UNIVERSITAT DE BARCELONA

Technological insights into a histopathological and protein composition analysis of aortic aneurysms in Marfan síndrome

Júlia López Guimet

UNIVERSITAT DE BARCELONA

Technological insights into a histopathological and protein composition analysis of aortic aneurysms in Marfan syndrome

Thesis submitted for the degree of Doctor of Philosophy

Júlia López Guimet

2018

Director: Dr. Gustavo Egea Guri

Programa de Doctorat Medicina i Recerca Translacional

Departament de Biomedicina,

Facultat de Medicina i Ciències de la Salut,

Universitat de Barcelona

This doctoral thesis was performed at Departament de Biomedicina in the Facultat de Medicina i Ciències de la Salut of Universitat de Barcelona under the supervision of Dr. Gustavo Egea Guri. This thesis was supported by Ayudas para contratos predoctorales (reference: BES-2013-065962) from the Ministerio de Economía y Competitividad.

Júlia López Guimet
(PhD candidate)

Dr. Gustavo Egea Guri
(director)

Barcelona, February of 2018

千里之行，始於足下

“Un llarg camí comença amb un sol pas”

“A journey of a thousand miles begins with a single step”

Lao-Tzu, Chinese philosopher (604 BC - 531 BC)

Dedicat als que m'estimen tant
que m'han aguantat durant tot aquest trajecte

ACKNOWLEDGEMENTS

Gustavo

Mama, Papa, Artur

Ferni

Tieta, tiet, Roger, Neus i nens

Hortencs, VéllèZahs

Yolanda

Jordi

Mike

Dasha

Thayna, Carla, Noelia, Bet, Javi

Annemie

miniCarla i Nacho

Fábio, Rafa

Lucía, Laia

HistoLab i annexes: Gerardo, Jordiet, Ana, Glòria, Sara, Cristina, Gemma, Helena, Núria, Unai, Verònica, Vane, Isaac, Ened, Raquel, Laura V., Georgina, Andrea

4ª planta: secres Carme, Núria i Mercè, Oriol, Mercè, Jordi A., Phil, Andrés, Paola, Sílvia, Esther, David

ICFO: Ómar o Omár, Mónica, Pablo, David, César, Susana, altre Jordi

Biofísica: Ignasi, MA, Juanjo, Brian, Daniel, Ramón

UoM: Alex, Catherine, Sarah, Matiss, Julen, Carina, Beth, Carmel, James, Vicky, Lucy

UPF: Patricia, Bart, Bruno, Chong

Laura O.&co, Sara, Sete, Folders, Jordi C., Dinorah, Parklife crowd, sciDF, més família

El Ministerio, UB, Boehringer, Diamond, Zeiss, ImageJ, MatLab, TMB, Duet, Picross, Wikipedia, Google, Vueling, Ryanair, Gmail, Instagram, Grammarly, TupperWare

GRÀCIES, GRACIAS, THANK YOU, OBRIGADA, ARIGATOU!

~ Namaste ~

CONTENTS

ABSTRACT

The aorta is the main artery of the body, whose function is to collect the blood ejected by the heart and distribute it to all tissues. The elastic degree of the aortic wall necessary to withstand blood pressure is mainly provided by the distribution of collagen fibres and elastic lamellae. Fibrilin-1 is an essential protein of the elastic lamellae, which is mutated in Marfan syndrome (MFS), a connective tissue disorder characterized by the formation of aortic aneurysms with a high risk of mortality. Multiphoton microscopy and the microCT, among other approaches, have been used to evaluate the structural characteristics of the aortic tissue, the but there is currently little information about the three-dimensional histopathological structure of the MFS aorta. Besides, the differences in the protein content with respect to the healthy aorta have been analysed by means of studies that used conventional cell culture, neglecting the effect of the mechanical forces that the vascular smooth muscle cells (VSMC) constantly perceive *in vivo* due to blood pressure.

In this context, we have developed four innovative technologies that have allowed us to generate new data on the histopathological structure and the protein content of the aorta MFS in comparison to healthy samples:

- A multiphoton microscopy and image processing methodology was applied to MFS mouse aortae to visualise and analyse the microscale morphology of the elastic lamellae. Bigger and more abundant fenestrae were observed in the aorta of MFS compared to those of the WT. With this results, fenestrae become potential markers of lamellar damage in MFS.

- A microCT and image processing protocol to evaluate the histological integrity of the aortic wall. This technology was applied to MFS and WT mice aortae, and an increase in the area and the thickness of the tunica media and other histological parameters was observed in relation to age progression (3, 6, and 9 months (mo)). This increase was parallel between WT and MFS, but the SMF 9mo showed values significantly higher than the WT 9m. Therefore, we hypothesise that the MFS aorta may undergo an accelerated middle-ageing process.

- A bioreactor of mechanical stretching to examine the protein content of VSMCs of healthy human aorta and MFS cultivated under *in vivo*-like mechanical conditions. The MFS cells showed an altered reaction to the administration of stretch, not related to the content or distribution of phenotypic markers. Therefore, the MFS VSMCs show altered cell-matrix communication not linked to the phenotype.

- Finally, by means of the systematic review of the scientific literature, the most complete human aortic tissue proteome to date was generated. It is divided into a healthy and an aneurysmal databases, containing 919 and 724 different proteins, respectively.

The application of these technologies has provided new knowledge in the field of vascular biology, especially with regard to Marfan syndrome.

RESUM

L'aorta és la principal artèria del cos, la funció de la qual és recollir la sang expulsada pel cor i distribuir-la cap a tots els teixits. El grau elàstic de la paret aòrtica necessari per a suportar la pressió sanguínia ve donat principalment per la distribució de fibres de col·lagen i lamel·les elàstiques. La fibrilina-1 és una proteïna essencial de les lamel·les elàstiques, la qual es troba mutada en la síndrome de Marfan (SMF), un trastorn del teixit connectiu caracteritzat per la formació d'aneurismes d'aorta amb alt risc de mortalitat. Per a avaluar les característiques estructurals del teixit aòrtic s'han utilitzat, entre d'altres, la microscòpia multifotó i el microCT, però avui encara hi ha poca informació sobre l'estructura histopatològica tridimensional de l'aorta SMF. D'altra banda, s'han analitzat les diferències en el contingut proteic respecte l'aorta sana mitjançant estudis que empraven cultiu cel·lular convencional, descuidant l'efecte de les forces mecàniques que les cèl·lules musculars llises vasculars (VSMC) perceben constantment *in vivo* a causa de la pressió arterial.

En aquest context, hem desenvolupat quatre tecnologies innovadores que han permès generar noves dades sobre l'estructura histopatològica i el contingut proteic de l'aorta SMF en comparació a mostres sanes:

- Una metodologia de microscòpia multifotó i de processament d'imatges es va aplicar a aortes de ratolins SMF per a visualitzar y analitzar la morfologia microscala de les lamel·les elàstiques. Es van observar fenestres més grans i abundants en l'aorta de SMF en comparació amb les del tipus WT; esdevenint les fenestres potencials marcadors del dany lamel·lar en la SMF.

- Un protocol de microCT i processament d'imatges per a avaluar la integritat histològica de la paret aòrtica. Aquesta tecnologia es va aplicar a aortes de ratolins SMF i WT, i es va observar un increment de l'àrea i el gruix de la túnica media i d'altres paràmetres histològics en relació amb la progressió en edat (3, 6 i 9 mesos (mo)). Aquest increment fou paral·lel entre WT i SMF, però el SMF 9mo mostrà valors significativament més alts que els WT 9mo. Per tant, plantegem la hipòtesi que l'aorta SMF deu patir un procés accelerat d'envelliment a edat adulta mitjana.

- Un biorreactor d'estirament mecànic per a examinar el contingut proteic de VSMCs d'aorta humana sana i SMF cultivades sota un ambient mecànic similar al real. Les cèl·lules SMF van mostrar una reacció alterada a l'administració de l'estirament, no relacionada amb el contingut ni distribució de marcadors fenotípics. Per tant, les VSMCs de SMF mostren una comunicació cèl·lula-matriu alterada no associada al fenotip.

- Finalment, mitjançant la revisió sistemàtica de la literatura científica es va generar el proteoma de teixit aòrtic humà més complet de l'actualitat, dividit entre les bases de dades sana i aneurismàtica, que contenen 919 i 724 proteïnes diferents, respectivament.

L'aplicació d'aquestes tecnologies ha proporcionat nous coneixements al camp de la biologia vascular, especialment pel que fa a la síndrome de Marfan.

ABBREVIATIONS

ADAM	A disintegrin and metalloproteinase
ADAMTS	A disintegrin and metalloproteinase with thrombospondin motif
AEBP1	Adipocyte enhancer-binding protein 1
BAV	Bicuspid aortic valve
BMP	Bone morphogenetic protein
BSA	Bovine serum albumin
CT	Computed tomography
D	Dynamic (bioreactor chip condition)
DOI	Digital object identifier
E	Static (bioreactor chip condition)
ECM	Extracellular matrix
EGF	Epidermal growth factor
EMILIN	Elastin microfibril interface located protein
FBN1	Human fibrillin-1 gene
Fbn1	Murine fibrillin-1 gene
FGF	Fibroblast growth factor
FN	Fibronectin coating
GAG	Glycosaminoglycans
GUI	Graphical user interface
IEL	Internal elastic lamina
LOX	Lysyl oxidase
LOXL	LOX-like
LTBP	Latent TGF-β binding proteins
MAGP	Microfibril-associated glycoprotein
MF	Marfan syndrome (mice or cell culture condition)
MFS	Marfan syndrome (human disease)
microCT	X-ray computed micro-tomography
MMP	Metalloproteinases
mo	months old
MRI	Magnetic resonance imaging

PBS	Phosphate-buffered saline
PCR	Polymerase chain reaction
PDL	Poly-D-lysine
PDMS	Polydimethylsiloxane
PFA	Paraformaldehyde
RNA	Ribonucleic acid
ROI	Region of interest
SD	Standard deviation
SEM	Scanning electron microscopy
SHG	Second harmonic generation
SLRP	Small-leucine-rich repeat proteoglycans
SM22α	Transgelin
SMA	Aortic smooth muscle actin
SOD	Superoxide dismutase
TBS	Tris-buffered saline
TBS-T	TBS-Tween buffer
TEM	Transmission electron microscopy
TGF	Transforming growth factor
TGM2	Protein-glutamine gamma-glutamyltransferase 2
TIMP	Tissue inhibitor of MMPs
TPEF	Two-photon excitation fluorescence
UV	Ultraviolet light
VSMCs	Vascular smooth muscle cells
WT	Wild-type (murine condition)
2D	Two-dimensional, two dimensions
3D	Three-dimensional, three dimensions

INTRODUCTION

1. The nature of the Aorta

The primary role of the cardiovascular system is to distribute essential substances to tissues and remove metabolic byproducts from them[1]. The heart is the pump of this system, and the vasculature is the closed network of tubes that propels blood from the heart to the tissues and back. In mammals, the aorta is the main and largest artery of the body, measuring 1.2 m in length and ~26 mm in diameter in a healthy adult human[2,3]. This vessel directly collects the blood ejected by the heart, and branches out into arteries of gradually diminishing diameter up to billions of capillaries that ultimately regroup into a single vena cava that discharges de blood back to the heart[4,5].

1.1. Anatomy of the aorta

The shape of the aorta is that of a candy cane, where the initial end emerges from the left ventricle of the heart, and the opposite end culminates by bifurcation at the lumbar region of the body[6,7]. Taking into account this shape, the aorta is divided into ascending, arch, and descending segments (figure 1A). The aortic descending part runs along the spine nourishing the thoracic organs, passes through the diaphragm, branches to supply the abdominal organs, and finally, it splits up into the two iliac arteries that irrigate the lower limbs[6–8]. Moreover, the vessels that supply blood to the animal's head and the upper limbs (brachiocephalic, left common carotid, and left subclavian arteries) arise from the aortic arch (figure 1B). In summary, the aorta passes through the chest and abdomen, allowing all organs and tissues to be perfused with oxygenated blood from the heart.

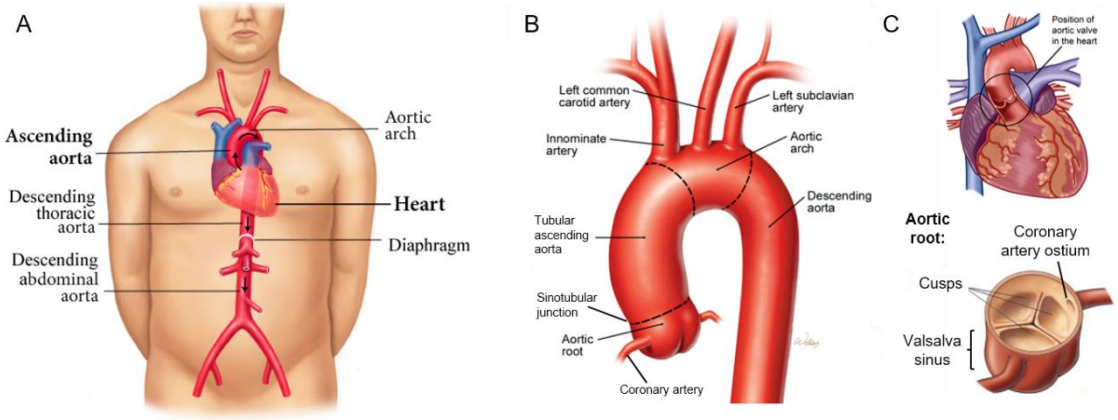

Figure 1. Anatomy of the aorta. A. Anatomical localisation of the whole aorta and its portions. B. Parts of the aorta confined within the thorax: ascending, arch, and thoracic descending. C. Aortic root localisation, disposition, and components.

The ascending aorta is constituted by the aortic root at the proximal end and the ascending tubular aorta that is a vertical tube that joins the aortic arch, the border between both ascending aorta parts is called the sinotubular junction (figure 1B)[7]. The aortic root is a physiologically dilated vessel space that is placed inside the heart and hosts the aortic semilunar valve, which regulates blood entrance to the aorta (figure 1C). This structure is a tricuspid valve, constituted by three cusps or leaflets, that opens passively due to blood ejection in systole and closes passively in diastole, impeding retrograde blood flux to heart[4,8]. The vessel tube of the root is constituted by three round dilatations in the shape of sacks, named Valsalva sinuses, that allow the valve leaflets to open up to 90º [2]. In addition, the origins (ostia) of the coronary arteries that irrigate the cardiac tissue arise from these sinuses (figure 1C).

1.2. Histology of the aorta

The aorta is classified as an elastic artery since its wall is structured to serve as conduct that pushes the blood forward. Accordingly, its wall is divided into three layers: tunicae intima, media and adventitia[9] (figure 2). The innermost layer named the tunica intima is composed of a continuous monolayer of endothelial cells and a thin subendothelial bed of loose connective tissue that together cover the luminal surface of the vessel[10]. The tunica media, the middle and thickest layer, is composed of a series of elastic lamellae alternating with circumferentially oriented layers of smooth muscle cells (VSMCs) (see below for further detail). The tunica adventitia, the outermost layer, is composed of loose fibroelastic connective tissue enriched in collagen fibres arranged longitudinally, fibroblasts, some elastic fibres, macrophages, small nerves and vasa vasorum[11]. Oxygen and nutrients are supplied to the aortic wall by simple diffusion from the lumen on one side, and, in the case of thick aortic walls (human, but not mice), on the outer side they are supplied by the *vasa vasorum* capillary network, which extends from the adventitia to the last layers of the tunica media[7,9]. The internal elastic lamina (IEL), which is the first lamella, separates tunicae intima and media, and the external elastic lamina often lines the boundary between tunicae media and adventitia[5].

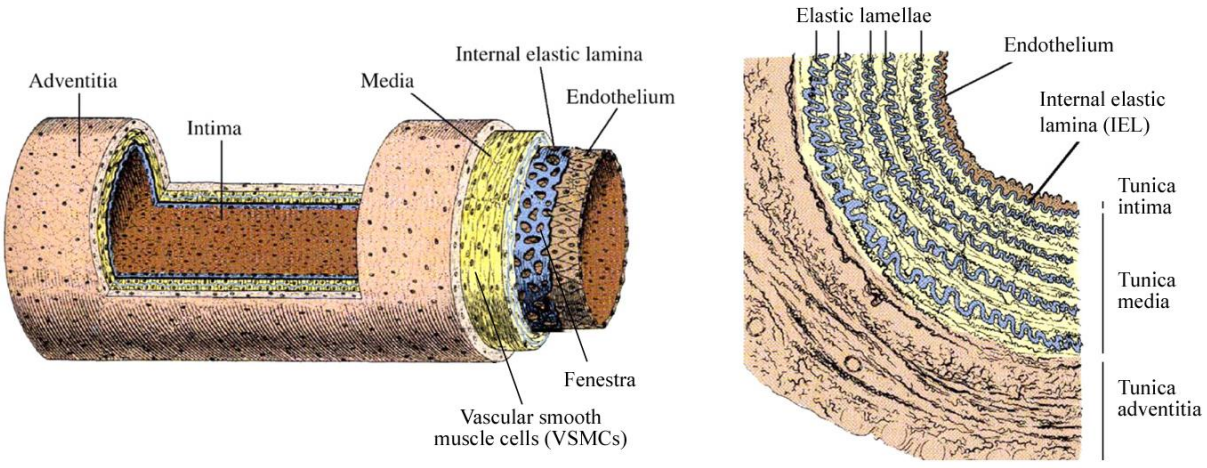

Figure 2. Histological elements in the aortic wall: tunicae intima, media, and adventitia, and intrinsic components. Adapted from ref.[12].

The tunica media has a complex, highly interrelated matrix structure that occupies most of the aortic wall's thickness. Within it, elastic lamellae or laminae are elastic fibres arranged as fenestrated sheets that organise as multiple concentric cylinders (figure 2). Additionally, lamellae are woven into a three-dimensional (3D) interconnecting network with thin elastic fibres connecting lamellae one to another and with the VSMCs[9]. The interlamellar space (i.e. between lamellae) is filled by VSMCs that are surrounded by extracellular matrix[A] (ECM) components such as collagen fibres, proteoglycans, signalling factors, and fibronectin[13,14].

1.3. Aortic biomechanics

Environmental cues in tissues can be classified into biochemical (pH, oxygenation, growth factors, cytokines, chemokines, hormones and lipoproteins) and biomechanical. Regarding the latter, the aortic wall is continuously subjected to three types of physiological mechanical stresses[B]: shear stresses originated from the blood flow rubbing the vessel lumen surface, circumferential stresses from the pulsatile blood pressure, and longitudinal stresses from surrounding tissue (mainly due to motion of the heart)[9]. To optimally bear aortic mechanical stresses, VSMCs orient in the circumferential direction, in contrast to the endothelial cells, which are oriented parallel to the blood flow direction in the vessel (figure 2, left panel)[8,11].

In the aorta, shear and longitudinal stresses are much smaller than the circumferential one[15]. In systole, the generated pressure by ventricle contraction pushes the blood through the aortic valve and onward the arterial tree (figure 3A). The aorta lumen expands to accommodate the whole volume of this ejected blood, and stores a fraction of the volume in the expanded part[4] (approximately the 50% of the ventricular stroke[16]). Then, during diastole, the vessel recoils progressively back to the initial diameter, propelling the stored blood volume forward even though no force is being exerted by the heart[5,11]. The specific structural arrangement and composition of the aorta wall allow this elastic response to the intermittent blood pumping by the heart, which serves to withstand the circumferential stress caused by the hemodynamic pressure (figure 3B)[7]. Additionally, the distension of the aorta with every heartbeat dampens the pulsatile nature of blood flow, turning the intermittent cardiac output into a nearly continuous flow downstream[1,5]. This phenomenon is the so-called Windkessel effect of the large arteries

[A] The extracellular matrix (ECM) is the three-dimensional, non-cellular structure that serves as framework for all tissues.

[B] Stress is the force applied to an object divided by the area over which that force is applied. Strain is the quantitative measure of the deformation of an object induced by a given force.

and is made possible by means of a specialised ECM uniquely designed to provide regulated elastic recoil[4,9,17].

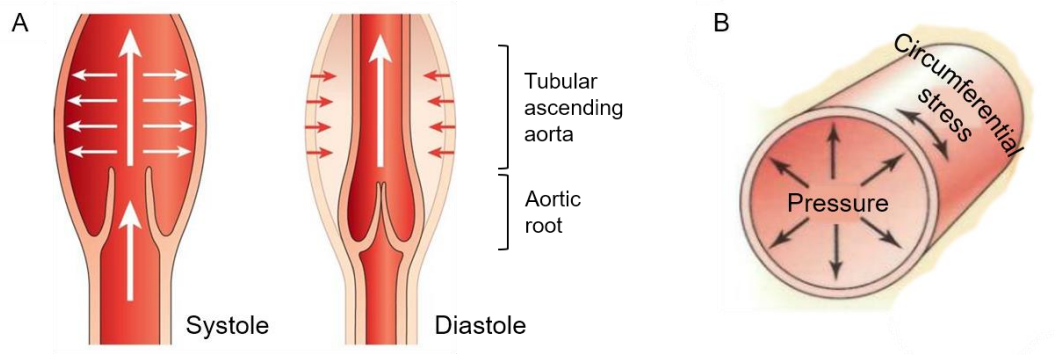

Figure 3. Circumferential stress occurring at the ascending aorta. A. Systolic blood ejected by the heart opens the aortic root cusps and flows through the ascending aorta. The blood volume pushes the vessel wall outwards, augmenting the volumetric capacity. In diastole, the walls recoil back to the initial size, pushing more blood forward. B. Schematic displaying the direction of the forces involved in the circumferential stress in the aortic wall. Adapted from ref. [4].

The tunica intima is particularly important in atherosclerosis and restenosis but participates little in the mechanical properties of the normal conducting vessel. Moreover, VSMCs do not contribute appreciably to the elastic behaviour of the aortic wall, as opposed to their crucial contraction role in smaller vessels[4,9]. Notably, the components of the arterial wall that account for the majority of the aorta mechanical properties are the collagen and elastin deposited by smooth muscle cells in the tunica media[9]. The large amount of elastin present in the tunica media makes the vessel highly distensible (i.e. compliant, elastic) so that it can effectively stretch to fit all the volume of ejected blood and gradually de-stretch afterwards[1]. Elastic lamellae are essentially a highly elastic network of fibres, capable of stretching more than 100% under physiological conditions and passively return to their original length when the tension is released[4,5]. Conversely, collagen fibres are far less extensible than lamellae, as they can be stretched only 3% to 4% under physiological conditions. Thus, the substantial distensibility or compliance of the aortic wall under normal conditions results mainly from the reversible extension of the elastic lamellae in the media[7]. Yet, the adventitial collagen fibres ultimately govern the tensile strength of the aortic wall to limit the extent of stretching and thereby prevent rupture of the tissue[2,11,18]. To provide this distention limit, collagen fibres are usually attached to the other components of the aortic wall with some slack, so that they are normally not under tension. The stretching of these other components takes up the slack, which then tautens the collagen fibres, and finally, they restrict greater distention of the tissue[4]. In addition, the elastin-to-collagen ratio is 70:30 at proximal aorta, allowing the maximum shock-absorbing effect of the cardiac output. With age, elastin content decreases whereas collagen increases, thus augmenting vascular stiffness in ageing[15].

As previously explained, the circumferential stresses occur when the blood pressure pulls apart the walls in the radial direction from the centre of the lumen, and thus stretch

the aortic wall (figure 3B). In particular, the mechanical pressure acts perpendicular to the direction of blood flow at 66 beats per minute in humans, which corresponds to a frequency of 1.1 Hz[19]. This generates circumferential stress in the wall, which in turn induces a ~13% strain in diameter (averaged value of data from refs. [19–21]). Then, the wall recoils back to its original size. This process is repeated cyclically for every heartbeat.

2. Aortic pathology: Aneurysm

As previously mentioned, aortic wall components are strictly structured to provide the elasticity needed for propelling the blood downstream[22,23]. Therefore, it is of fundamental importance to preserve its integrity in order to maintain effective vessel function[24,25]. In some vascular disease conditions, the aortic structure is severely altered, which compromises its vital role in blood conduction. Aortic diseases range from atherosclerotic stenosis to ulcer, calcification, thromboembolic disease, aneurysm, pseudoaneurysm, intramural haematoma, aortic tumours, and dissection. Similar to other arterial illnesses, aortic diseases may be diagnosed after a long period of asymptomatic development, or they may have an acute presentation[26].

2.1. Epidemiology of aortic aneurysms

Aneurysm is the second most frequent disease of the aorta after atherosclerosis[26]. This condition is the irreversible pathological dilatation of the aortic diameter with loss of wall parallelism[26,27] (figure 4A-B). Aortic aneurysms are currently a major health concern in the Western countries due to its high incidence and fatal outcome owing to dissection and rupture (figure 4C). They are the 20th cause of death in all ages in the United States of America (USA) in 2015, with more men affected than women[26], causing more deaths than human immunodeficiency virus (VIH)[28,29]. Although abdominal aorta aneurysms are more common, approximately 10.4 per 100,000 people in the USA develop thoracic aorta aneurysms each year[28]. However, the real number is likely to be higher since many cases often stay undiagnosed. To avoid undiagnosing life-threatening aneurysms, screening programs are progressively being implemented in the European primary care system[26].

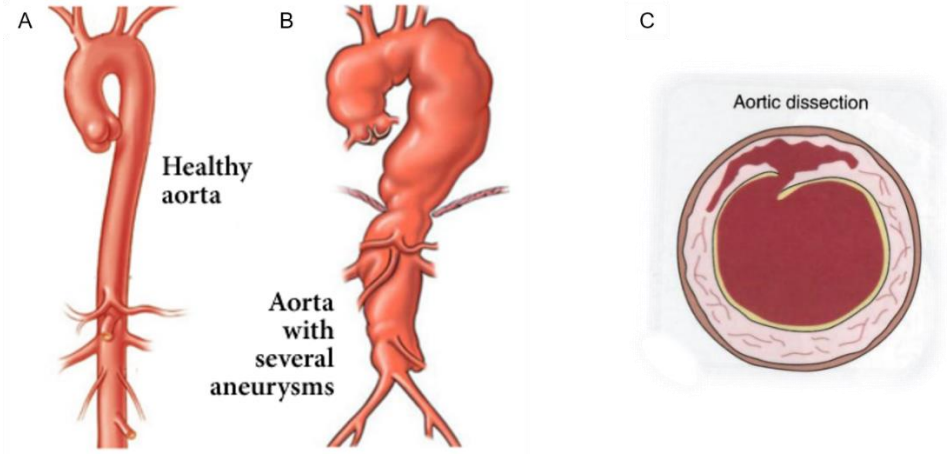

Figure 4. Aortic aneurysm and dissection schematics. A. Shape of a healthy human aorta. B. Shape of an aorta with aneurysms throughout all its length. C. Aortic wall dissection. Dark red marks luminal blood penetrating in between aortic wall layers.

2.2. Aetiology of aortic aneurysms

Aortic wall degeneration due to atherosclerosis is the most common cause of aortic aneurysms, especially of the abdominal portion[30,31]. Thus, age, male gender, cigarette smoking, atherosclerotic cardiovascular disease, and hypertension are risk factors associated with the presence of aneurysms[26,30]. Other causes of aortic aneurysm are genetic connective tissue disorders (Marfan, Loeys-Dietz, and vascular Ehlers-Danlos syndromes), congenital anomalies of the aortic valve (for instance, bicuspid aortic valve), familial genetic variants (coding for altered aortic smooth muscle actin (SMA), myosin-11, fibrillin-1, SMAD3, TGF-β (transforming growth factor-beta), and TGF-β receptor type-2 proteins, among others), inflammatory diseases (syphilitic, Takayasu and giant cell aortitis), and trauma[2,7,30,31]. Genetically triggered aneurysms behave differently from atherosclerotic aneurysms[7]. Many patients with connective tissue disorders also present bicuspid aortic valve, which increments the risk of aortic rupture and death. Furthermore, patients with an aortic aneurysm are at increased risk of cardiovascular events, mostly unrelated to the aneurysm, but plausibly related to inflammation and risk factors such as smoking or hypertension[26].

2.3. Prognosis of aortic aneurysms

An aneurysm is a clinically silent, but lethal, disease that is often asymptomatic before an acute event occurs: dissection or rupture of the aortic wall[26,28]. Dissection is the separation of aortic wall layers by intramural bleeding (figure 4C), often with subsequent formation of a false lumen[32]. Furthermore, an aortic rupture affects the whole thickness of the vessel wall, leading to haemorrhage towards surrounding tissues and fatal exsanguination[7,10]. Only 30-59% of patients with sudden aneurysm rupture reach the hospital alive, and an additional 27-40% die in the hospital[7,28]. The chance of aortic dissection occurrence is related to the aortic diameter[31], being more probable as the aneurysm grows[24,28,33]. In the ascending aorta, >60 mm is the diameter “hinge point” where there is a dramatic increase in the risk of acute complications[26,28]. To prevent premature death caused by aneurysm rupture, early clinical diagnosis and subsequent surveillance and treatment are essential.

2.4. Diagnosis of aortic aneurysms

The natural history of aneurysms is the gradual expansion of the aorta over a period of years and eventual rupture[7]. The long period of subclinical growth in the diameter is asymptomatic, thus aortic aneurysm detection is often an incidental finding on abdominal or chest radiography performed for other medical purposes[26]. Once identified, ultrasound echography (e.g. echocardiography) is the principal imaging method for aortic aneurysm monitoring in clinical practice (figure 5A-B), because of its ability to measure the aortic size and detect wall lesions, and because of its wide availability, painlessness, no risk,

and low cost[26,30]. Given that ultrasound-derived measurements of vessel diameter are not accurate at all, many experts recommend the use of ultrasound for follow-up of small aneurysms and the use of computed tomography (CT) or magnetic resonance imaging (MRI) for larger aneurysms and surgery planning[7,30]. These relatively non-invasive imaging modalities permit visualising the entire aorta in 3D to identify the affected parts adequately (figure 5C-E)[26,31]. Compared to MRI, CT requires a shorter time for image acquisition and processing, and it is a widely available technique[26]. Conversely, although contraindicated in patients with metal implants, MRI does not require dangerous ionising radiation as CT, thus it is highly suitable for serial follow-up studies in patients with known aortic disease. MRI also allows to visualise and measure blood flow, thus pulse wave velocities and wall shear stress can be determined[26].

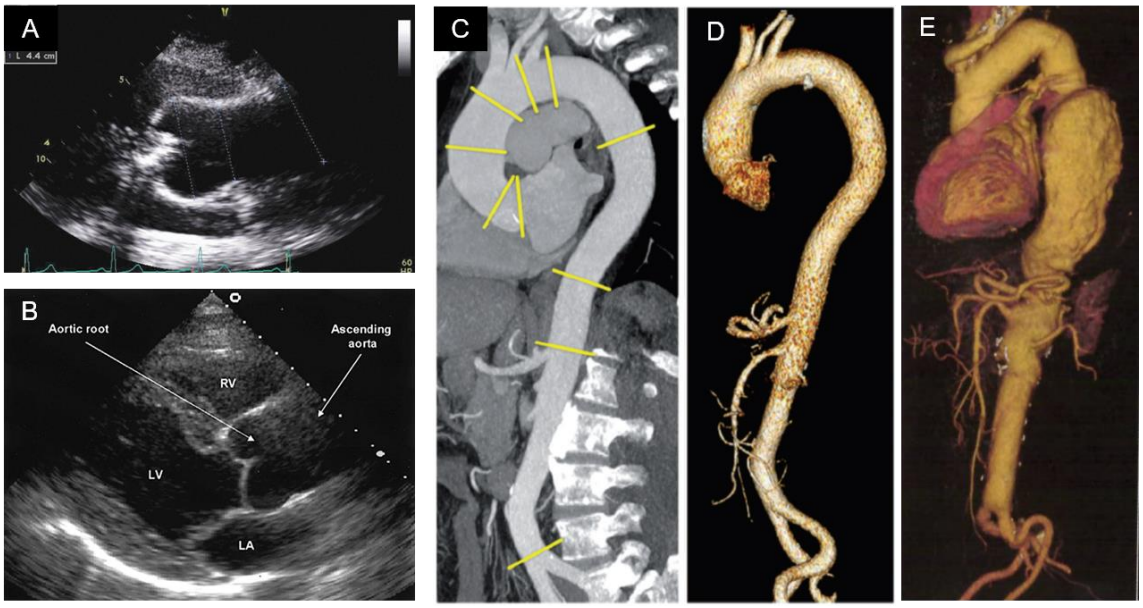

Figure 5. Diagnosis imaging of aortic aneurysms. A. Echocardiography of a healthy ascending aorta. B. Echocardiography of ascending aorta aneurysm. Note that the sinotubular junction, the border between the aortic root and the tubular ascending aorta, is no longer present. C. Slice of thorax CT, displaying the aorta, vertebrae, and other tissues[26]. D. 3D reconstruction of the aorta at the CT acquisition. E. 3D reconstruction of an aorta with a descending thoracic aneurysm. The heart is included in this reconstruction[2].

2.5. Treatment of aortic aneurysms

After detection of an aneurysm, yearly follow-up of the aortic diameter should be performed, since the greatest vascular diameter is the decisive element in establishing the aneurysm growth[30,31]. The aneurysmal thoracic aorta grows increasing by about 1 mm each year, yet growth in patients with familial thoracic aneurysms is accelerated at 2.1 mm/year rate[28]. Today, there is no effective treatment to slow down aneurysm growth. Thus, because of the tight relation of aneurysm and atherosclerosis, minimising cardiovascular risk factors is recommended. Hence, aortic aneurysm patients should give up smoking, perform moderate physical activity, avoid competitive sports, and control their blood pressure to reduce aortic wall stress[7,26,30]. The preferred

pharmacological approach to reduce blood pressure in the aneurysmal aorta is the administration of β-blocker drugs, like propranolol or atenolol[30,31]. However, although successful in animal models of abdominal aneurysms, two large clinical trials demonstrated no benefit of propranolol treatment in patients with small abdominal aneurysms[7]. In addition, statin use can be recommended for almost all patients with abdominal aneurysms based on the presence of coexisting atherosclerotic disease[7]. Moreover, other drugs, such as aspirin or renin-angiotensin inhibitors (like losartan), are nowadays administered in various centres for aneurysmal patients. Importantly, current pharmacological therapies for aneurysm often only benefit a small subset of aneurysm patients, possibly as a consequence of heterogeneity of the underlying disease pathology[34].

To prevent final rupture or dissection of the aorta, timely surgical operation on a patient with a known dilatation of the aorta is advised[30,31]. The rationale for elective surgical treatment of aneurysms is that it is a safer procedure than an emergency surgical intervention[28]. Indications for surgery are based mainly on aortic diameter and growth rate pondered by the underlying cause of the aneurysm (kind of disease or anomaly), and the balance between the risk of rupture against the surgical risk[26]. In general terms, surgical intervention of the aorta should be performed when the ascending aortic diameter reaches 55 mm and, in the setting of bicuspid aortic valve, Marfan syndrome, or familial thoracic aneurysm, when it reaches 50 mm[7]. Surgical treatment of aneurysms can be performed by open surgical repair or by endovascular aneurysm repair (EVAR), with most patients undergoing EVAR as it is a less invasive intervention[7]. Endovascular therapy is the implantation of a stent-graft inside the aneurysmal vessel to conduct blood through it, and thus avoiding blood pressure on the real aortic wall. Conversely, open surgical repair replaces the aneurysmal region by a prosthetic vessel graft that is sewn to the remaining aortic wall[2].

Nonetheless, aortic diameter alone is not sufficient to explain aortic dissection, and there is a need for additional risk markers[31]. Although the size of the aneurysm is the most important factor in predicting rupture, wall thickness, intraluminal thrombus thickness, and peak wall stress may also contribute to predicting risk for rupture[7]. For this reason, many research is and has been performed on understanding this pathology to finally develop earlier or more accurate diagnosis approaches.

2.6. Marfan syndrome

One of the genetic disorders leading to an aortic aneurysm is Marfan syndrome (MFS)[35]. MFS is the most frequent heritable connective tissue disorder[26], impacting on 1.5-17.2 out of 100,000 inhabitants in the general population[36], yet many affected individuals remain undiagnosed[30]. Symptomatology varies depending on the syndrome's severity, but it mainly affects the skeletal, ocular, and cardiovascular systems[37]. More specifically, patients may present a strong susceptibility to ascending aorta aneurysm, long-bone

overgrowth, scoliosis, eye lens dislocation, and dural ectasia (figure 6). The leading cause of premature death in MFS patients is acute aortic rupture, which is preceded by a long period of progressive dilatation of the sinuses of Valsalva at the ascending aorta[26,27,30,38]. The European Society of Cardiology recommends elective surgery in MFS patients who have a maximal aortic diameter ≥50 mm [26]. In contrast to the former life expectancy of MFS patients of 32 years, nowadays the application of an aortic prosthetic replacement allows patients to reach age expectancy up to 60 years[30].

MFS is caused by mutations in the fibrillin-1 gene (*FBN1*), inherited in an autosomal dominant manner, although about 30% of MFS cases are sporadic due to *de novo* mutations[38]. There are more than 3,000 reported different mutations throughout the *FBN1* gene leading to this disorder, but the most common are punctual missense[C] mutations usually at a calcium-binding epidermal growth factor (EGF)-like domain of the protein[35,39–41]. Moreover, *FBN1* mutations cause an alteration in the secondary structure of the protein, delayed secretion, or enhanced degradation susceptibility of fibrillin-1 [40]. The type and localisation of the mutation determine, in some cases, the seriousness and variety of symptoms, but the clinical utility of this correlation is nowadays low[38]. In addition, not all mutations in *FBN1* lead to MFS, some of them have been associated to other disorders such as Weill-Marchesani syndrome, a connective tissue disease that, contrary to MFS, is characterised by short stature and unusually short fingers and toes[38].

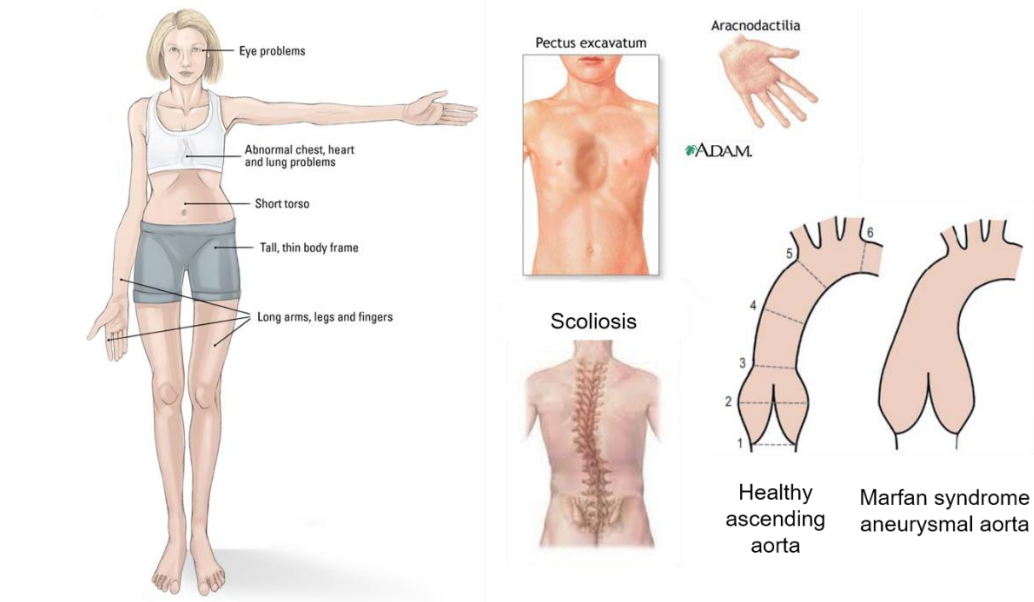

Figure 6. MFS patient characteristic features: long bone overgrowth (tall stature, long arms, legs and fingers (arachnodactyly)), indented breastbone (Pectus excavatum), spine deformities (scoliosis), and ascending aorta dilatation.

[C] Missense mutation occurs when a single nucleotide changes resulting in a codon change and a different amino-acid in the final protein.

2.7. Animal models for Marfan syndrome research

In order to study disease progression in depth, researchers have developed multiple animal models that recapitulate the clinical spectrum of human diseases. Generation of mouse models of MFS has proven to be an effective substitute to dissect the complexity of MFS pathogenesis[42]. A validated mouse model of MFS is the *Fbn1*$^{mgR/mgR}$, which expresses a reduced amount of normal fibrillin-1 [43]. These mice exhibit a more severe MFS symptomatology with lethal aneurysm dissection at age 2-3 months old[42]. Furthermore, one of the most representative models is the *Fbn1*$^{C1039G/+}$ murine model, in which a cysteine is substituted with a glycine at amino acid 1039 in an EGF domain of the protein[44], mimicking the most frequent type of mutation in human MFS patients. *Fbn1*$^{C1039G/+}$ mice express an equal amount of normal and mutant fibrillin-1, and compile the skeletal and aortic human pathological manifestations[42]. However, despite their aortic affectation, their life expectancy is standard and do not die of aortic dissection.

3. Structure and protein composition analysis techniques

The knowledge we currently have on the aortic structure and protein composition has been discovered by application of molecular biology and microscopy techniques.

Protein presence in tissue or in *in vitro* cultured cells is mainly achieved by using bulk whole protein composition approaches or by immune-based techniques specific for individual proteins. On the one hand, western blot and immunochemistry are the most common immune-based techniques for particular protein detection by antibodies in biological samples. On the other hand, two-dimensional gel electrophoresis plus subsequent mass spectrometry is the usual approach employed for assessment of bulk protein composition of a sample, since it rapidly and reliably identifies what proteins are present in the sample[45,46]. By applying these techniques, many information has been historically unravelled regarding the protein content of biological systems. The neXtProt database (https://www.nextprot.org/) gathers all the currently known expression patterns of proteins in a broad range of human, healthy and diseased, cells and tissues. This database annotates protein presence information obtained by immunochemistry (from the Human Protein Atlas database, www.proteinatlas.org), by mRNA expression (from Bgee database, https://bgee.org/), and by classical proteomics methods (from UniProt, www.uniprot.org). To date, the complete set of expressed proteins in the human body, i.e. the human proteome, contains 20,199 different proteins.

Furthermore, analysis methods employing microscopy have gradually unravelled information about composition and structure in biological samples. These methods allow in some cases the visualisation of the whole tissue or cell, and in other cases, enable the observation of specific elements or molecules wherever they are localised within the sample. There are many different microscopy techniques, relying on distinct optical phenomena, each one with its pros and cons. Besides, several steps must be done in advance to prepare the sample for optimal microscopy visualisation. Additionally, many microscopy techniques require subsequent computational processing of the acquired images to finally provide quantitative data relevant to researchers.

Here, microscopy will be the only technique to be extensively explained since this approach is directly related to the technology development performed in this thesis.

3.1. Basic concepts in optical physics

Microscopes are optical instruments that allow one to see small objects that are below the resolution limit of the human eye[47]. This limit is the ability to perceive two nearby

objects as two separate objects[48]. In fact, the human's eye is able to distinguish two objects that are at a distance of up to 0.1 mm (i.e. 100 µm), hence, 0.1 mm is our resolution limit. The size of most eukaryotic cells varies around 10 to 30 µm, whereas prokaryotic cells may be smaller. Thanks to the combination of different lenses, conventional optical microscopes provide a resolution limit up to 1 µm and electronic microscopes up to a 1 nm [47,49]. Thus, microscopes are fundamental elements for the study of the morphology of cells and tissues.

The range of colours that we perceive represents a very small portion of the electromagnetic spectrum (figure 7). Unlike humans, imaging machines cover almost the entire electromagnetic spectrum and also other important sources of energy, like acoustic, ultrasonic, and electronic (i.e. electron beams)[50]. Photons are the amounts of energy contained within electromagnetic waves. According to the energy per photon or the wavelength, the electromagnetic spectrum is grouped into (from highest energy to lowest, or from shortest wavelength to longest): gamma rays, X-rays, ultraviolet, visible light, infrared, microwaves and radio waves. Within the electromagnetic spectrum, the light spectrum ranges from ultraviolet to infrared, and the wavelength of the light determines its colour[48]. Thus, the wavelengths of light in the visible light spectrum range from 380 nm for violet light to 750 nm for red light, the infrared is longer than 750 nm, and the ultraviolet is shorter than 380 nm. White light is a combination of lights of different wavelengths in the visible spectrum (i.e. the normal light). It is important to note that the wavelength of an electromagnetic wave required to "see" an object must be of the same size as or smaller than the object[50].

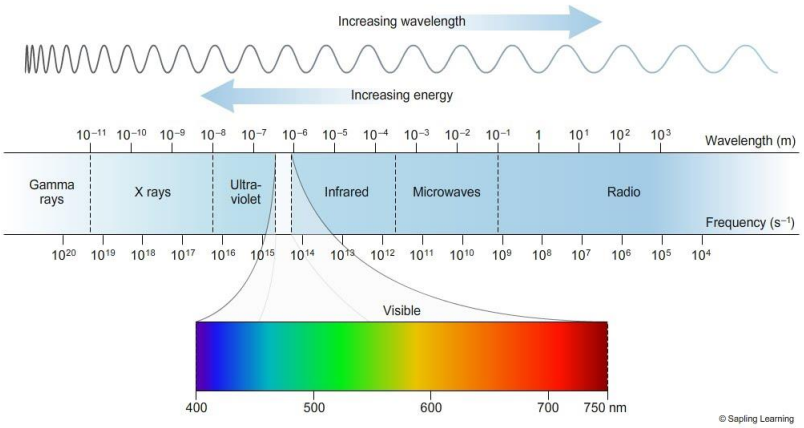

Figure 7. Electromagnetic spectrum. The visible light ranges from 380 to 750 nm (lower panel). X-rays are more energetic and have shorter wavelength than the visible light.

The different kinds of electromagnetic waves have very different effects upon biological objects. In this context, microscopes create a magnified, detailed image of seemingly invisible objects, based on the principles of light-tissue interaction[48]. When the light beam reaches a biological tissue, part of it penetrates the sample and part is reflected at the air-tissue interface[51]. Once inside, the penetrating light propagates while parts of it are absorbed, as well as scattered, and the rest is further transmitted across the whole

thickness of the sample without interaction. The process of light absorption is the transformation of light energy to some other form of energy (heat, sound, fluorescence) by specific tissue components such as melanin or haemoglobin. Scattering is the physical process where light is forced to deviate from a straight trajectory due to localised non-uniformities in the medium through which it passes. Light propagation within a tissue depends on the light's wavelength and on the scattering and absorption properties of tissue components, such as size, shape, density, and their refractive index (which defines the angle of deviation of the light beam due to reflection or scattering). Hence, light absorption and scattering determine how far light can penetrate into a specific tissue. Importantly, most of the microscopy images are generated by the incident light reflection or absorption produced by the sample being imaged[50].

3.2. Sample preparation for microscopy

Processing of biological samples is necessary to make them adequate for proper subsequent microscopy analysis while maintaining their *in vivo* native structure. The common steps in tissue or cell processing are: conservation by fixation, embedding within a solid scaffold block, sectioning or cutting thin laminas of the block, and highlighting the desired sample structures by staining or addition of marked antibodies (figure 8). Each of these steps holds variations depending on the type of biological sample, the structures to be observed, or the kind of microscope to be used. Moreover, each step induces modifications in the original specimen, which can lead to not-naturally-present artefacts.

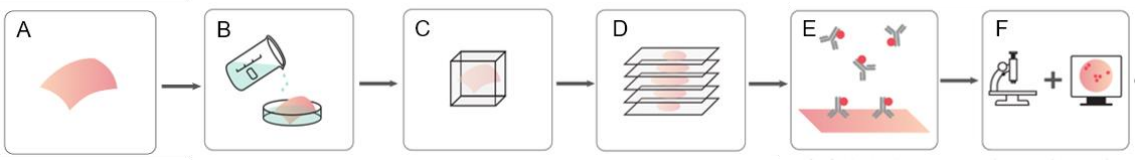

Figure 8. Sample preparation steps for microscopy analysis: sample extraction from animal (A), fixation (B), embedding (C), sectioning (D), staining or addition of a marked antibody (E), and visualisation using the microscope (F).

Since biological samples are extracted from their native place, fixation is required to stop the natural degradation occurring *post-mortem* (figure 8B)[52]. Fixation kills the cells and preserves the morphology of tissue and cellular components as similar to *in vivo* as possible. However, there is no universally ideal fixative, since each can be adequate for specific structures or microscopy techniques[47]. Particularly, the process of fixation can be done physically or chemically, but the latter is the most efficient and utilised approach. Biological samples can be fixed by freezing or heating, or by immersing them in chemical reagents like formol (formaldehyde), glutaraldehyde, paraformaldehyde (PFA), ethanol, methanol, potassium dichromate, osmium tetroxide, picric acid, and acetic acid. To reduce the time between sample obtaining and chemical fixation, in animal research, the

fixative reagent can be perfused. This method consists in introducing the fixative into the circulatory system of the animal before sacrifice, so that all tissues are “naturally” irrigated with the reagent and are uniformly fixed.

Microscopic assessment of tissues essentially requires translucent samples that permit the light beam to pass across them. Hence, it is necessary to obtain thin sections of the biological specimen to be examined. However, biological samples are not stiff enough for successfully cutting them into sufficiently thin laminas at uniform thickness[47]. Therefore, first, samples should be embedded within a solid and stable material that provides consistency for posterior sectioning (figure 8C)[52]. The most widely used material for biological sample embedding is paraffin wax (the constituting element of traditional candles) due to its low cost and ease of use. Paraffin includes the sample and also it infiltrates within the tissue by means of a serial process of dehydration, in which the tissue’s internal water is substituted by alcohol and then by paraffin[52]. Dehydrated samples are immersed in molten paraffin contained in a cubic mould. Then, all the set-up is placed in a cold place to solidify the paraffin and finally obtain a solid, cubic paraffin block that includes the biological sample within.

Once biological samples are fixed and embedded, the next step is to physically cut them into thin, uniform sections employing a microtome (figure 8D). This precision instrument performs a series of interrupted sections at a specific thickness (3 to 10 μm) to the paraffin block[47]. Besides, for thicker sections and/or in the case of soft samples (fresh or not paraffin embedded), a distinct microtome is used, the vibratome. Afterwards sectioning, the sample sections are placed on a microscopy glass slide.

Before observing the samples under the microscope, differential contrast between the diverse elements within the colourless tissue or cell has to be achieved. Selective staining of certain structures within the sample section increases the contrast and eases the microscopic study (figure 8E). Haematoxylin-eosin is among the most typically used stainings as it is a universal colourant for tissue that dyes cell nuclei in dark colour and dyes pink the cytoplasm and extracellular structures in various degrees of colouration[48]. Additionally, collagen in histological sections dyes blue with Mallory’s trichrome stain, green with Masson’s trichrome, and pink with eosin. There are dozens of different staining procedures specific for particular tissues.

To detect specific molecules instead of structures within the sample section, cyto- or histochemistry techniques are applied during the staining step (cyto- for cells, histo- for tissues)[47]. Taking advantage of the chemical properties of the molecules, these techniques can specifically detect sugars, nucleic acids (ex. DAPI for double-stranded DNA), lipids, proteins (ex. phalloidin for filamentous actin) or subgroups within the mentioned molecule types. Moreover, the immunohistochemistry or immunocytochemistry techniques perform the detection of a certain protein via its

recognition by a highly specific antibody[D] against this molecule (figure 9). The antibody is artificially marked with a fluorescent molecule, a peroxidase or phosphatase enzyme, or a colloidal gold particle to allow microscopy visualisation of the antibody-molecule binding complex[53]. Additionally, to increase the sensitivity of the technique, detection and marking are performed by two different antibodies: the primary and the secondary, respectively. The primary antibody specifically detects the interest molecule, and then, the secondary antibody linked to a marker recognises specifically the primary one (figure 9A-B)[48]. When performing the detection of more than one molecule in the same sample section, special care should be taken to avoid cross-reactivity: the primary antibody for detection of molecule A was obtained from host animal species Z, so secondary antibody for marking of A should recognize only Z antibodies; in turn, to detect molecule B, primary antibody was obtained from species Y and secondary antibody recognizes Y; if both primary antibodies were generated in Z animal species, secondary antibody would be marking both molecules A and B, without any chance for us to distinguish either; hence, when doing multiple detections, different primary antibodies should be originated in different host animal species. In summary, in the case that procedures are properly performed, immunochemistry is a highly specific and sensitive technique.

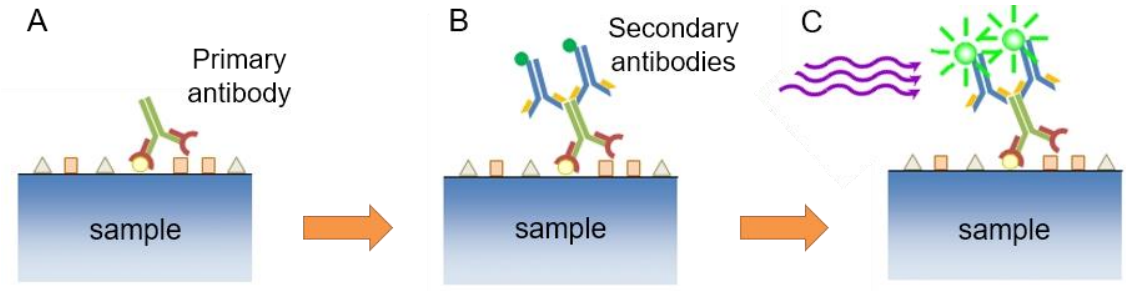

Figure 9. Immunochemistry functioning. A. Rabbit antibody specific for the round protein attaches only to its target. B. Secondary antibodies specific for rabbit antibody attach to their target. C. The marker in the secondary antibodies permits visualisation of the protein localisation in the sample. In this case, the marker is a fluorescent molecule that is excited by the incident light.

To conclude, fixed and stained sections of biological samples are mounted in between microscopy glass slides. An adequate mounting medium will allow optimal fluorescence emission, provide a suitable refractive index, and avoid spherical aberrations and early decay of fluorescence[47]. With this, the samples are ready for further observation under the microscope.

[D] An antibody, also known as an immunoglobulin, is a large, Y-shaped protein used by the natural immune system to neutralize pathogens. Each antibody specifically recognizes a unique molecule, called an antigen, and binds to it through the tips of the two short branches of its Y conformation. For immunofluorescence, a fluorochrome is attached to the tip of the antibody's long Y branch, without interfering with its function.

3.3. Microscopy image acquisition

3.3.1. Conventional microscopy

The widefield or conventional optical microscope bases its functioning on that white light passes across a biologic sample, illuminating the field of view[47]. The sample should be sufficiently thin so that the light beam can go through it. Structural details of the sample are visualised due to differences in the absorption of the light by different elements within the sample. Thus, the widefield microscope is fitted for stained, otherwise colourless, biological samples. Importantly, the sample is viewed as a sum of the focused region or plane plus the blurred image of all the out-of-focus planes (figure 10A)[48].

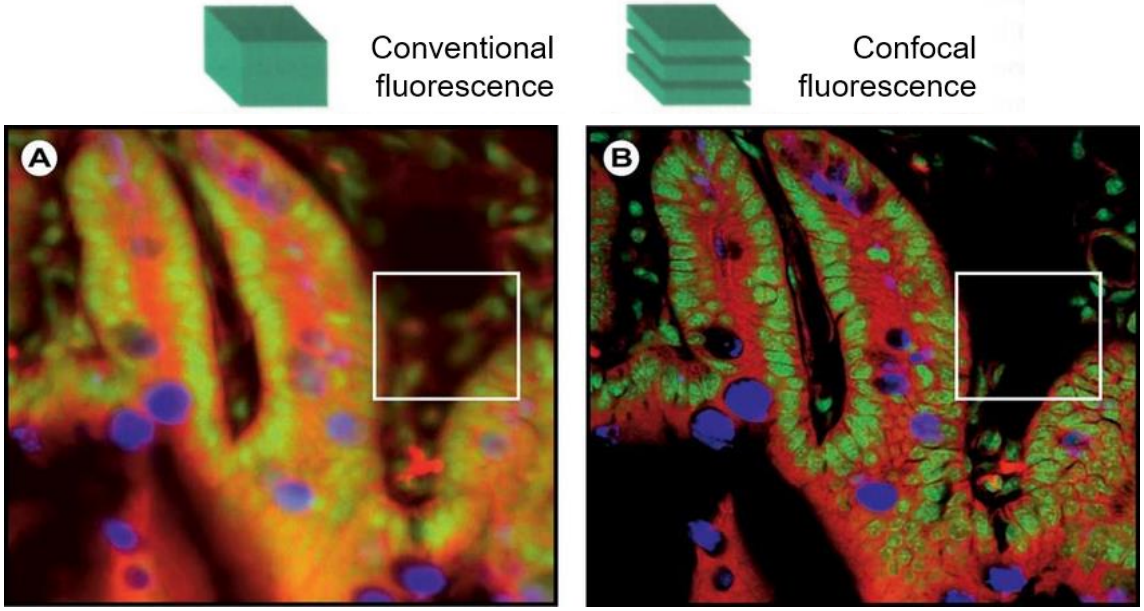

Figure 10. Example images of conventional (widefield) and confocal fluorescence of a mouse intestine section. In the wide field image (A), specimen planes outside the focal plane degrade the information of interest from the focal plane, and differently stained specimen details appear in mixed colour. In the confocal image (B), specimen details blurred in widefield imaging become distinctly visible, and the image contrast is greatly improved. Notice that out of focus signals cause additional structures to appear only in the widefield image (white box). Adapted from refs. [47,54].

Based on the conventional optical microscope, many other specific microscopes have been developed. The fluorescence microscope allows the detection of fluorescent molecules, named fluorochromes or fluorophores, which are those that are excited by absorbing light radiation at a specific wavelength and then emit light at a higher wavelength. In this manner, the fluorescent structures within the sample appear shiny on a dark background (the non-fluorescent rest of the sample) with sufficient contrast to permit detection (figure 10A)[52]. To this end, artificially added fluorochromes could be utilised, as well as, the natural fluorescence from the sample itself, emerging from endogenous autofluorescent molecules such as vitamins and elastin[47].

Immunofluorescent techniques employ natural antibodies[D] artificially linked to fluorochromes to detect within the sample the particular molecule the antibody is specific for (figure 9). There are several types of fluorochromes that can be attached to an antibody, such as FITC, Alexas, and Cys, and each one exhibits a characteristic light absorption/emission spectrum that allows visualisation in a certain colour[48]. In fact, it is possible to detect up to 5 different molecules at the same sample section by carefully choosing five different fluorochromes that do not have interfering absorption/emission spectra between them. The only modification needed in the microscope to visualise each fluorochrome colour is to change the excitation and emission optical filters, which is a quick, routine procedure in microscopy[48]. Besides, importantly, the fluorescence of fluorochromes tends to lose intensity with time due to depletion[47], whereas the autofluorescence of all the tissue augments with time due to natural degradation.

3.3.2. Laser scanning microscopy

Laser scanning microscopy is a form of optical microscopy in which a specific wavelength laser beam is used instead of white light. The confocal laser scanning microscope is an adaptation of a fluorescence microscope with a pinhole that allows visualising only a chosen particular, thin plane of illumination within the thickness of the whole sample (Z-axis)[47]. Hence, one can see only the fluorescence emerging in that particular focused plane, eliminating the fluorescence occurring in lower or upper out-of-focus level planes[48]. With this, confocal microscopy produces high-resolution images of optical sections of the sample (figure 10B), and can "section" all the sample providing a z-stack of optical section images. The parameters of z-stack acquisition, such as the thickness (z-step) and the number of optical sections, are tuned for the convenience of the study. Furthermore, it is possible to reconstruct a 3D rendering computationally out of a z-stack of a given sample, and this rendering can be virtually rotated and cut as desired.

Laser scanning microscopy is not only restricted to the use of externally added fluorochromes into the samples. Indeed, multiphoton laser scanning microscopy is able to confocally visualise fluorescent structures without the need for a pinhole, by taking advantage of nonlinear optics phenomena. This process is defined as the excitation of a fluorochrome by the simultaneous absorption of two or more infrared photons, which together sum up the required wavelength for its excitation; as opposed to the excitation by one single photon occurring in the conventional fluorescence events (linear optics process)[48,55]. As an advantage, the infrared light laser beam used in multiphoton microscopy can penetrate further inside the sample, as compared to conventional confocal microscopy, allowing to work with thicker samples. In addition, multiphoton microscopy produces far less photodamage to biological samples than one-photon fluorescence[55]. Nevertheless, multiphoton microscopy requires a very well aligned microscope setup.

The nonlinear optics process is called two-photon excitation fluorescence (TPEF) in the case of absorption of two photons by an endogenous or exogenous fluorochrome. A fluorochrome that is active by conventional one-photon absorption at a given wavelength can often be excited by two photons of twice the wavelength, yet the fluorescence quality might decrease[55]. Furthermore, the excitation by two photons of materials arranged as non-centrosymmetric structures, like collagen, microtubules, and muscle myosin, produces a nonlinear optical event similar to TPEF, called second harmonic generation (SHG). Both TPEF and SHG are currently used for high-resolution laser scanning microscopy in the biology field for visualisation of submicron structures (figure 11).

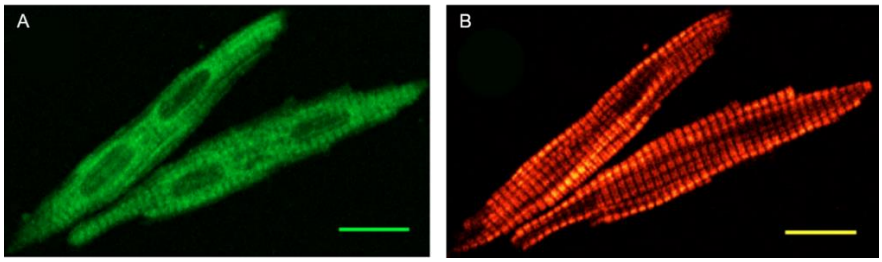

Figure 11. Two isolated binucleated cardiomyocytes as imaged with TPEF (A) and SHG (B)[56]. A. The TPEF signal is due to the cellular nonspecific autofluorescence that arises when a specific fixative is used to preserve cells. The four circular gaps correspond to cell nuclei. B. The SHG signal resolves the myosin filaments in cardiomyocytes. Scale bar = 15 µm.

3.3.3. Electron microscopy

Although analogous functioning to optical microscopes, electron microscopy irradiates samples with a beam of electrons instead of with a light beam (i.e. photons)[50]. This technique achieves higher resolution images compared to conventional microscopy since high power electron beams reach five orders of magnitude shorter wavelength than visible light, thus augmenting the resolution limit of the microscope[48]. There are two types of electron microscopy techniques: transmission electron microscopy (TEM) for ultra-high-resolution imaging of sample sections based on the electron density of their diverse endogenous structures, and scanning electron microscopy (SEM) for visualising the surface topography of the sample covered by metallic particles[47]. In Histology, TEM has historically served to unravel the microstructure of ECM components such as the various collagens. Complementarily, SEM has been useful for characterising the volumetric arrangement of the ECM.

3.3.4. X-ray computed micro-tomography (microCT)

To analyse the 3D structure of relatively large biological samples, optical and electron microscopy techniques can be combined with approaches to image several consecutive sections of the same sample. However, although there has been a considerable

improvement over the last decades, serial sectioning histology remains a tedious and specialised task[49].

Alternatively, the internal structures of large biological samples (up to cm^3) can be visualised without physical sectioning by X-ray computed micro-tomography (microCT)[49]. In this microscopy technique, the X-rays pass through the sample and are collected at the opposite end like in clinical X-ray radiographs, yet in microCT, the sample rotates providing several acquisitions (figure 12)[50]. Then, algorithms use the sensed data to construct a 3D rendering of the sample and provide virtual serial sections of it, just like in clinical CT (figure 12B-C and 5C-E). Biological samples for microCT do not necessarily require fixation, added contrast, or physical sectioning, hence living animals can be imaged with this approach. However, it is compulsory to use the phase-contrast modality of microCT to characterise soft tissues (i.e. non-calcified) at high resolution[57,58]. Furthermore, microCT can be performed at a synchrotron light source to achieve greater sample throughput as acquisition times are faster than when using an X-ray laboratory source. Synchrotrons are highly-demanded national facilities that act as giant microscopes as they generate light 10 billion times brighter than the sun[59].

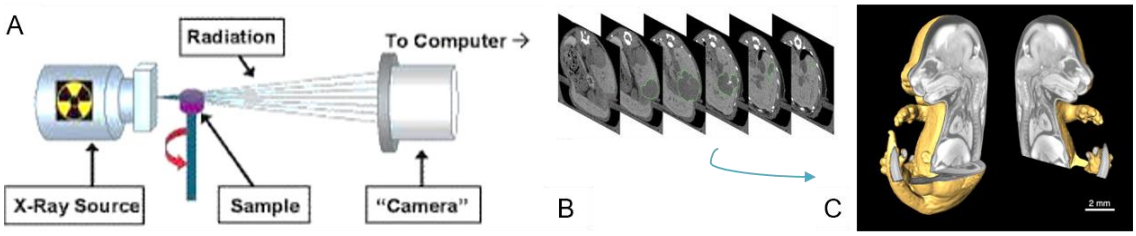

Figure 12. MicroCT basic functioning. A. X-rays are projected to the rotating sample and the camera collects the transmitted light. B. The detected signal is computationally reconstructed as a series of virtual sections of the sample. C. The scan sections can be used to build a 3D rendering of the sample. In this case, it is a mouse embryo[60].

3.4. Microscopy image processing and analysis

Currently, image analysis is applied to a wide range of fields such as robotics, medical imaging, astronomy, environmental studies, and archaeology[50]. The concept of image analysis in the context of histology refers to the extraction of significant information out of microscopy images, by employing computational image processing techniques[47]. Notably, whereas image processing modifies the original image yielding a transformed image, image analysis obtains quantitative data by performing measures on the transformed image.

In this framework, digital images are divided into pixels, which are small square areas, all of the same size, which constitute the minimum unit of an image (figure 13A)[47]. Each pixel displays a colour intensity or a grey level within it, which is translated to a discrete number from a defined scale (usually greyscale: from black to white) (figure 13B)[50]. Taking this into account, the maximum number of levels or intensities in an image is

defined by the number of bits that constitute it (bit depth): 2-bit images contain 2 levels (binary image, black and white), whereas 6-bit images contain 64, and 8-bit images contain 256 levels (figure 13C). In summary, the intensity of each pixel is defined by a number within the range of the bit depth of the image. An image with many levels has greater colour resolution than an image with lower bit depth. However, the human eye is only capable of distinguishing 64 grey levels, thus images over 6 bits do not provide additional visual information, yet this extra data might be relevant for the computer[47].

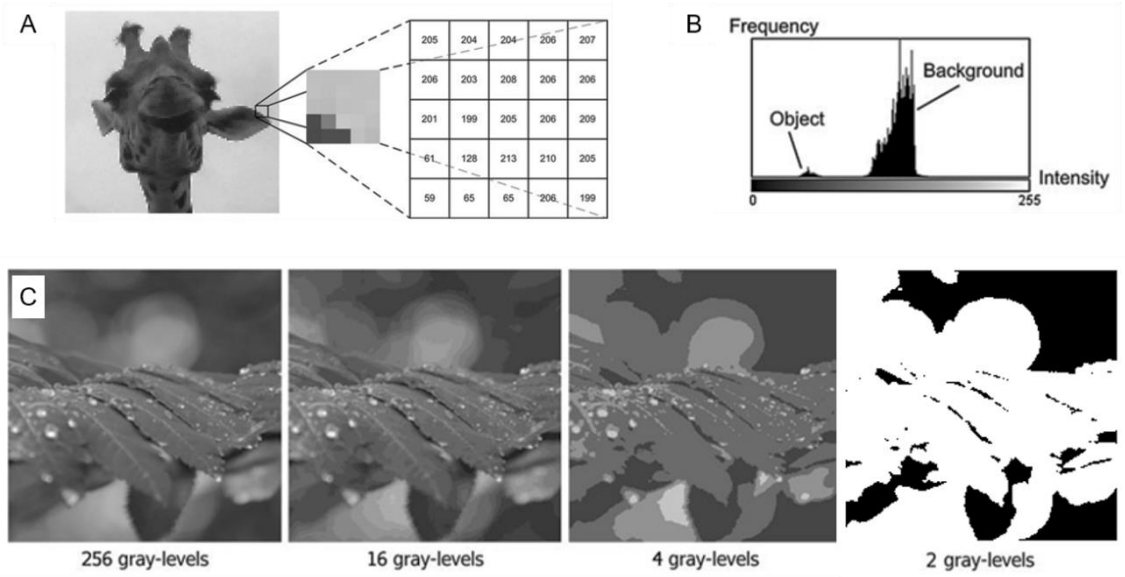

Figure 13. Images as arrays of pixels. A. Example image showing its decomposition into elemental pixels, each one with a level of grey or intensity value. B. Histogram of the intensity of all the pixels in an 8-bit image, grey levels range from 0 to 255. In this case, a few pixels belong to the object of interest, which is darker (closer to 0 intensity value) than the background pixels. C. Visualisation of the same image at different bit depths. Higher bit depth provides more grey levels, thus more detail. Last example is a binary image.

Image processing considers histological images as complex pictures, owing to its broad range of colours/levels, intensities, and textures, and also to the geometry of its objects that is often intricate and might not be completely defined[47]. These factors make challenging to segment the regions of interest (ROI) out of the original histological images, in order to finally measure features on them. Hence, previous image processing steps are needed to reduce the amount of information (i.e. detail) in the original image, and lastly be able to segment the ROI.

Essentially, image processing operations involve the application of arithmetic calculations to the values of grey level of each pixel in an image[50]. There are many image processing operations, thus, here, only the most commonly used in biomedicine will be briefly described: spatial and geometric operations, contrast improvement, thresholding, illumination correction, binary operations, and logical operations[47]. An image is rotated, translated, scaled, sharpened, and contrasted as desired to aid ROI visualisation. The contrast of an image is the difference in grey level between the highest and the lowest levels, hence it relates to the image's range of grey levels, which can spread throughout

the bit depth range of levels (from levels 0 to 255, in the case of 8-bit) or can occupy only a portion of this range (for instance, from levels 47 to 123). Manipulation of the contrast of an image serves to highlight certain features or to improve the general visualisation of the image (figure 14A). Besides, a thresholding operation localises all the pixels within an image that display a particular grey level (figure 14B). Illumination correction of the image is often necessary given that microscopes might present optical imperfections that lead to a heterogeneous illumination of the field of view[47]. The illumination correction is made by subtracting to the original image a white image, which is an image taken with the same microscope and setup parameters but without any sample. As well, other arithmetic operations on images are addition, the already mentioned subtraction, multiplication, and division, by other images or by particular numerical values. Logical operators (AND, OR and NOT) are also used to perform operations between two images, in order to obtain a resulting image with just the pixels present in both images (AND), with only the different pixels in both images (OR), or with only the pixels not present in any of both images (NOT) (figure 14C)[50]. Moreover, the operations on binary images called dilation and erosion consist in the addition or elimination, respectively, of a layer (or more) of pixels on the contour of a binary object (figure 14D)[47]. These binary operators are used to assemble single objects that need to be together or to separate individual objects, respectively.

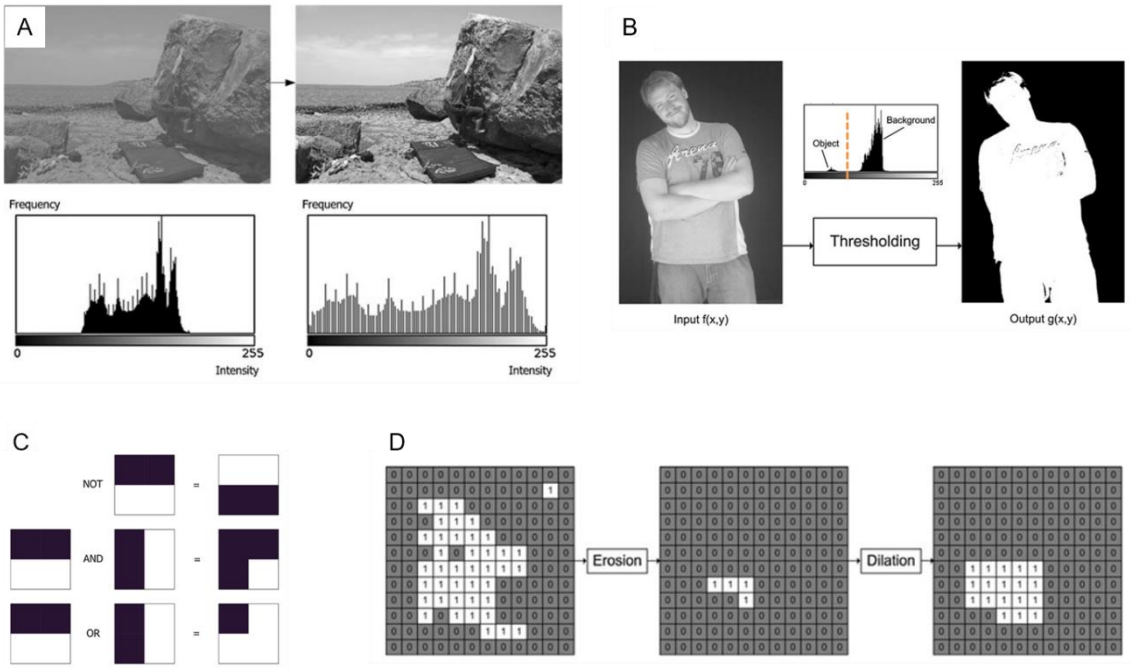

Figure 14. Examples of image processing operations. A. Contrast adjustment of an image: its histogram is stretched to occupy all the available grey levels. B. Thresholding selects the pixels from a specific range of grey levels and converts the image into binary. In this case, the ROI had brighter pixels than the background, so the threshold was set in between both intensities (orange dashed line). Notice that some parts of the man's T-shirt and hair were converted to black instead of white in the binary image because their pixels were as dark as the background. C. Logical operators explained in 4-pixel binary images. D. Erosion operation followed by dilation operation on a binary image. Although both operations subtract or add a single pixel to the whole contour of the white object, the process cannot recover the original image, given that it was a complex object.

By wisely using these and many other image processing operations, one can modify the original image to adequately emphasise the regions or objects of interest for their segmentation. Segmentation is defined as the process in which the ROI(s) is separated from the rest of the image[50]. There are countless segmentation methods based on the classification of the image pixels relying on their colour, intensity, aggrupation, spatial location, or shape or texture of the object containing the particular pixel[47]. Given the complexity of histological images, the employment of multiple segmentation criteria is required for an accurate delimitation of the ROI in the image.

Once the ROIs are extracted, quantification of their features is performed. Typically, morphological and densitometric are the two kinds of measurements applied to segmented objects. The morphology of the objects is defined by geometric characteristics such as number, area, perimeter, diameter, orientation, and distance between individual objects[47]. Additionally, densitometry measurement of the objects relies on the quantification of the grey levels within the object's pixels.

Image modification processes can be applied to digital images using the free software ImageJ [61]. For more complex or specialised image processing in 3D, a plausible option is to utilise ilastik free software[62]. Finally, for customised calculations on large amounts of images, writing a personalised MatLab code is a good alternative. Besides many other features, MatLab software (2016, The MathWorks Inc., Natick, Massachusetts, USA) allows the design of simple graphical user interfaces that permit an easy communication between the non-experienced user and the raw code.

4. Aortic wall structure and protein composition

The application of microscopy and molecular biology techniques has led to the discovery of a big part of today's knowledge of aorta protein composition and structure.

In the aorta, the ECM constitutes more than half of the mass of the wall and is mainly composed of collagen and elastin[63]. Other components, such as microfibrils, proteoglycans, and glycoproteins are all present within the extracellular space of the vessel wall. In the tunica media, the ECM is produced primarily by the VSMC during development, whereas in the adventitia, collagen is synthesised by the adventitial fibroblasts as in other connective tissues of the body[11]. In addition to providing physical support for cells, the ECM actively participates in the establishment and maintenance of differentiated tissues by acting as a source of both chemical and physical cues that modulate cell behaviour[64]. This crucial function is achieved through its complex chemical composition and organisation.

4.1. Whole aortic wall

4.1.1. Aortic wall microscopy imaging

Historically, the study of vascular tissue structure has relied primarily on the visualisation of two-dimensional (2D) stained transverse sections by optical microscopy. As previously explained, ECM dyes pink with the standard haematoxylin-eosin staining of histological sections (figure 15A). However, with this approach, elastic fibres are indistinguishable from the rest of the ECM. Hence, to visualise them, vascular samples are coloured with Verhoeff's stain that dyes lamellae in dark (figure 15B).

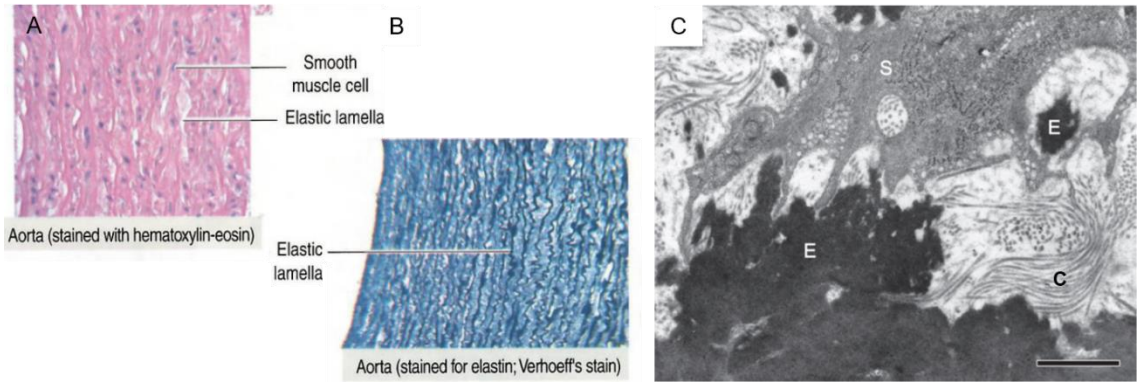

Figure 15. Aortic wall architecture. A. Hematoxylin-eosin staining of aortic tunica media[10]. B. Verhoeff's staining of tunicae intima and media. C. TEM imaging showing VSMC (S), elastic lamellae and fibres (E), and collagen fibres (C) [65]. Scale bar = 1 µm.

Electron microscopy has shown that the aortic media consists of lamellar units comprising concentric elastic lamellae and intervening VSMCs, elastic fibres, collagen fibres, and proteoglycans. VSMCs and lamellae are strongly interconnected to function as a whole structure to withstand the repeated motion of the aorta (figure 9C)[65].

Nevertheless, the knowledge obtained using these methodologies is inherently based on a two-dimensional perspective of the tissue (transverse cuts of the aortic vessel), which is highly limiting to determine the location, progression, and extension of the tunica media features when a 3D microstructural analysis is required. Therefore, for further insights, more sophisticated microscopy techniques have been progressively applied to the cardiovascular system, including the aorta[66,67]. Serial sectioning (combined with optical or electron microscopy) and confocal microscopy may be used to visualise the 3D micro- and nano-structure of small pieces of vascular tissue[13,49,65].

In particular, multiphoton microscopy is well suited for arterial wall imaging, since it permits visualisation of almost the entire wall, without the need for exogenous fluorochromes, or even sample fixation and embedding[68]. Based on endogenous tissue sources of nonlinear signals, the TPEF signal arises from the elastin content in elastic lamellae, and the SHG signal originates from collagen fibres located at the adventitia and interlamellar spaces (figure 10). Taking into account that these two matrix components make up most of the arterial tissue structure, multiphoton microscopy can disclose almost all the framework of an unstained aortic wall[68]. To date, some laboratories have applied this technique to image aortic samples in a conventional transverse perspective (XZ or YZ axes), as in standard histological preparations (figure 16A-B) [68,69]. A few other groups have applied multiphoton microscopy to image the tissue in an en-face view, and subsequently generated a three-dimensional rendering of it[70,71]. The en-face histological perspective consists of visualising the surface of the vessel (XY axes) along the depth of its wall (further detail at next section “Elastic lamellae”). An illustrative example of en-face visualisation is that obtained by endoscopic vascular imaging.

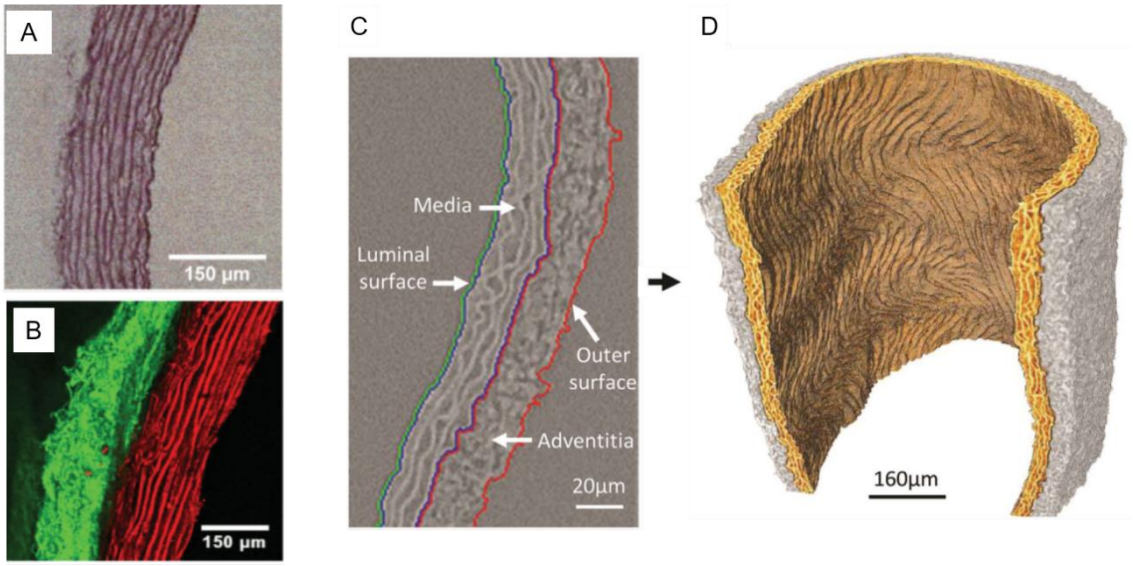

Figure 16. Aortic imaging by advanced microscopy techniques. A. Conventional histological preparation of rat aorta[68]. B. Multiphoton microscopy of the same vessel as in A. Elastic lamellae are marked in red, collagen in green. C. MicroCT slice of rat carotid artery[72]. D. 3D reconstruction of a microCT scan of rat carotid artery. Tunica media is marked in yellow.

Similar to multiphoton microscopy, phase-contrast microCT of vasculature does not need tissue staining or sectioning, nor contrast agent addition, to visualise the 3D microstructure of the sample[72]. Moreover, microCT allows imaging of samples of larger volumes, compared to multiphoton microscopy. Taking advantage of these benefits, Stergiopulos and coworkers[73] used microCT imaging at low resolution to map aortic tissue for subsequent histological analysis, whilst Assemat *et al.*[74] characterised aortic geometry for numerical simulations. Furthermore, Walton *et al*.[72] reported the visualisation of entire rat carotid arteries at high resolution, resolving sub-micron tissue structures (figure 16C-D). To our knowledge, there are few articles on vascular micro-scale imaging by microCT, yet none image the internal structure of the aortic tissue at high resolution.

However, these advanced 3D techniques need specialised machines and expertise, so researchers tend to continue using the 2D approach for histological studies.

4.1.2. Aortic wall protein composition

By means of molecular biology techniques, the scientific community has a clear consensus on the gross protein composition of the aorta. In general, this vessel is made of ECM, composed by collagen, elastin, microfibril components (fibrillins, fibulins, etc.), proteoglycans, and soluble molecules such as growth factors; and by cells, mainly VSMCs, whose protein content is explained later in this section.

Although this current knowledge on aortic protein composition, it does not exist an established human aorta proteome since the Human Protein Atlas comprises many human body tissues but not the aorta. Hence the data on aortic proteins stated at the neXtProt database is all based on indirect protein presence demonstration through RNA expression, which cannot be assumed as a definitive aortic proteome. To this goal, Didangelos *et al*.[75] attempted to establish the set of proteins present in control human aorta samples by mass spectrometry. They characterised 630 unique proteins in the aorta, which some of them had never been reported in the vascular tissues before, like podocan, sclerostin, and agrin. Nowadays, this is the only extensive list of proteins present in the healthy human aorta. Nonetheless, mass spectrometry is not an absolute technique, thus there are other proteins in the tissue that were not identified in Didangelos study, but are identified by immune-based studies, such as TGF-β.

4.2. Elastic lamellae

4.2.1. Elastic lamellae organisation

Elastic fibres in the aorta are arranged forming concentric, fenestrated sheets called lamellae. Elastic lamellae are a rubber-like material that accounts for most of the expansion of the aortic wall at normal systole pressure[4]. Particularly, lamellae are wavy when the aorta is non-pressurized, and straight when subjected to blood pressure[76]. Transversely sectioned, conventional histological preparations of the aortic wall show elastic lamellae arranged in almost equidistant parallel layers, whose number depends on the animal species and vessel calibre[77]; for instance, lamellae number is 7 to 8 on average for adult mice aorta[78] and 40 to 70 for humans[7,8,11]. Despite resembling parallel layers, lamellae branch regularly, resulting in a different number of lamellae in different anatomical positions of the same aortic portion[13]. Moreover, numerous direct connections between neighbouring lamellae are present in the tunica media, constituting a dense elastic fibre network at the interlamellar spaces (figure 17A). This network forms cage-like structures dividing adjacent SMCs, and often also connecting with them[13].

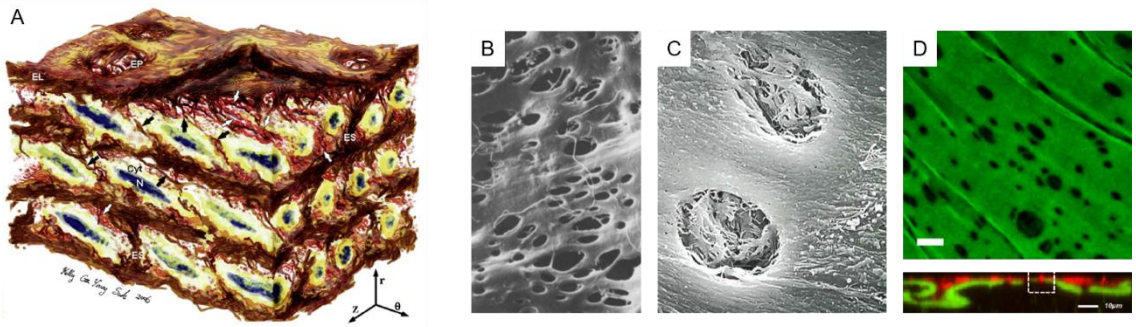

Figure 17. Lamellae architecture. A. Lamellae (marked in brown) structure as parallel fenestrated sheets, with VSMCs in between (in yellow), and interconnecting elastic fibres (in brown)[13]. B. SEM of human cerebral artery IEL[79]. C. SEM of rat aorta IEL fenestrae at x3,000 magnifications[80]. D. en-face TPEF imaging of rat mesenteric artery IEL. Lower panel displays the transverse view of the IEL and, in red, the endothelial cells of tunica intima[81]. Scale bar = 10 µm.

Lamellae surface presents physiological micro-scale holes of 1-10 µm in diameter, called fenestrae (figure 17B-D)[80]. Their size and density depend on the analysed vessel, animal species, and age[79,82,83]. Lamellae fenestrae allow cell communication and free flow of nutrients between one interlamellar space and the subsequent, especially between tunicae intima and media[5,80,84]. Additionally, it is thought that fenestrae contribute to the developmental modelling of the IEL[84]. Conventional transverse histological preparations are not an adequate method to study fenestrae owing to their small size and localisation at the surface of lamellae. Fenestrae can be visualised by SEM (figure 17B-C)[79]. However, this technique can only display the natural surface of the tissue, and hence studies have mainly focused on the outermost lamellae, the IEL[79,80]. Furthermore, the recent application of TPEF microscopy on rat artery samples has allowed the

visualisation and analysis of fenestrae from only the IEL [83,85], and has also been used in combination with exogenous fluorophores (figure 17D)[81].

4.2.2. Elastic lamellae synthesis

Elastic fibres, hence elastic lamellae, are composed of a core of elastin and a mantle of microfibrils[4,11]. Proelastin, the precursor of elastin, is cleaved within the cell and secreted as tropoelastin[10]. In the extracellular space, tropoelastin deposits on the surface of microfibrils and interacts with them to facilitate elastin fibre assembly and provide overall structure to the growing fibre[9,11]. Lysyl oxidase (LOX) family members oxidise lysine residues of tropoelastin to form covalent cross-links between and within tropoelastin molecules[9]. These bonds induce the aggregation of tropoelastin to build bundles of elastic fibres[18]. Although cross-linked, the individual tropoelastin molecules remain in a random-coil configuration. In addition, >80% of tropoelastin's lysine residues are crosslinked, resulting in 15 to 20 crosslinks per elastin unit[9]. Therefore, the produced elastin arrangement is a highly crosslinked 3D network of randomly coiled tropoelastin molecules[5,18]. The random coiling of tropoelastin molecules and the high degree of cross-linking between them enables the characteristic stretching and recoil properties of the elastic fibres that allow their rubber-like elastic behaviour (figure 18)[5,9].

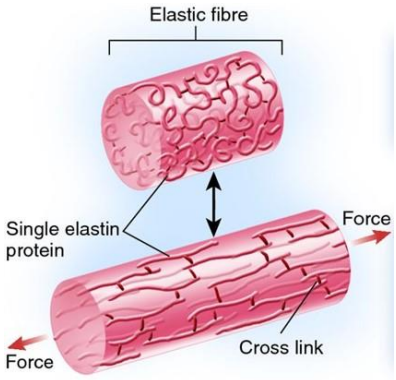

Figure 18. Elastic fibre micro-structural conformation in stretch and recoil. Stretching forces unroll the coiled tropoelastin molecules, without breaking the conformation of the elastic fibre.

4.2.3. Elastic lamellae microfibrils

The microfibrils involved in elastin assembly are composed of glycoproteins and have a diameter of approximately 10-15 nm[11,16]. The structural building blocks of the microfibril are the fibrillin molecules, which are stabilised by crosslinks catalysed by the protein-glutamine γ-glutamyltransferase 2 (former tissue transglutaminase, TGM2)[9,86]. The microfibrils are formed first, serving as a scaffold or template for subsequent deposition of tropoelastin monomers in a certain manner that the lysine residues are accessible for LOX crosslinking[9,11]. Moreover, microfibrils also regulate morphogenetic and tissue homeostatic programs through direct cell-matrix interactions or indirectly by modulating the activity of TGF-β and BMP (bone morphogenetic protein)[9]. Signalling induced by these two growth factors is a potent regulator mechanism of cell survival and differentiation, of tissue morphogenesis and homeostasis, and of cellular responses to injury[86]. Hence, microfibril integrity is crucial for overall tissue maintenance.

The human genome contains three fibrillins (1,2, and 3), yet fibrillin-1 is the most abundant in the mature aorta[9]. Fibrillins interact with cell surface integrins, elastin, heparin sulphate proteoglycans, TGF-β binding proteins (LTBPs), and BMP-7[87]. Fibrillin-1 has a crucial role in the sequestration and regulation of the activity of growth factors, especially of TGF-β, which is a key player in tissue homeostasis, and its deregulation is implicated in a variety of diseases[25].

Several other proteins associated with elastic lamellae microfibrils have been described in the aorta, but their role is not yet completely clear (figure 19)[9,27,86]. The best characterised are the latent TGF-β binding proteins (LTBP 1-4), EMILINs (elastin microfibril interface-located protein), microfibril-associated glycoproteins (MAGPs), and members of the fibulin family. The small glycoproteins MAGP-1 and -2 are constitutive components of most microfibrils[9,27]. Their presence is trivial for the elastin assembly function, but it is necessary for binding members of the TGF-β growth factor family. In addition, fibulins mediate cell adhesion through integrin receptors, influence cell growth and motility, and regulate elastic fibre synthesis[27,86]. They also interact with apolipoprotein A, LOX, LOX-like 1 (LOXL1), and superoxide dismutase (SOD) in arterial walls. All fibulins except -6 and -7 are found in elastic tissues, with fibulin-2 and -4 at the interface between the elastin core and its surrounding microfibrils, -1 located within the elastin core, and -5 associated to microfibrils[9]. Besides, EMILIN-1 has the ability to bind both tropoelastin and fibulin-5, suggesting that it may serve a bridging function between those two molecules[9]. Furthermore, LTBPs associated to microfibrils sequester TGF-β and regulate its availability in tissue[86,88].

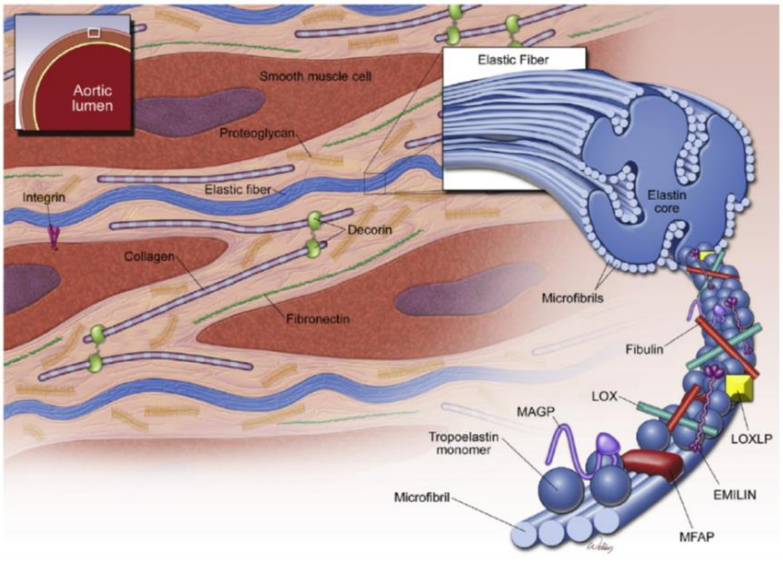

Figure 19. Elastic lamellae composition and surrounding key structural components of the tunica media[27]: elastin, microfibrils, vascular smooth muscle cells (VSMCs), collagen fibres, proteoglycans. Crosslinking of tropoelastin monomers by LOX forms elastic fibres, which in turn are covered by microfibrils. Microfibrils are composed of fibrillin and several microfibril-associated proteins, such as EMILINs, MAGPs, and fibulins. Elastic fibres in the aortic wall arrange as sheets, named lamellae.

4.3. Collagen

The collagen structure provides a supportive framework in the tissues, with binding sites for other ECM components, signalling molecules, and cells. In the aorta, collagen fibres are found in all three tunicae, especially forming large bundles in the adventitia and, to a minor extent, around the VSMCs of the media[63]. Each collagen fibre is composed of collagen subunits, made of three polypeptide α chains coiled to form a triple-stranded helix, held together by hydrogen bonds (figure 20)[5,8]. Collagens are a family of proteins that share the molecular triple helix structure but have α chains that differ in their amino-acid composition[9]. So far, there are 28 different types of collagen, made up by combinations of three out of more than 40 distinct α chains, each encoded by a separate gene[64]. The principal collagen fibre types in blood vessels are I and III, in tunica media and adventitia respectively, which are both classified as fibrillar collagens[4,9]. Importantly, although one type may predominate in a particular location, it should not be assumed that this is the only type present[5]. In fact, collagen types IV, V and VI have also been reported in aorta[9,23].

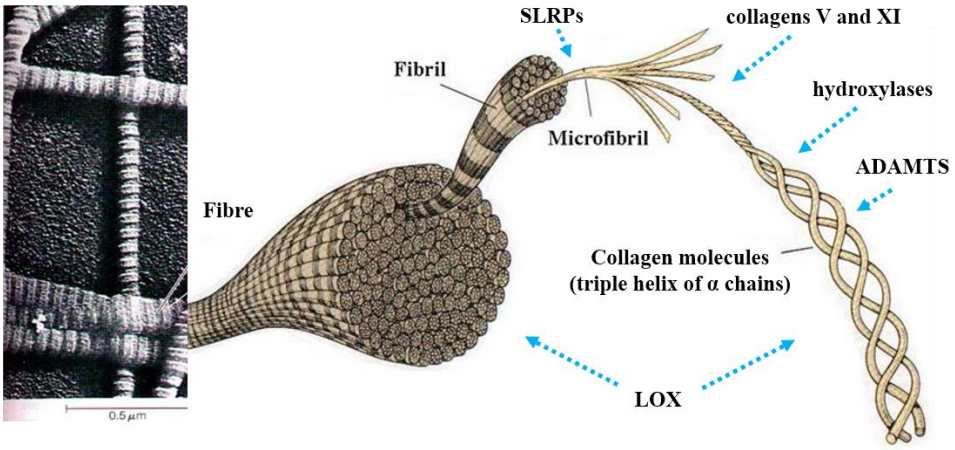

Figure 20. Organisation of collagen fibres. Collagen molecules are triple helixes of α chains. These molecules assemble into microfibrils, which in turn aggregate into collagen fibrils. Finally, a collagen fibre is the assembly of multiple fibrils. Some proteins involved in the collagen fibre synthesis are LOX, other collagens, small-leucine-rich repeat proteoglycans (SLRPs), and metalloproteinases (ADAMTS).

For fibrillar collagen synthesis, within the cell, three polypeptide α chains are wound around one another in a triple helix to generate a rope-like procollagen molecule (figure 20)[18]. Many proteins are involved in this helix formation, such as lysyl and prolyl hydroxylases, 78 kDa glucose-regulated proteins (GRP78) and GRP94[64]. Then, procollagen is secreted to the extracellular space, where it is converted into a collagen molecule by enzymatic cleavage of the non-helical tips of the procollagen conformation[11]. Removal of the peptide tips is carried out by collagen type-specific metalloproteinases from the ADAMTS (a disintegrin and metalloproteinase with thrombospondin motif), BMP1 and tolloid-like families, as well as by furin-like proprotein convertases[64]. After cleavage of procollagen into collagen, the molecules self-assemble into ordered polymers called collagen microfibrils, aided by collagens V and XI[64]. Then, multiple

microfibrils associate one to another forming collagen fibrils by interaction with certain small-leucine-rich repeat proteoglycans (SLRPs) and FACIT collagens (fibril-associated collagens with interrupted triple helices)[10,64]. Finally, the fibrils often aggregate into larger bundles, the collagen fibres (figure 20), which are stabilised by collagen intra- and intermolecular covalent crosslinks catalysed by LOXs (figure 20)[18,64]. This collagen supramolecular assembly is crosslinked to a greater or lesser degree depending on the required tensile strength[18].

4.4. Proteoglycans

Proteoglycans are characterised by a core multidomain protein that is covalently linked to multiple glycosaminoglycans (GAG), which are long, voluminous chains of repeating disaccharide[E] units[18,64]. This GAG component binds water to provide hydration and compressive resistance to the tissue[64]. Thus, proteoglycans form a highly hydrated, gel-like "ground substance" in which the cells, the ECM fibrous proteins, and various secreted signalling molecules are embedded and settle the tissue[18].

The proteoglycans found in greatest abundance in the vessel wall can be categorised into two classes: small (i.e. SLRPs) and large proteoglycans[9]. Versican is the largest proteoglycan in the vessel wall and has been localised at the aortic tunicae intima and media. It is known to have a wide variety of functions, including induction of cell adhesion, migration, and proliferation. Moreover, the GAG component of the large proteoglycan perlecan can inhibit VSMC proliferation and migration, and it binds to fibrillin-1, fibroblast growth factor (FGF), and elastin[86]. Besides, the function of the other large proteoglycan, aggrecan, in the vessel wall is unclear. Furthermore, SLRPs bind ECM molecules such as collagen, tropoelastin, fibronectin, TGF-β, cytokines, and fibrillin microfibrils, among others. The SLRP family in artery includes decorin, biglycan, fibromodulin, mimecan (osteoglycin), and lumican[9]. Decorin and biglycan are directly implicated in the process of elastic fibre formation and also regulate collagen packing[86].

4.5. Adhesive glycoproteins

Glycoproteins are ECM molecules constituted by protein chains linked to ramified polysaccharides[53]. Glycoproteins differ from proteoglycans in their higher proportion of protein and in characteristic differences in the nature of their polysaccharide side-chains. The subgroup of adhesive glycoproteins includes fibronectin, laminin, nidogen (former entactin), and vitronectin in the aortic tissue. They mediate attachment of cells to the tissue substrate (figure 21), given that most cells do not have the specific receptors to bind directly to other ECM molecules, such as structural fibres or soluble growth factors[5,18].

[E] A disaccharide is the sugar formed by two covalently linked monosaccharides (simple sugars).

Fibronectin assembles into fibrillar structures around cells and has two different functions in the aorta[64]. On the one hand, it has a structural role, as it modifies the mean stress and elastic properties of the vessel wall. On the other hand, fibronectin plays the role of "master organiser" of matrix assembly since it forms a bridge between cell surface receptors, i.e. integrins, and several ECM compounds such as collagen and proteoglycans[89]. The presence of fibronectin at the ECM controls the deposition, organisation, and stability of other matrix proteins, including collagen I, collagen III, and thrombospondin 1; and modulates cell migration, adhesion, proliferation, and phenotype of VSMC[90]. Specifically, in vessels, fibronectin surrounds closely the VSMCs forming a basal lamina-like layer that attaches cells to the ECM and transmits the mechanical cues happening at the microenvironment (figure 21)[14].

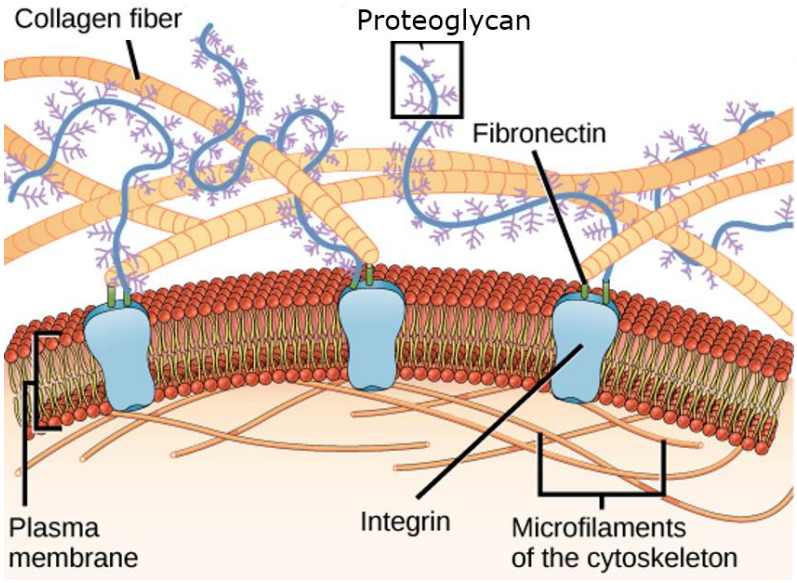

Figure 21. Overview of ECM organisation and connection with cells. Collagen fibres, proteoglycans and glycoproteins are abundant components of the ECM. Fibronectin links ECM components with cells through integrins, that are cell plasma membrane proteins. In turn, integrins connect with the intracellular cytoskeleton.

4.6. Remodelling proteases

The aortic ECM is a dynamic structure that is constantly rebuilt and remodelled to control tissue homeostasis and proper functionality, although at a slow pace[91,92]. Maintenance of a functional ECM requires the coordinated activation, both temporally and spatially, of complex sets of ECM proteins as well as the enzymes responsible for their synthesis and degradation[9]. Turnover or replacement of old ECM molecules requires their previous degradation. Proteolytic cleavage of ECM components is the main process during ECM degradation in remodelling, and besides regulating ECM composition, it releases biologically active molecules that were previously sequestered within the matrix (such as growth factors)[91]. The ECM is cleaved by a host of enzymes from different families of

proteases: matrix metalloproteinases (MMP), adamalysins (ADAMs and ADAMTSs), Ser proteases (such as neutrophil elastase and plasminogen activator) and cathepsins[63,91]. These enzymes are produced by the vascular cells and are stored in a latent form within the ECM until they are required[63]. Proteases are capable of completely proteolysing the entire ECM, therefore this process requires tight regulation to avoid excessive tissue degradation, especially in response to tissue injury[63,91].

The proteolytic degradation of aortic ECM mainly involves the MMPs, including collagenases, gelatinases, stromelysins, metalloelastases, and membrane type-matrix metalloproteinases[63]. Collectively, the 23 reported MMPs can degrade all ECM proteins, thus their activity is low in normal conditions[91], and in the case of tissue repair or disease, MMP activity will be highly stimulated[91]. Thus, MMPs have a crucial role in vascular ECM remodelling, during either physiological or pathological events. Furthermore, MMP activity is modulated by transcriptional level processes, by growth factors and cytokines (EGF, FGF, TGF-β), and by specific MMP activators and inhibitors (such as plasminogen/plasmin)[63]. Notably, the tissue inhibitor of MMPs (TIMP) family consists of four members (TIMP1-4) that reversibly inhibit the activity of MMPs, ADAMs, and ADAMTSs. The local MMP-to-TIMP ratio may determine the overall proteolytic activity in the tissue[91].

Turnover of collagen fibres is frequent and mediated by collagenase enzymes MMP-1, 2, 3 and 9 [12,23]. Conversely, elastin replacement is slow, because the majority of arterial elastin is laid down during the perinatal period and there is minimal elastin synthesis in the adult animal[9,23]. This explains why damage to the elastin component in the aorta cannot be properly repaired in adulthood.

4.7. Vascular smooth muscle cells (VSMCs)

4.7.1. Phenotypic modulation of VSMC

VSMCs are the most abundant cellular components of the aortic wall, whose function is to synthesise the ECM components of the tunica media[11]. VSMCs are commonly categorised into two kinds of phenotype that are defined by cell behaviour and intracellular protein content (figure 22). On the one hand, the contractile phenotype can be identified as a state in which cells are elongated and spindle-shaped. They present an assembled contractile apparatus within the cell cytoplasm, have low proliferative activity, and low migration[9,93]. Moreover, they contain the following protein contractile markers: aortic smooth muscle actin (SMA), transgelin (or SM22α, smooth muscle protein 22), myosin-11 (former smooth muscle myosin heavy chain, SMMHC), calponin, smoothelin, caldesmon, and vinculin[94,95]. Many of these proteins are part of the cell cytoskeleton's contractile apparatus. Particularly, SMA is the predominant actin isoform in VSMCs and locates typically in the contractile filaments that form the cell's

cytoskeleton in association with myosin[96]; and transgelin is a transformation and shape-change sensitive actin isoform whose function in contraction regulation is currently unclear[97]. On the other hand, cells in a synthetic phenotype show a cobblestone, epithelioid or rhomboid shape. Their cytoplasm is full of organelles, which synthesise great amounts of ECM and the necessary machinery to proliferate and migrate. Some protein markers that can be found in synthetic VSMC are myosin-11, myosin-9, and retinol-binding protein 1 (RBP1)[95].

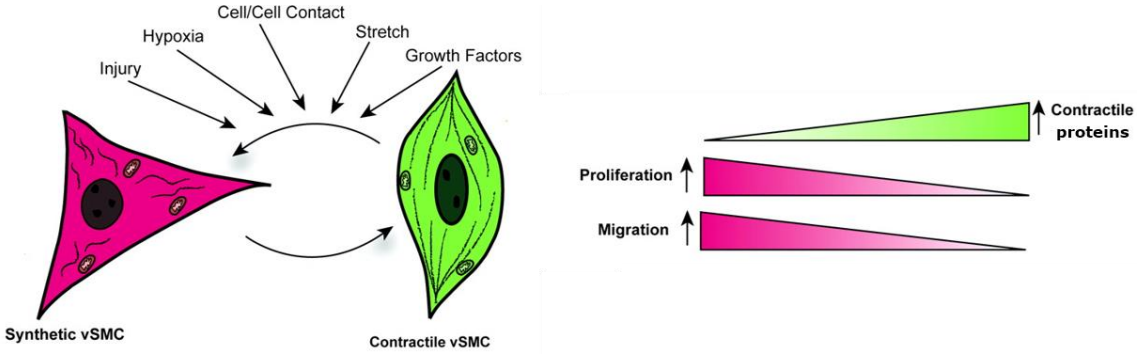

Figure 22. VSMCs phenotype modulation[98]. In response to a variety of stimuli, VSMCs switch between contractile phenotype and synthetic phenotype. Contractile phenotype is characterized by high expression of contractile proteins and low rates of proliferation and migration. Conversely, synthetic VSMCs express low levels of contractile proteins and have increased rates of proliferation and migration.

VSMC phenotype is determined through the integration of numerous environmental cues, including cytokines, cell-cell contact, ECM interactions, injury stimuli, and mechanical stresses (figure 22). Thus, regulation of phenotypic switching of VSMC is also a complex procedure that is influenced by many factors. In the healthy adult aorta, VSMCs proliferate slowly, presenting little synthetic phenotype[99]. Thus, they tend to be found in a contractile phenotype showing many of the contractile markers. However, vascular remodelling in normal development or in pathological conditions produces a phenotypic change towards a synthetic phenotype[100,101]. This change allows VSMC to increase the capacities of generating ECM, proliferating, and migrating, necessaries for the mentioned *in vivo* remodelling situations.

4.7.2. VSMC-ECM communication

In addition to providing the structural and mechanical properties required for vessel function, the aortic ECM delivers instructional signals that induce, define, and stabilise VSMC behaviour, and consequently modulate vascular remodelling[9,102]. These instructions can be in the form of biochemical molecules and/or mechanical stress diffusion. The effect of biochemical signals on vascular cells has been described earlier in this section, whereas the cell-mechanical stress interaction will be defined here.

The physical connections between the tunica media ECM and the cells embedded within it allow those cells to sense the mechanical cues happening in the environment due to blood pressure (mechanosensing). These cell-ECM links are established in cellular membrane assemblies called focal adhesions, and are constituted by essential proteins, such as integrins, filamin-A, and vinculin, that together connect with the actin cytoskeleton (figure 23A). Mechanosensed extracellular stimuli transduce to the cell cytoskeleton, and then this information is translated to other intracellular signalling pathways, which can finally modulate the aortic wall function, integrity, and response to damage (process of mechanotransduction)[103]. Specifically, cells are able to control the synthesis and degradation of matrix components and modify their behaviour according to the received biomechanical signals[25]. Therefore, the morphology, structure, and functionality of vascular cells are intimately linked to their local ECM environment. In the case of VSMCs, the cyclic stretching of the wall (i.e. circumferential stresses) directly influences their behaviour[23,96,102].

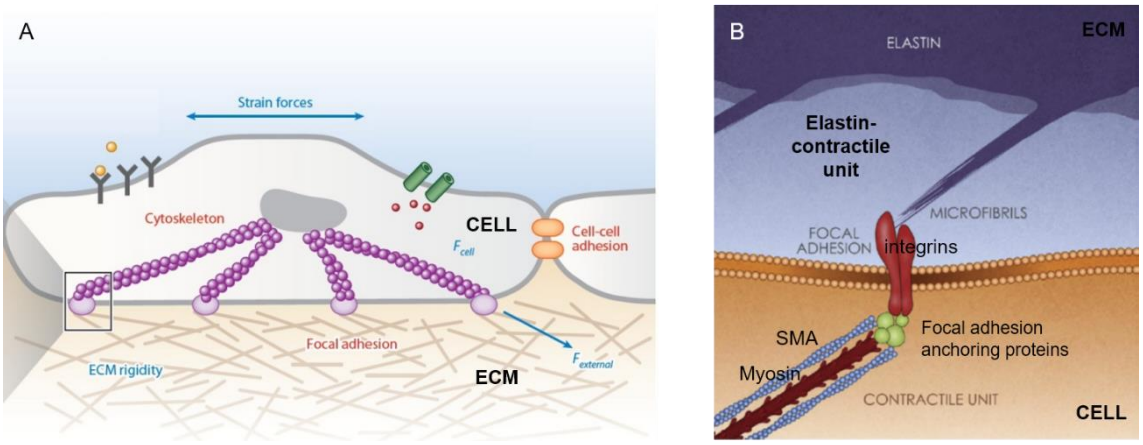

Figure 23. Cell-ECM communication. A. Cells are physically connected to the surrounding ECM through focal adhesions (light purple elements). Focal adhesions are composed by several intracellular anchoring proteins, including filamin-A, vinculin, paxilin, talin, α-actinin, and zyxin. Focal adhesions are also linked to the cell's cytoskeleton, which in turn is connected to the nucleus. B. The elastin-contractile unit in VSMCs[16]. Elastic lamellae protrusions link to focal adhesions at the cell membrane, and these link to the contractile apparatus or unit.

The elastin-contractile unit is a functional and structural unit in the aortic tunica media, which constitutes a direct connection between the VSMC and the lamellae (figure 23B)[16]. Extensions protrude from the elastic lamellae towards the interlamellar space and are attached to the focal adhesions in the VSMC cell membrane. Inside the VSMCs, the contractile apparatus is linked to the cytoplasmic side of the focal adhesions. This apparatus is composed of SMA-containing thin filaments and myosin thick filaments, along with regulatory proteins such as tropomyosin. Also, it interacts with the cytoskeleton, which is composed of nonmuscle actins, intermediate desmin-containing filaments, and focal adhesions. Contractile and cytoskeletal filaments are, in turn, anchored to the nuclear membrane through linkage between SMA and lamin A and other nuclear proteins[16]. This intertwined arrangement of ECM and cellular components, called

the elastin-contractile unit, is necessary for mechanotransduction. This unit is uniquely designed to transmit forces via integrins from the lamellae to the VSMCs, and thus may serve as a mechanosensor unit of the aortic wall. Specifically, the ECM endures the bulk of stress that is exerted on the vessel wall, which is typically 100-200 kPa, such that only 3-5 kPa is exerted on the VSMCs embedded on the aortic wall. The cells sense this stress via the elastin-contractile unit and proportionally regulate and remodel the ECM[16].

4.7.3. VSMCs cultured under stretch: bioreactors

For research purposes, many groups culture VSMCs *in vitro*. However, almost all *in vitro* studies are performed under conventional cell culture conditions, which only mimic the biochemical niche of VSMCs (O_2, CO_2, and surrounding protein concentrations) obviating the mechanical cues occurring *in vivo.* Therefore, taking into account that *in vivo* cell environment is established by biochemical and biomechanical signals, occasional studies have used bioreactors to culture cells under a more physiological condition[104]. Vascular bioreactors are platforms where cells are cultured as conventionally plus under a mechanical environment[105]. In the case of VSMCs, bioreactors are developed to perform different conditions of substrate[F] stretching to resemble the body's circumferential stress cycles due to blood flow. These *in vitro* devices can modulate stretch parameters such as its frequency, direction (uni-, bi- or equiaxial), pulsatility (constant or variable), and the percentage of deformation of the surface[106]. Hence, it is conceivable to mimic, in a laboratory, the physiological 1.1 Hz pulsatile, 13% strain, uniaxial stretch of the *in vivo* human ascending aorta (as defined earlier in the "1.3. Aortic biomechanics" section).

Furthermore, it exists only one commercial bioreactor (FlexerCell) for cell culture under stretch, yet it is an expensive device. Hence, many researchers have designed their own bioreactors. One of the latest and more physiological systems developed is a culture system in which VSMC are seeded on decellularised human umbilical veins, so they are placed on a completely natural ECM[107]. However, this method relies on the availability of adequate human vein donor samples. To overcome this drawback, researchers often use polydimethylsiloxane (PDMS), the most widely used silicon-based organic polymer, to construct the actual place of the bioreactor where cell seeding and culturing will be performed[108,109]. PDMS is an optically transparent, inert, and non-cytotoxic material capable of adopting any given shape. Fabrication of PDMS constructs only requires the mould of the desired shape and a source of heat (60ºC for 1 hour) to promote polymerisation of the PDMS from the viscous state to solid. In addition, plasma treatment is usually employed to strongly adhere together two PDMS constructs or pieces. This process activates the surface of the objects by oxidising its molecules, so that when both

[F] Substrate is the ground material where cells are attached.

surfaces are held together, they adhere by forming covalent bonds between the oxidised molecules of both sides.

It is noteworthy to state that the majority of the studies performed with vascular bioreactors or FlexerCell device used other cells than VSMCs, such as fibroblasts, HUVECS (human umbilical vein endothelial cells) or myoblasts[106,110]. The few studies performed with VSMCs in bioreactors reported, for instance, that after eight weeks of culture on stretching decellularised human umbilical veins, VSMC displayed higher proliferative capacity forming densely populated regions in the scaffold towards tunica intima and adventitia[107]. Besides, another group cultured VSMC on an artificial microchannel that acted as a blood vessel. Then, stretch was applied under different conditions as well as shear stress, emulating the two mechanical forces occurring due to blood flow[111]. Cytoskeleton organisation was analysed afterwards, and it indicated that the parallel alignment of the cytoskeleton to cyclic stretch was beneficial for VSMC adhesion, survival, and proliferation. In addition, many reports state that cyclic strain promotes a contractile phenotype in VSMCs[102].

Studies with VSMCs cultured under *in vitro* stretch do not extend much further than the data above, which is comprehensible due to the scarce availability of VSMC primary cell lines, the complexity the bioreactors add to the culturing procedure, and the high cost of acquiring a FlexerCell device.

5. Marfan aortic wall structure and protein composition

5.1. Histopathology of the aorta in Marfan syndrome

An aortic aneurysm is associated with chronic aortic wall inflammation, increased local expression of proteinases, excessive collagen deposition, and elastolysis[7,42]. In this context, conventional histological preparations of MFS aorta are characterised by a great tunica media disarrangement and fragmentation of lamellae. There is also an accumulation of proteoglycans at the interlamellar spaces, fibrotic collagen production, and loss of VSMCs (figure 24)[24,30,37,40]. All these traits worsen as the disease progresses.

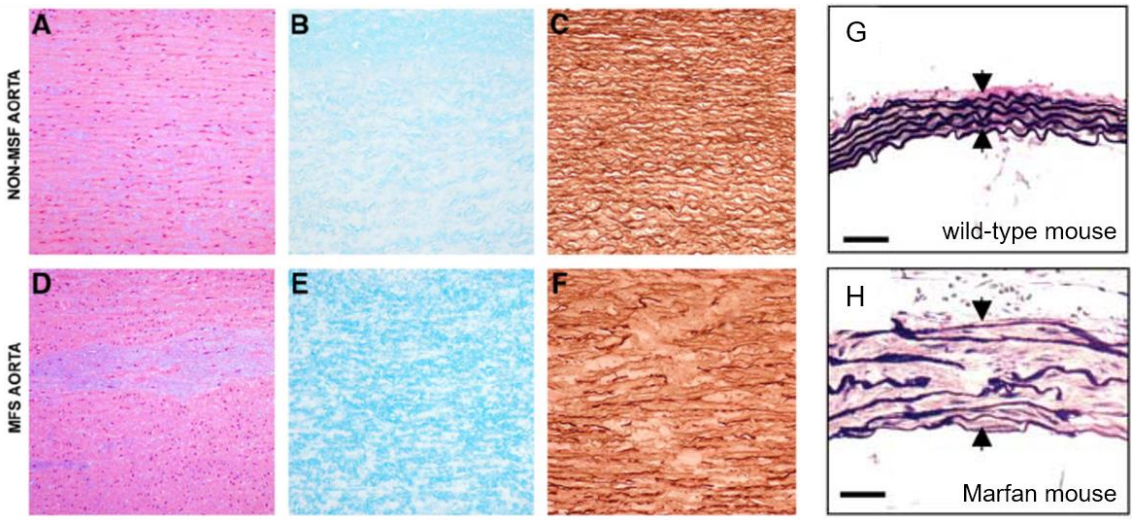

Figure 24. Conventional histological preparations of human (A-F) and mice (G-H), control (upper panels) and MFS (lower panels) transverse aortic wall. A, D. Haematoxylin-eosin staining, showing GAGs in lavender, and cell nuclei in purple[112]. B, E. Alcian blue staining, showing GAGs in darker blue. C, F. Verhoeff-van Gieson staining, showing elastic lamellae in darker brown. G, H. Verhoeff-van Gieson combined with haematoxylin-eosin staining, showing lamellae in purple and other ECM components in pink[113]. Scale bar = 50 µm. D-F, H. MFS samples display accumulation of GAGs, loss and fragmentation of lamellae, loss of cell nuclei, and thickening of the interlamellar spaces.

Histological Verhoeff-van Gieson staining of MFS murine aortae displays wall disruption similar to that in humans: the MFS *Fbn1*$^{C1039G/+}$ murine model shows the formation of ascending aortic aneurysm, with the accompanying destruction of elastic lamellae arrangement, thickening of the interlamellar spaces, and apoptosis of VSMCs (figure 24G-H)[44,113]. For research purposes, damage severity in mice aortae is often assessed by manually counting lamellae breaks in a transverse histological preparation of the aortic wall or by establishing a subjective score within a 1-to-4 damage scale[113,114]. However, these approaches are suitable for *post-mortem* aortic damage assessment as

they need a full-thickness piece of aorta subsequently prepared for optical microscopy imaging.

Moreover, TEM revealed the rupture of VSMC-lamella connections[115], and SEM demonstrated a significant loss of the interlamellar fibres that link neighbouring lamellae (figure 25A-D)[65]. En-face TPEF microscopy has been used in Marfan mice to observe elastic lamellae fenestrae changes and thus report an elastolytic process, but with low-resolution imaging and very limited quantitative analysis (figure 25E-F)[116,117]. To our knowledge, no further data is available on lamellae 3D microstructure features in health or disease.

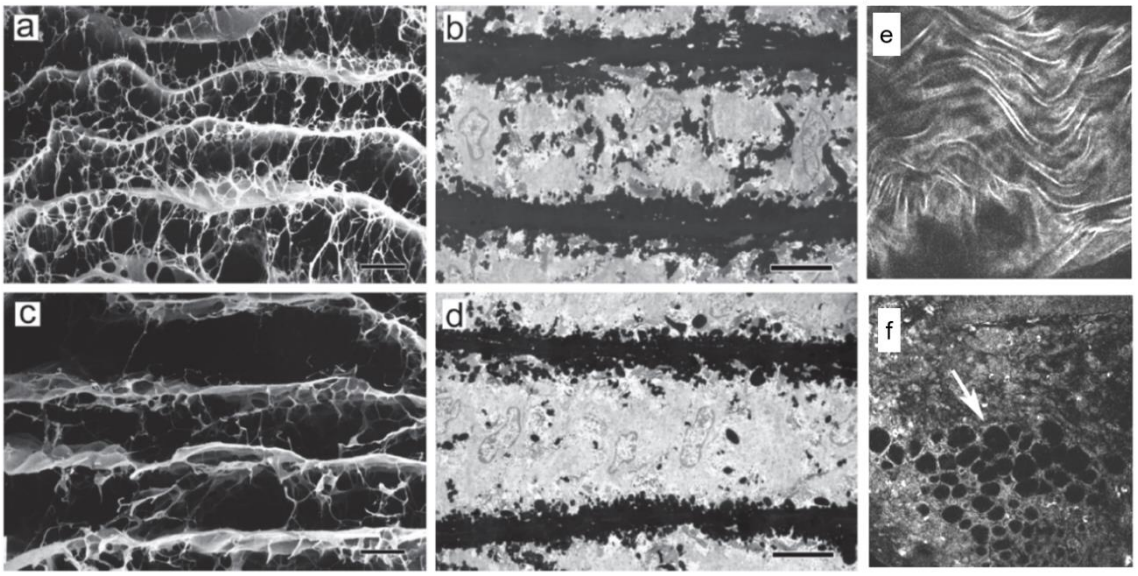

Figure 25. Advanced microscopy images of control (upper panels) and Marfan (lower panels) mice aortae lamellae. A,C. SEM transverse images showing lamellae and interlamellar elastic fibres[65]. Scale bar = 20 µm. B,D. TEM transverse images showing elastic lamellae and fibres (dark) and VSMCs (in between lamellae)[65]. Scale bar = 5 µm. E,F. En-face TPEF images displaying a lamella surface[117]. Arrow indicates enlarged fenestrae in Marfan.

5.2. Protein composition of the aorta in Marfan syndrome

Several proteomic studies have been conducted on aneurysmal aortic tissue, and they have identified the following potential protein biomarkers[G 118]:

Adipocyte enhancer-binding protein 1 (AEBP1)	Fibronectin	Peroxiredoxin-2	Thrombospondin-2
α-1-antitrypsin	Filamin-A	TGM2	Transthyretin

[G] A biomarker is a measurable indicator of some biological state or condition.

Apolipoprotein A1	Heat shock protein beta-1 (HspB1)	SOD	Triosephosphate isomerase
Collagen XII	MMP-12	Tenascin	Vimentin
Fibrinogen	Periostin	TIMP-1	Vitronectin

However, many proteomic studies of aneurysmal tissue do not classify the samples in relation to the underlying pathology of the sample donors. Thus, in some cases, they used MFS aneurysmal aortae, but the obtained results become an average between the MFS and non-MFS aneurysmal aortae protein content.

To date, only one article has performed a proteomic analysis of only MFS aortic tissue[119]. They found higher amounts of filamin-A C-terminal fragment, calponin-1, vinculin, and myosin-10 in aortic tunica media of MFS aneurysm samples than in controls. Moreover, using immune-based techniques, it was demonstrated that MFS aortae had decreased MMP-2, increased MMP-12, increased MMP-14, reduced TIMP-3, and elevated TIMP-2 compared to control tissue[120]. This observed MMP and TIMP portfolio was different to that obtained from non-MFS ascending aorta aneurysms.

Besides these large protein studies, many other articles report differential protein contents between MFS and control aortae. The elastin content in human MFS aorta is almost 50% lower than control[24,121]. In MFS mice, there is upregulation of MMP-2 and 9[122], and MMP-9 expression correlated with aortic wall zones affected by elastolysis of lamellae[123]. Furthermore, our group has previously found that there is an increase in the contractile phenotype markers in cultured Marfan VSMC compared to control aorta cells, as well as augmented TGF-β signaling[93]. But at the same time, MFS cells showed a higher collagen secretion rate[93]. Nonetheless, these experiments were performed in conventional *in vitro* conditions, excluding the essential influencing factor of mechanical signals.

5.3. Aortic aneurysm pathogenesis in Marfan syndrome

In latest decades, the previously stated findings on the structure and protein composition of the aorta, among many others, have provided significant knowledge about aneurysm initiation and progression in MFS. In brief, the various manifestations of MFS are today considered to be the result of an overall abnormality in the homeostasis of the ECM, in which reduced or mutated forms of fibrillin-1 lead to alterations in the mechanical properties of tissues, increased TGF-β activity and signalling, and loss of cell-ECM interactions[40].

As previously mentioned, normal fibrillin-1 is the principal component of aortic lamellae microfibrils. Apart from the evident structural role of microfibrils in the ECM, they sequester certain signalling molecules. In particular, TGF-β is retained and inactivated

by LTBP proteins adhered to microfibrils[25]. Taking this into account, in MFS aorta, insufficient or dysfunctional fibrillin-1 induces an aberrant assembly of the lamellae, an impaired mechanotransduction in VSMC, and an increase of free bioactive TGF-β[38]. In detail, reduced or mutated fibrillin-1 originates weak lamellae that wear out prematurely under the physiological strength of blood pressure and provide impaired mechanical stimuli to VSMCs[38]. Additionally, VSMCs in the MFS aorta receive increased signalling due to the pathological overactivation of TGF-β, including excessive phosphorylation of SMAD and MAPK (former ERK) proteins through the TFG-β receptors (TGFRs)[34,38]. These cues induce over-secretion of MMPs that results in inappropriate tissue remodelling leading to an amplified weakening of the aortic wall[25,34].

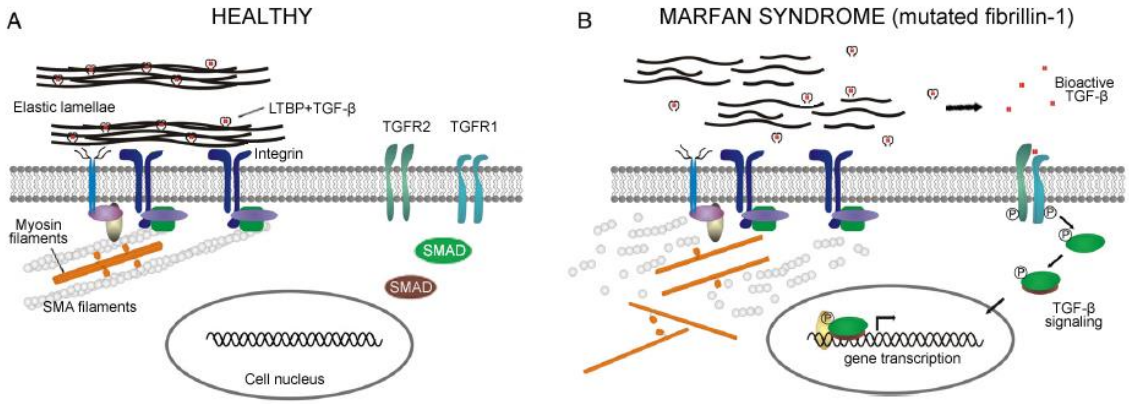

Figure 26. Hypothetical model of the pathogenic mechanism in aorta of MFS (adapted from ref. [124]). A. In healthy individuals, VSMCs sense the ECM via the elastin-contractile unit (lamellae, focal adhesion, and contractile apparatus). Also, TGF-β is sequestered by LTBP proteins associated to the fibrillin-containing microfibrils of the lamellae. B. Mutations in fibrillin-1 disrupt the tunica media ECM, leading to an altered mechanotransduction, and an increase of free, active TGF-β that promotes more intracellular signalling than in a healthy situation.

This explanatory model of pathogenesis allows understanding MFS aneurysm progression, as well as thoracic aortic aneurysm events due to other causes, since MFS has historically served as a prototype for thoracic aortic aneurysms[38,87]. Nevertheless, there are still knowledge gaps in this model that need further exploration. For instance, TGF-β has emerged as an important molecular factor of aneurysm progression. In MFS patients, higher levels of circulating TGF-β were shown to positively correlate with aortic root diameter and have therefore been proposed as biomarker for aortic risk[125]. TGF-β neutralising antibodies as well as the inhibition of TGF-β expression through cross-activating pathways have been shown to decrease aneurysm formation in the *Fbn1*$^{C1039G/+}$ animal model of MFS[113,126–128]. However, several subsequent studies have shown that TGF-β neutralisation increased aortic aneurysm size and rupture, for example in *Fbn1*$^{mgR/mgR}$ mice[129]. Thus, there is currently conflicting evidence for pathogenic versus protective roles for TGF-β in MFS aortic aneurysms[32]. The resolution of this conundrum might be relevant to find preventive or less invasive treatments for aneurysms occurring in MFS patients and related diseases.

OBJECTIVES

The overriding aim of this thesis was to perform a multi-scale and multi-approach analysis of the healthy and MFS aneurysmal-prone aorta based on the following idea:

“Innovative technologies can provide novel and relevant information about the histopathological remodelling and the protein content of the aortic wall in Marfan syndrome”

To corroborate this idea, the following specific objectives were posed:

1. Analyse the differential structural microscale arrangement of elastic lamellae in healthy and Marfan aortae by developing a multiphoton microscopy protocol.

2. Evaluate the differential histological integrity between healthy and Marfan aortic walls by implementing a microCT and image processing methodology.

3. Examine the differential protein levels associated with phenotypic modulation of healthy and MFS VSMCs cultured onto a newly designed bioreactor.

4. Assess the differential protein content between healthy and Marfan human aortae by creating a proteome database utilizing a literature-based analysis.

In this context, four novel technological methods were developed to generate relevant information on the structural and protein nature of the aorta. Taking into account the high component of technology development within this thesis, its description was incorporated in the results section, and afterwards, the application of the technology was characterised on MFS samples in comparison to healthy/wild-type ones. Additionally, given the diversity of each one of the four studies, the methods, results, and discussion sections were divided into four parts, plus a final joint discussion. The reader is encouraged to first read the results section, as the methods section is the finally established methodology after its development, explained at the results section.

MATERIALS AND METHODS

Part 1: High-resolution morphological approach to analyse elastic laminae injuries of the ascending aorta in a murine model of Marfan syndrome

1.1. Experimental animals and sample preparation

Nine-month-old Fbn1$^{C1039/+}$ mice and age-matched wild-type littermates were used in this study (n=4 for WT and n=6 for Marfan mice). Animal care and experimental procedures were approved by the University of Barcelona's independent Committee for Animal Welfare, according to the University of Barcelona's guidelines and the European Parliament Directive. The mice were on a C57B/6 genetic background and maintained as a heterozygous breeding colony in our animal room facility. Animals were sacrificed by isoflurane inhalation, and the aorta was surgically harvested from the aortic root until its suprarenal portion, and immediately rinsed in phosphate-buffered saline (PBS) and fixed in formol 10% overnight. Thereafter, aortae were cut longitudinally. The open aorta was placed on a glass slide covered with mowiol, and some small transverse cuts were performed to keep the tissue flat. Each aorta was mounted with the tunica intima facing the coverslip. For this study, only the tubular ascending aorta was used for imaging. A detailed map image of the entire sample was obtained by mosaic stitching of 308 bright field images of 0.8 x 0.5 mm field of view. Bright field images were acquired using a 10x 0.5 NA objective (Nikon) and Qimaging fast camera, with 0.46 µm pixel size.

Human aortic samples used for preliminary tests were collected from heart donors (n = 6) through the organ donation organisation at the Hospital Clínic i Provincial (Barcelona, Spain) and Hospital de Bellvitge de l'Hospitalet de Llobregat (Barcelona, Spain). Human tissues were collected with the required approvals from the Institutional Clinical Review Boards from both clinical centres and was accompanied by the patients' written consent conformed to the ethical guidelines of the 1975 Declaration of Helsinki.

1.2. Multiphoton microscope setup and image acquisition

The microscope setup consisted of a custom-made non-linear optics setting, based on a fully motorised Ti eclipse Nikon microscope. Multiphoton excitation was obtained using a Coherent mira900 titanium sapphire laser. The laser produced pulses of ~150 fs with a repartition rate of 76 MHz, and the power used at the back aperture of the objective

was 40 mW. To perform aorta imaging, the laser wavelength was set to 810 nm, producing at 405 nm a generation of second harmonic and efficient TPEF signals. The filters used were the following: Semrock FF720-SDi01-25x36 for TPEF/SHG generation; Semrock FF01750/SP-25 for TPEF detection; Semrock FF735-Di01-25x36 for SHG detection; and Semrock FF01-406/15-25 for forward SHG detection. Samples were visualised using a 40x 1.3 NA oil objective (Nikon) and the collection of the forward second harmonic signal was performed by means of a 1.4 NA oil immersion condenser. Image z-stacks of both signals (TPEF/elastin and SHG/collagen) were taken simultaneously by custom-made acquisition software coded in Labview. Image stacks were carried out at z-step 0.5 μm from the intima until 60 μm deep into the tissue. Acquisitions were taken at a pixel size of 0.29 μm, field of view 512x512 pixels, and averaged 5 times. Four image stacks at different anatomical locations were acquired for each aorta sample, and the exact location was assessed using the bright field image map of each sample.

1.3. Computational image processing

Quantitative data was obtained by an image processing protocol scripted in ImageJ macro language (figure 27). The elastin signal image stack was resliced to its YZ perspective, and automatically binary thresholded using the Niblack algorithm at radius 10 to generate an elastin binary mask. The resulting mask stack was separated into groups of 15 consecutive images (34 groups), and each group was manually processed to select the chosen elastic lamella and isolate it from the other lamellae. This segmented lamella mask stack was re-resliced to recover the XY perspective, and small errors of segmentation and thresholding were corrected by applying a binary erode routine of 50 iterations at range 5. Manual rectification of segmentation inaccuracies was executed when needed. The corrected lamella mask was applied to the original elastin image stack to obtain the isolated segmented lamella, and its maximal projection was created. Illumination intensity variations were adjusted. Sauvola local threshold at radius 5 was applied to the adjusted maximal projection image to create a fenestrae binary mask. Manual check and correction were performed to obtain a verified fenestrae dataset. From the fenestrae binary mask, individual area (μm^2) and density (fenestrae number/mm^2) of fenestrae greater than 1 μm^2 were measured for each lamella using the “analyse particles” algorithm. The number of elastic lamellae ruptures and their area were excluded from the analysis. The image processing protocol yielded maximal projections of 16 wild-type IEL, 16 wild-type 2^{nd} lamellae, 24 Marfan IEL and 24 Marfan 2^{nd} lamellae. A total of 6,400 fenestrae at all maximal projections were quantified.

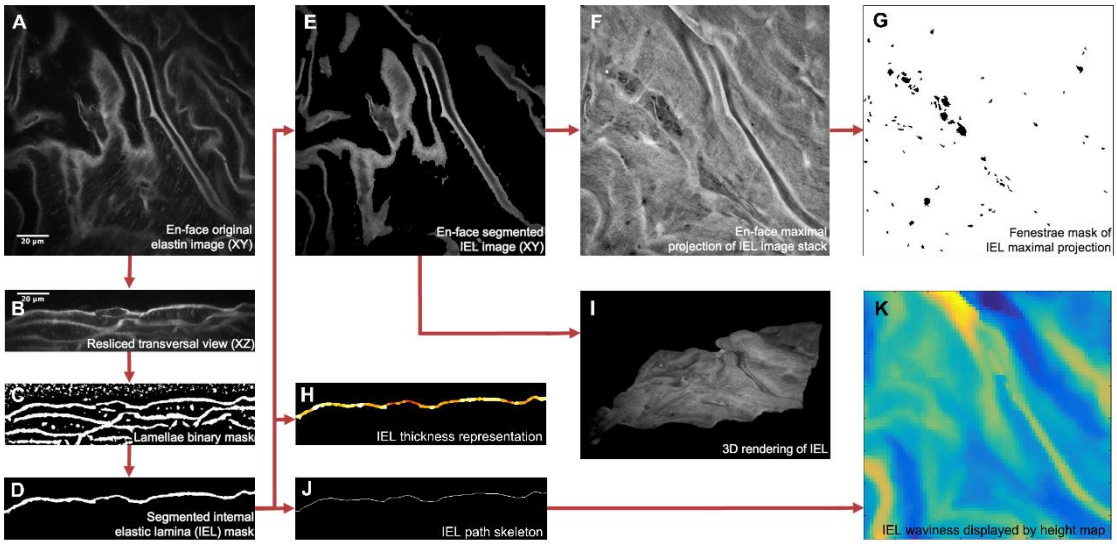

Figure 27. Image processing protocol to obtain en-face segmented elastic laminae and subsequent quantitative analysis. A. Representative image of an acquired original en-face TPEF stack. Elastin TPEF and background cell autofluorescence signals are visualized in grey scale. B. Representative image of the resliced original stack to transverse view. C. Representative image of the binary mask stack that was subsequently obtained. Elastin signal and some background spots are automatically marked in white, the rest of the tissue is marked in black. D. Representative image of segmented individual lamina mask stack. In this case, only the IEL mask was selected. E. Representative image of the resulting en-face IEL stack. F. En-face maximal projection comprised of all images within the IEL stack. G. Binary mask of all fenestrae seen at the maximal projection (F). H. Representative image of thickness display stack. Highest thickness is marked by white colour. I. 3D rendering of the lamella obtained from the IEL stack. J. Representative image of lamella skeleton image stack. K. Height map showing global lamella waviness. Yellow denotes low and dark blue high heights. Scale bar = 20 μm.

BoneJ plugin in ImageJ was used to automatically quantify lamella thickness from the segmented lamella stacks. For an accurate measurement, image stack voxel size was rescaled by 0.6 at the X and Y axis, so that voxels had isotropic dimensions (0.5x0.5x0.5 μm). Then the BoneJ specific measurement of thickness was applied onto each segmented lamella stack mask. Data was the mean thickness ±SD of the whole stack, and the programme provided a coloured representation of local thicknesses in each stack slice.

To quantify lamella waviness in ImageJ, the YZ segmented lamella mask stack was manually checked for any error in the continuity of the lamella. Next, 9 automated series of binary erode and dilate were applied to the lamella mask in order to smooth the mask surface without losing its path. The YZ mask stack was then converted into its skeleton (by the Skeletonize option), depicted as a black background and white single-pixeled line tracing the core path of the lamella and branches, in each one of the stack slices. The next step was to process the skeleton stack to erase all undesired branching. We developed a sophisticated automated algorithm run on MatLab (The MathWorks Inc., Natick, MA) that tracked each one of the white pixels in the skeleton and classified them into skeleton segments belonging to the lamellar core path or to a branch path. Once the

classification had been done in each stack slice, the algorithm joined only the core path skeleton segments to finally generate the clean lamella skeleton stack. However, due to simplification of the 3D lamella shape into a split 2D skeleton, the smooth lamellar continuity was somehow spoiled. Therefore, in ImageJ, 9 series of erode and dilate were used automatically, first in the XY perspective and then in the resulting YZ view. Finally, a complete clean accurate skeleton stack was obtained from each segmented lamella stack. Out of these, we applied another developed MatLab algorithm to generate height data. The algorithm tracked each white pixel in the YZ skeleton to get its height value in the Z axis, and relativised each value to the minimum height value of the whole skeleton. To eliminate noise or tiny details affecting the wave pattern, the XY image (made of the relativised height values) was rescaled by 0.15. Likewise, a possible general inclination of the lamella was also corrected from the relativised rescaled height image by subtracting its own 20 px Gaussian blurred image. In the end, these final height values were displayed as a height map where yellow denotes low heights and dark blue represents high ones.

1.4. Conventional histology

Formol-fixed mice aortae were dehydrated and embedded in paraffin. Five µm transverse sections were stained with Verhoeff-Van Gieson staining for visualisation of elastic fibres. The length of elastic laminae breaks was measured manually from 24 images, using ImageJ. The mean break length and standard deviation were calculated.

En-face TPEF lamellar rupture length corresponded to the rupture distance crossed by a vertical or horizontal line. To standardise, a 10x10 µm grid was superimposed on all the TPEF maximal projection images that showed lamellar ruptures (8 out of the 48 total Marfan images). Each rupture yielded multiple length values. The mean length of ruptures was calculated by averaging the multiple lengths obtained from all the ruptured images. The standard deviation was also calculated in order to show data dispersion. Ruptured images were relatively infrequent, distributed among half of the Marfan aortic samples, and their anatomical location was randomly selected.

1.5. Statistical method

Data were analysed using GraphPad Prism 6 (La Jolla, California, USA), and plotted as median and interquartile boxplots with minimum and maximum whiskers. As the datasets presented various distribution shapes, statistical analysis was carried out using the Kolmogorov-Smirnov nonparametric test. The value of $P \leq 0.05$ was considered statistically significant. The degree of significance was assigned as follows: * for $P \leq 0.05$, ** for $P \leq 0.01$, *** for $P \leq 0.001$, and **** for $P \leq 0.0001$.

Part 2: MicroCT imaging of remodelling and micro-scale damage in Marfan syndrome murine aorta

2.1. Experimental animals and sample preparation

Three, six, and nine-month-old Fbn1$^{C1039G/+}$ mice and age-matched wild-type littermates were used in this study (n=5 per group, 30 animals in total). Animal care and experimental procedures were approved by the University of Barcelona's independent Committee for Animal Welfare, according to the University of Barcelona's guidelines and the European Parliament Directive. The mice were on a C57B/6 genetic background and maintained as a heterozygous breeding colony in our animal room facility.

Animals were sacrificed by isoflurane inhalation, and their aorta was surgically harvested from the aortic root until its suprarenal portion. Mice aorta dissection was performed by first removing all the anatomical elements of their thorax. Secondly, once the aorta was visible, the adipose tissue was removed and the vessel was gently detached from the spine. Third, the aortic root was extracted from the inside of the heart by cutting the surrounding cardiac tissue. Also, the aortic arch branches were cut and the aorta at the abdominal level too. With this, the aorta was completely separated from the body. Finally, the aorta was placed on a Petri dish and, there, it was cleaned more thoroughly by removing blood and adipose tissue rests.

Samples were immediately rinsed in PBS and fixed in 4% PFA. Thereafter, aortae were dehydrated and embedded in paraffin, as for conventional histological preparations. Sample paraffin blocks were manually trimmed to remove embedding surplus surrounding the aortic vessel. Samples were vertically glued to a metal cryocap.

2.2. Synchrotron X-ray computed micro-tomography (microCT)

Aortic paraffin blocks were imaged at the I13-2 beamline of the Diamond Light Source (Didcot, Oxford, United Kingdom) by synchrotron phase-contrast microCT[72] (figure 28). Samples were scanned exposing them to the wide wavelength spectrum beam (pink beam, 20-25 keV) of synchrotron light at 0.14 seconds exposure time. The light was detected by a pco.4000 camera with a propagation distance of 200 mm. Scans consisted of 3001 projections over 180° at a 4x objective magnification, providing a 4.5x3 mm field of view and isotropic 1.1 µm voxel size. The region of interest of the sample was placed close to the centre of rotation to avoid imaging artefacts. Scan time was 15 minutes per sample (acquisition time, plus sample placement and acquisition setting).

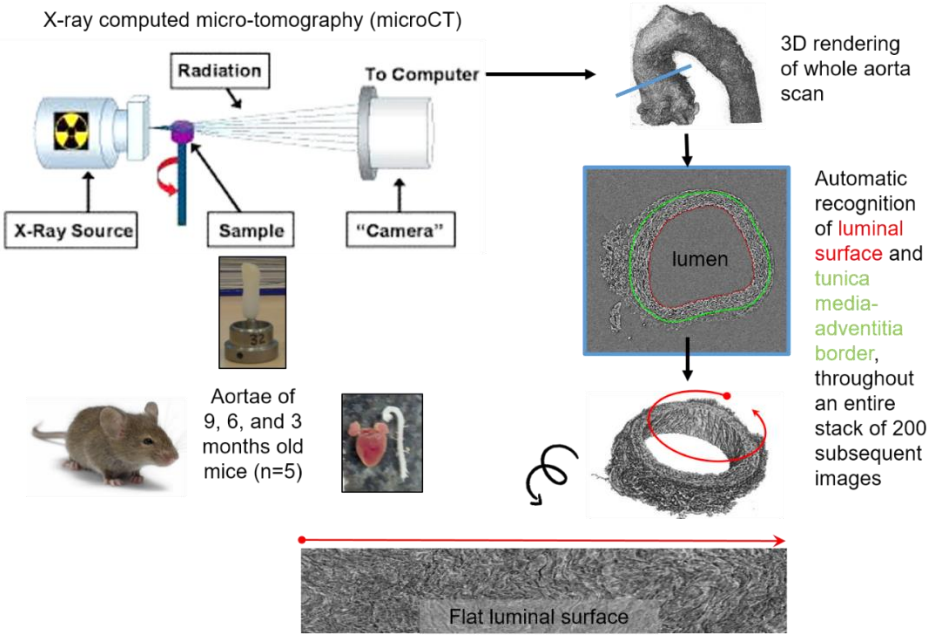

Figure 28. Study overview. Murine aortae were imaged by synchrotron-based microCT, and the obtained scans were computationally processed to evaluate histological parameters of tunica media (between the luminal surface in red and the media-adventitia border in green) and flat luminal surface morphology.

2.3. Computational image processing

Synchrotron scans were reconstructed via filtered back projection, with flat and dark correction and ring artefact suppression, without Paganin filtering, using the software provided at Diamond Light Source[130]. After this, the reconstructed image stacks were composed of 2,671 32-bit greyscale TIFF images each. Aortic image stacks were processed in Avizo software (FEI, Thermo Fisher Scientific) to generate a 3D volume-rendered image of the whole aortic vessel, by segmenting tissue out of surrounding paraffin by means of brightness threshold. The stacks were virtually rotated and resampled to obtain an image stack orthogonal to the ascending aorta tube, yielding perfect transverse virtual cuts of this vessel region. Finally, stacks were saved as 16-bit unsigned TIFF format. When necessary, any dirt or air bubble artefact present in the luminal paraffin was manually erased by painting on it with the same grey colour as paraffin, with ImageJ.

For 2D histological quantification, a central 200-images-portion of the ascending aorta stack was selected in all the samples. This cropped image stack was visualised and quantified by an in-house graphical user interface (GUI) developed in MatLab, which performed histological parameter quantification and also the necessary previous image processing. Briefly, every single image was firstly binarised to segment the aortic wall out of the surrounding external paraffin. Several morphological operations were applied to smoothen the segmentation. Then, to segment the tunica media from the adventitia, a first limit was automatically calculated by the GUI. To do that, the thickness of the aortic wall was computed in all the image slices by computing the Euclidean distance transform

of the binary mask and a line was established at the middle of the aortic wall throughout the circumference (this line was placed equidistant from both the wall-lumen and the adventitia-paraffin limits, so that it divided the aortic wall into two halves). Subsequently, the limit between media and adventitia layers was defined by dilating the mask that enclosed the inner half of the aortic wall, with a structural element of 0.35*minimum thickness of the aortic wall. This size of the morphological dilation was defined after visual inspection of several images, as it approximately fitted the real media-adventitia limit for all the different aortae sample groups.

The centreline of the aorta tube was calculated by performing a spline interpolation of all the lumen centroids computed in all the image slices. After automatically finding the centreline, a local Cartesian to Polar coordinates transformation was applied in order to virtually open the aorta, which meant that the aortic wall was converted from a ring into a straight line (fig 1C and 1D). This was achieved by using each point of the limit between the lumen and the aorta wall as a local centre for the coordinate values swap. The polar coordinates of the calculated media-adventitia limit were smoothened using a spline function. The GUI enabled the user to modify the limits manually in order to improve the automatic estimation of the media-adventitia limit. It is noteworthy to state that it was necessary to modify only 2 slices per sample out of the 200 being measured, since the GUI readjusted the rest of the images relying on the manual modifications. In summary, the media-adventitia and lumen-aorta limits were automatically found by the GUI, which allowed the generation of tunica media, aortic wall and lumen masks.

Once the media-adventitia limit was accurately delimited, the thickness of the tunica media, its cross-sectional area and the area occupied by lamellae were computed. The thickness was obtained by calculating the Euclidean distance between the media-adventitia and the media-lumen limits in each image slice. The distribution of all the thickness values in the aorta circumference of a slice was plotted as a histogram and then fitted to a Gaussian, and thus, the mean thickness and standard deviation were achieved for each slice in the stack. Cross-sectional area was calculated as the area of the tunica media mask. Then the medial mean thickness and mean cross-sectional area of the whole 200-slices stack and their standard deviations were obtained. To calculate the lamella area, the “highly contrasted lamellae” were segmented out by brightness thresholding the tunica media images, as the intensity of its pixels was higher than the rest of the image. Then the total number of lamella pixels was counted and divided by the area of the media to compute the % of medial space occupied by lamellae. Subtraction of lamellar area to the total medial area yielded the area occupied by the interlamellar spaces.

In the case of some aneurysmal samples, the GUI was not able to perform the media-adventitia limit nor the virtual opening step, since the vessel circumference was not circular but completely irregular. To overcome this issue, the brightest parts of the images (mainly lamellae) were thresholded and then a watershed algorithm was applied to the resulting binary mask un ImageJ, thus obtaining a mask of a closed tube. Next,

the ilastik software was used to identify and segment the lumen from all 200 slices, by means of the carving workflow. The resulting lumen mask was applied to the original images in order to create an aortic image stack with a black lumen instead of with a grey lumen. Then, the media-adventitia limit was manually outlined to allow segmentation of tunica media out of the rest of the image. With this, the in-house GUI was used to calculate the tunica media cross-sectional area and pixel amount, but it was not able to compute the thickness due to the irregularities in the vessel circumference. Therefore, the medial thickness of only two irregular samples was manually measured using ImagJ.

Lumen diameter values were obtained by approximating the vessel internal circumference to an ellipse and averaging its major and minor axes.

The luminal surface of the samples was obtained for all the whole ascending aorta region, which included a different number of image slices depending on the sample (anywhere from 200 to 800 slices). This region's image stack was virtually opened and lumen and tunica media were labelled, following the previously described procedure using the GUI. Next, using an in-house ImageJ macro, we were able to delineate the border between the lumen and the aortic wall, which corresponds to the location of the IEL. Binary dilatation of this limit by 7 pixels was the ideal to segment the entire IEL. Finally, we resliced the segmented IEL stack to the en-face perspective and generated the maximal projection of all the images to obtain the visualisation of the luminal surface. Quantification of lamella breaks in the maximal projection image was done by manually delimitating their contour and measuring their area, in ImageJ.

The 3D volume render of aortic tissue was generated using Blender software after manually processing the images with ImageJ. In brief, a small portion of the entire aortic scan was selected, and intensity threshold was applied to obtain the mask of the lamellae. Manual smoothening and cleaning of the mask was required. Then, a contour mesh was generated for the mask stack in Paraview software[131], rendering a lamellae 3D volume of the aortic tissue piece. Next, the number of mesh faces was reduced using Instant meshes software. Finally, the volumetric mesh of the lamellae was visualised by Blender software and a movie was recorded.

2.4. Statistical method

Data were analysed using GraphPad Prism 6 (La Jolla, California, USA), and plotted as the 5 data points corresponding to the mean value of each sample, and the group mean ± standard deviation (SD). Since the data did not follow a Gaussian distribution and also presented various distribution shapes, statistical analysis was carried out using the Kolmogorov-Smirnov nonparametric test. In the specifically mentioned cases, the F-test was applied to evaluate differences in data dispersion between groups, instead of differences in the mean value. The degree of significance was assigned as follows: # $P < 0.08$; * $P \leq 0.05$, ** $P \leq 0.01$, and *** $P \leq 0.001$.

Part 3: Impact of *in vivo*-like stretch on the phenotypic modulation of VSMCs of Marfan syndrome patients

3.1. Extraction of human VSMCs

Human VSMCs were isolated from tunica media of control and Marfan ascending aortas of patients using the primary culture explants methodology performed in our lab[93]. In brief, the aorta tube was opened longitudinally with a scalpel blade, and the endothelium monolayer was removed by scraping. Aorta was cleaned of fatty tissue and separated from intima and adventitia layers by peeling using forceps. Once the tunica media was isolated, it was placed in a new Petri dish with 5 mL of serum-free 231 medium (Gibco, USA), and it was cut into 1x1 mm cubes, named explants. Aortic media explants were transferred to 100 mm culture dishes and covered with 4 mL of 231 culture medium supplemented with 25 mL smooth muscle growth supplement from Gibco, supplemented with 25mL 100 mg/mL streptomycin and 100 U/L penicillin (i.e. complete medium). Cell cultures were maintained at 37°C in a humidified 5% CO_2 atmosphere. Explants were left undisturbed for 4 days to prevent detachment, and afterwards, the medium was changed every 4 days. One or two weeks later, once VSMCs had migrated out from the explants, the cells were trypsinised and routinely subcultured. Cells were frozen in DMSO and kept in a liquid nitrogen tank until we wanted to use them for the experiments. Primary cultures have limited expansion so they were used for experiments between passages 3 to 8.

3.2. Stretch bioreactor

The bioreactor consisted of a cell culture platform (chip) connected to a vacuum system (figure 29), as will be thoroughly explained in the Results section.

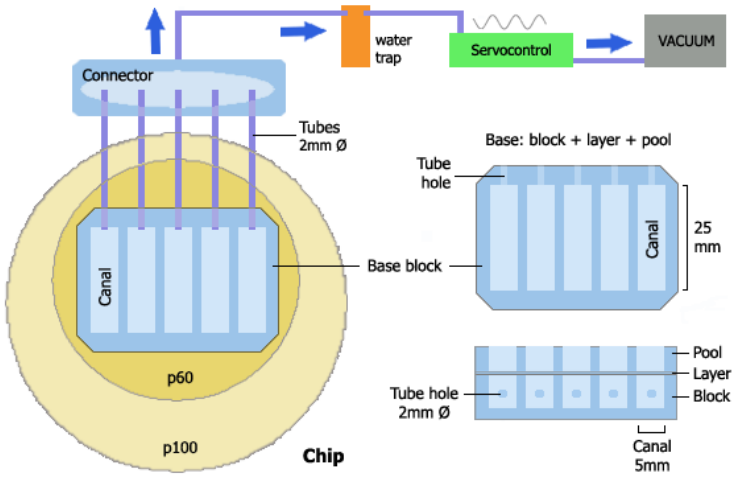

Figure 29. Stretch bioreactor components.

To fabricate the chip, each piece was made separately, and a new chip was built for each experiment. The pressure chamber, membrane, culture chamber, and connector were made of PDMS 1:10 mix (1 g of curing agent per 10 g of PDMS) in specifically shaped moulds. Once PDMS was poured into each mould, it was solidified at 60ºC for 1 hour.

On the lateral of the block, a P60 and a P100 culture dishes, five 2 mm holes were made with a 2 mm skin punch or drill for later introduction of tubes. Then, a 20 µm thick membrane was generated. Rectangular glasses were washed thoroughly with ethanol and were activated with high potency plasma treatment for 30 seconds. Then, we exposed the glass to Repel Silane vapour, which was used to prevent PDMS from sticking too much on the glass surface. Liquid PDMS was poured onto the activated glass, and the glass+PDMS was placed into a spin coater machine at 1000 rpm for 1 minute to achieve a membrane at the desired thickness (20 µm). After this spinning step, the glass+PDMS was placed onto a slide warmer (95ºC) during 20 minutes to solidify the PDMS membrane.

To assemble the complete chip, in order to facilitate the adhesion, the membrane and the pressure chamber were activated again with plasma treatment and attached one to another. To ensure the correct union between them, the borders were sealed with PDMS. Then the pressure chamber+membrane block was separated from the glass, and was glued with liquid PDMS to a P60 culture dish and, in turn, this P60 was glued to a P100. Next, 2 mm tubes were introduced through the holes of the P100, P60, and pressure chamber, and after, every hole was sealed with PDMS. Once the chip was constructed, its mechanical performance was checked by connecting it to the vacuum system. If the membrane stretched properly under cyclic negative pressure application, the chip was finally prepared for posterior cell culture: sterilisation by ultraviolet light (UV) for 1 hour, sealed with Parafilm (Sigma), and storage at room temperature until it was needed for an experiment. Each chip was disposable, just like normal culture cell dishes, so chips were built every time from scratch for each experiment.

3.3. VSMC culture onto chip

Two or three weeks before the experiment, frozen human VSMCs were thawed and cultured to achieve enough cell number to seed them onto chips. On the chip cell seeding day, a culture chamber and the surface of a chip (membrane) were activated with plasma treatment, at maximum power for 1 minute. The culture chamber was adhered to the membrane, and the whole chip assembly was sterilised by UV for 20 minutes. Then the membrane was coated with fibronectin (F4759, Sigma) at 10 µg/mL for 1h at 37ºC, placed into the incubator. Meanwhile, cells were detached from the conventional culture dishes with trypsin (1 mL), centrifuged, resuspended in serum-free 231 media (Gibco, USA), and counted. Once fibronectin coating incubation was finished, canals were

carefully rinsed with phosphate-buffered saline (PBS), and then, cells were seeded at different cell concentration regarding its posterior use:

- 60,000 cells were seeded on the canals aimed to carry out protein extracts.
- 30,000 cells per canal were seeded for posterior immunocytochemistry analysis.

Cell cultures on chip were maintained in an incubator at 37ºC in a humidified 5% CO_2 atmosphere and were nourished with complete 231 media that was changed every 3 days, as it is conventionally done. Cells were left unstretched overnight to allow their adhesion to the chip membrane, and the day after, the vacuum system was activated to generate stretching of the membrane. Finally, the effect of stretch on the VSMCs was analysed by immunocytochemistry and western blot at different exposure times: 0 (no stretch, only overnight adhesion), 3 and 7 days. Each replicate experiment involved the same primary cell line seeded at the same time onto three chips, each one intended for one of the 3 exposure times.

Conventional cell culture at 0, 3 and 7 days was also performed as comparison control condition (inherently unstretched). Cells were seeded onto 230 mm^2 round coverslips for immunocytochemistry (30,000 cells) or 962 mm^2 culture wells for western blot (240,000 cells). Those substrates were fibronectin-coated as in the chips, or were not coated as in conventional experiments. Cell seeding was made at the same time for conventional and for chip cultures, and both cell cultures were kept in the same incubator. We performed this experiment with VSMCs from three different Marfan patients, as well as three different control patients.

For the bioreactor's optimisation tests, the following coating procedures were applied:

- Poly-D-lysine (PDL) coating. Incubation during 2 hours at 37ºC of 10 µg/mL PDL on the PDMS substrate, and posterior drying at the laminar flow cabinet.
- Collagen coating. Incubation during 3 hours at 37ºC of 10 µg/mL collagen on the PDMS substrate, and posterior rinsing with PBS.
- Gelatin coating. Dilution of 0.1 g of gelatin powder in 50 mL PBS, then incubation of this 0.2% gelatin on the PDMS substrate during 1 hour at 37ºC, and posterior rinsing with PBS.
- PDL-collagen or PDL gelatin coatings. First, PDL coating as described above, and secondly, collagen or gelatin coating as detailed above.

3.4. VSMC immunofluorescence

For immunocytochemistry analysis, VSMC seeded on the canals or glass coverslips were fixed with 4% PFA in PBS for 10 minutes and rinsed afterwards in PBS thrice. Subsequently, cells were incubated with 50 mM ammonium chloride pH 7.4 for 20 minutes to block the reactivity of aldehyde groups of the PFA. Then, the samples were rinsed in PBS and permeabilised with PBS 0,1% saponin 1% bovine serum albumin (BSA) for 10 minutes. Primary antibodies were incubated for 1 hour in a humid, dark

chamber. After rinsing the cells thrice, they were incubated with the secondary antibodies plus phalloidin-FITC for 45 minutes. All the antibodies were diluted in PBS 1%BSA. The membranes of the chip in which the immunostaining had been performed were dissected with a scalpel, cutting through their rectangular contour. The cut membranes were mounted with the mounting medium DAPI-fluoromount-G on microscopy glass slides and covered with a rectangular coverslip. In the case of immunostaining of cells on coverslips, coverslips were mounted on slides with the same mounting medium. All the procedure was performed at room temperature.

Stained structures by this protocol were ECM collagen I (goat anti-collagen I, 1/40, Abcam; + Alexa Fluor® 488 anti-goat, 1/250, Abcam), cytoplasm SMA (mouse anti-SMA, 1/500, Sigma; + Cyanine Cy™3 anti-mouse, 1/250, Jackson), transgelin (rabbit anti-transgelin, 1/500, Abcam; + Alexa Fluor® 647 anti-rabbit, 1/250, Invitrogen), actin cytoskeleton (FITC-labelled phalloidin, 1/500, Sigma), focal adhesions (mouse anti-vinculin, 1/400, Sigma; Alexa Fluor ® 546 anti-mouse, 1/250, Jackson) and nuclei (DAPI, from the DAPI-fluoromount-G mounting medium, Southern Biotechnology Associates).

Fibrillin-1 immunocytochemistry was performed following the methanol protocol adapted by Dr Reinhart's lab. In brief, samples were fixed, blocked, and permeabilised during exactly 5 minutes with 70% metOH+30% acetone cooled at -20ºC. Then, samples were incubated with 10% FBS for 30 minutes, rinsed, and the antibodies were added orderly as described in the above immunofluorescence protocol. Used antibodies were: rabbit anti-fibrillin-1, 1/1000, provided by Dr Reinhart, and Alexa Fluor® 488 anti-rabbit, 1/250, Molecular Probes.

Focal adhesion staining by anti-vinculin-A546 antibody complex was imaged with the 60X objective. Focal adhesions of ten cells of 10 images for each condition were analysed by ImageJ applying a threshold that distinguished the vinculin staining. With this, the number and the size of vinculin stain spots were measured. Hence, the number of focal adhesions per cell area (density) and the ratio between vinculin area and cell area (cell occupation percentage) were obtained.

In the case of cell directionality assessment, actin cytoskeleton staining by FITC-phalloidin was imaged with the microscope 10X objective with the Hokawo program. The direction of all cells was manually marked in five images of each condition of each experiment. All direction marks were analysed by ImageJ thresholding to obtain their angle value. Angle values ranged originally from 0º to 180º, so values in the range of 90º to 180º were converted to the range of 0º to 90º by a simple conversion factor. Also, the angles were corrected by the angle of the chip's cut membrane, since not all mounted membranes were placed exactly horizontal, in parallel to the microscope slide. Once the angle conversions were done, the direction of all cells was quantitatively analysed in reference to applied stretch direction.

SMA staining was viewed in an epifluorescence microscope, and Cast software was used to count the number of cells (nuclei by DAPI), the number of cells with SMA fibres, with diffuse SMA staining (without fibres), and without SMA staining.

3.5. VSMC protein analysis

Cells seeded on chips were lysed adding 200 µL of RIPA lysis buffer (10 mM Tris-HCl pH 7.5, 1 mM EDTA pH 7.5, 0,5mM EGTA, 1% Triton X-100, 0,1% sodium deoxycholate, 0,1% sodium dodecyl sulfate (SDS); 140 mM NaCl) containing proteases (Aproptin 1/1000, Pepstatin A 1/1000, Leupeptin 1/1000, and Phenylmethylsulfonyl fluoride 1/200) and phosphatase inhibitors (Sodium Orthovanadate 1/100) into the chip canals. The membrane was softly scrapped with a scraper for the cells to detach and start to lysate by the action of the buffer. Cell lysates were placed into an eppendorf, homogenised with a 30G needle (30 strokes), and left 30 minutes on ice. After, they were centrifuged at 1000 g for 10 minutes at 4ºC. The supernatant was placed into a new eppendorf, and protein concentration was determined with the colourimetric DC Protein Assay from Bio-Rad (Hercules, CA, USA).

Western blot was performed using 5 or 10 µg of protein lysates. Samples were prepared by mixing the protein lysate with 5 µL of loading buffer 5X, containing 10% β-mercaptoethanol. They were loaded on a 10% SDS -polyacrylamide gel, subjected to electrophoresis for ~80 min (35 mA per gel) and transferred to nitrocellulose membranes (Promega, USA). The membranes were blocked with 5% BSA diluted in Tris-buffered saline (TBS). Then, they were incubated overnight with primary antibodies, diluted in TBS with Tween buffer (TBS-T) (20mM Tris-HCl, 150 mM NaCl, 0.1% Tween-20) containing 0.02% of sodium azide and 1% of BSA. Used primary antibodies were: anti-SMA (mouse 1/4000, Sigma), anti-transgelin (rabbit 1/7500, Abcam), anti-collagen I (goat, 1/1000, Millipore), anti-elastin (mouse, 1/5000, Sigma), anti-calponin-1 (rabbit, 1/1000, Sigma), anti-alpha-actin (mouse, 1/20000, Sigma), and loading control anti-GAPDH (mouse 1/1000, Abcam). The following day, blots were rinsed three times with TBS-T for 10 minutes and were incubated with anti-mouse IgG HRP conjugate (1/3000; Promega) or anti-rabbit IgG HRP conjugate (1/3000, Promega) secondary antibodies for 1h in 2,5% BSA diluted in TBS-T. Blots were rinsed thrice with TBS-T for 10 minutes and were covered with western blotting luminol reagent (Santa Cruz, Delaware, CA, USA) on a cassette. Bands were visualised by exposure of the membrane to hyperfilm (Amersham Pharmacia Biotech, Uppsala, Sweden) in a dark room. Band intensities were measured by densitometry scanning of the film using ImageJ software.

3.6. VSMC RNA analysis

Total RNA (ribonucleic acid) was isolated using TRIzol protocol (Invitrogen, USA). Briefly, culture media was removed, cells were washed in PBS, and samples were homogenised in 200 µL TRizol using a scrapper. After incubation of the lysed samples for 5 min at room temperature to permit the complete dissociation of the nucleoprotein complexes, 150 µL of chloroform was added. Cold centrifugation at 12000 g for 15 minutes separated the mixtures into three phases: lower red, phenol-chloroform, protein phase, middle viscous white, DNA-containing phase, and the upper colourless, aqueous RNA phase. The RNA was precipitated from the aqueous phase by mixing it with 375 µL cold isopropanol and centrifuging it again. The RNA pellet was washed with 75% ethanol and left to dry. RNA pellet was finally dissolved in 20 µL of RNase-free water. The RNA concentration and purity were quantified by Nanodrop (Agilent, USA).

cDNA from 1 µg total RNA was synthesised at a thermal cycler using the High Capacity Reverse Transcriptase kit (Applied Biosystems, USA), following the conventional PCR (polymerase chain reaction) procedure. Subsequently, the cDNA products were used to detect collagen I, myocardin and GAPDH expression by 1.5% agarose electrophoresis in combination with the KAPA2Gfast kit. Gel bands were visualised and imaged in an ultraviolet light chamber.

3.7. Statistical method

All data were analysed using GraphPad Prism software (La Jolla, California, USA). Significance degree was assigned as follows: *P value <0.05; ** P value <0.01; ***P value < 0.001; ****P value <0.0001.
Focal adhesion quantitative data were expressed as the mean ± SD of vinculin area and of the number of focal adhesions per μm^2. Statistical analysis was carried out by nonparametric Mann-Whitney test since a small size sample should be assumed as non-Gaussian.
Analysis of SMA staining patterns was expressed as the mean of the percentage of cells with each corresponding staining pattern.
Western blot data were expressed as the mean ± SD. The ratio between the protein content of SMA and transgelin was made in relation to the loading control GAPDH. Statistical analysis was performed with a two-way ANOVA.

Part 4: Definition of a literature-based proteome of the human aorta

4.1. Literature processing and database building

Manual literature review aided by previous text mining filtering were adapted from Hibbert *et al*.[132]. In brief, all published scientific articles containing information about proteins in human aorta were sought at the Web of Science database (more detail is explained at the Results section). The information of all the retrieved articles in this search was extracted as plain text using the webpage's "save to" utility. Then, a custom-made bioinformatics text mining code processed the extracted data to provide an MS Excel spreadsheet listing the relevant keywords contained in the abstracts of all the articles[132]. Manual revision of each article record was performed to detect the articles that actually provided information on specific proteins present in the human aortic tissue. When one relevant article was found, it was carefully read, and the following information was extracted and put in an MS Access database: protein name, technique used for protein presence detection (mass spectrometry and/or immune-based methods), article unique DOI, and, if stated, protein location within tissue (tunicae intima, media, adventitia and/or other), aortic portion (ascending, abdominal, descending thoracic, or aortic root), age and sex of sample donor, and affectation that occasioned the aortic tissue donation. Afterwards, the database protein record was complemented with general information about the individual protein: official name, UniProt accession number, and encoding gene name. In the onset of an article that mentioned an already annotated protein in the database, its DOI was added to the already existing protein record. Once revision of the whole article list was finished, we assumed that the proteome was complete. Notably, all this procedure was performed to generate two databases that contain the human Aorta Proteome and the human Aortic Aneurysm Proteome.

RESULTS

Part 1: High-resolution morphological approach to analyse elastic laminae injuries of the ascending aorta in a murine model of Marfan syndrome

In the context described in the introduction section, our aim was to provide further insights into the characterisation of elastic lamellae microstructure. Therefore, a confocal multiphoton microscopy and computational methodology was developed, which generated the en-face TPEF image of segmented individual lamellae from unstained whole aortic samples. Then, this methodology was applied to ascending aorta samples of Marfan syndrome mice, as a histopathological model of tunica media alterations that typically occur in aortic aneurysms.

1.1. Technology development: Multiphoton microscopy and image processing

1.1.1. Optimisation of multiphoton microscopy acquisition

To obtain high-quality en-face images of intact mice aortae that allowed a detailed assessment of lamellae microstructural alterations, a new method was established involving tissue preparation, image acquisition, processing, and analysis. Image acquisition by confocal multiphoton microscopy was performed at Institut de Ciències Fotòniques (ICFO) premises. Their setup was a custom-made multiphoton microscope, which permitted parallel visualisation of TPEF and SHG, among other signals. The first attempt to image murine aortic tissue demonstrated that this setup was able of simultaneous visualisation of the elastic lamellae by elastin TPEF signal and collagen fibres by SHG (figure 30) of a vascular sample. Thereafter, one could perform an en-face (XY perspective) confocal stack running into the tissue in the Z-axis (z-stack) to acquire the whole thickness of the sample, and then the stack could be visualised transversally (XZ or YZ perspectives, figure 30A) and in 3D (XYZ, figure 30B) by ImageJ software.

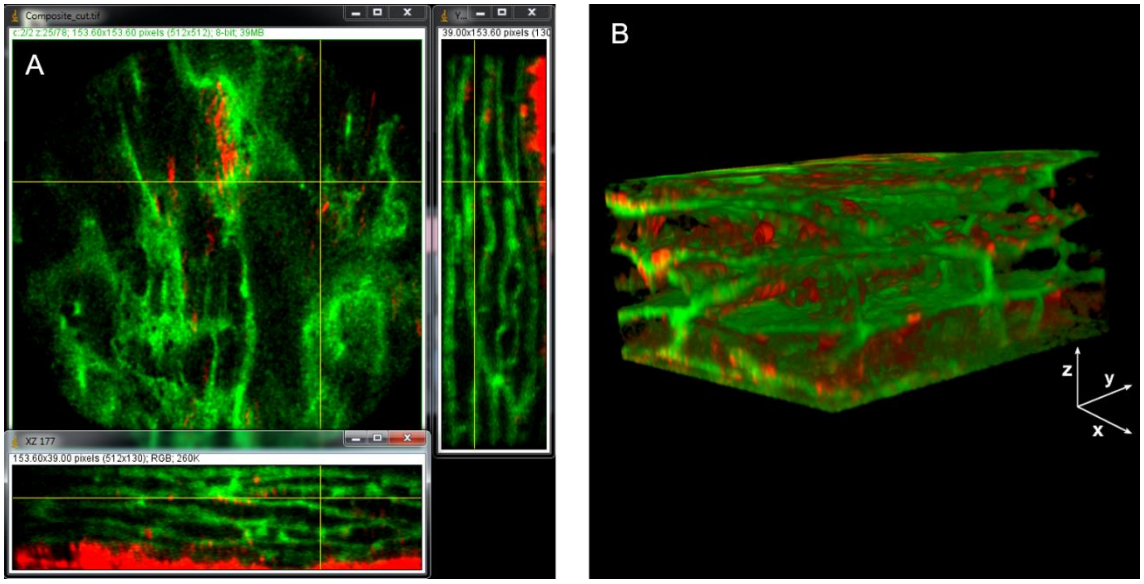

Figure 30. Representations of a multiphoton confocal z-stack of murine aortic tissue. A. Z-stack displayed by ImageJ orthogonal views utility. The central panel shows a particular image of the originally acquired en-face z-stack, while the lateral and lower panels show the two possible transversal perspectives of the tissue (YZ and XZ). B. Volumetric rendering of the tunica media of murine aortic tissue. Elastin is marked in green, collagen in red.

Despite performing the acquisition in a dark room, these first images were noisy (see that black zones in figure 30 are crowded with diffuse green granules). To overcome this issue, the microscope was covered with a black cape, which effectively attenuated the surrounding light (figure 31). Thus, the use of this cape was mandatory for subsequent captures.

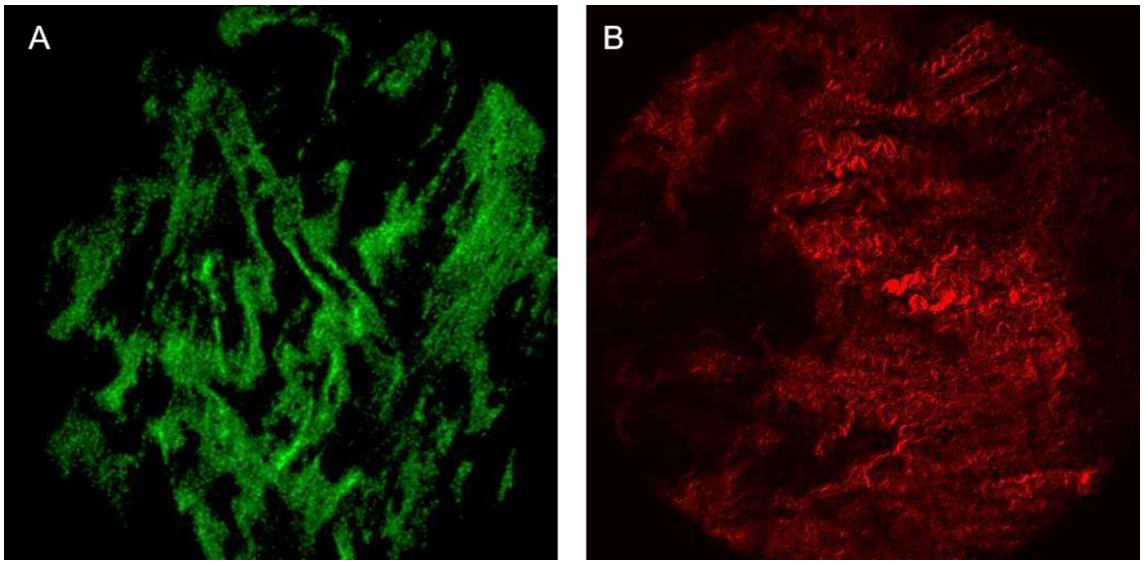

Figure 31. Multiphoton confocal acquisition of murine aortic tissue, using a black cape. A. Single confocal image of TPEF signal corresponding to elastic lamellae. B. Single confocal image of SHG signal corresponding to medial collagen fibres. In comparison to figure 1, note that image noise was almost inexistent.

For these first acquisitions, laser power was set to 30 mW so that it was possible to capture collagen both from the tunica media and the adventitia in the same z-stack (figure 32). However, to obtain sharper and more intense images of medial collagen, laser power should be augmented (figure 32C). Conversely, the laser should be turned down to desaturate the adventitial collagen images (figure 32A).

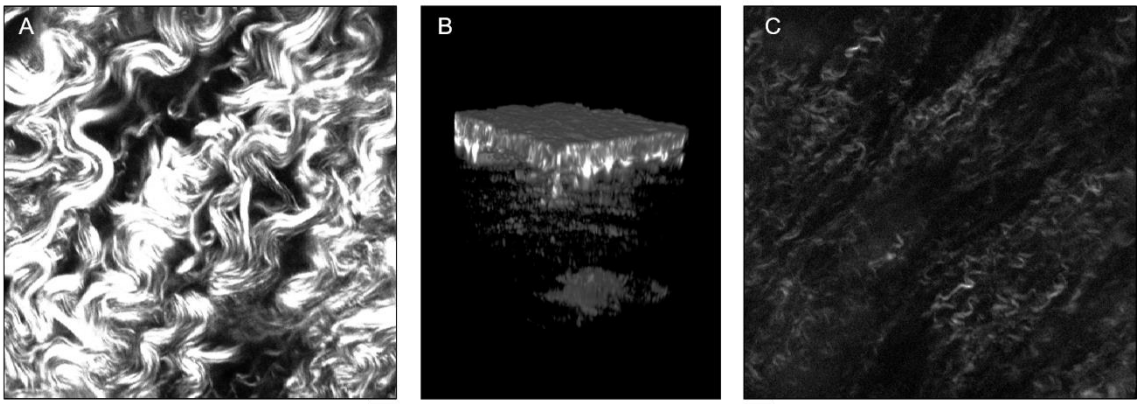

Figure 32. SHG confocal acquisition of murine aortic tissue at 30 mW laser power. A. Single confocal image of SHG signal at the tunica adventitia level. Signal saturation happens in the absolute white regions. B. Volumetric rendering of SHG signal z-stack of the aorta. Both tunicae collagens were distinguishable by their brightness intensity: adventitial collagen mesh on top, and medial collagen below and arranged in layers. C. Single confocal image of SHG signal at the tunica media level. Medial collagen is here visualised at low intensity.

Besides, in these assays, some samples had the aortic tissue placed with the endothelium in contact with the coverslip, and others on the opposite side. The comparison of both situations evidenced that the adventitia layer produced a drastic effect on the microscope light: when the light crossed the adventitia first, its intensity was highly attenuated, and consequently, the tunica media was hardly imaged (figure 33A). This loss of signal was due to ordinary light absorption by the abundant collagen mesh, and it was evident at ~50 μm inside the tissue. In contrast, light incidence firstly through the tunica intima had a milder effect on the light intensity, consequently, the tissue could be imaged further down (figure 33B). Taking this into account, as the aim was to study the tunica media, the subsequent samples were all mounted with the tunica intima placed in contact with the coverslip, i.e. placed facing the light source.

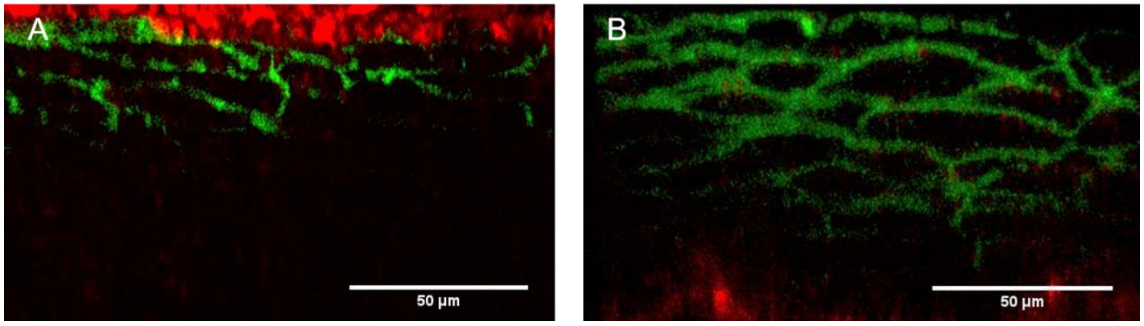

Figure 33. Microscope light penetration into an aortic tissue sample. A. Tunica adventitia placed in front of the light source. B. Tunica intima placed in front of the light source. Notice the depth of the light penetration in each case. Light incidence comes from the top of the figure. Elastin is marked in green, collagen in red. Scale bar = 50 µm.

In addition, the stack z-step size was set in accordance to the Nyquist criterion: in order to not lose information, the sampling rate should be 2*B (in our case, B is the length of the z-stack in the Z-axis). Taking into account that tissue thickness of our aortic samples was around 80 µm, but some samples achieved 100 µm, the z-stack length was grossly averaged to 100 µm since the z-stacks had to cover the full thickness of the tissue. Accordingly, sampling rate was required to be (2*100=) 200 images per stack, implying a 0.5 µm z-step size. Consequently, all z-stacks from now on were acquired with this z-step size, even though the sample was thinner than 100 µm.

In summary, the subsequent aortic tissue z-stacks were consistently performed at 0.5 µm z-step size, with total surrounding light deprivation, and laser power higher than 30 mW.

1.1.2. Optimisation of the sample preparation

Up to this point, the used samples were randomly-located, small pieces of paraformaldehyde (PFA) fixed aortae that were positioned flat in between the microscopy mounting glasses. To standardise the sample preparation protocol for this study, first, the fixation reagent was verified. Formol and glutaraldehyde were tested, besides PFA (figure 34). The result was that formol provided a more uniform and intense fluorescence signal than PFA (compare figure 34B versus A). Besides, glutaraldehyde fixation converted the elastin TPEF pattern to “blue” and stimulated the emergence of autofluorescence of the interlamellar space components (figure 34C). Therefore, formol was established as the standard fixation reagent.

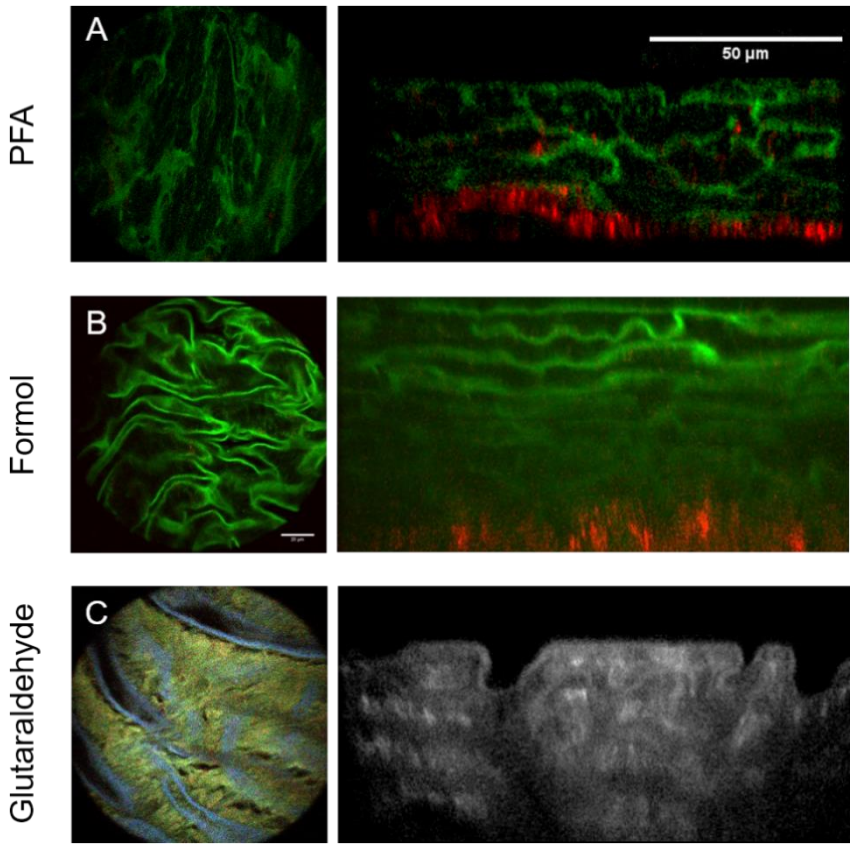

Figure 34. Fixation reagents assessment. En-face (left column) and transverse (right column) confocal images of murine aorta fixed with PFA (A), formol (B), or glutaraldehyde (C). In A and B, elastin is marked in green and collagen in red. In C, elastin is marked in blue and the interlamellar space components in yellow (colour resulting from the mixture of the green and red fluorescence channels). The transverse image is displayed without colouring to show the presence of fluorescence everywhere in the wall. Tunica intima is placed at the top of all the transverse images. Scale bar = 50 µm.

Despite the encouraging results of the first acquisitions, other parameters required verification. This is the case for the tissue structural modifications owing to sample fixation and flattening. A mouse was perfused with formol in order to obtain an aorta fixed at physiological pressure to have a realistic reference. Two narrow rings were dissected from this aorta, and one of them was cut to open the ring circumference. Both intact and open perfusion-fixed rings were mounted on microscope slides, in the transverse position, and were imaged by multiphoton microscopy. The obtained images of both perfused rings showed that lamellae were straightened due to the applied intraluminal pressure by the perfusion procedure (figure 35A and D). Additionally, another murine aorta was harvested the same day as the microscopy acquisition, and two rings were dissected out: one was left fresh to know the native configuration of unpressurised lamellae, and the other was directly fixed by immersion in formol. Moreover, transverse images of the samples used up to this experiment were added to the analysis, as a representation of a fixed and then open sample. Examination of these samples' acquisitions revealed that the lamellae in these latter three conditions had a similar wavy aspect (figure 35), demonstrating that neither fixation nor ring opening after fixation leads

to significant modification in lamellae conformation. Besides, this wavy aspect was like that displayed in conventional histological preparations often presented in published articles. Therefore, open vessel fixed samples were a valid representation of an unpressurised aorta.

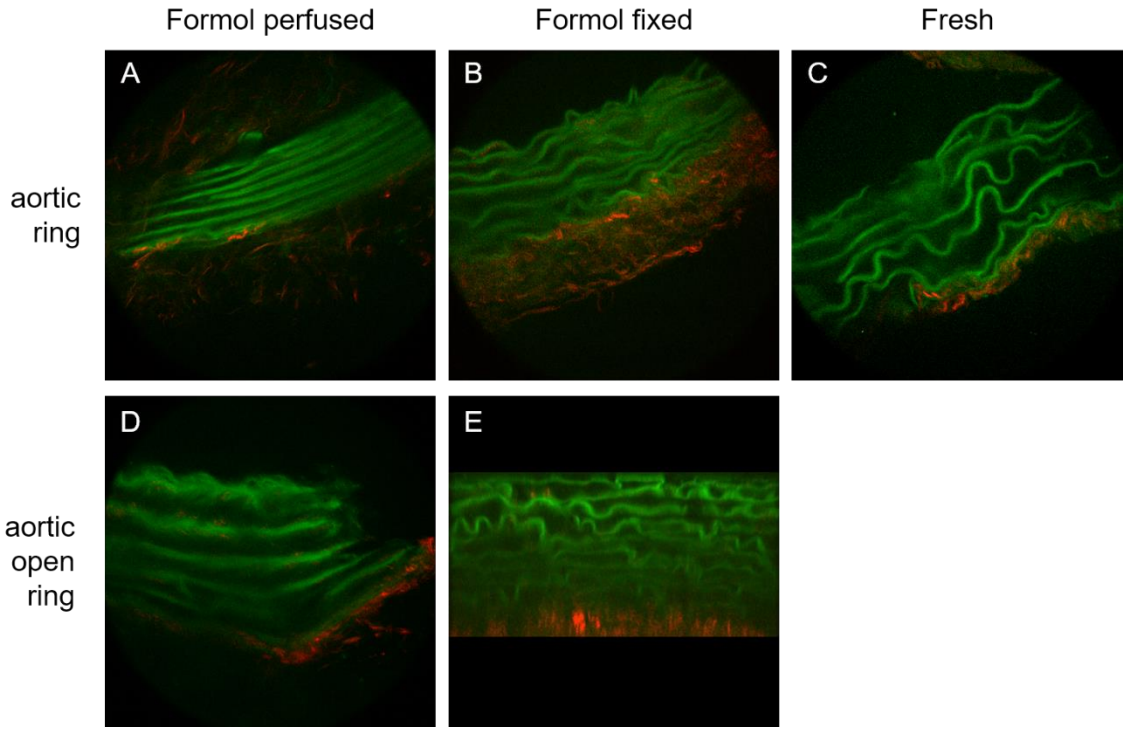

Figure 35. Assessment of lamellae conformation in different fixation procedures. A. Formol-perfused aortic ring sample. B. Aortic ring sample fixed in formol. C. Fresh aortic ring sample without fixation. Note the initiation of degradation. D. Open formol-perfused aortic ring sample. E. Aortic sample fixed in formol and then cut open. This image belongs to a previously acquired en-face z-stack.

Next, the uniformity of lamellae structure along the aorta tube was verified. A prominent difference between the aortic root and the tubular ascending aorta was observed in terms of lamellae wrinkling (figure 36). This change was clearly seen in bright field microscopy (figure 36A) and also at TPEF signal acquisition (figure 36B). Specifically, in the aortic root, lamellae were very straight, and there was almost no interlamellar space (figure 36A), resembling a pressurised vessel (figures 35A and D). Conversely, the tubular ascending aorta presented wavy lamellae paths and, at least, a few microns separation between lamellae. As aortic aneurysms typically occur at the tubular ascending aorta of $Fbn1^{C1039G/+}$ mice, in the following acquisitions, we focused on this anatomical zone.

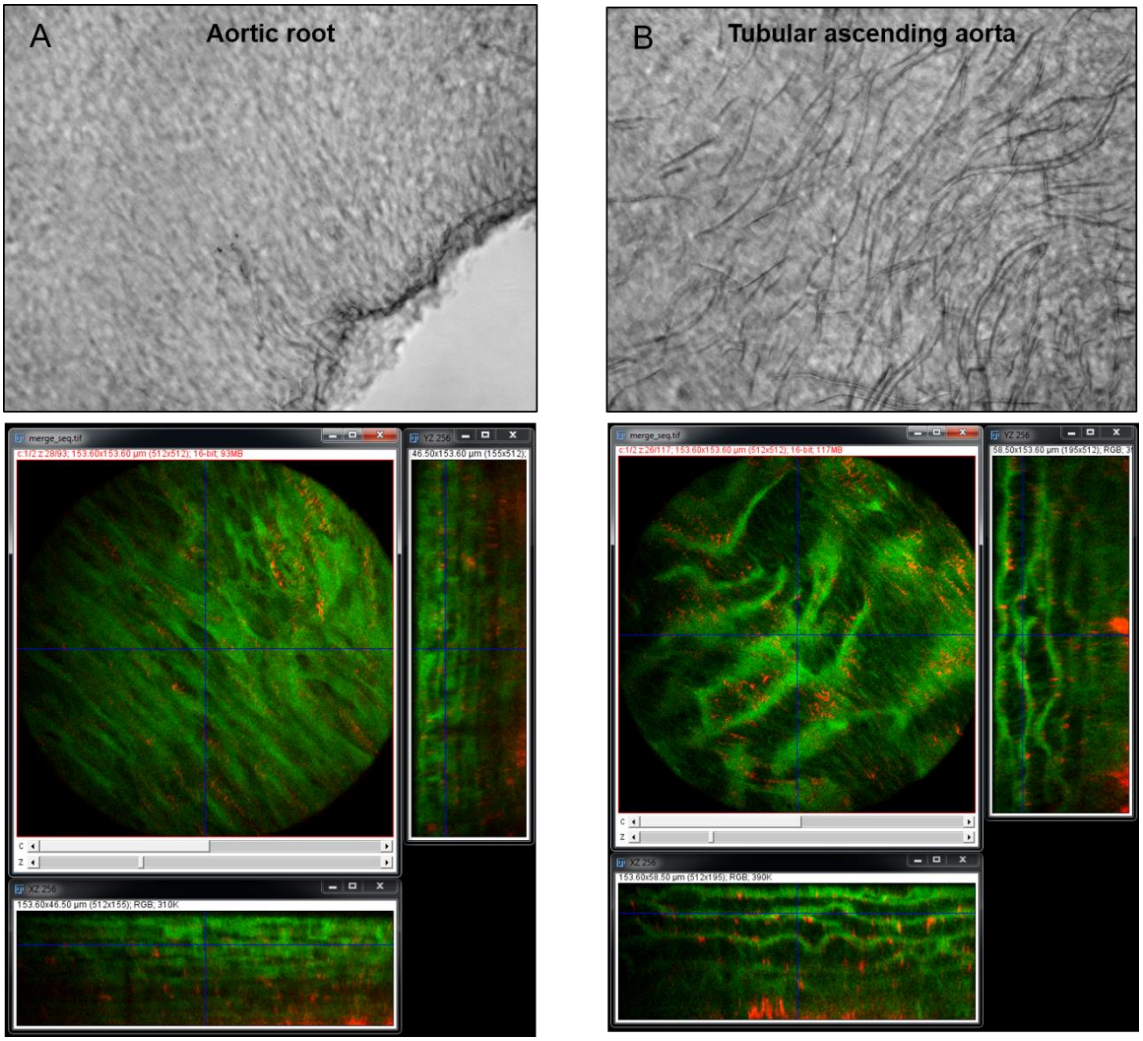

Figure 36. Lamellae conformation at different anatomical sites. Aortic tissue imaging at the bright field (upper panels) and the multiphoton (lower panels) microscopies of aortic root (A) and tubular ascending aorta (B). Multiphoton microscopy panels show the sample at en-face (central) and transverse (lateral and below) perspectives, with elastin in green and collagen in red.

Moreover, in some previously imaged aortae, we noticed that second acquisition after two months displayed TPEF signal also for aortic cells, besides lamellae. See the large endothelial cells on top of the IEL, and the VSMCs packed between lamellae in figure 37A and B, respectively. Often, the directionality of the cells was evident.

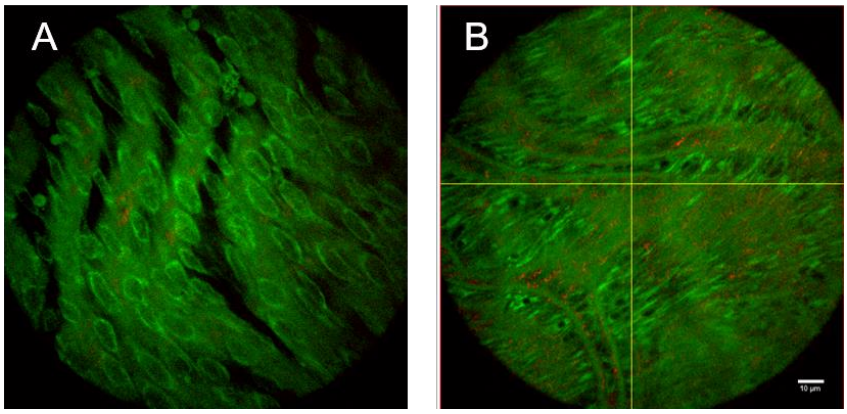

Figure 37. Aortic cell autofluorescence. A. Endothelial cells at tunica intima, plus the initiation of the IEL. B. VSMCs at tunica media, all aligned to the same direction. Elastin is marked in green, collagen in red. Scale bar = 10 µm.

The cell autofluorescence was a problem because its signal was indistinguishable from the elastin one (figure 37 and 38). The most probable explanation for this phenomena was that, in general, samples continued slowly degrading even though they were fixed, and cell autofluorescence emergence was an indication of this degradation. To verify this hypothesis, some samples used one month before were imaged, and the new images were compared to the old ones (figure 38B versus A). Indeed, the appearance of cell autofluorescence was obvious. Thus, we established that no more than 30 days could pass between animal sacrifice and microscopy acquisition.

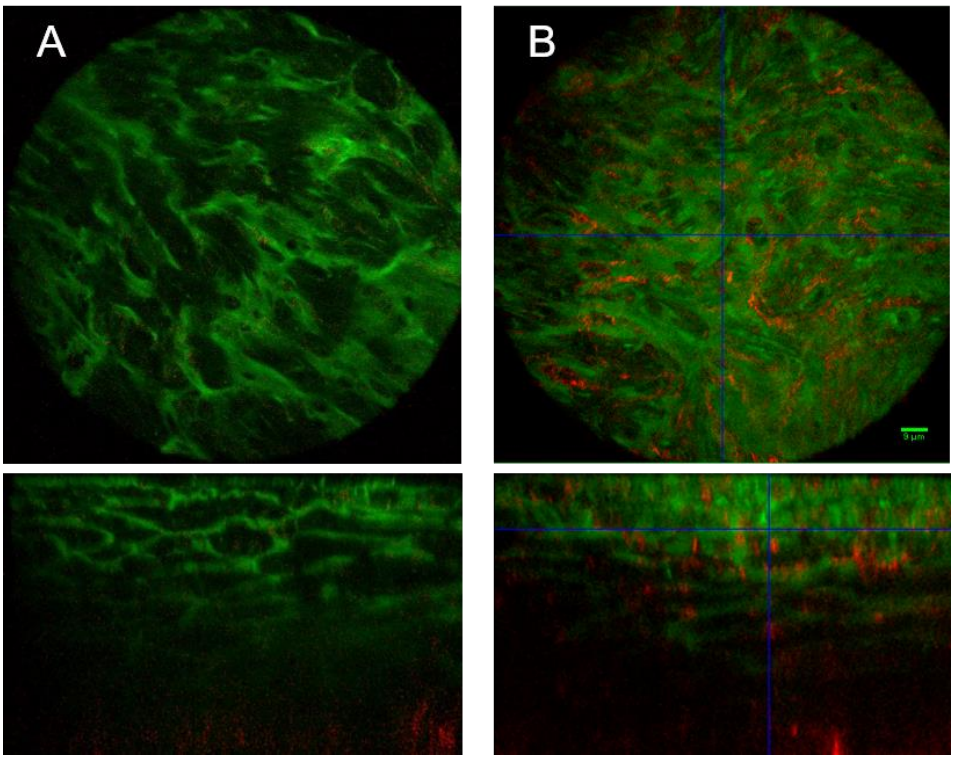

Figure 38. Aortic cell autofluorescence emergence in the same sample. A. Initial images of the aortic sample at en-face (upper panel) and transverse (lower) perspectives. B. Images of the same sample after 40 days. Note the apparition of green fluorescence in between lamellae. Collagen signal was sharper in B due to the microscopy acquisition improvements made during the 40 days. Elastin is marked in green, collagen in red. Scale bar = 9 µm.

In summary, the following definitive acquisitions were performed by applying all the established sample and microscope variables:

- formol fixed and afterwards cut-open aortae,
- recently sacrificed animal,
- endothelium facing the light source,
- imaging of the tubular ascending aorta,
- acquisition in total darkness,

- 0.5 µm z-step size,
- laser power higher than 30 mW.

Notably, acquisitions consisted of an en-face z-stack of confocal images, beginning at the tunica intima and running until the elastin signal became too low for accurately visualise lamellae.

Furthermore, the gathered knowledge on mice aorta imaging was implemented to make acquisitions of human aortic samples (figure 39). However, taking into account that the thickness of human tissue was ten times thicker than the murine, it was not possible for the microscope light to pass through the human tissue. Consequently, samples had to be physically cut into ~100 µm thick slices. To do so, the human samples were embedded in low melting agarose and were cut with a vibratome. Transverse imaging of the obtained slices revealed that human aortic tissue was more complex than that of mice (figure 39A). Despite several attempts, it was very hard to cut the sample in parallel to the luminal surface, thus we were not able to achieve any en-face visualisation of the human tissue (figure 39B and C). For this reason, we decided to continue the project with mice aortae and to keep the human samples for perhaps a second phase of the study.

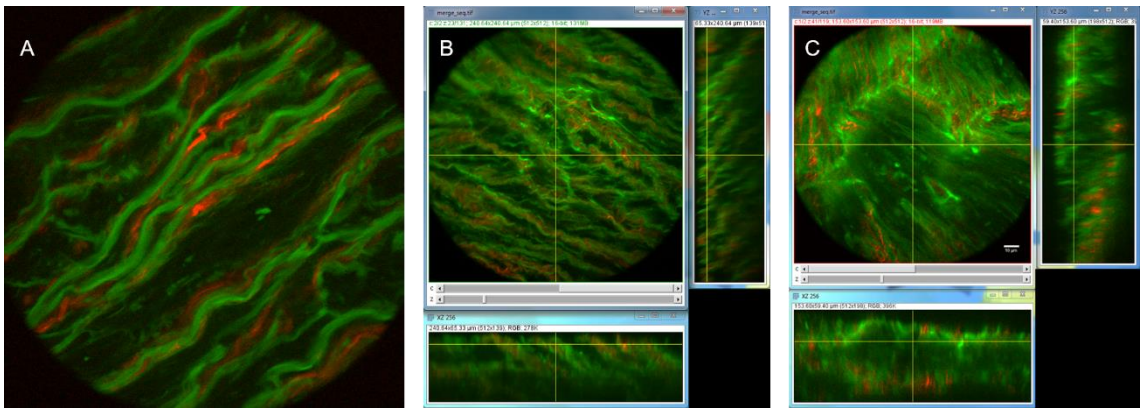

Figure 39. Human aortic tissue acquisitions by multiphoton microscopy. A. Transverse perspective of the human aortic wall. B and C. Oblique perspectives of the human aortic wall as attempts to obtain en-face slices. Note that the cut in C is closer to be in parallel to the lamellae or luminal surface than B. Elastin is marked in green, collagen in red.

1.1.3. Image processing of aortic elastin z-stacks

Once image acquisition parameters were fully optimised, quantification of histological features on the en-face tissue images was performed. However, to precisely measure those features in a standardised manner, images needed additional computational processing before. Hence, we first proceeded by observing the particularities of the images and then by scripting code to process them in accordance with the observations.

The series of consecutive transverse images of TPEF elastin signal often showed the progression of lamella branching, small breaks, crosslinking between neighbouring lamellae, and/or abrupt ending of lamellae (figure 40). These findings showed that aortic elastic lamellae were arranged in a 3D cage-like network, with irregularities that disrupted the apparent parallel arrangement seen in conventional histological preparations.

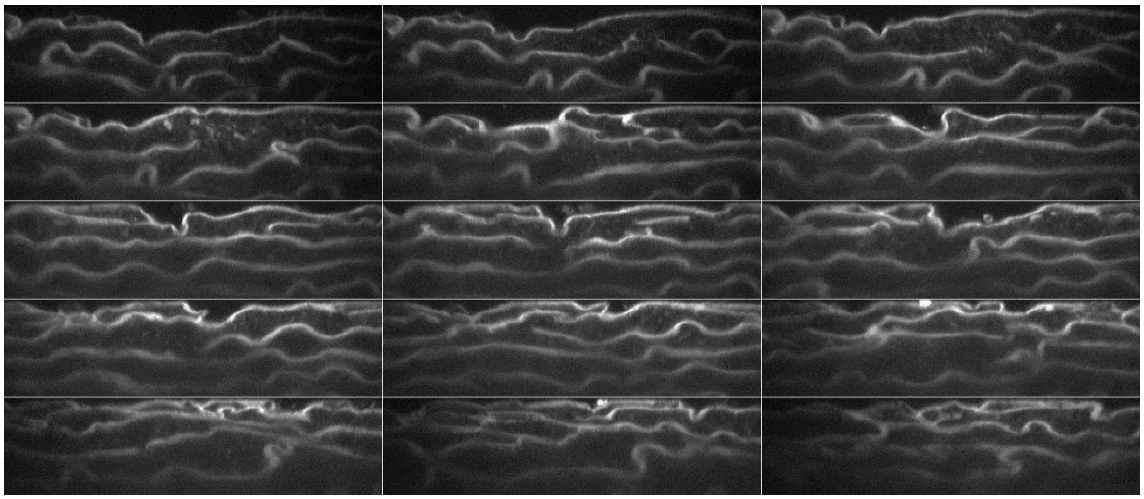

Figure 40. Consecutive image sequence of elastin signal at transverse perspective. Sequential progression is from left to right. Brighter grey signal displays elastic lamellae. Progression throughout the volume shows lamellae branching, crosslinking, and breaks.

However, the transverse view did not allow detailed lamellae microstructure visualisation. Hence, segmentation of individual lamellae out of the acquired TPEF z-stack was then necessary. Consequently, to work with *clean* individual elastic lamella images, a semi-automatic segmentation protocol was developed in ImageJ software that processed the original elastin stack (figure 41) (for further detail, refer to the Materials and methods section). Briefly, each en-face z-stack (XY) (figure 41A) was virtually resliced to build its corresponding transverse image stack (YZ) (figure 41B), and then binary auto-threshold function was used to discriminate the elastin signal from the background (figure 41C). The chosen elastic lamella was then manually selected, and a new mask image stack was created with only this selection (figure 41D). The complete lamella mask stack was resliced back to the en-face view, and it was applied to the original one (figure 41A) to generate the image z-stack only of the selected individual elastic lamella (figure 41E). Finally, all the images of the lamella z-stack were joined into a maximal projection in the Z axis (figure 41F), in order to produce a single image that provided the 3D information of the lamella.

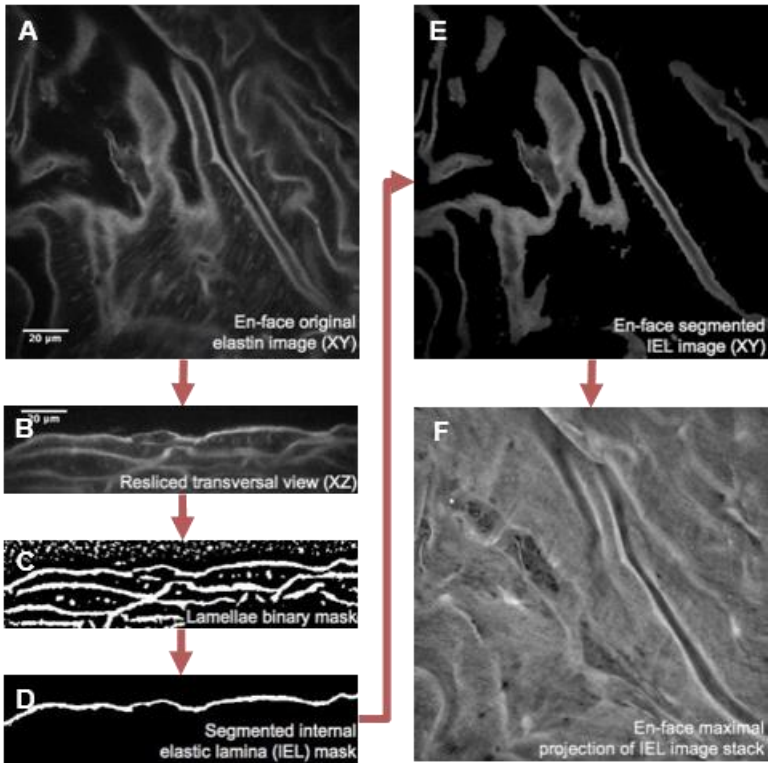

Figure 41. Image processing protocol to obtain en-face segmented elastic laminae. A. Single confocal image of an original en-face TPEF z-stack. Elastin TPEF and low background autofluorescence signals are visualised in grey scale. B. Representative image of the transverse stack obtained by reslicing the original stack. C. Representative image of the binary mask stack that was subsequently obtained by thresholding. Elastin signal and some background spots are automatically marked in white, the rest of the tissue is marked in black. D. Representative image of segmented individual lamina mask stack. In this case, only the IEL mask was selected. E. Single confocal image of the resulting en-face IEL z-stack. F. En-face maximal projection comprised of all images within the IEL stack. Scale bar = 20 µm.

It is relevant to state that the developed ImageJ method had several automatic steps, but the segmentation of the lamellae was basically manual as their shapes were excessively irregular for a simple computer code to understand it. Some subsequent manual correction was also required to recover the original pixels placed within the fenestrae and ruptures (completely black spots in figure 42 upper panel). Additionally, the illumination of the images was corrected by subtracting a white image.

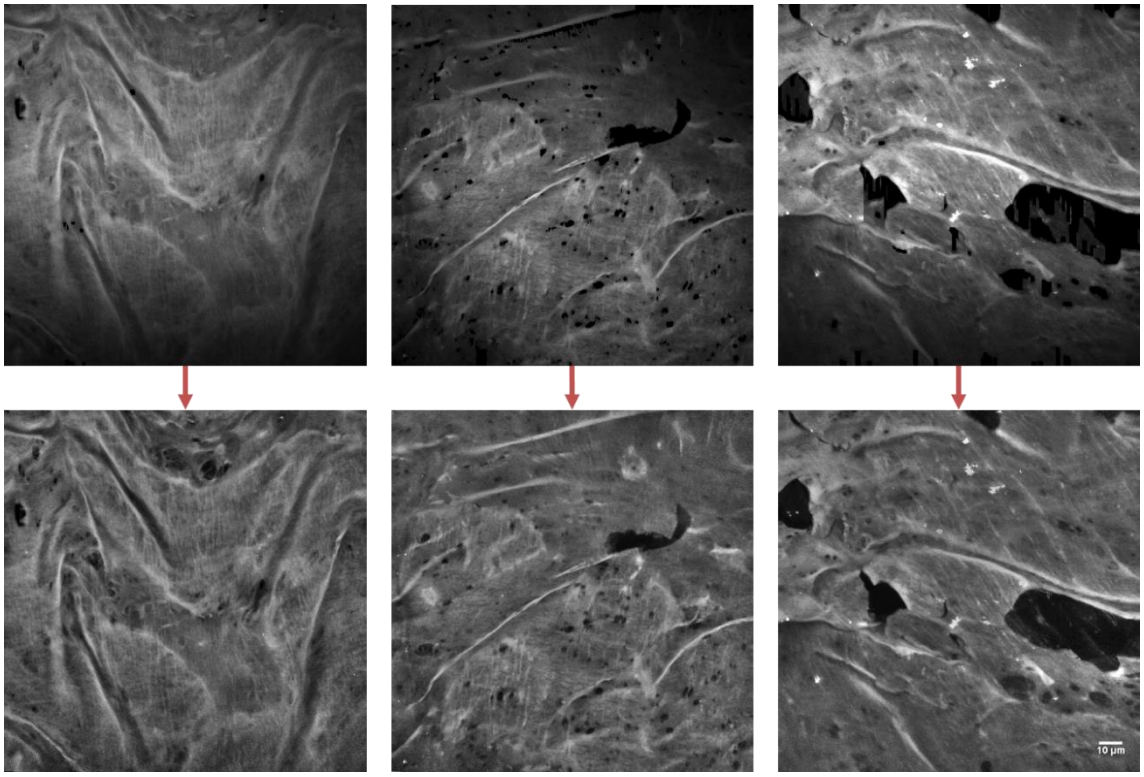

Figure 42. Manual correction of lamellae maximal projections. Upper panel shows maximal projections obtained after threshold and segmentation. The lower panel shows the same maximal projections after detailed manual correction and illumination flattening. Scale bar = 10 µm.

Furthermore, the maximal projection revealed topological and structural information of a single lamella, as it displayed its surface (figures 41F and 42). Dark holes in the maximal projection of individual lamella were identified as lamellar fenestrations, and they were selected and extracted to constitute a fenestrae map (figure 43C). From this map, morphological analysis was carried out to assess the density and size of fenestrae.

Another lamellar feature that could be evaluated from the image acquisitions was the waviness of each lamella. To this aim, a new approach was developed based on measuring the height of each lamella pixel at the en-face z-stack (figure 43). This procedure, however, required a single Z-axis height value per XY pixel position. To this aim, a protocol combining ImageJ and MatLab software was created, which produced a single-pixel skeleton of the lamella and removed any existent branching on it (for further detail, refer to the Materials and methods section). Once the lamella skeleton was *clean* (figure 43F), the MatLab code evaluated its waviness in terms of height variation in the Z-axis. Height values were organised into histograms and waviness maps represented by colours ranging from yellow (the lowest height) to dark blue (the highest height) (figure 43G).

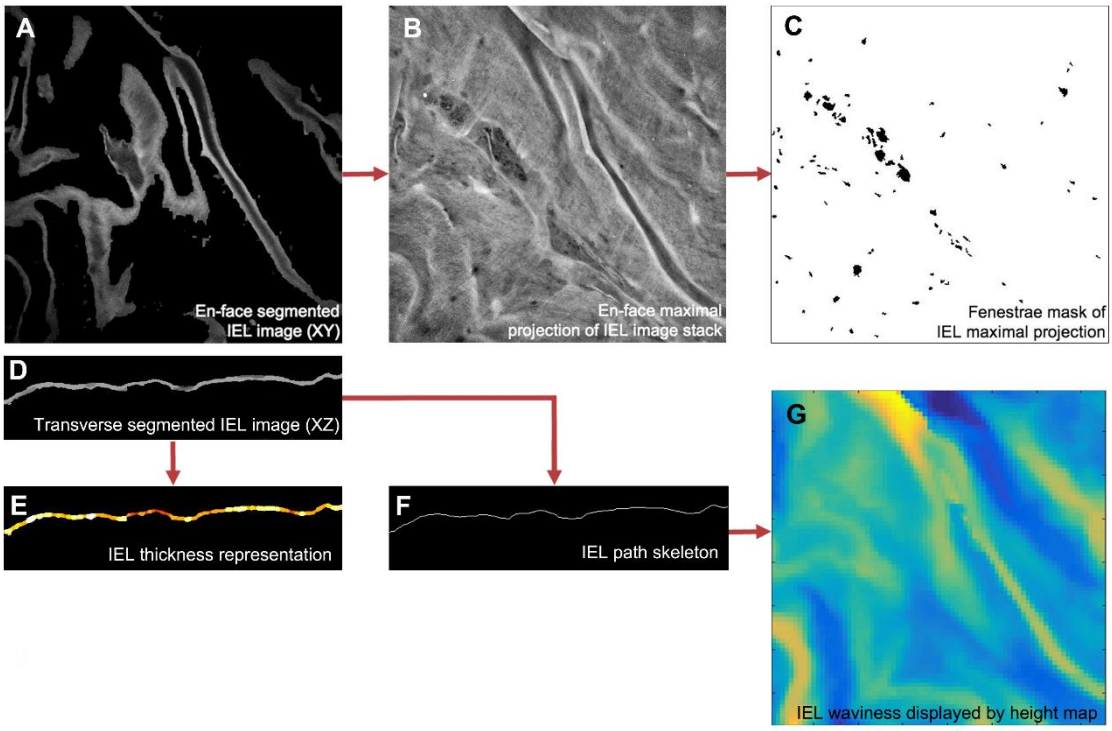

Figure 43. Image processing for quantitative analysis. A. Single confocal image of the en-face segmented IEL z-stack. B. En-face maximal projection of the IEL stack. C. Binary map of all fenestrae seen at the maximal projection (B). D. Single transverse image of segmented IEL stack. E. Single image of thickness display stack. Highest thickness is marked by white colour. F. Single image of lamella skeleton image stack. G. En-face height map showing global lamella waviness. Yellow denotes low height and dark blue high height.

Moreover, the images could also be used to assess lamellae thickness, without any further procedure, by applying the already published BoneJ plugin for ImageJ. This program quantified lamella thickness and generated a visual colour representation from blue (lowest thickness) to white (highest thickness) (figure 43E).

1.2. Technology application to murine Marfan aortae

As explained above, a complete methodology was developed for quantifying lamellae morphological features. Next, the aforementioned methodology was applied to examine in detail the elastic lamellae in the ascending aortic tissue in wild-type (WT, n=4) and Marfan mice (MF; *Fbn1*$^{C1039G/+}$ model, n=6). To begin, the entire aorta was dissected from the animal and immediately fixed in formol. Then, the vessel was cut in half longitudinally and mounted with the tunica intima facing onto the cover slide. Four en-face z-stack acquisitions were randomly taken from the tubular ascending portion of each aorta sample. The IEL and the elastic lamina located just underneath it (2nd lamina) were segmented and analysed (figures 41 and 43). In particular, the maximal projection of each of the segmented lamellae was generated, and fenestrae density and size data

was quantified from them. Lamellae thickness and waviness were also measured for each image stack.

Observing the samples, the transverse view of the aortic wall obtained by TPEF (figure 44A and C) closely matched what was seen in conventional histological preparations using Verhoeff-van Gieson staining (figure 44B and D). Specifically, Marfan tissue visualised by both techniques showed lamellae disruptions and disarrangement (figure 44C and D) compared to WT tissue (figure 44A and B).

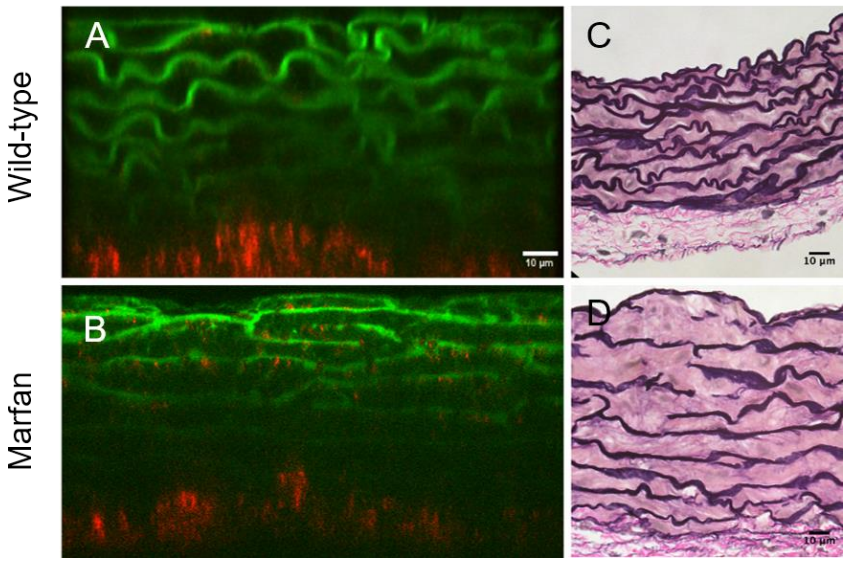

Figure 44. Transverse aortic tissue visualisation by multiphoton microscopy (A and C) and conventional histology (B and D) of wild-type (A and B) and Marfan (C and D) samples. In multiphoton images, elastin is marked in green and collagen in red. Conventional histological preparations were set using Verhoeff-van Gieson staining that marked lamellae in purple. Scale bars, 10 µm.

The multiphoton en-face maximal projections showed that the IEL in WT animals had a flat, continuous aspect with unevenly distributed small fenestrae, which are visualised as small black holes (figure 45A). In contrast, the IEL in Marfan mice showed more prominent fenestrae and occasional large ruptures (figure 45B). Despite having an identical genetic background, Marfan mice showed variable lamina aspect patterns. However, the differences with WT mice were evident. Additionally, the structural differences between WT and Marfan 2nd laminae were even more evident than in the IEL (figure 45). To note, the lamellae shown in figure 16 are matched pairs, which means that in reality, each 2nd laminae corresponds to the IEL displayed above it. In some cases, the 2nd lamella exhibited the imprint of the IEL waves (see last WT lamellae pair in figure 45).

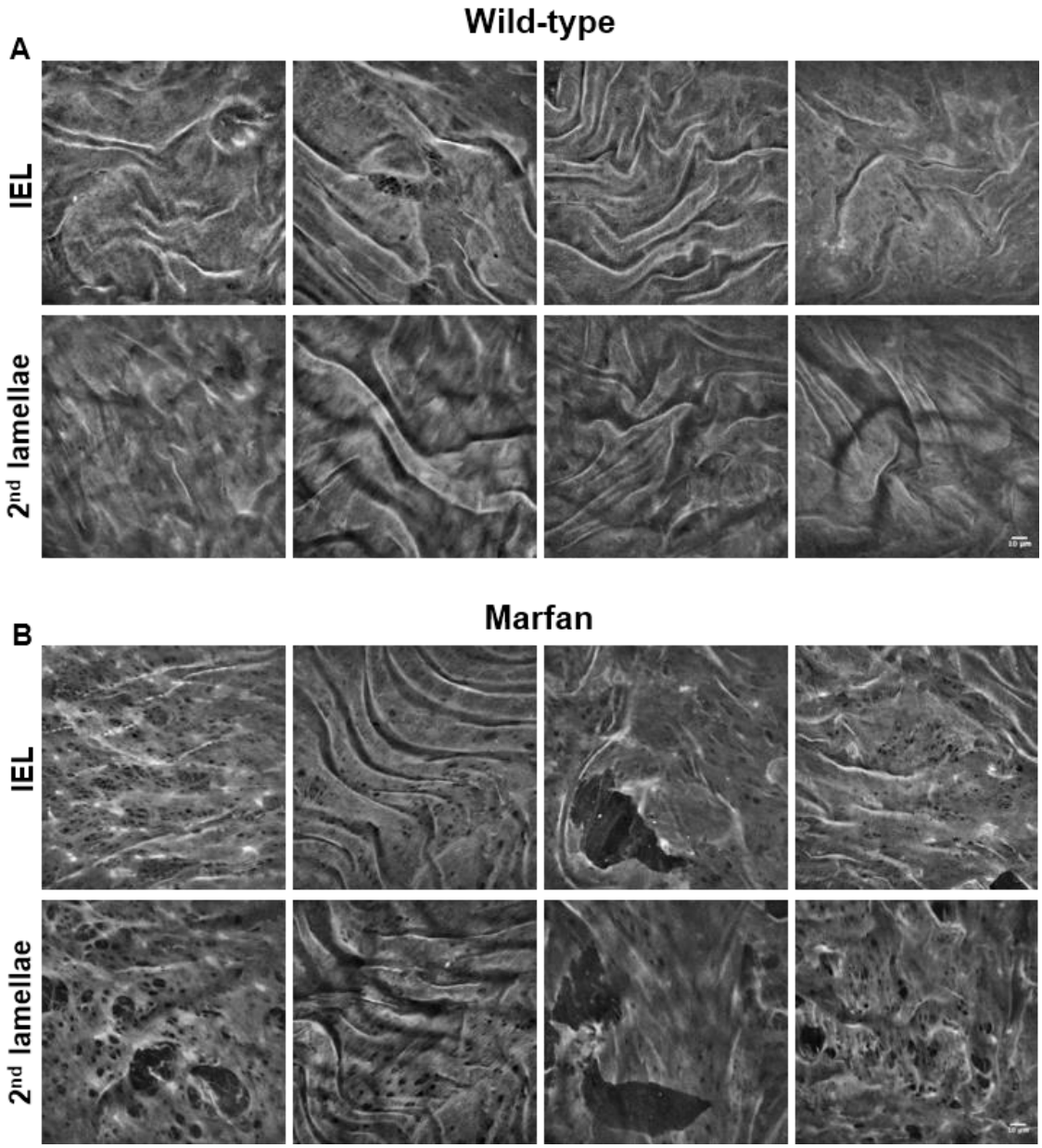

Figure 45. Representative en-face maximal projections of wild-type and Marfan aortic elastic laminae. Maximal projections of segmented IEL and 2nd lamina of WT (A) and Marfan (B) aortae. IEL and 2nd laminae images of each column belong to the same z-stack acquisition. In addition, each column corresponds to a different animal. Fenestrae are seen as black holes of variable size. Big polygonal black holes were considered ruptures and were excluded from fenestrae quantification. Scale bar = 10 μm.

It could be postulated that these lamellar ruptures might be merely caused by sample handling during animal surgery. To elucidate this, the length of the rupture's hole was measured at different points in the en-face maximal projection, mimicking the quantification of the length of elastic laminae breaks performed when aortae are examined transversally in classic histological preparations. Thus, to resemble conventional histological sectioning, a regular grid was used that marked all the horizontal and vertical lines where length measurements should be performed for all ruptures. As a result, the maximal projection rupture length was on average 20.71 μm at IEL and 30.73 μm at the 2nd lamellae. Altogether, the length of Marfan ruptures was 26.52

µm (± 19.29 µm) in our en-face images. For comparative reasons, the length of elastic laminae breaks was quantified at 24 conventional histological preparations of Marfan aortae, giving a mean length of 20.95 µm (± 19.47 µm). In conclusion, the values obtained from en-face and transversal histology were very similar and therefore, the ruptures in Marfan en-face images of IEL and 2nd lamellae (figure 45B, third column panels from the left) corresponded to the classical elastic laminae breaks observed by conventional histological methods, and were not primarily caused by sample handling. Moreover, importantly, only 8 out of the 48 total Marfan images showed ruptures.

In reference to lamellae quantification, fenestrae density was 2.5 fold higher in Marfan IEL than in WT IEL (figure 46A; median values: 2.14 fenestrae/mm^2 in WT vs 5.53 fenestrae/mm^2 in MFS). Marfan mice also had significantly larger fenestrae than WT mice (figure 46B; 2.07 µm^2 in WT vs 2.25 µm^2 in MFS). Consequently, the total area of elastic lamina occupied by fenestrae in the field of view was clearly larger in Marfan mice.

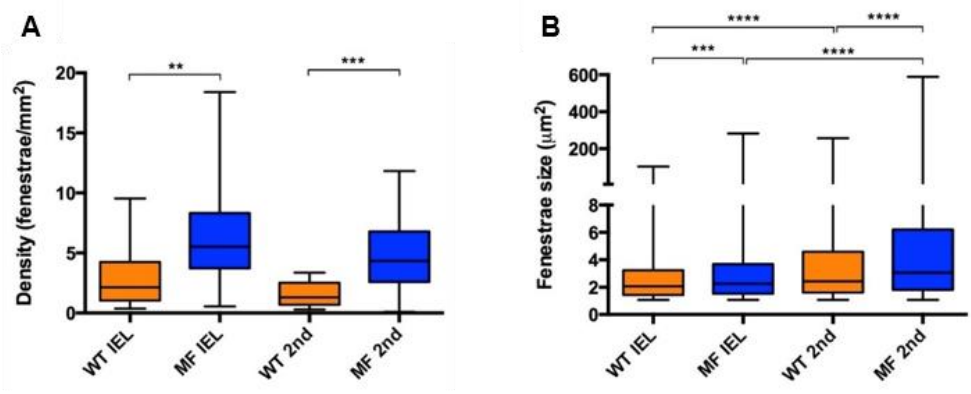

Figure 46. Quantitative analysis of density and size of fenestrae seen in IEL and 2nd elastic laminae from en-face maximal projection images. Fenestrae density (A) and size (B) seen in WT (orange) and Marfan (MF, blue) IEL and 2nd lamellae. Statistical significance between groups is indicated by asterisks and defined in the Materials and methods section. Interquartile boxplots with minimum and maximum whiskers. Forty maximal projections were analysed, and a total of 6,400 fenestrae were quantified.

The 2nd elastic laminae were segmented and analysed in the same way as the IEL. The results of quantitative analysis of the 2nd laminae were very similar to those obtained in the IEL when we compared WT and Marfan mice. Fenestrae density and size were significantly greater in the 2nd lamellae of Marfan mice than in WT mice (figure 46; density: 1.29 fenestrae/mm^2 WT vs 4.34 fenestrae/mm^2 in MFS; size: 2.43 µm^2 WT vs 3.06 µm^2 in MFS). No differences in fenestrae density were observed between the IEL and 2nd lamellae in WT and Marfan mice (figure 46A). However, there was a significant increase in the size of fenestrae between IEL and the 2nd lamellae in WT and Marfan aortae (figure 46B), which was more pronounced in Marfan aortae (WT: 2.07µm^2 in IEL vs. 2.43 µm^2 in 2nd lamina; MFS: 2.25 µm^2 in IEL vs. 3.06 µm^2 in 2nd lamina).

Next, a systematic analysis of the density and size of fenestrae was performed in different anatomical locations of the tubular ascending aorta. The locations were defined as proximal, central, and distal in the longitudinal plane, and as concavity and convexity in the circumferential plane (figure 47A-C). A qualitative examination of images of the

regions above revealed that laminae obtained in the convexity and proximal zones apparently had more microstructural damage (figure 47D and E).

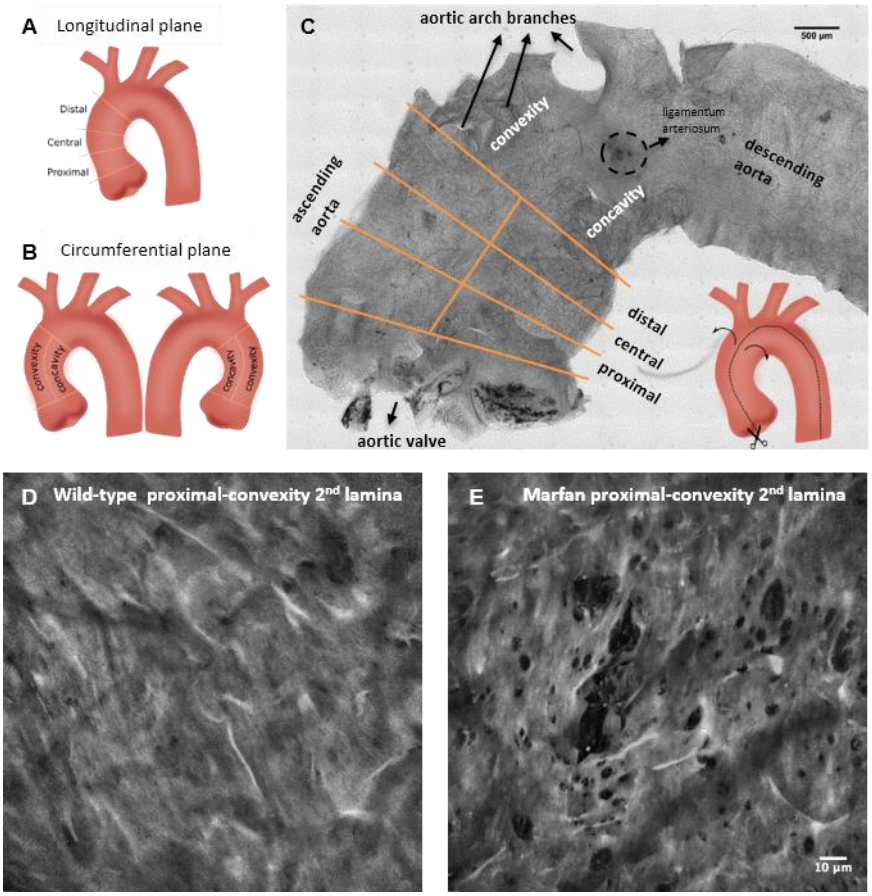

Figure 47. Anatomical regionalisation of ascending aorta used in this study. A and B. Schematic drawings of defined tubular ascending aorta anatomical regions used in our study in longitudinal (A) and circumferential (B) planes. C. Bright field image map of the longitudinally open aorta (as shown in the inset schematic drawing) and the corresponding regions. D and E. Representative maximal projections acquired in the proximal-convex region of WT (D) and Marfan (E) aortae. Scale 500 µm in C and 10 µm in D, E.

Indeed, statistically significant differences were observed between WT and Marfan mice in the IEL and in the 2nd elastic lamina, mainly in the proximal and convex regions. In particular, the median density of fenestrae in proximally located IEL (figure 48A) and 2nd laminae (figure 48B) were 7.5 and 6 times higher respectively in Marfan than in WT mice (IEL: 1.02 fenestrae/mm^2 WT vs 7.60 fenestrae/mm^2 in MFS; 2nd lamella: 1.14 fenestrae/mm^2 in WT vs 6.74 fenestrae/mm^2 in MFS). Moreover, Marfan fenestrae were significantly larger at proximal and distal IEL (figure 48C), and at proximal and central 2nd laminae (figure 48D).

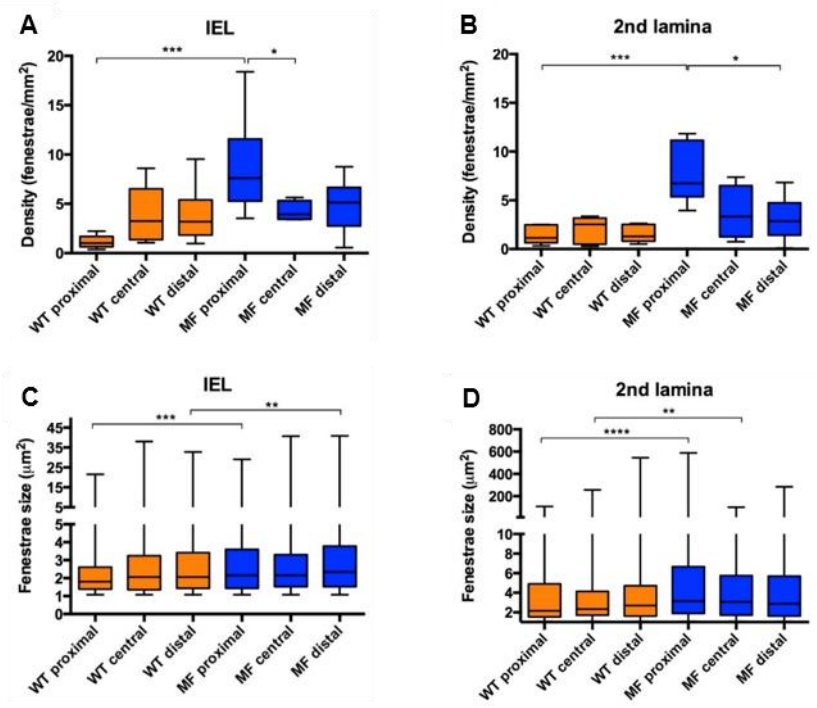

Figure 48. Quantitative analysis of fenestrae in IEL and 2nd laminae in the longitudinal plane of the tubular ascending aorta. The density of fenestrae in the IEL (A) and 2nd lamina (B), and their respective individual fenestrae size (C and D, respectively) measured at different longitudinal plane locations (proximal, central and distal) of WT (orange) and Marfan (MF, blue) ascending aortae. Statistical significance between groups is indicated by asterisks. Interquartile boxplots with minimum and maximum whiskers. Forty maximal projections were analysed, and a total of 6,400 fenestrae were quantified.

The circumferential partition of data (figure 49) showed that fenestrae density in WT IEL located at the concavity (cv) was significantly higher than that at the convexity (cx) of the aorta (figure 49A; 1.78 fenestrae/mm^2 in cx vs 5.81 fenestrae/mm^2 in cv). However, this was not the case for WT 2nd laminae (figure 49B; 1.27 fenestrae/mm^2 in cx, and 2.46 fenestrae/mm^2 in cv). In contrast, Marfan IEL fenestrae density ranges at concavity and convexity (2.8-9.1 fenestrae/mm^2) were highly similar to that at WT concavity (2.7-9 fenestrae/mm^2), and greater than at WT convexity (1-2.5 fenestrae/mm^2) (figure 49A). At the 2nd laminae, Marfan fenestrae density was similar to that at the Marfan IEL (compare MFcx with MFcv in figure 49A and B), and higher than 2nd laminae WT density in both circumferential regions (figure 49B), but was only significant at the convex region. We observed a significant difference in the size of fenestrae between Marfan and WT convexities both at the IEL and the 2nd laminae (Figs. 49C and D, respectively; IEL: 1.98 µm^2 in WT vs 2.25 µm^2 in MFS; 2nd laminae: 2.52 µm^2 in WT vs 3.06 µm^2 in MFS). In summary, structural injuries in the Marfan ascending aortae were regionalised, and were preferentially accumulated in the convexity region of the circumferential plane, and mainly in the proximal region of the longitudinal plane.

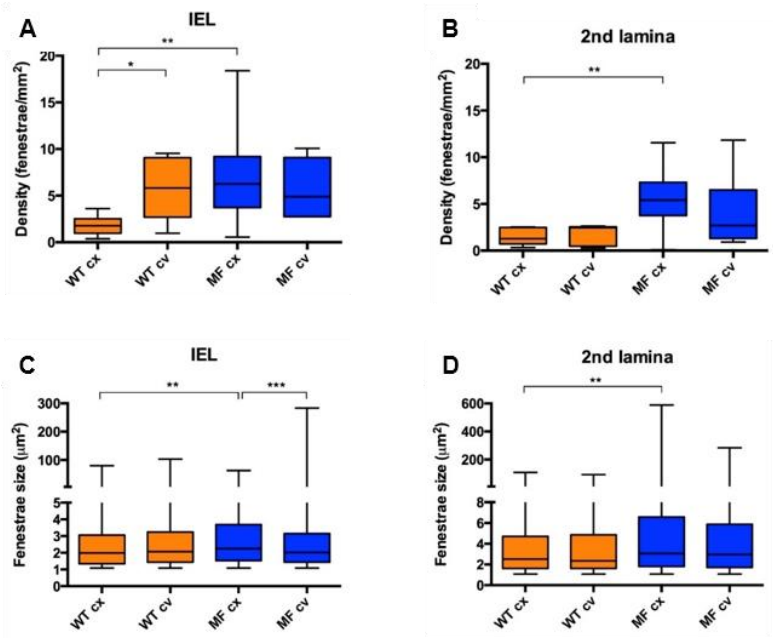

Figure 49. Quantitative analysis of fenestrae in IEL and 2nd laminae in the circumferential plane of the tubular ascending aorta. The density of fenestrae at the IEL (A) and 2nd lamina (B), and their respective individual fenestrae size (C and D) measured at different circumferential plane locations (convexity/cx and concavity/cv) of WT (orange) and Marfan (MF, blue) ascending aortae. Statistical significance between groups is indicated by asterisks. Interquartile boxplots with minimum and maximum whiskers. Forty maximal projections were analysed, and a total of 6,400 fenestrae were quantified.

Finally, potential differences between WT and Marfan mice were also examined regarding lamellae thickness and waviness. Lamellae thickness showed that in WT and Marfan, IEL and 2nd lamellae were on average 2.7–3.0 µm, without significant differences between them (figure 50A). Also, the measurement of waviness showed that WT and Marfan lamellae had the same spectrum of height values (figure 50B and C).

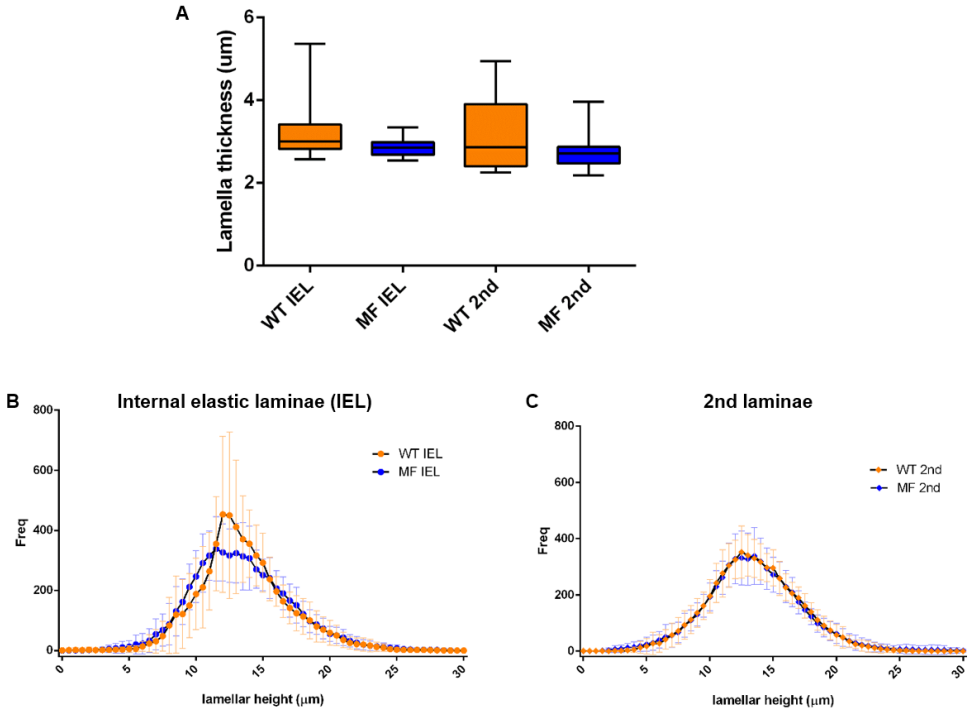

Figure 50. Quantitative analysis of lamella thickness and waviness. A. Thickness in wild-type (orange) and Marfan (blue) IEL and 2nd laminae. B and C. Waviness by lamella local height histogram of IEL (B) and 2nd laminae (C).

In addition, we visually analysed adventitial collagen acquired by SHG signal (figure 51). However, we could not distinguish any quantifiable feature, nor we could see differences between WT and MF samples.

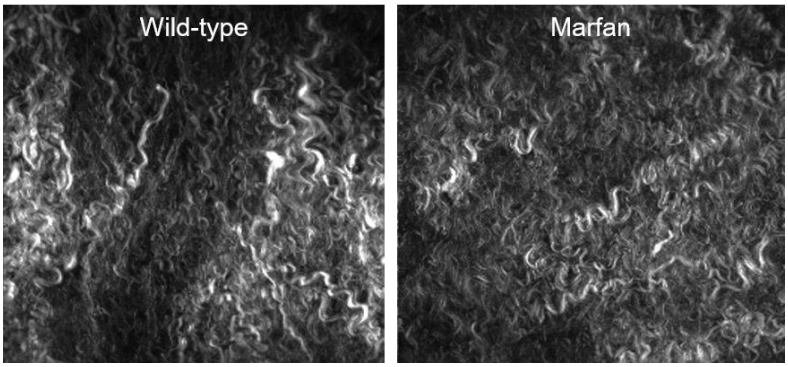

Figure 51. Adventitial collagen visualisation in wild-type and Marfan tubular ascending aorta samples.

Part 2: MicroCT imaging of remodelling and micro-scale damage in Marfan syndrome murine aorta

Vascular tissue structure is commonly analysed by manual quantification on conventional histological preparations. Although this practice has generated much knowledge in the field, it lacks the possibility of three-dimensional assessment of the tissue volume. To overcome this issue, serial cut studies have been performed, yet this kind of tissue processing damages the sample, leading to artefacts in the acquired images. In this context, microCT arises as an alternative given that it is a technique that works in the three dimensions and images the whole sample at once without cutting it. In addition, computational image processing of the microCT scans might provide an automatic and objective quantification of tissue structure features.

Taking into account this scenario, we have developed a methodology involving aorta imaging by synchrotron-based phase-contrast microCT and subsequent automatic image processing. Once optimised, we applied this methodology to wild-type and Marfan mice aortae, and analysed different histological parameters of the arterial wall.

2.1. Technology development: microCT and image processing

2.1.1. Optimisation of microCT acquisition

The aorta from the aortic root to the upper abdominal level (figure 52A) was extracted from mice as described in the Materials and methods section. As for conventional histological preparations, entire aortae were fixed in 4% PFA overnight, followed by dehydration in an ethanol series, and then embedding in paraffin wax. Additionally, embedding was done under vacuum to remove any air bubble within the vessels. Also, the wax surplus around the sample was trimmed to minimise the amount of external paraffin that could attenuate the light arrival to the tissue (figure 52B). Finally, the paraffin-embedded aortae were glued vertically onto a metal cryocap to provide standing stability to the samples (figure 52B).

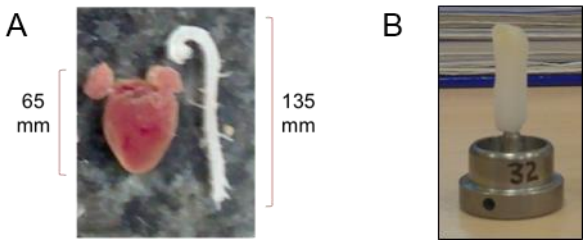

Figure 52. Aorta sample preparation. A. Murine heart (left) and aorta (right) after animal dissection and vessel cleaning. The aorta portion is from the root to the upper abdominal level. B. Paraffin-embedded aorta block already trimmed and glued onto a metal cryocap.

Once the samples were prepared, we scanned them by synchrotron microCT without staining or sectioning, adapting the expertise from Walton *et al*.[72] on laboratory microCT. In detail, we were awarded a 5-days timeslot at the synchrotron I13 beamline at the Diamond Light Source, Didcot, Oxford, United Kingdom. There, we performed phase-contrast X-ray tomography first testing different parameter variations, and then, scanning all the project's aortae.

To begin, an aorta (paraffin block + metal cryocap) was placed onto the magnetic sample stage in front of the objective, and three tomographic scans were performed to find the best light propagation distance: 150, 200, or 400 mm. The rest of acquisition parameters were as in standard conditions, using the pink light beam, acquiring 6001 projections over 180º, and performing a filtered back projection reconstruction. In addition, the pco.4000 camera at 4x magnification was used, so that the acquired scan had a wide field of view (4.5 x 3.0 mm) at high resolution (isotropic 1.1 µm voxel size). The resulting scan evidenced that these settings permitted successful sample imaging (figure 53). Particularly they allowed the acquisition of the whole aorta length in only two acquisitions, one of the thoracic aorta, and the other of the abdominal aorta. Moreover, comparing the three scans obtained applying the different propagation distances, it was clear that 200 mm yielded the best image sharpness (figure 53B).

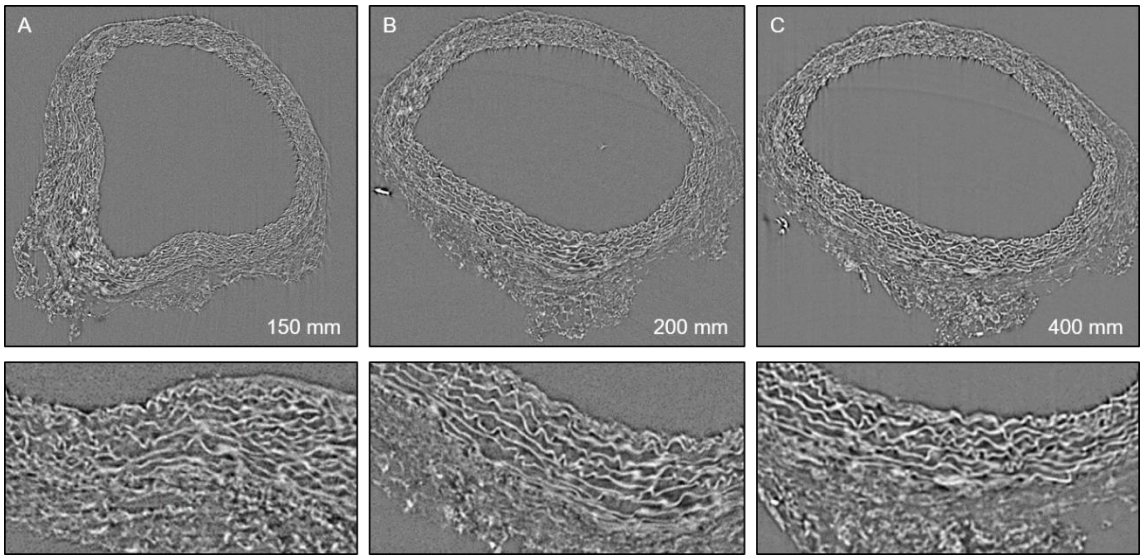

Figure 53. Transverse virtual cuts of an aorta by synchrotron microCT at 150 mm (A), 200 mm (B), and 400 mm (C) light propagation distances. The sharpness of the image is best seen in the tunica media of the lower half of the vessel circumference (lower panel zoomed images). Spike artefacts are present particularly at the upper half of the vessel circumference, evidencing that the centre of rotation is placed "below" the image.

Furthermore, these first scans evidenced image artefacts in the shape of spikes that blurred the details of the tissue (figure 53, upper half of the vessel circumference). This

phenomenon was caused by a high distance between the sample and the centre of rotation of the sample stage. Thus, it was crucial to place the centre of rotation close to the middle of the aortic lumen. Although not always possible due to aorta tortuosity, in the following scans, we tried to accurately place the sample core focalised to the centre of rotation.

The next test involved the assessment of the number of scan projections, since this parameter directly determined the scan time. Taking into account that the exposure of the pink beam was of ~0.14 seconds per projection, we sought to reduce the number of projections in the scans. Hence, 6001 projections were tested, as before, and also 3001 projections. Surprisingly, both scans images were similar, and the reduction of projections did not affect scan contrast or sharpness (figure 54). Moreover, the scanning time diminished from 14 to 7 minutes. Therefore, 3001 projections was established as a standard setting for definitive aortic scans.

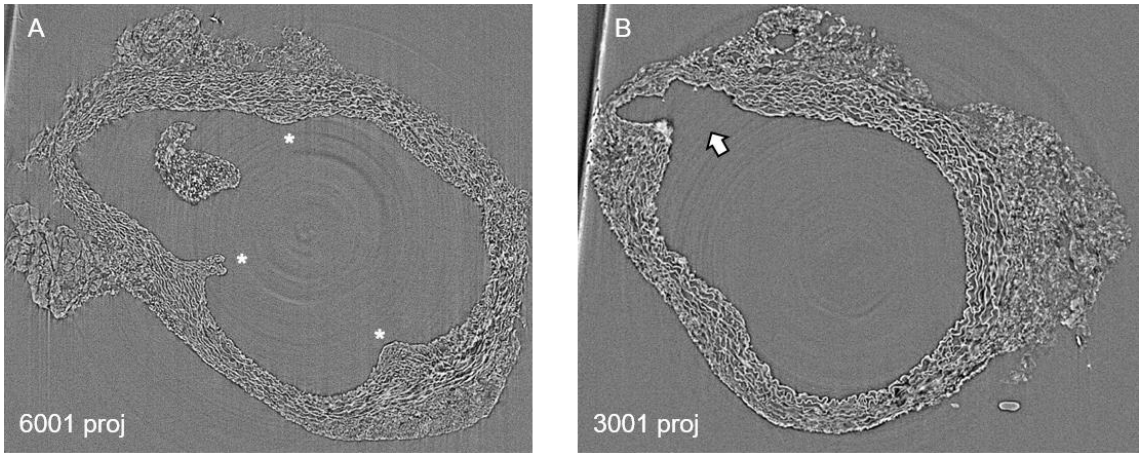

Figure 54. Transverse virtual cuts of an aorta by synchrotron microCT at 6001 (A) and 3001 projections (B). These cuts belong to the aortic root portion, denoted by the initiation of aortic valve septa (A, marked by asterisks) or the entrance of a coronary artery (B, marked by an arrow). Notice the concentric rings that evidence the centre of rotation lying in the middle of the lumen.

2.1.2. Aortic microCT scan comprehension

After mandatory scan reconstruction, microCT scans were stacks of greyscale tiff images. In particular, the aortic scans consisted in the whole volume of the aorta divided into ~2,600 subsequent images (named slices). In the portion of the ascending aorta, those slices were transverse virtual cuts of the vessel, displaying the tissue as in conventional histological preparations. As shown in figure 55, one could distinguish the tunicae media and adventitia in those images. In detail, tunica media is composed of the concentric elastic lamellae, which are brighter than the interlamellar space. The adventitia rendered as a dense mesh surrounding the tunica media, with spots as bright as lamellae. The amount of adventitia was usually higher at the inner curvature of the aorta (upper side in figure 55A-B) than in the rest of the vessel circumference. Although

the tunica intima should be present in contact with the luminal paraffin, this cellular layer did not produce enough phase-contrast to be displayed in the microCT scan images. Thus, the luminal surface visualised in the aorta microCT scans was the IEL, the innermost element of the tunica media.

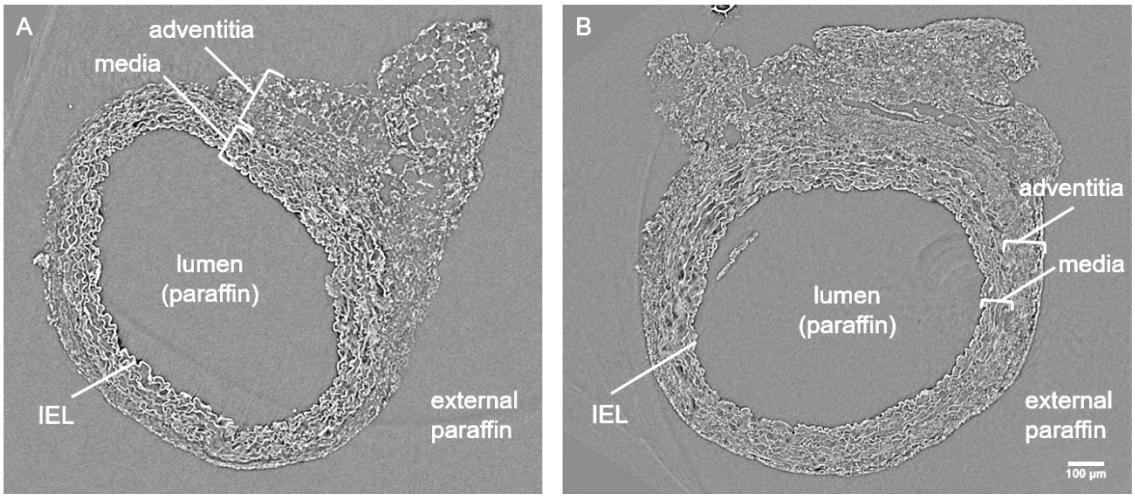

Figure 55. Two illustrative examples of microCT transverse virtual cut slices of mice ascending aortae. Histological structures are marked. Scale bar = 100 µm.

Nevertheless, the singularity of microCT in comparison to conventional histological techniques was the possibility to assess the volume of a tissue specimen. Indeed, microCT aortic scans went from the aortic root to the arch (figure 56): one could progressively see the emergence of the aortic valve leaflets (slice 50 to 400 in figure 56), the appearance of the coronary arteries (slices 150, 350, and 500), the tubular portion of the ascending aorta (slice 600 to 1150) and the initiation of vessel bending at the aortic arch (slice 1200 in figure 56).

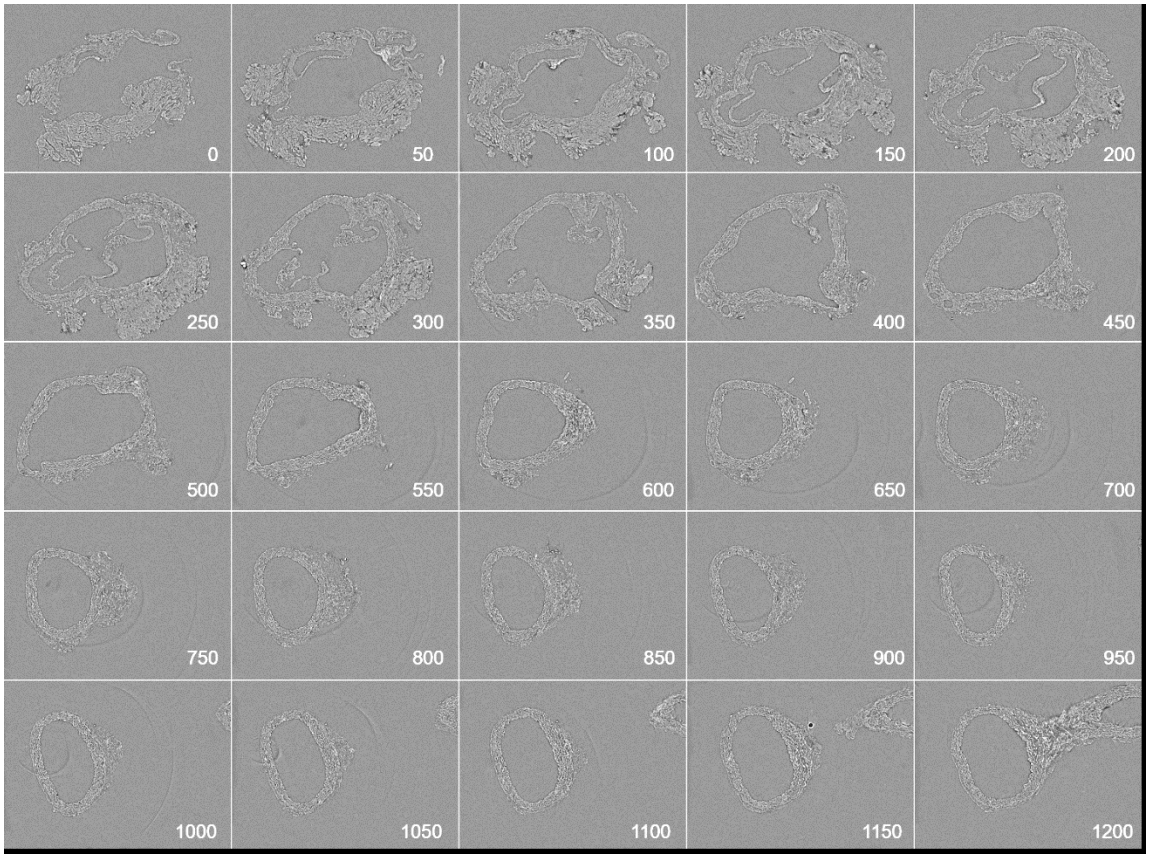

Figure 56. Aorta scan progression from the aortic root (slice 0) to the aortic arch (slice 1200).

Furthermore, the microCT scans served to generate the whole aorta 3D volume rendering in Avizo software (figure 57). Renders could be of the entire organ (figure 57A), and the vessel interior could be accessed disclosing the luminal surface (figure 57B), where one could observe the wall wrinkles caused by the unpressurisation of the aorta without blood pressure. Any piece of the scan could be virtually isolated, such as the tubular portion of the ascending aorta (figure 57C). Additionally, to visualise the aortic valve, the vessel portion corresponding to the aortic root could be virtually extracted (figure 57D for tricuspid valve and E for bicuspid valve), or the whole 3D render could be combined with a slice (figure 57F).

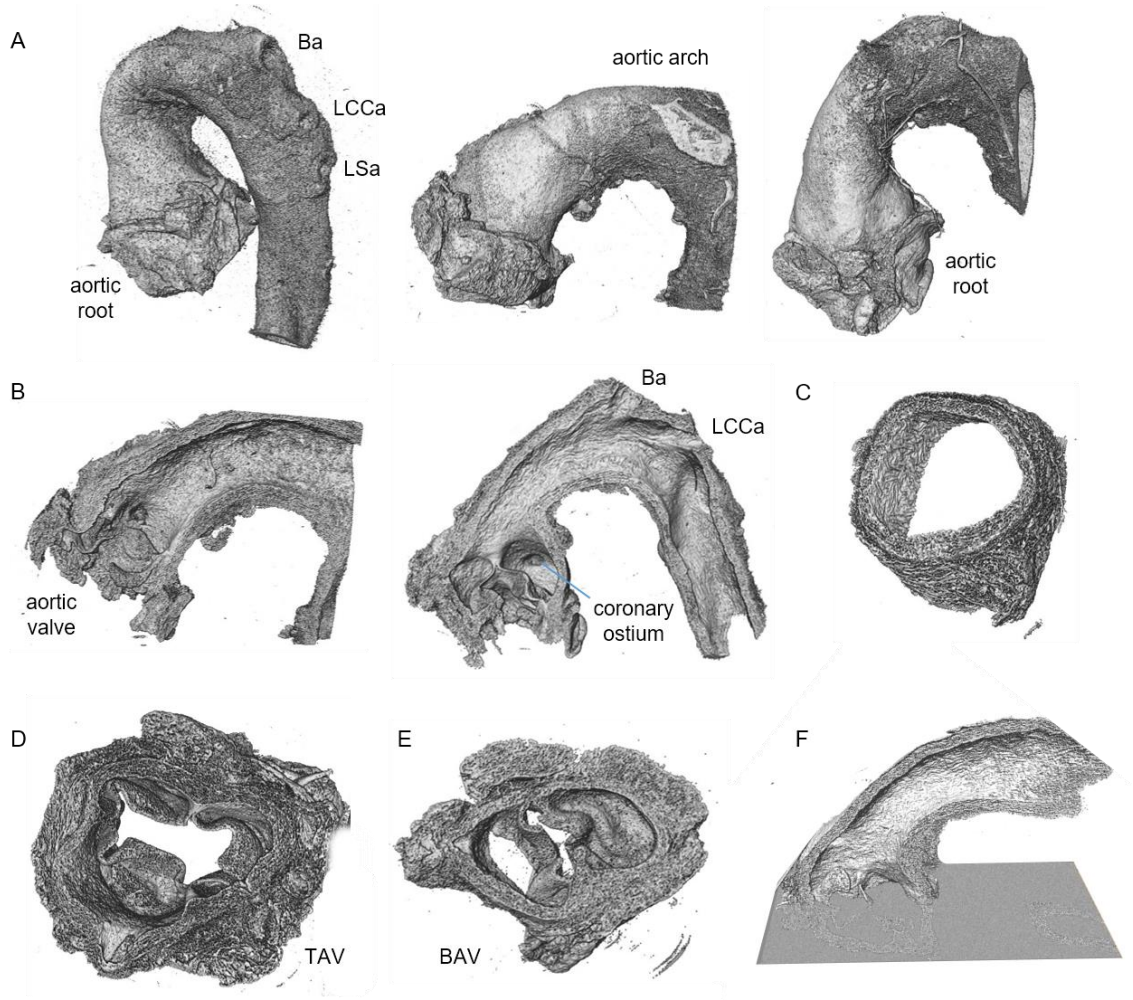

Figure 57. Three-dimensional renderings of mice aortae. A. Whole vessel from the aortic root to the descending or arch. In the first render, note the entrance at the arch of its three branching arteries: brachiocephalic artery (Ba), left common carotid artery (LCCa) and left subclavian artery (LSa). B. Inside of aortae, where it is shown the luminal surface, the aortic valve, coronary ostium and two of the arch arteries' entrance (Ba and LCCa). C. Tubular ascending aorta portion. D. Tricuspid aortic valve (TAV). E. Pathological bicuspid aortic valve (BAV). F. Tricuspid aortic valve represented by a combination of 3D render and transverse slice.

Moreover, with these high-resolution scans, the microstructure of the lamellae network was observable, and in some cases, it was disrupted (figure 58). Conventionally, lamellae breaks are observed in single transverse sections of the arterial wall (equivalent to only one slice of figure 58A). However, breaks are not a bi-dimensional entity but a volumetric structure, and are unlikely to be confined only to the region visualised in the single section but many will extend to preceding and following sections. Hence, a sequence of consecutive sections could provide insight on the extension of a particular lamella break. Figure 58A shows an image sequence belonging to the wall of an aneurysmal aorta, which presents several lamellae breaks. Throughout this sequence, distinct breaks appear, grow, and terminate at various sites within the tunica media. A break might start as a gap in one lamella (yellow box at slice 20 in figure 58A) and progressively grow affecting neighbouring lamellae, and might finally implicate all the

lamellae in the media (see slice 340 in figure 58A). This break progression can also be easily visualised by means of 3D rendering (figure 58B and C) to be virtually explored in detail.

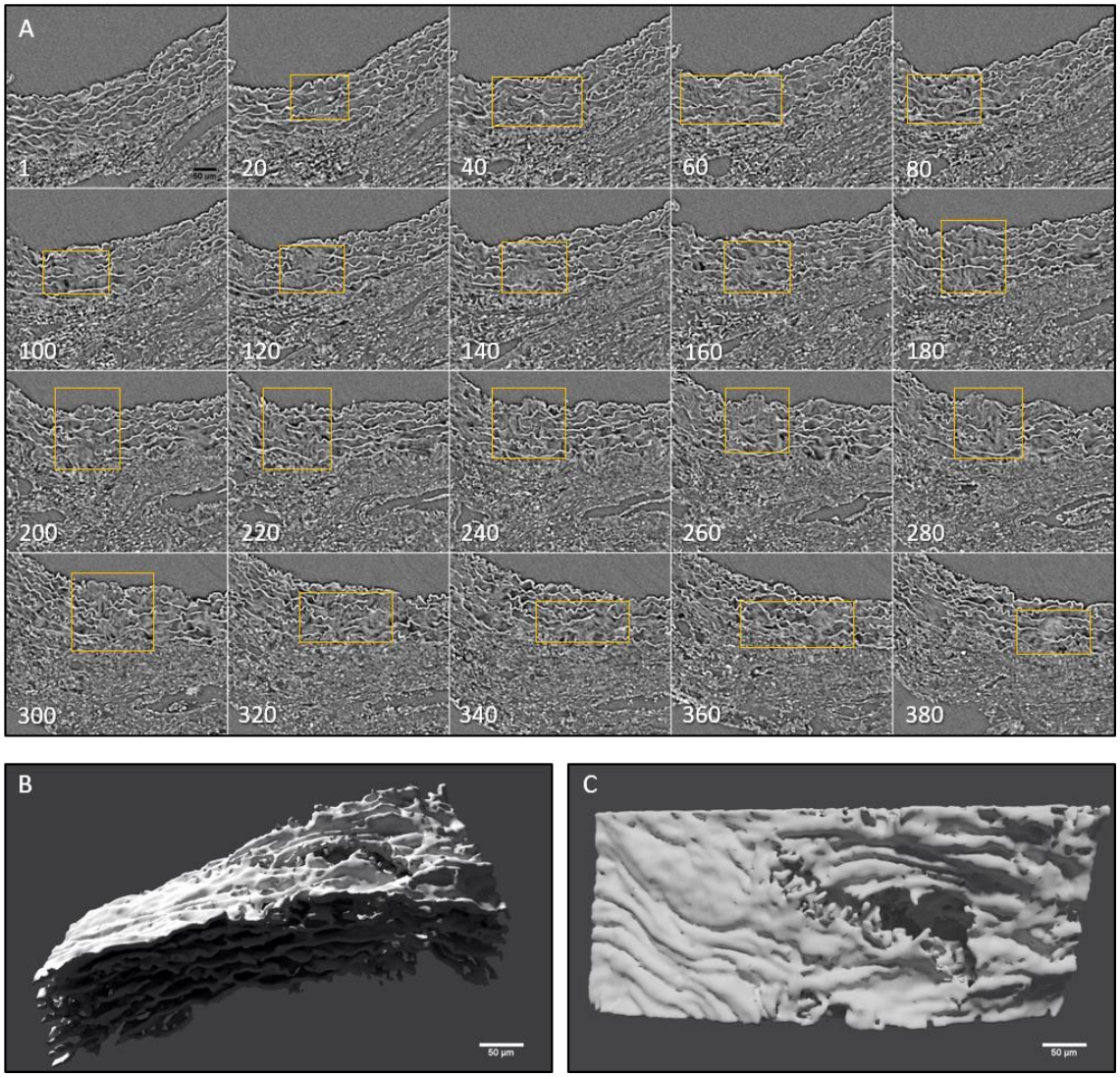

Figure 58. Visualisation of lamella break extension. A. Transverse slice sequence of aortic wall showing the course of the lamellae and the emergence and progression of a lamellae break gradually affecting many layers (yellow box). B and C. Lateral (B) and en-face (C) view of the volumetric render of the same tissue portion as in A. The prominent break corresponded to the one clearly observable in slice 260 of A. Notice the extension and depth of the break. Only tunica media lamellae are rendered. Scale bar = 50 µm.

In addition, some aortae showed mild intimal hyperplasia, evidenced by an amorphous mass attached to the luminal surface (figure 59). This mass had the same grey level as the interlamellar space and, in some spots, it was united to the elements in the interlamellar space (see first slices in figure 59). Also, in this case, the attached mass progressed as a floating mass in the lumen (from the second row on, in figure 59).

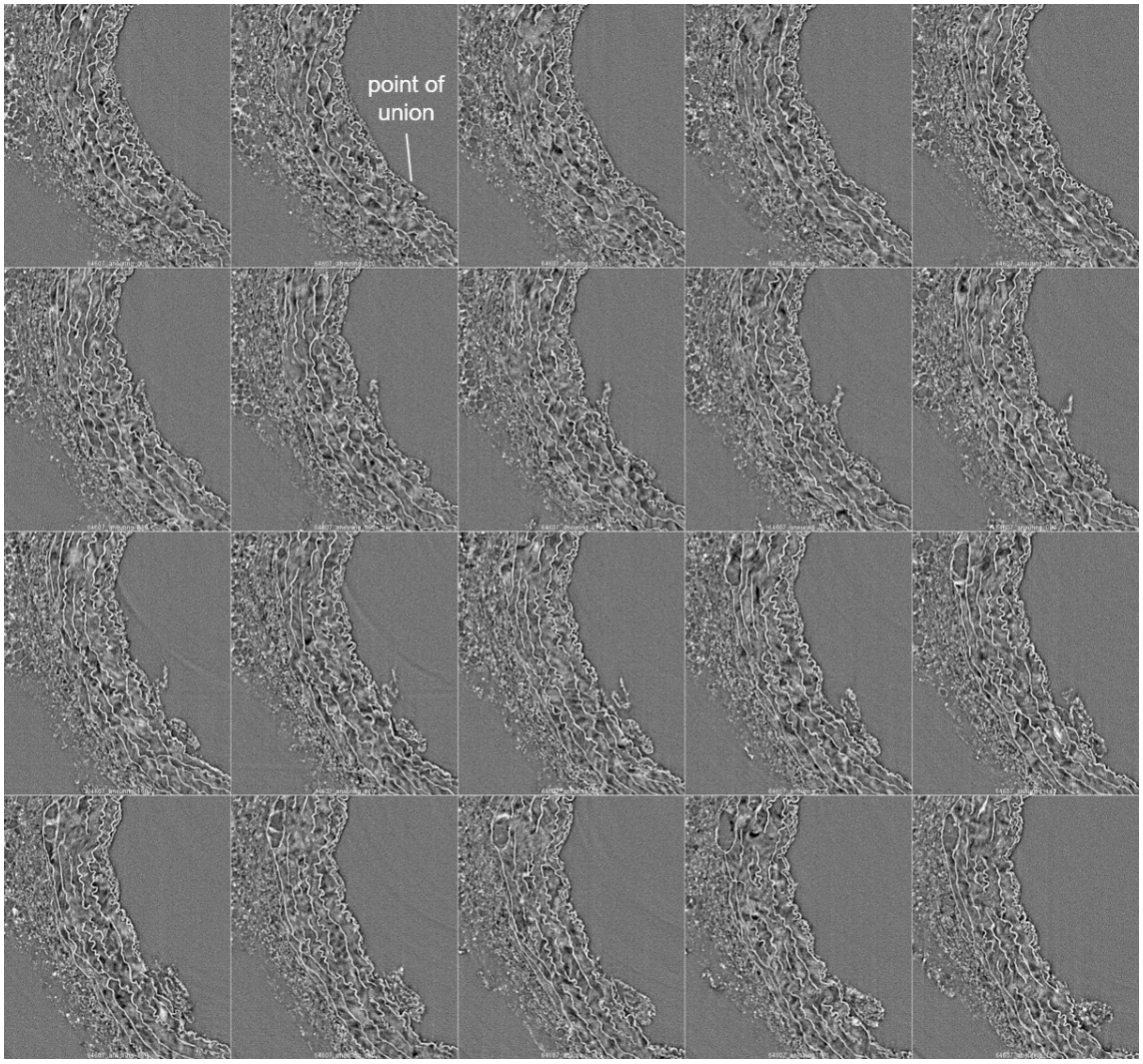

Figure 59. Mild intimal hypertrophy image sequence of mice aorta. First rows show the junction between the amorphous mass and the interlamellar space.

2.1.3. Image processing of aortic wall 3D scans

The quantification of histological parameters on these datasets was performed onto 200 consecutive slices of each sample at the same tubular ascending aorta level, in order to provide a robust mean value per sample. Quantified parameters were: ascending aorta diameter, tunica media thickness and cross-sectional area, and tunica media area corresponding to lamellae and to interlamellar space (figure 60).

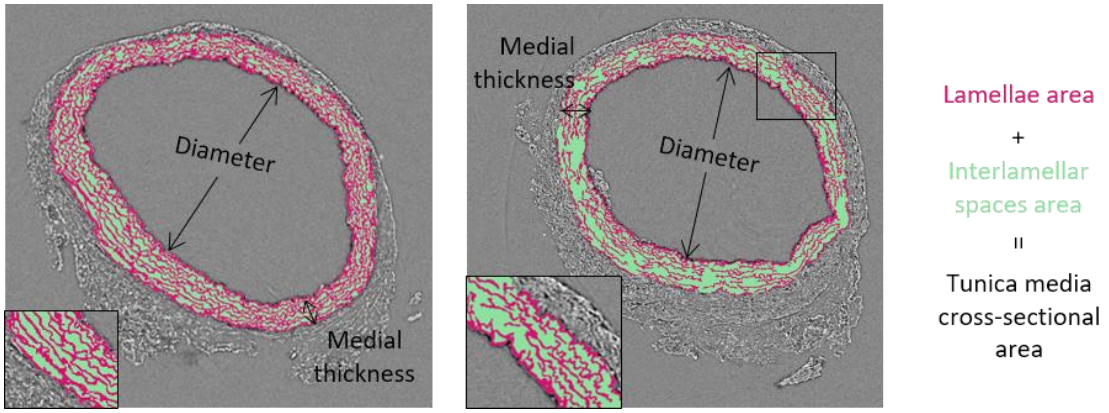

Figure 60. Illustrative schematic of the histological parameters quantified in microCT transverse aortic slices. Two example images with zoomed inset.

To assess these parameters, a computational image processing protocol was developed, which prepared the images and quantified the histological features automatically. Particularly, a graphical user interface (GUI) was created in MatLab to facilitate its adoption by programming-inexperienced users (figure 61).

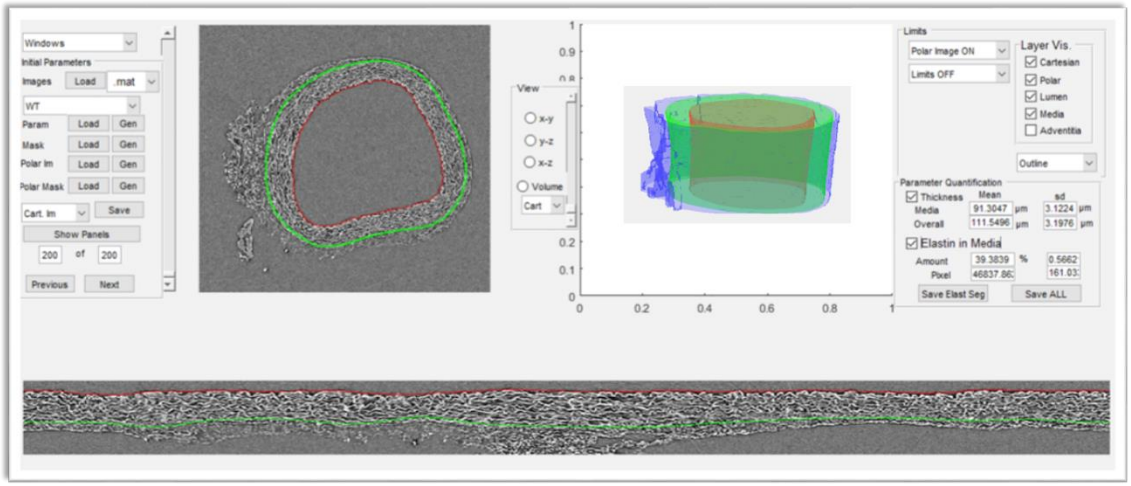

Figure 61. Screenshot of the developed GUI that permits interaction between the user and the program. Loading and computation panels are on the left. In the centre, the GUI displays the original aorta image on the left, the open aorta image down, and the 3D render of the lumen-media (red), media-adventitia (green) and adventitia-paraffin (blue) limits. On the upper right, one can choose which displays or limits to show. And the quantification panel is placed in the right centre.

In brief, the in-house algorithm loaded an aorta image stack, and it segmented the tissue out of the paraffin and the tunica media out of the tissue, for each image. The first segmentation was obtained by simple brightness thresholding, but the second required intensive computation as it was based on a mathematical relation. Specifically, the thickness of tunica media was not constant, but different throughout the vessel circumference and also varied for the different sample groups. Moreover, it was difficult to properly distinguish both tunicae based solely on greyscale intensity since they were very similar. Therefore, we sought a mathematical manner of outlining the media-adventitia limit that was applicable to all sample conditions. The media-adventitia limit

(green line at figure 61) was found to be placed approximately at a distance "0.35*minimum wall thickness (of each particular sample)" from the middle of the aorta wall, throughout the vessel circumference (refer to the Materials and methods section for further detail). This mathematical relation fitted for most of the wild-type and Marfan aortae regardless the age.

Then, the program computed the transformation of the aortic vessel image from Cartesian to Polar coordinates, which permitted to virtually open the vessel circumference (lower display in figure 61). The obtained open image was used to apply the calculated media-adventitia limit and, if necessary, to manually correct any error. Once the tunica media was precisely segmented, the algorithm computed its thickness, area and the area occupied by lamellae and by the interlamellar space, in each of the stack's images.

Moreover, the virtually open images were also useful for visualisation of the luminal surface. As previously explained, in the aortic microCT scans, the IEL was the structure that was apparently in contact with the luminal paraffin. Hence, an ImageJ macro was developed to segment the IEL from the aorta open stacks and change the point of view so that the IEL was seen en-face (figure 62) (refer to the Materials and methods section for further detail). With this, the visualisation of the luminal surface was achieved like it is seen in clinical vascular endoscopy.

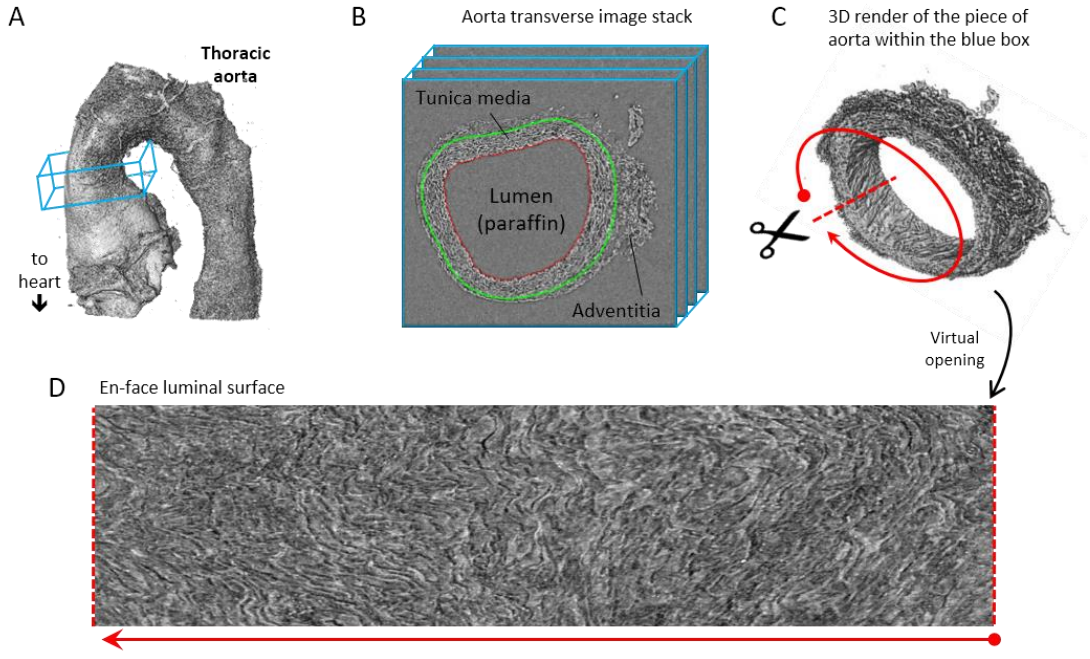

Figure 62. Image processing steps for aorta microCT scans. A. Volumetric rendering of an aorta scan from the aortic root to descending thoracic aorta. A stack of the tubular ascending aorta (blue box) was selected for further processing. B. The blue-box slices were computationally processed to segment the tunica media (enclosed between the red and the green lines) and calculate histological parameters. C. Abstract representation of the virtual opening step of the aorta piece. D. Resulting flat luminal surface of IEL segmentation at the en-face view, after the virtual opening of the tubular ascending aorta.

In summary, the image processing methodology, on the one hand, extracted the tunica media of ascending aorta images and quantified its histological features; and on the other hand, it segmented the IEL, opened it, and displayed it as a flat luminal surface (figure 62).

2.2. Technology application to murine Marfan aortae

Once the microCT acquisition settings and the image processing algorithms were optimised, we applied them to Marfan mice studies. In particular, 30 aortae from wild-type (WT) and Marfan *Fbn1*$^{C1039G/+}$ mice (MF), at age 3, 6, and 9 months old (mo) (n=5 per condition) were fixed, dehydrated, and paraffin embedded. All these murine aortae were imaged by phase-contrast microCT at Diamond synchrotron, all the datasets were modified by image processing algorithms, and different histological parameters of the aorta wall were analysed.

2.2.1. Quantitative analysis of histological features

Collectively, all wild-type aortae showed a normal candy-cane shape (figure 63A), and the ascending aorta conduit was circular or ellipsoid (figure 63B) with the lumen diameter ranging from 0.3 to 0.9 mm. Marfan samples were more heterogeneous (figure 63C-E) than WT, and evident aneurysms occurred in one of 6mo mouse and in three of 9mo mice (figure 63E). Owing to this heterogeneity in Marfan aortae, to compare dataset dispersion (statistical F-test; dashed lines in the graphs) instead of the mean values (Kolmogorov-Smirnov non-parametric test; continuous lines) was key to compute statistical differences in this condition.

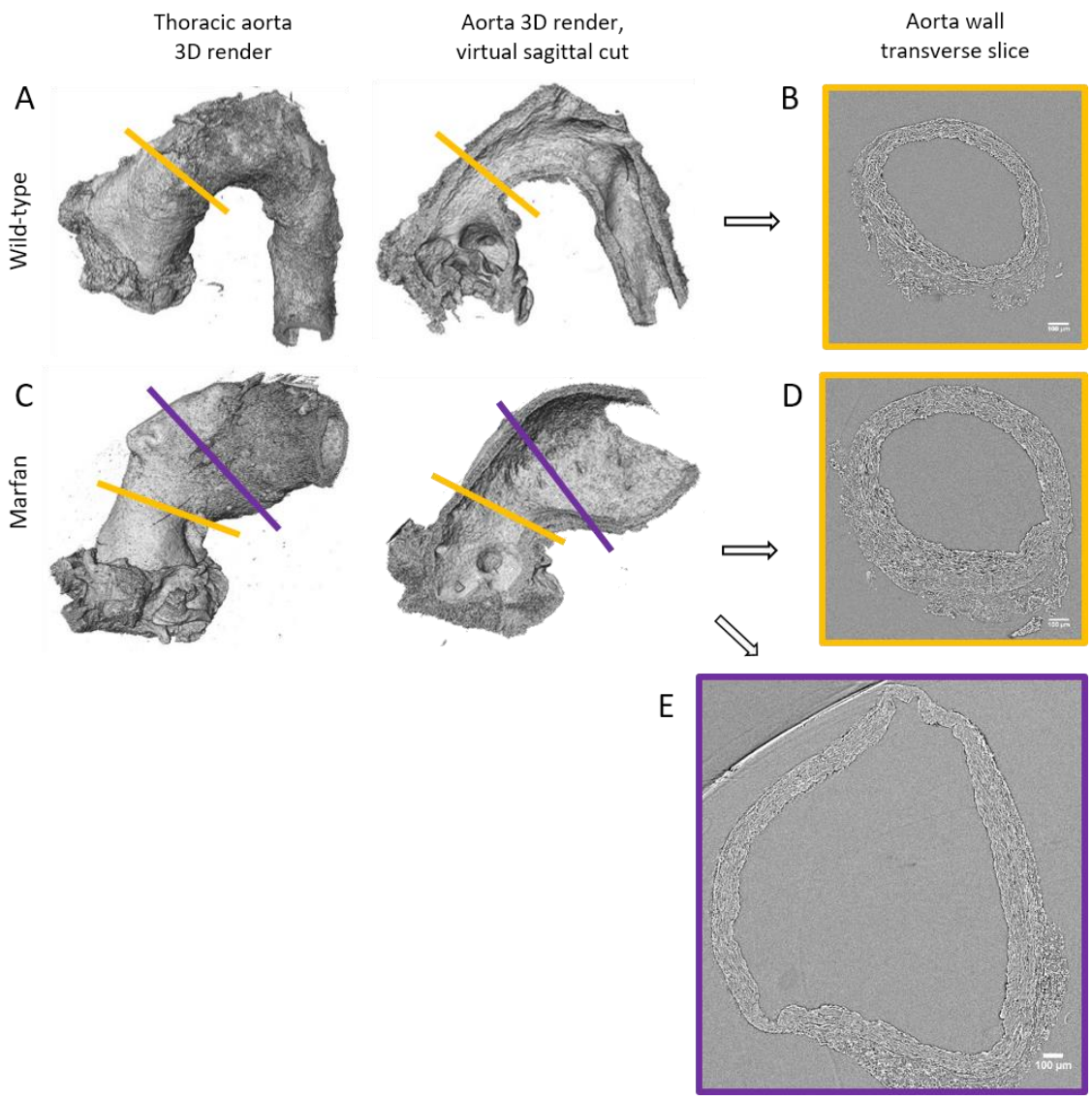

Figure 63. Synchrotron-based microCT scan examples of wild-type and Marfan mice aortae. A. Wild-type aorta volumetric rendering. B. Transverse slice of wild-type aorta, corresponding to the yellow line mark in A. C. Volumetric rendering of a Marfan aneurysmal aorta, with two different zones: non-dilated (yellow line) and dilated (purple line) zones. D. Transverse slice of a Marfan aneurysmal aorta at the non-dilated zone (yellow line in C). E. Transverse slice of a Marfan aneurysmal aorta at the dilated zone (purple line in C). Scale bars, 100 µm.

More in detail, tunica media of the WT ascending aorta showed no or scarce lamellar breaks (figure 64). Conversely, structural remodelling of the tunica media of Marfan aortae along age stages and in comparison to WT was clearly seen qualitatively (figure 64). Lamellae breaks augmented with age and aneurysm occurrence, and so did the interlamellar space.

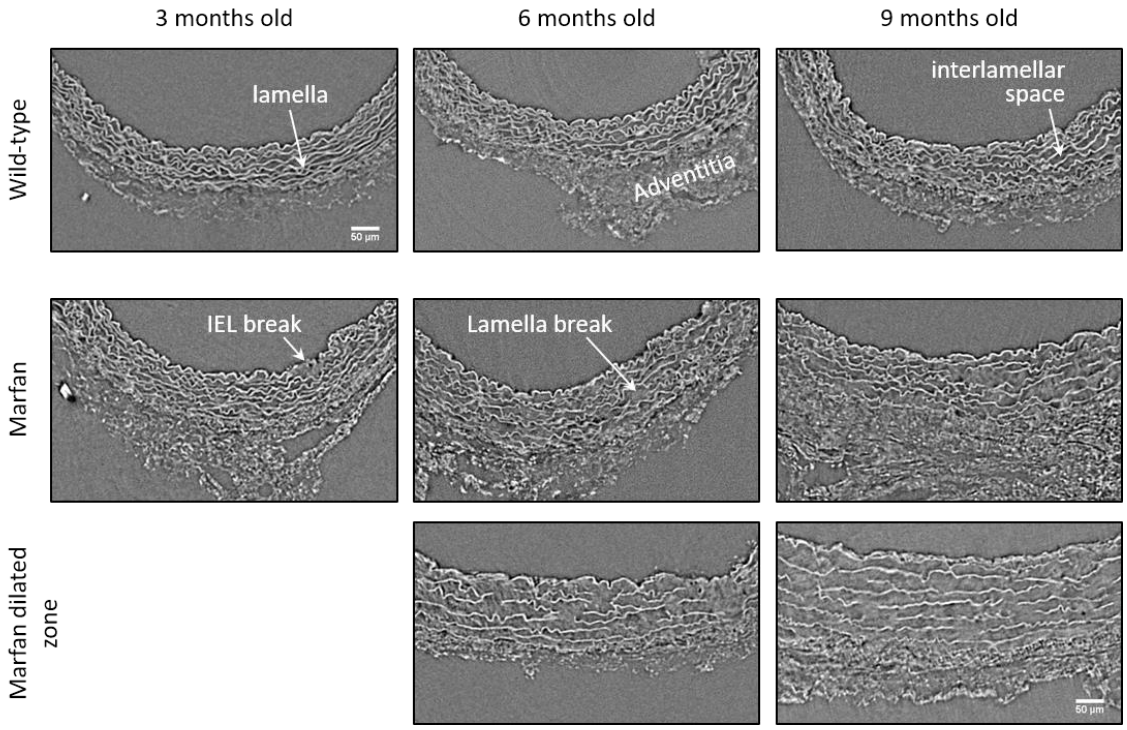

Figure 64. Representative transverse slices from microCT scans of wild-type and Marfan mice aortae at age 3, 6, and 9 months old. Scale bar = 50 µm.

These histological changes were verified quantitatively. In the case of WT samples, ascending aorta mean diameter remained homogeneous throughout the three studied age stages (figure 65A, means, 3mo=0.61±0.02, 6mo=0.60±0.03, 9mo=0.66±0.03 mm), although a slight growth was corroborated by a P value<0.08. Similarly, tunica media thickness increased with age (figure 65B, means 3mo=77±4, 6mo=81±8, 9mo=84±5 µm), but this increase was not significant when considering P≤0.05 (figure 65B). However, this analysis does not take into account the richness of these microCT data sets which characterise anatomical variation along the vessel axis. Comparing the frequency distributions of media thickness measurements for each slice from each animal (n = 1000 slices per condition group) there was a clear shift towards greater media thickness with age (figure 65C), which might be biologically significant even though not statistically different at conventional P value. Hence, it might be relevant to state that WT diameter and media thickness mean values increased significantly with age taking into account P<0.08.

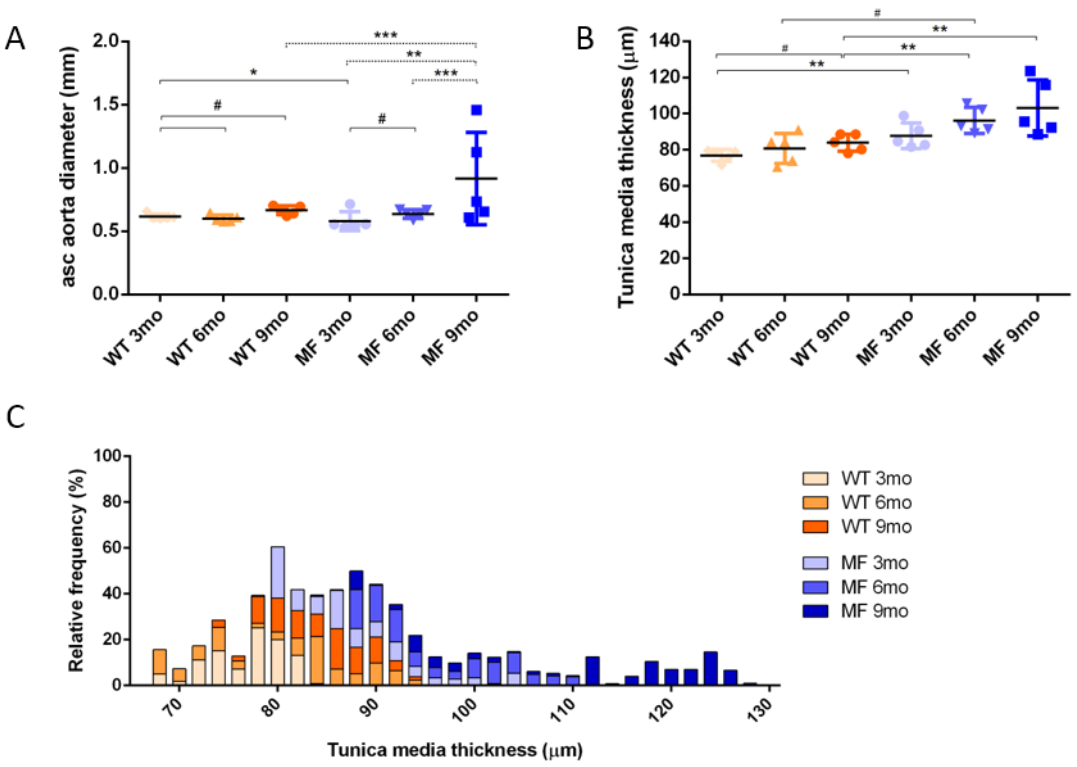

Figure 65. Transverse histological feature measurements in wild-type (WT) and Marfan (MF) mice aortae at 3, 6, and 9 months old. A. Ascending aorta luminal diameter (unpressurised). B. Tunica media thickness mean values of each aorta. C. Frequency distribution of the 200 thickness values per aorta. Values are the mean±SD; #P ≤ 0.08, *P ≤ 0.05, **P ≤ 0.01, and ***P ≤ 0.001.

Moreover, the cross-sectional area of the WT tunica media augmented also with age (figure 66A, means 3mo=0.18±0.01, 6mo=0.19±0.01, 9mo=0.21±0.01 mm^2, P<0.08), most likely because of the increase of the aorta diameter and of the media thickness. This age-associated growth of WT tunica media was mainly due to the significant parallel increase in both the area of lamellae (figure 66C, 3mo=0.07±0.003, 6mo=0.08±0.004, 9mo=0.09±0.003 mm^2) and of the interlamellar space (figure 66D, 3mo=0.10±0.007, 6mo=0.11±0.008, 9mo=0.13±0.01 mm^2). Since both medial constituents augmented at the same rate, their medial percentage remained constant with age progression (figure 66B, lamella 3mo=42±1, 6mo=42±1, 9mo=41%±2; interlamellar space 3mo=58±1, 6mo=58±1, 9mo=59%±2).

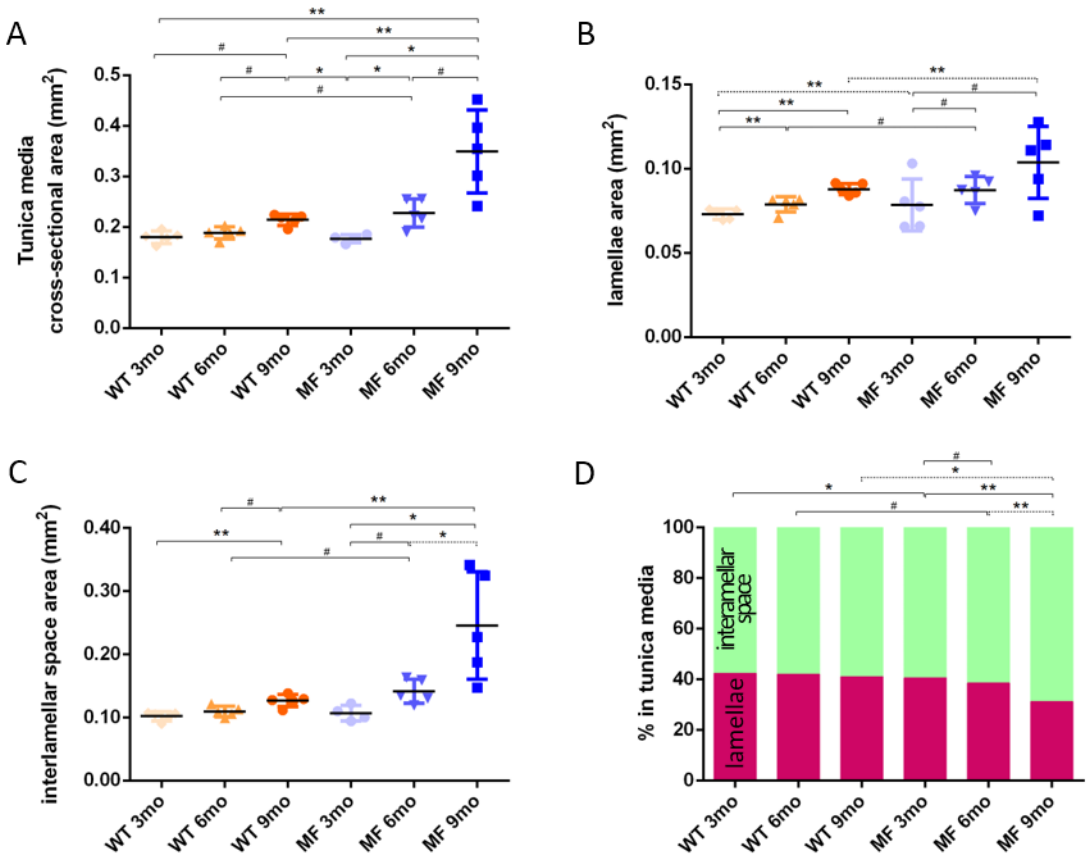

Figure 66. Transverse histological feature measurement in wild-type (WT) and Marfan (MF) mice aortae at 3, 6, and 9 months old. A. Tunica media cross-sectional area. B. Tunica media area occupied by lamellae. C. Tunica media area occupied by the interlamellar space. D. Tunica media percentage composition. Results are the mean±SD; #P ≤ 0.08, *P≤ 0.05, **P ≤ 0.01, and ***P ≤ 0.001.

In the other hand, in Marfan aortae, a significant increase was observed in the luminal diameter in relation to age (figure 65A, 3mo=0.58±0.07, 6mo=0.64±0.03, 9mo=0.92±1.13 mm). Besides, the progressive thickening tendency of the tunica media was observed (figure 65B, 3mo=88±7, 6mo=96±7, 9mo=103±15 µm) in comparison to WT (mean of ages=80±6 µm), together with the significant enlargement of the tunica media cross-sectional area (figure 66A, 3mo=0.18±0.007, 6mo=0.23±0.027, 9mo=0.35±0.082 mm^2), and the gradual decrease of the percentage medial space occupied by lamellae (figure 66D, MF 3mo=40±1, 6mo=38±2, 9mo=31%±9 of media, wild-type mean of ages 42%±1). This change in lamellae percentage was principally not caused by a reduction in lamellae area (figure 66B), but by a two-fold increase in the area of the interlamellar space (figure 66C, 3mo=0.11±0.01, 6mo=0.14±0.02, 9mo=0.25±0.08 mm^2).

Regarding WT and MF datasets together, MF 9mo aortae displayed significantly higher values than same age WT specimens in all the quantified histological parameters: MF 9mo had larger diameter, thicker tunica media, and bigger media, lamellae and interlamellar space areas than WT 9mo (figures 65 and 66). MF tunica media thickness

and lamellae percentage were already increased at age 3mo (figures 65B and 66D), whereas the MF areas at 6mo were higher than the WT 6mo (figure 66). Finally, MF 6mo aortae showed higher tunica media thickness than WT 9mo vessels (figure 65B).

One MF 6mo and one MF 9mo developed localized ascending aorta aneurysms that had an adjacent non-dilated zone, as displayed in figure 63 (yellow line for non-dilated, purple line for dilated). In addition, two MF 9mo mice showed an aneurysm that occupied the whole ascending aorta, hence no adjacent non-dilated zone existed. In this context, up to now, the quantitative analysis of this study was performed on the same ascending aorta region for all samples. Thus, the MF 9mo group included measurements at "normal" non-dilated zones from three animals, and also measurements at the dilated zones of the two aortas without non-dilated zone. Taking this into account, to evaluate more in detail the impact of aneurysm occurrence on the remodelling of the MF aortic wall, the analysis of the histological parameters was categorised into non-dilated (MF 3,6 and 9mo in figure 65 and 66) and dilated (MF dilated in figure 67, and purple line in figure 63) groups. Thus, the histological parameter values of the two entirely dilated aortae previously assessed in the MF 9mo group (dark blue dataset in figures 65 and 66) were now transferred to the MF dilated group (purple dataset in figure 67).

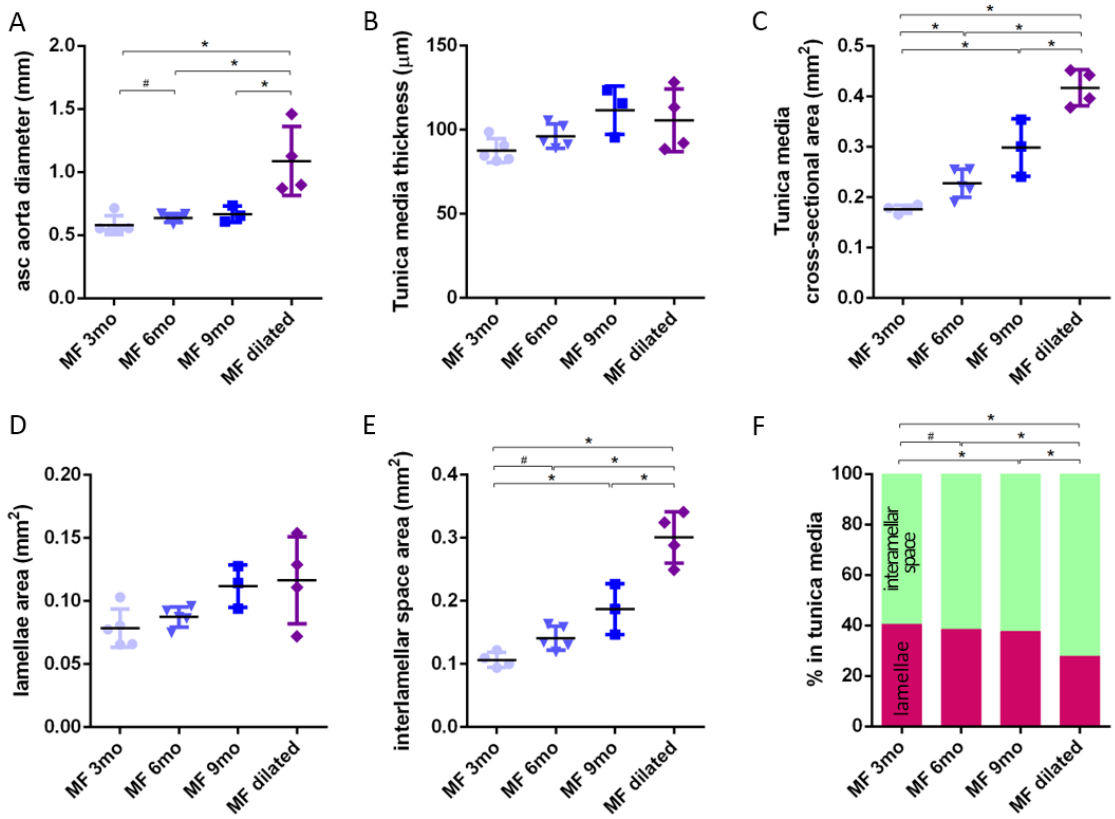

Figure 67. Transverse histological parameters in dilated and non-dilated aged Marfan (MF) mice aortae. Anatomically evident dilated MF aortae were grouped apart (purple data, and purple line in figure 12). A. Ascending aorta luminal diameter (unpressurised). B. Tunica media thickness mean values. C. Tunica media cross-sectional area. D. Tunica media area occupied by lamellae. E. Tunica media area occupied by the

interlamellar space. F. Tunica media percentage composition. Values are the mean ± SD; #P ≤ 0.08, *P ≤ 0.05, **P ≤ 0.01, and ***P ≤ 0.001.

Comparative analysis of this new MF dataset categorisation revealed that, in most cases, histological features were significantly higher in the dilated aorta zone group (represented in purple) compared to the younger Marfan groups (blue-based coloured datasets) (figure 67). Dilated zones obviously had a greater diameter than the other MF groups (figure 67A, 1.09±0.27 mm vs mean of ages 0.62±0.06 mm). Likewise, tunica media cross-sectional area also significantly increased in MF dilated compared to the other MF groups (figure 67C, 3mo=0.18±0.008, 6mo=0.23±0.028, 9mo=0.30±0.056, dilated=0.42±0.035 mm^2), as well as the interlamellar space area (figure 67E, 3mo, 0.11±0.01; 6mo, 0.14±0.02; 9mo, 0.19±0.04; dilated, 0.30±0.04 mm^2). However, the tunica media thickness and the lamellae area remained similar in all Marfan groups (figures 67B and 67D; mean of MF conditions 100.3±10.5 µm and 0.09±0.02 mm^2, respectively). Altogether resulted in the significant decrease of the percentage of lamellae in media (figure 67F, MF aortae in %: 3mo, 40±1; 6mo, 38±2; 9mo, 37±2; dilated, 27±8 of media). Particularly, non-dilated and non-aneurysmal MF 9mo samples did not show different diameter, media thickness and lamellae area, compared to MF 6mo and MF 3mo. Moreover, a higher tunica media and interlamellar space areas were only observed between MF 9mo and MF 3mo, but no longer between MF 9mo and MF 6mo, as happened prior to dataset categorisation. This structural remodelling was clearly seen in the aortic wall images (figure 64).

2.2.2. Lamellae luminal surface break analysis

To get an informative single image of damage progression in the aortic wall, the luminal surface of ascending aortae was virtually generated for all the samples to visualise the breaks occurring in the IEL at en-face perspective. Representative luminal surface images of WT and MF aortae at different ages are shown in figure 68, in which it can be seen the IEL breaks and their extension. Note that IEL breaks are viewed as dark irregular cracks. Luminal surface images denote the break severity evolution with disease progression (figure 68).

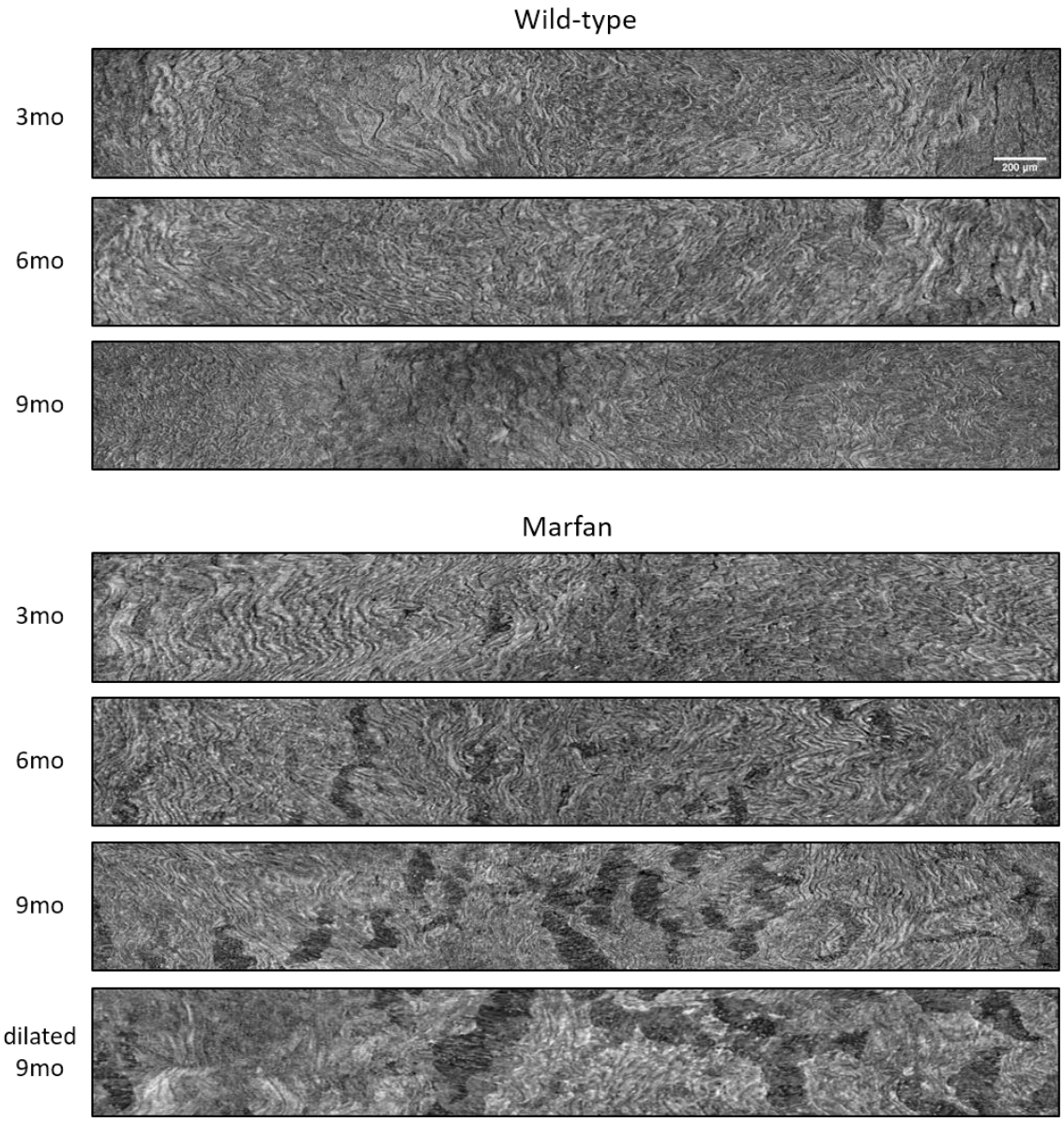

Figure 68. Representative images of ascending aorta luminal surface of wild-type and Marfan aortae at different age stages. IEL breaks are visualised as irregular dark cracks. Scale bar = 200 µm.

On the one hand, WT luminal surfaces of any age were wavy and continuous (figure 68). Occasionally, they presented a small break (figure 69A, luminal surface space occupied by breaks 3mo=0±0, 6mo=0.6±0.4, 9mo=0.3%±0.3) and/or darker zones owing to intimal mild hypertrophy (figure 69). On the other hand, Marfan luminal surfaces showed several lamella breaks, mainly in the longitudinal axis, whose number and extension progressively increased with age (figure 68). Indeed, the total luminal surface space occupied by breaks significantly increased with age (figure 69A, Marfan 3mo=0.3±0.5, 6mo=2.5±1.3, 9mo= 10%±10) and with aneurysm manifestation (figure 69B, 9mo=6.6±6.1, dilated=15%±8.3).

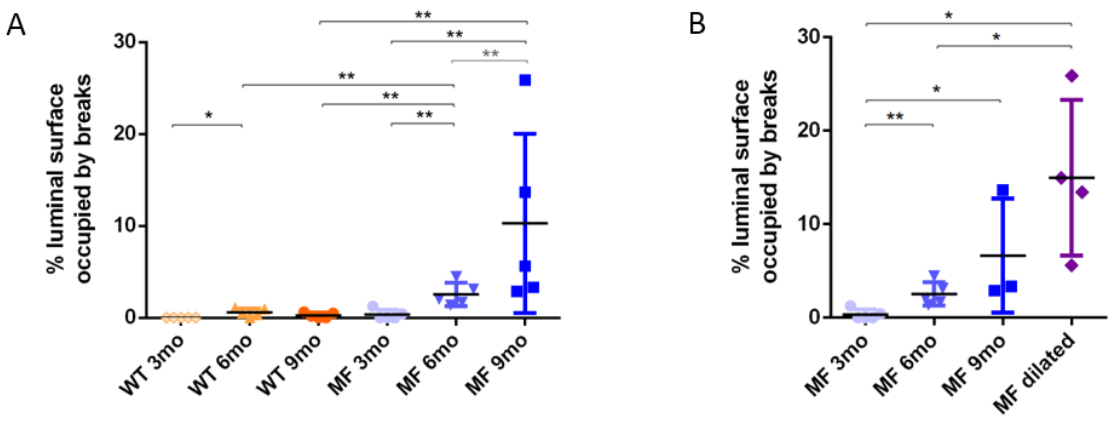

Figure 69. Luminal surface breaks analysis. A. Percentage of ascending aorta luminal surface occupied by breaks. B. Percentage of ascending aorta luminal surface occupied by breaks, after categorising aneurysmal datasets into dilated and non-dilated. Results are the mean±SD; *P≤0.05, **P≤0.01.

Moreover, the anatomical location of the luminal surface breaks was evaluated in four different ascending aorta locations: outer curvature, inner curvature, frontal, and dorsal sides. Even though not significant in most cases, Marfan damaged samples showed a tendency to present more luminal surface breaks at the outer curvature than in the rest of the vessel circumference (figure 70).

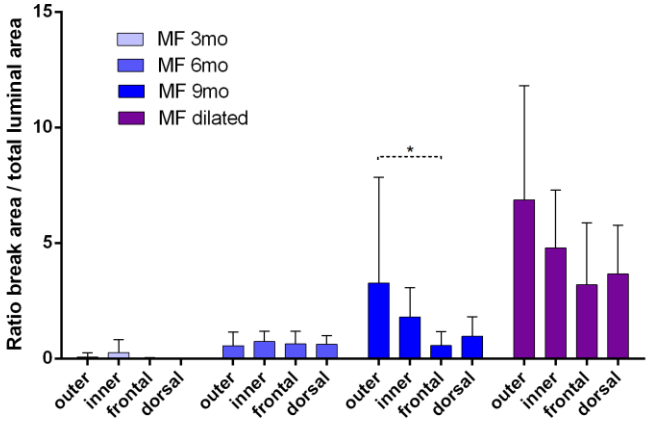

Figure 70. Luminal surface break quantification in different anatomical regions of ascending aorta. Results are the mean±SD; *P≤0.05.

Part 3: Impact of *in vivo*-like stretch on the phenotypic modulation of VSMCs of Marfan syndrome patients

Taking into account that stretching is a key component of VSMC physiological environment, other groups have already seen that *in vitro* applied mechanical forces have a key role in the modification of VSMC's phenotype that can affect their contractile protein levels[102]. Moreover, physiological mechanical forces trigger the reorganisation of cell stress actin fibres[111].

Previous results in our laboratory show that Marfan aortic tissue and cultured VSMC overexpress contractile makers, such as SMA, transgelin, calponin1, smoothelin, and the contractile machinery regulator myocardin[93]. However, all these data were acquired culturing cells on conventional *in vitro* conditions. For this reason, here we have designed and optimised a novel bioreactor device that allows culturing cells under *in vivo*-like stretching *in vitro* conditions. After demonstrating its overall suitable functioning, as a proof of concept, this bioreactor was employed to seed control and Marfan VSMCs, and its effect was assessed on their cytoskeleton organisation and contractile protein levels.

3.1. Technology development: stretch bioreactor

3.1.1. Origin of the device

The bioreactor employed in this project was an adaptation of an original bioreactor developed at the group of Dr Daniel Navajas from the Biophysics and Bioengineering unit of our Department. Their design was meant for hypoxia treatment of mesenchymal cells, hence it was aimed at controlling gas circulation within the bioreactor[133]. We performed several modifications to finally convert this hypoxia bioreactor into a stretch-inducing device for VSMCs.

The original bioreactor consisted of a single-use cell culture platform and a permanent gas source system. The platform, named chip, had a surface where cells were seeded and that was permeable to gases but not to liquids. This surface was a 10 µm-thick membrane placed on top of a well (figure 71). The well was a hole on a PDMS block that served as a gas chamber where gas circulation was introduced through the gas source pipe system. The chip was made of PDMS silicone placed within a conventional cell culture dish for an improved manipulation. A new chip had to be constructed for each

experiment, but fabrication was possible in the laboratory (refer to the Materials and methods section for more detail).

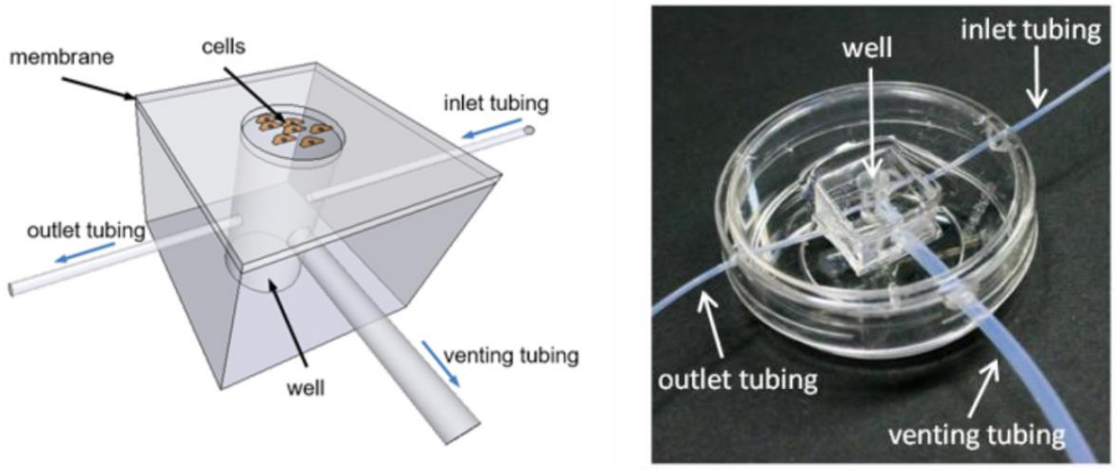

Figure 71. Original bioreactor's chip from which we developed our stretching bioreactor. Cells are seeded onto the portion of the membrane covering the well. Tubes connected the well of the chip to the gas source system. In order to facilitate chip handling, it is all attached to a P35 culture dish. Pictures originally published at ref. [133].

3.1.2. Mechanical stimulus optimisation

The first change on the original device was the substitution of the gas source system by a vacuum system, which applied negative pressurisation to aspirate the air within the wells. This modification was relevant because as the negative pressure reached the chip, it deformed the membrane downward and consequently applied stretch to the cells seeded on top (figure 72).

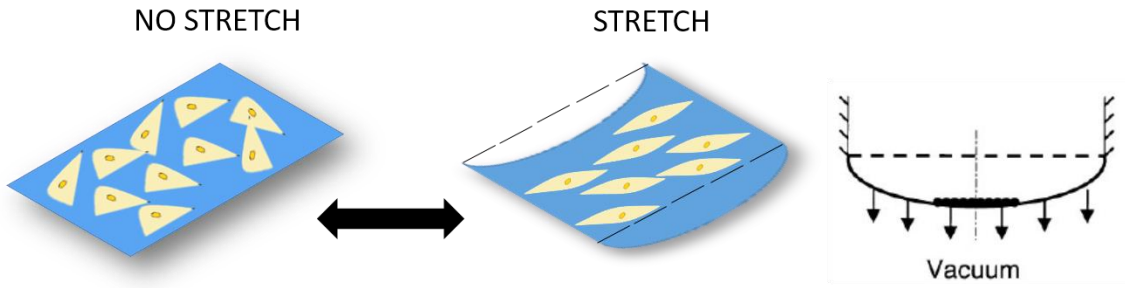

Figure 72. Schematic drawing of membrane stretch application. When negative pressurisation (i.e. vacuum) is activated, the otherwise flat chip membrane gets deformed downward and cells (in yellow) too.

Also, the shape of the wells was changed from circular to rectangular (now named canals), and their size was augmented, to accomplish a uniaxial membrane stretching. In detail, circular wells under negative pressurisation displayed a circumferential strain of the membrane (figure 73A). Conversely, rectangular canals under negative pressurisation implied stretch through the long and the short sides of the membrane

(figure 73B). Despite this biaxial strain, the tension at the long side of the rectangle (transverse direction) was greater than the tension at the short side (axial), due to the ratio between both sides' lengths. Hence, only cells placed very close to the short side edge sensed the axial stretch, but all the cells seeded on the membrane felt the transverse stretch. Taking this into account, we excluded, in posterior analyses, the cells close to the short side edge of the canal, in order to quantify only the effect of the transverse stretch on cells (uniaxial strain) (figure 73C). Additionally, membrane deformation from the centre to the side edges decreases gradually to zero at the edge[134]. Therefore, cells seeded at the edges are not subjected to deformation.

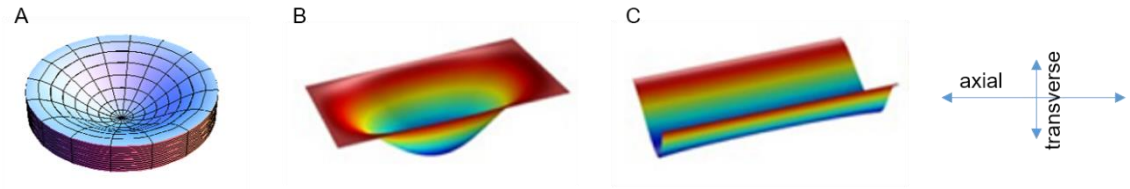

Figure 73. Stretch directions under negative pressure. A. Circular wells deform downward circumferentially. B. Rectangular canals display axial and transverse stretch of the membrane. C. Excluding the membrane portions next to the short sides, only transverse deformation occurs.

The surface dimensions of the cell culture were feasible up to 75x50 mm, which was the maximum size of the platform where the membrane was fabricated. Subtracting the margins and the space occupied by the chip's walls, the stretching-effective cell culture surface in a chip was 625 mm^2. However, due to the fabrication process, it was not possible to achieve a 625 mm^2 membrane on top of the chip without intermediate pillars for additional support. Hence, this area was divided into five equal 25x5 mm canals, with 125 mm^2 culture surface each and resistant side-pillars of 2 mm thickness (figure 74). A rigid, plastic mould was fabricated with these dimensions to serve as a cast for the subsequently constructed chips. To sum up the changes in design, the chip had a rectangular aspect with five rectangular canals, all within a P60 cell culture dish (figure 74C) and connected to a vacuum system.

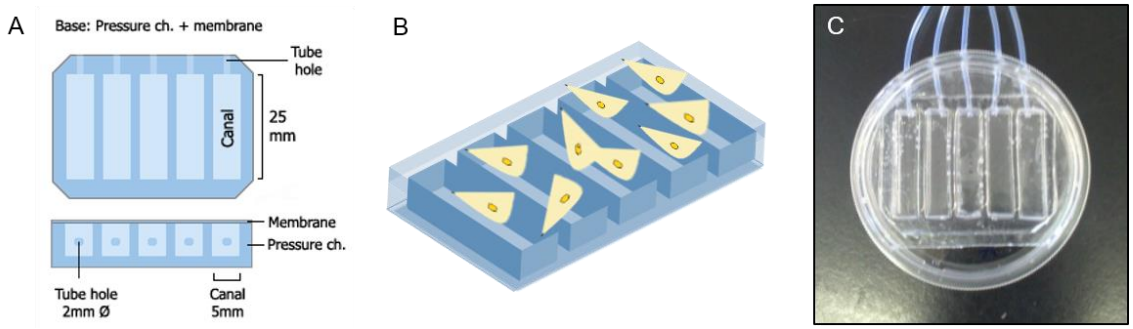

Figure 74. Chip shape and arrangement. A. Chip was composed of a PDMS pressure chamber and a thin PDMS membrane on top. B. The pressure chamber divided the membrane into 5 canals where stretch occurs. Cell culture is on the membrane. C. Picture of a chip with latest improvements: pressure chamber plus membrane within a P60 culture dish.

Next step was to optimise the vacuum system conditions to yield a mechanical behaviour similar to that occurring at the physiological aorta: sinusoidal cyclic uniaxial stretching at 1 Hz and 13% deformation or strain. The vacuum system performance was established by a servo controller instrument that monitored the pressure signal parameters before arriving at the chip, such as negative pressure magnitude, waveform, and frequency. However, the real negative pressure magnitude at the chip level was different to that monitored by the servo controller since the resistance caused by the conducting tubes delayed the pressure signal movement. Therefore, we established a real 13% negative pressure at the chip level by quantifying the deformation of the membrane *in situ*. We used a dissecting microscope to measure the change in distance between the microscope focused on the membrane at no pressure and at pressurisation. This displacement procedure was repeated 3 times for each negative pressure magnitude achieved by the servo controller: 10, 20, and 30 mmHg. The following mathematical deduction was used to find the membrane deformation value in the transverse axis out of the obtained focus displacements:

Lateral section of the pressurised membrane was approximated to an arc of a circle, where the arc width (W) was the original unpressurized membrane width (5 mm), and the arc height (H) was the measured focus displacement distance.

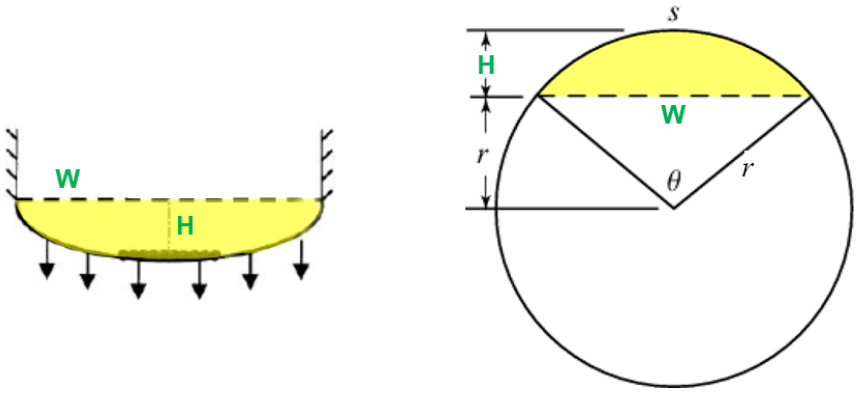

1. Radius of circle (*r*) given the width (W) and height (H) of the arc:

$$r = \frac{H}{2} + \frac{W^2}{8H}$$

2. Arc angle (*θ*) given the circle radius (*r*):

$$\cos\theta = \frac{a^2 + b^2 - c^2}{2ab} = \frac{r^2 + r^2 - W^2}{2rr}$$

3. Arc length (*s*) given the arc angle (*θ*):

$$s = 2\pi r * (\frac{\theta}{360})$$

4. Deformation ratio by comparing the unpressurized (W) and the pressurised (*s*) widths.

With this calculus, the membrane deformation was obtained for each pressure level, as stated in table 1. In the end, the servo controller was set to 20 mmHg in order to achieve the physiological 13% stretch deformation. Nevertheless, the overall system allowed maximum pressure frequency at 0.81 Hz as to maintain the 13% of deformation. An increase in the frequency of stretch would mean a decrease in the percentage of deformation of the membrane. Taking this into account, we decided that deformation was more important than frequency. Thus, in summary, the aortic bioreactor was set to subject cultured cells to a pulsatile stretch of 13% deformation and 0.81 Hz frequency.

Table 1. Membrane deformation rate under different pressure magnitudes.

Pressure magnitude	Focus displacement (n=3)	Average membrane strain
0 mmHg	0 mm	0%
10 mmHg	0.62, 0.83, 0.65 mm	5.14%
20 mmHg	1.11, 1.20, 1.04 mm	12.97%
30 mmHg	1.29, 1.51, 1.40 mm	19.97%

Furthermore, three separate chips were connected to active pulsatile negative pressurisation during 10 days with culture medium on top to assess whether the liquid permeated the chip's membrane. Once the determined time passed, no liquid had gone through the membrane. The focus displacement procedure was done again on these chips to evaluate any pressure performance changes in comparison to intact chips. As described before, the membrane deformation percentage was calculated for each pressure magnitude, and resulting values were displayed in table 2. Comparing deformation values before and after pressurisation during 10 days (table 1 vs table 2), we concluded that the chips' membranes did not suffer substantial mechanical fatigue after culturing under stretch.

Table 2. Deformation rate under different pressure magnitudes of stretched membranes for 10 days.

Pressure magnitude	Focus displacement (n=3)	Average membrane strain
0 mmHg	0 mm	0%
10 mmHg	0.45, 0.79, 0.65 mm	4.18%
20 mmHg	0.82, 1.23, 1.11 mm	11.38%
30 mmHg	1.35, 1.39, 1.37 mm	18.71%

In sum, the aortic bioreactor consisted of a single-use cell culture chip and a permanent vacuum system (figure 75). The vacuum system was composed of a vacuum machine, a servo controller to monitor the pressure, and a water trap to retain any liquid leak and

avoid its penetration into the servo controller that could damage it. All components were connected by means of flexible plastic tubes, and were all placed outside (but close to) the cell culture incubator. The chips were put inside the incubator, and connected to the vacuum system. The tube from the water trap to the chip had to enter into the incubator, thus it was covered by a rigid sheath that protected the tube from being pressed by the incubator door. Once inside, the tube was joined to a PDMS connector that distributed equally the pressure signal to the 5 different canals of a chip, using 2 mm diameter tubes previously sealed into the chip. Moreover, it was possible to connect up to three chips to the system at the same time, only by adding one or two T connectors.

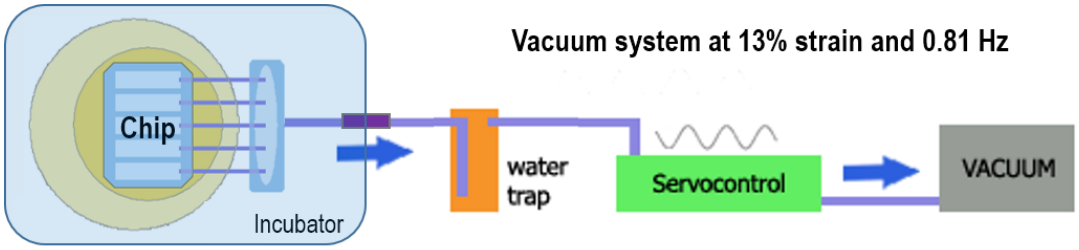

Figure 75. Schematic of the aortic bioreactor. The chip within an incubator received the negative pressure signal originated by the vacuum machine and modulated by the servo controller. The water trap prevented water drops from the incubator part to go inside the vacuum system.

3.1.3. Cell adhesion to chip

VSMCs were tested to adhere to PDMS, as it was the conforming material of the chip's membrane. Since the thickness of the whole chip was too high to allow the visualisation of the seeded cells by an inverted conventional microscope, first adhesion experiments had to be done on PDMS surfaces outside the chip. Hence, PDMS flat laminas of thickness 1 mm were fabricated and placed at the bottom of the wells of cell culture multi-well plates.

Different standard surface coatings were applied to the PDMS laminas to promote cell adhesion and prevent cell detachment due to substrate stretching: collagen, gelatin, poly-D-lysine (PDL), or fibronectin. Then, primary VSMCs were seeded on top. As a result, cells were almost not able to adhere to PDMS without a coating and formed small detached, floating clusters (figure 76A). Coatings facilitated cell adhesion to PDMS, but cells in gelatin tended to form bigger detached clusters after adhesion to the substrate (figure 76B). Moreover, although PDL and fibronectin coatings stimulated cell adhesion to the substrate (figure 76C and D), after 3-5 culturing days, the entire monolayer of adhered cells usually detached from the PDMS (figure 76E) and crumpled while floating in the culture well (figure 76F).

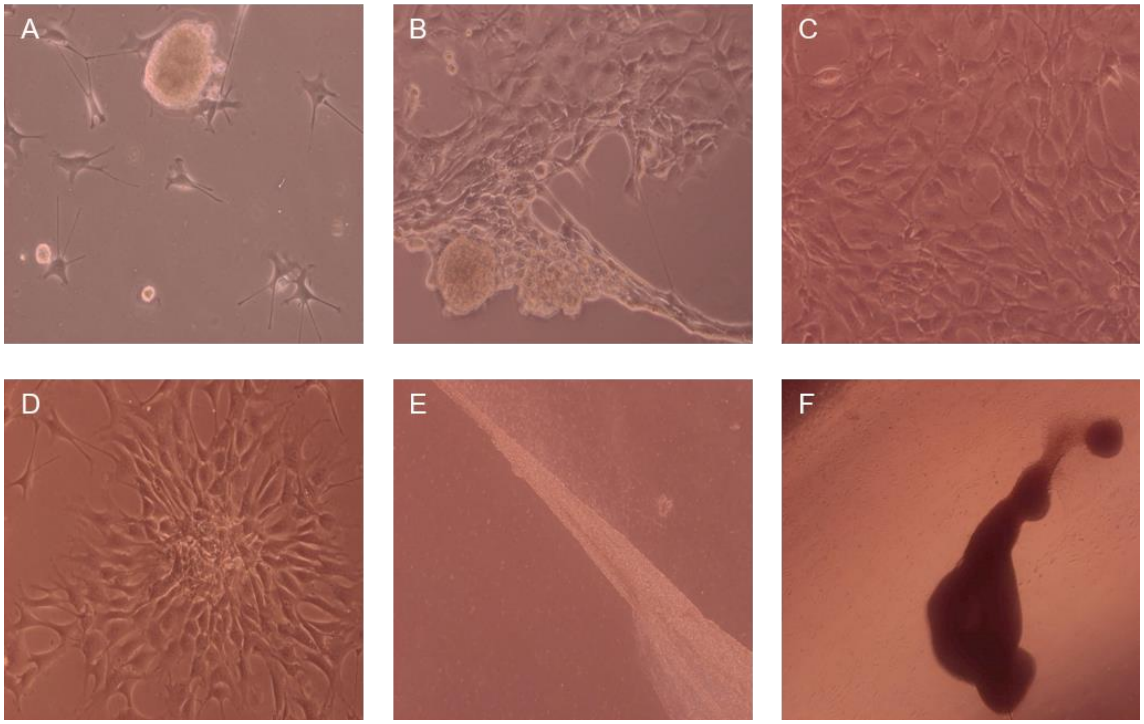

Figure 76. Cell culture onto coated PDMS. A. No coating. B. Gelatin coating. C. Fibronectin coating. D. PDL coating. E. Cell monolayer detachment from PDMS. F. Crumpled detached cell monolayer.

To enhance coating attachment to the PDMS substrate, a previous step of standard plasma treatment was inserted in the protocol: 30 seconds at the maximum power of surface plasma activation. This procedure led to correct cell adhesion in all coating conditions (figure 77). Furthermore, cells on fibronectin and on PDL+collagen were also able to proliferate up to confluence and to spread themselves throughout all the available coated substrate (figure 77B and F). Owing to the effect of the plasma treatment, cells did not detach from the substrate after 7 days of culture.

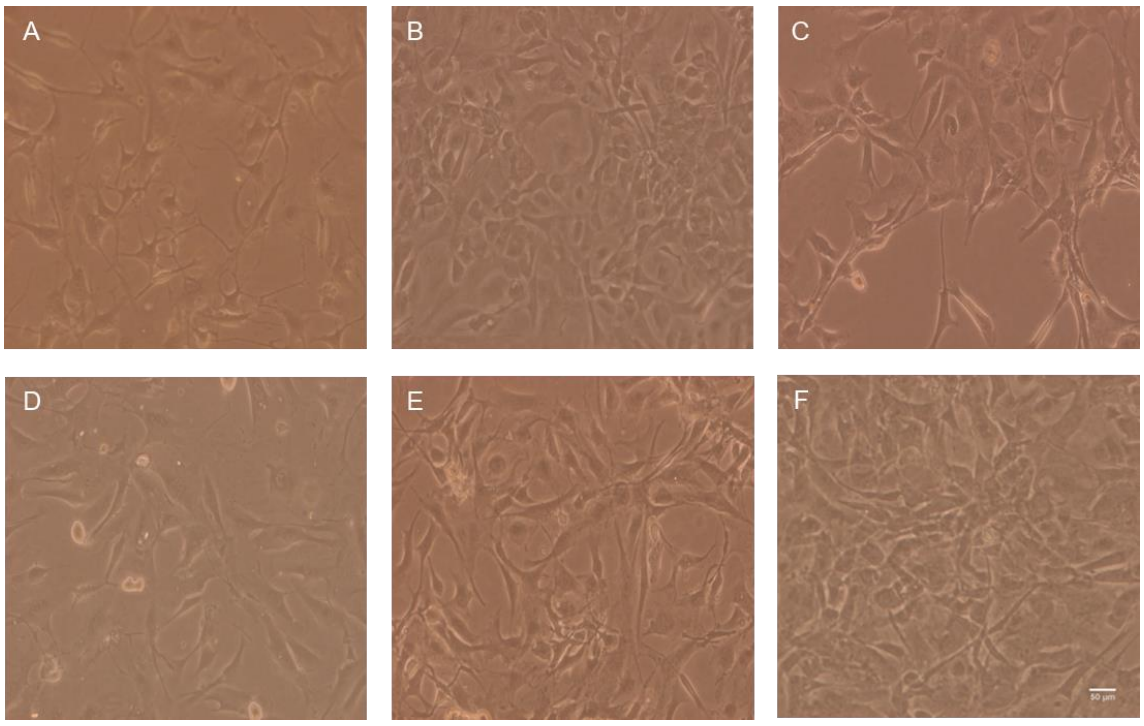

Figure 77. Cell culture onto coated PDMS with previous plasma treatment. A. No coating. B. Fibronectin coating. C. PDL+gelatin coating. D. PDL coating. E. Collagen coating. F. PDL+collagen coating. Scale bar = 50 µm.

In the next assay, cells were seeded on PDMS laminas coated with fibronectin or PDL+collagen, as previous experiments showed their successful performance. Cells were cultured for 7 days and the medium was supplemented with 50 µg/mL ascorbic acid to stimulate the ECM secretion by cells[93,135]. ECM formation was assessed by performing immunofluorescence of collagen since it is one of the main components of aortic tunica media ECM. Indeed, cells in these both coating conditions generated a three-dimensional mesh of collagen fibres (figure 78).

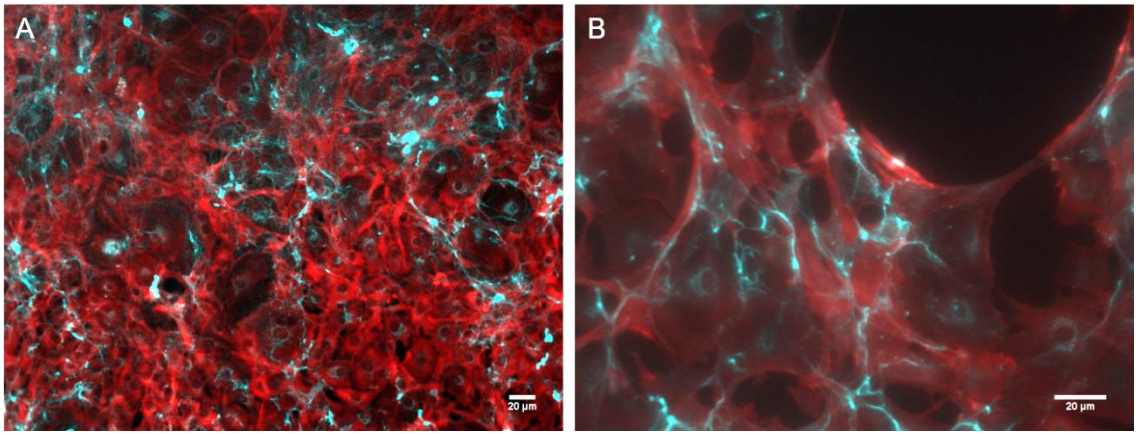

Figure 78. Immunofluorescence of cells (actin cytoskeleton marked in red) and collagen fibres (marked in cyan). A. Cell culture on PDMS lamina coated with PDL+ collagen. B. Cell culture on PDMS lamina coated with fibronectin. Scale bar = 20 µm.

In the case of PDL+collagen, we observed that collagen coating was obviously labelled by the anti-collagen I antibody of the immunofluorescence procedure (see the blue labelling outside the places where cells are located in figure 79). This drawback plus the required time of incubation (5 hours), refrained us from using collagen in the standard coating procedure for chips, and established fibronectin coating as the optimal chip coating. In detail, fibronectin coating protocol involved the incubation of 10 µg/mL commercial fibronectin on the plasma-activated PDMS substrate during 1 hour at 37ºC.

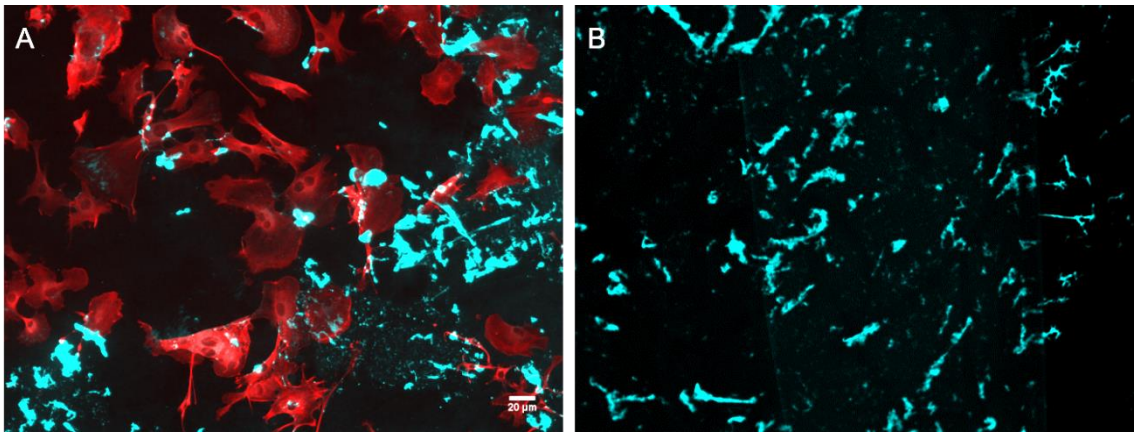

Figure 79. Immunofluorescence of cells (actin cytoskeleton in red) and collagen fibres (in cyan) onto PDMS lamina coated with PDL+collagen. A. Zone at the edge of a group of cells. B. Zone without cells. Note collagen staining where no cells are present. Scale bar = 20 µm.

This determination on fibronectin coating for cell adhesion to PDMS was transferred to actual cell seeding onto chips. However, a new element had to be introduced into the chip design first, in order to retain the cell culture medium on the canals. A five-canal culture chamber was created to fit on top of the chip's membrane coinciding with the five canals of the chip pressure chamber (figure 80). The culture chamber allowed 500 µL of culture medium per canal, which was an adequate volume for cell culturing on a 125 mm^2 area. On the experiment day, a culture chamber was attached to the chip immediately after plasma treatment, taking advantage of the material attachment properties that plasma activation provides. However, on the 2nd day of culture, the culture chamber slowly detached from the chip, leading to a loss of cell culture medium. Hence, plasma treatment time was increased to 1 minute, in order to guarantee culture chamber attachment to the chip for at least 7 days.

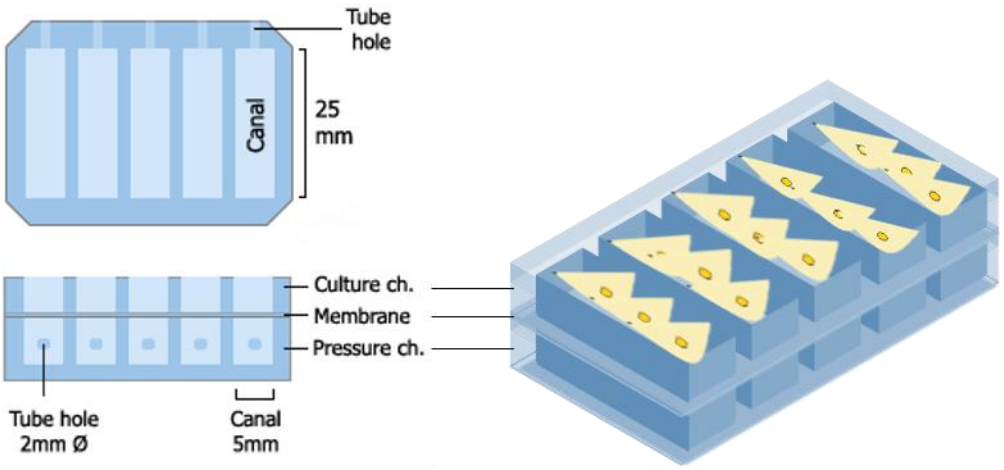

Figure 80. Chip components. A chip was composed of a PDMS pressure chamber, a PDMS membrane, and a PDMS culture chamber on top. The culture chamber divided cell culture into 5 separated canals.

To conclude, 10 µg/mL fibronectin coating with previous plasma treatment worked fine for cell attachment to chip membrane. The seeding protocol in detail consisted in:

1- on the day of the experiment, a plasma treatment was performed on the chip at maximum power for 1 minute;

2- the culture chamber was firmly attached to the chip;

3- 20 minutes of ultraviolet light sterilisation were applied to the chip, since all the previous steps were done out of an antiseptic ambient;

4- the membrane was coated with fibronectin at concentration 10 µg/mL for 1 hour at 37ºC (incubator);

5- the coated membrane was rinsed thrice with PBS and the cells in culturing medium were gently pipetted in the canals;

6- the seeded chip was finally placed into a cell culture incubator at 37ºC in a humidified 5% CO_2 atmosphere;

7- the culturing medium was changed every 2 days.

After 7 days, a phalloidin immunocytochemistry procedure was performed to demonstrate cell presence on the chips (figure 81A) (this methodology is explained in detail at the following section “Immunocytochemistry, protein, and mRNA analysis in the bioreactor”). The same procedure was done with another chip, but in this case, the stretch stimulus was activated the day after cell seeding. Particularly, cells were left unstretched overnight to allow a strong adhesion to the chip’s membrane and avoid cell detachment when the vacuum system was activated to generate stretching of the membrane. The immunofluorescence images demonstrated that this procedure was successful in maintaining cells onto the chip’s membrane even in stretching condition (figure 81B).

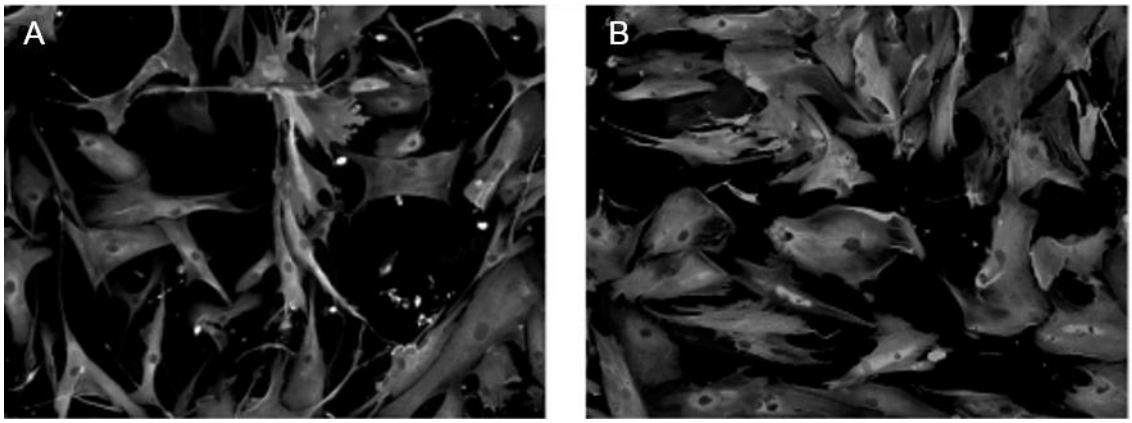

Figure 81. Cell actin cytoskeleton immunofluorescence. A. Cell culture on chip during 7 days. B. Cell culture on chip during 7 days under stretching condition.

3.1.4. Cell culture on chip

Once the bioreactor’s mechanical performance and cell adhesion were optimised, cell culture parameters were standardised for subsequent experiments. The number of seeded cells was the next variable to optimise, in order to achieve cell confluence the day after seeding for ideal posterior analyses. We conducted experiments comparing 40,000, 60,000 and 100,000 cells seeded onto a chip’s canal (figure 82). The concluding result was that 60,000 cells per canal was the ideal cell seeding number to yield overnight confluence (figure 82B). Taking into account the posterior use of a canal, cells were seeded to confluence (60,000 cells) for protein and mRNA analysis, and were seeded to semi-confluence (30,000) for posterior immunocytochemistry so that individual cells could be appropriately observed under the microscope.

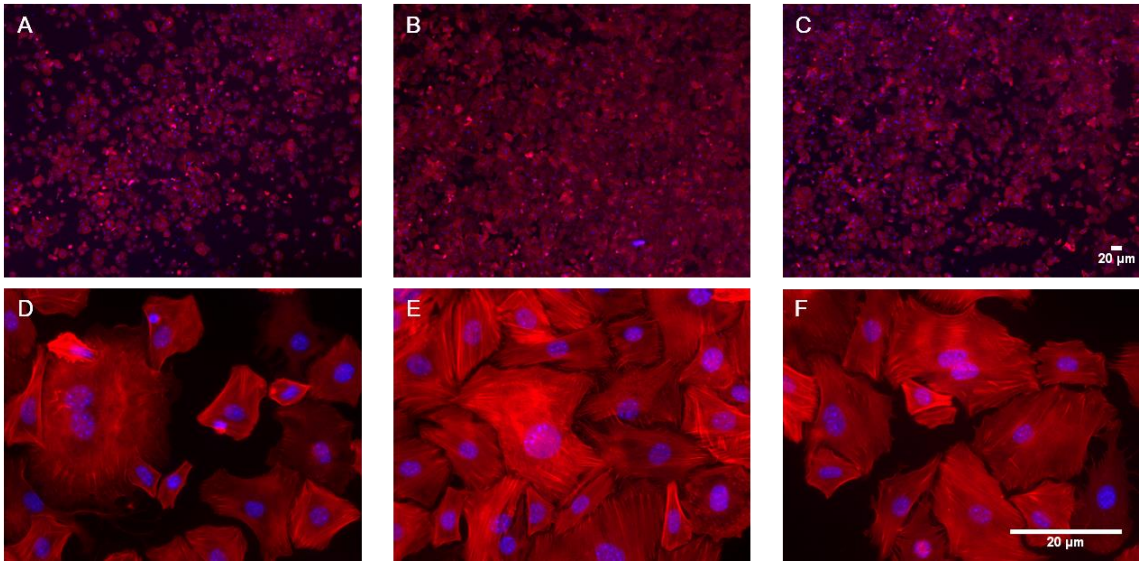

Figure 82. Cell confluence assessment after overnight attachment to chip. Immunocytochemistry of 40,000 (A, D), 60,000 (B, E) and 100,000 (C, F) cell seeding conditions. Cell actin cytoskeleton marked in red, cell nuclei marked in purple. Scale bar = 20 µm.

Although chips were sterilised with ultraviolet light before cell seeding, some experimental chips were contaminated by bacteria or fungi. This fact made clear that sterilisation and cleaning ought to be more severe, since chips were fabricated on the non-sterile general workbench and there was too much manipulation within the incubator. Hence, a step of ultraviolet sterilisation during 1 hour was introduced right after chip fabrication termination. Next, chips remained sealed until the experiment day. Then, the chip was opened to perform the usual established steps for cell seeding: plasma treatment and culture chamber attachment in a non-germ-free environment, 20 minutes of ultraviolet light sterilisation, fibronectin coating and cell seeding in a sterile laminar flow cabinet. Besides, all bioreactor experiments were performed in a separate incubator only meant for this purpose, which was cleaned and disinfected for each new experiment.

Another fact that was evident in long-term culture within chips was the evaporation of culture medium due to incubator conditions. This phenomenon is common in conventional cell culture, albeit it is not apparent since culture dishes are usually filled with exceeding cell culture medium. In our case, the chips had a little amount of medium (500 µL per canal) combined with an extended evaporation surface (~125 mm^2), which led to the evaporation of half of the medium in one night. To overcome this issue, the chip was entirely glued into a P100 cell culture dish and this dish was filled with sterilised water, so that the total amount of evaporation surface at the chip was increased. With this improvement, there was very little evaporation of culture medium.

Adding this new element to the device, the final aspect of an optimised chip is as illustrated in figure 83.

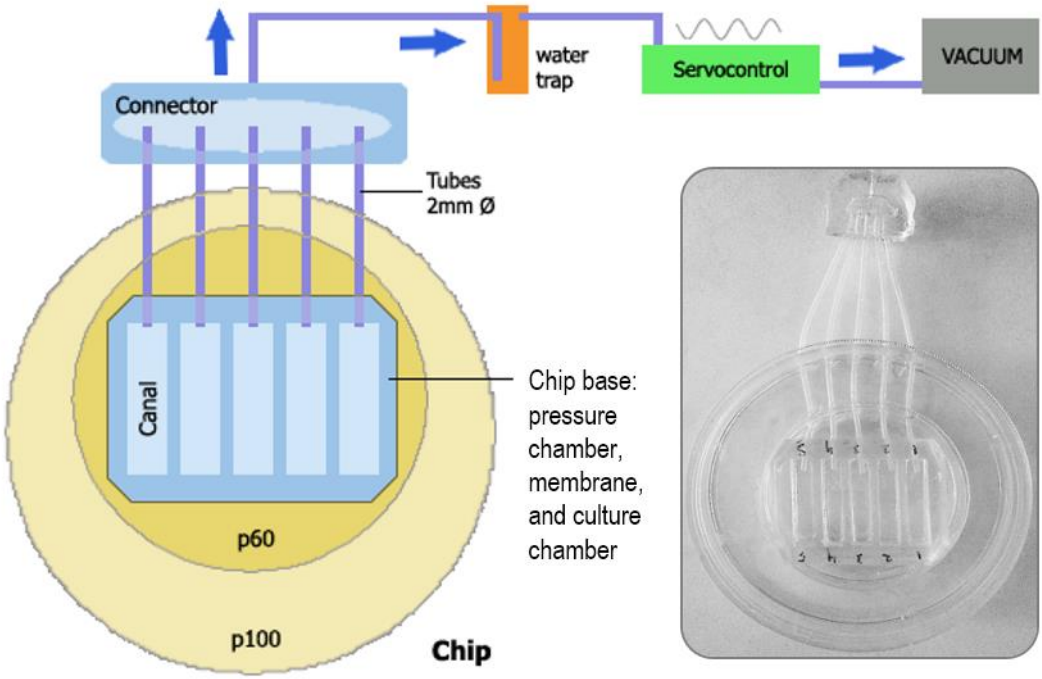

Figure 83. Final stretching bioreactor components.

3.1.5. Immunocytochemistry, protein, and mRNA analysis in the bioreactor

After cell culture on a chip, the collection of cell lysate for protein and mRNA analysis was performed as usual, but using an adapted scrapper. This scraper was cut to fit inside a canal and had to be used gently not to tear the fragile membrane. Cell lysis reagent was initially TRIzol so that protein and mRNA could be extracted from the same sample. However, the protein concentration obtained with this procedure was too low, making not feasible to extract mRNA and protein from the same sample with TRIzol. Hence, the subsequent experiments used different canals for each component extraction, protein or mRNA, and for further protein analysis, the conventional RIPA lysis buffer was used for protein and TRIzol for mRNA. Verification assays of protein and mRNA quantity demonstrated that cell lysate from a whole chip could yield ~100 µg of protein or 101.5 ng/µL of mRNA, which was sufficient for subsequent analyses. At protein level, elastin, actin, collagen, and calponin-1 proteins presence were checked by western blot on control samples of cells seeded on chips (figure 84A). Also, collagen I, myocardin, and GAPDH mRNA presence were checked by PCR on control samples of cells seeded on chips (figure 84B). With these verifications, we concluded that protein and mRNA analyses were possible on cells cultured on bioreactor chips.

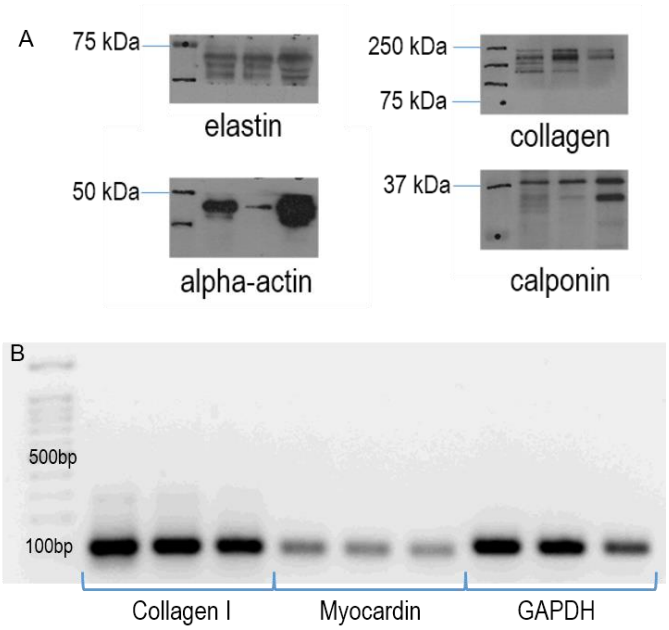

Figure 84. Example of protein (A) and mRNA (B) analysis of control cell lysate from bioreactor chip culture.

On the other hand, the standard immunocytochemistry procedure was performed entirely on the chip since the membrane was not as rigid as a coverslip to be accurately handled as in a conventional manner. The steps were the same as in a standard paraformaldehyde procedure, but all reagents were poured onto the chip's canals, and in the end, the membrane was dissected with a scalpel and mounted between a microscope slide and a coverslip (refer to the Materials and methods section for more detail). It is important to note that all liquids on the chip had to be gently removed by a micropipette instead of with a vacuum aspirator that could fatally suckle the chip's membrane and tear it. As a proof of concept, we did an ECM immunofluorescence to verify the proper functioning of the established protocol. Fibrillin-1 and collagen I were stained on control samples of cells cultured on chips under stretching conditions during 7 days. A prominent ECM was observed (figure 85 and 86). These experiments jointly with the immunostainings for cell confluence and adhesion assays demonstrated the possibility of performing immunocytochemistry procedures on the chips.

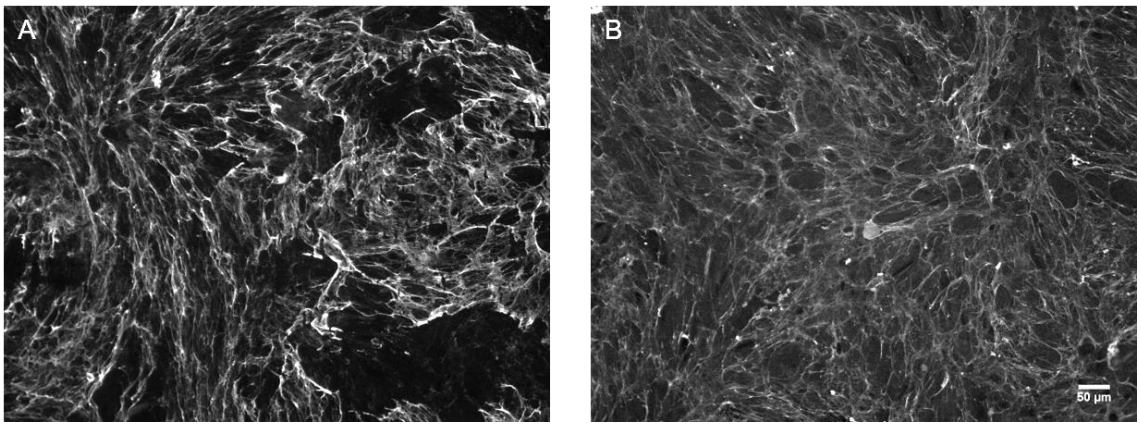

Figure 85. Immunofluorescence marking collagen I (A) and fibrillin-1 (B). Scale bar = 50 µm.

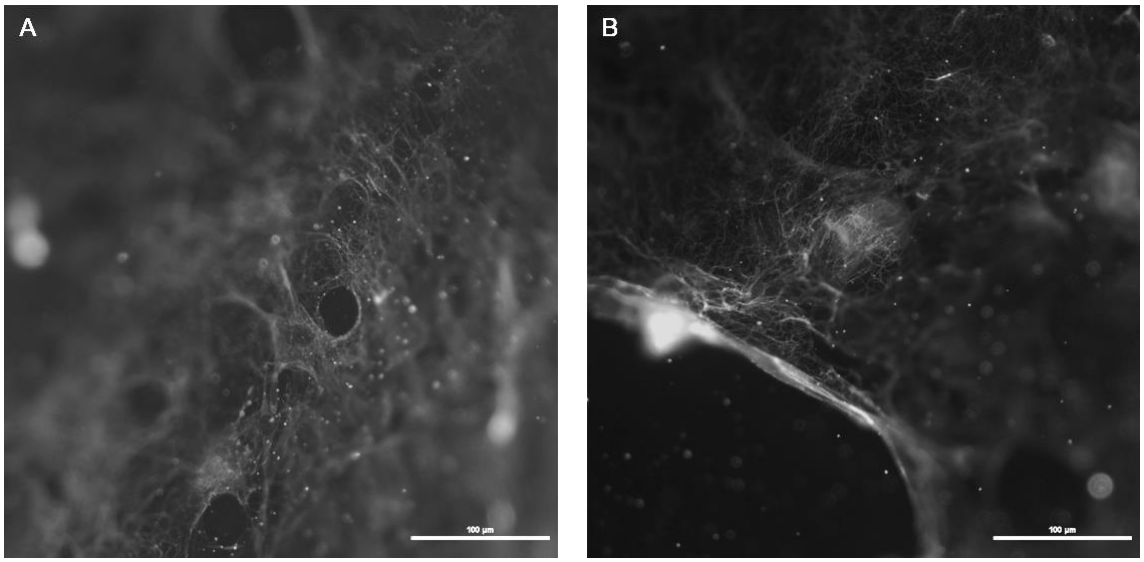

Figure 86. Confocal images of collagen staining. A. Collagen mesh at the centre of cell culture. B. Collagen mesh at the edge of a cell group. Scale bar = 100 µm.

In addition, PDMS membranes alone were assessed for autofluorescence and for unspecific antibody binding. An immunocytochemistry procedure was applied to intact chip membranes without seeded cells. Microscopy examination of these samples revealed no staining. Therefore, PDMS membranes had no autofluorescence and did not bind to random primary or secondary antibodies or BSA.

3.2. Technology application to human Marfan VSMCs

3.2.1. Study overview

Once all bioreactor parameters were optimised, we applied the device for Marfan syndrome studies. To evaluate the effect of mechanical stretching on VSMCs at different exposure times, stretched cells cultured on chip were compared to cells cultured on chips but without the stretch, as well as to cells seeded on conventional culture substrates (glass coverslips for immunocytochemistry and 6-well polystyrene culture plates for western blot). Chips with activated stretch condition were named “dynamic cultures”, whereas conventional culturing and non-stretching chips were called “static cultures”. VSMC culture conditions were maintained during 0 (only overnight adhesion), 3, and 7 days under stretch. In accordance with the mentioned culture parameters, we have established the following nomenclature (visually explained in figure 87). Samples of cells seeded on chips were named with an “E” for static or a “D” for dynamic, plus the number of culture days (0, 3, or 7). In addition, some specified conventional culture substrates were fibronectin-coated to see if this coating, also used on chip seeding, was responsible for any possible difference on the results. Thus, samples of cells seeded on conventional

substrates were designated with the culturing days' number followed by the specification of fibronectin coating presence: positive or negative (labelled FN+ or FN-). Note the abbreviated nomenclature for each condition in Figure 17, as it will be used in the following sections.

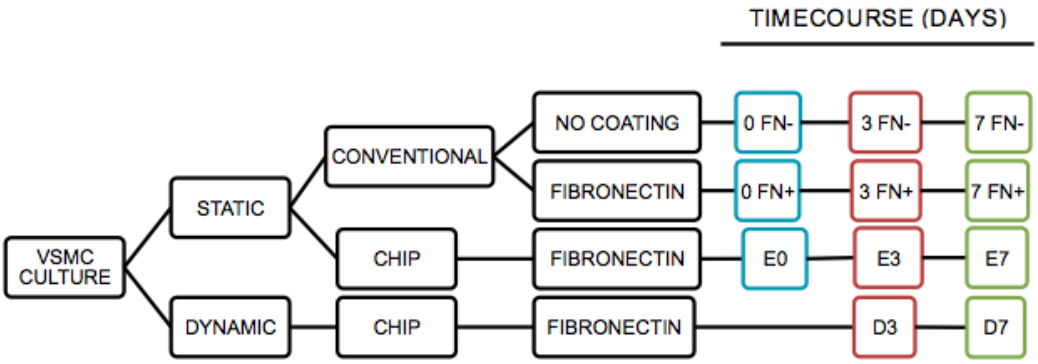

Figure 87. Labelling of the different conditions in which the cells were seeded depending on the substrate, coating and time.

3.2.2. Focal adhesion analysis

To demonstrate real cell adhesion to the chip's membrane, we analysed the vinculin staining as an approximation of focal adhesion distribution in the cells. Immunocytochemistry of vinculin and actin staining was carried out on cells seeded onto a chip without stretch (static) and onto glass coverslip (the conventional immunofluorescence substrate). In addition, this assay was performed with control and Marfan VSMCs. Indeed, for both genotypes, the vinculin linked to the actin stress fibres was clearly observed (figure 88).

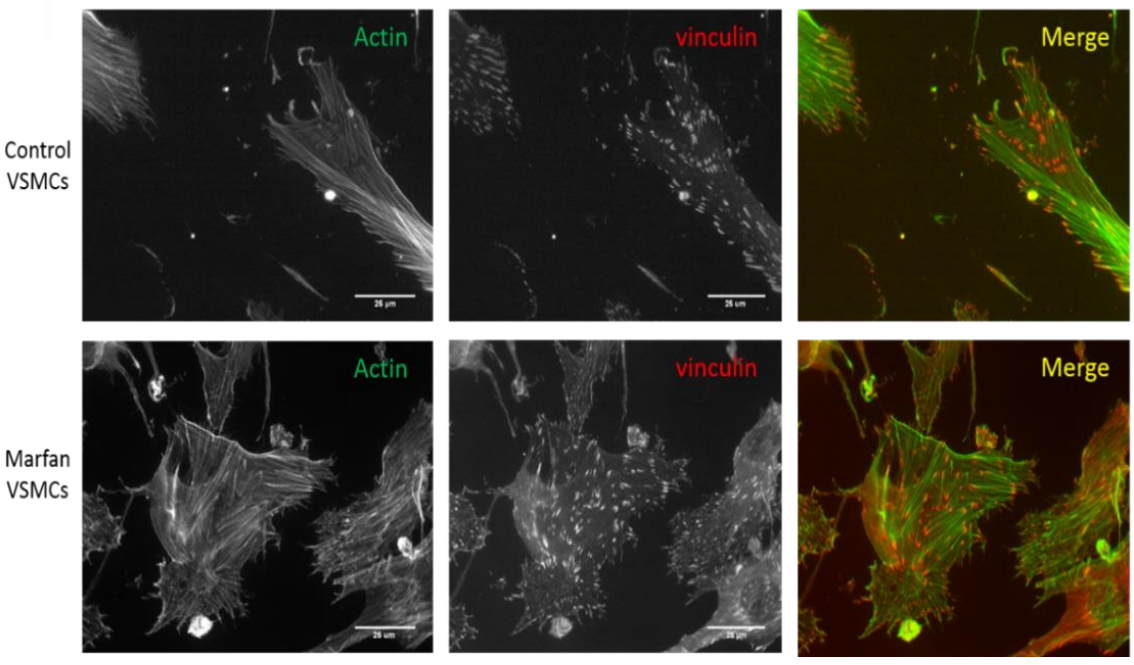

Figure 88. Focal adhesion immunofluorescence. Control and Marfan VSMCs seeded on chips without stretch activation. Scale bar = 25 µm.

Focal adhesion quantitative analysis was performed in terms of the vinculin area related to total cell area and the density of focal adhesion. On the one hand, we studied the area in the aforementioned two culturing conditions for both VSMCs genotypes (figure 89A). Importantly, there were significant differences between the static coverslip and the static chip conditions in control and in Marfan VSMCs: VSMCs had greater focal adhesion area on the rigid surface of coverslips than on the soft surface of the chip's membrane. On the other hand, we also studied the density of focal adhesion (number/µm^2) under these conditions and genotypes (figure 89B). There was a significant difference between the static coverslip and the static membrane controls. The Marfan results remained highly similar between both culture conditions.

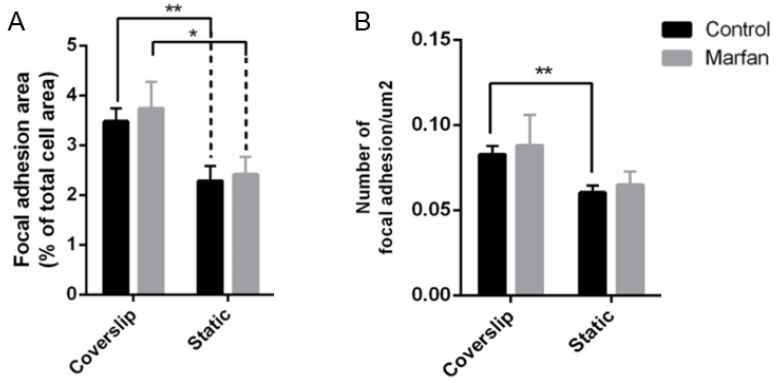

Figure 89. Focal adhesion quantitative analysis. A. Focal adhesion area related to total cell area on control and Marfan VSMCs cultured on coverslip or static chip. B. Number of focal adhesions per µm^2 on control and Marfan VSMCs cultured on coverslip or static chip. Control VSMCs samples, n=3; Marfan VSMCs samples, n=3. Ten cells were analysed per replicate of each genotype. * P value <0,05; ** P value <0,01.

3.2.3. Cultured VSMC orientation

The direction of the cultured cells was considered a parameter of mechanically induced cytoskeletal reorganisation by the effect of imposed stretch. Therefore, the directionality of control and Marfan VSMC was studied by actin cytoskeleton immunofluorescence staining. A tendency of alignment towards the stretch direction was observed in some conditions both from control and Marfan samples (figure 90).

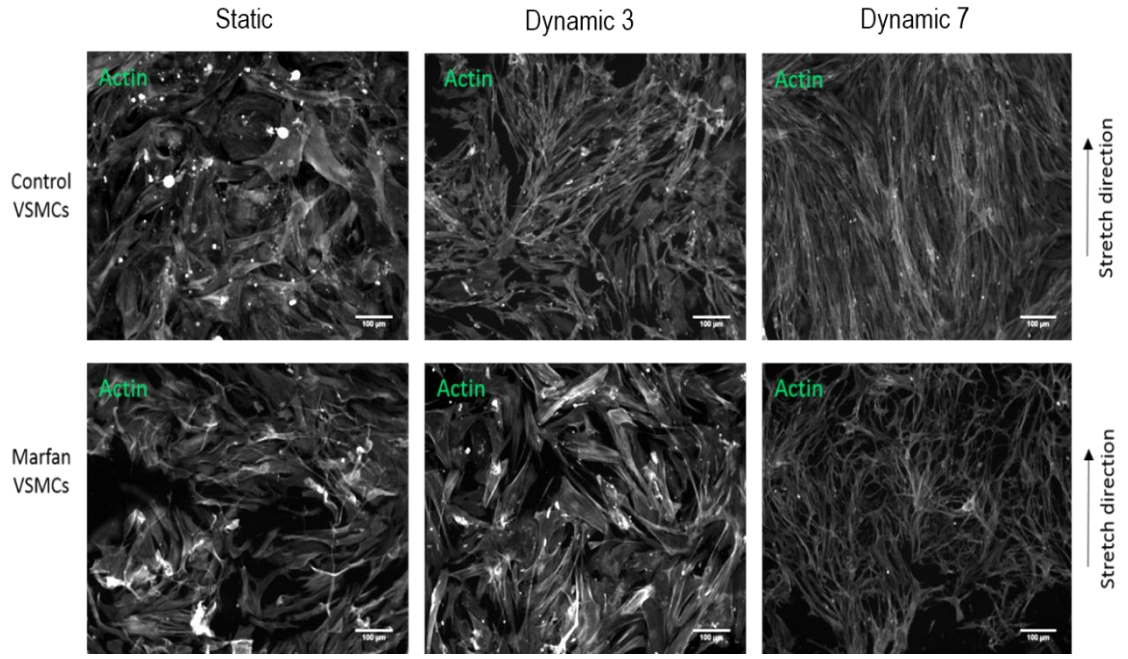

Figure 90. Control and Marfan VSMCs cytoskeleton immunofluorescence. Representative images of some conditions are shown. Actin cytoskeleton staining of static (E0), dynamic 3, and dynamic 7 conditions of Marfan and control VSMCs. Scale bar = 100 µm.

To quantify this cell alignment tendency, the direction of each cell present in an image of actin staining was manually marked, and their direction angle in relation to the applied stretch direction was measured (figure 91). Cell angle values ranged from 0º to 180º, being 0º the stretch direction. Biologically, it is relevant that cells orient parallel, perpendicular, or oblique to stretch direction, but it is irrelevant if obliquity is on the left or on the right sides. Hence being oriented in the range of 90 to 180 degrees is biologically the same as being oriented in the range of 0º to 90º. Thus, values in the range of 90º to 180º were converted to the range of 0º to 90º.

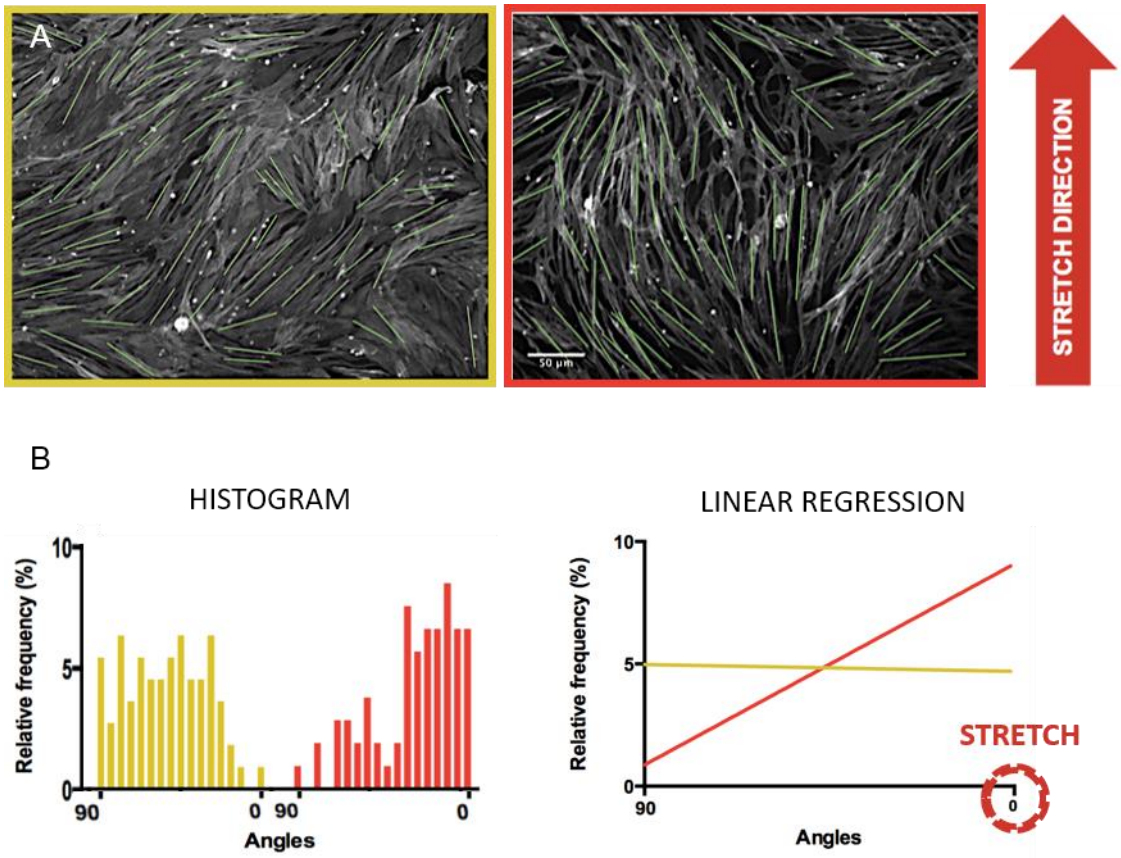

Figure 91. Example of cell directionality analysis. A. Example images of cell directionality assessment. Marfan VSMCs on two conditions, static 0 (yellow) and dynamic 7 (red) with the directionality of the cells marked in green, ready for the following angle analysis. Scale bar = 50 µm. B. Graphs of cell directionality assessment of example images in figure 91. Marfan VSMCs on two conditions, static 0 (yellow) and dynamic 7 (red). Both graphs plot relative frequency by angle direction from 90º to 0º. Importantly, 0º is the stretch direction.

Cell directionality was analysed related to the alignment of cells towards the stretch direction (0º). Obtained cell directionality values were represented using two types of graphs: histogram and linear regression analysis representation graph (figure 91). Histogram graphs showed the distribution of cell directionality regarding frequency of each angle group (from 90º to 0º in groups of ten angles). Linear regression was obtained to assess statistical significance between histogram distributions of all the conditions. It generated a slope that represented the global distribution of the histogram and computed whether the histogram slope was significantly different to zero. Zero represented horizontality, which meant the absence of pendent. In our study, a horizontal slope meant that there was no preferential cell alignment to any angle, so cells individually had random directionalities (yellow example in figure 91). Conversely, slopes significantly different to zero had a pendent. If the slope tended to higher angles (downhill), the cell alignment was perpendicular to stretch direction. In contrast, if the slope tended to lower angles (uphill), cell alignment was parallel to stretch (red example in figure 91).

With this methodology, the influence of long time stretch application on control and Marfan VSMCs direction alignment was analysed. Histogram graph distributions revealed control VSMCs cultured on chips under static condition overnight (E0) and under the dynamic condition for three days (D3) were equally oriented in all directions (figure 92A), meaning that cells were not aligned to any particular direction. Notably, control VSMCs cultured under the dynamic condition for seven days (D7) showed an alignment towards the stretch direction (0º). Analysis of linear regression graphs showed that D7 control VSMCs' slope was significantly non-zero (figure 92B), demonstrating a significant trend to the stretch direction angle.

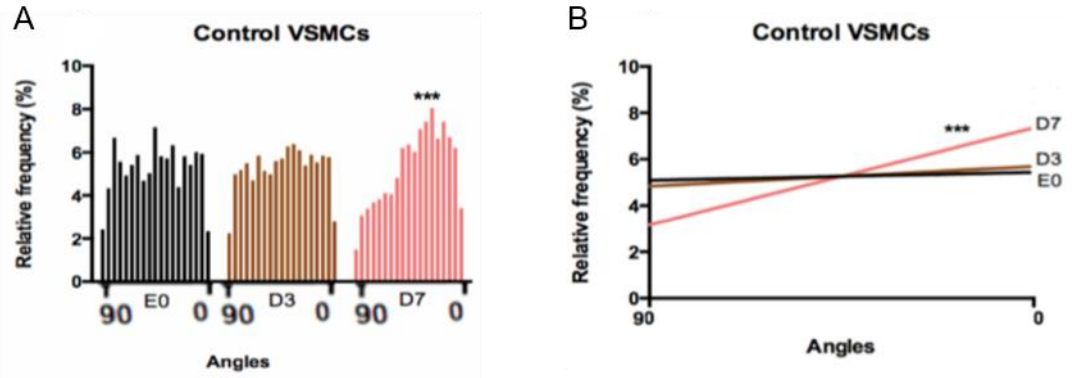

Figure 92. Directionality assessment of control VSMCs under stretch exposure on chips. A. Histogram of control VSMCs directionality frequencies under static and dynamic conditions. B. Linear regression of control VSMCs directionality based on the histogram values. Control samples, n =3. Approximately 1,000 cells were counted per replicate. ***P value <0.001. E0 corresponds to static 0 days, D3 to dynamic 3 days, and D7 to dynamic 7 days.

Moreover, Marfan VSMCs cultured under E0 condition also remained randomly oriented in all directions as the control counterparts (figure 93A). Furthermore, Marfan VSMCs cultured under dynamic conditions for 3 or 7 days (D3 or D7) showed a slight tendency toward low angles. However, any Marfan VSMCs slope was significantly non-zero, although it could be observed that the generated linear regression of D3 and D7 was not horizontal but slightly sloped (Figure 93B). In summary, both genotypes showed a tendency to align towards stretch direction at seven days of exposure to stretch, although only control cells had a statistically significant result.

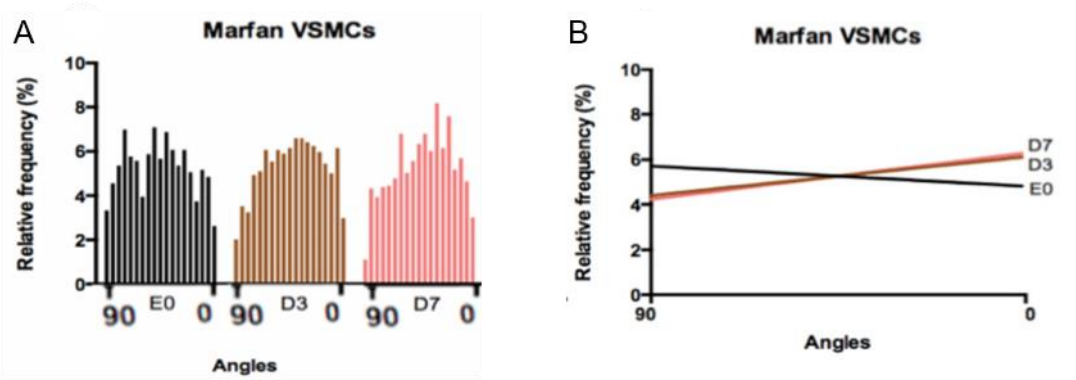

Figure 93. Directionality assessment of Marfan VSMCs under stretch exposure on chips. A. Histogram of Marfan VSMCs directionality frequencies under static and dynamic conditions. B. Linear regression of Marfan VSMCs directionality based on the histogram values. Marfan samples, n=3. Approximately 1,000 cells were counted per replicate. E0 corresponds to static 0 days, D3 to dynamic 3 days, and D7 to dynamic 7 days.

Furthermore, we completed our experiments by adding a whole set of cell culture control conditions: conventional culture (seeded on glass coverslip with or without fibronectin coating) as well as static culture on chips at the established different culture days (figure 94). The cell directionality of those samples was evaluated, and the obtained results were compared to the previous ones. Altogether, control VSMCs showed significant alignment on 0 FN-, 7 FN-, E7 and D7, but it was not towards the stretch direction in most cases (figure 94A). The condition 3 FN- on control cells also displayed a tendency to align perpendicular to the stretch, but it was not statistically significant. Moreover, Marfan VSMCs only displayed significant alignment towards the stretch on condition E3, and it was towards the opposite direction of stretch (figure 94B).

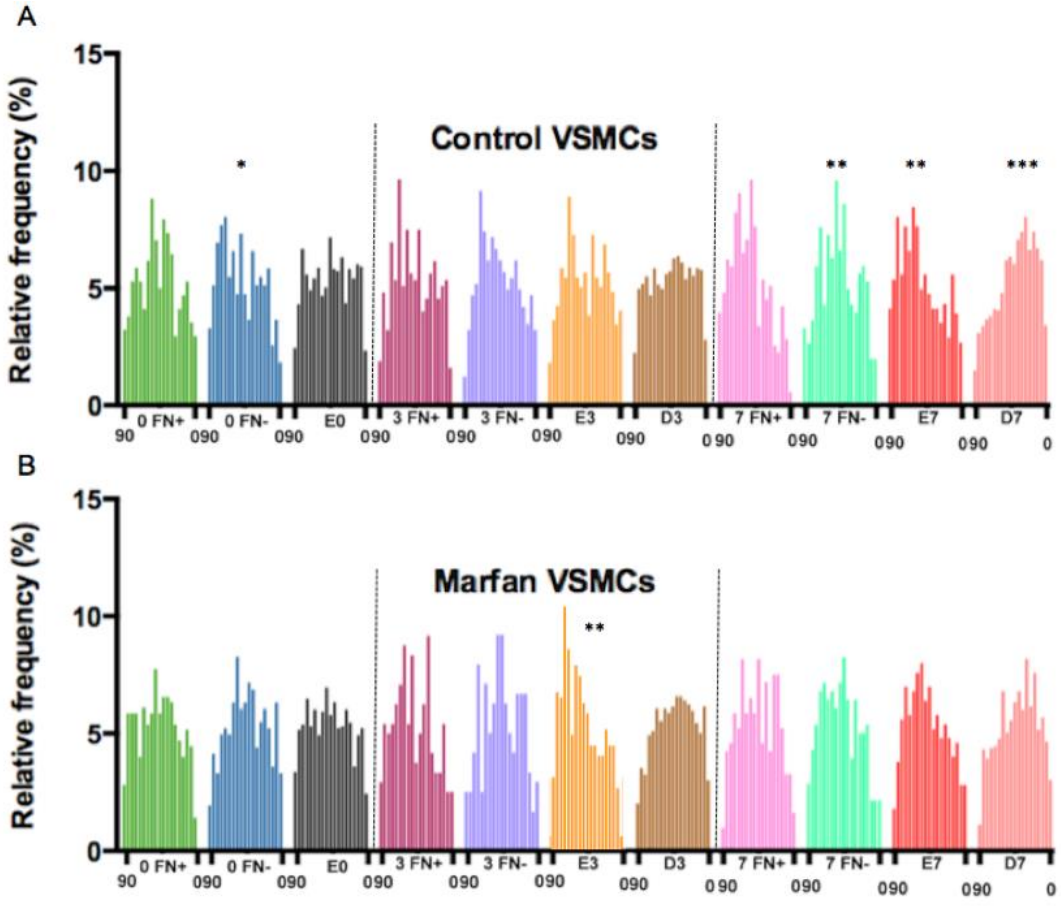

Figure 94. Directionality of the eleven different conditions for both genotypes, control (A) and Marfan (B). Control samples, n=3; Marfan samples, n=3. Approximately 1,000 cells were counted per replicate of each genotype. *P value <0.05; ** P value <0.01; ***P value <0.001. FN- corresponds to coverslip; FN+ to coverslip with fibronectin coating; E0,3,7 to static chip for 0,3 and 7 days; and D3 and D7 to dynamic chip for 3 and 7 days (refer to section 3.2.1 for culture condition details).

In summary, most of the assayed culture conditions rendered randomly placed cells, but control cells subjected to 7 days of stretch exposure were aligned toward the stretch direction. Also, control cells seeded on non-coated coverslips tended to align towards 90º, as well as, the ones cultured 7 days on a static chip. Furthermore, differential culturing substrate seemed not to have this same effect on Marfan VSMCs, with the exception of culture on static chip for 3 days (E3).

3.2.4. Cell distribution of contractile phenotype markers in VSMCs

To assess the cellular distribution of the main contractile phenotype marker proteins, an immunocytochemistry protocol was carried out to stain SMA, transgelin, and F-actin proteins. Gross observation of the contractile markers showed that SMA staining worked well and cells showed good staining (figure 95). Conversely, transgelin showed diffuse, unspecific staining in cell cytoplasm (figure 96). We could not optimise the transgelin staining, so it was not possible to analyse it quantitatively.

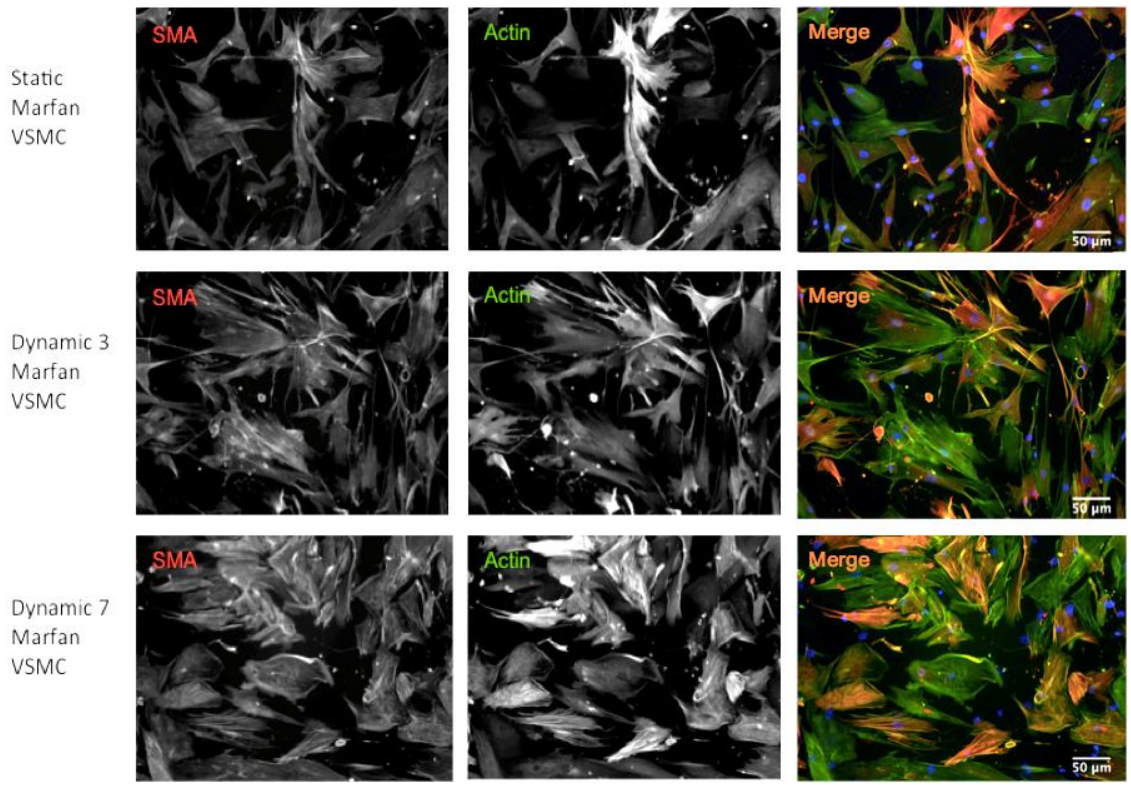

Figure 95. Immunofluorescence staining of SMA, F-actin, and DAPI and the merged image of the three stainings. Representative images of some conditions are shown: Marfan VSMCs cultured on a chip under static condition overnight and under dynamic condition for three days and seven days. Green corresponds to actin staining, red corresponds to SMA staining, blue corresponds to DAPI nuclei staining, and orange corresponds to colocalization between SMA and actin proteins. Scale bar = 50 µm.

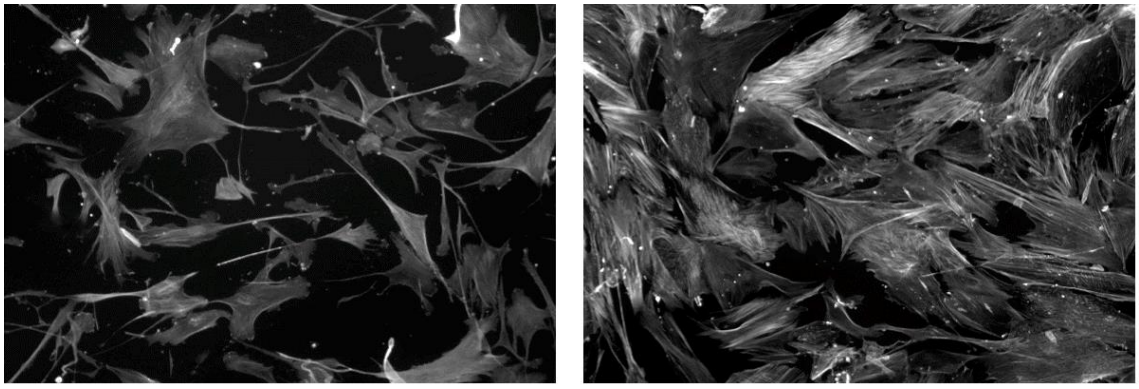

Figure 96. Immunofluorescence staining of transgelin, example images.

To integrate the SMA observations along with quantitative values, the cytoplasmic distribution pattern of SMA was measured in the samples. To do so, the occurrence percentage of each of three different SMA staining patterns was quantified: VSMC with organised fibres positively stained for SMA (SMA+fibres+); VSMC with cytosolic diffuse SMA staining (SMA+fibres-), which meant that these cells had SMA monomers but they were not assembled into fibres; and negative staining for SMA (SMA-), meaning these cells had very low expression of SMA (figure 97). Actin and DAPI staining allowed the visualisation of all cells, particularly those without SMA staining.

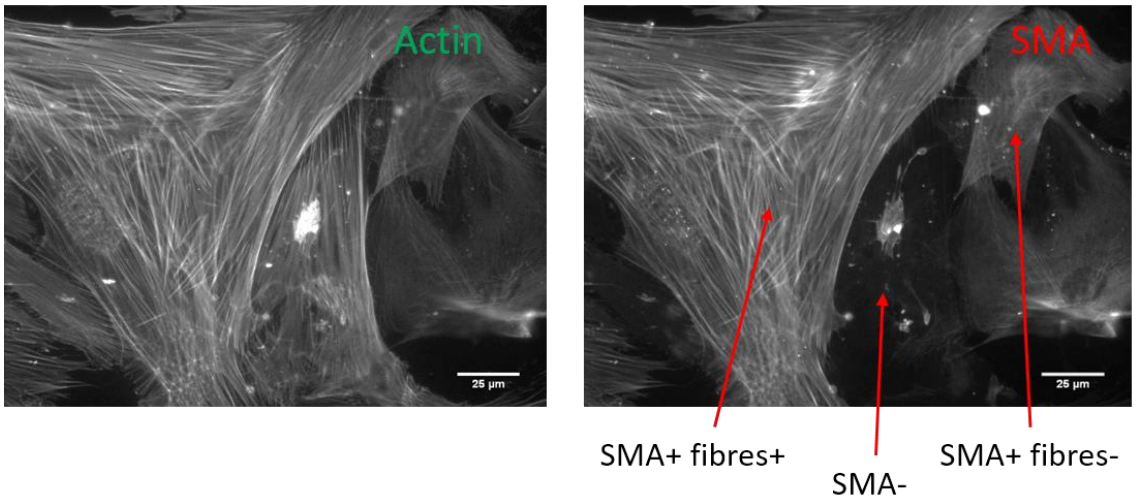

Figure 97. Example image of the actin cytoskeleton and SMA staining of same cells to illustrate the different SMA cytoplasmic distribution patterns: SMA+fibres+, SMA+fibres-, and SMA-. Scale bar = 25 µm.

Percentage of cells with these staining patterns was done for control and Marfan VSMCs (figure 98). In summary, the percentage of cells with each staining pattern was similar between all conditions of both VSMCs genotypes. Furthermore, statistical analysis showed no significant differences between any conditions (figure 98).

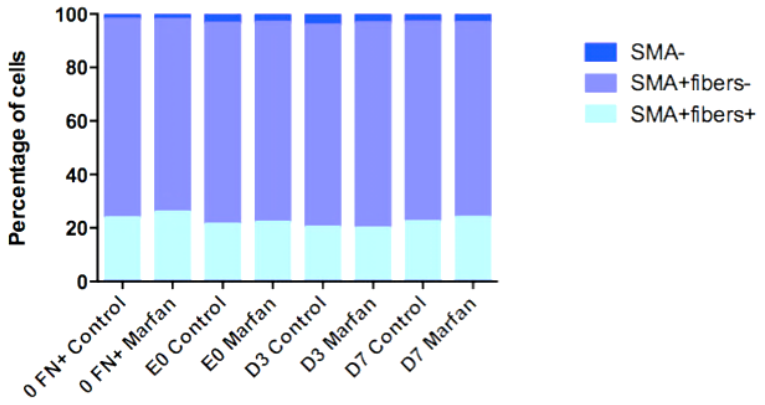

Figure 98. Analysis of the SMA staining pattern. Plots of the percentage of control and Marfan cells with each SMA staining pattern in each condition. Control VSMCs samples, n=3; Marfan VSMCs samples, n=3. Approximately 1,500 cells were analysed per replicate of each genotype.

3.2.5. Contractile marker levels in VSMCs

Finally, the contractile marker protein levels were analysed in control and Marfan VSMCs in relation to different exposures to stretching condition. Protein extraction and western blot analysis were performed for each one of the eleven conditions (figure 99). As a result, SMA and transgelin protein levels remained similar between different static and dynamic conditions in control and Marfan VSMCs (figure 99B and C). However, although not significant, Marfan VSMCs showed, more contractile protein quantity than control VSMCs, in the majority of the culture conditions (darker bars vs lighter bars at figure 99B and C).

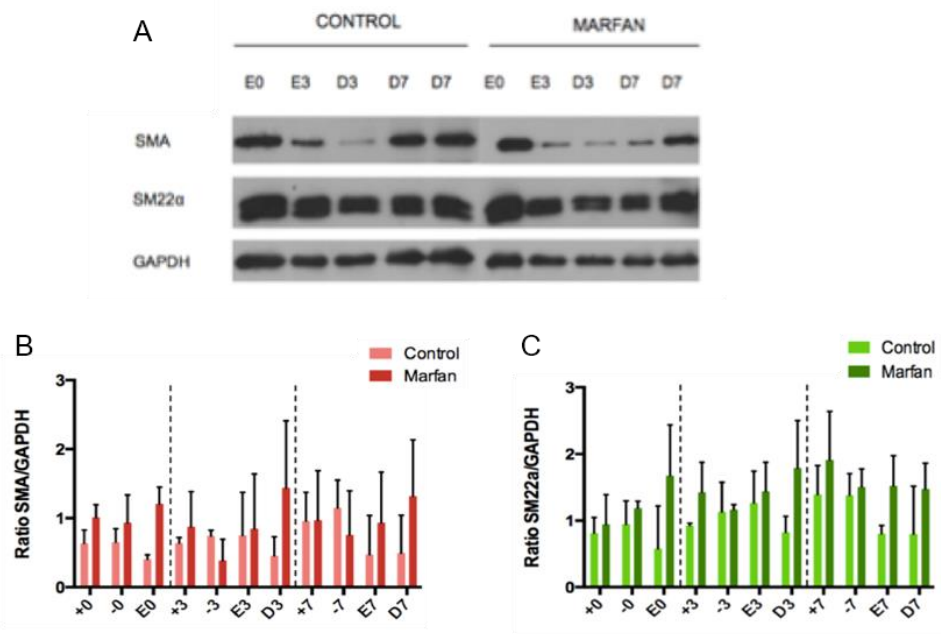

Figure 99. Contractile protein marker levels in VSMCs. A. Representative western blot bands of indicated SMA and transgelin or SM22α contractile proteins in control and Marfan VSMCs cultured at all the study conditions. B and C. Quantitative analysis of the indicated contractile protein levels from control and Marfan VSMCs. Protein levels were expressed as the ratio between protein and GAPDH, the loading control. Control, n=3; Marfan, n=3. Bar graphs represented by mean ± SD.

Part 4: Definition of a literature-based proteome of the human aorta

Taking into account that current protein databases are incomplete regarding the aortic tissue, we sought to build a thorough Aorta Proteome. Since aortic tissue is a difficult kind of sample to obtain from humans, it was ethically mandatory to exploit all publicly available data instead of performing actual protein analysis on tissue. Specifically, we took advantage of the work previously published by hundreds of researchers and we collected all the relevant information they reported on protein presence in human aorta. With this we constructed a database containing all the proteins that have been reported in human aortic tissue, together with extra information such as details of the used samples, experimental method of protein assessment, associated disease, and article(s) where it is mentioned. This procedure was based on that performed by Sherratt and co-workers on the Manchester Skin Proteome[132].

4.1. Technology development: literature processing and database

Aiming to gather all the current knowledge on protein presence in aortic tissue, we performed a meticulous literature revision. Up to November 2017, there were in total 142 million scientific publications included in the Web of Science (WOS) (https://clarivate.libguides.com/webofscienceplatform/coverage). To avoid reviewing all those publications to find those specifically reporting protein presence in human aortic tissue, we filtered them by introducing the following specifications at the WOS search engine[H]:

- aort* → includes: aorta, aortic, aortae, aortas.
- AND human OR patient* OR subject* OR individual* OR participant* OR donor*
- AND (each protein name) → a search was done for each of the 20,239 currently reviewed proteins by Uniprot, plus for their alternative protein names.
- [in English]
- [only scientific articles] → excluding books, proceedings, reviews, and meeting abstracts.
- [from year 2000 to 2016] → to avoid scanned old articles that cannot be read by a computer.

[H] An asterisk in search procedures broadens the search by finding keywords that start with the same letters. AND will search sources that mention all the stated keywords, whereas OR will search sources that mention either stated keyword.

With this search keywords and parameters, the WOS retrieved 22,318 scientific articles that their topic was related to aorta, human, and any protein.

Once the abstracts of all those articles were downloaded, we were exclusively interested in the articles where authors employed human aortic tissue samples. However, taking into account that WOS search engine looked for keywords at the article's abstract and title but also in the articles referenced by the article of interest, many articles' abstracts did not actually display the "aort*" and "human/patient/etc." keywords. In addition, many articles used other animals' aortae or aortic cell cultures instead of human aortic tissue. Hence, it was necessary to discard these false positive articles. For this purpose, a bioinformatics code processed all the downloaded article abstracts to assess the occurrence of the following specific keywords:

- aort*
- human, patient*, subject*, individual*, participant*, donor*
- [any protein name]
- proteom*
- mass spec*, MS
- immunohisto*, histochem*, stain*, "western blot*", ELISA
- "mice /rat /rabbit /porcine /bovine /murine aort*"
- "human aortic endothelial cells"
- "human aortic smooth muscle cells"

The output of this process was a spreadsheet file listing all the 22,318 articles' unique DOIs (digital object identifier) arranged by alphabetical order of the first protein name mentioned at their abstract (table 3). The rest of the columns after the DOI and the first mentioned protein included the other sought keywords that were also mentioned at the abstract.

row	Article DOI	First mentioned protein	Other keyword	Other keyword	Other keyword	Other keyword
1	10.1093/cvr/cvv027	5'-nucleotidase	aort.*	human		
2	10.3727/096368912X657701	Alpha-1-antitrypsin	von_Willebrand_ factor	aort.*	mouse_ aort.*	donor*
3	10.1074/jbc.M703115200	Aladin	aort.*			
4	10.1371/journal.pone.072111	Alpha-1-antichymotrypsin	Carbonic_ anhydrase_1	Vitronectin	proteom.*	mass_ spectrometry
5	10.1006/mvre.2001.2384	Angio-associated_ migratory_ cell_protein	aort.*			
6	10.1093/cvr/cvt245	Angiotensin-converting_enzyme_2	Angiotensin-converting_enzyme	Apolipo-protein _ E	aort.*	
7	10.1073/pnas.1001253107	Angiotensin-converting_enzyme_2	Low-density_ lipoprotein_ receptor	aort.*	human	human_ aortic_ endothelial_ cells
8	10.1016/j.regpep.2010.9.005	Angiotensin-converting_enzyme_2	Angiotensin-converting_enzyme	Profilin-1	aort.*	
9	10.1089/ars.2014.6070	Angiotensin-converting_enzyme_2	Angiotensin-converting_enzyme	stain.*	mouse_ aort.*	
10	10.1161/ATVBAHA.114.30613	Angiotensin-converting_enzyme_2	Angiotensin-converting_enzyme	immunohisto.*	aort.*	subject.*

Table 3. Example of article list classified by interest keywords. Green box marks the indispensable mentions and yellow box marks the mentions that can be positive or negative, depending on the other keyword mentions in the same abstract. Red box marks the abstracts that are not going to be further examined due to its mentioned keywords list.

With this list we were able to easily identify which abstracts should be further examined manually (i.e. reading by a person). If an abstract mentioned the “aort*” keyword, it was further read (1st- 3rd, 5th-8th and 9th DOI rows at table 3), with the exception of those where the “aorta” mention was related to another animal or cell culture and “human/patient/etc.” was not mentioned (9th DOI row at table 3). Conversely, if “aort*” was not mentioned, the abstract was not assessed (4th DOI row at table 3). This protocol assumed that authors usually declared the use of human aortic tissue at the abstract of their article, since it is a very difficult biological sample to obtain.

Following this strategy, we immediately learnt that the abstracts that mentioned both the “aort*” and “human/patient/etc.” keywords (first and 10th DOI rows at table 3) were the most likely to contain useful information for our purpose. Nevertheless, many abstracts mentioned these two keywords at the introductory part or at the final future perspectives section of the abstract, which indeed was a mention not related to the samples they employed, and hence, it was information not relevant for our aim. Also, other articles that were discarded after abstract assessment were those that studied the human aorta *in vivo* for calcification, stenosis, or regurgitation analysis, and did not work on protein examination within the tissue. In addition, clinical articles that only used the aorta for blood extraction or for vessel clamping were dismissed too. Finally, articles that analysed

mRNA or that employed other human vessels than aorta were also discarded. In summary, only the abstracts that demonstrated protein analysis on human aortic tissue were accepted for further reading of the full article.

After applying this strategy to the originally obtained 22,318 articles, more than a half were further read, and only 268 articles provided useful information on protein presence in the human aortic tissue. In particular, these articles demonstrated the presence of 1086 unique proteins by means of mass spectrometry and/or immune-based techniques (western blotting, immunohistochemistry, and ELISA). The reported information of these proteins in these articles was gathered in a database. Thus the proteome database contained the following information for each protein record: the Uniprot accession number, the article(s) where the protein presence in aorta was reported, the specific information on the samples used (donor age and sex, aortic region, tissue layer), the analysis technique, and reported relation to diseases. With all this gathered information, we established the human healthy Aorta Proteome and the human Aortic Aneurysm Proteome, which are completely listed in the Appendix section of this thesis.

4.2. Technology application to human aorta data

4.2.1. The human healthy Aorta Proteome

Regarding the healthy human aorta, literature review revealed the presence of 919 different proteins in the tissue. This number was higher than any other reported aorta proteomic characterization to date, being the greatest of 630 proteins[75] (figure 100A). Additionally, our Aorta Proteome contained all the proteins retrieved by searching aort* at UniProt and at the Human Protein Atlas (figure 100B). It is noteworthy to state that aort* mentions in these two databases was related to disease description, instead of annotation of protein presence in the aortic tissue, neither healthy or diseased.

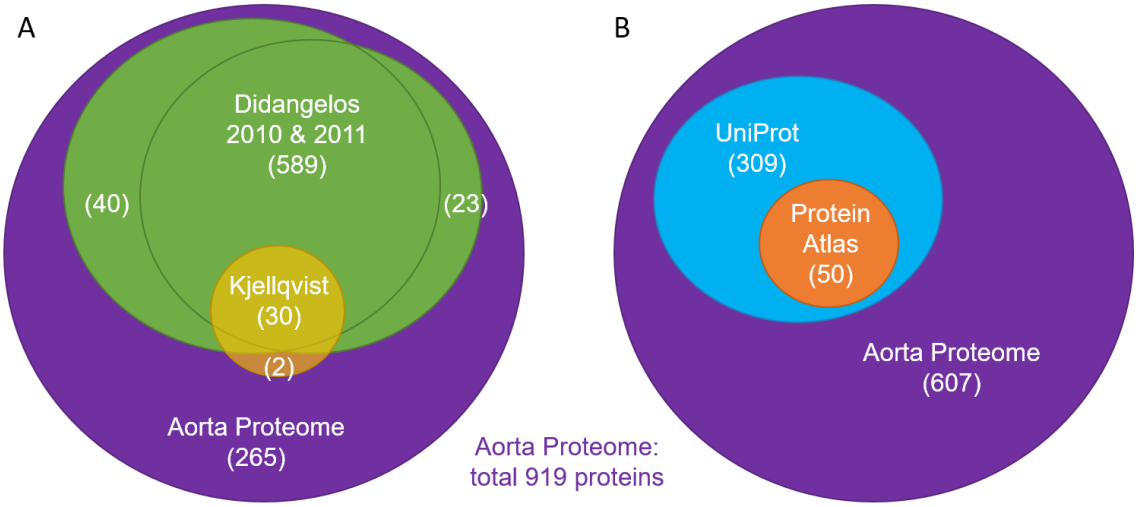

Figure 100. Total protein number relationship between different proteomic sources. A. The here presented Aorta Proteome (purple) was composed by proteins reported at Didangelos *et al.* 2010 (629 proteins)[75], Didangelos *et al.* 2011 (612)[136], Kjellqvist *et al.* 2013 (32)[137], among other minor sources. B. The Aorta Proteome included all the UniProt and the Human Protein Atlas protein records that mention aort*.

The aortic presence of each protein in the database was reported by one or more published articles, and each report was performed by mass spectrometry and/or by immune-based techniques (western blot, immunohistochemistry, and ELISA). For further analysis, reliability of protein presence in aortic tissue was determined by the number of articles that reported it and the diversification of the reporting techniques. Taking this into account, the most proved protein presences where those validated by both experimental methodologies.

Specifically, the 81% of total proteins in the Aorta Proteome was validated by mass spectrometry and the remaining 29% by immune-based methods (figure 101). Many database proteins were validated by more than one report (72%). In particular, the Aorta Proteome had 90 totally validated proteins (10%) out of 919, so their aortic presence was guaranteed by diverse reports and techniques. Conversely, the 28% of the proteome was only validated in a single article, either by mass spectrometry or immune-based methods, hence there was a moderate confidence level for their real presence in aortic tissue.

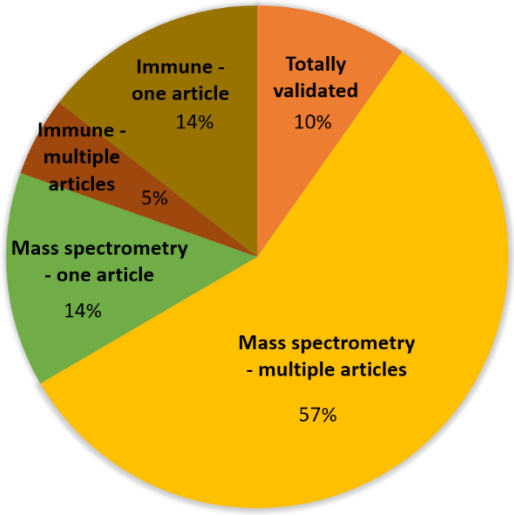

Figure 101. Validation sources of protein presence in aorta. Proteins in the Aorta Proteome were validated by one or more articles, and by mass spectrometry and/or immune-based techniques.

More in detail, within the totally validated protein group there were some of the “most popular”[138] aortic proteins: elastin, collagens, fibrillin-1, LTBP-1, fibronectin, TIMP-1, MMP-2, myosin-11, aortic smooth muscle actin (also known as SMA), smoothelin, and transgelin. In table 4, one can get an insight of the available information in the Aorta Proteome database regarding these proteins: official name, UniProt accession number, encoding gene, experimental validation technique (immune-based and/or mass spectrometry), reporting articles of protein presence, protein location in aortic tissue

(tunicae intima, media and/or adventitia), and data about the sample donors (aortic region source, age, sex, and type of control patient). Refer to the Annex 1 for the full list of proteins of the human Aorta Proteome and their associated information. To note, many reports did not state all of this information, thus, the Aorta Proteome had, in some cases, blank spaces.

Protein name	UniProt Accession number	Gene name	Protein presence technique	#DOIs	Protein location	Tissue location	Age	Sex	Type of control sample
72 kDa type IV collagenase	P08253	MMP2	Immuno; Mass Spec	11	intima; media	ascending, abdominal	64.1, 71.5, 61, 60.9, 25, 20, 68.9, 37.5	B	autopsy CV healthy; CABG; valve replacement
Actin, aortic smooth muscle	P62736	ACTA2	Immuno; Mass Spec	13	intima; media	abdominal, ascending	47.3, 39.7, 40	B	autopsy CV healthy; CABG; valve replacement
Collagen alpha-1(III) chain	P02461	COL3A1	Immuno; Mass Spec	5	media	ascending	47.7	B	other
Elastin	P15502	ELN	Immuno; Mass Spec	5	media	abdominal, ascending	46.1, 59.8	M	other
Fibrillin-1	P35555	FBN1	Immuno; Mass Spec	4		thoracic, ascending	35, 37.5	B	valve replacement
Latent-transforming growth factor beta-binding protein 1	Q14766	LTBP1	Immuno; Mass Spec	4	intima; media	ascending			valve replacement
Metalloproteinase inhibitor 1	P01033	TIMP1	Immuno; Mass Spec	7	adventitia; media	abdominal, ascending	48, 64.1, 69, 51, 68.9, 37.5	B	CABG; other
Myosin-11	P35749	MYH11	Immuno; Mass Spec	5	media	ascending	37.5	B	valve replacement
Smoothelin	P53814	SMTN	Immuno; Mass Spec	4	intima; media	ascending	37.5,39.7	B	valve replacement
Transgelin	Q01995	TAGLN	Immuno; Mass Spec	7	media	ascending	37.5,60	B	CABG; valve replacement

Table 4. The Aorta Proteome database information of ten relevant proteins in aorta research. Columns correspond to (from left to right): official name of the protein, UniProt accession number, kind of protein analysis technique used for tissue presence assessment, number of articles reporting the protein in tissue, location of protein within the tissue (if reported or if deducible from histological images), aortic portion of the employed samples, average age of sample donors in each report (in years), their biological sex (male, female, or both; M, F, or B), and type of control sample referring to cardiovascular healthy donor autopsy sample, coronary artery bypass grafting (CABG) patient sample, valve replacement patient sample, or other.

Taking into account the source of the examined control samples in the reports, the vast majority of the samples was obtained from ascending aorta of valve replacement surgery patients (70%), and only the 4% of the whole proteome was validated on actual cardiovascular healthy donor autopsy samples (figure 102A). Moreover, average age of sample donors was 42 ± 11 years old, although it ranged from foetal stage to 76 years (figure 102B). Both biological sexes were equally represented in the database records (figure 102C). Therefore, we established that the Aorta Proteome was globally representative of ascending aorta of middle-aged, aorta-healthy individuals. Yet, information regarding younger, descending aorta, and/or completely cardiovascular healthy samples was also included in the database. Importantly, there were 33 proteins assessed on cardiovascular healthy autopsy donor aortae, of which 13 were totally

validated (for instance, MMP-2, SMA, and SOD1) and 20 were only assessed by immune-based techniques (such as MMP-9 and MAPKs).

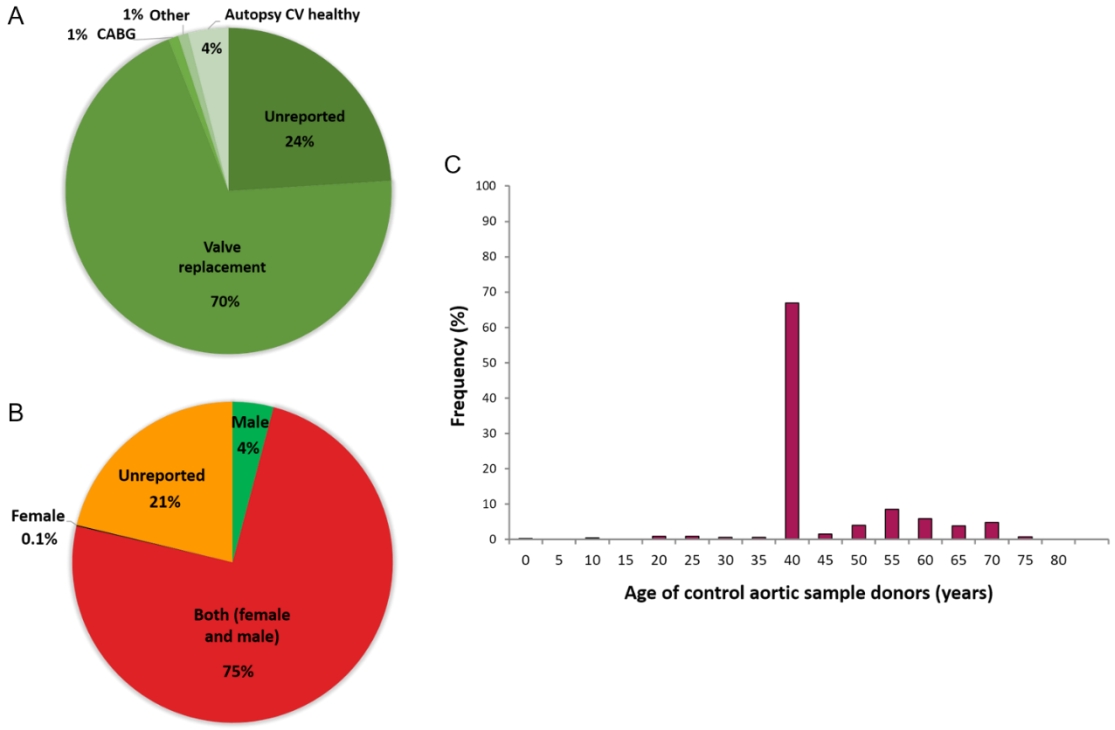

Figure 102. Population data of the reported control aortic samples. A. Type of control sample: valve replacement surgery, coronary artery bypass graft (CABG) surgery, cardiovascular (CV) healthy donor autopsy, other, or unreported in the source article. B. Biological sex of sample donors: source articles worked on male, female, or both kinds of samples. C. Frequency histogram of age of control aortic sample donors.

As for the total 919 proteins in the healthy Aorta Proteome, 279 were described in relation to aortic diseases. The most frequently reported aortopathy was aneurysm, and the rest of diseases were occasionally mentioned (dissection, calcified aorta, aging, atherosclerosis, aortic stiffening, and valve pathology).

Furthermore, in reference to the compiled proteins in our Aorta Proteome, their location within the tissue was scarcely reported in the articles (only in the 26% of cases; figure 103A). This meant that, in most articles, total tissue lysates were employed, but they did not mention it. Regarding the actually located proteins, most of them corresponded to the tunica media (13% of total proteome), and the rest belonged to tunicae intima, adventitia, and the periaortic adipose tissue (8, 4, and 1%, respectively). In addition, more than half of the Aorta Proteome were intracellular proteins (61%; figure 103B; for instance, histones, ribosomal proteins, ATP synthase subunits, SMADs, and tubulin chains). Extracellular proteins, such as chemokines and immunity complement molecules, constituted the 29% of the total Aorta Proteome. ECM proteins were the less diverse group in the Aorta Proteome (10%) and it was composed by 66% glycoproteins, 21% collagens, and 13% proteoglycans (figure 103C).

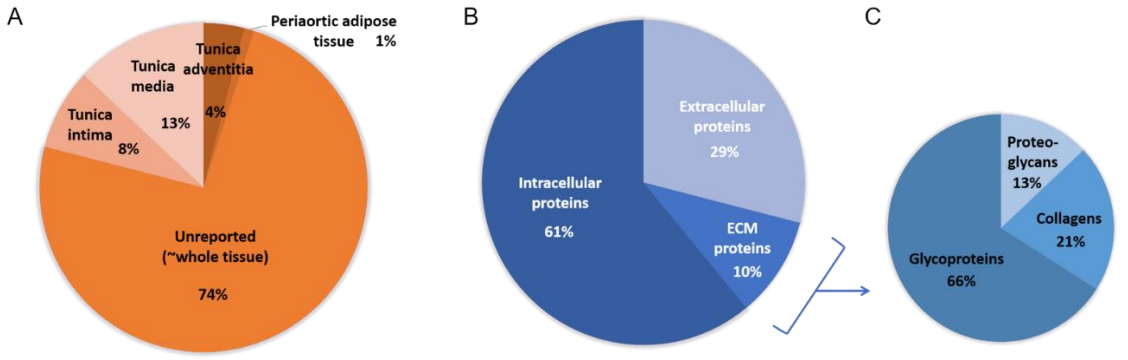

Figure 103. Overall protein data. A. Reported protein location within the aortic tissue: tunicae intima, media, adventitia, periaortic adipose tissue, or whole tissue or unreported. B. Protein classification relying on sub-tissue location: intracellular, extracellular, or ECM component. C. Classification of ECM proteins into glycoproteins, collagens, or proteoglycans.

Given that elastic lamellae fragmentation is the most evident aortic histological feature in the event of aneurysm, we checked the existence of lamellae proteins in the Aorta Proteome (table 5). Elastin, the most abundant component of elastic lamellae, was completely validated in human aortic tissue by several reports and both assessment techniques. This was exactly the same for fibrillin-1, but fibrillin-2, was not reported by any article in human control aortic tissue. Main fibulins (1, 2, and 5) were existent in the Aorta Proteome, although not fibulins 3 and 4. Moreover, the presence of the lamellae associated proteins families LOXs and LTBPs in control aorta tissue was seldom reported. Conversely, biglycan, decorin, fibronectin, TGM2 (formerly tissue transglutaminase) and vitronectin were completely validated (table 5), hence their presence in human aortic tissue was guaranteed.

Biglycan	✓ ✓	Fibulin -3	✗	LOXL2	✗
Decorin	✓ ✓	Fibulin -4	✗	LOXL3	✗
Elastin	✓ ✓	Fibulin -5	✓ ✓	MFAP2 (MAGP-1)	✗
EMILIN -1	✓	Ficolin-2 (EBP-37)	✗	MFAP3	✗
EMILIN -2	✗	LTBP -1	✓ ✓	MFAP4	✓
Fibrillin -1	✓ ✓	LTBP-2	✓	MFAP5 (MAGP-2)	✓
Fibrillin -2	✗	LTBP-3	✗	TGM2	✓ ✓
Fibronectin	✓ ✓	LTPB -4	✓	TGFβ-i protein ig-h3	✓
Fibulin -1	✓ ✓	Lysyl oxidase (LOX)	✗	Versican	✓
Fibulin -2	✓	LOXL1	✓	Vitronectin	✓ ✓

✓ Validated by mass spectrometry
✓ Validated by immune-based techniques
✗ Not in the Aorta Proteome (human healthy tissue)

Table 5. Existence of lamellae components and associated proteins in the Aorta Proteome, and statement of validation technique of their presence in human control aortic tissue.

Additionally, the presence of VSMC contractile phenotype markers in control aortic tissue, such as SMA, transgelin, myosin-11, smoothelin, calponin, and vinculin, was

totally validated (table 6). The synthetic phenotype protein marker myosin-11 was also double validated, but myosin-9 was only assessed by mass spectrometry, and RBP1 was not reported in aortic tissue.

Calponin-1	✓ ✓
Myosin-9	✓
Myosin-10	✓
Myosin-11	✓ ✓
RBP1	✗
SMA	✓ ✓
Smoothelin	✓ ✓
Transgelin	✓ ✓
Vimentin	✓ ✓
Vinculin	✓

Table 6. Existence of VSMC phenotype associated proteins in the Aorta Proteome, and statement of validation technique of their presence in human control aortic tissue.

4.2.2. The human Aortic Aneurysm Proteome

The same literature review was performed searching for protein presence in human MFS aortic tissue. Nonetheless, only 32 proteins were reported, including SMAD2 (more phosphorylated than control samples), transgelin (downregulated), TGF-β1 (upregulated), decorin (upregulated in tunica media), vinculin (upregulated), and nitric oxide synthases (NOS2 upregulated, NOS3 downregulated). Therefore, we broadened our study by searching protein presence in human aneurysmal aortic tissue. Importantly, there was one protein solely reported in Marfan aneurysmal tissue: fructose-bisphosphate aldolase C.

The human Aortic Aneurysm Proteome contained 724 protein records, and comprised data from bulk proteomic analyses[119,136,137,139,140] and from individual immune-based studies (figure 104). In detail, 10% of the total proteins was certainly validated by both techniques, whereas the 76% was assessed only by mass spectrometry (12% demonstrated in several articles, plus 64% corroborated in one article) and the rest by immunohistochemistry or western blot (9% in several articles, 5% in one article). Totally validated protein percentage was similar to that of the healthy Aorta Proteome. Surprisingly, proteins like MMP-2, MMP-9, CD68, IL6, and IL8, have been reported many times by immunohistochemistry and western blot in human aneurysmal aortae, but were not found by mass spectrometry studies. Refer to the Annex 2 for the full list of proteins of the human Aortic Aneurysm Proteome and their associated information.

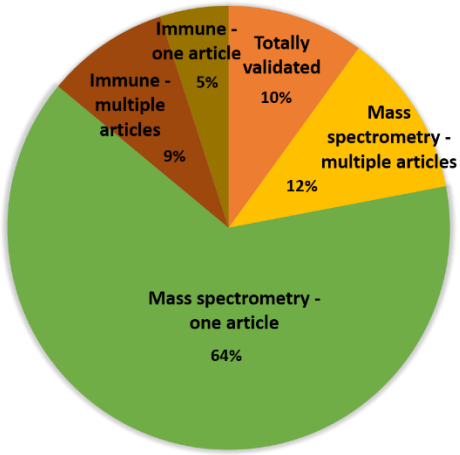

Figure 104. Validation sources of protein presence in aneurysmal aorta. Proteins in the Aortic Aneurysm Proteome were validated by one or more articles, and by mass spectrometry and/or immune-based techniques.

The majority of the protein data within the proteome was originated from abdominal aortic aneurysms (87%), but source articles did not state the underlying cause of the pathology in most cases (85%) (figure 105A). Taking into account the current knowledge on epidemiology and aetiology of abdominal aneurysms, we assumed that the cause of these aneurysms was atherosclerotic disease. Additionally, the rest of the data (13%) was obtained from aneurysmal ascending aortae of MFS (4%) and bicuspid aortic valve (9%) patients. Moreover, the whole set of aortic samples, either abdominal or ascending, were principally extracted from senior men, with an average age of 66 years old (figure 105B-C).

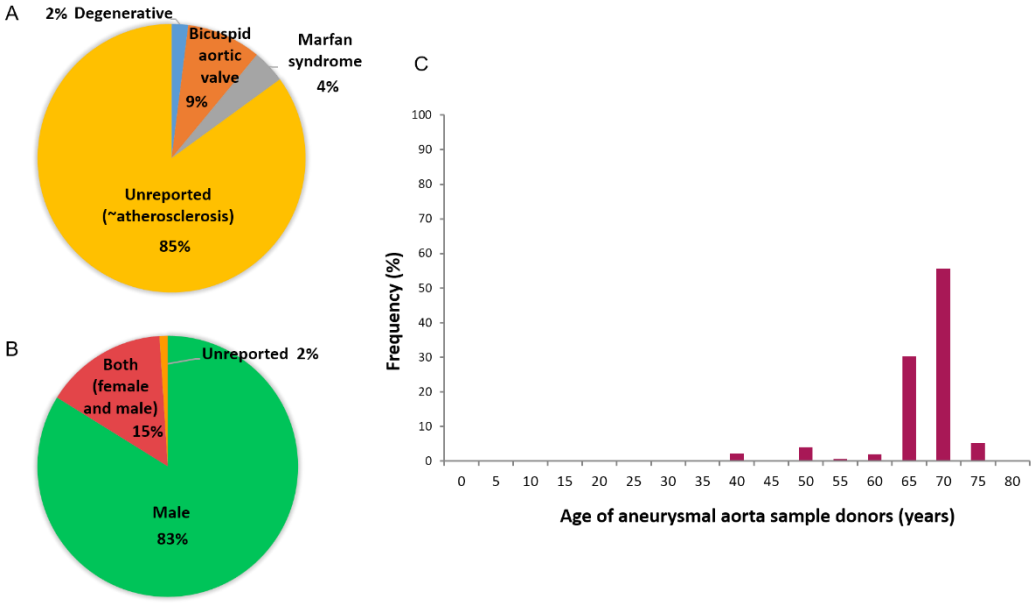

Figure 105. Population data of the reported aneurysmal aortic samples. A. Cause of the aortic aneurysm: unreported (being most likely due to atherosclerosis), degenerative, bicuspid aortic valve, and Marfan syndrome. B. Biological sex of sample donors: source articles worked on male, female, or both kinds of samples. C. Frequency histogram of age of aneurysmal aortic sample donors.

Protein location in the tissue was often unreported or performed on the whole tissue without specific allusion in the source article (89%) (figure 106A). Only few proteins were reported in particular locations: 2% at tunica intima, 4% at tunica media, 3% at tunica adventitia, 1% at inflammation regions within the aortic wall, and 1% at the adjacent thrombus. Moreover, the kind of protein pattern was similar to that of the healthy Aorta Proteome. More than half of the Aortic Aneurysm Proteome were intracellular proteins, and 31% were soluble extracellular proteins (figure 106B). The remaining 11% were ECM proteins, composed by 63% glycoproteins, 22% collagens, and 15% proteoglycans (figure 106C).

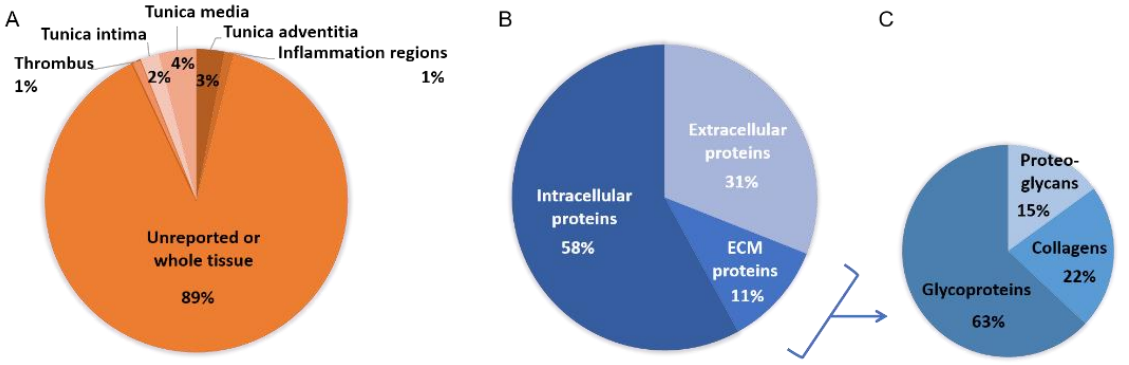

Figure 106. Overall protein data. A. Reported protein location within the aortic tissue: tunicae intima, media, adventitia, inflammation regions, thrombus, or whole tissue or unreported. B. Protein classification relying on sub-tissue location: intracellular, extracellular, or ECM component. C. Classification of ECM proteins into glycoproteins, collagens, or proteoglycans.

Furthermore, aortic wall ECM proteins were analysed in detail in the Aortic Aneurysm Proteome (table 7, second column). Surprisingly, elastin was only validated by immune-based techniques, and fibrillin-1 only by mass spectrometry. Several collagen chains were present in the database, and many were totally validated. Proteoglycans and adhesive glycoproteins, such as fibronectin, vitronectin, thrombospondin-2, tenascin, decorin, and biglycan, were also assessed by both kinds of techniques. Elastic lamellae associated proteins were in some cases present in the Aortic Aneurysm Proteome (like EMILIN-1, fibulin-1 and 5, LOX, and MFAP-4) but only partially validated. Additionally, proteins involved in remodelling processes were abundant in the aneurysmal aorta reports, as the presence of MMP-12, 14, 2, 9, TIMP-1, 2, 3, and α-1-antitrypsin, was described in the human diseased tissue. Moreover, EMILIN-2, fibrillin-2, fibulin-4, ficolin-2, LOXL2, LOXL3, and MFAP-2 were not reported either in the aneurysm nor the healthy proteomes (tables 5 and 7).

AEBP1	✓ ✓	↑	Fibulin-5	✓ ✓	↓	MMP-2	✓	↑
Alpha-1-antitrypsin	✓ ✓	=, ↑, ↓	Ficolin-2	✘*		MMP-9	✓	↑
Apolipoprotein A1	✓	↑, ↓	LOX	✓	**unique**	Tenascin	✓ ✓	↑
Biglycan	✓ ✓	=	LOXL1	✓	=	TGM2	✓ ✓	↑, ↓
Collagen III (COL3A1)	✓ ✓	↓	LOXL2	✘*		Thrombo-spondin-2	✓ ✓	↑
Collagen XII (COL12A1)	✓ ✓	↑	LOXL3	✘*		TIMP-1	✓ ✓	=, ↑, ↓
Decorin	✓ ✓	=, ↑	MFAP-2	✘*		TIMP-2	✓	↑, ↓
Elastin	✓	↓	MFAP-4	✓	↑, ↓	TIMP-3	✓ ✓	↑
EMILIN-1	✓	=	MFAP-5	✓	=	Transthyretin	✓ ✓	↓
EMILIN-2	✘*		MMP-12	✓ ✓	**unique**	Versican	✓	↓
Extracellular SOD	✓ ✓	↓	MMP-14	✓	↑	Vitronectin	✓ ✓	↑
Fibrillin-1	✓	↑						
Fibrillin-2	✘*							
Fibrinogen	✓							
Fibronectin	✓ ✓	↑						
Fibulin-1	✓	↓						
Fibulin-2	✘							
Fibulin-4	✘*							

✓ Validated by mass spectrometry

✓ Validated by immune-based techniques

✘ Not in the Aorta Aneurysm Proteome

✘* Not in any Proteome

↑ Higher protein level than control samples

↓ Lower protein level than control samples

= Same protein level than control samples

unique Not in the healthy Aorta Proteome

Table 7. Existence of ECM proteins in the Aortic Aneurysm Proteome, statement of validation technique of their presence in human aneurysmal aortic tissue, and report of protein level changes in relation to control tissue. Protein level changes could be described by more than one published article and these reports could be contradictory. Hence, in the database we annotated all possible scenarios.

The Aortic Aneurysm Proteome also contained information on the changes in the protein levels as compared to control tissue, when reported by the source articles (table 7, third column). In general, MMP expression was augmented, but TIMPs and α-1-antitrypsin (an inhibitor of serine proteases) displayed different expression patterns depending on the reporting article results. Elastin, extracellular SOD [Cu-Zn], fibulin-1, transthyretin, fibulin-5, and versican were diminished in aneurysmal tissue. Conversely, vitronectin, tenascin, and fibronectin were increased. Fibrillin-1 was also augmented, but, importantly, it was reported on abdominal aneurysm samples not related to MFS.

Moreover, proteins related to VSMC functioning and phenotype were also present in the Aortic Aneurysm Proteome: calponin-1, filamin-A, myosins, SMA, smoothelin, transgelin, vimentin, and vinculin (table 8A). However, synthetic phenotype marker RBP1 was not reported by any article in human aortic aneurysm tissue, but, in turn, it was not even reported for healthy tissue (table 6). Regarding the present markers, either phenotype proteins were augmented compared to control samples, except for SMA and transgelin that reports described contradictory protein level changes. In addition, TGF-β signalling

proteins in aneurysmal aorta were present, and augmented or similar as compared to control tissue (table 8B). To our surprise, no article reported TGF-β receptors in human aneurysmal aorta samples.

A

Calponin-1	✓ ✓	↑
Filamin-A	✓ ✓	↑
HspB1	✓	
Myosin-9	✓	
Myosin-10	✓ ✓	↑
Myosin-11	✓	
Peroxiredoxin-2	✓ ✓	
RBP1	✘*	
SMA	✓ ✓	=, ↑, ↓
Smoothelin	✓	↑
Transgelin	✓ ✓	=, ↑, ↓
Triosephosphate isomerase	✓	
Vimentin	✓ ✓	=, ↓
Vinculin	✓	↑

✓ Validated by mass spectrometry

✓ Validated by immune-based techniques

✘ Not in the Aorta Aneurysm Proteome

✘* Not in any Proteome

↑ Higher protein level than control samples

↓ Lower protein level than control samples

= Same protein level than control samples

unique Not in the healthy Aorta Proteome

B

LTBP-1	✓ ✓	=
LTBP-2	✓	=, ↑
LTBP-3	✘*	
LTBP-4	✘	
MAPK 1 (ERK-2)	✓ ✓	
MAPK 3 (ERK-1)	✓	
SMAD2	✓	
SMAD3	✘	
TGF-β1	✓	↑
TGF-β2	✓	=
TGF-β3	✓	=
TGFβ-i protein ig-h3	✓	↑
TGFR-1	✘	
TGFR-2	✘*	

Table 8. Existence of VSMC proteins in the Aortic Aneurysm Proteome relative to cell phenotype (A) and TGF-β signalling (B), statement of validation technique of their presence in human aneurysmal aortic tissue, and report of protein level changes in relation to control tissue. Protein level changes could be described by more than one published article and these reports could be contradictory. Hence, in the database we annotated all possible scenarios.

Besides, there were 188 proteins reported in aneurysmal tissue but not in healthy human aorta tissue. Within this unique protein group there were four collagen alpha chains, MMP-12, LOX, ADAM17, RBP4, and several immunity-related proteins (complement factors and antibody chains).

DISCUSSION

Part 1: High-resolution morphological approach to analyse elastic laminae injuries of the ascending aorta in a murine model of Marfan syndrome

In this study, we reported the implementation of a new multiphoton microscopy image processing method for elastic lamellae microstructure examination, based on obtaining series of en-face images from unstained aortic tissue. We used healthy and MFS murine aortae as tissue models and determined the anatomical distribution of fenestrae alterations that occur in elastic laminae.

In the last decade, a lot of data have been generated about histological damage in the aortic wall in MFS, using routine histological techniques following the conventional sequence of fixation, paraffin embedding, sectioning and histological staining. Technological improvements in microscopy and, importantly, in image processing have provided a new panorama to the histopathology field[13]. Accordingly, here we applied en-face multiphoton microscopy and a segmentation protocol to assess lamellae morphology. The advantages of our new approach are: (i) it can produce high-resolution en-face confocal stacks that enable detailed visualization of histological structures; (ii) it can obtain quantitative information belonging to the three dimensions XYZ, which increases our understanding of 3D histological arrangements; and (iii) the entire aortic vessel can be viewed, for straightforward monitoring of different anatomical regions.

1.1. Analysis of lamellae 3D microstructural data

Although TPEF confocal microscopy has been used to obtain the elastin signal of vessels in other studies[68], our report is the first to our knowledge in which a semi-automatic image processing protocol is systematically implemented to segment individual lamellae and quantitatively analyse histological microstructural changes. Furthermore, this unique analysis was performed on en-face images of ascending aorta tunica media of a murine model of MFS, in which elastic fibre ruptures are known to be associated with the formation and progression of aortic aneurysm[44]. Related previous studies in MFS reported “disruptions” in en-face images from pressurized adult MFS descending aortae, but without any quantitative analysis[116]; and also reported a ≈40 µm “hole” diameter measurement based on non-segmented lamellae of diseased tissues only (from another MFS murine model)[117]. In addition, the measurement of elastic laminae features of transversely viewed parts of Marfan mice aortae obtained by multiphoton microscopy was reported as an alternative to conventional histological methods[141]. Here, we

complement these studies and highlight the relevance of en-face multiphoton microscopy and image processing for generating quantitative 3D microstructural data on individual elastic lamellae. We report new histopathological alterations in the aortic media in the murine *Fbn1*$^{C1039G/+}$ model of MFS: lamellae in the ascending aorta show larger and more fenestrae than WT tissue. The density of fenestrae in Marfan elastic laminae is at least double than that found in WT. These fenestrae alterations probably represent lamellar micro-damage, which could be directly related to the characteristic elastic lamellae fragmentation and disarrangement happening in Marfan aortae[141]. Thus, we propose the density of fenestrae as a potential aortic microscale damage marker. The hypothetical future application of our imaging and processing method as a basis for the vascular endoscopy examination of MFS patients or related diseases might provide an early evaluation tool for aortic histological damage prior to the irreversible appearance of the aneurysm.

Interestingly, our results show that alterations in the density and size of fenestrae did not occur uniformly in the entire Marfan ascending aortic media, but were mostly restricted to the proximal and convex regions. This is in accordance with results reported by Trachet *et al*.[142] in the ascending aorta of angiotensin II-infused ApoE$^{-/-}$ mice. Using conventional histological techniques, they reported that the largest aortic wall dissections occurred in the outer convex quadrant, which corresponds to the central part of the aortic convexity. We speculate that the regionalized structural changes reported here could be due to a preferential impact of the blood flow on the convex and proximal ascending aortic regions. It is known that deviant blood flow can be caused by aortic valve dysfunction[3]. In particular, the convexity of ascending aorta is the preferential blood flow impact zone found in bicuspid aortic valve disease[143], which is accompanied by differential lamellae fragmentation and matrix protein expression patterns in comparison to the concavity[144]. In the case of MFS patients, aortic root dilatation usually entails aortic valve dysfunction[145], which in turn causes aortic blood flow disturbance[145,146] leading to mild or moderate aortic regurgitation[146,147]. Therefore, it is reasonable to hypothesize that MFS disturbed flow could be mainly impacting on this particular anatomical zone, just as happens in bicuspid aortic valve pathology. This premise should be confirmed by further detailed hemodynamic studies on Marfan patients and murine models, which to our knowledge are not currently available.

A recent paper reported a transmural gradient of lamellar injury, in which elastic laminae break number varies significantly amongst lamellae[142]. In particular, central lamellae including the 2nd showed more breaks than peripheral ones. The results of our comparisons of fenestrae density and size between the IEL and the 2nd lamina also suggest a histological injury gradient, where the damage is more severe in the 2nd lamina than in the IEL. Again, we can only speculate about the significance of this difference. It could be related to intrinsic robustness of the IEL, whose structure and organization might be better adapted to support the mechanical impact of blood flow than the rest of laminae. In this respect, aortic transmural mechanical behaviour has been studied in relation to transmural structural properties[148,149]. Results show that the porcine thoracic

descending aorta wall is divided into transverse outer and inner tunica media halves, which differ in their mechanical and molecular composition. In addition, the alignment of bovine elastic and collagen fibres due to mechanical load varies in lamellae localized close to the endothelium and in the subsequent lamellae[150]. We are aware that this variance cannot be directly extrapolated to mice, due to differences in the animal model used and the aortic portion examined in terms of wall thickness and lamellae number. Nonetheless, it cannot be discarded that similar structural variance between lamellae occurs in mice as well. Our results suggest that this variance might take place between IEL and successive lamellae. In the case of Marfan mice aortae, we hypothesise that the weakness of the tunica media[121] plus the intrinsically different primary structure of each lamina could explain the here reported dissimilar injury pattern occurring between the 2nd laminae and the IEL.

Regarding the other lamellar parameters assessed by our methodology, it was previously shown by SEM that medial elastic laminae of adult rat aorta were 2-3 μm thick and had an irregular profile[151]. Moreover, an average of 2.74 μm was reported in mouse[152]. Therefore, our lamella thickness values (2.7-3.0 μm) are in accordance with those measured in mouse[152] and rat aortae[151,153].

There are few data about lamellae undulation assessment either in health or disease. Wolinsky and Glagov[76] established the waviness index, which consisted in obtaining the ratio of the lamellar length to the straight line distance between two reference points. Other developed undulation assessment techniques quantified the folding[154] and fibre angular undulation[69] of lamellae. Globally, these three methods are all based on individual transversal sections, and hence they provide 2D data. Conversely, our waviness quantification approach takes into account area values as in earth topography studies, and therefore it is much more informative about the 3D structure of the tissue. With this method, we showed no differences in lamellar waviness between WT and Marfan aortic tissue.

Part 2: MicroCT imaging of remodelling and micro-scale damage in Marfan syndrome murine aorta

In this study, we show a potential outcome of using synchrotron-based microCT imaging in vascular biology: to image large volumes of aortic tissue at microscale resolution. Aortic scans of WT and Marfan mice (3, 6, and 9 months old) were automatically processed by our in-house image processing code to quantify a variety of histological features, providing at the same time highly informative 3D-based morphology images of the ascending aorta luminal surface. Besides, all the histological parameters here reported have been quantified onto 200 consecutive images, which has yielded a robust mean value for each sample, as opposed to the one-to-ten sections usually measured in conventional histology. Altogether, this study represents a significant insight in the understanding of structural alterations at micro-scale resolution occurring in the tunica media of aortic aneurysms in Marfan syndrome. Additionally, this study allows to infer some conclusions about aortic wall remodelling with early and middle ages (3 to 9 months old), and complements other ageing studies that use elder mice (24 months old)[78].

2.1. Validation of the transverse histological feature values in microCT images

To demonstrate the validity of microCT for vascular histological feature assessment, we compared the obtained quantitative data with that already published. For instance, unpressurized ascending aorta diameter of wild-type animals (~600 µm) was coincident to that thoroughly measured by mechanical studies (ascending aorta inner diameter ~675 µm at 0 mmHg, 6-months-old *Fbn1*$^{+/+}$ mice)[78]. The diameter data cannot be compared to that reported in other publications because this feature is commonly measured *in vivo* by ultrasound and, hence, in pressurised aorta. However, Mariko *et al.*[78] also performed this *in vivo* measurement for the same aortae mentioned above, yielding 1.7 mm systolic to 1.48 mm diastolic diameters of ascending aorta of 5 to 7 months old *Fbn1*$^{+/+}$ mice. This diameter size is ordinary for mice[129,142,155], thus we can extrapolate that our aortic diameter measurements of WT mice are correct.

Regarding the aortic tunica media thickness, diverse values have been previously reported: ~85 µm at 3-months-old wild-type mice[156] (85 comes from 95 µm of the reported total wall minus 10 µm [142] of the expected adventitia), ~75 µm at 3-months-old wild-type mice[142], ~70 µm at ~3-months-old wild-type mice[152], and ~55 and ~83 µm

media thickness at ~8-months-old wild-type and Marfan mice, respectively[113]. Our measurement of thickness of tunica media in 3-months-old wild-type mice (77 µm) was similar to that previously reported (85, 75, and 70 µm)[142,152,156]. Despite this coincidence, the remaining previously reported value was lower than ours. However, this same report measured a 1.5-fold increase in Marfan tunica media thickness compared to that of wild-type[113,116], which is close to our resulting 1.2-fold widening (84 and 103 µm media thickness in wild-type and Marfan 9mo samples, respectively). Taking into account this similarity in ratio, it is feasible to attribute the absolute value discrepancy to the different imaging and quantification methods used by both groups. We are confident of our quantitative analysis since with computational quantification the potential human-induced bias is omitted, and also we have used of a large number of images, which provides a robust average.

Wild-type tunica media cross-sectional area measured in our study (0.19 mm^2 in average) agreed with the ~0.2 mm^2 reported on wild-type 5-6 months old mice[157]. Furthermore, Chung *et al.*[122] earlier published the changes in elastic fibres' area percentage in tunica media in differently aged mice and confirmed that lamellae area remained constant at ~50% in wild-type 3, 6, and 9-months-old aortic arches, and that Marfan non-aneurysmal thoracic aorta at 3 months-old was similar to the wild-type, but it decreased to ~44% in 6 and 9 months old mice, and to ~34% at 9-months-old aneurysmal samples. Notice that these values followed the same tendency and ratios as our results, but approximately 10 points above, as our results showed constant wild-type lamellae area at 42% and Marfan decreasing from 40% at 3mo to 31% at 9mo, and to 27% at dilated zones. This shift between their results and ours could be explained by the use of different imaging approaches (histological stainings[122] vs phase-contrast), which might alter differently the real size of lamellae. In conclusion, our quantitative analysis of several histological features is in accordance with those previously reported in WT and MF aortae using other imaging approaches. Hence, high-resolution microCT stands as a valid imaging technique for vascular wall assessment at transverse perspective, and it could be applied for the study of tissue remodelling associated to aneurysms.

2.2. Age-dependent histological remodelling in wild-type and Marfan aortic walls

Both in WT and Marfan aortae, we observed a gradual age-dependent increase in the luminal diameter, tunica media thickness, and cross-sectional area mean values. Similar results were also present for the lamellae and interlamellar space areas, but whereas in WT mice the resulting lamellae concentration remained invariant with age, in Marfan, a decrease was produced due to a two-fold increase of the interlamellar space area. Notably, Marfan aortae during age progression showed a similar tendency as WT for most of the examined histomorphometric parameters, but in the end, MF 9mo (without categorising datasets) showed significantly greater values than WT 9mo, that is higher

ascending aorta diameter, tunica media thickness, and the areas of the media, lamellae and interlamellar space. Moreover, tunica media thickness at MF 3mo was as elevated as in WT 9mo. In general terms, our results with the haploinsuficiency model of Marfan syndrome (*Fbn1*$^{C1039/+}$) complement previous ones using a hypomorphic model (*Fbn1*$^{+/mg\Delta}$)[78], which together suggest that the genetic deficiency of fibrillin-1 seems to represent a pathological model of accelerated ageing in large arteries.

The aged-dependent increase in the thickness of the WT tunica media resulted from the parallel increase in lamellae and interlamellar space areas. Although it is reported that there is almost no elastin deposition during adulthood[9,23], here we observed a significant increase in wild-type elastic lamellae area with ageing. Nevertheless, nowadays it is not known which components provide microCT contrast to lamellae. Thus, we postulate that other lamellae components, but not elastin, might be overexpressed, causing an increase in lamellae area. The future use of phase-contrast microCT in mice models genetically defective for fibrillins, fibulins, or other lamellae components will undoubtedly help to solve this question.

Notably, Marfan aortae showed a similar age-related tendency as WT for most of the examined histological parameters: higher ascending aorta diameter, tunica media thickness, and the area of the media, caused by more lamellae area but proportionally a lot more interlamellar space area. Yet at 9mo, Marfan aortae showed significantly greater values than WT 9mo, indicating an exponential increase in tissue remodelling. Hence, the histological features examined as potential indicators of structural remodelling in WT and MF tunica media suggest that in both models, the age-dependent tunica media changes are similar, but in MF they occur in an accelerated manner. Furthermore, this increase in MF 9mo values was mainly caused by dilated aortic datasets, because when these were categorized apart, MF 9mo (non-dilated) displayed similar values to those of WT 9mo, and MF dilated was significantly different to the rest of MF groups in most of the parameters. We hypothesise that the histological parameters that were not altered when dilated and non-dilated datasets were separated, are the ones directly implicated in ageing and Marfan disease progression, but not in the aneurysmal evolution. Hence, lamellae area and tunica media thickness are not related to aneurysmal tissue remodelling. In fact, Marfan medial thickness was already augmented at 3 months old, age in which there was no aneurysm occurrence.

Furthermore, significant lamella damage, i.e. luminal surface breaks, also occurred before (6mo) the appearance of an aneurysm (9mo). Moreover, although early lamellae fragmentation has been already documented in Marfan syndrome[114,122], this is the first report that visualises damage in the luminal surface of the vessel. These breaks resembled those IEL cracks mentioned by Robertson and Watton[23], which are a form of mechanically-induced damage. We suggest that these breaks/cracks start as a small rupture between abnormally enlarged fenestrae[158] (as reported in the part 1 of this thesis), and progressively extend due to high tensile circumferential stresses[15]. Therefore, our data of lamellae break/crack progression caused by tensile stress failure

might be of interest for the research groups working on computational modelling of aneurysms[17,159] and blood flow simulations[143]. In fact, the mechanical interpretation of this data might provide an explanation to previously published reports on the altered mechanical behaviour of Marfan aortae[116,122,160]. Moreover, these IEL breaks might be related to contrast agent infiltration within the aortic wall, as suggested by Logghe *et al*[161].

Finally, we have to note that for some histomorphometric parameters the observed age-depended increases did not always reach the usually accepted statistical significance (at least a $P \leq 0.05$), but this does not necessarily mean that they are not having a biological impact in tissue homeostasis[162]. We are strongly confident of our quantitative analysis since the obtained final average values came from the non-human-biased measurement of 200 images per sample, which is not the case for conventional histology analyses. Also, all the datasets, except MF 9mo, showed homogeneous average values with low dispersion. Therefore, the mentioned image processing outputs were satisfactory to assess MF murine aortae as a model of aneurysmal formation in comparison to age-dependent WT aortic remodelling.

2.3. Potentiality of vascular tissue imaging by phase-contrast microCT

High-resolution phase-contrast microCT is here revealed as a valid and potent technique for the study of vascular tissues providing both a transverse and 3D perspectives. This imaging approach overcomes the limits imposed by conventional histological methods such as small size, staining, and sectioning of samples. Indeed, X-ray phase-contrast microCT imaging offers the great advantage to visualise large volumes of unstained and unsectioned soft tissues, providing new structural information that helps to understand tissues and organs in health and disease (Tsukube *et al*.[163] and references therein). Although here we used *ex vivo* synchrotron-based microCT imaging, laboratory microCT devices are already capable of performing high-resolution acquisitions of vascular samples, in detriment to scanning time[72]. Therefore, the examination of luminal surface damage by microCT is a novel and feasible way of aneurysm assessment in research. Moreover, microCT devices are currently capable of *in vivo* vascular imaging[164–166], and it might only need a bit of further instrumental improvement to achieve higher resolution scans that permit visualisation of vascular microarchitecture *in vivo*. Thus, probably in a near future the luminal surface of aorta could be monitored *in vivo* by microCT to obtain microstructural information of the aneurysm in real time, complementing the data provided by echocardiography, in pre-clinical research and clinical diagnosis[167].

Part 3: Impact of *in vivo*-like stretch on the phenotypic modulation of VSMCs of Marfan syndrome patients

The overriding aim of this thesis part was to build a custom-made system to culture VSMCs in a pseudo-physiological environment. To this aim, we have successfully developed a stretching bioreactor that subjected VSMCs to an *in vivo*-like mechanical environment, and we have assessed its influence on proteins associated to phenotypic modulation.

3.1. Functioning assessment of the stretch bioreactor

The implemented aortic bioreactor was built to serve as a cell culture platform providing a stretching stimulus that mimicked the *in vivo* environment. The intensity and frequency of this stimulus were set taking into account the physiological values for these parameters: 13% strain at 1.1 Hz [19–21]. Nonetheless, the overall bioreactor system was able to produce the exact physiological strain rate, but at slightly lower frequency (0.81 Hz). We accepted this shortfall given that the mechanical environment achieved by the aortic bioreactor was highly similar to that of a human aorta, and that no other setup improvement could accomplish the required 1 Hz (aside from acquiring the FlexerCell© instrumentation).

Besides, the aortic bioreactor was proved valid for culture of human primary VSMCs, by previously applying a fibronectin coating and plasma treatment to the culture surface (the chip membrane). Posterior protein analysis by adapted immunofluorescence and western blot techniques was also successfully demonstrated. In addition, effective long-term culture of cells with and without stretch application was confirmed by means of these techniques. Furthermore, the effect of stretch stimulus on control cell directionality demonstrated that VSMCs actually sensed the mechanical tension occurring on the culturing substrate and reacted to it (mechanotransduction).

Cell attachment to the membrane was evidenced by focal adhesion assessment. Control and Marfan VSMCs seeded on chips displayed numerous focal adhesions, yet their area was significantly lower than that of cells seeded on coverslips without fibronectin. Moreover, chip-cultured control VSMCs had significantly lower number of focal adhesions than conventionally-cultured cells. Paraphrasing, VSMCs were firmly attached to the bioreactor substrate, but they required less strong adhesion than on a stiff surface as glass coverslips. This result is in accordance with earlier reports stating

that focal adhesions are smaller in soft substrates, and also the number of focal adhesions is almost significantly lower[168,169]. At the same time, contractile filaments are less abundant in the cytoplasm of cells on soft substrates, as they are unable to generate a notable traction when pulling the unstable elements conforming the soft surrounding environment. Conversely, in stiff substrates, the sufficient traction reinforces cell-substrate attachment allowing the establishment and growth of multiple focal adhesions[169].

In summary, with these experiments, we demonstrated the validity of the mechanical environment created by the aortic bioreactor for the long-term culture of human primary VSMCs and the posterior protein analysis.

3.2. Interpretation of cultured VSMCs orientation

Cell directionality towards the stretch direction in the case of cells cultured on coverslips (FN- and FN+ conditions) was negligible, because the substrate was circular and had no actual stretch direction. Hence, the stretch direction as an orientation indicator was only valid for cells cultured on chip, either static or dynamic. For coverslips, cell directionality assessment was only relevant for collective cell alignment, regardless the direction.

Control cells cultured onto coverslips without fibronectin coating (conventional culture) frequently showed a significant collective alignment. In contrast, VSMCs seeded on coverslips with fibronectin coating did not tend to collectively align as individual cells were randomly oriented. In the case of culture onto chips for 7 days, either static or dynamic, the substrate (fibronectin-coated soft PDMS) drove control cells to collectively align. Hence, the stiff glass substrate promoted cell alignment, but its combination with a soft fibronectin coating stimulated a scattering in cell directions. Moreover, cells on chips (always with fibronectin coating) were collectively aligned. In summary, whatever the direction the cells aligned to, fibronectin seems to produce a chaotic effect on glass and an organising effect on PDMS. Indeed, it has previously been reported that the stiffness of the substrate can trigger changes on cell behaviour[170] (for instance, the above explanation on focal adhesions). However, fibronectin itself might not be the cause of this behaviour shift because in both cases the stiffness is the same: that provided by the fibronectin coating. The difference relies on the underlying substrate, which is glass or PDMS. We suggest that the fibronectin coating might detach from the glass substrate when cells pull from it to spread and migrate. This detachment may happen in some regions and depending on the amount of pulling cells. Thus, cells might turn the completely coated coverslips to patched, that is with alternating soft and stiff parts. This irregular fibronectin coating might induce “confusing” signals to VSMCs, and hence, might promote a random orientation of cells.

Regarding the aligned cells, we hypothesise that general alignment of cells on coverslips could be a consequence of a “collective intelligence” process of cells[171], in which the first

cells that adhered to the substrate influenced the other ones to align in their same direction[172]. Additionally, in the case of the chip's rectangular membranes, the cell directionality was also influenced by the shape of the substrate since control cells after 7 days of static culture were aligned parallel to the long axis of the rectangle. However, this alignment shifted to perpendicular (i.e. towards the stretch direction) when control cells were cultured under dynamic conditions. This fact was relevant because VSMCs in the aortic tissue (*in vivo*) arrange circumferentially aligned, which is parallel to the direction of the physiologic stretch tension[8,11]. Therefore, we showed that control VSMCs cultured under dynamic condition tended to align towards the bioreactor's stretch direction, as it occurs *in vivo*.

3.3. Effect of *in vivo*-like stretch onto Marfan VSMCs

As previously explained, static control cells tended to align perpendicular to the stretch direction, but stretching stimulus induced control cells to align parallel to its direction, as this was the optimal state to bear the mechanical tension. In contrast, Marfan cells showed scarce collective alignment in any condition. Particularly in dynamic chips, cells were less aligned towards the stretch direction in comparison to control, since histogram shift indicated a tendency without reaching statistical significance. This tendency started at day 3, which was earlier than in control cultures (day 7). We postulate that this alteration of the proper cell alignment when a stretching stimulus was applied might be due to an altered cell-ECM signalling in Marfan VSMCs. This impaired mechanotransduction process could be caused by a failure in the initial mechanosensing or in the execution of cell migration in response to the mechanical stimulus. Thus, cell-ECM linking proteins or contractile proteins might be affected. These proteins, in turn, might be permanently altered by the aberrant fibrillin-1 ECM occurring in the Marfan condition (demonstrated in parts 1 and 2 of this thesis). In summary, the altered reaction of Marfan cells to substrate stretching might be a consequence of an impaired communication between the cell and its surrounding ECM.

To unravel this question, further experiments were required to see whether this different directionality behaviour of Marfan VSMCs was due to a variation in any protein of the cell-ECM anchoring or the phenotypic modulation signalling pathways. To begin with, the vinculin in Marfan cells showed a similar expression distribution to that of control cells. Moreover, the contractile protein per excellence, SMA, was evaluated in terms of cytosolic staining patterns. It showed no significant differences between all conditions in both cell genotypes. Furthermore, there were no specific SMA and transgelin protein level differences between control and Marfan VSMCs seeded in culture dishes and in chips, subjected to static and dynamic conditions. Hence, we postulate that the abnormal cell-ECM communication in human Marfan VSMCs over time exposure to stretch is, in principle, not related to focal adhesion constitution by vinculin, or to SMA subcellular distribution, or to total SMA and transgelin protein content in cells. These results open

the door to explore other proteins that might be involved in the altered mechanotransduction process in Marfan syndrome, such as myosins or integrins associated to fibronectin binding. We also propose the evaluation of the focal adhesion protein filamin-A, since an increase in its fragmentation has been reported in aortic aneurysms of MFS patients[119].

3.4. Effect of *in vivo*-like stretch onto human VSMC phenotypic modulation

As explained at the Introduction section, VSMCs contractile phenotype is principally distinguished by the overexpression of contractile markers SMA and transgelin[93], and cell phenotype modulation can be promoted by mechanical stimuli[95,173]. For these reasons, we expected a change in the levels of SMA and transgelin on cells seeded under stretch conditions in comparison to the static cultures. Nonetheless, both protein levels remained similar in control and Marfan VSMCs under stretch compared to the static counterparts. Therefore, unexpectedly, we observe that there is no phenotypic switch involving SMA and transgelin in stretch-cultured human VSMCs. However, we propose that cell phenotype should be analysed using more markers other than these two contractile markers, given that VSMCs phenotype is considered, by some authors, as a continuous spectrum between the contractile and synthetic states in which there are more than two phenotypes[95,99,102]. In fact, in *in vitro* settings, some studies found VSMCs to be in intermediate phenotypes, for instance, in Marfan aorta, contractile protein upregulation occurred in parallel to increased synthesis of collagen I [93].

Taking this into account, in our experiments, SMA and transgelin might not be sufficiently representative of phenotypic changes happening in human primary VSMCs cultured under stretch stimulus. Therefore, other markers such as calponin-1, smoothelin, or myosin-11 should be considered for further analysis, as well as secreted ECM proteins like collagens and proteoglycans.

Part 4: Definition of a literature-based proteome of the human aorta

To date there is not a well-established human aorta proteome[174–176]. The leading protein databases, namely UniProt and the Human Protein Atlas, do not provide direct protein information on the aortic tissue[132]. In addition, the biggest mass spectrometry proteomic analyses on human healthy and aneurysmal aortic tissue state 630 and 522 proteins, respectively[75,136]. However, mass spectrometry is not an absolute technique[138,175,177], thus there exist other proteins in the tissue that were not identified by those studies. In this context, we have gathered all the published scientific information regarding protein presence strictly only in the human aortic tissue[132]. As a result, we state that there are at least 919 different proteins in the human healthy Aorta Proteome and 724 proteins in the human Aortic Aneurysm Proteome. Out of these total proteins, there exists solid demonstration of presence of 659 and 198 proteins, respectively, in aortic tissue, validated by more than one article or technique.

4.1. General information provided by our aortic Proteomes

In reference to the sources of the protein data, it is important to highlight that the variability of human samples and the processing of the samples varied for each source article. As an advantage of establishing a proteome, gathering all the data of those articles minimises the peculiarities or false positives of individual studies[177]. Thus, the here developed proteomes stand as databases that provide averaged information about protein presence in the aorta. This means that the Aortic Aneurysm Proteome can be utilised to acquire information for all types of aneurysms. But, it should be kept in mind that the proteome might be more representative of the kind of samples that are the majority in the database, which, in the case of the Aortic Aneurysm Proteome are atherosclerotic ageing-associated, abdominal aortic aneurysmal samples of senior men. Furthermore, the Aorta Proteome is actually not representing a completely healthy population, as it is obviously infrequent to obtain this kind of aortic samples[118]. Instead, the Aorta Proteome mainly contains information about ascending aorta of middle-aged, aorta-healthy individuals that were subjected to a valve replacement surgery intervention. Nevertheless, for practical reasons, this data can be extrapolated as healthy population information, but should be interpreted with caution[118].

Besides, it is important to note that the aphorism “the absence of evidence is not evidence of absence” applies for the here presented study[175]. In other words, the proteins listed in the Proteomes could be not the only ones existing in the aortic tissue. Given the

limitations of mass spectrometry[175,177], it is plausible to keep in mind that (few) other proteins in the aorta samples are not being detected, especially those at low concentrations in tissue. Proof of this is the relevant proportion of protein records in the Proteomes only validated by immune-based techniques (19% in healthy and 14% in aneurysmal tissues), such as interleukin-6, -8, MMP-9, -14, TIMP-2, TGF-β1, 2, and 3, in both Proteomes. In addition, it is possible that proteins not detected by mass spectrometry are also not identified by immune-based techniques due to unavailability of specific antibodies, inaccessibility of the antigen, or merely due to that no research group has had the interest to look for the protein in human aortic tissue. Furthermore, the absence of a protein in the Proteomes could be caused by a human error during the literature review process. On the one hand, the reader could have missed a useful article(s) during manual revision of the abstracts. On the other hand, the authors of the articles may have written other protein name not officially stated at the UniProt database or did not specify the "human/patient/etc." or "aort*" keywords in their abstract, hence the WOS search engine or the bioinformatics algorithm were not able to filter this article as a positive match. Last but not the least, it also could be that certain proteins are not present in the human aorta. However, this affirmation should be backed by experimental verification. In fact, a very reduced number of proteins, like MMP-2 and -13, were reported in human aorta by some articles[136,178,179], whereas other articles stated that there was no presence of these proteins in the aorta[180,181].

4.2. Protein-specific analysis of the aortic Proteomes

Examining changes in the proteome might provide insights into understanding the molecular mechanisms of diseases[177]. Regarding the variation in the aneurysm Proteome in comparison to the healthy one, we found that 146 proteins had significantly altered levels and 188 proteins were only reported for the diseased tissue. These proteins were diverse, but our detailed analysis demonstrated that many of them were related to tissue remodelling (MMPs and TIMPs), inflammation and fibrosis (TGF-β1, interleukins, collagens), VSMC phenotype (SMA, transgelin, vinculin), and aortic ECM structure (proteoglycans, adhesive glycoproteins, and lamellae components). Indeed, these mentioned functions are those already known to be involved in the aneurysm pathogenesis. In particular, transgelin and vinculin were reported to be altered in MF aneurysmal aortae, in contrast to the results obtained in part 3 of this thesis. Nonetheless, in some cases, the same protein was reported to show different alteration patterns depending on the various source articles, and their experimental conditions. For instance, transgelin in aneurysmal tissue displayed the same[136], higher[137], or even lower protein levels[119,140,182] in comparison to control samples. Thus, by scrutinising the proteome, one can get the full picture of the alterations occurring within the tissue, identifying the sites where there is controversy or there is a need for additional analysis.

4.3. Potentiality of proteome establishment

Importantly, the proteome is a summary of the current knowledge on protein presence in the aorta. Above we have indicated some of the benefits for the scientific community of establishing a proteome: it is useful as an information baseline reference that provides the big picture of the whole protein content in the tissue, whereas also links to sources with detailed information about each protein. These advantages are relevant since a proteome can serve as a starting point for further deepening or large array exploratory studies[175,183]. Additionally, the checking of a proteome before launching a research project could avoid duplicating protein validations that are already reported, which is a crucial issue given the low availability of human aortic tissue for scientific purposes. In the field of vascular tissue, the consultation of our Proteome databases might reduce the number of redundant experiments and help focus the assays towards specific proteins proven to be of interest[138]. Moreover, our Proteomes will support large-scale molecular phenotyping of aneurysmal patients in the era of precision medicine, as proteomic reports based on mass spectrometry already do[175,176].

Furthermore, the simple methodology here presented based on literature reviewing can be applied to other tissues, conditions, or animal species, only by adjusting the specific keywords during Web of Science search and bioinformatics processing. In fact, we have already published the human Skin Proteome[132], and we are currently performing the human Cartilage Proteome. Notably, this methodology could be accelerated by machine learning implementation so that new proteomes could be built more efficiently, and the already existing proteomes could constantly be updated with the newest published articles.

Final remarks

We have successfully accomplished four novel technologies to analyse different aspects of the histopathological structure and protein content of healthy and aneurysmal-prone MFS aortae:

- Multiphoton microscopy and image processing by ImageJ protocol
- Synchrotron-based microCT and image processing by MatLab method
- Bioreactor for aortic cell culture subjected to mechanical stretch
- Human Aorta and Aortic Aneurysm Proteomes

The application of these technologies provides new information in the field of vascular biology. Particularly, MFS disease progression affects the IEL, the innermost ECM structure in the aortic wall, which can be accessed using clinical endoscopy. The IEL gets gradually disrupted like an old cloth subjected to stretching forces: first, at the microscale, the naturally-occurring fenestrae enlarge[158], and then, these disruptions continue growing becoming big lamellae breaks of hundreds of micrometres. All these alterations are involved in the aberrant cell-ECM communication happening in MFS. We can affirm that in this context, SMA and transgelin total protein levels in VSMCs are not responsible for the aberrant MFS mechanotransduction, and neither is the cytosolic distribution of SMA and vinculin (at least, in our laboratory conditions). However, the proteome analysis has shown that aneurysmal aortic tissue of MFS patients actually presents altered levels of SMA, transgelin, and vinculin proteins in comparison to control tissue. Notably, tissue manipulation is not the same as for *in vitro* cultured VSMCs, hence, these results are not fully comparable. Nonetheless, this discrepancy stresses out the importance of establishing standard protocols and comparative studies to precisely know the difference between the experimental models and what occurs in a tissue/organ context in reality.

CONCLUSIONS

1. The analysis of the microstructure of elastic lamellae of arteries is feasible using the here developed multiphoton microscopy and image processing protocol. Its application established the density of aortic fenestrae as a potential microscale damage marker in Marfan syndrome histopathology, being mainly accumulated in the proximal and convex regions of the ascending aorta.

2. The evaluation of tissue remodelling in the vascular wall is achievable by employing the here implemented microCT and image processing methodology. Its application revealed that the aortic wall of middle-aged Marfan mice displays a histopathological remodelling resembling that of an accelerated middle-ageing process.

3. The examination of the behaviour and content of vascular smooth muscle cells cultured under an *in vivo*-like mechanical environment is possible by utilising the here designed stretch bioreactor. Its application proved that aortic vascular smooth muscle cells from Marfan patients show an altered cell-ECM communication, which is not related to a phenotypic switch defined by SMA or transgelin.

4. The assessment of the current scientific information about protein presence in the human aorta is plausible by performing a systematic literature review. Its application yielded the Aorta Proteome and the Aortic Aneurysm Proteome databases, which stand as the largest aortic proteomes to date, and will serve as a baseline reference for the vascular biology scientific community.

PUBLICATIONS AND CONFERENCE COMMUNICATIONS

The following section includes the publications and conference communications derived from the research conducted by the PhD candidate during her thesis.

- Lopez-Guimet J, Andilla J, Loza-Alvarez P, Egea G. High-Resolution Morphological Approach to Analyse Elastic Laminae Injuries of the Ascending Aorta in a Murine Model of Marfan Syndrome. Sci Rep. 2017;7(1):1505. Available at: http://dx.doi.org/10.1038/s41598-017-01620-8 . IF = 4.259, Q1.

  This article is available at Appendix 3 of this thesis.

- Lopez-Guimet J *et al*. MicroCT imaging of remodelling and micro-scale damage in Marfan syndrome murine aorta. *Under review.*

- Lopez-Guimet J *et al*. Novel morphological approaches to analyse elastic lamellae damagein murine Marfan syndrome aortae. Oral presentation and poster at the *Elastin, Elastic Fibers & Microfibrils – Gordon Research Seminar and Conference*. 29th July – 4th August 2017, University of New England, USA.
- Lopez-Guimet J *et al*. High-resolution morphological study by two-photon excitation microscopy of the aortic wall in a murine model of Marfan syndrome. Oral presentation at the *9th European Elastin Meeting*, 17-19th June 2016, Stuttgart, Germany.
- Lopez-Guimet J *et al*. Synchrotron X-ray micro-tomography of aged and diseased cardiovascular tissues. Oral presentation and poster at the *Tomography for Scientific Advancement symposium*, 3-4th September 2015, University of Manchester, UK.

REFERENCES

1. Koeppen BM, Stanton BA. *Berne & Levy Physiology*. 6th ed. Philadelphia: Mosby; 2008.

2. Hutchison SJ. *Enfermedades Aórticas: Atlas de Diagnóstico Clínico Por Imagen*. Barcelona: Elsevier; 2010.

3. Back M, Gasser TC, Michel J-B, Caligiuri G. Biomechanical factors in the biology of aortic wall and aortic valve diseases. *Cardiovasc Res*. 2013;99(2):232-241. doi:10.1093/cvr/cvt040.

4. Boron WF, Boulpaep EL. *Medical Physiology*. Philadelphia: Elsevier; 2005.

5. Fawcett DW. *A Textbook of Histology*. 12th ed. New York: Chapman & Hall; 1994.

6. Testut L, Latarjet A. *Compendio de Anatomía Descriptiva*. Barcelona: Salvat; 1983.

7. Mann DL, Zipes DP, Libby P, Bonow RO. *Braunwald's Heart Disease: A Textbook of Cardiovascular Medicine*. 10th ed. Philadelphia: Elsevier; 2015.

8. Gartner LP, Hiatt JL. *Texto Atlas de Histología*. 3rd ed. McGraw-Hill Interamericana; 2008.

9. Wagenseil JE, Mecham RP. Vascular extracellular matrix and arterial mechanics. *Physiol Rev*. 2009;89(3):957-989. doi:10.1152/physrev.00041.2008.

10. Kierszenbaum AL, Tres LL. *Histology and Cell Biology: An Introduction to Pathology*. 4th ed. Philadelphia: Elsevier; 2016.

11. Ross MH, Kaye GI, Pawlina W. *Histología: Texto Y Atlas Color Con Biología Celular Y Molecular*. 4th ed. Buenos Aires: Editorial Médica Panamericana; 2004.

12. Junqueira LC, Carneiro J. *Histología Básica*. 6th ed. Barcelona: Masson; 2005.

13. O'Connell MK, Murthy S, Phan S, et al. The three-dimensional micro- and nanostructure of the aortic medial lamellar unit measured using 3D confocal and electron microscopy imaging. *Matrix Biol*. 2008;27(3):171-181. doi:10.1016/j.matbio.2007.10.008.

14. Dingemans KP, Teeling P, Lagendijk JH, Becker AE. Extracellular matrix of the human aortic media: an ultrastructural histochemical and immunohistochemical study of the adult aortic media. *Anat Rec*. 2000;258(1):1–14.

15. Lee RT, Kamm RD. Vascular Mechanics for the Cardiologist. *J Am Coll Cardiol*. 1994;23(6):1289-1295. doi:10.1016/0735-1097(94)90369-7.

16. Karimi A, Milewicz DM. Structure of the Elastin-Contractile Units in the Thoracic Aorta and How Genes That Cause Thoracic Aortic Aneurysms and Dissections Disrupt This Structure. *Can J Cardiol*. 2016;32(1):26-34. doi:10.1016/j.cjca.2015.11.004.

17. Emmott A, Garcia J, Chung J, et al. Biomechanics of the Ascending Thoracic Aorta: A Clinical Perspective on Engineering Data. *Can J Cardiol*. 2016;32(1):35-47. doi:10.1016/j.cjca.2015.10.015.

18. Alberts B, Bray D, Lewis J, Raff M, Roberts K, Watson JD. *Molecular Biology of the Cell*. 2nd ed. New York: Garland; 1989.

19. Teixido-Tura G, Redheuil A, Rodríguez-Palomares J, et al. Aortic biomechanics by magnetic resonance: Early markers of aortic disease in Marfan syndrome regardless of aortic dilatation? *Int J Cardiol*. 2014;171(1):56-61. doi:10.1016/j.ijcard.2013.11.044.

20. van Prehn J, Vincken KL, Muhs BE, et al. Toward endografting of the ascending aorta: insight into dynamics using dynamic cine-CTA. *J Endovasc Ther*. 2007;14(4):551-560. doi:10.1583/1545-1550(2007)14[551:TEOTAA]2.0.CO;2.

21. Morrison TM, Choi G, Zarins CK, Taylor C a. Circumferential and longitudinal cyclic strain of the human thoracic aorta: Age-related changes. *J Vasc Surg*. 2009;49(4):1029-1036. doi:10.1016/j.jvs.2008.11.056.

22. Cheng JK, Wagenseil JE. Extracellular matrix and the mechanics of large artery development. *Biomech Model Mechanobiol*. 2012;11:1169-1186. doi:10.1007/s10237-012-0405-8.

23. Robertson AM, Watton PN. Mechanobiology of the Arterial Wall. In: Becker S, Kuznetsov A, eds. *Transport in Biological Media*. Elsevier; 2013:275-347. doi:10.1016/B978-0-12-415824-5.00008-4.

24. Tsamis A, Krawiec JT, Vorp DA. Elastin and collagen fibre microstructure of the human aorta in ageing and disease: a review. *J R Soc Interface*. 2013;10:1-22. doi:10.1098/rsif.2012.1004.

25. El-Hamamsy I, Yacoub MH. Cellular and molecular mechanisms of thoracic aortic aneurysms. *Nat Rev Cardiol*. 2009;6(12):771-786. doi:10.1038/nrcardio.2009.191.

26. Erbel R, Aboyans V, Boileau C, et al. 2014 ESC Guidelines on the diagnosis and treatment of aortic diseases. *Eur Heart J*. 2014;35(41):2873-2926. doi:10.1093/eurheartj/ehu281.

27. Wu D, Shen YH, Russell L, Coselli JS, LeMaire SA. Molecular mechanisms of thoracic aortic dissection. *J Surg Res*. 2013;184(2):907-924. doi:10.1016/j.jss.2013.06.007.

28. Chau KH, Elefteriades JA. Natural history of thoracic aortic aneurysms: size matters, plus moving beyond size. *Prog Cardiovasc Dis*. 2013;56(1):74-80. doi:10.1016/j.pcad.2013.05.007.

29. Centers for Disease Control and Prevention N. *20 Leading Causes of Death in United States*.; 2015. https://webappa.cdc.gov/sasweb/ncipc/leadcause.html.

30. Lavall D, Schäfers H-J, Böhm M, Laufs U. Aneurysms of the ascending aorta. *Dtsch Arztebl Int*. 2012;109(13):227. http://www.ncbi.nlm.nih.gov/pmc/articles/PMC3334714/.

31. Cozijnsen L, Braam RL, Waalewijn RA, et al. What is new in dilatation of the

ascending aorta? Review of current literature and practical advice for the cardiologist. *Circulation*. 2011;123(8):924-928. doi:10.1161/CIRCULATIONAHA.110.949131.

32. Tellides G. Further Evidence Supporting a Protective Role of Transforming Growth Factor-β (TGFβ) in Aortic Aneurysm and dissection. *Arterioscler Thromb Vasc Biol*. 2017;37:1983-1986. doi:10.1161/ATVBAHA.117.310031.

33. Tremblay D, Leask RL. Remodelling and pathology development associated with aneurysmal ascending aortic tissues. *Can J Chem Eng*. 2011;89(1):13-22. doi:10.1002/cjce.20455.

34. Wilson NK, Gould RA, Gallo E, Consortium ML. Pathophysiology of aortic aneurysm: insights from human genetics and mouse models. *Pharmacogenomics*. 2016;17(18):2071-2080.

35. Dietz HC, Cutting GR, Pyeritz RE, et al. Marfan Syndrome caused by a recurrent de novo missense mutation in the fibrillin gene. *Nature*. 1991;352:337-339.

36. von Kodolitsch Y, de Backer J, Bannas P, et al. Perspectives on the revised Ghent criteria for the diagnosis of Marfan syndrome. *Appl Clin Genet*. 2015;8:137-155. doi:10.2147/TACG.S60472.

37. Dietz HC, Loeys B, Carta L, Ramirez F. Recent progress towards a molecular understanding of Marfan syndrome. *Am J Med Genet Part C Semin Med Genet*. 2005;139C(1):4-9. doi:10.1002/ajmg.c.30068.

38. De Backer J, Renard M, Campens L, et al. Marfan Syndrome and Related Heritable Thoracic Aortic Aneurysms and Dissections. *Curr Pharm Des*. 2015;21(28):4061-4075. doi:10.1161/01.CIR.0000078634.33124.95.

39. Ramachandra CJ a., Mehta A, Guo KWQ, Wong P, Tan J Le, Shim W. Molecular pathogenesis of Marfan syndrome. *Int J Cardiol*. 2015;187:585-591. doi:10.1016/j.ijcard.2015.03.423.

40. Cañadas V, Vilacosta I, Bruna I, Fuster V. Marfan syndrome. Part 1: pathophysiology and diagnosis. *Nat Rev Cardiol*. 2010;7(5):256-265. doi:10.1038/nrcardio.2010.30.

41. Zeyer KA, Reinhardt DP. Engineered mutations in fibrillin-1 leading to Marfan syndrome act at the protein, cellular and organismal levels. *Mutat Res Mutat Res*. 2015;765:7-18. doi:10.1016/j.mrrev.2015.04.002.

42. Cook JR, Carta L, Galatioto J, Ramirez F. Cardiovascular manifestations in Marfan syndrome and related diseases; multiple genes causing similar phenotypes. *Clin Genet*. May 2014:1-10. doi:10.1111/cge.12436.

43. Pereira L, Lee SY, Gayraud B, et al. Pathogenetic sequence for aneurysm revealed in mice underexpressing fibrillin-1. *Proc Natl Acad Sci U S A*. 1999;96(7):3819-3823. http://www.pubmedcentral.nih.gov/articlerender.fcgi?artid=22378&tool=pmcentrez&rendertype=abstract.

44. Judge DP, Biery NJ, Keene DR, et al. Evidence for a critical contribution of haploinsufficiency in the complex pathogenesis of Marfan syndrome. *J Clin Invest*. 2004;114(2):172-181. doi:10.1172/JCI200420641.

45. Simpson RJ. *Proteins and Proteomics*. Cold Spring Harbor Laboratory Press; 2003.

46. Mas Oliva J. *Diagnóstico Molecular En Medicina*. 2nd ed. Mexico D.F.: Manual Moderno; 2007.

47. Montuenga Badía L, Esteban Ruiz FJ, Calvo González A. *Técnicas de Histología Y Biología Celular*. Barcelona: Elsevier; 2009.

48. Spector DL, Goldman RD. *Basic Methods in Microscopy*. New York: Cold Spring Harbor Laboratory Press; 2006.

49. Shearer T, Bradley RS, Hidalgo-Bastida LA, Sherratt MJ, Cartmell SH. Three-dimensional visualisation of soft biological structures by X-ray computed micro-tomography. *J Cell Sci*. 2016;0:1-10. doi:10.1242/jcs.179077.

50. Gonzalez RC, Woods RE. *Digital Image Processing*. 3rd ed. Pearson Prentice Hall; 2008.

51. Tuchin V V. Tissue Optics and Photonics: Light-Tissue Interaction. *J Biomed Photonics Eng*. 2015;1(2):98-134. doi:10.18287/jbpe-2015-1-2-98.

52. Culling CFA. *Handbook of Histopathological and Histochemical Techniques*. 3rd ed. Butterworths; 1974.

53. Young B, Heath JW. *Wheather's Histología Funcional*. 4th ed. Madrid: Harcourt; 2000.

54. Ishikawa-Ankerhold HC, Ankerhold R, Drummen GP. Advanced fluorescence microscopy techniques —FRAP, flip, flap, FRET and FLIM. *Molecules*. 2012;17:4047-4132. doi:10.3390/molecules17044047.

55. So PTC. Two-photon Fluorescence Light Microscopy. *eLS*. 2001. doi:10.1038/npg.els.0002991.

56. Wallace SJ, Morrison JL, Botting KJ, Kee TW. Second-harmonic generation and two-photon-excited autofluorescence microscopy of cardiomyocytes: quantification of cell volume and myosin filament. *J Biomed Opt*. 2008;13(6). doi:10.1117/1.3027970.

57. Willner M, Bech M, Herzen J, et al. Quantitative X-ray phase-contrast computed tomography at 82 keV. *Opt Express*. 2013;21(4). doi:10.1364/OE.21.004155.

58. Marenzana M, Hagen CK, Borges DN, et al. Synchrotron- and phase-contrast imaging for imaging mouse articular cartilage in the absence of radiopaque contrast agents. *Philos Trans R Soc*. 2014;372. doi:10.1098/rsta.2013.0127.

59. Diamond Light Source D. About synchrotrons. http://www.diamond.ac.uk/Home/About/FAQs/About-Synchrotrons.html.

60. Wong MD, Dorr AE, Walls JR, Lerch JP, Henkelman RM. A novel 3D mouse embryo atlas based on micro-CT. 2012;3256:3248-3256. doi:10.1242/dev.082016.

61. Schneider CA, Rasband WS, Eliceiri KW. NIH Image to ImageJ: 25 years of image analysis. *Nat Methods*. 2012;9(7):671-675. doi:10.1038/nmeth.2089.

62. Sommer C, Straehle C, Ullrich K, Hamprecht FA. ilastik: Interactive Learning and Segmentation Toolkit. *Eighth IEEE Int Symp Biomed Imaging (ISBI), Proc*. 2011:230-233.

63. Bou-Gharios G, Ponticos M, Rajkumar V, Abraham D. Extra-cellular matrix in vascular networks. *Cell Prolif*. 2004;37:207-220.

64. Mouw JK, Ou G, Weaver VM. Extracellular matrix assembly: a multiscale deconstruction. *Nat Rev Mol Cell Biol*. 2014;15(12):771-785. doi:10.1038/nrm3902.

65. Nakashima Y. Pathogenesis of aortic dissection: Elastic fiber abnormalities and aortic medial weakness. *Ann Vasc Dis*. 2010;3(1):28-36. doi:10.3400/avd.AVD.

66. Hope MD, Hope TA. Functional and molecular imaging techniques in aortic aneurysm disease. *Curr Opin Cardiol*. 2013;28(6):609-618. doi:10.1097/HCO.0b013e3283644beb.

67. Campagnola PJ, Dong C-Y. Second harmonic generation microscopy: principles and applications to disease diagnosis. *Laser Photon Rev*. 2011;5(1):13-26. doi:10.1002/lpor.200910024.

68. Boulesteix T, Pena A-MA-M, Pagès N, et al. Micrometer scale ex vivo multiphoton imaging of unstained arterial wall structure. *Cytom Part*. 2006;69A(1):20-26. doi:10.1002/cyto.a.20196.

69. Tsamis A, Phillippi JA, Koch RG, et al. Fiber micro-architecture in the longitudinal-radial and circumferential-radial planes of ascending thoracic aortic aneurysm media. *J Biomech*. 2013;46(16):2787-2794. doi:10.1016/j.jbiomech.2013.09.003.

70. Megens RTA, Reitsma S, Schiffers PHM, et al. Two-photon microscopy of vital murine elastic and muscular arteries. *J Vasc Res*. 2007;44(2):87-98. doi:10.1159/000098259.

71. Zadrozny LM, Neufeld EB, Lucotte BM, et al. Study of the development of the mouse thoracic aorta three-dimensional macromolecular structure using two-photon microscopy. *J Histochem Cytochem*. 2015;63(1):8-21. doi:10.1369/0022155414559590.

72. Walton LA, Bradley RS, Withers PJ, et al. Morphological Characterisation of Unstained and Intact Tissue Micro-architecture by X-ray Computed Micro- and Nano-Tomography. *Sci Rep*. 2015;5:10074. doi:10.1038/srep10074.

73. Trachet B, Fraga-Silva RA, Piersigilli A, et al. Dissecting abdominal aortic aneurysm in Ang II-infused mice: suprarenal branch ruptures and apparent luminal dilatation. *Cardiovasc Res*. 2015;105(2):213-222. doi:10.1093/cvr/cvu257.

74. Assemat P, Armitage JA, Siu KK, et al. Three-dimensional numerical simulation of blood flow in mouse aortic arch around atherosclerotic plaques. *Appl Math Model*. 2014;38(17-18):4175-4185. doi:10.1016/j.apm.2014.01.004.

75. Didangelos A, Yin X, Mandal K, Baumert M, Jahangiri M, Mayr M. Proteomics Characterization of Extracellular Space Components in the Human Aorta. *Mol Cell Proteomics*. 2010;9:2048-2062. doi:10.1074/mcp.M110.001693.

76. Wolinsky H, Glagov S. Structural Basis for the Static Mechanical Properties of the Aortic Media. *Circ Res*. 1964;14(5):400-413. doi:10.1161/01.RES.14.5.400.

77. Wolinsky H, Glagov S. A Lamellar Unit of Aortic Medial Structure and Function in Mammals. *Circ Res*. 1967;20(1):99-111. doi:10.1161/01.RES.20.1.99.

78. Mariko B, Pezet M, Escoubet B, et al. Fibrillin-1 genetic deficiency leads to pathological ageing of arteries in mice. *J Pathol*. 2011;224(1):33-44. doi:10.1002/path.2840.

79. Campbell GJ, Roach MR. Fenestrations in the internal elastic lamina at bifurcations of human cerebral arteries. *Stroke*. 1981;12(4):489-496. doi:10.1161/01.STR.12.4.489.

80. Ushiki T. Collagen Fibers, Reticular Fibers and Elastic Fibers. A Comprehensive Understanding from a Morphological Viewpoint. *Arch Histol Cytol*. 2002;65(2):109-126. doi:10.1679/aohc.65.109.

81. Kirby BS, Bruhl A, Sullivan MN, Francis M, Dinenno FA, Earley S. Robust internal elastic lamina fenestration in skeletal muscle arteries. *PLoS One*. 2013;8(1):1-11. doi:10.1371/journal.pone.0054849.

82. Roach MR. The pattern of elastin in the aorta and large arteries of mammals. *Ciba Found Symp*. 1983;100(1):37-55.

83. Sandow SL, Gzik DJ, Lee RMKW. Arterial internal elastic lamina holes: Relationship to function? *J Anat*. 2009;214(2):258-266. doi:10.1111/j.1469-7580.2008.01020.x.

84. Wong LC, Langille BL. Developmental remodeling of the internal elastic lamina of rabbit arteries: effect of blood flow. *Circ Res*. 1996;78(5):799-805. doi:10.1161/01.RES.78.5.799.

85. Arribas SM, Briones AM, Bellingham C, et al. Heightened aberrant deposition of hard-wearing elastin in conduit arteries of prehypertensive SHR is associated with increased stiffness and inward remodeling. *Am J Physiol Heart Circ Physiol*. 2008;295(6):H2299-H2307. doi:10.1152/ajpheart.00155.2008.

86. Kielty CM, Stephan S, Sherratt MJ, Williamson M, Shuttleworth CA. Applying elastic fibre biology in vascular tissue engineering. *Philos Trans R Soc Lond B Biol Sci*. 2007;362(1484):1293-1312. doi:10.1098/rstb.2007.2134.

87. Jondeau G, Michel JB, Boileau C. The translational science of Marfan syndrome. *Heart*. 2011;97:1206-1214. doi:10.1136/hrt.2010.212100.

88. Chaudhry SS, Cain SA, Morgan A, Dallas SL, Shuttleworth CA, Kielty CM. Fibrillin-1 regulates the bioavailability of TGFβ1. *J Cell Biol*. 2007;176(3):355-367. doi:10.1083/jcb.200608167.

89. Halper J. *Progress in Heritable Soft Connective Tissue Diseases*. Springer Netherlands; 2014.

90. Martinez-Lemus LA, Hill MA, Meininger GA. The Plastic Nature of the Vascular Wall: A Continuum of Remodeling Events Contributing to Control of Arteriolar Diameter and Structure. *Physiol*. 2009;24:45-57. doi:10.1152/physiol.00029.2008.

91. Bonnans C, Chou J, Werb Z. Remodelling the extracellular matrix in development and disease. *Nat Rev Mol Cell Biol*. 2014;15(12):786-801. doi:10.1038/nrm3904.

92. Humphrey JD. Vascular Adaptation and Mechanical Homeostasis at Tissue, Cellular, and Sub-cellular Levels. *Cell Biochem Biophys*. 2008;50:53-78. doi:10.1007/s12013-007-9002-3.

93. Crosas-Molist E, Meirelles T, López-Luque J, et al. Vascular smooth muscle cell phenotypic changes in patients with Marfan syndrome. *Arterioscler Thromb Vasc Biol*. 2015;35(4):960-972. doi:10.1161/ATVBAHA.114.304412.

94. Moiseeva EP. Adhesion receptors of vascular smooth muscle cells and their functions. *Cardiovasc Res*. 2001;52(January):372-386.

95. Rensen SSM, Doevendans PAFM, van Eys GJJM. Regulation and characteristics of vascular smooth muscle cell phenotypic diversity. *Netherlands Hear J*. 2007;15(3):100-108.

96. Yamin R, Morgan KG. Deciphering actin cytoskeletal function in the contractile vascular smooth muscle cell. *J Physiol*. 2012;590(17):4145-4154. doi:10.1113/jphysiol.2012.232306.

97. Zhang R, Shi L, Zhou L, et al. Transgelin as a therapeutic target to prevent hypoxic pulmonary hypertension. *Am J Physiol - Lung Cell Mol Physiol*. 2014;306:574-583. doi:10.1152/ajplung.00327.2013.

98. Davis-Dusenbery BN, Wu C, Hata A. Micromanaging Vascular Smooth Muscle Cell Differentiation and Phenotypic Modulation. *Arterioscler Thromb Vasc Biol*. 2011;31:2370-2377. doi:10.1161/ATVBAHA.111.226670.

99. Siow RCM, Pearson JD. Vascular Smooth Muscle Cells. In: Murray JC, ed. *Angiogenesis Protocols. Methods in Molecular Medicine™*. Humana Press; 2001.

100. Lesauskaite V, Tanganelli P, Sassi C, et al. Smooth Muscle Cells of the Media in the Dilatative Pathology of Ascending Thoracic Aorta: Morphology, Immunoreactivity for Osteopontin, Matrix Metalloproteinases, and Their Inhibitors. *Hum Pathol*. 2001;32(9):1003-1011. doi:10.1053/hupa.2001.27107.

101. Mao N, Gu T, Shi E, Zhang G, Yu L, Wang C. Phenotypic switching of vascular smooth muscle cells in animal model of rat thoracic aortic aneurysm. *Interact Cardiovasc Thorac Surg*. 2015;21:62-70. doi:10.1093/icvts/ivv074.

102. Riha GM, Lin PH, Lumsden AB, Yao Q, Chen C. Roles of Hemodynamic Forces in Vascular Cell Differentiation. *Ann Biomed Eng*. 2005;33(6):772-779. doi:10.1007/s10439-005-3310-9.

103. Humphrey JD, Schwartz MA, Tellides G, Milewicz DM. Role of Mechanotransduction in Vascular Biology: Focus on Thoracic Aortic Aneurysms and Dissections. *Circ Res*. 2015;116(8):1448-1461. doi:10.1161/CIRCRESAHA.114.304936.

104. Albinsson S, Bhattachariya A, Hellstrand P. Stretch-dependent smooth muscle differentiation in the portal vein-role of actin polymerization, calcium signaling, and microRNAs. *Microcirculation*. 2014;21:230-238. doi:10.1111/micc.12106.

105. Qiu J, Zheng Y, Hu J. Biomechanical regulation of vascular smooth muscle cell functions: from in vitro to in vivo understanding. *J R Soc Interface*. 2014;11. doi:10.1098/rsif.2013.0852.

106. Cui Y, Hameed FM, Yang B, et al. Cyclic stretching of soft substrates induces spreading and growth. *Nat Commun*. 2015;6:1-8. doi:10.1038/ncomms7333.

107. Tosun Z, McFetridge PS. Variation in Cardiac Pulse Frequencies Modulates vSMC Phenotype Switching During Vascular Remodeling. *Cardiovasc Eng Technol*. 2015;6(1):59-70. doi:10.1007/s13239-014-0204-8.

108. Moraes C, Chen J-H, Sun Y, Simmons CA. Microfabricated arrays for high-throughput screening of cellular response to cyclic substrate deformation. *Lab Chip*. 2010;10(2):227-234. doi:10.1039/b914460a.

109. Huh D, Kim HJ, Fraser JP, et al. Microfabrication of human organs-on-chips. *Nat Protoc*. 2013;8(11):2135-2157. doi:10.1038/nprot.2013.137.

110. Boccafoschi F, Mosca C, Bosetti M, Cannas M. The role of mechanical stretching in the activation and localization of adhesion proteins and related intracellular molecules. *J Cell Biochem*. 2011;112(5):1403-1409. doi:10.1002/jcb.23056.

111. Zheng W, Jiang B, Wang D, Zhang W, Wang Z, Jiang X. A microfluidic flow-stretch chip for investigating blood vessel biomechanics. *Lab Chip*. 2012;12(18):3441-3450. doi:10.1039/c2lc40173h.

112. Romaniello F, Mazzaglia D, Pellegrino A, et al. Aortopathy in Marfan syndrome : an update. *Cardiovasc Pathol*. 2014;23:261-266. doi:10.1016/j.carpath.2014.04.007.

113. Habashi JP, Judge DP, Holm TM, et al. Losartan, an AT1 antagonist, prevents aortic aneurysm in a mouse model of Marfan Syndrome. *Science (80-)*. 2006;312(5770):117-121. doi:10.1126/science.1124287.

114. Uriarte JJ, Meirelles T, Gorbenko Del Blanco D, et al. Early Impairment of Lung Mechanics in a Murine Model of Marfan Syndrome. *PLoS One*. 2016;11(3):e0152124. doi:10.1371/journal.pone.0152124.

115. Dingemans KP, Teeling P, van der Wal AC, Becker AE. Ultrastructural pathology of aortic dissections in patients with Marfan syndrome: *Cardiovasc Pathol*. 2006;15(4):203-212. doi:10.1016/j.carpath.2006.03.004.

116. Haskett D, Doyle JJ, Gard C, et al. Altered tissue behavior of a non-aneurysmal descending thoracic aorta in the mouse model of Marfan syndrome. *Cell Tissue Res*. 2012;347(1):267-277. doi:10.1007/s00441-011-1270-y.

117. Ju X, Ijaz T, Sun H, et al. IL-6 regulates extracellular matrix remodeling associated with aortic dilation in a fibrillin-1 hypomorphic mgR/mgR mouse model of severe marfan syndrome. *J Am Heart Assoc*. 2014;3(1):e000476-e000476. doi:10.1161/JAHA.113.000476.

118. Abdulkareem N, Skroblin P, Jahangiri M, Mayr M. Proteomics in aortic aneurysm – What have we learnt so far? *Proteomics Clin Appl*. 2013;7:504-515. doi:10.1002/prca.201300016.

119. Pilop C, Aregger F, Gorman RC, et al. Proteomic Analysis in Aortic Media of Patients With Marfan Syndrome Reveals Increased Activity of Calpain 2 in Aortic Aneurysms. *Circulation*. 2009;120:983-991. doi:10.1161/CIRCULATIONAHA.108.843516.

120. Ikonomidis JS, Jones JA, Barbour JR, et al. Expression of Matrix Metalloproteinases and Endogenous Inhibitors Within Ascending Aortic Aneurysms of Patients With Marfan Syndrome. *Circulation*. 2006;114. doi:10.1161/CIRCULATIONAHA.105.000810.

121. Abraham PA, Perejda AJ, Carnes WH, Uitto J. Marfan syndrome. Demonstration of abnormal elastin in aorta. *J Clin Invest*. 1982;70(6):1245-1252.

122. Chung AWY, Au Yeung K, Sandor GGS, Judge DP, Dietz HC, Van Breemen C. Loss of elastic fiber integrity and reduction of vascular smooth muscle contraction resulting from the upregulated activities of matrix metalloproteinase-2 and -9 in the thoracic aortic aneurysm in Marfan syndrome. *Circ Res*. 2007;101(5):512-522. doi:10.1161/CIRCRESAHA.107.157776.

123. Bunton TE, Biery NJ, Myers L, Gayraud B, Ramirez F, Dietz HC. Phenotypic alteration of vascular smooth muscle cells precedes elastolysis in a mouse model of Marfan syndrome. *Circ Res*. 2001;88(1):37-43. doi:10.1161/01.RES.88.1.37.

124. Renard M, Callewaert B, Baetens M, et al. Novel MYH11 and ACTA2 mutations reveal a role for enhanced TGF β signaling in FTAAD. *Int J Cardiol*. 2013;165(2):314-321. doi:10.1016/j.ijcard.2011.08.079.

125. Matt P, Schoenhoff F, Habashi J, et al. Circulating Transforming Growth Factor-beta in Marfan Syndrome. *Circulation*. 2009;120:526-533. doi:10.1161/CIRCULATIONAHA.108.841981.

126. Holm TM, Habashi JP, Doyle JJ, et al. Noncanonical TGFbeta signaling contributes to aortic aneurysm progression in Marfan syndrome mice - supplementary. *Science (80-)*. 2011;332(6027):358-361. doi:332/6027/358 [pii]\r10.1126/science.1192149.

127. Lavoie P, Robitaille G, Agharazii M, Ledbetter S, Lebel M, Larivière R. Neutralization of transforming growth factor-β attenuates hypertension and prevents renal injury in uremic rats. *J Hypertens*. 2005;23(10). doi:16148614.

128. Habashi JP, Doyle JJ, Holm TM, et al. Angiotensin II Type 2 Receptor Signaling Attenuates Aortic Aneurysm in Mice Through ERK Antagonism. *Science (80-)*. 2011;332(April):361-366. doi:10.1126/science.1192152.

129. Cook JR, Clayton NP, Carta L, et al. Dimorphic Effects of Transforming Growth Factor-β Signaling During Aortic Aneurysm Progression in Mice Suggest a Combinatorial Therapy for Marfan Syndrome. *Arterioscler Thromb Vasc Biol*. 2015;35:911-917. doi:10.1161/ATVBAHA.114.305150.

130. Titarenko S, Withers PJ, Yagola A. An analytical formula for ring artefact suppression in X-ray tomography. *Appl Math Lett*. 2010;23:1489-1495. doi:10.1016/j.aml.2010.08.022.

131. Ahrens J, Geveci B, Law C. *ParaView: An End-User Tool for Large Data*

Visualization, Visualization Handbook. Elsevier; 2005.

132. Hibbert SA, Ozols M, Griffiths CEM, Watson REB, Bell M, Sherratt MJ. Defining tissue proteomes by systematic literature review. *Sci Rep*. 2018:1-10. doi:10.1038/s41598-017-18699-8.

133. Campillo N, Jorba I, Schaedel L, Casals B, Gozal D. A Novel Chip for Cyclic Stretch and Intermittent Hypoxia Cell Exposures Mimicking Obstructive Sleep Apnea. *Front Physiol*. 2016;7(319). doi:10.3389/fphys.2016.00319.

134. Williams JL, Chen JH, Belloli DM. Strain fields on cellstressing devices employing clamped circular elastic diaphragms as substrates. *J Biomech Eng*. 1992;114(3):377-384.

135. Cukierman E. Preparation of Extracellular Matrices Produced by Cultured Fibroblasts. In: *Current Protocols in Cell Biology*. ; 2002.

136. Didangelos A, Yin X, Mandal K, et al. Extracellular Matrix Composition and Remodeling in Human Abdominal Aortic Aneurysms: A Proteomics Approach. *Mol Cell Proteomics*. 2011;10. doi:10.1074/mcp.M111.008128.

137. Kjellqvist S, Maleki S, Olsson T, et al. A Combined Proteomic and Transcriptomic Approach Shows Diverging Molecular Mechanisms in Thoracic Aortic Aneurysm Development in Patients with Tricuspid- And Bicuspid Aortic Valve. *Mol Cell Proteomics*. 2013;12:407-425. doi:10.1074/mcp.M112.021873.

138. Omenn GS. Advances of the HUPO Human Proteome Project with broad applications for life sciences research. *Expert Rev Proteomics*. 2017;14(2):109-111. doi:10.1080/14789450.2017.1270763.

139. Farina A, Chambery A, Esposito S, et al. Proteomic pro fi ling of medial degeneration in human ascending aorta. *Clin Biochem*. 2010;43:387-396. doi:10.1016/j.clinbiochem.2009.10.015.

140. Molacek J, Mares J, Treska V, Houdek K, Baxa J. Proteomic analysis of the abdominal aortic aneurysm wall. *Surg Today*. 2014;44:142-151. doi:10.1007/s00595-012-0480-6.

141. Cui JZ, Tehrani AY, Jett KA, Bernatchez P, van Breemen C, Esfandiarei M. Quantification of aortic and cutaneous elastin and collagen morphology in Marfan syndrome by multiphoton microscopy. *J Struct Biol*. 2014;187(3):242-253. doi:10.1016/j.jsb.2014.07.003.

142. Trachet B, Piersigilli A, Fraga-Silva RA, et al. Ascending Aortic Aneurysm in Angiotensin II-Infused Mice: Formation, Progression, and the Role of Focal Dissections. *Arterioscler Thromb Vasc Biol*. 2016;36:673-681. doi:10.1161/ATVBAHA.116.307211.

143. Atkins SK, Cao K, Rajamannan NM, Sucosky P. Bicuspid aortic valve hemodynamics induces abnormal medial remodeling in the convexity of porcine ascending aortas. *Biomech Model Mechanobiol*. 2014;13(6):1209-1225. doi:10.1007/s10237-014-0567-7.

144. Cotrufo M, Della Corte A, De Santo LS, et al. Different patterns of extracellular matrix protein expression in the convexity and the concavity of the dilated aorta with bicuspid aortic valve: Preliminary results. *J Thorac Cardiovasc Surg*.

2005;130(2):504-511. doi:10.1016/j.jtcvs.2005.01.016.

145. Dormand H, Mohiaddin RH. Cardiovascular magnetic resonance in Marfan syndrome. *J Cardiovasc Magn Reson*. 2013;15:33. doi:10.1186/1532-429X-15-33.

146. Bogren HG, Mohiaddin RH, Yang GZ, Kilner PJ, Firmin DN. Magnetic resonance velocity vector mapping of blood flow in thoracic aortic aneurysms and grafts. *J Thorac Cardiovasc Surg*. 1995;110(3):704-714. doi:10.1016/S0022-5223(95)70102-8.

147. Hope MD, Hope TA, Meadows AK, et al. Bicuspid aortic valve: four-dimensional MR evaluation of ascending aortic systolic flow patterns. *Radiology*. 2010;255(1):53-61. doi:10.1148/radiol.09091437.

148. Hemmasizadeh A, Autieri M, Darvish K. Multilayer material properties of aorta determined from nanoindentation tests. *J Mech Behav Biomed Mater*. 2012;15:199-207. doi:10.1016/j.jmbbm.2012.06.008.

149. Hemmasizadeh A, Tsamis A, Cheheltani R, et al. Correlations between transmural mechanical and morphological properties in porcine thoracic descending aorta. *J Mech Behav Biomed Mater*. 2015;47:12-20. doi:10.1016/j.jmbbm.2015.03.004.

150. Timmins LH, Wu Q, Yeh AT, Moore JE, Greenwald SE. Structural inhomogeneity and fiber orientation in the inner arterial media. *Am J Hear Circ Physiol*. 2010;298:1537-1545. doi:10.1152/ajpheart.00891.2009.

151. Ushiki T, Murakumo M. Scanning Electron Microscopic Studies of Tissue Elastin Components Exposed by a KOH-Collagenase or Simple KOH Digestion Method. *Arch Histol Cytol*. 1991;54(4):427-436. doi:10.1679/aohc.54.427.

152. Clark TE, Lillie MA, Vogl AW, Gosline JM, Shadwick RE. Mechanical contribution of lamellar and interlamellar elastin along the mouse aorta. *J Biomech*. 2015;48(13):3599-3605. doi:10.1016/j.jbiomech.2015.08.004.

153. Briones AM, González JM, Somoza B, et al. Role of elastin in spontaneously hypertensive rat small mesenteric artery remodelling. *J Physiol*. 2003;552(Pt 1):185-195. doi:10.1113/jphysiol.2003.046904.

154. Blomgren B, Göktürk C. A novel method for quantification of the folding of elastic laminae in elastic arteries. *Micron*. 2008;39(5):623-630. doi:10.1016/j.micron.2007.03.010.

155. Lee L, Cui JZ, Cua M, et al. Aortic and Cardiac Structure and Function Using High-Resolution Echocardiography and Optical Coherence Tomography in a Mouse Model of Marfan Syndrome. *PLoS One*. 2016;11(11):e0164778. doi:10.1371/journal.pone.0164778.

156. Howell DW, Popovic N, Metz RP, Wilson E. Regional changes in elastic fiber organization and transforming growth factor β signaling in aortas from a mouse model of marfan syndrome. *Cell Tissue Res*. 2014;358(3). doi:10.1007/s00441-014-1993-7.

157. Fan LM, Douglas G, Bendall JK, et al. Endothelial cell-specific reactive oxygen species production increases susceptibility to aortic dissection. *Circulation*.

2014;129:2661-2672. doi:10.1161/CIRCULATIONAHA.113.005062.

158. López-Guimet J, Andilla J, Loza-Alvarez P, Egea G. High-Resolution Morphological Approach to Analyse Elastic Laminae Injuries of the Ascending Aorta in a Murine Model of Marfan Syndrome. *Sci Rep*. 2017;7:1505. doi:10.1038/s41598-017-01620-8.

159. Sokolis DP, Kritharis EP, Giagini AT, Lampropoulos KM, Papadodima SA, Iliopoulos DC. Biomechanical response of ascending thoracic aortic aneurysms: association with structural remodelling. *Comput Methods Biomech Biomed Engin*. 2012;15(3):231-248. doi:10.1080/10255842.2010.522186.

160. Bellini C, Korneva A, Zilberberg L, Ramirez F, Rifkin DB, Humphrey JD. Differential Ascending and Descending Aortic Mechanics Parallel Aneurysmal Propensity in a Mouse Model of Marfan Syndrome. *J Biomech*. 2016;49(12):2383-2389. doi:10.1016/j.jbiomech.2015.11.059.

161. Logghe G, Trachet B, Aslanidou L, et al. Propagation-based phase-contrast synchrotron imaging of aortic dissection in mice: from individual elastic lamella to 3D analysis. *Sci Rep*. 2018;8(2223). doi:10.1038/s41598-018-20673-x.

162. Lovell DP. Biological Importance and Statistical Significance. *J Agric Food Chem*. 2013;61:8340-8348. doi:10.1021/jf401124y.

163. Tsukube T, Hoshino M, Yagi N. X-ray phase-contrast tomography opens new era for cardiovascular research. *Eur Hear J - Cardiovasc Imaging*. 2017;18(December):742-743. doi:10.1093/ehjci/jew327.

164. Starosolski Z, Villamizar CA, Rendon D, et al. Ultra High-Resolution In vivo Computed Tomography Imaging of Mouse Cerebrovasculature Using a Long Circulating Blood Pool Contrast Agent. *Sci Rep*. 2015;5(10178):10178. doi:10.1038/srep10178.

165. Nebuloni L, Kuhn GA, Vogel J, Müller R. A Novel In Vivo Vascular Imaging Approach for Hierarchical Quantification of Vasculature Using Contrast Enhanced Micro-Computed Tomography. *PLoS One*. 2014;9(1):e86562. doi:10.1371/journal.pone.0086562.

166. Das NM, Hatsell S, Nannuru K, et al. In Vivo Quantitative Microcomputed Tomographic Analysis of Vasculature and Organs in a Normal and Diseased Mouse Model. *PLoS One*. 2016;11(2):e0150085. doi:10.1371/journal.pone.0150085.

167. Donath T, Pfeiffer F, Bunk O, et al. Toward Clinical X-ray Phase-Contrast CT. Demonstration of Enhanced Sort-Tissue Contrast in Human Specimen. *Invest Radiol*. 2010;45(7):445-452.

168. Guo W, Frey MT, Burnham NA, Wang Y. Substrate Rigidity Regulates the Formation and Maintenance of Tissues. *Biophys J*. 2006;90:2213-2220. doi:10.1529/biophysj.105.070144.

169. Lee S, Kumar S. Actomyosin stress fiber mechanosensing in 2D and 3D. *F1000Research*. 2016;5. doi:10.12688/f1000research.8800.1.

170. Handorf AM, Zhou Y, Halanski MA, Li W. Tissue Stiffness Dictates Development, Homeostasis, and Disease Progression. *Organogenesis*.

2015;11:1-15. doi:10.1080/15476278.2015.1019687.

171. Sunyer R, Trepat X. Mechanobiology of collective cell systems. *Biofísica*. 2017;7.

172. He S, Liu C, Li X, Ma S, Huo B, Ji B. Dissecting Collective Cell Behavior in Polarization and Alignment on Micropatterned Substrates. *Biophys J*. 2015;109:489-500. doi:10.1016/j.bpj.2015.06.058.

173. Beamish JA, He P, Kottke-Marchant K, Marchant RE. Molecular Regulation of Contractile Smooth Muscle Cell Phenotype: Implications for Vascular. *Tissue Eng*. 2010;16(5). doi:10.1089/ten.teb.2009.0630.

174. Mayr M. Vascular Proteomics – The Forgotten Blood Vessels. *Proteo*. 2013;7:463. doi:10.1002/prca.201370044.

175. Lam MPY, Ping P, Murphy E. Proteomics Research in Cardiovascular Medicine and Biomarker Discovery. *J Am Coll Cardiol*. 2016;68(25). doi:10.1016/j.jacc.2016.10.031.

176. Mokou M, Lygirou V, Vlahou A, Mischak H. Proteomics in cardiovascular disease: recent progress and clinical implication and implementation. *Expert Rev Proteomics*. 2017;14(2). doi:10.1080/14789450.2017.1274653.

177. Zerkowski H-R, Grussenmeyer T, Matt P, Grapow M, Engelhardt S, Lefkovits I. Proteomics Strategies in Cardiovascular Research. *J Proteome Res*. 2004;3:200-208. doi:10.1021/pr034079t CCC:

178. Annabi B, Shédid D, Ghosn P, et al. Differential regulation of matrix metalloproteinase activities in abdominal aortic aneurysms. *J Vasc Surg*. 2002;35:539-546. doi:10.1067/mva.2002.121124.

179. Tromp G, Gatalica Z, Skunca M, et al. Elevated expression of matrix metalloproteinase-13 in abdominal aortic aneurysms. *Ann Vasc Surg*. 2004;18(4):414-420. doi:10.1007/s10016-004-0050-5.

180. Lizarbe TR, Tarín C, Aracil E, Orte LM, Zaragoza C. Nitric Oxide Induces the Progression of Abdominal Aortic Aneurysms through the Matrix Metalloproteinase Inducer EMMPRIN. *Am J Pathol*. 2009;175(4):1421-1430. doi:10.2353/ajpath.2009.080845.

181. Huusko T, Salonurmi T, Taskinen P, et al. Elevated messenger RNA expression and plasma protein levels of osteopontin and matrix metalloproteinase types 2 and 9 in patients with ascending aortic aneurysms. *J Thorac Cardiovasc Surg*. 2013;145(4):1117-1123. doi:10.1016/j.jtcvs.2012.04.008.

182. Ailawadi G, Moehle CW, Pei H, et al. Smooth muscle phenotypic modulation is an early event in aortic aneurysms. *J Thorac Cardiovasc Surg*. 2009;138(6):1392-1399. doi:10.1016/j.jtcvs.2009.07.075.

183. Ngo D, Sinha S, Shen D, et al. Aptamer-Based Proteomic Profiling Reveals Novel Candidate Biomarkers and Pathways in Cardiovascular Disease. *Circulation*. 2016;134:270-285. doi:10.1161/CIRCULATIONAHA.116.021803.

APPENDIX

Appendix 1.
Aorta Proteome list

AORTA PROTEOME

Protein Name	UniProt#	Gene Name	DOI or PMID	#DOI	Experimental Evidence	Aorta location	Wall Location	Age	Sex	Type of control sample	Associated disease
14-3-3 protein beta/alpha	P31946	YWHAB	10.1074/mcp.M112.021873, 10.1002	2	Mass Spec	ascending				valve replacement	increased in ascending aneurysm
14-3-3 protein epsilon	P62258	YWHAE	10.1074/mcp.M111.008128, 10.1002	3	Mass Spec	ascending		37.5	B	valve replacement	
14-3-3 protein eta	Q04917	YWHAH	10.1002/prca.201200064		Mass Spec						
14-3-3 protein gamma	P61981	YWHAG	10.1074/mcp.M111.008128, 10.1002	3	Mass Spec	ascending		37.5	B	valve replacement	
14-3-3 protein theta	P27348	YWHAQ	10.1074/mcp.M112.021873, 10.1074	4	Mass Spec	ascending		37.5	B	valve replacement	augmented in ascending aneurysm
14-3-3 protein zeta/delta	P63104	YWHAZ	10.1074/mcp.M112.021873, 10.1074/mcp.M111.008128, 10.1002/prca.201200064, 10.1074/mcp.M110.001693	4	Mass Spec	ascending		37.5	B	valve replacement	increased in TAV and BAV asc dilation. 10.1021/pr070380o says there's no 14-3-3zeta in control aortae
1-phosphatidylinositol 4,5-bisphosphate	P51178	PLCD1	10.1074/mcp.M111.008128, 10.1074	2	Mass Spec	ascending		37.5	B	valve replacement	
3-hydroxyacyl-CoA dehydrogenase type-	Q99714	HSD17B10	10.1074/mcp.M111.008128, 10.1074	2	Mass Spec	ascending		37.5	B	valve replacement	
3-hydroxyanthranilate 3,4-dioxygenase	P46952	HAAO	10.1074/mcp.M111.008128, 10.1074	2	Mass Spec	ascending		37.5	B	valve replacement	
3-hydroxybutyrate dehydrogenase type	Q9BUT1	BDH2	10.1074/mcp.M111.008128, 10.1074	2	Mass Spec	ascending		37.5	B	valve replacement	
40S ribosomal protein S14	P62263	RPS14	10.1074/mcp.M111.008128, 10.1074	2	Mass Spec	ascending		37.5	B	valve replacement	
40S ribosomal protein S15a	P62244	RPS15A	10.1074/mcp.M111.008128, 10.1074	2	Mass Spec	ascending		37.5	B	valve replacement	
40S ribosomal protein S16	P62249	RPS16	10.1074/mcp.M111.008128, 10.1074	2	Mass Spec	ascending		37.5	B	valve replacement	
40S ribosomal protein S19	P39019	RPS19	10.1074/mcp.M111.008128, 10.1074	2	Mass Spec	ascending		37.5	B	valve replacement	
40S ribosomal protein S2	P15880	RPS2	10.1074/mcp.M111.008128, 10.1074	2	Mass Spec	ascending		37.5	B	valve replacement	
40S ribosomal protein S20	P60866	RPS20	10.1074/mcp.M111.008128, 10.1074	2	Mass Spec	ascending		37.5	B	valve replacement	
40S ribosomal protein S21	P63220	RPS21	10.1074/mcp.M111.008128, 10.1074	2	Mass Spec	ascending		37.5	B	valve replacement	
40S ribosomal protein S25	P62851	RPS25	10.1074/mcp.M111.008128, 10.1074	2	Mass Spec	ascending		37.5	B	valve replacement	
40S ribosomal protein S27	P42677	RPS27	10.1074/mcp.M111.008128, 10.1074	2	Mass Spec	ascending		37.5	B	valve replacement	
40S ribosomal protein S3	P23396	RPS3	10.1074/mcp.M111.008128, 10.1074	2	Mass Spec	ascending		37.5	B	valve replacement	
40S ribosomal protein S3a	P61247	RPS3A	10.1074/mcp.M111.008128, 10.1074	2	Mass Spec	ascending		37.5	B	valve replacement	
40S ribosomal protein S4, X isoform	P62701	RPS4X	10.1074/mcp.M111.008128, 10.1074	2	Mass Spec	ascending		37.5	B	valve replacement	
40S ribosomal protein S5	P46782	RPS5	10.1074/mcp.M111.008128, 10.1002	3	Mass Spec	ascending		37.5	B	valve replacement	
40S ribosomal protein S8	P62241	RPS8	10.1074/mcp.M111.008128, 10.1074	2	Mass Spec	ascending		37.5	B	valve replacement	
40S ribosomal protein S9	P46781	RPS9	10.1074/mcp.M111.008128, 10.1074	2	Mass Spec	ascending		37.5	B	valve replacement	
40S ribosomal protein SA	P08865	RPSA	10.1074/mcp.M111.008128, 10.1074	2	Mass Spec	ascending		37.5	B	valve replacement	
5'-nucleotidase	P21589	NT5E	10.1093/cvr/cvv027		Immuno	aortic valve		58	B		augmented in calcific disease
60 kDa heat shock protein, mitochondria	P10809	HSPD1	10.1074/mcp.M111.008128, 10.1002	3	Mass Spec	ascending		37.5	B	valve replacement	
60S acidic ribosomal protein P0	P05388	RPLP0	10.1074/mcp.M111.008128, 10.1074	2	Mass Spec	ascending		37.5	B	valve replacement	
60S ribosomal protein L11	P62913	RPL11	10.1074/mcp.M111.008128, 10.1074	2	Mass Spec	ascending		37.5	B	valve replacement	
60S ribosomal protein L12	P30050	RPL12	10.1074/mcp.M111.008128, 10.1074	2	Mass Spec	ascending		37.5	B	valve replacement	
60S ribosomal protein L13	P26373	RPL13	10.1074/mcp.M111.008128, 10.1074	2	Mass Spec	ascending		37.5	B	valve replacement	
60S ribosomal protein L17	P18621	RPL17	10.1074/mcp.M111.008128, 10.1074	2	Mass Spec	ascending		37.5	B	valve replacement	
60S ribosomal protein L18	Q07020	RPL18	10.1074/mcp.M111.008128, 10.1074	2	Mass Spec	ascending		37.5	B	valve replacement	
60S ribosomal protein L18a	Q02543	RPL18A	10.1074/mcp.M111.008128, 10.1074	2	Mass Spec	ascending		37.5	B	valve replacement	
60S ribosomal protein L23	P62829	RPL23	10.1074/mcp.M111.008128, 10.1074	2	Mass Spec	ascending		37.5	B	valve replacement	
60S ribosomal protein L24	P83731	RPL24	10.1074/mcp.M111.008128, 10.1074	2	Mass Spec	ascending		37.5	B	valve replacement	
60S ribosomal protein L26-like 1	Q9UNX3	RPL26L1	10.1074/mcp.M111.008128, 10.1074	2	Mass Spec	ascending		37.5	B	valve replacement	
60S ribosomal protein L27a	P46776	RPL27A	10.1074/mcp.M111.008128, 10.1074	2	Mass Spec	ascending		37.5	B	valve replacement	
60S ribosomal protein L30	P62888	RPL30	10.1074/mcp.M111.008128, 10.1074	2	Mass Spec	ascending		37.5	B	valve replacement	
60S ribosomal protein L36	Q9Y3U8	RPL36	10.1074/mcp.M111.008128, 10.1074	2	Mass Spec	ascending		37.5	B	valve replacement	
60S ribosomal protein L4	P36578	RPL4	10.1074/mcp.M111.008128, 10.1074	2	Mass Spec	ascending		37.5	B	valve replacement	
60S ribosomal protein L6	Q02878	RPL6	10.1074/mcp.M111.008128		Mass Spec	ascending		37.5	B	valve replacement	
60S ribosomal protein L9	P32969	RPL9	10.1074/mcp.M111.008128, 10.1074	2	Mass Spec	ascending		37.5	B	valve replacement	
6-phosphogluconolactonase	O95336	PGLS	10.1074/mcp.M111.008128, 10.1074	2	Mass Spec	ascending		37.5	B	valve replacement	
72 kDa type IV collagenase	P08253	MMP2	10.1053/hupa.2001.27107, 10.1111/eci.12618, 10.1016/j.amjhyper.2004.11.011, 10.1016/j.atherosclerosis.2004.11.021, 10.1161/HYPERTENSIONAHA.107.089409, 10.1074/mcp.M110.001693, 10.1067/mva.2002.121124, 10.1074/mcp.M111.008128, 10.1042/CS20140696	11	Immuno;Mass Spec	ascending, abdominal	intima;media	64.1, 71.5, 61, 60.9, 25, 20, 68.9, 37.5	B	autopsy CV healthy;CABG;valve replacement	less active in aneurysm, augmented in aneurysm, dissection, aging and atheromatous plaques, 10.1016/j.jtcvs.2012.04.008 says there's no mmp2 in control ascending. Not detected in abdominal aneurysm by mass spect
78 kDa glucose-regulated protein	P11021	HSPA5	10.1074/mcp.M111.008128, 10.1074	3	Mass Spec	ascending		37.5	B	valve replacement	
Acetyl-CoA acetyltransferase, mitochond	P24752	ACAT1	10.1074/mcp.M111.008128, 10.1074/mcp.M1		Mass Spec	ascending		37.5	B	valve replacement	
Actin, alpha cardiac muscle 1	P68032	ACTC1	10.1074/mcp.M111.008128, 10.1074	2	Mass Spec	ascending		37.5	B	valve replacement	
Actin, alpha skeletal muscle	P68133	ACTA1	10.1016/j.ejcts.2009.07.025, 10.1067/mva.2002.121124	2	Immuno;Mass Sp	ascending		68.9	B, M	CABG	decreased in aneurysm, increased in aneurysm and in dissection
Actin, aortic smooth muscle	P62736	ACTA2	10.14670/HH-27.103, 10.1111/j.1440-1827.2011.02699.x, 10.1161/CIRCRESAHA.110.235390,10.1161/HYPERTENSIONAHA.107.089409, 10.1161/ATVBAHA.115.305529, 10.1002/prca.201200064, 10.1016/j.jtcvs.2009.07.075, 10.1074/mcp.M110.001693, 10.1002/path.2516	13	Immuno;Mass Spec	abdominal, ascending	intima;media	47.3, 39.7, 40	B	autopsy CV healthy;CABG;valve replacement	increased in aneurysm, increased in dissection adventitia, decreased in aneurysm and medial dissection
Actin, cytoplasmic 1	P60709	ACTB	10.1074/mcp.M111.008128, 10.1002	5	Immuno;Mass Spec	thoracic, ascending		37.5,59, 68.9	B	CABG;valve replacement	
Actin-related protein 2	P61160	ACTR2	10.1074/mcp.M111.008128, 10.1074	3	Mass Spec	ascending		37.5	B	valve replacement	
Actin-related protein 2/3 complex subun	O15144	ARPC2	10.1074/mcp.M111.008128, 10.1074	2	Mass Spec	ascending		37.5	B	valve replacement	
Actin-related protein 2/3 complex subun	P59998	ARPC4	10.1074/mcp.M111.008128, 10.1002	3	Mass Spec	ascending		37.5	B	valve replacement	
Actin-related protein 2/3 complex subun	Q9BPX5	ARPC5L	10.1074/mcp.M111.008128, 10.1074	2	Mass Spec	ascending		37.5	B	valve replacement	
Actin-related protein 3	P61158	ACTR3	10.1074/mcp.M111.008128, 10.1002	3	Mass Spec	ascending		37.5	B	valve replacement	
Adenosylhomocysteinase	P23526	AHCY	10.1074/mcp.M111.008128, 10.1074	2	Mass Spec	ascending		37.5	B	valve replacement	
Adenylate kinase isoenzyme 1	P00568	AK1	10.1074/mcp.M111.008128, 10.1002	3	Mass Spec	ascending		37.5	B	valve replacement	
Adenylyl cyclase-associated protein 1	Q01518	CAP1	10.1074/mcp.M111.008128, 10.1002	3	Mass Spec	ascending		37.5	B	valve replacement	
Adenylyl cyclase-associated protein 2	P40123	CAP2	10.1074/mcp.M110.001693		Mass Spec	ascending				valve replacement	
Adipocyte enhancer-binding protein 1	Q8IUX7	AEBP1	10.1002/prca.201200064, 10.1074/n	3	Immuno;Mass Sp	ascending		37.5	B	valve replacement	augmented in aneurysm
Adiponectin	Q15848	ADIPOQ	20145358, 10.1002/prca.201200064	2	Immuno;Mass Sp	abdominal	periaortic adipose tissue			autopsy CV healthy	decreased in atherosclerosis
ADP/ATP translocase 2	P05141	SLC25A5	10.1002/prca.201200064		Mass Spec						
ADP/ATP translocase 3	P12236	SLC25A6	10.1074/mcp.M111.008128, 10.1074	2	Mass Spec	ascending		37.5	B	valve replacement	
ADP-ribosylation factor 1	P84077	ARF1	10.1002/prca.201200064		Mass Spec						
ADP-ribosylation factor 6	P62330	ARF6	10.1159/000339430		Immuno	descending thorac	intima				
Aggrecan core protein	P16112	ACAN	10.1002/prca.201200064, 10.1074/mcp.M110.001693, 10.1074/mcp.M111.008128	3	Mass Spec	ascending		37.5	B	valve replacement	decreased in abdominal aneurysm
Agrin	O00468	AGRN	10.1074/mcp.M111.008128, 10.1074	2	Immuno;Mass Sp	ascending	intima	37.5	B	valve replacement	
Alcohol dehydrogenase [NADP(+)]	P14550	AKR1A1	10.1074/mcp.M111.008128, 10.1074	2	Mass Spec	ascending		37.5	B	valve replacement	
Alcohol dehydrogenase 1B	P00325	ADH1B	10.1074/mcp.M111.008128, 10.1002	3	Mass Spec	ascending		37.5	B	valve replacement	
Alcohol dehydrogenase class-3	P11766	ADH5	10.1074/mcp.M111.008128, 10.1002	3	Mass Spec	ascending		37.5	B	valve replacement	
Aldehyde dehydrogenase X, mitochondr	P30837	ALDH1B1	10.1074/mcp.M111.008128, 10.1074	3	Mass Spec	ascending		37.5	B	valve replacement	
Aldehyde dehydrogenase, mitochondria	P05091	ALDH2	10.1074/mcp.M111.008128, 10.1016	3	Mass Spec	abdominal, scending		37.5,53.91	B	valve replacement	
Aldo-keto reductase family 1 member C2	P52895	AKR1C2	10.1002/prca.201200064		Mass Spec						
Aldose 1-epimerase	Q96C23	GALM	10.1074/mcp.M111.008128, 10.1074	2	Mass Spec	ascending		37.5	B	valve replacement	
Alpha-1-acid glycoprotein 1	P02763	ORM1	10.1074/mcp.M111.008128, 10.1002	3	Mass Spec	ascending		37.5	B	valve replacement	

Alpha-1-antichymotrypsin	P01011	SERPINA3	10.1074/mcp.M111.008128, 10.389	4	Immuno;Mass Sp	ascending, abdomi	adventitia;intima	37.5	B	valve replacement	decreased in abdominal aneurysm
Alpha-1-antitrypsin	P01009	SERPINA1	10.1074/mcp.M111.008128, 10.101	4	Immuno;Mass Sp	ascending		37.5,58	B,M	other;valve replacement	decreased in aneurysm and in dissection
Alpha-1B-glycoprotein	P04217	A1BG	10.1074/mcp.M111.008128, 10.107	2	Mass Spec	ascending		37.5	B	valve replacement	
Alpha-2A adrenergic receptor	P08913	ADRA2A	10.1152/ajpheart.00268.2003		Immuno	ascending	adventitia	1-44	B		
Alpha-2-antiplasmin	P08697	SERPINF2	10.1002/prca.201200064		Mass Spec						
Alpha-2-HS-glycoprotein	P02765	AHSG	10.1093/ndt/gfp137		Immuno		intima;media	68	B		augmented in CDK patients
Alpha-2-macroglobulin	P01023	A2M	10.1074/mcp.M111.008128, 10.100	3	Mass Spec	ascending		37.5	B	valve replacement	
Alpha-actinin-1	P12814	ACTN1	10.1074/mcp.M112.021873, 10.1074/mcp.M111.008128, 10.1074/mcp.M110.001693, 10.1002/prca.201200064	4	Mass Spec	ascending		37.5	B	valve replacement	increased in dilation, increased or decreased in BAV dilation
Alpha-actinin-4	O43707	ACTN4	10.1074/mcp.M111.008128, 10.100	3	Mass Spec	ascending		37.5	B	valve replacement	increased in TAV and BAV dilation
Alpha-aminoadipic semialdehyde dehyd	P49419	ALDH7A1	10.1074/mcp.M111.008128, 10.107	2	Mass Spec	ascending		37.5	B	valve replacement	
Alpha-crystallin B chain	P02511	CRYAB	10.1074/mcp.M111.008128, 10.100	3	Mass Spec	ascending		37.5	B	valve replacement	
Alpha-enolase	P06733	ENO1	10.1074/mcp.M112.021873, 10.1074/mcp.M111.008128, 10.1016/j.jvs.2011.10.033, 10.1016/j.ejcts.2009.07.025, 10.1002/prca.201200064, 10.1074/mcp.M110.001693	6	Mass Spec	abdominal, ascending		37.5,53.91	B, M	valve replacement	not affected in abdominal aneurysm, augmented in aneurysm and diminished in dissection
Alpha-parvin	Q9NVD7	PARVA	10.1074/mcp.M111.008128, 10.100	3	Mass Spec	ascending				valve replacement	
Angiogenin	P03950	ANG	10.1016/j.jvs.2006.11.020		Immuno	abdominal	adventitia;media	55	B		
Angiopoietin-1	Q15389	ANGPT1	10.1093/cvr/cvu196		Immuno	ascending	adventitia;media	51	B		augmented in aneurysm, not sure if control aorta has it because suppl info is not available online
Angiopoietin-2	O15123	ANGPT2	10.1093/cvr/cvu196		Immuno	ascending	adventitia;media	51	B		augmented in degenerative aneurysm, not sure if control aorta has it because suppl info is not available online
Angiotensin-converting enzyme	P12821	ACE	10.1161/HYPERTENSIONAHA.107.089409		Immuno	descending	intima	20	M	autopsy CV healthy	auigmented with aging
Angiotensin-converting enzyme 2	Q9BYF1	ACE2	10.1161/ATVBAHA.114.304613, 10.1161/HYP		Immuno	abdominal, ascend	intima;media	53.6, 50, 4	M,B		Upregulated in BAV, less in abdominal aneurysm
Angiotensinogen	P01019	AGT	10.1016/j.atherosclerosis.2009.01.003, 10.1097/FJC.0000000000000276, 10.1093/abbs/gmv047	3	Immuno	ascending		50, 60	B	autopsy CV healthy;CABG	augmented in ascending thoracic and idiopathic ascending aortic aneurysm, in abdominal aneurysm and atherosclerosis
Ankyrin-3	Q12955	ANK3	10.1074/mcp.M111.008128, 10.107	2	Mass Spec	ascending		37.5	B	valve replacement	
Annexin A1	P04083	ANXA1	10.1074/mcp.M112.021873, 10.107	4	Mass Spec	ascending		37.5	B	valve replacement	
Annexin A11	P50995	ANXA11	10.1074/mcp.M111.008128, 10.107	2	Mass Spec	ascending		37.5	B	valve replacement	
Annexin A2	P07355	ANXA2	10.1074/mcp.M111.008128, 10.101	4	Mass Spec	abdominal, ascending		37.5,53.91	B	valve replacement	decreased in abdominal aneurysm
Annexin A3	P12429	ANXA3	10.1074/mcp.M111.008128, 10.100	3	Mass Spec	ascending		37.5	B	valve replacement	
Annexin A4	P09525	ANXA4	10.1074/mcp.M112.021873, 10.107	4	Mass Spec	ascending		37.5	B	valve replacement	
Annexin A5	P08758	ANXA5	10.1074/mcp.M112.021873, 10.107	5	Mass Spec	abdominal, ascending		37.5,53.91	B	valve replacement	decreased in abdominal aneurysm
Annexin A6	P08133	ANXA6	10.1074/mcp.M111.008128, 10.100	3	Mass Spec	ascending		37.5	B	valve replacement	
Annexin A7	P20073	ANXA7	10.1074/mcp.M111.008128, 10.107	2	Mass Spec	ascending		37.5	B	valve replacement	
Antileukoproteinase	P03973	SLPI	10.1074/mcp.M111.008128, 10.107	3	Mass Spec	ascending		37.5	B	valve replacement	not detected in abdominal aneurysm
Antithrombin-III	P01008	SERPINC1	10.1074/mcp.M111.008128, 10.100	3	Mass Spec	ascending		37.5	B	valve replacement	
AP-2 complex subunit alpha-1	O95782	AP2A1	10.1074/mcp.M110.001693		Mass Spec	ascending				valve replacement	
Apelin	Q9ULZ1	APLN	10.1016/j.carpath.2014.02.003		Immuno	abdominal	intima;media				negatively correlated with aortic atherosclerosis
Apelin receptor	P35414	APLNR	10.1016/j.carpath.2014.02.003		Immuno	abdominal	intima;media				positively correlated with aortic atherosclerosis
Apolipoprotein A-I	P02647	APOA1	10.1161/CIRCULATIONAHA.108.843516, 10.1161/CIRCULATIONAHA.113.002624, 10.1002/prca.201200064, 10.1074/mcp.M110.001693, 10.1074/mcp.M111.008128	5	Immuno;Mass Sp	ascending		60, 23, 37.	B	other;valve replacement	augmented in atherosclerosis and abdominal aneurysm, decreased in Marfan aneurysm
Apolipoprotein A-IV	P06727	APOA4	10.1002/prca.201200064, 10.1074/m	3	Mass Spec	ascending		37.5	B	valve replacement	
Apolipoprotein B-100	P04114	APOB	10.1016/j.atherosclerosis.2009.01.038, 10.1161/hs1101.098520 , 10.1002/prca.201200064, 10.1074/mcp.M110.001693, 10.1074/mcp.M111.008128	5	Immuno;Mass Sp	abdominal, ascend	intima	1, 7.9, 0, 4	B	valve replacement	augmented with aging and abdominal aneurysm
Apolipoprotein D	P05090	APOD	10.1074/mcp.M110.001693, 10.1074/mcp.M111.008128	2	Mass Spec	ascending		37.5	B	valve replacement	augmented in abdominal aneurysm
Apolipoprotein E	P02649	APOE	10.1002/prca.201200064, 10.1074/mcp.M110.001693, 10.1074/mcp.M111.008128	3	Mass Spec	ascending		37.5	B	valve replacement	augmented in abdominal aneurysm
Aquaporin-1	P29972	AQP1	10.1002/prca.201200064		Mass Spec						
Aspartate aminotransferase, cytoplasmi	P17174	GOT1	10.1074/mcp.M111.008128, 10.107	2	Mass Spec	ascending		37.5	B	valve replacement	
Aspartate aminotransferase, mitochond	P00505	GOT2	10.1074/mcp.M111.008128, 10.107	2	Mass Spec	ascending		37.5	B	valve replacement	
Asporin	Q9BXN1	ASPN	10.1074/mcp.M111.008128, 10.107	2	Mass Spec	ascending		37.5	B	valve replacement	
Astrocytic phosphoprotein PEA-15	Q15121	PEA15	10.1002/prca.201200064		Mass Spec						
ATP synthase subunit alpha, mitochondr	P25705	ATP5A1	10.1074/mcp.M111.008128, 10.100	3	Mass Spec	ascending		37.5	B	valve replacement	
ATP synthase subunit beta, mitochondri	P06576	ATP5B	10.1074/mcp.M111.008128, 10.101	4	Mass Spec	abdominal, ascending		37.5,53.91	B	valve replacement	
ATP synthase subunit gamma, mitochon	P36542	ATP5C1	10.1074/mcp.M111.008128, 10.107	2	Mass Spec	ascending		37.5	B	valve replacement	
ATP synthase subunit O, mitochondrial	P48047	ATP5O	10.1074/mcp.M111.008128, 10.107	2	Mass Spec	ascending		37.5	B	valve replacement	
ATP-dependent RNA helicase A	Q08211	DHX9	10.1074/mcp.M111.008128, 10.107	2	Mass Spec	ascending		37.5	B	valve replacement	
ATP-dependent RNA helicase DDX1	Q92499	DDX1	10.1074/mcp.M111.008128, 10.107	2	Mass Spec	ascending		37.5	B	valve replacement	
ATP-dependent RNA helicase DDX3X	O00571	DDX3X	10.1074/mcp.M111.008128		Mass Spec	ascending		37.5	B	valve replacement	
Azurocidin	P20160	AZU1	10.1074/mcp.M110.001693		Mass Spec	ascending				valve replacement	
BAG family molecular chaperone regulat	O95817	BAG3	10.1074/mcp.M110.001693		Mass Spec	ascending				valve replacement	
Band 3 anion transport proteinBand 3 ar	P02730	SLC4A1	10.1002/prca.201200064		Mass Spec						
Basal cell adhesion molecule	P50895	BCAM	10.1074/mcp.M111.008128, 10.107	2	Mass Spec	ascending		37.5	B	valve replacement	
Basement membrane-specific heparan s	P98160	HSPG2	10.1002/prca.201200064, 10.1074/m	3	Mass Spec	ascending		37.5	B	valve replacement	decreased in abdominal aneurysm
Basigin	P35613	BSG	10.1016/j.atherosclerosis.2004.11.021		Immuno		intima	25			augmented in atheromatous plaque, 10.2353/ajpath.2009.080845 and 10.1042/CS20080235 say that control aortas do not have basigin
Beta-2-glycoprotein 1	P02749	APOH	10.1074/mcp.M111.008128, 10.107	3	Mass Spec	ascending		37.5	B	valve replacement	
Biglycan	P21810	BGN	10.1002/prca.201200064,10.1074/m	4	Immuno;Mass Sp	ascending	media	37.5	B	valve replacement	decreased in aneurysm
Biliverdin reductase A	P53004	BLVRA	10.1074/mcp.M111.008128, 10.107	2	Mass Spec	ascending		37.5	B	valve replacement	
Bone morphogenetic protein 2	P12643	BMP2	10.1093/ndt/gfp137		Immuno		intima;media	68	B		augmented in calcified aorta

Bone morphogenetic protein 4	P12644	BMP4	10.1074/mcp.M111.008128, 10.1161	3	Immuno;Mass Sp	abdominal, ascend	media	37.5	B	valve replacement	prominent expression in foam cells in the lipid core of atheroma
Brain acid soluble protein 1	P80723	BASP1	10.1074/mcp.M111.008128, 10.1074	2	Mass Spec	ascending		37.5	B	valve replacement	
Breast cancer anti-estrogen resistance p	P56945	BCAR1	10.1038/srep17189		Immuno	ascending	intima;media	62	B		augmented in aortic stiffening
Brefeldin A-inhibited guanine nucleotide	Q9Y6D5	ARFGEF2	10.1074/mcp.M111.008128, 10.1074	2	Mass Spec	ascending		37.5	B	valve replacement	
Bromodomain adjacent to zinc finger do	Q9UIF8	BAZ2B	10.1074/mcp.M111.008128, 10.1074	2	Mass Spec	ascending		37.5	B	valve replacement	
BTB/POZ domain-containing protein KCT	Q96CX2	KCTD12	10.1074/mcp.M111.008128, 10.1074	2	Mass Spec	ascending		37.5	B	valve replacement	
Cadherin-1	P12830	CDH1	10.1074/mcp.M111.008128, 10.1074	2	Mass Spec	ascending		37.5	B	valve replacement	
Cadherin-13	P55290	CDH13	10.1016/j.carpath.2014.02.003, 10.1002/prca		Immuno;Mass Sp	abdominal	intima;media				less in atherosclerosis
Caldesmon	Q05682	CALD1	10.1074/mcp.M111.008128, 10.1002	3	Mass Spec	ascending		37.5	B	valve replacement	
Calmodulin-1	P0DP23	CALM1	10.1074/mcp.M111.008128, 10.1074	3	Mass Spec	ascending		37.5	B	valve replacement	
Calnexin	P27824	CANX	10.1002/prca.201200064		Mass Spec						
Calpain small subunit 1	P04632	CAPNS1	10.1002/prca.201200064		Mass Spec						
Calpain-1 catalytic subunit	P07384	CAPN1	10.14670/HH-11-691, 10.1161/HYPERTENSIONAHA.112.196840	2	Immuno	ascending, descend	intima;media	61.6, 20	B, M		increased expression with aging and ascending aneurysm
Calpain-2 catalytic subunit	P17655	CAPN2	10.1161/CIRCULATIONAHA.108.843	4	Immuno;Mass Sp	ascending	intima;media	60,61.6, 2	B, M	valve replacement	increased in atherosclerosis
Calpastatin	P20810	CAST	10.14670/HH-11-691		Immuno	ascending	media	61.6	B		augmented in aneurysm
Calponin-1	P51911	CNN1	10.1074/mcp.M111.008128, 10.1161	4	Immuno;Mass Sp	ascending	intima;media	37.5	B	valve replacement	increased in Marfan aneurysm
Calponin-2	Q99439	CNN2	10.1002/prca.201200064		Mass Spec						
Calponin-3	Q15417	CNN3	10.1074/mcp.M111.008128, 10.1002	3	Mass Spec	ascending		37.5	B	valve replacement	
Calreticulin	P27797	CALR	10.1002/prca.201200064, 10.1074/m	3	Mass Spec	ascending		37.5	B	valve replacement	
cAMP-dependent protein kinase type I-a	P10644	PRKAR1A	10.1074/mcp.M110.001693		Mass Spec	ascending				valve replacement	
Carbonic anhydrase 1	P00915	CA1	10.1074/mcp.M111.008128, 10.1002	3	Mass Spec	ascending		37.5	B	valve replacement	
Carbonic anhydrase 2	P00918	CA2	10.1002/prca.201200064		Mass Spec						
Carbonyl reductase [NADPH] 1	P16152	CBR1	10.1074/mcp.M111.008128, 10.1002	3	Mass Spec	ascending		37.5	B	valve replacement	
Carboxypeptidase Q	Q9Y646	CPQ	10.1074/mcp.M111.008128, 10.1074	2	Mass Spec	ascending		37.5	B	valve replacement	
Cartilage oligomeric matrix protein	P49747	COMP	10.1074/mcp.M110.001693, 10.1074/mcp.M111.008128	2	Mass Spec	ascending		37.5	B	valve replacement	not detected in abdominal aneurysm
Caspase-1	P29466	CASP1	10.1016/j.hlc.2014.04.256		Immuno	ascending	media	61.5	B	CABG	
Caspase-3	P42574	CASP3	10.1016/j.jtcvs.2009.07.075		Immuno	ascending	media			CABG	higher in aneurysm
Cathepsin B	P07858	CTSB	10.1111/j.1365-2613.2012.00819.x	1	Immuno		intima;media	52.9	B		augmented in abdominal aneurysm media
Cathepsin D	P07339	CTSD	10.1016/j.atherosclerosis.2009.01.003, 10.1111/j.1365-2613.2012.00819.x, 10.1074/mcp.M110.001693, 10.1002/prca.201200064, 10.1074/mcp.M111.008128	5	Immuno;Mass Sp	ascending	intima;media	52.9, 37.5	B	autopsy CV healthy;valve replacement	augmented in abdominal aneurysm
Cathepsin G	P08311	CTSG	10.1016/j.jvs.2014.06.004, 10.1002/	5	Immuno;Mass Sp	abdominal, ascending		37.5,50	B	autopsy CV healthy;valve replacement	augmented in abdominal aneurysm and atherosclerosis
Cathepsin K	P43235	CTSK	10.1111/j.1365-2613.2012.00819.x, 10.2353/ajpath.2007.060522	2	Immuno	abdominal	intima;media	52.9, 48	B		augmented in aneurysm (pro- and active forms)
Cathepsin L1	P07711	CTSL	10.1111/j.1365-2613.2012.00819.x,	3	Immuno	abdominal, ascending		52.9, 48	B		augmented in abdominal aneurysm (pro- and active forms)
Cathepsin S	P25774	CTSS	10.1111/j.1365-2613.2012.00819.x, 10.2353/ajpath.2007.060522	2	Immuno	abdominal	intima	52.9, 48	B		augmented in aneurysm (pro- and active forms) and appearing in its media. 10.1074/mcp.M111.008128 says there's no cathepsin S in control aorta
Cathepsin Z	Q9UBR2	CTSZ	10.1074/mcp.M110.001693, 10.1002/prca.201200064, 10.1074/mcp.M111.008128	3	Mass Spec	ascending		37.5	B	valve replacement	decreased in abdominal aneurysm or not detected
Caveolin-1	Q03135	CAV1	10.1074/mcp.M111.008128, 10.1002	3	Mass Spec	ascending		37.5	B	valve replacement	
C-C motif chemokine 15	Q16663	CCL15	10.1016/j.jvs.2006.11.020		Immuno	abdominal		55	B		
C-C motif chemokine 2	P13500	CCL2	10.1161/CIRCULATIONAHA.111.0834	4	Immuno	abdominal	intima;media	68.9, 20, 5	M, B	autopsy CV healthy	augmented in aneurysm and aging
C-C motif chemokine 22	O00626	CCL22	10.1016/j.jvs.2006.11.020		Immuno	abdominal		55	B		
C-C motif chemokine 3	P10147	CCL3	10.1161/CIRCULATIONAHA.111.0834	1	Immuno	abdominal					augmented in abdominal aneurysm
C-C motif chemokine 5	P13501	CCL5	10.1161/CIRCULATIONAHA.111.0834	4	Immuno	abdominal, ascend	adventitia;intima	68.9, 55	B		augmented in abdominal aneurysm
C-C motif chemokine 7	P80098	CCL7	10.1016/j.jvs.2006.11.020		Immuno	abdominal		55	B		
CCR4-NOT transcription complex subuni	A5YKK6	CNOT1	10.1074/mcp.M111.008128, 10.1074	2	Mass Spec	ascending		37.5	B	valve replacement	
CD59 glycoprotein	P13987	CD59	10.1002/prca.201200064		Mass Spec						
CD9 antigen	P21926	CD9	10807738, 10.1002/prca.201200064	2	Immuno;Mass Sp	thoracic descending		17.5		autopsy CV healthy	CD9 is very weak or virtually negative in non-atherosclerotic aortae, and it is strong in atherosclerotic
Cell division control protein 42 homolog	P60953	CDC42	10.1002/prca.201200064		Mass Spec						
Cell surface glycoprotein MUC18	P43121	MCAM	10.1074/mcp.M111.008128, 10.1002	3	Mass Spec	ascending		37.5	B	valve replacement	
Centlein	Q9NXG0	CNTLN	10.1074/mcp.M111.008128, 10.1074	2	Mass Spec	ascending		37.5		valve replacement	
Centromere-associated protein E	Q02224	CENPE	10.1074/mcp.M111.008128, 10.1074	2	Mass Spec	ascending		37.5		valve replacement	
Ceruloplasmin	P00450	CP	10.1074/mcp.M110.001693, 10.1074	2	Mass Spec	ascending		37.5	B	valve replacement	augmented in abdominal aneurysm
cGMP-dependent protein kinase 1	Q13976	PRKG1	10.1002/prca.201200064, 10.1074/mcp.M110		Mass Spec	ascending				valve replacement	
Chloride intracellular channel protein 1	O00299	CLIC1	10.1074/mcp.M111.008128, 10.1074	3	Mass Spec	ascending		37.5		valve replacement	
Chloride intracellular channel protein 4	Q9Y696	CLIC4	10.1074/mcp.M112.021873, 10.1002	2	Mass Spec	ascending				valve replacement	
Chymase	P23946	CMA1	10.1074/mcp.M111.008128, 10.1161/CIRCULATIONAHA.109.849679, 10.1016/j.atherosclerosis.2009.01.003, 10.1074/mcp.M110.001693	4	Immuno;Mass Sp	abdominal, ascending		37.5,41.9,	B	autopsy CV healthy;valve replacement	augmented in abdominal aneurysm and atherosclerosis
Clathrin heavy chain 1	Q00610	CLTC	10.1074/mcp.M111.008128, 10.1002	2	Mass Spec			37.5		valve replacement	
Clusterin	P10909	CLU	10.1111/j.1365-2362.2009.02216.x,	4	Immuno;Mass Sp	valve, ascending		60, 37.5	M, B	valve replacement	increased in aortic valve pathology and abdominal aneurysm
Coagulation factor IX	P00740	F9	10.1074/mcp.M111.008128, 10.1002	3	Mass Spec	ascending		37.5		valve replacement	
Coagulation factor XIII A chain	P00488	F13A1	10.1002/prca.201200064		Mass Spec						
Cofilin-1	P23528	CFL1	10.1074/mcp.M111.008128, 10.1002	3	Mass Spec	ascending		37.5		valve replacement	
Cofilin-2	Q9Y281	CFL2	10.1074/mcp.M111.008128, 10.1074	2	Mass Spec	ascending		37.5		valve replacement	
Coiled-coil domain-containing protein 18	Q8N715	CCDC185	10.1074/mcp.M111.008128, 10.1074	2	Mass Spec	ascending		37.5	B	valve replacement	
Cold-inducible RNA-binding protein	Q14011	CIRBP	10.1016/j.surg.2016.01.007		Immuno			>50			augmented in abdominal aneurysm
Collagen alpha-1(I) chain	P02452	COL1A1	10.1093/icvts/ivs421, 10.1016/j.athc	6	Immuno;Mass Sp	ascending		47.7, 37.5	B	other;valve replacement	decreased in aneurysm, augmented in ascending disection

Collagen alpha-1(III) chain	P02461	COL3A1	10.1016/j.ejvs.2014.10.018, 10.1093/icvts/ivs421, 10.1067/mva.2000.109743, 10.1016/j.athoracsur.2009.04.030, 10.1161/CIRCULATIONAHA.105.000 240, 10.1074/mcp.M110.001693	6	Immuno;Mass Sp	ascending	media	58,47.7	B	CABG;other	decreased in aneurysm and in myocardial infarction, augmented in ascending dissection and aneurysm
Collagen alpha-1(IV) chain	P02462	COL4A1	10.1074/mcp.M111.008128, 163775	4	Immuno;Mass Sp	ascending		37.5,33	B	valve replacement	augmented in aneurysm
Collagen alpha-1(V) chain	P20908	COL5A1	10.1074/mcp.M111.008128, 10.1016	3	Immuno;Mass Sp	ascending		37.5	B	other;valve replacement	augmented in aneurysm
Collagen alpha-1(VI) chain	P12109	COL6A1	10.1002/prca.201200064, 10.1074/n	3	Mass Spec	ascending		37.5	B	valve replacement	
Collagen alpha-1(VIII) chain	P27658	COL8A1	10.1074/mcp.M111.008128, 10.1002	3	Mass Spec	ascending		37.5	B	valve replacement	
Collagen alpha-1(XI) chain	P12107	COL11A1	10.1016/j.athoracsur.2009.04.030		Immuno	ascending				other	increased in aneurysm
Collagen alpha-1(XII) chain	Q99715	COL12A1	10.1002/prca.201200064, 10.1074/n	3	Immuno;Mass Sp	ascending		37.5	B	valve replacement	augmented in abdominal aneurysm
Collagen alpha-1(XIV) chain	Q05707	COL14A1	10.1002/prca.201200064, 10.1074/n	3	Mass Spec	ascending		37.5	B	valve replacement	decreased in abdominal aneurysm
Collagen alpha-1(XV) chain	P39059	COL15A1	10.1002/prca.201200064, 10.1074/n	3	Mass Spec	ascending		37.5	B	valve replacement	
Collagen alpha-1(XVIII) chain	P39060	COL18A1	10.1002/prca.201200064, 10.1074/n	3	Mass Spec	ascending		37.5	B	valve replacement	decreased in abdominal aneurysm
Collagen alpha-1(XXII) chain	Q8NFW1	COL22A1	10.1074/mcp.M111.008128		Mass Spec	ascending		37.5	B	valve replacement	
Collagen alpha-1(XXVIII) chain	Q2UY09	COL28A1	10.1074/mcp.M110.001693		Mass Spec	ascending				valve replacement	
Collagen alpha-2(I) chain	P08123	COL1A2	10.2353/ajpath.2007.060522, 10.101	6	Immuno;Mass Sp	abdominal, ascending		47.7, 37.5	B	other;valve replacement	augmented in ascending dissection and abdominal aneurysm and dissection
Collagen alpha-2(IV) chain	P08572	COL4A2	10.1074/mcp.M111.008128, 10.1002	4	Immuno;Mass Sp	thoracic, ascending		37.5,59	B	valve replacement	decreased in some aortopathies
Collagen alpha-2(V) chain	P05997	COL5A2	10.1074/mcp.M111.008128, 10.1016/j.athoracsur.2009.04.030, 10.1074/mcp.M110.001693	3	Immuno;Mass Sp	ascending		37.5	B	other;valve replacement	augmented in aneurysm, 10.1074/mcp.M111.008128 says there's no collagen a-2(V) in control ascending aorta
Collagen alpha-2(VI) chain	P12110	COL6A2	10.1002/prca.201200064, 10.1074/n	3	Mass Spec	ascending		37.5	B	valve replacement	
Collagen alpha-2(VIII) chain	P25067	COL8A2	10.1074/mcp.M111.008128, 10.1074	2	Mass Spec	ascending		37.5	B	valve replacement	
Collagen alpha-3(VI) chain	P12111	COL6A3	10.1002/prca.201200064, 10.1074/n	4	Mass Spec	ascending		37.5	B	valve replacement	augmented in abdominal aneurysm
Collagen alpha-6(IV) chain	Q14031	COL4A6	10.1074/mcp.M111.008128, 10.1074	2	Mass Spec	ascending		37.5	B	valve replacement	
Collagenase 3	P45452	MMP13	10.2353/ajpath.2007.060522, 10.1007/s10016-004-0050-5	2	Immuno	abdominal, whole	media	48		unknown	10.2353/ajpath.2009.080845 says that control aortas do not have mmp13
Complement C1q subcomponent subuni	P02745	C1QA	10.1002/prca.201200064		Mass Spec						
Complement C1q subcomponent subuni	P02746	C1QB	10.1074/mcp.M111.008128, 10.1002	3	Mass Spec	ascending		37.5	B	valve replacement	
Complement C1q subcomponent subuni	P02747	C1QC	10.1074/mcp.M111.008128, 10.1002	3	Mass Spec	ascending		37.5	B	valve replacement	
Complement C1q tumor necrosis factor-	Q9BXJ0	C1QTNF5	10.1074/mcp.M111.008128, 10.1074	2	Mass Spec	ascending		37.5	B	valve replacement	
Complement C1r subcomponent	P00736	C1R	10.1074/mcp.M111.008128, 10.1074	2	Mass Spec	ascending		37.5	B	valve replacement	
Complement C1s subcomponent	P09871	C1S	10.1074/mcp.M111.008128, 10.1074	2	Mass Spec	ascending		37.5	B	valve replacement	
Complement C3	P01024	C3	10.1074/mcp.M111.008128, 10.111	4	Immuno;Mass Sp	valve, ascending		37.5,60	B,M	valve replacement	increased in aortic valve pathology
Complement C4-A	P0C0L4	C4A	10.1074/mcp.M111.008128, 10.1002	3	Mass Spec	ascending		37.5	B	valve replacement	
Complement C4-B	P0C0L5	C4B	10.1002/prca.201200064		Mass Spec						
Complement C5	P01031	C5	10.1111/j.1365-2362.2009.02216.x,	2	Immuno;Mass Sp	valve		60	M		increased in aortic valve pathology
Complement component C6	P13671	C6	10.1074/mcp.M111.008128		Mass Spec	ascending		37.5	B	valve replacement	
Complement component C8 beta chain	P07358	C8B	10.1074/mcp.M111.008128, 10.1074	2	Mass Spec	ascending		37.5	B	valve replacement	
Complement component C8 gamma cha	P07360	C8G	10.1074/mcp.M111.008128, 10.1074	2	Mass Spec	ascending		37.5	B	valve replacement	
Complement component C9	P02748	C9	10.1074/mcp.M111.008128, 10.1002	3	Mass Spec	ascending		37.5	B	valve replacement	
Complement decay-accelerating factor	P08174	CD55	10.1002/prca.201200064, 10.1074/n	2	Mass Spec	ascending				valve replacement	
Complement factor B	P00751	CFB	10.1074/mcp.M111.008128, 10.1074	3	Mass Spec	ascending		37.5	B	valve replacement	
Complement factor H	P08603	CFH	10.1074/mcp.M111.008128, 10.1002	3	Mass Spec	ascending		37.5	B	valve replacement	
Complement factor H-related protein 1	Q03591	CFHR1	10.1074/mcp.M111.008128, 10.1002	3	Mass Spec	ascending		37.5	B	valve replacement	
Connective tissue growth factor	P29279	CTGF	10.1177/1708538112472282, 10.101	4	Immuno	ascending	adventitia;media	62.1, 59, 4	B	valve replacement	increased in thoracic aneurysm and dissection
Coronin-1A	P31146	CORO1A	10.1002/prca.201200064		Mass Spec						
Coronin-1C	Q9ULV4	CORO1C	10.1074/mcp.M111.008128, 10.1002	3	Mass Spec	ascending		37.5	B	valve replacement	
C-reactive protein	P02741	CRP	10.1159/000362997, 10.1016/j.athe	3	Immuno	abdominal	intima;media	68.9, 10, 6	B		augmented in aneurysm
Creatine kinase B-type	P12277	CKB	10.1074/mcp.M111.008128, 10.1074	2	Mass Spec	ascending		37.5	B	valve replacement	
C-type lectin domain family 11 member	Q9Y240	CLEC11A	10.1074/mcp.M111.008128, 10.1074	2	Mass Spec	ascending		37.5	B	valve replacement	
Cyclic nucleotide-gated cation channel b	Q9NQW8	CNGB3	10.1074/mcp.M111.008128		Mass Spec	ascending		37.5	B	valve replacement	
Cyclin-dependent kinase 2	P24941	CDK2	10.1067/mlc.2003.23		Immuno	ascending		64			
Cyclin-dependent kinase 4	P11802	CDK4	10.1067/mlc.2003.23		Immuno	ascending		64			
Cyclin-dependent kinase inhibitor 1	P38936	CDKN1A	10.1067/mlc.2003.23		Immuno	ascending		64			
Cyclin-dependent kinase inhibitor 1B	P46527	CDKN1B	10.1067/mlc.2003.23		Immuno	ascending		64			
Cystatin-B	P04080	CSTB	10.1074/mcp.M111.008128, 10.1002	3	Mass Spec	ascending		37.5	B	valve replacement	
Cystatin-C	P01034	CST3	10.1111/j.1365-2613.2012.00819.x, 10.2353/ajpath.2007.060522	2	Immuno	abdominal	intima	52.9, 48	B		less or more in abdominal aneurysm
Cysteine and glycine-rich protein 1	P21291	CSRP1	10.1074/mcp.M111.008128, 10.1002	3	Mass Spec	ascending		37.5	B	valve replacement	
Cysteine and glycine-rich protein 2	Q16527	CSRP2	10.1074/mcp.M111.008128, 10.1002	3	Mass Spec	ascending		37.5	B	valve replacement	
Cysteine-rich protein 2	P52943	CRIP2	10.1074/mcp.M111.008128, 10.1002	3	Mass Spec	ascending		37.5	B	valve replacement	
Cytochrome b-c1 complex subunit 2, mit	P22695	UQCRC2	10.1074/mcp.M111.008128, 10.1074	2	Mass Spec	ascending		37.5	B	valve replacement	
Cytochrome c	P99999	CYCS	10.1074/mcp.M111.008128, 10.1074	2	Mass Spec	ascending		37.5	B	valve replacement	
Cytochrome P450 1A1	P04798	CYP1A1	10.1055/s-0034-1367735		Immuno	ascending	adventitia;intima;m	58.13	B	CABG	augmented in aneurysm
Cytoplasmic dynein 1 heavy chain 1	Q14204	DYNC1H1	10.1074/mcp.M111.008128, 10.1002	3	Mass Spec	ascending		37.5	B	valve replacement	
Cytoplasmic dynein 1 intermediate chair	Q13409	DYNC1I2	10.1074/mcp.M111.008128		Mass Spec	ascending		37.5	B	valve replacement	
Cytosol aminopeptidase	P28838	LAP3	10.1074/mcp.M111.008128, 10.1074	2	Mass Spec	ascending		37.5	B	valve replacement	
D-3-phosphoglycerate dehydrogenase	O43175	PHGDH	10.1074/mcp.M111.008128, 10.1074	2	Mass Spec	ascending		37.5	B	valve replacement	
Decorin	P07585	DCN	10.1074/mcp.M110.001693, 10.1002/path.2516, 10.1074/mcp.M111.008128	3	Immuno;Mass Sp	ascending	adventitia;intima	37.5	B	valve replacement	augmented in abdominal aneurysm, in media in aneurysm
Dedicator of cytokinesis protein 9	Q9BZ29	DOCK9	10.1074/mcp.M111.008128, 10.1074	2	Mass Spec	ascending		37.5	B	valve replacement	
Delta(3,5)-Delta(2,4)-dienoyl-CoA isome	Q13011	ECH1	10.1074/mcp.M111.008128, 10.1074	2	Mass Spec	ascending		37.5	B	valve replacement	
Dermatan-sulfate epimerase-like protein	Q8IZU8	DSEL	10.1074/mcp.M111.008128		Mass Spec	ascending		37.5	B	valve replacement	
Dermatopontin	Q07507	DPT	10.1002/prca.201200064, 10.1074/n	3	Mass Spec	ascending		37.5	B	valve replacement	
Desmin	P17661	DES	10.1074/mcp.M111.008128, 10.1159	3	Immuno;Mass Sp	infrarenal, ascendi	intima;media	37.5,47	B	valve replacement	decreased in abdominal aneurysm
Desmoplakin	P15924	DSP	10.1074/mcp.M110.001693		Mass Spec	ascending				valve replacement	
Destrin	P60981	DSTN	10.1074/mcp.M111.008128, 10.1002	3	Mass Spec	ascending		37.5	B	valve replacement	
Dihydropteridine reductase	P09417	QDPR	10.1074/mcp.M111.008128, 10.1074	2	Mass Spec	ascending		37.5	B	valve replacement	
Dihydropyrimidinase-related protein 2	Q16555	DPYSL2	10.1074/mcp.M111.008128, 10.1002	3	Mass Spec	ascending		37.5	B	valve replacement	
Dihydropyrimidinase-related protein 3	Q14195	DPYSL3	10.1074/mcp.M111.008128, 10.1074	3	Mass Spec	ascending		37.5	B	valve replacement	
DNA repair protein REV1	Q9UBZ9	REV1	10.1074/mcp.M110.001693		Mass Spec	ascending				valve replacement	
DNA-(apurinic or apyrimidinic site) lyase	P27695	APEX1	10.1074/mcp.M111.008128, 10.1074	2	Mass Spec	ascending		37.5	B	valve replacement	
Drebrin	Q16643	DBN1	10.1074/mcp.M111.008128, 10.1074	2	Mass Spec	ascending		37.5	B	valve replacement	
Dual specificity mitogen-activated prote	Q02750	MAP2K1	10.1016/j.jamcollsurg.2012.06.414		Immuno						more phosphorilated in abdominal aneurysm
Dual specificity mitogen-activated prote	P36507	MAP2K2	10.1016/j.jamcollsurg.2012.06.414		Immuno						more phosphorilated in abdominal aneurysm
Dual specificity protein phosphatase 3	P51452	DUSP3	10.1074/mcp.M111.008128, 10.1074	2	Mass Spec	ascending		37.5	B	valve replacement	
Dystrophin	P11532	DMD	10.1017/S1047951105000144, 10.1074/mcp.		Immuno;Mass Sp	arch, ascending	intima;media	11	M	valve replacement	disarranged in aortic coarctation
E3 ubiquitin/ISG15 ligase TRIM25	Q14258	TRIM25	10.1016/j.mce.2003.12.008		Immuno		intima				
Echinoderm microtubule-associated pro	O00423	EML1	10.1074/mcp.M111.008128, 10.1074/mcp.M1		Mass Spec	ascending		37.5	B	valve replacement	

Echinoderm microtubule-associated pro	O95834	EML2	10.1074/mcp.M111.008128, 10.1074/mcp.M1		Mass Spec	ascending		37.5	B	valve replacement	
EF-hand domain-containing protein D1	Q9BUP0	EFHD1	10.1002/prca.201200064		Mass Spec						
EGF-containing fibulin-like extracellular	Q12805	EFEMP1	10.1002/prca.201200064, 10.1074/m	3	Mass Spec	ascending		37.5	B	valve replacement	
EGF-containing fibulin-like extracellular	O95967	EFEMP2	10.1177/1708538112473976		Immuno	ascending		58	B		less in aortic dissection
EH domain-containing protein 2	Q9NZN4	EHD2	10.1074/mcp.M111.008128, 10.1002	3	Mass Spec	ascending		37.5	B	valve replacement	
EH domain-containing protein 3	Q9NZN3	EHD3	10.1074/mcp.M111.008128, 10.1074	2	Mass Spec	ascending		37.5	B	valve replacement	
Elastin	P15502	ELN	10.1016/j.jvs.2012.09.062, 10.1093/icvts/ivs421, 10.1002/ajmg.a.37638, 10.1002/prca.201200064, 10.1016/j.jvs.2010.11.035	5	Immuno;Mass Sp	abdominal, ascending	media	46.1, 59.8	M	other	decreased in dissection and ruptured abdominal aneurysm
Elongation factor 1-alpha 1	P68104	EEF1A1	10.1074/mcp.M111.008128, 10.1074	2	Mass Spec	ascending		37.5	B	valve replacement	
Elongation factor 1-gamma	P26641	EEF1G	10.1074/mcp.M111.008128, 10.1074	2	Mass Spec	ascending		37.5	B	valve replacement	
Elongation factor 2	P13639	EEF2	10.1002/prca.201200064, 10.1074/mcp.M110		Mass Spec	ascending				valve replacement	
EMILIN-1	Q9Y6C2	EMILIN1	10.1074/mcp.M111.008128, 10.1002	3	Mass Spec	ascending		37.5	B	valve replacement	
Endoglin	P17813	ENG	10.1093/cvr/cvu196		Immuno	ascending	adventitia	51	B		decreased in aneurysm
Endoplasmin	P14625	HSP90B1	10.1074/mcp.M111.008128, 10.1002	3	Mass Spec	ascending		37.5	B	valve replacement	
Endothelin-1 receptor	P25101	EDNRA	10.1097/00005344-200036051-00109		Immuno		media				
ERO1-like protein alpha	Q96HE7	ERO1A	10.1074/mcp.M111.008128, 10.1074	2	Mass Spec	ascending		37.5	B	valve replacement	
Erythrocyte band 7 integral membrane p	P27105	STOM	10.1002/prca.201200064		Mass Spec						
Estrogen sulfotransferase	P49888	SULT1E1	10.1016/S0002-9440(10)63492-X, 10	2	Immuno	abdominal	media	57.7,24	B		varies depending on atherosclerotic stage
Eukaryotic initiation factor 4A-II	Q14240	EIF4A2	10.1074/mcp.M111.008128, 10.1074	2	Mass Spec	ascending		37.5	B	valve replacement	
Eukaryotic translation initiation factor 4	O43432	EIF4G3	10.1074/mcp.M111.008128, 10.1074	2	Mass Spec	ascending		37.5	B	valve replacement	
Eukaryotic translation initiation factor 4	Q9NRA8	EIF4ENIF1	10.1074/mcp.M111.008128		Mass Spec	ascending		37.5	B	valve replacement	
Eukaryotic translation initiation factor 4	Q15056	EIF4H	10.1002/prca.201200064		Mass Spec						
Extracellular superoxide dismutase [Cu-Zn]	P08294	SOD3	10.1074/mcp.M110.001693, 10.1002	3	Immuno;Mass Sp	ascending		37.5	B	valve replacement	decreased in abdominal aneurysm
Ezrin	P15311	EZR	10.1002/prca.201200064		Mass Spec						
F-actin-capping protein subunit alpha-1	P52907	CAPZA1	10.1074/mcp.M111.008128		Mass Spec	ascending		37.5	B	valve replacement	
F-actin-capping protein subunit beta	P47756	CAPZB	10.1074/mcp.M111.008128, 10.1002	3	Mass Spec	ascending		37.5	B	valve replacement	
Far upstream element-binding protein 2	Q92945	KHSRP	10.1074/mcp.M111.008128, 10.1074	2	Mass Spec	ascending		37.5	B	valve replacement	
Fatty acid-binding protein, heart	P05413	FABP3	10.1074/mcp.M111.008128, 10.1074	2	Mass Spec	ascending		37.5	B	valve replacement	
Fermitin family homolog 2	Q96AC1	FERMT2	10.1074/mcp.M111.008128, 10.1002	3	Mass Spec	ascending		37.5	B	valve replacement	
Fermitin family homolog 3	Q86UX7	FERMT3	10.1002/prca.201200064		Mass Spec						
Ferritin heavy chain	P02794	FTH1	10.1074/mcp.M111.008128, 10.1074	3	Immuno;Mass Sp	ascending, abdominal		37.5,64.9	B,M	valve replacement	aneurysm
Ferritin light chain	P02792	FTL	10.1074/mcp.M111.008128, 10.1002	4	Immuno;Mass Sp	ascending, abdominal		37.5,64.9	B,M	valve replacement	aneurysm
Ferritin, mitochondrial	Q8N4E7	FTMTFTMT	10.1159/000362997		Immuno	abdominal		68.9			augmented in aneurysm
Fibrillin-1	P35555	FBN1	10.1159/000157436, 10.1002/prca.201200064, 10.1074/mcp.M110.001693, 10.1074/mcp.M111.008128	4	Immuno;Mass Sp	thoracic, ascending		35, 37.5	B	valve replacement	increased in abdominal aneurysm
Fibrinogen alpha chain	P02671	FGA	10.1074/mcp.M111.008128, 10.1002	4	Mass Spec	ascending		37.5		valve replacement	
Fibrinogen beta chain	P02675	FGB	10.1074/mcp.M112.021873, 10.1074	5	Mass Spec	ascending		37.5		valve replacement	
Fibrinogen gamma chain	P02679	FGG	10.1074/mcp.M112.021873, 10.1074	4	Mass Spec	ascending		37.5		valve replacement	augmented in aneurysm
Fibroblast growth factor 1	P05230	FGF1	10.1093/cvr/cvu196		Immuno	ascending	adventitia;media	51	B		augmented in aneurysm
Fibromodulin	Q06828	FMOD	10.1002/prca.201200064, 10.1074/mcp.M110		Mass Spec	ascending		37.5	B	valve replacement	
Fibronectin	P02751	FN1	10.1016/j.ijcard.2011.08.079, 10.101	6	Immuno;Mass Sp	abdominal, ascend	intima;media	39.7, 37.5	B	other;valve replacement	augmented in aneurysm
Fibulin-1	P23142	FBLN1	10.1002/prca.201200064, 10.1074/mcp.M110.001693, 10.1074/mcp.M111.008128, 10.1016/j.jvs.2010.11.035	4	Immuno;Mass Sp	ascending		46.1, 37.5	M, B	valve replacement	decreased in aortic dissection and abdominal aneurysm
Fibulin-2	P98095	FBLN2	10.1074/mcp.M110.001693		Mass Spec	ascending				valve replacement	
Fibulin-5	Q9UBX5	FBLN5	10.1093/cvr/cvw082, 10.1074/mcp.M	4	Immuno;Mass Sp	ascending	media	37.5	B	valve replacement	decreased in abdominal aneurysm
Filamin A-interacting protein 1-like	Q4L180	FILIP1L	10.1074/mcp.M111.008128, 10.1074	2	Mass Spec	ascending		37.5	B	valve replacement	
Filamin-A	P21333	FLNA	10.1074/mcp.M111.008128, 10.1002	3	Mass Spec	ascending		37.5	B	valve replacement	
Filamin-binding LIM protein 1	Q8WUP2	FBLIM1	10.1074/mcp.M112.021873, 10.1074	4	Mass Spec	ascending		37.5	B	valve replacement	augmented in BAV dilation
Filamin-C	Q14315	FLNC	10.1074/mcp.M111.008128, 10.1074	2	Mass Spec	ascending		37.5	B	valve replacement	
Focal adhesion kinase 1	Q05397	PTK2	10.1038/srep17189		Immuno	ascending	intima;media	62	B		augmented in aortic stiffening
Four and a half LIM domains protein 1	Q13642	FHL1	10.1074/mcp.M111.008128, 10.1016/j.jvs.2010.11.113, 10.1002/prca.201200064, 10.1074/mcp.M110.001693	4	Immuno;Mass Sp	ascending		47.4	M	autopsy CV healthy;valve replacement	decreased in dissection
Four and a half LIM domains protein 2	Q14192	FHL2	10.1074/mcp.M111.008128, 10.1074	3	Mass Spec	ascending		37.5	B	valve replacement	
Four and a half LIM domains protein 3	Q13643	FHL3	10.1002/prca.201200064		Mass Spec						
Four and a half LIM domains protein 5	Q5TD97	FHL5	10.1074/mcp.M111.008128, 10.1074	2	Mass Spec	ascending		37.5	B	valve replacement	
Fructose-bisphosphate aldolase A	P04075	ALDOA	10.1074/mcp.M111.008128, 10.1074	3	Mass Spec	ascending		37.5	B	valve replacement	
Fructose-bisphosphate aldolase C	P09972	ALDOC	10.1161/CIRCULATIONAHA.108.843516		Mass Spec	ascending		60	B	valve replacement	decreased in Marfan aneurysm
Fumarylacetoacetase	P16930	FAH	10.1074/mcp.M111.008128, 10.1074	2	Mass Spec	ascending		37.5	B	valve replacement	
Galectin-1	P09382	LGALS1	10.1074/mcp.M112.021873, 10.1074	4	Mass Spec	ascending		37.5	B	valve replacement	increased in TAV and BAV asc dilation
Galectin-3	P17931	LGALS3	10.1074/mcp.M111.008128, 10.1074	2	Mass Spec	ascending		37.5	B	valve replacement	
Galectin-3-binding protein	Q08380	LGALS3BP	10.1074/mcp.M111.008128, 10.1002	3	Mass Spec	ascending		37.5	B	valve replacement	
Gamma-enolase	P09104	ENO2	10.1074/mcp.M111.008128, 10.1074	2	Mass Spec	ascending		37.5	B	valve replacement	
Gamma-synuclein	O76070	SNCG	10.1074/mcp.M111.008128, 10.1074	2	Mass Spec	ascending		37.5	B	valve replacement	
Gelsolin	P06396	GSN	10.1074/mcp.M112.021873, 10.1074	4	Mass Spec	ascending		37.5	B	valve replacement	augmented in TAV and BAV ascending dilation
Glia-derived nexin	P07093	SERPINE2	10.1161/ATVBAHA.113.301327	1	Immuno	ascending	media	54	B		augmented in aneurysm, 10.1074/mcp.M111.008128 says there's no glia-derived nexin in control ascending aorta
Glucose-6-phosphate isomerase	P06744	GPI	10.1074/mcp.M111.008128, 10.1002	3	Mass Spec	ascending		37.5	B	valve replacement	
Glucosidase 2 subunit beta	P14314	PRKCSH	10.1074/mcp.M111.008128, 10.1074	2	Mass Spec	ascending		37.5	B	valve replacement	
Glutamate dehydrogenase 1, mitochond	P00367	GLUD1	10.1074/mcp.M111.008128, 10.1074	2	Mass Spec	ascending		37.5	B	valve replacement	
Glutamine-rich protein 2	Q9H0J4	QRICH2	10.1074/mcp.M111.008128, 10.1074	2	Mass Spec	ascending		37.5	B	valve replacement	
Glutathione peroxidase 3	P22352	GPX3	10.1074/mcp.M111.008128, 10.1002	3	Mass Spec	ascending		37.5	B	valve replacement	
Glutathione S-transferase A4	O15217	GSTA4	10.1080/01926230500369907		Immuno	arch	media	22	B		augmented in atherosclerotic plaques
Glutathione S-transferase Mu 3	P21266	GSTM3	10.1074/mcp.M111.008128, 10.1074	2	Mass Spec	ascending		37.5	B	valve replacement	
Glutathione S-transferase omega-1	P78417	GSTO1	10.1074/mcp.M111.008128, 10.1074	2	Mass Spec	ascending		37.5	B	valve replacement	
Glutathione S-transferase P	P09211	GSTP1	10.1074/mcp.M111.008128, 10.1055	4	Immuno;Mass Sp	ascending		37.5,58.13	B	CABG;valve replacement	augmented in aneurysm
Glutathione synthetase	P48637	GSS	10.1074/mcp.M111.008128, 10.1074	2	Mass Spec	ascending		37.5	B	valve replacement	
Glyceraldehyde-3-phosphate dehydrogenase	P04406	GAPDH	10.1074/mcp.M112.021873, 10.1074/mcp.M111.008128, 10.1016/j.jvs.2011.10.033, 10.1002/path.2516, 10.1002/prca.201200064, 10.1016/j.atherosclerosis.2009.01.003, 10.1074/mcp.M110.001693	7	Immuno;Mass Sp	thoracic, abdominal, ascending		37.5,53.91, 50	B	valve replacement	reduced in abdominal aneurysm, augmented in ascending TAV and BAV dilation
Glycogen phosphorylase, brain form	P11216	PYGB	10.1074/mcp.M111.008128, 10.1002	3	Mass Spec	ascending		37.5	B	valve replacement	
Glycogenin-1	P46976	GYG1	10.1074/mcp.M111.008128, 10.1074	2	Mass Spec	ascending		37.5	B	valve replacement	
Glyoxalase domain-containing protein 4	Q9HC38	GLOD4	10.1074/mcp.M111.008128, 10.1074	2	Mass Spec	ascending		37.5	B	valve replacement	
Group 10 secretory phospholipase A2	O15496	PLA2G10	10.1016/j.atherosclerosis.2006.08.062		Immuno		intima;media				augmented in atheriosclerosis
Group 3 secretory phospholipase A2	Q9NZ20	PLA2G3	10.1016/j.atherosclerosis.2006.08.062		Immuno		intima;media				augmented in atheriosclerosis

Group IID secretory phospholipase A2	Q9UNK4	PLA2G2D	10.1016/j.atherosclerosis.2006.08.062		Immuno		intima;media				augmented in atheriosclerosis
Group IIE secretory phospholipase A2	Q9NZK7	PLA2G2E	10.1016/j.atherosclerosis.2006.08.062		Immuno		media				augmented in atheriosclerosis
Growth/differentiation factor 15	Q99988	GDF15	10.1159/000362997		Immuno	abdominal		68.9			augmented in aneurysm
GTPase Kras	P01116	KRAS	10.1074/mcp.M111.008128, 10.1074	2	Mass Spec	ascending		37.5	B	valve replacement	
GTP-binding nuclear protein Ran	P62826	RAN	10.1074/mcp.M111.008128, 10.1002	3	Mass Spec	ascending		37.5	B	valve replacement	
Guanine nucleotide exchange factor DBS	O15068	MCF2L	10.1074/mcp.M111.008128, 10.1074	2	Mass Spec	ascending		37.5	B	valve replacement	
Guanine nucleotide-binding protein G(I),	P62873	GNB1	10.1074/mcp.M111.008128, 10.1074	2	Mass Spec	ascending		37.5	B	valve replacement	
Guanine nucleotide-binding protein G(I),	P62879	GNB2	10.1074/mcp.M111.008128, 10.1074	2	Mass Spec	ascending		37.5	B	valve replacement	
Guanine nucleotide-binding protein G(o	P09471	GNAO1	10.1074/mcp.M111.008128, 10.1074	2	Mass Spec	ascending		37.5	B	valve replacement	
Guanine nucleotide-binding protein subu	P29992	GNA11	10.1002/prca.201200064		Mass Spec						
Haptoglobin	P00738	HP	10.1074/mcp.M111.008128, 10.1074	2	Mass Spec	ascending		37.5	B	valve replacement	
Heat shock 70 kDa protein 1A	P0DMV8	HSPA1A	10.1074/mcp.M111.008128, 10.1074	2	Mass Spec	ascending		37.5	B	valve replacement	
Heat shock 70 kDa protein 1B	P0DMV9	HSPA1B	10.1074/mcp.M110.001693	1	Mass Spec	ascending		37.5	B	valve replacement	
Heat shock 70 kDa protein 4	P34932	HSPA4	10.1074/mcp.M111.008128, 10.1074	2	Mass Spec	ascending		37.5	B	valve replacement	
Heat shock cognate 71 kDa protein	P11142	HSPA8	10.1074/mcp.M111.008128, 10.1002	3	Mass Spec	ascending		37.5	B	valve replacement	
Heat shock protein beta-1	P04792	HSPB1	10.1074/mcp.M112.021873, 10.1074	5	Immuno;Mass Sp	ascending		37.5,47.4	B,M	autopsy CV healthy;valve replacement	augmented in dissection
Heat shock protein beta-6	O14558	HSPB6	10.1074/mcp.M111.008128, 10.1002	3	Mass Spec	ascending		37.5	B	valve replacement	
Heat shock protein beta-7	Q9UBY9	HSPB7	10.1074/mcp.M111.008128, 10.1074	2	Mass Spec	ascending		37.5	B	valve replacement	
Heat shock protein HSP 90-alpha	P07900	HSP90AA1	10.1074/mcp.M111.008128, 10.1002	3	Mass Spec	ascending		37.5	B	valve replacement	
Heat shock protein HSP 90-beta	P08238	HSP90AB1	10.1074/mcp.M112.021873, 10.1074	4	Mass Spec	ascending		37.5	B	valve replacement	increased in TAV and BAV asc dilation
Heat shock-related 70 kDa protein 2	P54652	HSPA2	10.1074/mcp.M111.008128, 10.1074	2	Mass Spec	ascending		37.5	B	valve replacement	
Hematopoietic progenitor cell antigen CD34	P28906	CD34	10.1159/000439169, 10.1016/j.jvs.2009.03.055		Immuno	abdominal, infrarenal	adventitia;intima	66.1,46.6	B,M	autopsy CV healthy	associated to adipose-derived stem cells appearance in abdominal aneurysm, augmented in aneurysm
Heme-binding protein 2	Q9Y5Z4	HEBP2	10.1074/mcp.M111.008128, 10.1074	2	Mass Spec	ascending				valve replacement	
Hemicentin-1	Q96RW7	HMCN1	10.1002/prca.201200064		Mass Spec						10.1074/mcp.M111.008128 says there's no hemicentin-1 in control ascending aorta
Hemoglobin subunit alpha	P69905	HBA1 , HBA2	10.1074/mcp.M112.021873, 10.1074	5	Mass Spec	ascending		37.5,60	B	valve replacement	decreased in Marfan, BAV and unknown aneurysm
Hemoglobin subunit beta	P68871	HBB	10.1074/mcp.M112.021873, 10.1074	5	Mass Spec	ascending		37.5,60	B	valve replacement	decreased in Marfan, BAV and unknown aneurysm
Hemoglobin subunit delta	P02042	HBD	10.1074/mcp.M112.021873, 10.1074	4	Mass Spec	ascending		37.5	B	valve replacement	decreased in Marfan, BAV and unknown aneurysm
Hemopexin	P02790	HPX	10.1074/mcp.M111.008128, 10.1002	3	Mass Spec	ascending		37.5	B	valve replacement	
Heparin cofactor 2	P05546	SERPIND1	10.1074/mcp.M111.008128, 10.1074	2	Mass Spec	ascending		37.5	B	valve replacement	
Hepatocyte growth factor	P14210	HGF	10.1093/cvr/cvu196		Immuno	ascending	adventitia;media	51	B		decreased in aneurysm
Hepatoma-derived growth factor	P51858	HDGF	10.1074/mcp.M110.001693, 10.1074	2	Mass Spec	ascending		37.5	B	valve replacement	
Heterochromatin protein 1-binding prot	Q5SSJ5	HP1BP3	10.1074/mcp.M111.008128, 10.1074	2	Mass Spec	ascending		37.5	B	valve replacement	
Heterogeneous nuclear ribonucleoprote	P51991	HNRNPA3	10.1074/mcp.M111.008128		Mass Spec	ascending		37.5	B	valve replacement	
Heterogeneous nuclear ribonucleoprote	Q14103	HNRNPD	10.1074/mcp.M111.008128, 10.1074	2	Mass Spec	ascending		37.5	B	valve replacement	
Heterogeneous nuclear ribonucleoprote	P55795	HNRNPH2	10.1074/mcp.M110.001693		Mass Spec	ascending				valve replacement	
Heterogeneous nuclear ribonucleoprote	P61978	HNRNPK	10.1002/prca.201200064		Mass Spec						
Heterogeneous nuclear ribonucleoprote	P52272	HNRNPM	10.1074/mcp.M111.008128, 10.1074	2	Mass Spec	ascending		37.5	B	valve replacement	
Heterogeneous nuclear ribonucleoprote	O43390	HNRNPR	10.1074/mcp.M111.008128, 10.1074	2	Mass Spec	ascending		37.5	B	valve replacement	
Heterogeneous nuclear ribonucleoprote	Q00839	HNRNPU	10.1074/mcp.M111.008128, 10.1074	2	Mass Spec	ascending		37.5	B	valve replacement	
Heterogeneous nuclear ribonucleoprote	Q9BUJ2	HNRNPUL1	10.1074/mcp.M111.008128		Mass Spec	ascending		37.5	B	valve replacement	
Heterogeneous nuclear ribonucleoprote	Q1KMD3	HNRNPUL2	10.1074/mcp.M111.008128		Mass Spec	ascending		37.5	B	valve replacement	
Heterogeneous nuclear ribonucleoprote	P22626	HNRNPA2B1	10.1074/mcp.M111.008128, 10.1002	3	Mass Spec	ascending		37.5	B	valve replacement	
Heterogeneous nuclear ribonucleoprote	P07910	HNRNPC	10.1074/mcp.M111.008128, 10.1074	2	Mass Spec	ascending		37.5	B	valve replacement	
High mobility group protein B1	P09429	HMGB1	10.1074/mcp.M111.008128, 10.1074	2	Mass Spec	ascending		37.5	B	valve replacement	
Histidine-rich glycoprotein	P04196	HRG	10.1002/prca.201200064		Mass Spec						
Histone deacetylase 1	Q13547	HDAC1	10.1242/dmm.024513	1	Immuno	abdominal		58	B	autopsy CV healthy	augmented in aneurysm
Histone deacetylase 2	Q92769	HDAC2	10.1242/dmm.024513	1	Immuno	abdominal		58	B	autopsy CV healthy	augmented in abdominal aneurysm
Histone deacetylase 4	P56524	HDAC4	10.1242/dmm.024513	1	Immuno	abdominal		58	B	autopsy CV healthy	augmented in aneurysm
Histone deacetylase 7	Q8WUI4	HDAC7	10.1242/dmm.024513	1	Immuno	abdominal		58	B	autopsy CV healthy	augmented in aneurysm
Histone deacetylase 9	Q9UKV0	HDAC9	10.1161/STROKEAHA.111.000217		Immuno		intima;media				
Histone H1.2	P16403	HIST1H1C	10.1074/mcp.M111.008128, 10.1074	2	Mass Spec	ascending		37.5	B	valve replacement	
Histone H1.4	P10412	HIST1H1E	10.1074/mcp.M111.008128, 10.1074	2	Mass Spec	ascending		37.5	B	valve replacement	
Histone H1.5	P16401	HIST1H1B	10.1074/mcp.M111.008128, 10.1074	2	Mass Spec	ascending		37.5	B	valve replacement	
Histone H2A type 1-B/E	P04908	T1H2AB, HIST1H	10.1002/prca.201200064		Mass Spec						
Histone H2A type 1-D	P20671	HIST1H2AD	10.1074/mcp.M111.008128		Mass Spec	ascending		37.5	B	valve replacement	
Histone H2A type 2-A	Q6FI13	HIST2H2AA3	10.1074/mcp.M110.001693		Mass Spec	ascending				valve replacement	
Histone H2A type 2-C	Q16777	HIST2H2AC	10.1002/prca.201200064		Mass Spec						
Histone H2A.Z	P0C0S5	H2AFZ	10.1002/prca.201200064		Mass Spec						
Histone H2B type 1-B	P33778	HIST1H2BB	10.1074/mcp.M111.008128, 10.1074	2	Mass Spec	ascending		37.5	B	valve replacement	
Histone H2B type 1-C/E/F/G/I	P62807	HIST1H2BC	10.1074/mcp.M111.008128, 10.1074	2	Mass Spec	ascending		37.5	B	valve replacement	
Histone H2B type 1-K	O60814	HIST1H2BK	10.1002/prca.201200064		Mass Spec						
Histone H3.1	P68431	HIST1H3A	10.1074/mcp.M111.008128		Mass Spec	ascending		37.5	B	valve replacement	
Histone H3.3	P84243	H3F3A, H3F3B	10.1242/dmm.024513, 10.1002/prca	2	Immuno;Mass Sp	abdominal	media	58	B	autopsy CV healthy	decreased in aneurysm
Histone H4	P62805	HIST1H4A	10.1074/mcp.M111.008128, 10.1002	3	Mass Spec	ascending		37.5	B	valve replacement	
Homeobox protein MSX-2	P35548	MSX2	10.1093/ndt/gfp137		Immuno		intima;media	68	B		augmented in calcified aorta
Hsc70-interacting protein	P50502	ST13	10.1074/mcp.M111.008128, 10.1074	2	Mass Spec	ascending		37.5	B	valve replacement	
Hyaluronan and proteoglycan link protei	P10915	HAPLN1	10.1074/mcp.M111.008128, 10.1002	3	Mass Spec	ascending		37.5	B	valve replacement	
Hypoxia-inducible factor 1-alpha	Q16665	HIF1A	10.1159/000318806		Immuno		media				increased in abdominal aneurysm
Ig alpha-1 chain C region	P01876	IGHA1	10.1074/mcp.M111.008128, 10.1002	3	Mass Spec	ascending		37.5	B	valve replacement	
Ig gamma-1 chain C region	P01857	IGHG1	10.1074/mcp.M111.008128, 10.1002	3	Mass Spec	ascending		37.5	B	valve replacement	
Ig gamma-2 chain C region	P01859	IGHG2	10.1074/mcp.M111.008128, 10.1074	3	Mass Spec	ascending		37.5	B	valve replacement	
Ig gamma-3 chain C region	P01860	IGHG3	10.1074/mcp.M111.008128, 10.1074	3	Mass Spec	ascending		37.5	B	valve replacement	
Ig heavy chain V-I region 5	P01602	IGKV1-5	10.1002/prca.201200064		Mass Spec						
Ig heavy chain V-III region BRO	P01766		10.1074/mcp.M111.008128, 10.1074	2	Mass Spec	ascending		37.5	B	valve replacement	
Ig heavy chain V-III region CAM	P01768		10.1002/prca.201200064		Mass Spec						
Ig kappa chain C region	P01834	IGKC	10.1074/mcp.M111.008128, 10.1074	3	Mass Spec	ascending		37.5	B	valve replacement	
Ig kappa chain V-III region SIE	P01620		10.1002/prca.201200064		Mass Spec						
Ig kappa chain V-III region WOL	P01623		10.1074/mcp.M111.008128, 10.1074	2	Mass Spec	ascending		37.5	B	valve replacement	
Ig lambda-1 chain C regions	P0CG04	IGLC1	10.1074/mcp.M111.008128, 10.1074	2	Mass Spec	ascending		37.5	B	valve replacement	
Ig lambda-2 chain C regions	P0DOY2	IGLC2	10.1002/prca.201200064		Mass Spec						
Ig mu chain C region	P01871	IGHM	10.1074/mcp.M111.008128, 10.1074/mcp.M1		Mass Spec	ascending		37.5	B	valve replacement	
Immunoglobulin superfamily containing	O14498	ISLR	10.1074/mcp.M110.001693	1	Mass Spec	ascending				valve replacement	
Inactive carboxypeptidase-like protein X	Q8N436	CPXM2	10.1074/mcp.M110.001693, 10.1074	2	Mass Spec	ascending		37.5	B	valve replacement	
Inosine-5'-monophosphate dehydrogena	P12268	IMPDH2	10.1074/mcp.M110.001693		Mass Spec	ascending				valve replacement	
Inositol monophosphatase 1	P29218	IMPA1	10.1074/mcp.M111.008128, 10.1074	2	Mass Spec	ascending		37.5	B	valve replacement	
Insulin-like growth factor-binding protein 1	P08833	IGFBP1	10.1159/000362997, 10.1093/cvr/cvu196	2	Immuno	abdominal, ascending	adventitia;media	51	B		augmented in aneurysm in media and diminished in adventitia
Insulin-like growth factor-binding protei	P18065	IGFBP2	10.1093/cvr/cvu196		Immuno	ascending	adventitia	51	B		decreased in aneurysm
Insulin-like growth factor-binding protein 3	P17936	IGFBP3	10.1093/cvr/cvu196		Immuno	ascending	adventitia;media	51	B		aneurysm, not sure if control aorta has it because suppl info is not available online

Insulin-like growth factor-binding protein 7	Q16270	IGFBP7	10.1002/prca.201200064, 10.1074/mcp.M110.001693, 10.1074/mcp.M111.008128	3	Mass Spec	ascending		37.5	B	valve replacement	augmented in abdominal aneurysm
Integrin alpha-1	P56199	ITGA1	10.1002/prca.201200064		Mass Spec						
Integrin alpha-5	P08648	ITGA5	10.1074/mcp.M110.001693		Mass Spec	ascending				valve replacement	
Integrin alpha-7	Q13683	ITGA7	10.1074/mcp.M111.008128, 10.1074	2	Mass Spec	ascending		37.5	B	valve replacement	
Integrin alpha-8	P53708	ITGA8	10.1074/mcp.M111.008128, 10.1002	3	Mass Spec	ascending		37.5	B	valve replacement	
Integrin alpha-lib	P08514	ITGA2B	10.1002/prca.201200064		Mass Spec						
Integrin alpha-M	P11215	ITGAM	10.1155/2015/456582		Immuno		adventitia;media	71.42	B		augmented in abdominal aneurysm
Integrin alpha-V	P06756	ITGAV	10.1074/mcp.M111.008128, 10.1074	2	Mass Spec	ascending		37.5	B	valve replacement	
Integrin beta-1	P05556	ITGB1	10.1074/mcp.M111.008128, 10.1002	3	Mass Spec	ascending		37.5	B	valve replacement	
Integrin beta-3	P05106	ITGB3	10.1002/prca.201200064		Mass Spec						
Integrin-linked protein kinase	Q13418	ILK	10.1074/mcp.M111.008128, 10.1002	3	Mass Spec	ascending		37.5	B	valve replacement	
Inter-alpha-trypsin inhibitor heavy chain	P19827	ITIH1	10.1074/mcp.M111.008128, 10.1074	2	Mass Spec	ascending		37.5	B	valve replacement	
Inter-alpha-trypsin inhibitor heavy chain	P19823	ITIH2	10.1074/mcp.M111.008128, 10.1074	2	Mass Spec	ascending		37.5	B	valve replacement	
Inter-alpha-trypsin inhibitor heavy chain	Q14624	ITIH4	10.1074/mcp.M111.008128, 10.1074	2	Mass Spec	ascending		37.5	B	valve replacement	
Inter-alpha-trypsin inhibitor heavy chain	Q86UX2	ITIH5	10.1074/mcp.M111.008128, 10.1074	2	Mass Spec	ascending		37.5	B	valve replacement	
Intercellular adhesion molecule 1	P05362	ICAM1	10.1159/000362997		Immuno	abdominal		68.9			augmented in aneurysm
Interferon gamma	P01579	IFNG	10.1161/CIRCULATIONAHA.111.0834	2	Immuno	abdominal, ascend	intima;media	54.6	B		increased in aneurysm
Interferon regulatory factor 7	Q92985	IRF7	10.1074/mcp.M111.008128, 10.1074	2	Mass Spec	ascending		37.5	B	valve replacement	
Interferon-inducible protein AIM2	O14862	AIM2	10.1016/j.jvs.2013.03.048		Immuno		adventitia;intima; media	45	M		10.2119/molmed.2013.00162 says there's only AIM2 at adventitial single infiltrating cells at healthy aorta
Interleukin enhancer-binding factor 2	Q12905	ILF2	10.1074/mcp.M111.008128, 10.1074	2	Mass Spec	ascending		37.5	B	valve replacement	
Interleukin enhancer-binding factor 3	Q12906	ILF3	10.1074/mcp.M111.008128, 10.1074	2	Mass Spec	ascending		37.5	B	valve replacement	
Interleukin-1 beta	P01584	IL1B	10.1007/s00268-002-6690-0, 10.101	4	Immuno	infra-renal, ascend	media	54.6	B	unknown	increased in aneurysm and dissection
Interleukin-17A	Q16552	IL17A	10.1161/CIRCULATIONAHA.111.0834	1	Immuno	abdominal					increased in abdominal aneurysm
Interleukin-2	P60568	IL2	10.1016/j.jvs.2006.11.020		Immuno	abdominal		55	B		
Interleukin-23 subunit alpha	Q9NPF7	IL23A	10.1161/CIRCULATIONAHA.111.083451		Immuno	ascending					augmented in abdominal aneurysm
Interleukin-6	P05231	IL6	10.1007/s10353-007-0339-z, 10.1016/j.jvs.2006.11.020, 10.1016/j.athoracsur.2015.05.009	3	Immuno	infra-renal, abdominal, thoracic		59.5, 55	B		augmented in aneurysm, 10.1159/000362997 says there's no IL6 in normal aorta
Interleukin-8	P10145	CXCL8	10.1161/CIRCULATIONAHA.111.0834	4	Immuno	ascending, infra-re	adventitia	51, 59.9, 5	B		augmented in aneurysm
Interstitial collagenase	P03956	MMP1	10.14670/HH-11-691, 10.1089/ars.2005.7.1195	2	Immuno	ascending, abdominal	media	61.6	B		augmented in aneurysm, 10.1053/hupa.2001.27107 says thare's no MMP1 in control ascending aortae
Isocitrate dehydrogenase [NADP] cytopl	O75874	IDH1	10.1074/mcp.M111.008128, 10.1074	2	Mass Spec	ascending		37.5	B	valve replacement	
Isocitrate dehydrogenase [NADP], mitoc	P48735	IDH2	10.1002/prca.201200064		Mass Spec						
Junctophilin-2	Q9BR39	JPH2	10.1074/mcp.M111.008128, 10.1074	2	Mass Spec	ascending		37.5	B	valve replacement	
Kallistatin	P29622	SERPINA4	10.1074/mcp.M111.008128, 10.1074/mcp.M110.001693	2	Mass Spec	ascending		37.5	B	valve replacement	10.1074/mcp.M111.008128 says there's no kallistatin in control ascending aorta
Keratin, type I cytoskeletal 10	P13645	KRT10	10.1074/mcp.M111.008128, 10.1002	3	Mass Spec	ascending		37.5	B	valve replacement	
Keratin, type I cytoskeletal 14	P02533	KRT14	10.1074/mcp.M111.008128, 10.1074	2	Mass Spec	ascending		37.5	B	valve replacement	
Keratin, type I cytoskeletal 16	P08779	KRT16	10.1074/mcp.M111.008128, 10.1074	2	Mass Spec	ascending		37.5	B	valve replacement	
Keratin, type I cytoskeletal 27	KRT27	Q7Z3Y8	10.1074/mcp.M111.008128		Mass Spec	ascending		37.5	B	valve replacement	
Keratin, type I cytoskeletal 9	P35527	KRT9	10.1074/mcp.M111.008128, 10.1002	3	Mass Spec	ascending		37.5	B	valve replacement	
Keratin, type II cytoskeletal 1	P04264	KRT1	10.1074/mcp.M111.008128, 10.1002	3	Mass Spec	ascending		37.5	B	valve replacement	
Keratin, type II cytoskeletal 2 epidermal	P35908	KRT2	10.1074/mcp.M111.008128, 10.1002	3	Mass Spec	ascending		37.5	B	valve replacement	
Keratin, type II cytoskeletal 5	P13647	KRT5	10.1074/mcp.M110.001693		Mass Spec	ascending				valve replacement	
Keratin, type II cytoskeletal 6C	P48668	KRT6C	10.1074/mcp.M111.008128		Mass Spec	ascending		37.5	B	valve replacement	
Kinectin	Q86UP2	KTN1	10.1074/mcp.M111.008128, 10.1074	2	Mass Spec	ascending		37.5	B	valve replacement	
Kinesin heavy chain isoform 5A	Q12840	KIF5A	10.1074/mcp.M110.001693		Mass Spec	ascending				valve replacement	
Kit ligand	P21583	KITLG	10.1016/j.jvs.2009.03.055		Immuno	infrarenal	intima	46.6	B		neovessels in aneurysm
KN motif and ankyrin repeat domain-cor	Q63ZY3	KANK2	10.1074/mcp.M111.008128, 10.1074	2	Mass Spec	ascending		37.5	B	valve replacement	
Lactadherin	Q08431	MFGE8	10.1161/CIRCRESAHA.108.187088, 1	6	Immuno;Mass Sp	descending, thorac	intima;media	19, 68, 60	B	autopsy CV healthy;valve replacement	augmented in aneurysm, aging, and dissection
Lactotransferrin	P02788	LTF	10.1074/mcp.M111.008128, 10.1002	3	Mass Spec	ascending		37.5	B	valve replacement	
Lactoylglutathione lyase	Q04760	GLO1	10.1002/prca.201200064		Mass Spec						
Lamina-associated polypeptide 2, isofor	P42166	TMPO	10.1074/mcp.M111.008128, 10.1074	2	Mass Spec	ascending		37.5	B	valve replacement	
Lamin-B2	Q03252	LMNB2	10.1074/mcp.M111.008128, 10.1074	2	Mass Spec	ascending		37.5	B	valve replacement	
Laminin subunit alpha-2	P24043	LAMA2	16377578		Immuno			33			decreased in ascending aneurysm
Laminin subunit alpha-3	Q16787	LAMA3	10.1074/mcp.M111.008128, 10.1074	2	Mass Spec	ascending			B	valve replacement	
Laminin subunit alpha-4	Q16363	LAMA4	10.1074/mcp.M110.001693		Mass Spec	ascending				valve replacement	not detected in abdominal aneurysm
Laminin subunit alpha-5	O15230	LAMA5	10.1002/prca.201200064, 10.1074/n	3	Mass Spec	ascending		37.5	B	valve replacement	decreased in abdominal aneurysm
Laminin subunit beta-1	P07942	LAMB1	16377578		Immuno			33			10.1074/mcp.M111.008128 says there's no laminin beta 1 in control ascending aorta
Laminin subunit beta-2	P55268	LAMB2	10.1074/mcp.M111.008128, 163775	4	Immuno;Mass Sp	ascending		37.5,33	B	valve replacement	
Laminin subunit gamma-1	P11047	LAMC1	10.1074/mcp.M111.008128, 10.1155	4	Immuno;Mass Sp	thoracic, ascending		37.5,59	B	valve replacement	augmented in Marfan
Latent-transforming growth factor beta-binding protein 1	Q14766	LTBP1	10.4261/1305-3825.DIR.3844-10.1, 1	4	Immuno;Mass Sp	ascending	intima;media			valve replacement	augmented in aneurysm
Latent-transforming growth factor beta-	Q14767	LTBP2	10.1002/prca.201200064, 10.1074/n	3	Mass Spec	ascending		37.5	B	valve replacement	
Latent-transforming growth factor beta-binding protein 4	Q8N2S1	LTBP4	10.1002/prca.201200064, 10.1074/n	3	Mass Spec	ascending		37.5	B	valve replacement	not detected in abdominal aneurysm
Left-right determination factor 1	O75610	LEFTY1	10.1074/mcp.M111.008128, 10.1074	2	Mass Spec	ascending		37.5	B	valve replacement	
Leiomodin-1	P29536	LMOD1	10.1074/mcp.M111.008128, 10.1074	3	Mass Spec	ascending		37.5	B	valve replacement	
Leptin	P41159	LEP	20145358	1	Immuno	abdominal	periaortic adipose tissue			autopsy CV healthy	augmented in atherosclerosis
Leptin receptor	P48357	LEPR	10.3349/ymj.2000.41.1.68	1	Immuno		intima	28			augmented in atherosclerosis
Leucine-rich alpha-2-glycoprotein	P02750	LRG1	10.1074/mcp.M111.008128, 10.1074	2	Mass Spec	ascending		37.5	B	valve replacement	
Leukocyte elastase inhibitor	P30740	SERPINB1	10.1074/mcp.M110.001693, 10.1074	2	Mass Spec	ascending		37.5	B	valve replacement	
LIM and cysteine-rich domains protein 1	Q9NZU5	LMCD1	10.1074/mcp.M111.008128, 10.1074	3	Mass Spec	ascending		37.5	B	valve replacement	
LIM and senescent cell antigen-like-cont	P48059	LIMS1	10.1074/mcp.M111.008128, 10.1002	2	Mass Spec			37.5	B	valve replacement	
LIM and senescent cell antigen-like-cont	Q7Z4I7	LIMS2	10.1074/mcp.M110.001693		Mass Spec	ascending				valve replacement	
LIM and SH3 domain protein 1	Q14847	LASP1	10.1074/mcp.M111.008128, 10.1074	3	Mass Spec	ascending		37.5	B	valve replacement	
LIM domain-binding protein 3	O75112	LDB3	10.1074/mcp.M111.008128, 10.1074	2	Mass Spec	ascending		37.5	B	valve replacement	
Lipoma-preferred partner	Q93052	LPP	10.1074/mcp.M111.008128, 10.1074	3	Mass Spec	ascending		37.5	B	valve replacement	
Lipopolysaccharide-binding protein	P18428	LBP	10.1002/prca.201200064		Mass Spec						
Liver carboxylesterase 1	P23141	CES1	10.1074/mcp.M111.008128, 10.1074	2	Mass Spec	ascending		37.5	B	valve replacement	
L-lactate dehydrogenase A chain	P00338	LDHA	10.1074/mcp.M112.021873, 10.1074	4	Immuno;Mass Sp	ascending		37.5	B	valve replacement	augmented in aneurysm
L-lactate dehydrogenase B chain	P07195	LDHB	10.1074/mcp.M111.008128, 10.1002	3	Mass Spec	ascending		37.5	B	valve replacement	
Low affinity immunoglobulin gamma Fc	P31994	FCGR2B	10.1159/000362997		Immuno	abdominal		68.9			augmented in aneurysm
Low molecular weight phosphotyrosine	P24666	ACP1	10.1074/mcp.M111.008128, 10.1074	2	Mass Spec	ascending		37.5	B	valve replacement	
Lumican	P51884	LUM	10.1097/HJH.0b013e3282f4b3d0, 10	4	Immuno;Mass Sp	ascending	media	59, 37.5	M, B	valve replacement	
Lymphotoxin-alpha	P01374	LTA	10.1016/j.jvs.2006.11.020		Immuno	abdominal		55	B		augmented in aneurysm
Lysozyme C	P61626	LYZ	10.1074/mcp.M111.008128, 10.1002	3	Mass Spec	ascending				valve replacement	
Lysyl oxidase homolog 1	Q08397	LOXL1	10.1074/mcp.M111.008128, 10.1074	2	Mass Spec	ascending				valve replacement	
Macrophage colony-stimulating factor 1	P09603	CSF1	10.1016/j.jvs.2006.11.020		Immuno	abdominal		55	B		augmented in aneurysm
Macrophage migration inhibitory factor	P14174	MIF	10.1089/ars.2005.7.1195, 10.1002/prca.2012		Immuno;Mass Sp	abdominal	media				aneurysm

Macrophage-capping protein	P40121	CAPG	10.1074/mcp.M111.008128, 10.1074	2	Mass Spec	ascending		37.5	B	valve replacement	
Macrosialin	P34810	CD68	10.1016/j.atherosclerosis.2009.01.038, 10.1093/ndt/gfp137, 10.1161/CIRCRESAHA.108.173682, 10.1016/j.atherosclerosis.2011.06.008, 10.1093/cvr/cvr080, 10.1161/ATVBAHA.115.305529	6	Immuno	abdominal	intima;media	10, 68, 44, 64	B		increased in abdominal aneurysm, or not, increased in CDK calcified intima, 10.2119/molmed.2013.00162 says there's no CD68 in healthy aorta
Major vault protein	Q14764	MVP	10.1074/mcp.M111.008128, 10.1074	2	Mass Spec	ascending				valve replacement	
Malate dehydrogenase, cytoplasmic	P40925	MDH1	10.1074/mcp.M111.008128, 10.1074	2	Mass Spec	ascending		37.5	B	valve replacement	
Malate dehydrogenase, mitochondrial	P40926	MDH2	10.1074/mcp.M111.008128, 10.1002	3	Mass Spec	ascending		37.5	B	valve replacement	
Mast cell carboxypeptidase A	P15088	CPA3	10.1074/mcp.M110.001693		Mass Spec	ascending				valve replacement	
Mast/stem cell growth factor receptor Kit	P10721	KIT	10.1161/CIRCRESAHA.108.173682		Immuno	thoracic descending		44	B		more phosphorilated in abdominal aneurysm
Matrilin-2	O00339	MATN2	10.1074/mcp.M110.001693		Mass Spec	ascending				valve replacement	
Matrilysin	P09237	MMP7	10.1093/cvr/cvu196, 10.1016/j.humpath.200		Immuno	ascending		51, 50.4	B		augmented in aneurysm
Matrix Gla protein	P08493	MGP	10.1074/mcp.M111.008128, 10.1093/ndt/gfp137, 10.1161/hq1201.100229, 10.1074/mcp.M110.001693	4	Immuno;Mass Sp	abdominal, ascending	adventitia;intima; media	37.5,68	B	valve replacement	augmented in calcified aorta, prominent expression in foam cells in the lipid core of atheroma
Matrix metalloproteinase-14	P50281	MMP14	10.1067/mva.2001.115962, 10.1067/mva.2002.121124		Immuno	infrarenal, ascending		68.9	B	CABG	higher active form in abdominal aneurysm
Matrix metalloproteinase-19	Q99542	MMP19	10.1093/cvr/cvu196		Immuno	ascending		51	B		augmented in aneurysm
Matrix metalloproteinase-9	P14780	MMP9	10.14670/HH-11-691, 10.1016/j.jctvs.2006.07.036, 10.1161/hs1101.098520, 10.1053/hupa.2001.27107, 10.1371/journal.pone.0070057, 10.1016/j.atherosclerosis.2004.11.021, 10.1161/HYPERTENSIONAHA.107.089409, 10.1093/cvr/cvu196, 10.1016/j.jvs.2010.11.035	9	Immuno	abdominal, thoracic, descending, ascending	adventitia;intima; media	61.6, 61.4, 7.9, 0, 42.5, 71.5, 44.6, 25, 20, 51, 46.1	B, M	autopsy CV healthy	less active in aneurysm, augmented in thoracic aneurysm or not, in dissection, in aging, and in atheromatous plaque, 10.1016/j.jtcvs.2012.04.008 says there's no mmp9 in control ascending, 10731924 says MMP9 is at minimal thickened intima of controls
Membrane primary amine oxidase	Q16853	AOC3	10.1074/mcp.M111.008128, 10.1074/mcp.M110.001693, 10.1002/prca.201200064	3	Mass Spec	ascending		37.5	B	valve replacement	AOC exists in aorta but it's reported by radiometry at 10.1006/taap.2001.9238
Metal transporter CNNM4	Q6P4Q7	CNNM4	10.1074/mcp.M111.008128, 10.1074	2	Mass Spec	ascending		37.5	B	valve replacement	
Metalloproteinase inhibitor 1	P01033	TIMP1	10.1016/j.jvs.2012.09.062, 10.1016/j.jctvs.2006.07.036, 10.1016/j.jtcvs.2012.04.008, 10.2353/ajpath.2007.060522, 10.1093/cvr/cvu196, 10.1067/mva.2002.121124, 10.1074/mcp.M111.008128	7	Immuno;Mass Spec	abdominal, ascending	adventitia;media	48, 64.1, 69, 51, 68.9, 37.5	B	CABG;other	decreased or augmented or the same in aneurysm, 10.1053/hupa.2001.27107 says thare's no TIMP1 in control ascending aortae
Metalloproteinase inhibitor 2	P16035	TIMP2	10.1016/j.jvs.2012.09.062, 10.1053/hupa.2001.27107, 10.1016/j.amjhyper.2004.11.011, 10.1016/j.atherosclerosis.2004.11.021, 10.1067/mva.2002.121124	5	Immuno	abdominal, ascend	intima;media	71.5, 60.9	B	CABG;other	decreased in aneurysm, augmented in atheromatous plaque, aneurysm and dissection, 10731924 says TIMP2 is at minimal thickened intima of controls
Metalloproteinase inhibitor 3	P35625	TIMP3	10.1074/mcp.M110.001693, 10.1067	3	Immuno;Mass Sp	ascending		68.9, 37.5	B	CABG;valve replacement	augmented in aneurysm
Metalloproteinase inhibitor 4	Q99727	TIMP4	10.1093/cvr/cvu196		Immuno	ascending	adventitia;media	51	B		decreased in aneurysm
Methyl-CpG-binding protein 2	P51608	MECP2	10.1074/mcp.M111.008128, 10.1074	2	Mass Spec	ascending		37.5	B	valve replacement	
MICOS complex subunit MIC60	Q16891	IMMT	10.1074/mcp.M111.008128, 10.1074	2	Mass Spec	ascending		37.5	B	valve replacement	
Microfibril-associated glycoprotein 4	P55083	MFAP4	10.1074/mcp.M112.021873, 10.1016	5	Mass Spec	abdominal, ascending		53.91, 37.5	B	valve replacement	decreased in abdominal and ascending aneurysm
Microfibrillar-associated protein 5	Q13361	MFAP5	10.1074/mcp.M111.008128		Mass Spec	ascending		37.5	B	valve replacement	
Microsomal glutathione S-transferase 3	O14880	MGST3	10.1002/prca.201200064		Mass Spec						
Microtubule-associated protein 1B	P46821	MAP1B	10.1074/mcp.M111.008128, 10.1002	3	Mass Spec	ascending		37.5	B	valve replacement	
Microtubule-associated protein 4	P27816	MAP4	10.1074/mcp.M111.008128, 10.1074	2	Mass Spec	ascending		37.5	B	valve replacement	
Mimecan	P20774	OGN	10.1074/mcp.M112.021873, 10.1002/prca.201200064, 10.1074/mcp.M110.001693, 10.1074/mcp.M111.008128	4	Mass Spec	ascending		37.5	B	valve replacement	decreased in abdominal aneurysm, and in ascending TAV and BAV dilation
Mitogen-activated protein kinase 1	P28482	MAPK1	10.1016/j.jamcollsurg.2012.06.414, 10.1093/abbs/gmv047, 10.1007/s10735-013-9558-8, 10.1111/eci.12618	4	Immuno	ascending, abdominal	adventitia;media	47.3, 61	B		augmented in dissection (p-erk), idiopathic ascending aneurysm (p-erk) and nonruptured aneurysm
Mitogen-activated protein kinase 14	Q16539	MAPK14	10.1016/j.jvs.2010.11.113, 10.1093/abbs/gmv047	2	Immuno	ascending		47.4	M	autopsy CV healthy	augmented in dissection and idiopathic ascending aortic aneurysm
Mitogen-activated protein kinase 3	P27361	MAPK3	10.1093/abbs/gmv047, 10.1007/s10735-013-9558-8, 10.1111/eci.12618	3	Immuno	ascending, abdominal		47.3, 61	B		augmented in dissection (p-erk), idiopathic ascending aneurysm (p-erk) and nonruptured aneurysm
Mitogen-activated protein kinase 8	P45983	MAPK8	10.1093/abbs/gmv047	1	Immuno	ascending				autopsy CV healthy	more phosphorilated in idiopathic ascending aortic aneurysm
Mitogen-activated protein kinase 9	P45984	MAPK9	10.1093/abbs/gmv047	1	Immuno	ascending				autopsy CV healthy	more phosphorilated in idiopathic ascending aortic aneurysm
Moesin	P26038	MSN	10.1074/mcp.M111.008128, 10.1093	5	Immuno;Mass Sp	ascending		37.5,59	B,M	valve replacement	
MORC family CW-type zinc finger protei	Q86VD1	MORC1	10.1074/mcp.M111.008128, 10.1074	2	Mass Spec	ascending		37.5	B	valve replacement	
Mothers against decapentaplegic homolog 2	Q15796	SMAD2	10.1016/j.ijcard.2011.08.079, 10.1161/ATVBAHA.114.304412, 10.1024/0301-1526/a000133, 10.4261/1305-3825.DIR.3844-10.1, 10.1093/cvr/cvq291, 10.1002/path.2516, 10.1161/ATVBAHA.113.301327	7	Immuno	thoracic, ascending	intima;media	54	B		more phosphorylated in aneurysm, in non-syndromic dissection and in Marfan aneurysm, augmented in Marfan aorta interstices
Mothers against decapentaplegic homolog 3	P84022	SMAD3	10.1024/0301-1526/a000133, 10.1093/cvr/cvq291	2	Immuno	ascending					augmented in Marfan aorta interstices
Mothers against decapentaplegic homolog 4	Q13485	SMAD4	10.1024/0301-1526/a000133, 10.1093/cvr/cvq291	2	Immuno	ascending					augmented in Marfan syndrome
Mothers against decapentaplegic homolog 7	O15105	SMAD7	10.1024/0301-1526/a000133, 10.1093/cvr/cvq291	2	Immuno	ascending					augmented in Marfan aorta nuclei
Mucin-16	Q8WXI7	MUC16	10.1074/mcp.M111.008128, 10.1074	2	Mass Spec	ascending		37.5	B	valve replacement	
Multidrug resistance-associated protein	O15439	ABCC4	10.1074/mcp.M111.008128, 10.1074	2	Mass Spec	ascending		37.5	B	valve replacement	
Myeloblastin	P24158	PRTN3	10.1002/prca.201200064, 10.1074/m	2	Mass Spec	ascending				valve replacement	
Myeloperoxidase	P05164	MPO	10.1093/ndt/gfp137, 10.1002/prca.2	4	Immuno;Mass Sp	ascending	intima;media	68, 37.5	B	valve replacement	augmented in abdominal aneurysm
Myosin light chain kinase, smooth muscl	Q15746	MYLK	10.1074/mcp.M111.008128, 10.1074	3	Mass Spec	ascending		37.5	B	valve replacement	
Myosin light polypeptide 6	P60660	MYL6	10.1074/mcp.M112.021873, 10.1074	4	Mass Spec	ascending		37.5	B	valve replacement	augmented in TAV and BAV asc dilation
Myosin regulatory light chain 12B	O14950	MYL12B	10.1074/mcp.M112.021873, 10.1074	4	Mass Spec	ascending		37.5	B	valve replacement	augmented in BAV dilation
Myosin regulatory light polypeptide 9	P24844	MYL9	10.1074/mcp.M112.021873, 10.1074	4	Mass Spec	ascending		37.5	B	valve replacement	augmented in BAV asc dilation

Myosin-10	P35580	MYH10	10.1074/mcp.M111.008128, 10.1002	3	Mass Spec	ascending		37.5	B	valve replacement	
Myosin-11	P35749	MYH11	10.1074/mcp.M111.008128, 10.1038	5	Immuno;Mass Sp	ascending	media	37.5	B	valve replacement	increased in aneurysm
Myosin-4	Q9Y623	MYH4	10.1002/path.2516		Immuno	thoracic					
Myosin-7B	A7E2Y1	MYH7B	10.1074/mcp.M111.008128, 10.1074	2	Mass Spec	ascending		37.5	B	valve replacement	
Myosin-9	P35579	MYH9	10.1074/mcp.M111.008128, 10.1002	3	Mass Spec	ascending		37.5	B	valve replacement	
Myosin-IIIb	Q8WXR4	MYO3B	10.1002/prca.201200064		Mass Spec						
N(G),N(G)-dimethylarginine dimethylam	O95865	DDAH2	10.1074/mcp.M111.008128, 10.1074	2	Mass Spec	ascending		37.5	B	valve replacement	
NAD(P)H dehydrogenase [quinone] 1	P15559	NQO1	10.1016/S0891-5849(00)00310-5		Immuno						
NADH dehydrogenase [ubiquinone] 1 alp	O95182	NDUFA7	10.1074/mcp.M111.008128, 10.1074	2	Mass Spec	ascending		37.5	B	valve replacement	
NADH-cytochrome b5 reductase 3	P00387	CYB5R3	10.1074/mcp.M111.008128, 10.1002	3	Mass Spec	ascending		37.5	B	valve replacement	
NADH-ubiquinone oxidoreductase 75 kD	P28331	NDUFS1	10.1074/mcp.M111.008128, 10.1074	2	Mass Spec	ascending		37.5	B	valve replacement	
Nascent polypeptide-associated comple	Q13765	NACA	10.1074/mcp.M111.008128, 10.1074	2	Mass Spec	ascending		37.5	B	valve replacement	
Nck-associated protein 5-like	Q9HCH0	NCKAP5L	10.1074/mcp.M111.008128, 10.1074/mcp.M1		Mass Spec	ascending		37.5	B	valve replacement	
Nesprin-1	Q8NF91	SYNE1	10.1074/mcp.M111.008128, 10.1074	2	Mass Spec	ascending		37.5	B	valve replacement	
Nesprin-2	Q8WXH0	SYNE2	10.1074/mcp.M111.008128, 10.1074	2	Mass Spec	ascending		37.5	B	valve replacement	
Nestin	P48681	NES	10.1074/mcp.M110.001693		Mass Spec	ascending				valve replacement	
Neuroblast differentiation-associated pr	Q09666	AHNAK	10.1074/mcp.M111.008128, 10.1002	3	Mass Spec	ascending		37.5	B	valve replacement	
Neuropilin-1	O14786	NRP1	10.1093/ejcts/ezu118	1	Immuno	ascending	adventitia;intima;	54	B	CABG	
Neutrophil collagenase	P22894	MMP8	10.2353/ajpath.2007.060522, 10.1159/000362997, 10.1016/j.jss.2010.05.030	3	Immuno	abdominal		48, 68.9, 57.4	B		augmented in abdominal aneurysm (pro- and active protease)
Neutrophil defensin 1	P59665	DEFA1 , DEFA1B	10.1074/mcp.M111.008128, 10.1074	3	Mass Spec	ascending		37.5	B	valve replacement	augmented in abdominal aneurysm
Neutrophil elastase	P08246	ELANE	10.1002/prca.201200064		Mass Spec						
Nexilin	Q0ZGT2	NEXN	10.1074/mcp.M111.008128, 10.1074	2	Mass Spec	ascending		37.5	B	valve replacement	
Nicotinamide phosphoribosyltransferase	P43490	NAMPT	20145358	1	Immuno	abdominal	periaortic adipose tissue			autopsy CV healthy	augmented in atherosclerosis
Nidogen-1	P14543	NID1	10.1002/prca.201200064, 10.1074/n	3	Mass Spec	ascending		37.5	B	valve replacement	
Nidogen-2	Q14112	NID2	10.1074/mcp.M111.008128, 10.1074	2	Mass Spec	ascending		37.5	B	valve replacement	
Nitric oxide synthase, endothelial	P29474	NOS3	10.1155/2014/760694		Immuno	thoracic		59	B	valve replacement	diminished in aortopathies
Nitric oxide synthase, inducible	P35228	NOS2	10.1155/2014/760694		Immuno	thoracic		59	B	valve replacement	augmented in aortopathies, 10.1016/S0741-5214(03)00148-4 and 10.2353/ajpath.2009.080845 says that control aortas do not have iNOS
Nitrogen permease regulator 2-like prot	Q8WTW4	NPRL2	10.1074/mcp.M110.001693		Mass Spec	ascending				valve replacement	
NLR family CARD domain-containing pro	Q7RTR2	NLRC3	10.1074/mcp.M111.008128		Mass Spec	ascending		37.5	B	valve replacement	
Non-POU domain-containing octamer-bi	Q15233	NONO	10.1111/his.12434		Immuno	ascending	adventitia;media	47.8	B		decreased in disection
NSFL1 cofactor p47	Q9UNZ2	NSFL1C	10.1074/mcp.M111.008128, 10.1074	2	Mass Spec	ascending		37.5	B	valve replacement	
Nuclear receptor subfamily 1 group I me	O75469	NR1I2	10.1093/cvr/cvr330		Immuno		media				
Nucleolin	P19338	NCL	10.1074/mcp.M111.008128, 10.1074	2	Mass Spec	ascending		37.5	B	valve replacement	
Nucleoside diphosphate kinase B	P22392	NME2	10.1074/mcp.M111.008128, 10.1002	3	Mass Spec	ascending		37.5	B	valve replacement	
Nucleosome assembly protein 1-like 4	Q99733	NAP1L4	10.1074/mcp.M111.008128, 10.1074	2	Mass Spec	ascending		37.5	B	valve replacement	
Obscurin	Q5VST9	OBSCN	10.1002/prca.201200064		Mass Spec						
Omega-amidase NIT2	Q9NQR4	NIT2	10.1074/mcp.M111.008128, 10.1074	2	Mass Spec	ascending		37.5	B	valve replacement	
Oncostatin-M	P13725	OSM	10.1016/j.jvs.2006.11.020		Immuno	abdominal		55	B		augmented in aneurysm
Ornithine decarboxylase	P11926	ODC1	10.1097/HJH.0b013e3282f4b3d0		Immuno	ascending	media	59	M		
Osteocalcin	P02818	BGLAP	10.1097/HJH.0b013e3282f4b3d0, 10.1093/ndt/gfp137, 10.1161/hq1201.100229	3	Immuno	ascending, abdominal	adventitia;intima; media	59, 68	M, B		augmented in calcified aorta, prominent expression in foam cells in the lipid core of atheroma
Osteopontin	P10451	SPP1	10.1016/j.ejvs.2014.10.018, 10.1016/j.jtcvs.2012.04.008, 21894406, 10.1053/hupa.2001.27107, 10.1093/ndt/gfp137, 10.1177/1708538112472282	6	Immuno	ascending	intima;media	58,25.4, 71.5, 68, 62.1	B	CABG;unknown	augmented in aneurysm, dissection and calcified aorta, (trustworthy-21894406? diminished in aneurysm, dissection and coronary artery disease)
Palladin	Q8WX93	PALLD	10.1074/mcp.M111.008128, 10.1002	3	Mass Spec	ascending		37.5	B	valve replacement	
Pappalysin-1	Q13219	PAPPA	10.1074/mcp.M111.008128, 10.1074	2	Mass Spec	ascending		37.5	B	valve replacement	
PDZ and LIM domain protein 1	O00151	PDLIM1	10.1074/mcp.M111.008128, 10.1002	3	Mass Spec	ascending		37.5	B	valve replacement	
PDZ and LIM domain protein 3	Q53GG5	PDLIM3	10.1074/mcp.M112.021873, 10.1074	4	Mass Spec	ascending		37.5	B	valve replacement	
PDZ and LIM domain protein 4	P50479	PDLIM4	10.1074/mcp.M111.008128, 10.1074	2	Mass Spec	ascending		37.5	B	valve replacement	
PDZ and LIM domain protein 5	Q96HC4	PDLIM5	10.1074/mcp.M111.008128, 10.1074	2	Mass Spec	ascending		37.5	B	valve replacement	
PDZ and LIM domain protein 7	Q9NR12	PDLIM7	10.1074/mcp.M111.008128, 10.1002	3	Mass Spec	ascending		37.5	B	valve replacement	
Pentraxin-related protein PTX3	P26022	PTX3	10.1093/cvr/cvu196		Immuno	ascending	adventitia;media	51	B		aneurysm: augmented in media and diminished in adventitia
Peptidyl-prolyl cis-trans isomerase A	P62937	PPIA	10.1074/mcp.M111.008128, 10.1002	3	Mass Spec	ascending		37.5	B	valve replacement	
Peptidyl-prolyl cis-trans isomerase B	P23284	PPIB	10.1074/mcp.M111.008128, 10.1074	2	Mass Spec	ascending		37.5	B	valve replacement	
Perilipin-4	Q96Q06	PLIN4	10.1074/mcp.M110.001693	1	Mass Spec	ascending				valve replacement	
Periostin	Q15063	POSTN	10.1002/prca.201200064, 10.1074/n	3	Immuno;Mass Sp	ascending		37.5	B	valve replacement	
Peroxiredoxin-1	Q06830	PRDX1	10.1074/mcp.M111.008128, 10.1002	3	Mass Spec	ascending		37.5	B	valve replacement	
Peroxiredoxin-2	P32119	PRDX2	10.1074/mcp.M111.008128, 10.1002	3	Mass Spec	ascending		37.5	B	valve replacement	
Peroxiredoxin-5, mitochondrial	P30044	PRDX5	10.1074/mcp.M111.008128, 10.1002	3	Mass Spec	ascending		37.5	B	valve replacement	
Peroxiredoxin-6	P30041	PRDX6	10.1074/mcp.M111.008128, 10.1002	3	Mass Spec	ascending		37.5	B	valve replacement	
Persephin	O60542	PSPNPSPN	10.1093/cvr/cvu196		Immuno	ascending	media	51	B		augmented in aneurysm, not sure if control aorta has it because suppl info is not available online
Phosphatase and actin regulator 1	Q9C0D0	PHACTR1	10.1016/j.atherosclerosis.2016.04.025		Immuno		intima				marked expression of PHACTR1 in immune cells in atherosclerosis
Phosphate carrier protein, mitochondria	Q00325	SLC25A3	10.1074/mcp.M111.008128, 10.1074	2	Mass Spec	ascending		37.5	B	valve replacement	
Phosphatidylethanolamine-binding prot	P30086	PEBP1	10.1074/mcp.M111.008128, 10.1002	3	Mass Spec	ascending		37.5	B	valve replacement	
Phosphoglucomutase-1	P36871	PGM1	10.1074/mcp.M111.008128, 10.1074	3	Mass Spec	ascending		37.5	B	valve replacement	
Phosphoglucomutase-like protein 5	Q15124	PGM5	10.1074/mcp.M111.008128, 10.1002	3	Mass Spec	ascending		37.5	B	valve replacement	
Phosphoglycerate kinase 1	P00558	PGK1	10.1074/mcp.M111.008128, 10.1016	4	Mass Spec	ascending		37.7,58	B,M	valve replacement	decreased in aneurysm and increased in dissection
Phosphoglycerate mutase 1	P18669	PGAM1	10.1074/mcp.M111.008128, 10.1016	4	Mass Spec	abdominal, ascending		37.7,53.91	B	valve replacement	
Phospholipase A2, membrane associated	P14555	PLA2G2A	10.1074/mcp.M111.008128, 10.1016	3	Immuno;Mass Sp	ascending	intima;media	37.5	B	valve replacement	augmented in atherosclerosis
Pigment epithelium-derived factor	P36955	SERPINF1	10.1093/cvr/cvu196, 10.1002/prca.2	4	Immuno;Mass Sp	ascending	adventitia;media	51, 37.5	B	valve replacement	augmented in abdominal aneurysm
Pituitary-specific positive transcription factor 1	P28069	POU1F1	10.1093/ndt/gfp137		Immuno		intima;media	68	B		augmented in calcified aorta
Placenta growth factor	P49763	PGF	10.1093/cvr/cvu196		Immuno	ascending	adventitia;media	51	B		aneurysm, not sure if control aorta has it because suppl info is not available online
Plasma protease C1 inhibitor	P05155	SERPING1	10.1074/mcp.M111.008128, 10.111	3	Immuno;Mass Sp	valve, ascending		37.5,60	B,M	valve replacement	increased in aortic valve pathology
Plasminogen	P00747	PLG	10.1074/mcp.M111.008128, 10.1093	4	Immuno;Mass Sp	ascending	media	37.5,51	B	valve replacement	augmented in aneurysm
Plasminogen activator inhibitor 1	P05121	SERPINE1	10.1159/000339304, 10.1093/cvr/cvu196, 10.1161/ATVBAHA.113.301327, 19190555	4	Immuno	ascending, abdomi	adventitia;media	47, 51, 54	B		augmented in aneurysm, decreased in abdominal aneurysm
Plastin-2	P13796	LCP1	10.1002/prca.201200064, 10.1074/mcp.M110		Mass Spec	ascending				valve replacement	
Plastin-3	P13797	PLS3	10.1074/mcp.M111.008128, 10.1002	3	Mass Spec	ascending		37.5	B	valve replacement	
Platelet basic protein	P02775	PPBP	10.1002/prca.201200064		Mass Spec						

Platelet endothelial cell adhesion molecule	P16284	PECAM1	10.1159/000439169, 10.1093/cvr/cvr080, 10.1161/CIRCRESAHA.110.235390, 10.1161/ATVBAHA.115.305529, 10.1016/j.jvs.2009.03.055, 10.1016/j.atherosclerosis.2011.06.008	6	Immuno	abdominal, infrarenal	intima;media	66.1, 69.1,64, 46.6	B,M	autopsy CV healthy	associated to adipose-derived stem cells appearance in abdominal aneurysm, increased in aneurysm and atheromatous aortae
Platelet factor 4	P02776	PF4	10.1002/prca.201200064, 10.1093/c	2	Immuno;Mass Sp	ascending	adventitia;media	51	B		decreased in aneurysm
Platelet glycoprotein Ib beta chain	P13224	GP1BB	10.1002/prca.201200064		Mass Spec						
Platelet-derived growth factor subunit A	P04085	PDGFA	10.1093/cvr/cvu196		Immuno	ascending	media	51	B		decreased in aneurysm
Pleckstrin	P08567	PLEK	10.1002/prca.201200064		Mass Spec						
Plectin	Q15149	PLEC	10.1074/mcp.M111.008128, 10.1074	3	Mass Spec	ascending		37.5	B	valve replacement	
Podocan	Q7Z5L7	PODN	10.1074/mcp.M110.001693, 10.1074	2	Immuno;Mass Sp	ascending	intima	37.5	B	valve replacement	
Podoplanin	Q86YL7	PDPN	10.1016/j.thromres.2012.01.003, 10.1371/journal.pone.0089983, 10.1371/journal.pone.0089830	3	Immuno	abdominal	adventitia;media	47, 66.5	M, B		augmented in atherosclerosis, appears in media in aneurysm
Poly(rC)-binding protein 2	Q15366	PCBP2	10.1074/mcp.M111.008128, 10.1074	2	Mass Spec	ascending		37.5	B	valve replacement	
Polyadenylate-binding protein 1	P11940	PABPC1	10.1074/mcp.M111.008128, 10.1074	2	Mass Spec	ascending		37.5	B	valve replacement	
Polycystin-1	P98161	PKD1	10.1074/mcp.M111.008128, 10.1074	2	Mass Spec	ascending		37.5	B	valve replacement	
Polycystin-2	Q13563	PKD2	11134244		Immuno		media				
Polymerase I and transcript release facto	Q6NZI2	PTRF	10.1074/mcp.M111.008128, 10.1002	3	Mass Spec	ascending		37.5	B	valve replacement	
Potassium/sodium hyperpolarization-act	Q9UL51	HCN2	10.1074/mcp.M111.008128		Mass Spec	ascending		37.5	B	valve replacement	
Prelamin-A/C	P02545	LMNA	10.1074/mcp.M111.008128, 10.1016	5	Immuno;Mass Sp	ascending		37.5,73, 5	B, M	valve replacement	diminished in aneurysm and in dissection
Prenylated Rab acceptor protein 1	Q9UI14	RABAC1	10.1002/prca.201200064		Mass Spec						
Probable cysteine--tRNA ligase, mitocho	Q9HA77	CARS2	10.1074/mcp.M111.008128		Mass Spec	ascending		37.5	B	valve replacement	
Procollagen C-endopeptidase enhancer	Q15113	PCOLCE	10.1074/mcp.M110.001693, 10.1074	3	Mass Spec	ascending		37.5	B	valve replacement	
Pro-epidermal growth factor	P01133	EGF	10.1016/j.jvs.2006.11.020		Immuno	abdominal		55	B		
Profilin-1	P07737	PFN1	10.1074/mcp.M111.008128, 10.1002	3	Mass Spec	ascending		37.5	B	valve replacement	
Profilin-2	P35080	PFN2	10.1074/mcp.M111.008128, 10.1074	2	Mass Spec	ascending		37.5	B	valve replacement	
Progesterone receptor	P06401	PGR	10.1507/endocrj.52.245		Immuno	abdominal	media	53.7	B		
Programmed cell death 6-interacting pro	Q8WUM4	PDCD6IP	10.1074/mcp.M111.008128, 10.1002	3	Mass Spec	ascending		37.5	B	valve replacement	
Prokineticin-1	P58294	PROK1	10.1093/cvr/cvu196		Immuno	ascending	media	51	B		augmented in aneurysm, not sure if control aorta has it because suppl info is not available online
Prolargin	P51888	PRELP	10.1074/mcp.M111.008128, 10.1002	3	Mass Spec	ascending		37.5	B	valve replacement	
Proliferating cell nuclear antigen	P12004	PCNA	10.1067/mlc.2003.23		Immuno	ascending		64			
Proliferation-associated protein 2G4	Q9UQ80	PA2G4	10.1074/mcp.M110.001693		Mass Spec	ascending				valve replacement	
Prolow-density lipoprotein receptor-related protein 1	Q07954	LRP1	10.1074/mcp.M111.008128, 10.1016	4	Immuno;Mass Spec	abdominal, ascending	adventitia;media	37.5,45, 52.92	B	valve replacement	decreased in abdominal aneurysm
Properdin	P27918	CFP	10.1074/mcp.M111.008128, 10.1074	2	Mass Spec	ascending		37.5	B	valve replacement	
Prosaposin	P07602	PSAP	10.1002/prca.201200064, 10.1074/n	3	Mass Spec	ascending		37.5	B	valve replacement	not detected in abdominal aneurysm
Prostacyclin synthase	Q16647	PTGIS	10.1002/prca.201200064		Mass Spec						
Prostaglandin E synthase	O14684	PTGES	10.1194/jlr.M042481		Immuno	abdominal	adventitia	56.3	B		augmented in aneurysm
Prostaglandin E2 receptor EP4 subtype	P35408	PTGER4	10.1194/jlr.M042481, 10.1016/j.ajpa	2	Immuno	abdominal		45	M	autopsy CV healthy	
Prostaglandin G/H synthase 1	P23219	PTGS1	10.1016/j.bbalip.2006.09.015		Immuno		intima	51	F		
Prostaglandin G/H synthase 2	P35354	PTGS2	10.1194/jlr.M042481, 10.1016/j.atherosclerosis.2006.08.062	2	Immuno	abdominal	adventitia;media	56.3	B		augmented in abdominal aneurysm, 10731924 says COX2 is at minimal thickened intima of controls and many in atherosclerosis
Proteasome activator complex subunit 1	Q06323	PSME1	10.1074/mcp.M111.008128, 10.1074	2	Mass Spec	ascending		37.5	B	valve replacement	
Proteasome subunit alpha type-1	P25786	PSMA1	10.1074/mcp.M111.008128, 10.1074	2	Mass Spec	ascending		37.5	B	valve replacement	
Proteasome subunit alpha type-2	P25787	PSMA2	10.1074/mcp.M111.008128, 10.1074	2	Mass Spec	ascending		37.5	B	valve replacement	
Proteasome subunit alpha type-3	P25788	PSMA3	10.1074/mcp.M110.001693		Mass Spec	ascending				valve replacement	
Proteasome subunit alpha type-6	P60900	PSMA6	10.1074/mcp.M111.008128, 10.1074	2	Mass Spec	ascending		37.5	B	valve replacement	
Proteasome subunit alpha type-7	O14818	PSMA7	10.1074/mcp.M111.008128, 10.1074	2	Mass Spec	ascending		37.5	B	valve replacement	
Proteasome subunit alpha type-7-like	Q8TAA3	PSMA8	10.1074/mcp.M111.008128, 10.1074	2	Mass Spec	ascending		37.5	B	valve replacement	
Proteasome subunit beta type-5	P28074	PSMB5	10.1074/mcp.M111.008128, 10.1074	2	Mass Spec	ascending		37.5	B	valve replacement	
Proteasome subunit beta type-6	P28072	PSMB6	10.1074/mcp.M111.008128, 10.1074	2	Mass Spec	ascending		37.5	B	valve replacement	
Proteasome subunit beta type-8	P28062	PSMB8	10.1038/srep15730		Immuno			65.5	M		
Protein AMBP	P02760	AMBP	10.1074/mcp.M111.008128, 10.1002	3	Mass Spec	ascending		37.5	B	valve replacement	
Protein deglycase DJ-1	Q99497	PARK7	10.1074/mcp.M112.021873, 10.1074	4	Mass Spec	ascending		37.5	B	valve replacement	increased in TAV and BAV asc dilation
Protein disulfide-isomerase	P07237	P4HB	10.1074/mcp.M111.008128, 10.1002	3	Mass Spec	ascending		37.5	B	valve replacement	
Protein disulfide-isomerase A3	P30101	PDIA3	10.1074/mcp.M111.008128, 10.1002	3	Mass Spec	ascending		37.5	B	valve replacement	
Protein disulfide-isomerase A4	P13667	PDIA4	10.1074/mcp.M111.008128, 10.1074	2	Mass Spec	ascending		37.5	B	valve replacement	
Protein disulfide-isomerase A6	Q15084	PDIA6	10.1074/mcp.M111.008128, 10.1074	2	Mass Spec	ascending		37.5	B	valve replacement	
Protein FAM83F	Q8NEG4	FAM83F	10.1074/mcp.M111.008128, 10.1074	2	Mass Spec	ascending		37.5	B	valve replacement	
Protein kinase C delta-binding protein	Q969G5	PRKCDBP	10.1002/prca.201200064, 10.1074/mcp.M110		Mass Spec	ascending				valve replacement	
Protein Niban	Q9BZQ8	FAM129A	10.1074/mcp.M111.008128, 10.1002	3	Mass Spec	ascending		37.5	B	valve replacement	
Protein NOV homolog	P48745	NOV	10.1074/mcp.M111.008128, 10.1074	2	Mass Spec	ascending		37.5	B	valve replacement	
Protein phosphatase 1 regulatory subun	O14974	PPP1R12A	10.1002/prca.201200064		Mass Spec						
Protein phosphatase 1 regulatory subun	O60237	PPP1R12B	10.1074/mcp.M111.008128, 10.1074	2	Mass Spec	ascending		37.5	B	valve replacement	
Protein phosphatase 1 regulatory subun	Q96A00	PPP1R14A	10.1002/prca.201200064		Mass Spec						
Protein phosphatase 1 regulatory subun	Q15435	PPP1R7	10.1074/mcp.M111.008128, 10.1074	2	Mass Spec	ascending		37.5	B	valve replacement	
Protein S100-A10	P60903	S100A10	10.1002/prca.201200064		Mass Spec						
Protein S100-A11	P31949	S100A11	10.1074/mcp.M111.008128, 10.1002	3	Mass Spec	ascending		37.5	B	valve replacement	
Protein S100-A4	P26447	S100A4	10.1074/mcp.M111.008128, 10.1371	4	Immuno;Mass Sp	thoracic, ascending	media	37.5,44.6	B	other;valve replacement	augmented in thoracic aneurysm
Protein S100-A6	P06703	S100A6	10.1074/mcp.M111.008128, 10.1002	3	Mass Spec	ascending		37.5	B	valve replacement	
Protein S100-A8	P05109	S100A8	10.1002/prca.201200064, 10.1074/mcp.M110.001693, 10.1074/mcp.M111.008128	3	Mass Spec	ascending		37.5	B	valve replacement	augmented in abdominal aneurysm
Protein S100-A9	P06702	S100A9	10.1002/prca.201200064, 10.1074/mcp.M110.001693	2	Mass Spec	ascending				valve replacement	10.1074/mcp.M111.008128 says there's no Protein S100-A9 in control ascending aorta
Protein SET	Q01105	SET	10.1074/mcp.M111.008128, 10.1074	2	Mass Spec	ascending		37.5	B	valve replacement	
Protein unc-13 homolog B	O14795	UNC13B	10.1074/mcp.M110.001693		Mass Spec	ascending				valve replacement	
Protein virilizer homolog	Q69YN4	VIRMA	10.1074/mcp.M112.021873		Mass Spec	ascending				valve replacement	
Protein-glutamine gamma-glutamyltransferase 2	P21980	TGM2	10.1074/mcp.M112.021873, 10.1074	7	Immuno;Mass Sp	abdominal, thoracic desc, ascending	intima;media	37.5,68, 4	B	other;valve replacement	augmented in aging, abdminal and ascending aneurysm and in CDK calcified aorta media
Protein-L-isoaspartate(D-aspartate) O-m	P22061	PCMT1	10.1074/mcp.M111.008128, 10.1074	2	Mass Spec	ascending		37.5	B	valve replacement	
Prothrombin	P00734	F2	10.1002/prca.201200064		Mass Spec						
Protocadherin Fat 4	Q6V0I7	FAT4	10.1074/mcp.M111.008128, 10.1074	2	Mass Spec	ascending		37.5	B	valve replacement	
Purine nucleoside phosphorylase	P00491	PNP	10.1002/prca.201200064		Mass Spec						
Puromycin-sensitive aminopeptidase	P55786	NPEPPS	10.1074/mcp.M111.008128, 10.1074	2	Mass Spec	ascending		37.5	B	valve replacement	
Putative elongation factor 1-alpha-like 3	Q5VTE0	EEF1A1P5	10.1002/prca.201200064		Mass Spec						
Putative hydroxypyruvate isomerase	Q5T013	HYI	10.1074/mcp.M111.008128, 10.1074	2	Mass Spec	ascending		37.5	B	valve replacement	
Pyruvate kinase PKM	P14618	PKM	10.1074/mcp.M111.008128, 10.1002	3	Mass Spec	ascending		37.5	B	valve replacement	
Quinone oxidoreductase	Q08257	CRYZ	10.1074/mcp.M111.008128, 10.1074	2	Mass Spec	ascending		37.5	B	valve replacement	
Rab GDP dissociation inhibitor alpha	P31150	GDI1	10.1074/mcp.M111.008128, 10.1074	2	Mass Spec	ascending		37.5	B	valve replacement	
Rab GDP dissociation inhibitor beta	P50395	GDI2	10.1074/mcp.M111.008128, 10.1002	3	Mass Spec	ascending		37.5	B	valve replacement	
RAC-alpha serine/threonine-protein kina	P31749	AKT1	10.1161/CIRCRESAHA.112.300735		Immuno	descending thoracic		61.3	B		aneurysm, dissection
RAC-beta serine/threonine-protein kinas	P31751	AKT2	10.1161/CIRCRESAHA.112.300735		Immuno	descending thoracic		61.3	B		aneurysm, dissection
Radixin	P35241	RDX	10.1074/mcp.M111.008128, 10.1074	2	Mass Spec	ascending		37.5	B	valve replacement	
Ras GTPase-activating-like protein IQGA	P46940	IQGAP1	10.1074/mcp.M111.008128, 10.1074	3	Mass Spec	ascending		37.5	B	valve replacement	
Ras GTPase-activating-like protein IQGA	Q13576	IQGAP2	10.1074/mcp.M111.008128		Mass Spec	ascending		37.5	B	valve replacement	

Ras suppressor protein 1	Q15404	RSU1	10.1074/mcp.M111.008128, 10.1002	3	Mass Spec	ascending		37.5	B	valve replacement	
Ras-related C3 botulinum toxin substrate	P63000	RAC1	10.1074/mcp.M111.008128, 10.1074	2	Mass Spec	ascending		37.5	B	valve replacement	
Ras-related protein Rab-10	P61026	RAB10	10.1002/prca.201200064		Mass Spec						
Ras-related protein Rab-11A	P62491	RAB11A	10.1074/mcp.M110.001693		Mass Spec	ascending				valve replacement	
Ras-related protein Rab-7a	P51149	RAB7A	10.1074/mcp.M111.008128, 10.1074	2	Mass Spec	ascending		37.5	B	valve replacement	
Ras-related protein Rap-1A	P62834	RAP1A	10.1074/mcp.M111.008128, 10.1074	2	Mass Spec	ascending		37.5	B	valve replacement	
Ras-related protein Rap-1b	P61224	RAP1B	10.1002/prca.201200064		Mass Spec						
Ras-related protein R-Ras	P10301	RRAS	10.1074/mcp.M111.008128, 10.1002	3	Mass Spec	ascending		37.5	B	valve replacement	
Receptor-interacting serine/threonine-p	Q13546	RIPK1	10.1161/CIRCRESAHA.116.304899		Immuno	abdominal	media				
Receptor-interacting serine/threonine-p	Q9Y572	RIPK3	10.1161/CIRCRESAHA.116.304899		Immuno	abdominal	media				augmented in aneurysm
Receptor-type tyrosine-protein phospha	Q13332	PTPRS	10.1074/mcp.M110.001693		Mass Spec	ascending				valve replacement	
Renin receptor	O75787	ATP6AP2	10.1016/j.atherosclerosis.2009.01.003	1	Immuno			50	B	autopsy CV healthy	augmented in atherosclerosis
Resistin	Q9HD89	RETN	10.1152/ajpheart.00431.2009, 10.1074/mcp.M110.001693	2	Immuno;Mass Sp	ascending	media			valve replacement	augmented in atherosclerosis
Reticulon-4	Q9NQC3	RTN4	10.1161/ATVBAHA.107.140913, 10.1002/prca.201200064	2	Immuno;Mass Sp	ascending					deceased in atherosclerotic arteries
Retinal dehydrogenase 1	P00352	ALDH1A1	10.1074/mcp.M111.008128, 10.1016	3	Mass Spec	abdominal, ascending		37.5,53.91	B	valve replacement	decreased in abdominal aneurysm
Retinitis pigmentosa 1-like 1 protein	Q8IWN7	RP1L1	10.1074/mcp.M111.008128, 10.1074	2	Mass Spec	ascending		37.5	B	valve replacement	
Retinoic acid receptor responder protein 2	Q99969	RARRES2	20145358, 10.1186/1471-2261-14-56	2	Immuno	abdominal	media;periaortic adipose tissue				augmented in atherosclerosis, hypertension and aging, presence in periaortic fat
Rho GDP-dissociation inhibitor 1	P52565	ARHGDIA	10.1074/mcp.M111.008128, 10.1002	3	Mass Spec	ascending		37.5	B	valve replacement	
Rho GDP-dissociation inhibitor 2	P52566	ARHGDIB	10.1074/mcp.M111.008128, 10.1002	3	Mass Spec	ascending		37.5	B	valve replacement	
Rho GTPase-activating protein 1	Q07960	ARHGAP1	10.1074/mcp.M111.008128, 10.1002	3	Mass Spec	ascending		37.5	B	valve replacement	
Rho-related GTP-binding protein RhoC	P08134	RHOC	10.1074/mcp.M111.008128, 10.1002	3	Mass Spec	ascending		37.5	B	valve replacement	
Ribonuclease inhibitor	P13489	RNH1	10.1074/mcp.M111.008128, 10.1002	3	Mass Spec	ascending		37.5	B	valve replacement	
RNA cytidine acetyltransferase	Q9H0A0	NAT10	10.1074/mcp.M111.008128, 10.1074	2	Mass Spec	ascending		37.5	B	valve replacement	
RNA-binding motif protein, X chromosor	P38159	RBMX	10.1074/mcp.M111.008128, 10.1074	2	Mass Spec	ascending		37.5	B	valve replacement	
Runt-related transcription factor 2	Q13950	RUNX2	10.1093/ndt/gfp137		Immuno		intima;media	68	B		augmented in calcified aorta, 10.1038/sj.ki.5002353 says that there's no CBFA1 in control aorta
S-adenosylmethionine synthase isoform	Q00266	MAT1A	10.1074/mcp.M111.008128, 10.1074	2	Mass Spec	ascending		37.5	B	valve replacement	
Scavenger receptor cysteine-rich type 1	Q86VB7	CD163	10.14670/HH-11-691, 10.1016/j.ijcard.2015.08.053	2	Immuno	ascending, abdominal	intima	61.6	B		augmented in aneurysm or not
Sclerostin	Q9BQB4	SOST	10.1074/mcp.M111.008128, 10.1074/mcp.M110.001693	2	Immuno;Mass Sp	ascending	intima	37.5	B	valve replacement	not detected in abdominal aneurysm
Secernin-1	Q12765	SCRN1	10.1074/mcp.M111.008128, 10.1074	2	Mass Spec	ascending		37.5	B	valve replacement	
Secreted frizzled-related protein 1	Q8N474	SFRP1	10.1074/mcp.M110.001693, 10.1074/mcp.M111.008128	2	Mass Spec	ascending		37.5	B	valve replacement	not detected in abdominal aneurysm
Secreted frizzled-related protein 3	Q92765	FRZB	10.1074/mcp.M110.001693, 10.1074	2	Mass Spec	ascending		37.5	B	valve replacement	
Selenium-binding protein 1	Q13228	SELENBP1	10.1074/mcp.M111.008128, 10.1074	2	Mass Spec	ascending		37.5	B	valve replacement	
Sepiapterin reductase	P35270	SPR	10.1074/mcp.M111.008128, 10.1074	2	Mass Spec	ascending		37.5	B	valve replacement	
Septin-11	Q9NVA2	SEPT11	10.1074/mcp.M111.008128, 10.1074	2	Mass Spec	ascending		37.5	B	valve replacement	
Septin-2	Q15019	SEPT2	10.1074/mcp.M111.008128, 10.1002	3	Mass Spec	ascending		37.5	B	valve replacement	
Septin-7	Q16181	SEPT7	10.1074/mcp.M111.008128, 10.1074	2	Mass Spec	ascending		37.5	B	valve replacement	
Septin-9	Q9UHD8	SEPT9	10.1074/mcp.M111.008128, 10.1074	2	Mass Spec	ascending		37.5	B	valve replacement	
Serine protease HTRA1	Q92743	HTRA1	10.1074/mcp.M111.008128, 10.1002	3	Mass Spec	ascending		37.5	B	valve replacement	
Serine/arginine-rich splicing factor 1	Q07955	SRSF1	10.1074/mcp.M111.008128, 10.1074	2	Mass Spec	ascending		37.5	B	valve replacement	
Serine/threonine-protein kinase ATR	Q13535	ATR	10.1074/mcp.M111.008128, 10.1074	2	Mass Spec	ascending		37.5	B	valve replacement	
Serine/threonine-protein phosphatase 2	P30153	PPP2R1A	10.1002/prca.201200064		Mass Spec						
Serine/threonine-protein phosphatase 2	Q15257	PPP2R4	10.1074/mcp.M111.008128, 10.1074	2	Mass Spec	ascending		37.5	B	valve replacement	
Serine/threonine-protein phosphatase 5	P53041	PPP5C	10.1074/mcp.M111.008128, 10.1074	2	Mass Spec	ascending		37.5	B	valve replacement	
Serotransferrin	P02787	TF	10.1074/mcp.M112.021873, 10.1074	5	Immuno;Mass Sp	ascending, abdominal		37.5,64.9	B,M	valve replacement	
Serpin A12	Q8IW75	SERPINA12	20145358	1	Immuno	abdominal	periaortic adipose tissue			autopsy CV healthy	augmented in atherosclerosis
Serpin B6	P35237	SERPINB6	10.1074/mcp.M111.008128, 10.1074	2	Mass Spec	ascending		37.5	B	valve replacement	
Serpin H1	P50454	SERPINH1	10.1074/mcp.M111.008128, 10.1074	2	Mass Spec	ascending		37.5	B	valve replacement	
Serum albumin	P02768	ALB	10.1074/mcp.M112.021873, 10.1074	4	Mass Spec	ascending		37.5	B	valve replacement	
Serum amyloid P-component	P02743	APCS	10.1074/mcp.M112.021873, 10.1161/CIRCULATIONAHA.108.843516, 10.1074/mcp.M110.001693, 10.1002/prca.201200064, 10.1074/mcp.M111.008128	5	Mass Spec	ascending		60, 37.5	B	valve replacement	augmented in abdominal aneurysm and in BAV dilation, or decreased in Marfan aneurysm
S-formylglutathione hydrolase	P10768	ESD	10.1074/mcp.M111.008128, 10.1002	3	Mass Spec	ascending		37.5	B	valve replacement	
SH3 and PX domain-containing protein 2	A1X283	SH3PXD2B	10.1074/mcp.M111.008128, 10.1074	2	Mass Spec	ascending		37.5	B	valve replacement	
SH3 domain-binding glutamic acid-rich-l	O75368	SH3BGRL	10.1074/mcp.M111.008128, 10.1002	2	Mass Spec			37.5	B	valve replacement	
SH3 domain-binding glutamic acid-rich-l	Q9H299	SH3BGRL3	10.1002/prca.201200064, 10.1074/m	2	Mass Spec	ascending					
Signal transducer and activator of transc	P42224	STAT1	10.1016/j.jvs.2009.11.075		Immuno	abdominal					augmented in aneurysm
Signal transducer and activator of transc	P40763	STAT3	10.1016/j.yjmcc.2015.08.014		Immuno						activated in abdominal aneurysm
Smoothelin	P53814	SMTN	10.1074/mcp.M111.008128, 10.1161	4	Immuno;Mass Sp	ascending	intima;media	37.5,39.7	B	valve replacement	augmented in Marfan aneurysm
Somatomedin-B and thrombospondin ty	Q8IVN8	SBSPON	10.1074/mcp.M110.001693, 10.1074	2	Mass Spec	ascending		37.5	B	valve replacement	decreased in abdominal aneurysm
Sorbin and SH3 domain-containing prote	Q9BX66	SORBS1	10.1074/mcp.M111.008128, 10.1002	3	Mass Spec	ascending		37.5	B	valve replacement	
Sorbin and SH3 domain-containing prote	O94875	SORBS2	10.1074/mcp.M111.008128, 10.1002	3	Mass Spec	ascending		37.5	B	valve replacement	
Sortilin	Q99523	SORT1	10.1371/journal.pone.0084969		Immuno		intima	67			augmented in fibroatheromatous plaque
Sorting nexin-18	Q96RF0	SNX18	10.1074/mcp.M111.008128, 10.1074	2	Mass Spec	ascending		37.5	B	valve replacement	
Sorting nexin-3	O60493	SNX3	10.1074/mcp.M111.008128, 10.1074	2	Mass Spec	ascending		37.5	B	valve replacement	
SPARC	P09486	SPARC	10.1161/hq1201.100229		Immuno	abdominal	adventitia;media				prominent expression in foam cells in the lipid core of atheroma
SPARC-like protein 1	Q14515	SPARCL1	10.1074/mcp.M110.001693, 10.1074	2	Mass Spec	ascending		37.5	B	valve replacement	not detected in abdominal aneurysm
SPARC-related modular calcium-binding	Q9H3U7	SMOC2	10.1074/mcp.M111.008128, 10.1074	2	Mass Spec	ascending		37.5	B	valve replacement	not detected in abdominal aneurysm
Spectrin alpha chain, non-erythrocytic 1	Q13813	SPTAN1	10.1161/CIRCULATIONAHA.108.843516, 10.1074/mcp.M111.008128, 10.1074/mcp.M110.001693	3	Immuno;Mass Sp	ascending, abdominal		60,37.5	B	valve replacement	increased fragmentation in MF and BAV asc aneurysm
Spectrin beta chain, non-erythrocytic 1	Q01082	SPTBN1	10.1074/mcp.M111.008128, 10.1002	3	Mass Spec	ascending		37.5	B	valve replacement	
Splicing factor, proline- and glutamine-ri	P23246	SFPQ	10.1074/mcp.M111.008128, 10.1074	2	Mass Spec	ascending		37.5	B	valve replacement	
Spondin-1	Q9HCB6	SPON1	10.1074/mcp.M110.001693, 10.1074	2	Mass Spec	ascending		37.5	B	valve replacement	not detected in abdominal aneurysm
Src substrate cortactin	Q14247	CTTN	10.1002/prca.201200064		Mass Spec						
Staphylococcal nuclease domain-contair	Q7KZF4	SND1	10.1074/mcp.M111.008128, 10.1074	2	Mass Spec	ascending				valve replacement	
Steryl-sulfatase	P08842	STS	10.1016/S0002-9440(10)63492-X		Immuno	abdominal	media	57.7	B		varies depending on atherosclerotic stage
Stress-70 protein, mitochondrial	P38646	HSPA9	10.1074/mcp.M111.008128, 10.1074	2	Mass Spec	ascending		37.5	B	valve replacement	
Stress-induced-phosphoprotein 1	P31948	STIP1	10.1074/mcp.M111.008128, 10.1074	2	Mass Spec	ascending		37.5	B	valve replacement	
Stromal cell-derived factor 1	P48061	CXCL12	10.1016/j.jvs.2006.11.020		Immuno	abdominal		55	B		
Stromelysin-1	P08254	MMP3	10.14670/HH-11-691, 10.1161/01.RE	4	Immuno	ascending	media	61.6, 51, 5	B		augmented in aneurysm
Succinate dehydrogenase [ubiquinone] f	P31040	SDHA	10.1074/mcp.M111.008128, 10.1074	2	Mass Spec	ascending		37.5	B	valve replacement	
Succinate dehydrogenase [ubiquinone] i	P21912	SDHB	10.1074/mcp.M111.008128, 10.1074	2	Mass Spec	ascending		37.5	B	valve replacement	
Superoxide dismutase [Cu-Zn]	P00441	SOD1	10.1074/mcp.M111.008128, 10.1016	5	Immuno;Mass Sp	ascending	intima;media	37.5,47.4,	M,B	autopsy CV healthy;valve replacement	decreased in dissection

Superoxide dismutase [Mn], mitochondrial	P04179	SOD2	10.1074/mcp.M111.008128, 10.1093	3	Immuno;Mass Sp	ascending	intima;media	37.5,68	B	valve replacement	augmented in calcified aorta
Supervillin	O95425	SVIL	10.1074/mcp.M110.001693		Mass Spec	ascending				valve replacement	
Synaptic vesicle membrane protein VAT-	Q99536	VAT1	10.1074/mcp.M111.008128, 10.1074	2	Mass Spec	ascending		37.5	B	valve replacement	
Synaptopodin	Q8N3V7	SYNPO	10.1074/mcp.M111.008128, 10.1002	3	Mass Spec	ascending		37.5	B	valve replacement	
Synaptopodin-2	Q9UMS6	SYNPO2	10.1074/mcp.M111.008128, 10.1074	2	Mass Spec	ascending		37.5	B	valve replacement	
Synemin	O15061	SYNM	10.1074/mcp.M111.008128, 10.1074	2	Mass Spec	ascending		37.5	B	valve replacement	
Talin-1	Q9Y490	TLN1	10.1074/mcp.M111.008128, 10.1002	3	Mass Spec	ascending		37.5	B	valve replacement	
Target of Nesh-SH3	Q7Z7G0	ABI3BP	10.1074/mcp.M110.001693, 10.1074	2	Mass Spec	ascending		37.5	B	valve replacement	decreased in abdominal aneurysm
T-complex protein 1 subunit gamma	P49368	CCT3	10.1074/mcp.M111.008128, 10.1074	2	Mass Spec	ascending		37.5	B	valve replacement	
T-complex protein 1 subunit theta	P50990	CCT8	10.1074/mcp.M111.008128, 10.1074	2	Mass Spec	ascending		37.5	B	valve replacement	
Tenascin	P24821	TNC	10.1111/j.1440-1827.2011.02699.x, 10.1074/mcp.M110.001693, 10.1074/mcp.M111.008128	3	Immuno;Mass Sp	abdominal, ascending	media	37.5	B	autopsy CV healthy;valve replacement	increased in abdominal aneurysm, 16377578 says there's no tenascin in normal aortae
Tenascin-X	P22105	TNXB	10.1161/CIRCULATIONAHA.104.513	3	Immuno;Mass Sp	ascending	adventitia;intima;	37.5	B	valve replacement	decreased in aneurysm
Tensin-1	Q9HBL0	TNS1	10.1002/prca.201200064, 10.1074/n	2	Mass Spec	ascending		37.5	B	valve replacement	
Testin	Q9UGI8	TES	10.1074/mcp.M111.008128, 10.1074	2	Mass Spec	ascending		37.5	B	valve replacement	
Tetranectin	P05452	CLEC3B	10.1002/prca.201200064, 10.1074/n	3	Mass Spec	ascending		37.5	B	valve replacement	
TGF-beta receptor type-1	P36897	TGFBR1	10.1024/0301-1526/a000133		Immuno						attenuated in Marfan syndrome
Thioredoxin	P10599	TXN	10.1074/mcp.M111.008128, 10.1002	3	Mass Spec	ascending		37.5	B	valve replacement	
Thioredoxin domain-containing protein	Q8NBS9	TXNDC5	10.1074/mcp.M111.008128, 10.1074	2	Mass Spec	ascending		37.5	B	valve replacement	
Thioredoxin reductase 1, cytoplasmic	Q16881	TXNRD1	10.1074/mcp.M111.008128, 10.1002	3	Mass Spec	ascending		37.5	B	valve replacement	
Thioredoxin-like protein 1	O43396	TXNL1	10.1074/mcp.M111.008128, 10.1074	2	Mass Spec	ascending		37.5	B	valve replacement	
Thrombomodulin	P07204	THBD	10.1161/ATVBAHA.115.305529		Immuno		intima				in abdominal aneurysm switches to tunica media
Thrombopoietin	P40225	THPO	10.1016/j.jvs.2006.11.020		Immuno	abdominal		55	B		
Thrombospondin-1	P07996	THBS1	10.1002/prca.201200064, 10.1093/c	4	Immuno;Mass Sp	ascending	adventitia;media	51, 37.5	B	valve replacement	augmented in aneurysm
Thrombospondin-2	P35442	THBS2	10.1093/cvr/cvu196, 10.1002/prca.201200064	2	Immuno;Mass Sp	ascending	media				augmented in aneurysm, 10.1074/mcp.M111.008128 says there's no thrombospondin-2 in control ascending aorta
Thymidine phosphorylase	P19971	TYMP	10.1093/cvr/cvu196		Immuno	ascending	media	51	B		augmented in aneurysm, not sure if control aorta has it because suppl info is not available online
Thymosin beta-4	P62328	TMSB4X	10.1016/j.jprot.2015.06.005	1	Immuno	ascending	intima;media	76	B	autopsy CV healthy	overexpression in atherosclerosis
Tissue factor	P13726	F3	10.1093/cvr/cvu196		Immuno	ascending	adventitia;media	51	B		aneurysm, not sure if control aorta has it because suppl info is not available online
Tissue factor pathway inhibitor 2	P48307	TFPI2	10.1161/hq0102.101842		Immuno		intima				augmented in atherosclerotic tissue
Tissue-type plasminogen activator	P00750	PLAT	10.1097/01.LAB.0000073127.46392.9D		Immuno	ascending		51.1			
Titin	Q8WZ42	TTN	10.1074/mcp.M111.008128, 10.1002	2	Mass Spec	ascending		37.5	B	valve replacement	
Toll-like receptor 3	O15455	TLR3	10.1016/j.atherosclerosis.2015.06.014		Immuno	infrarenal	media				augmented in abdominal aneurysm
Toll-like receptor 4	O00206	TLR4	10.1016/j.atherosclerosis.2015.06.01	3	Immuno	infrarenal	media				augmented in abdominal aneurysm
Transaldolase	P37837	TALDO1	10.1074/mcp.M111.008128, 10.1074	2	Mass Spec	ascending		37.5	B	valve replacement	
Transcription activator BRG1	P51532	SMARCA4	10.1093/ejcts/ezu215		Immuno		media				augmented in thoracic aneurysm
Transcription factor SOX-9	P48436	SOX9	10.1093/cvr/cvw082		Immuno	abdominal	media				decreased in abdominal aneurysm, 10.1038/sj.ki.5002353 says there's no sox9 in control and it is present in calcified aorta
Transcription initiation factor TFIID subu	Q7Z7C8	TAF8	10.1074/mcp.M111.008128, 10.1074	2	Mass Spec	ascending		37.5	B	valve replacement	
Transcriptional repressor p66-beta	Q8WXI9	GATAD2B	10.1074/mcp.M111.008128		Mass Spec	ascending		37.5	B	valve replacement	
Transferrin receptor protein 1	P02786	TFRC	10.1161/ATVBAHA.115.305586, 10.1	2	Immuno	ascending, abdomi	media	74, 64.9	B,M	valve replacement	increased in aneurysm
Transforming growth factor beta-1	P01137	TGFB1	10.1093/cvr/cvu196, 10.1093/ndt/gf	5	Immuno	ascending, thoraci	intima;media	51, 68	B		augmented in CDK patients, in aneurysm and in cytoplasm of Marfan syndrome
Transforming growth factor beta-1-induced transcript 1 protein	O43294	TGFB1I1	10.1002/prca.201200064, 10.1074/n	3	Mass Spec	ascending		37.5	B	valve replacement	decreased in abdominal aneurysm
Transforming growth factor beta-2	P61812	TGFB2	10.1002/path.2516		Immuno	ascending					
Transforming growth factor beta-3	P10600	TGFB3	10.1002/path.2516		Immuno	ascending					
Transforming growth factor-beta-induced protein ig-h3	Q15582	TGFBI	10.1074/mcp.M111.008128, 10.1002	3	Mass Spec	ascending		37.5	B	valve replacement	augmented in abdominal aneurysm
Transgelin	Q01995	TAGLN	10.1074/mcp.M112.021873, 10.1074/mcp.M111.008128, 10.1161/CIRCULATIONAHA.108.843516, 10.1161/ATVBAHA.114.304412, 10.1016/j.jtcvs.2009.07.075, 10.1002/prca.201200064, 10.1074/mcp.M110.001693	7	Immuno;Mass Sp	ascending	media	37.5,60	B	CABG;valve replacement	decreased in unknown aneurysm. Increased in BAV asc dilation. Not affected in Marfan aneurysm or decreased
Transgelin-2	P37802	TAGLN2	10.1074/mcp.M112.021873, 10.1074	4	Mass Spec	ascending		37.5	B	valve replacement	increased in TAV and BAV asc dilation
Transitional endoplasmic reticulum ATPa	P55072	VCP	10.1074/mcp.M111.008128, 10.1002	3	Mass Spec	ascending		37.5	B	valve replacement	
Transketolase	P29401	TKT	10.1074/mcp.M111.008128, 10.1002	3	Mass Spec	ascending		37.5	B	valve replacement	
Transmembrane protein 43	Q9BTV4	TMEM43	10.1002/prca.201200064		Mass Spec						
Transthyretin	P02766	TTR	10.1074/mcp.M112.021873, 10.1074	4	Immuno;Mass Sp	ascending	intima	37.5	B	valve replacement	decreased in BAV asc dilation
Trifunctional enzyme subunit alpha, mito	P40939	HADHA	10.1074/mcp.M111.008128, 10.1074	2	Mass Spec	ascending		37.5	B	valve replacement	
Trifunctional enzyme subunit beta, mito	P55084	HADHB	10.1074/mcp.M111.008128, 10.1074	2	Mass Spec	ascending		37.5	B	valve replacement	
Triosephosphate isomerase	P60174	TPI1	10.1074/mcp.M111.008128, 10.1016	4	Immuno;Mass Sp	abdominal, ascending		37.5,53.91	B	valve replacement	decreased in abdominal aneurysm
Tropomyosin alpha-1 chain	P09493	TPM1	10.1074/mcp.M111.008128, 10.1002	3	Mass Spec	ascending		37.5	B	valve replacement	
Tropomyosin alpha-4 chain	P67936	TPM4	10.1074/mcp.M111.008128, 10.1002	3	Mass Spec	ascending		37.5	B	valve replacement	
Tropomyosin beta chain	P07951	TPM2	10.1074/mcp.M112.021873, 10.1074	5	Mass Spec	abdominal, ascending		37.5,53.91	B	valve replacement	augmented in TAV and BAV asc dilation
Trypsin-3	P35030	PRSS3	10.1002/prca.201200064		Mass Spec						
Tryptase alpha/beta-1	Q15661	TPSAB1	10.1161/CIRCRESAHA.111.243758, 1	4	Immuno;Mass Sp	descending thorac	adventitia	41.9, 44, 3	B	valve replacement	augmented in abdominal aneurysm and advanced atherosclerosis
Tubulin alpha-1A chain	Q71U36	TUBA1A	10.1074/mcp.M111.008128, 10.1002	3	Mass Spec	ascending		37.5	B	valve replacement	
Tubulin alpha-1B chain	P68363	TUBA1B	10.1002/prca.201200064, 10.1074/n	2	Mass Spec	ascending				valve replacement	
Tubulin alpha-1C chain	Q9BQE3	TUBA1C	10.1002/prca.201200064		Mass Spec						
Tubulin alpha-4A chain	P68366	TUBA4A	10.1074/mcp.M111.008128, 10.1002	3	Mass Spec	ascending		37.5	B	valve replacement	
Tubulin beta chain	P07437	TUBB	10.1074/mcp.M112.021873, 10.1074	4	Mass Spec	ascending		37.5	B	valve replacement	increased in TAV and BAV dilation
Tubulin beta-1 chain	Q9H4B7	TUBB1	10.1002/prca.201200064		Mass Spec						
Tubulin beta-2A chain	Q13885	TUBB2A	10.1074/mcp.M111.008128, 10.1002	2	Mass Spec			37.5	B	valve replacement	
Tubulin beta-4A chain	P04350	TUBB4A	10.1002/prca.201200064		Mass Spec						
Tubulin beta-4B chain	P68371	TUBB4B	10.1074/mcp.M111.008128, 10.1074	3	Mass Spec	ascending		37.5	B	valve replacement	
Tubulin beta-6 chain	Q9BUF5	TUBB6	10.1074/mcp.M111.008128, 10.1074	2	Mass Spec	ascending		37.5	B	valve replacement	
Tubulointerstitial nephritis antigen-like	Q9GZM7	TINAGL1	10.1074/mcp.M112.021873, 10.1074	4	Mass Spec	ascending		37.5	B	valve replacement	

Tumor necrosis factor	P01375	TNF	10.1016/j.jvs.2012.09.062, 10.1161/	5	Immuno	abdominal, infra-re	intima;media	68, 59.5	B	other;unknown	augmented in calcified aorta and abdominal aneurysm
Tumor necrosis factor ligand superfamily	P50591	TNFSF10	10.1016/j.bbrc.2007.03.209		Immuno						
Tumor necrosis factor ligand superfamily	O14788	TNFSF11	10.1097/HJH.0b013e3282f4b3d0, 10	3	Immuno	ascending, abdomi	intima;media	59, 68	M, B		
Tumor necrosis factor receptor superfan	O00220	TNFRSF10A	10.1016/j.bbrc.2007.03.209		Immuno						
Tumor necrosis factor receptor superfamily member 11A	Q9Y6Q6	TNFRSF11A	10.1093/ndt/gfp137		Immuno		intima;media	68	B		augmented in calcified aorta
Tumor necrosis factor receptor superfamily member 11B	O00300	TNFRSF11B	10.1161/CIRCULATIONAHA.104.464727, 19351609, 10.1016/j.bbrc.2007.03.209, 10.1093/ndt/gfp137, 10.1161/hq1201.100229	5	Immuno	thoracic, abdomina	intima;media	68	B		augmented in atherosclerosis, decreased/augmented in abdominal aneurysm
Type-1 angiotensin II receptor	P30556	AGTR1	10.1161/HYPERTENSIONAHA.107.089409, 10.1161/01.CIR.0000035655.45453.D2, 10.1016/j.atherosclerosis.2009.01.003	3	Immuno	ascending		20, 50	M, B	autopsy CV healthy	augmented in abdominal aneurysm, in atherosclerosis and with aging
Type-2 angiotensin II receptor	P50052	AGTR2	10.1016/j.atherosclerosis.2009.01.003	1	Immuno			50	B	autopsy CV healthy	augmented in abdominal aneurysm and atherosclerosis
Ubiquitin carboxyl-terminal hydrolase is	P09936	UCHL1	10.1074/mcp.M111.008128, 10.1002	3	Mass Spec	ascending		37.5	B	valve replacement	
Ubiquitin-40S ribosomal protein S27a	P62979	RPS27A	10.1074/mcp.M111.008128, 10.1074	2	Mass Spec	ascending		37.5	B	valve replacement	
Ubiquitin-conjugating enzyme E2 N	P61088	UBE2N	10.1002/prca.201200064		Mass Spec						
Ubiquitin-conjugating enzyme E2 variant	Q15819	UBE2V2	10.1074/mcp.M111.008128, 10.1074	2	Mass Spec	ascending		37.5	B	valve replacement	
Ubiquitin-like modifier-activating enzym	P22314	UBA1	10.1074/mcp.M111.008128, 10.1002	3	Mass Spec	ascending		37.5	B	valve replacement	
UMP-CMP kinase	P30085	CMPK1	10.1074/mcp.M111.008128, 10.1074	2	Mass Spec	ascending		37.5	B	valve replacement	
Unconventional myosin-Ic	O00159	MYO1C	10.1074/mcp.M111.008128, 10.1002	3	Mass Spec	ascending		37.5	B	valve replacement	
Unconventional myosin-Id	O94832	MYO1D	10.1074/mcp.M111.008128, 10.1074	3	Mass Spec	ascending		37.5	B	valve replacement	
Unconventional myosin-XVIIIb	Q8IUG5	MYO18B	10.1074/mcp.M111.008128, 10.1074	2	Mass Spec	ascending		37.5	B	valve replacement	
Urotensin-2	O95399	UTS2	10.1016/j.atherosclerosis.2004.03.023		Immuno		intima				augmented in aneurysm and in atherosclerosis
UTP--glucose-1-phosphate uridylyltransf	Q16851	UGP2	10.1074/mcp.M111.008128, 10.1074	2	Mass Spec	ascending		37.5	B	valve replacement	
UV excision repair protein RAD23 homol	P54727	RAD23B	10.1074/mcp.M111.008128, 10.1074	2	Mass Spec	ascending		37.5	B	valve replacement	
Vascular endothelial growth factor A	P15692	VEGFA	10.3349/ymj.2000.41.1.68, 10.1093/cvr/cvr080, 10.1093/cvr/cvu196	3	Immuno	ascending	intima;media	28, 64, 51	B		augmented or diminished in abdominal aneurysm and atherosclerosis
Vasodilator-stimulated phosphoprotein	P50552	VASP	10.1074/mcp.M111.008128, 10.1002	3	Mass Spec	ascending		37.5	B	valve replacement	
Versican core protein	P13611	VCAN	10.1002/prca.201200064, 10.1074/r	3	Mass Spec	ascending		37.5	B	valve replacement	decreased in abdominal aneurysm
Vimentin	P08670	VIM	10.1074/mcp.M112.021873, 10.1074/mcp.M111.008128, 10.1016/j.jvs.2011.10.033, 10.1016/j.ejcts.2009.07.025, 10.1002/prca.201200064, 10.1093/cvr/cvt205, 10.1074/mcp.M110.001693	7	Immuno;Mass Sp	abdominal, ascending	media	53.91, 59, 58, 53.91	B, M	valve replacement	not affected in abdominal aneurysm, thoracic aneurysm, decreased in aneurysm and increased in dissection
Vinculin	P18206	VCL	10.1074/mcp.M111.008128, 10.1002	3	Mass Spec	ascending		37.5	B	valve replacement	
Vinexin	O60504	SORBS3	10.1074/mcp.M111.008128, 10.1074	2	Mass Spec	ascending		37.5	B	valve replacement	
Vitamin D-binding protein	P02774	GC	10.1074/mcp.M111.008128, 10.116	4	Mass Spec	ascending		37.5,60	B	valve replacement	decreased in Marfan aneurysm
Vitronectin	P04004	VTN	10.1510/icvts.2010.238139, 10.1074	4	Immuno;Mass Sp	ascending	adventitia	37.5	B	valve replacement	10.1074/mcp.M111.008128 says there's no vitronectin in control ascending aorta
Voltage-dependent anion-selective chan	P21796	VDAC1	10.1074/mcp.M110.001693		Mass Spec	ascending				valve replacement	
Voltage-dependent anion-selective chan	P45880	VDAC2	10.1074/mcp.M110.001693		Mass Spec	ascending				valve replacement	
von Willebrand factor	P04275	VWF	10.1194/jlr.M042481, 10.1002/prca.	4	Immuno;Mass Sp	abdominal, ascend	adventitia;intima;r	56.3, 51	B		augmented in aneurysm
von Willebrand factor A domain-contain	Q6PCB0	VWA1	10.1074/mcp.M110.001693		Mass Spec	ascending				valve replacement	
WD repeat-containing protein 1	O75083	WDR1	10.1074/mcp.M111.008128, 10.1002	3	Mass Spec	ascending		37.5	B	valve replacement	
WNT1-inducible-signaling pathway prote	O76076	WISP2	10.1074/mcp.M110.001693		Mass Spec	ascending				valve replacement	
Xaa-Pro dipeptidase	P12955	PEPD	10.1186/1471-2350-12-14		Immuno		adventitia;media	73	M		
Zinc-alpha-2-glycoprotein	P25311	AZGP1	10.1074/mcp.M111.008128, 10.1074	2	Mass Spec	ascending		37.5	B	valve replacement	
Zyxin	Q15942	ZYX	10.1074/mcp.M111.008128, 10.1074	3	Mass Spec	ascending		37.5	B	valve replacement	

Appendix 2. Aortic Aneurysm Proteome list

AORTIC ANEURYSM PROTEOME

Protein Name	UniProt#	Gene Name	DOI or PMID	#DOI	Experimental Evidence	Aorta location	Wall Location	Age	Sex	Aneurysm cause	Relation to control
14-3-3 protein beta/alpha	P31946	YWHAB	10.1074/mcp.M112.021873		Mass Spec	ascending				BAV, unknown	unknown aneurysm higher than in control
14-3-3 protein epsilon	P62258	YWHAE	10.1074/mcp.M111.008128		Mass Spec	abdominal		>65	M		
14-3-3 protein gamma	P61981	YWHAG	10.1074/mcp.M111.008128		Mass Spec	abdominal		>65	M		
14-3-3 protein theta	P27348	YWHAQ	10.1074/mcp.M112.021873		Mass Spec	ascending				BAV, unknown	unknown aneurysm higher than in control
14-3-3 protein zeta/delta	P63104	YWHAZ	10.1074/mcp.M112.021873, 10.1074	2	Mass Spec	ascending, abdominal		>65	M	BAV,unknown	higher than in control
2,4-dienoyl-CoA reductase, mitochondria	Q16698	DECR1	10.1074/mcp.M111.008128		Mass Spec	abdominal		>65	M		not in healthy aorta proteome
40S ribosomal protein S16	P62249	RPS16	10.1074/mcp.M111.008128		Mass Spec	abdominal		>65	M		
40S ribosomal protein S19	P39019	RPS19	10.1074/mcp.M111.008128		Mass Spec	abdominal		>65	M		
40S ribosomal protein S25	P62851	RPS25	10.1074/mcp.M111.008128		Mass Spec	abdominal		>65	M		
40S ribosomal protein S3	P23396	RPS3	10.1074/mcp.M111.008128		Mass Spec	abdominal		>65	M		
40S ribosomal protein SA	P08865	RPSA	10.1074/mcp.M111.008128		Mass Spec	abdominal		>65	M		
60 kDa heat shock protein, mitochondria	P10809	HSPD1	10.1074/mcp.M111.008128		Mass Spec	abdominal		>65	M		
60S acidic ribosomal protein P0	P05388	RPLP0	10.1074/mcp.M111.008128		Mass Spec	abdominal		>65	M		
60S ribosomal protein L11	P62913	RPL11	10.1074/mcp.M111.008128		Mass Spec	abdominal		>65	M		
60S ribosomal protein L12	P30050	RPL12	10.1074/mcp.M111.008128		Mass Spec	abdominal		>65	M		
60S ribosomal protein L18	Q07020	RPL18	10.1074/mcp.M111.008128		Mass Spec	abdominal		>65	M		
60S ribosomal protein L23	P62829	RPL23	10.1074/mcp.M111.008128		Mass Spec	abdominal		>65	M		
60S ribosomal protein L30	P62888	RPL30	10.1074/mcp.M111.008128		Mass Spec	abdominal		>65	M		
60S ribosomal protein L7a	P62424	RPL7A	10.1074/mcp.M111.008128		Mass Spec	abdominal		>65	M		not in healthy aorta proteome
72 kDa type IV collagenase	P08253	MMP2	10.1159/000339304, 10.1016/j.jvs.2010.01.057, 10.1016/j.angio.2014.12.001, 10.1371/journal.pone.0070057, 10.1111/eci.12618, 10.1016/j.atherosclerosis.2013.10.035,10.1016/j.jtcvs.2009.07.075, 10.1016/j.jvs.2012.09.062 , 10.1016/S0002-9440(10)64447-1	10	Immuno	ascending, abdominal,thoracic	adventitia;inflamation regions;intima;media;thrombus;wall lysate	64,73,74, 67,71,63, 66.9	B,M	sporadic, unknown	higher than in control
78 kDa glucose-regulated protein	P11021	HSPA5	10.1139/Y09-085, 10.1074/mcp.M11	2	Immuno;Mass Spe	abdominal		>65,70	M,B		
Acid ceramidase	Q13510	ASAH1	10.1074/mcp.M111.008128		Mass Spec	abdominal		>65	M		not in healthy aorta proteome
Actin, alpha cardiac muscle 1	P68032	ACTC1	10.1007/s00595-012-0480-6, 10.107	2	Mass Spec	abdominal		68,>65	B,M		lower than in control
Actin, alpha skeletal muscle	P68133	ACTA1	10.1016/j.ejcts.2009.07.025, 10.1067/mva.2002.121124	2	Immuno;Mass Spe	ascending,abdominal		56,67.2	B,M		abdominal lower than in control, ascending higher
Actin, aortic smooth muscle	P62736	ACTA2	10.1161/ATVBAHA.114.304412, 10.1093/cvr/cvt205, 10.1093/cvr/cvu196, 10.1161/ATVBAHA.115.305529, 10.1111/j.1440-1827.2011.02699.x, 10.1042/CS20080235, 10.1016/j.atherosclerosis.2011.06.008, 10.1016/j.clinbiochem.2009.10.015, 10.1074/mcp.M111.008128	10	Immuno;Mass Spe	ascending,abdominal	media	73,41,63, 54,60,70, 48.3,>65	B,M	Marfan, BAV, unknown, non-Marfan non-BAV	same or lower than in control
Actin, cytoplasmic 1	P60709	ACTB	10.1016/j.jvs.2011.10.033, 10.1067/	5	Immuno;Mass Spe	abdominal		69,67.2,73	B,M	not Marfan	same as in control
Actin, gamma-enteric smooth muscle	P63267	ACTG2	10.1016/j.jvs.2008.08.097, 10.1016/	2	Mass Spec	abdominal,ascending		73.5,48.3	B	BAV, unknown	not in healthy proteome
Actin-related protein 2	P61160	ACTR2	10.1074/mcp.M111.008128		Mass Spec	abdominal		>65	M		
Actin-related protein 2/3 complex subun	O15143	ARPC1B	10.1074/mcp.M111.008128		Mass Spec	abdominal		>65	M		not in healthy proteome
Actin-related protein 2/3 complex subun	P59998	ARPC4	10.1074/mcp.M111.008128		Mass Spec	abdominal		>65	M		
Actin-related protein 3	P61158	ACTR3	10.1074/mcp.M111.008128		Mass Spec	abdominal		>65	M		
Adenylate kinase isoenzyme 1	P00568	AK1	10.1074/mcp.M111.008128		Mass Spec	abdominal		>65	M		
Adenylosuccinate lyase	P30566	ADSL	10.1074/mcp.M111.008128		Mass Spec	abdominal		>65	M		
Adenylyl cyclase-associated protein 1	Q01518	CAP1	10.1074/mcp.M111.008128		Mass Spec	abdominal		>65	M		
Adhesion G-protein coupled receptor G4	Q8IZF6	ADGRG4	10.1074/mcp.M111.008128		Mass Spec	abdominal		>65	M		not in healthy proteome
Adipocyte enhancer-binding protein 1	Q8IUX7	AEBP1	10.1074/mcp.M111.008128		Immuno;Mass Spe	abdominal	inflamation regions;media	>65	M		higher than in control
Aggrecan core protein	P16112	ACAN	10.1074/mcp.M111.008128		Mass Spec	abdominal		>65	M		lower than in control
Agrin	O00468	AGRN	10.1074/mcp.M111.008128		Mass Spec	abdominal		>65	M		same as in control
Alcohol dehydrogenase [NADP(+)]	P14550	AKR1A1	10.1074/mcp.M111.008128		Mass Spec	abdominal		>65	M		
Alcohol dehydrogenase 1B	P00325	ADH1B	10.1007/s00595-012-0480-6, 10.107	2	Mass Spec	abdominal		68,>65	B,M		lower than in control
Aldehyde dehydrogenase, mitochondrial	P05091	ALDH2	10.1016/j.jvs.2011.10.033	1	Mass Spec	abdominal		69	B	not Marfan, not inflammatory disease	lower than in control
Alpha-1-acid glycoprotein 1	P02763	ORM1	10.3892/ijmm.2012.985, 10.1074/m	2	Mass Spec	abdominal		>65	M		
Alpha-1-acid glycoprotein 2	P19652	ORM2	10.1074/mcp.M111.008128		Mass Spec	abdominal		>65	M		not in healthy proteome
Alpha-1-antichymotrypsin	P01011	SERPINA3	10.3892/ijmm.2012.994, 10.1074/m	2	Immuno;Mass Spe	abdominal	adventitia;intima	>65	M		lower than in control
Alpha-1-antitrypsin	P01009	SERPINA1	10.3892/ijmm.2012.985, 10.1016/j.atherosclerosis.2011.05.002, 10.1016/j.ejcts.2009.07.025, 10.1007/s00595-012-0480-6, 10.1074/mcp.M111.008128	5	Immuno;Mass Spe	ascending, abdominal	thrombus;wall lysate	70,56,68, >65	B,M		abdominal aneurysm higher than in control, ascending lower than or same as in control
Alpha-1B-glycoprotein	P04217	A1BG	10.1074/mcp.M111.008128		Mass Spec	abdominal		>65	M		
Alpha-2-antiplasmin	P08697	SERPINF2	10.1074/mcp.M111.008128		Mass Spec	abdominal		>65	M		
Alpha-2-HS-glycoprotein	P02765	AHSG	10.3892/ijmm.2012.985, 10.1074/m	2	Immuno;Mass Spe	abdominal,thoracic		>65	M		
Alpha-2-macroglobulin	P01023	A2M	10.1074/mcp.M111.008128		Mass Spec	abdominal		>65	M		
Alpha-actinin-1	P12814	ACTN1	10.3892/ijmm.2012.985, 10.1074/mcp.M112.021873, 10.1074/mcp.M111.008128	3	Mass Spec	ascending, thoracic,abdominal		>65	M	BAV, unknown	higher than in control, higher or lower than control when it is BAV aneurysm
Alpha-actinin-4	O43707	ACTN4	10.1074/mcp.M112.021873, 10.1016	3	Mass Spec	ascending, abdominal		48.3,>65	B,M	BAV, unknown	higher than in control
Alpha-crystallin B chain	P02511	CRYAB	10.3892/ijmm.2012.985	1	Mass Spec	thoracic					
Alpha-enolase	P06733	ENO1	10.3892/ijmm.2012.985, 10.1016/j.j	7	Mass Spec	ascending, thoracic,abdominal		69,56,68, 48.3,>65	B,M	not Marfan,BAV, unkown	lower or higher than in control or the same
Angiogenin	P03950	ANG	10.1016/j.jvs.2006.11.020, 10.3892/	2	Immuno;Mass Spe	thoracic,abdominal		74	M	unknown,atherosclerosis	same as in control
Angiopoietin-1	Q15389	ANGPT1	10.1093/cvr/cvu196	1	Immuno	ascending	adventitia;media	54	B	Marfan,BAV,degenerative	higher than in control
Angiopoietin-2	O15123	ANGPT2	10.1093/cvr/cvu196	1	Immuno	ascending	adventitia;media	54	B	Marfan,BAV,degenerative	higher than in control
Angiopoietin-related protein 2	Q9UKU9	ANGPTL2	10.1161/ATVBAHA.112.247866		Immuno	abdominal	inflamation regions	74	B		
Angiotensinogen	P01019	AGT	10.1016/j.atherosclerosis.2009.01.003		Immuno	abdominal		70.5	M		higher than in control
Ankyrin repeat domain-containing prote	Q9UPS8	ANKRD26	10.1074/mcp.M111.008128		Mass Spec	abdominal		>65	M		not in healthy proteome
Annexin A1	P04083	ANXA1	10.1074/mcp.M112.021873, 10.1074	2	Mass Spec	ascending, abdominal		>65	M	BAV, unknown	
Annexin A2	P07355	ANXA2	10.1016/j.jvs.2011.10.033, 10.1007/	3	Mass Spec	abdominal		69,68,>65	B,M	not Marfan	same as in control or lower
Annexin A4	P09525	ANXA4	10.1510/icvts.2010.238139, 10.1074	3	Mass Spec	ascending, abdominal		70,>65	B,M	BAV,unknown	
Annexin A5	P08758	ANXA5	10.1016/j.jvs.2011.10.033, 10.1074/	4	Mass Spec	ascending, abdominal		69,68,>65	B,M	not Marfan, BAV,unknown	lower than in control
Annexin A6	P08133	ANXA6	10.1074/mcp.M111.008128		Mass Spec	abdominal		>65	M		
Antithrombin-III	P01008	SERPINC1	10.1074/mcp.M111.008128		Mass Spec	abdominal		>65	M		
AP-2 complex subunit alpha-1	O95782	AP2A1	10.1074/mcp.M111.008128		Mass Spec	abdominal		>65	M		

Apolipoprotein A-I	P02647	APOA1	10.3892/ijmm.2012.985, 10.1510/icv	5	Mass Spec	ascending, abdominal		70,48.3,38,>65	B,M	Marfan, BAV, unknown	higher or lower than in control
Apolipoprotein A-II	P02652	APOA2	10.3892/ijmm.2012.985	1	Mass Spec	abdominal					not in healthy proteome
Apolipoprotein A-IV	P06727	APOA4	10.3892/ijmm.2012.985, 10.1074/m	2	Mass Spec	abdominal		>65	M		same as in control
Apolipoprotein B-100	P04114	APOB	10.3892/ijmm.2012.985, 10.1074/m	2	Mass Spec	abdominal		>65	M		higher than in control
Apolipoprotein C-III	P02656	APOC3	10.3892/ijmm.2012.985	1	Mass Spec	abdominal,thoracic					not in healthy proteome
Apolipoprotein D	P05090	APOD	10.1074/mcp.M111.008128		Mass Spec	abdominal		>65	M		higher than in control
Apolipoprotein E	P02649	APOE	10.3892/ijmm.2012.985, 10.1074/m	2	Mass Spec	abdominal,thoracic		>65	M		higher than in control
Apolipoprotein L1	O14791	APOL1	10.1074/mcp.M111.008128		Mass Spec	abdominal		>65	M		
Apolipoprotein(a)	P08519	LPA	10.3892/ijmm.2012.985	1	Mass Spec	abdominal					not in healthy proteome
Apoptosis regulator BAX	Q07812	BAX	10.1139/Y09-085	1	Immuno	abdominal		70	B		not in healthy proteome
Apoptosis regulator Bcl-2	P10415	BCL2	10.1139/Y09-085	1	Immuno	abdominal		70	B		not in healthy proteome
Arachidonate 5-lipoxygenase	P09917	ALOX5	10.1007/s00109-008-0413-4	1	Immuno	abdominal	media				not in healthy proteome
Armadillo repeat-containing X-linked pro	Q9P291	ARMCX1	10.1074/mcp.M111.008128		Mass Spec	abdominal		>65	M		not in healthy proteome
Asporin	Q9BXN1	ASPN	10.1074/mcp.M111.008128		Mass Spec	abdominal		>65	M		same as in control
Ataxin-7-like protein 1	Q9ULK2	ATXN7L1	10.1074/mcp.M111.008128		Mass Spec	abdominal		>65	M		not in healthy proteome
ATP synthase subunit alpha, mitochondri	P25705	ATP5A1	10.1074/mcp.M111.008128		Mass Spec	abdominal		>65	M		
ATP synthase subunit beta, mitochondria	P06576	ATP5B	10.1016/j.jvs.2011.10.033, 10.1074/	2	Mass Spec	abdominal		69,>65	B,M	not Marfan	same as in control
ATP synthase subunit gamma, mitochon	P36542	ATP5C1	10.1074/mcp.M111.008128		Mass Spec	abdominal		>65	M		
Band 3 anion transport protein	P02730	SLC4A1	10.3892/ijmm.2012.985	1	Mass Spec	abdominal					
Basement membrane-specific heparan s	P98160	HSPG2	10.1074/mcp.M111.008128		Mass Spec	abdominal		>65	M		lower than in control
Basigin	P35613	BSG	10.2353/ajpath.2009.080845, 10.10	3	Immuno	ascending,abdomi	intima;media	71,67,60	B,M	non-Marfan non-BAV, unknown	higher than in control
B-cell receptor CD22	P20273	CD22	10.1186/1471-2350-12-14	1	Immuno	abdominal	adventitia	73	M		not in healthy proteome
Bcl-2 homologous antagonist/killer	Q16611	BAK1	10.1139/Y09-085	1	Immuno	abdominal		70	B		not in healthy proteome
Beta-2-glycoprotein 1	P02749	APOH	10.3892/ijmm.2012.985, 10.1510/icv	3	Mass Spec	abdominal		70,>65	B,M		
Biglycan	P21810	BGN	10.3892/ijmm.2012.985, 10.1002/pa	3	Immuno;Mass Spe	ascending, abdomi	media	>65	M	Marfan,BAV,degenerative	same as in control
Biliverdin reductase A	P53004	BLVRA	10.1074/mcp.M111.008128		Mass Spec	abdominal		>65	M		
B-lymphocyte antigen CD20	P11836	MS4A1	10.1371/journal.pone.0053882, 10.1	9	Immuno	abdominal	adventitia	69,73,66,7	B,M	unknown, degenerative	not in healthy proteome
Brain acid soluble protein 1	P80723	BASP1	10.1074/mcp.M111.008128		Mass Spec	abdominal		>65	M		
BTB/POZ domain-containing protein KCT	Q96CX2	KCTD12	10.1074/mcp.M111.008128		Mass Spec	abdominal		>65	M		
C4b-binding protein alpha chain	P04003	C4BPA	10.1074/mcp.M111.008128		Mass Spec	abdominal		>65	M		not in healthy proteome
Cadherin-1	P12830	CDH1	10.1074/mcp.M111.008128		Mass Spec	abdominal		>65	M		
Cadherin-13	P55290	CDH13	10.1074/mcp.M111.008128		Mass Spec	abdominal		>65	M		
Caldesmon	Q05682	CALD1	10.3892/ijmm.2012.985, 10.1074/m	2	Mass Spec	abdominal,thoracic		>65	M		
Calmodulin	P62158	CALM1	10.1016/j.clinbiochem.2009.10.015, 10.1074/		Mass Spec	ascending, abdominal		48.3,>65	B,M	BAV, unknown	
Calpain-1 catalytic subunit	P07384	CAPN1	10.14670/HH-11-691	1	Immuno	ascending	media	64	B	not Marfan	higher than in control
Calpain-2 catalytic subunit	P17655	CAPN2	10.14670/HH-11-691, 10.1161/CIRCULATIONAHA.108.843516	2	Immuno	ascending	media	64,38,57	B	not Marfan, Marfan,BAV	same as in control
Calpastatin	P20810	CAST	10.14670/HH-11-691	1	Immuno	ascending	media	64	B	not Marfan	higher than in control
Calponin-1	P51911	CNN1	10.3892/ijmm.2012.985, 10.1161/AT	5	Immuno;Mass Spe	ascending, abdominal		41,48.3,38,>65	B,M	Marfan,BAV,unknown	higher than in control
Calponin-3	Q15417	CNN3	10.1074/mcp.M111.008128		Mass Spec	abdominal		>65	M		
Calreticulin	P27797	CALR	10.1510/icvts.2010.238139, 10.1016	3	Mass Spec	ascending, abdominal		70,48.3,>6	B,M	BAV,unknown	same as in control
Carbonic anhydrase 1	P00915	CA1	10.1074/mcp.M111.008128		Mass Spec	abdominal		>65	M		
Carbonic anhydrase 2	P00918	CA2	10.1074/mcp.M111.008128		Mass Spec	abdominal		>65	M		
Carbonic anhydrase 9	Q16790	CA9	10.3109/14017431.2016.1158416		Immuno	ascending		64	B		not in healthy proteome
Carbonyl reductase [NADPH] 1	P16152	CBR1	10.1074/mcp.M111.008128		Mass Spec	abdominal		>65	M		
Carboxypeptidase B2	Q96IY4	CPB2	10.3892/ijmm.2012.985	1	Mass Spec	abdominal					not in healthy proteome
Carcinoembryonic antigen-related cell a	P13688	CEACAM1	10.1016/j.atherosclerosis.2011.05.00	1	Immuno	abdominal	thrombus	70	B		not in healthy proteome
Carcinoembryonic antigen-related cell a	P31997	CEACAM8	10.1093/cvr/cvp048	1	Immuno	abdominal	adventitia;thrombus	70	M	degenerative	not in healthy proteome
Cartilage acidic protein 1	Q9NQ79	CRTAC1	10.1074/mcp.M111.008128		Mass Spec	abdominal		>65	M		not in healthy proteome
Cartilage oligomeric matrix protein	P49747	COMP	10.1074/mcp.M111.008128		Mass Spec	abdominal		>65	M		same as in control
Caspase-3	P42574	CASP3	10.1139/Y09-085, 10.1002/path.4534, 10.1016/j.jtcvs.2009.07.075	3	Immuno	ascending,abdominal		70	B	not connective disorders, unknown	higher than in control
Catalase	P04040	CAT	10.1074/mcp.M111.008128		Mass Spec	abdominal		>65	M		not in healthy proteome
Catenin alpha-1	P35221	CTNNA1	10.1074/mcp.M111.008128		Mass Spec	abdominal		>65	M		not in healthy proteome
Cathelicidin antimicrobial peptide	P49913	CAMP	10.1161/ATVBAHA.116.307786	1	Immuno	abdominal					not in healthy proteome
Cathepsin B	P07858	CTSB	10.1016/j.jvs.2007.08.015, 10.1074/	2	Immuno;Mass Spe	abdominal		73,>65	B,M		
Cathepsin D	P07339	CTSD	10.3892/ijmm.2012.985, 10.1016/j.atherosclerosis.2009.01.003, 10.1074/mcp.M111.008128	3	Immuno;Mass Spe	abdominal	adventitia;inflammation regions	70.5,>65	M		same as in control
Cathepsin G	P08311	CTSG	10.1016/j.atherosclerosis.2009.01.00	2	Immuno;Mass Spe	abdominal	adventitia;media	70.5,>65	M		higher than in control
Cathepsin K	P43235	CTSK	10.1371/journal.pone.0053882, 10.1	4	Immuno	abdominal		69,74,72.5	B		higher than in control
Cathepsin L1	P07711	CTSL	10.1016/j.jvs.2010.01.057, 10.2353/	4	Immuno	abdominal		74,72.5,73	B		higher than in control
Cathepsin S	P25774	CTSS	10.1371/journal.pone.0053882, 10.1	5	Immuno;Mass Spe	abdominal		69,74,72.5	B,M		higher than in control
C-C motif chemokine 15	Q16663	CCL15	10.1016/j.jvs.2006.11.020	1	Immuno	abdominal		74	M	atherosclerotic	same as in control
C-C motif chemokine 17	Q92583	CCL17	10.1016/j.jvs.2006.11.020	1	Immuno	abdominal		74	M	atherosclerotic	not in healthy proteome
C-C motif chemokine 2	P13500	CCL2	10.1371/journal.pone.0053882, 10.1159/000362997, 10.1016/j.jvs.2006.11.020, 10.1161/CIRCULATIONAHA.108.806505, 10.1007/s00109-008-0413-4, 10.1042/CS20070352, 10.1093/cvr/cvu196	7	Immuno	ascending, abdominal		69,69,74,73,72,54	B,M	unknown,atherosclerosis, Marfan,BAV,degenerative	higher than in control
C-C motif chemokine 22	O00626	CCL22	10.1016/j.jvs.2006.11.020	1	Immuno	abdominal		74	M	atherosclerotic	same as in control
C-C motif chemokine 3	P10147	CCL3	10.1371/journal.pone.0053882	1	Immuno	abdominal		69	B		
C-C motif chemokine 4	P13236	CCL4	10.1371/journal.pone.0053882, 10.1	3	Immuno	abdominal		69,73,72	B		not in healthy proteome
C-C motif chemokine 5	P13501	CCL5	10.1159/000362997, 10.1016/j.jvs.2	3	Immuno	abdominal	adventitia;thrombus	69,74,70	M,B	degenerative,atherosclerosis	higher than in control
C-C motif chemokine 7	P80098	CCL7	10.1016/j.jvs.2006.11.020	1	Immuno	abdominal		74	M	atherosclerotic	same as in control
C-C motif chemokine 8	P80075	CCL8	10.1016/j.jvs.2006.11.020	1	Immuno	abdominal		74	M	atherosclerotic	not in healthy proteome
CCAAT/enhancer-binding protein alpha	P49715	CEBPA	10.1161/CIRCULATIONAHA.108.8065	3	Immuno	abdominal		73,74,72	B,M		not in healthy proteome
CCAAT/enhancer-binding protein beta	P17676	CEBPB	10.1161/CIRCULATIONAHA.108.8065	3	Immuno	abdominal		73,74,72	B,M		not in healthy proteome
CCAAT/enhancer-binding protein delta	P49716	CEBPD	10.1161/CIRCULATIONAHA.108.8065	3	Immuno	abdominal		73,74,72	B,M		not in healthy proteome
CD5 antigen-like	O43866	CD5L	10.1074/mcp.M111.008128		Mass Spec	abdominal		>65	M		not in healthy proteome
Ceruloplasmin	P00450	CP	10.3892/ijmm.2012.985, 10.1074/m	2	Immuno;Mass Spe	abdominal		>65	M		higher than in control
Chloride intracellular channel protein 1	O00299	CLIC1	10.1074/mcp.M111.008128		Mass Spec	abdominal		>65	M		
Chloride intracellular channel protein 4	Q9Y696	CLIC4	10.1074/mcp.M112.021873		Mass Spec	ascending				BAV, unknown	
Chymase	P23946	CMA1	10.1161/CIRCULATIONAHA.109.8496	3	Immuno;Mass Spe	abdominal	adventitia;media	79,70.5,>65	B,M		higher than in control
Clathrin heavy chain 1	Q00610	CLTC	10.1074/mcp.M111.008128		Mass Spec	abdominal		>65	M		
Clusterin	P10909	CLU	10.1139/Y09-085, 10.3892/ijmm.201	3	Immuno;Mass Spe	abdominal		>65,70	M,B		higher than in control
Coagulation factor IX	P00740	F9	10.3892/ijmm.2012.985, 10.1074/m	2	Mass Spec	abdominal		>65	M		
Coagulation factor XIII B chain	P05160	F13B	10.1074/mcp.M111.008128		Mass Spec	abdominal		>65	M		not in healthy proteome
Cofilin-1	P23528	CFL1	10.1074/mcp.M111.008128		Mass Spec	abdominal		>65	M		
Coiled-coil domain-containing protein 80	Q76M96	CCDC80	10.1074/mcp.M111.008128		Mass Spec	abdominal		>65	M		not in healthy proteome
Cold-inducible RNA-binding protein	Q14011	CIRBP	10.1016/j.surg.2016.01.007	1	Immuno	abdominal	media	62	B		higher than in control
Collagen alpha-1(I) chain	P02452	COL1A1	10.3892/ijmm.2012.985, 10.1016/j.e	5	Immuno;Mass Spe	ascending,thoracic	media	>65,41,70	M,B	unknown, Marfan	same as or lower than in control
Collagen alpha-1(III) chain	P02461	COL3A1	10.3892/ijmm.2012.985, 10.1016/j.e	5	Immuno;Mass Spe	ascending,abdominal		>65,63,70	M,B	not Marfan, not BAV, unknown	lower or higher than in control
Collagen alpha-1(IV) chain	P02462	COL4A1	16377578, 10.1074/mcp.M111.0081	2	Immuno;Mass Spe	abdominal,ascending		>65,56	M,B	unknown,BAV	same as in control
Collagen alpha-1(VI) chain	P12109	COL6A1	10.1074/mcp.M111.008128		Mass Spec	abdominal		>65	M		same as in control
Collagen alpha-1(VII) chain	Q02388	COL7A1	10.1074/mcp.M111.008128		Mass Spec	abdominal		>65	M		not in healthy proteome
Collagen alpha-1(VIII) chain	P27658	COL8A1	10.1074/mcp.M111.008128		Mass Spec	abdominal		>65	M		same as in control
Collagen alpha-1(XI) chain	P12107	COL11A1	10.1016/j.athoracsur.2009.04.030		Immuno	ascending					higher than in control
Collagen alpha-1(XII) chain	Q99715	COL12A1	10.1074/mcp.M111.008128		Immuno;Mass Spe	abdominal		>65	M		higher than in control

Collagen alpha-1(XIV) chain	Q05707	COL14A1	10.3892/ijmm.2012.985, 10.1074/m	2	Mass Spec	abdominal		>65	M		lower than in control
Collagen alpha-1(XV) chain	P39059	COL15A1	10.1074/mcp.M111.008128		Mass Spec	abdominal		>65	M		same as in control
Collagen alpha-1(XVIII) chain	P39060	COL18A1	10.1074/mcp.M111.008128		Mass Spec	abdominal		>65	M		lower than in control
Collagen alpha-1(XXI) chain	Q96P44	COL21A1	10.1074/mcp.M111.008128		Mass Spec	abdominal		>65	M		not in healthy proteome
Collagen alpha-2(I) chain	P08123	COL1A2	10.3892/ijmm.2012.985, 10.1016/j.e	6	Immuno;Mass Spe	abdominal, thoraci	media	>65,72.5,7	B, M	unknown, Marfan	higher or lower than in control
Collagen alpha-2(IV) chain	P08572	COL4A2	10.1155/2014/760694, 10.1074/mcp	2	Immuno;Mass Spe	ascending,abdominal		>65	M	Marfan&related, unknown	same as in control
Collagen alpha-2(V) chain	P05997	COL5A2	10.1016/j.athoracsur.2009.04.030, 1	2	Immuno;Mass Spe	ascending,abdominal		>65	M		higher than in control
Collagen alpha-2(VI) chain	P12110	COL6A2	10.1007/s00595-012-0480-6, 10.107	2	Mass Spec	abdominal		68,>65	B,M		same as in control or higher
Collagen alpha-2(VIII) chain	P25067	COL8A2	10.1074/mcp.M111.008128		Mass Spec	abdominal		>65	M		same as in control
Collagen alpha-2(XI) chain	P13942	COL11A2	10.1016/j.clinbiochem.2009.10.015,	2	Mass Spec	ascending, abdominal		48.3,>65	B,M	BAV,unknown	not in healthy proteome
Collagen alpha-3(VI) chain	P12111	COL6A3	10.1510/icvts.2010.238139, 10.1074	2	Mass Spec	abdominal		70,>65	M		higher than in control
Collagen alpha-4(IV) chain	P53420	COL4A4	10.1074/mcp.M111.008128		Mass Spec	abdominal		>65	M		not in healthy proteome
Collagenase 3	P45452	MMP13	10.1159/000228900, 10.1016/j.atherosclerosis.2011.05.002, 10.1007/s10016-004-0050-5, 10.2353/ajpath.2009.080845, 10.2353/ajpath.2007.060522	4	Immuno	abdominal	inflamation regions;intima;media;thrombus	71,70,71, 72.5	B,M		
Complement C1q subcomponent subuni	P02746	C1QB	10.1074/mcp.M111.008128		Mass Spec	abdominal		>65	M		
Complement C1q subcomponent subuni	P02747	C1QC	10.3892/ijmm.2012.985, 10.1074/m	2	Mass Spec	abdominal,thoracic		>65	M		
Complement C1q tumor necrosis factor-	Q9BXJ1	C1QTNF1	10.1093/eurheartj/ehv649	1	Immuno	thoracic					
Complement C1r subcomponent	P00736	C1R	10.1074/mcp.M111.008128		Mass Spec	abdominal		>65	M		
Complement C1s subcomponent	P09871	C1S	10.1074/mcp.M111.008128		Mass Spec	abdominal		>65	M		
Complement C2	P06681	C2	10.1074/mcp.M111.008128		Mass Spec	abdominal		>65	M		not in healthy proteome
Complement C3	P01024	C3	10.3892/ijmm.2012.985, 10.1074/m	2	Mass Spec	abdominal,thoracic		>65	M		
Complement C4-A	P0C0L4	C4A	10.1074/mcp.M111.008128		Mass Spec	abdominal		>65	M		
Complement C5	P01031	C5	10.1074/mcp.M111.008128		Mass Spec	abdominal		>65	M		
Complement component C6	P13671	C6	10.1074/mcp.M111.008128		Mass Spec	abdominal		>65	M		
Complement component C7	P10643	C7	10.1074/mcp.M111.008128		Mass Spec	abdominal		>65	M		not in healthy proteome
Complement component C8 alpha chain	P07357	C8A	10.1074/mcp.M111.008128		Mass Spec	abdominal		>65	M		not in healthy proteome
Complement component C8 beta chain	P07358	C8B	10.1074/mcp.M111.008128		Mass Spec	abdominal		>65	M		
Complement component C8 gamma cha	P07360	C8G	10.1074/mcp.M111.008128		Mass Spec	abdominal		>65	M		
Complement component C9	P02748	C9	10.3892/ijmm.2012.985, 10.1074/m	2	Mass Spec	abdominal		>65	M		
Complement factor B	P00751	CFB	10.1074/mcp.M111.008128		Mass Spec	abdominal		>65	M		
Complement factor D	P00746	CFD	10.1074/mcp.M111.008128		Mass Spec	abdominal		>65	M		not in healthy proteome
Complement factor H	P08603	CFH	10.1074/mcp.M111.008128		Mass Spec	abdominal		>65	M		
Complement factor H-related protein 1	Q03591	CFHR1	10.1074/mcp.M111.008128		Mass Spec	abdominal		>65	M		
Complement factor H-related protein 2	P36980	CFHR2	10.1074/mcp.M111.008128		Mass Spec	abdominal		>65	M		not in healthy aorta proteome
Complement factor H-related protein 5	Q9BXR6	CFHR5	10.1074/mcp.M111.008128		Mass Spec	abdominal		>65	M		not in healthy proteome
Complement factor I	P05156	CFI	10.1074/mcp.M111.008128		Mass Spec	abdominal		>65	M		not in healthy proteome
Connective tissue growth factor	P29279	CTGF	10.1177/1708538112472282, 10.101	3	Immuno	ascending	media	63,64	B	unkwnown, non-syndromic TAAD, not BAV	higher than in control
Core histone macro-H2A.1	O75367	H2AFY	10.1074/mcp.M111.008128		Mass Spec	abdominal		>65	M		not in healthy proteome
Cortactin-binding protein 2	Q8WZ74	CTTNBP2	10.1074/mcp.M111.008128		Mass Spec	abdominal		>65	M		not in healthy proteome
C-reactive protein	P02741	CRP	10.1159/000362997	1	Immuno	abdominal		69	B		higher than in control
C-type lectin domain family 11 member	Q9Y240	CLEC11A	10.1074/mcp.M111.008128		Mass Spec	abdominal		>65	M		same as in control
C-type lectin domain family 4 member C	Q8WTT0	CLEC4C	10.1161/ATVBAHA.116.307786	1	Immuno	abdominal					not in healthy proteome
C-X-C motif chemokine 10	P02778	CXCL10	10.1371/journal.pone.0053882	1	Immuno	abdominal		69	B		not in healthy proteome
C-X-C motif chemokine 5	P42830	CXCL5	10.1016/j.jvs.2006.11.020	1	Immuno	abdominal		74	M	atherosclerotic	not in healthy proteome
Cyclic AMP-dependent transcription fact	P18848	ATF4	10.1002/path.4534	1	Immuno	thoracic				not connective disorders	not in healthy proteome
Cystatin-A	P01040	CSTA	10.1016/j.jvs.2007.08.015		Immuno	abdominal		73	B		not in healthy proteome
Cystatin-B	P04080	CSTB	10.1016/j.jvs.2007.08.015, 10.1074/	2	Immuno;Mass Spe	abdominal		73,>65	B,M		
Cystatin-C	P01034	CST3	10.1016/j.jvs.2008.09.055, 10.2353/	4	Immuno	abdominal		75,72.5,71	B		lower than in control
Cysteine and glycine-rich protein 1	P21291	CSRP1	10.3892/ijmm.2012.985, 10.1007/s0	2	Mass Spec	abdominal,thoracic		68,>65	B,M		lower than in control
Cysteine and glycine-rich protein 2	Q16527	CSRP2	10.1074/mcp.M111.008128		Mass Spec	abdominal		>65	M		
Cysteine-rich protein 2	P52943	CRIP2	10.1074/mcp.M111.008128		Mass Spec	abdominal		>65	M		
Cytochrome P450 1A1	P04798	CYP1A1	10.1055/s-0034-1367735	1	Immuno		media	61	B	not BAV, not connective tissue disorder	higher than in control
Cytochrome P450 2C19	P33261	CYP2C19	10.1074/mcp.M111.008128		Mass Spec	abdominal		>65	M		not in healthy proteome
Cytosol aminopeptidase	P28838	LAP3	10.1074/mcp.M111.008128		Mass Spec	abdominal		>65	M		
Decorin	P07585	DCN	10.3892/ijmm.2012.985, 10.1002/pa	3	Immuno;Mass Spe	ascending, abdomi	adventitia;intima;media	>65	M	Marfan,BAV,degenerative	higher than in control or the same
Dedicator of cytokinesis protein 9	Q9BZ29	DOCK9	10.1074/mcp.M111.008128		Mass Spec	abdominal		>65	M		
Delta-aminolevulinic acid dehydratase	P13716	ALAD	10.1074/mcp.M111.008128		Mass Spec	abdominal		>65	M		not in healthy proteome
Dermatopontin	Q07507	DPT	10.3892/ijmm.2012.985, 10.1074/m	2	Mass Spec	abdominal,thoracic		>65	M		same as in control
Desmin	P17661	DES	10.1159/000339304	1	Immuno	abdominal		73	B		lower than in control
Desmoplakin	P15924	DSP	10.1074/mcp.M111.008128		Mass Spec	abdominal		>65	M		
Destrin	P60981	DSTN	10.1007/s00595-012-0480-6, 10.107	2	Mass Spec	abdominal		68,>65	B,M		lower than in control
Dihydropyrimidinase-related protein 2	Q16555	DPYSL2	10.1074/mcp.M111.008128		Mass Spec	abdominal		>65	M		
Dihydropyrimidinase-related protein 3	Q14195	DPYSL3	10.1074/mcp.M111.008128		Mass Spec	abdominal		>65	M		
Disintegrin and metalloproteinase doma	P78536	ADAM17	10.1042/CS20030189, 10.1016/j.ath	2	Immuno	abdominal		72,70	B		not in healthy proteome
DNA damage-inducible transcript 3 protein	P35638	DDIT3	10.1002/path.4534	1	Immuno	thoracic				not connective disorders	not in healthy proteome
Dual specificity mitogen-activated protein kinase kinase 1	Q02750	MAP2K1	10.1016/j.jamcollsurg.2012.06.414	1	Immuno	abdominal					more phosphorilated in abdominal aneurysm than control
Dual specificity mitogen-activated protein kinase kinase 2	P36507	MAP2K2	10.1016/j.jamcollsurg.2012.06.414	1	Immuno	abdominal					more phosphorilated in abdominal aneurysm than control
Dynein heavy chain 2, axonemal	Q9P225	DNAH2	10.1074/mcp.M111.008128		Mass Spec	abdominal		>65	M		not in healthy proteome
E3 ubiquitin-protein ligase HUWE1	Q7Z6Z7	HUWE1	10.1074/mcp.M111.008128		Mass Spec	abdominal		>65	M		not in healthy proteome
E3 ubiquitin-protein ligase PDZRN3	Q9UPQ7	PDZRN3	10.1074/mcp.M111.008128		Mass Spec	abdominal		>65	M		not in healthy proteome
E3 ubiquitin-protein ligase UBR4	Q5T4S7	UBR4	10.1074/mcp.M111.008128		Mass Spec	abdominal		>65	M		not in healthy proteome
Ecto-NOX disulfide-thiol exchanger 2	Q16206	ENOX2	10.1074/mcp.M111.008128		Mass Spec	abdominal		>65	M		not in healthy proteome
EF-hand domain-containing protein D2	Q96C19	EFHD2	10.1074/mcp.M111.008128		Mass Spec	abdominal		>65	M		
EGF-containing fibulin-like extracellular	Q12805	EFEMP1	10.1074/mcp.M111.008128		Mass Spec	abdominal		>65	M		Same as control
EGF-like repeat and discoidin I-like doma	O43854	EDIL3	10.1074/mcp.M111.008128		Mass Spec	abdominal		>65	M		not in healthy proteome
EH domain-containing protein 2	Q9NZN4	EHD2	10.3892/ijmm.2012.985	1	Mass Spec	thoracic					
Elastin	P15502	ELN	10.1016/j.ejvs.2015.03.021, 10.1016/j.jvs.2012.09.062	2	Immuno	abdominal	media	70,66.9	B,M		ruptured aneurysm has less elastin than control
Elongation factor 1-alpha 1	P68104	EEF1A1	10.1074/mcp.M111.008128		Mass Spec	abdominal		>65	M		
Elongation factor 1-gamma	P26641	EEF1G	10.1074/mcp.M111.008128		Mass Spec	abdominal		>65	M		
Elongation factor 2	P13639	EEF2	10.1074/mcp.M111.008128		Mass Spec	abdominal		>65	M		
EMILIN-1	Q9Y6C2	EMILIN1	10.1074/mcp.M111.008128		Mass Spec	abdominal		>65	M		same as in control
Endoglin	P17813	ENG	10.1093/cvr/cvu196	1	Immuno	ascending	adventitia	54	B	Marfan,BAV,degenerative	lower than in control
Endoplasmin	P14625	HSP90B1	10.1074/mcp.M112.021873, 10.1007	3	Mass Spec	ascending, abdominal		68,>65	B,M	BAV, unknown	higher than in control
Eosinophil cationic protein	P12724	RNASE3	10.1074/mcp.M111.008128		Mass Spec	abdominal		>65	M		not in healthy proteome
Ephrin type-A receptor 5	P54756	EPHA5	10.1074/mcp.M111.008128		Mass Spec	abdominal		>65	M		not in healthy proteome
Epidermal growth factor	Q6QBS2	EGF	10.1016/j.jvs.2006.11.020	1	Immuno	abdominal		74	M	atherosclerotic	same as in control
ETS domain-containing protein Elk-1	P19419	ELK1	10.1093/cvr/cvt205	1	Immuno	ascending		63	B		not in healthy proteome
Extracellular superoxide dismutase [Cu-2	P08294	SOD3	10.1074/mcp.M111.008128		Immuno;Mass Spe	abdominal		>65	M		lower than in control
F-actin-capping protein subunit alpha-1	P52907	CAPZA1	10.1074/mcp.M111.008128		Mass Spec	abdominal		>65	M		
F-actin-capping protein subunit beta	P47756	CAPZB	10.1074/mcp.M111.008128		Mass Spec	abdominal		>65	M		
F-box/LRR-repeat protein 19	Q6PCT2	FBXL19	10.1074/mcp.M111.008128		Mass Spec	abdominal		>65	M		not in healthy proteome
Ferritin heavy chain	P02794	FTH1	10.1074/mcp.M111.008128		Mass Spec	abdominal		>65	M		
Ferritin light chain	P02792	FTL	10.1074/mcp.M111.008128		Mass Spec	abdominal		>65	M		
Ferritin, mitochondrial	Q8N4E7	FTMT	10.1159/000362997	1	Immuno	abdominal		69	B		higher than in control

Fibrillin-1	P35555	FBN1	10.1074/mcp.M111.008128	1	Mass Spec	abdominal		>65	M		higher than in control
Fibrinogen alpha chain	P02671	FGA	10.3892/ijmm.2012.985, 10.1074/m	2	Mass Spec	abdominal,thoracic		>65	M		
Fibrinogen beta chain	P02675	FGB	10.3892/ijmm.2012.985, 10.1510/icv	4	Mass Spec	abdominal,thoracic		70,>65	B,M		
Fibrinogen gamma chain	P02679	FGG	10.3892/ijmm.2012.985, 10.1074/m	4	Mass Spec	ascending,thoracic,abdominal		68,>65	B,M	BAV,unknown	unknown aneurysm higher than in control
Fibroblast growth factor 1	P05230	FGF1	10.1093/cvr/cvu196	1	Immuno	ascending	media	54	B	Marfan,BAV,degenerative	higher than in control
Fibrocystin	P08F94	PKHD1	10.1074/mcp.M111.008128		Mass Spec	abdominal		>65	M		not in healthy proteome
Fibromodulin	Q06828	FMOD	10.1074/mcp.M111.008128		Mass Spec	abdominal		>65	M		same as in control
Fibronectin	P02751	FN1	10.1016/j.ijcard.2011.08.079, 10.101	3	Immuno;Mass Spe	abdominal,ascendi	media	>65	M		higher than in control
Fibulin-1	P23142	FBLN1	10.1074/mcp.M111.008128		Mass Spec	abdominal		>65	M		lower than in control
Fibulin-5	Q9UBX5	FBLN5	10.3892/ijmm.2012.985, 10.1093/cv	3	Immuno;Mass Spe	abdominal,thoracic		70,>65	M		lower than in control
Ficolin-3	O75636	FCN3	10.1074/mcp.M111.008128		Mass Spec	abdominal		>65	M		not in healthy proteome
Filamin-A	P21333	FLNA	10.3892/ijmm.2012.985, 10.1161/CI	3	Immuno;Mass Spe	ascending, abdominal		38,>65	B,M	Marfan	higher than in control
Filamin-B	O75369	FLNB	10.1074/mcp.M111.008128		Mass Spec	abdominal		>65	M		not in healthy proteome
Filamin-binding LIM protein 1	Q8WUP2	FBLIM1	10.1074/mcp.M112.021873, 10.107	2	Mass Spec	ascending, abdominal		>65	M	BAV,unknown	BAV higher than in control
Filamin-C	Q14315	FLNC	10.1074/mcp.M111.008128		Mass Spec	abdominal		>65	M		
Four and a half LIM domains protein 1	Q13642	FHL1	10.1074/mcp.M111.008128		Mass Spec	abdominal		>65	M		
Four and a half LIM domains protein 2	Q14192	FHL2	10.1074/mcp.M111.008128		Mass Spec	abdominal		>65	M		
Fructose-bisphosphate aldolase A	P04075	ALDOA	10.1074/mcp.M111.008128		Mass Spec	abdominal		>65	M		
Fructose-bisphosphate aldolase C	P09972	ALDOC	10.1161/CIRCULATIONAHA.108.843516		Mass Spec	ascending		38	B	Marfan	lower than in control
Galectin-1	P09382	LGALS1	10.1074/mcp.M112.021873, 10.1016	3	Mass Spec	ascending, abdominal		48.3,>65	B,M	BAV,unknown	same as in control or higher
Galectin-3	P17931	LGALS3	10.1016/j.atherosclerosis.2011.06.00	2	Immuno;Mass Spe	abdominal		70,>65	B,M		
Galectin-3-binding protein	Q08380	LGALS3BP	10.1074/mcp.M111.008128		Mass Spec	abdominal		>65	M		same as in control
GATOR complex protein NPRL2	Q8WTW4	NPRL2	10.1074/mcp.M111.008128		Mass Spec	abdominal		>65	M		not in healthy proteome
Gelsolin	P06396	GSN	10.1074/mcp.M112.021873, 10.107	2	Mass Spec	ascending, abdominal		>65	M	BAV,unknown	higher than in control
Glia-derived nexin	P07093	SERPINE2	10.1161/ATVBAHA.113.301327, 10.1	2	Immuno;Mass Spe	ascending, abdomi	media	55, >65	B, M	Marfan, BAV, degenerative	higher than in control
Glucose-6-phosphate isomerase	P06744	GPI	10.1074/mcp.M111.008128		Mass Spec	abdominal		>65	M		
Glutamate dehydrogenase 1, mitochond	P00367	GLUD1	10.1074/mcp.M111.008128		Mass Spec	abdominal		>65	M		
Glutathione peroxidase 1	P07203	GPX1	10.1074/mcp.M111.008128		Mass Spec	abdominal		>65	M		not in healthy proteome
Glutathione peroxidase 3	P22352	GPX3	10.1074/mcp.M111.008128		Mass Spec	abdominal		>65	M		
Glutathione S-transferase omega-1	P78417	GSTO1	10.1074/mcp.M111.008128		Mass Spec	abdominal		>65	M		
Glutathione S-transferase P	P09211	GSTP1	10.3892/ijmm.2012.985, 10.1055/s-0034-1367735	2	Immuno;Mass Spe	thoracic	media	61	B	not BAV, not connective tissue disorder	higher than in control
Glyceraldehyde-3-phosphate dehydroge	P04406	GAPDH	10.1093/cvr/cvt205, 10.1016/j.jvs.20	7	Immuno;Mass Spe	ascending, abdominal		63,69,70, 68,>65	B,M	not Marfan,BAV, unknown	lower or higher than in control or the same
Glycogenin-1	P46976	GYG1	10.1074/mcp.M111.008128		Mass Spec	abdominal		>65	M		
Granulins	P28799	GRN	10.1074/mcp.M111.008128		Mass Spec	abdominal		>65	M		not in healthy proteome
Granulocyte colony-stimulating factor	P09919	CSF3	10.1371/journal.pone.0053882, 10.1	4	Immuno	abdominal		69,74,73,7	B,M	unknown,atherosclerosis	not in healthy proteome
Granulocyte-macrophage colony-stimula	P04141	CSF2	10.1016/j.jvs.2006.11.020, 10.1161/	3	Immuno	abdominal		74,73,72	B,M	unknown,atherosclerosis	not in healthy proteome
Granzyme A	P12544	GZMA	10.1161/CIRCULATIONAHA.108.8065	1	Immuno	abdominal		73	B		not in healthy proteome
Group 10 secretory phospholipase A2	O15496	PLA2G10	10.1016/j.atherosclerosis.2010.08.05	1	Immuno	abdominal					
Growth/differentiation factor 15	Q99988	GDF15	10.1159/000362997	1	Immuno	abdominal		69	B		higher than in control
Growth-regulated alpha protein	P09341	CXCL1	10.1016/j.jvs.2006.11.020	1	Immuno	abdominal		74	M	atherosclerotic	not in healthy proteome
Guanine nucleotide-binding protein G(I)	P62873	GNB1	10.1074/mcp.M111.008128		Mass Spec	abdominal		>65	M		
Guanine nucleotide-binding protein G(I)	P62879	GNB2	10.1074/mcp.M111.008128		Mass Spec	abdominal		>65	M		
Guanine nucleotide-binding protein G(o	P09471	GNAO1	10.1074/mcp.M111.008128		Mass Spec	abdominal		>65	M		
Haptoglobin	P00738	HP	10.3892/ijmm.2012.985, 10.1074/m	2	Mass Spec	abdominal		>65	M		
Haptoglobin-related protein	P00739	HPR	10.1074/mcp.M111.008128		Mass Spec	abdominal		>65	M		not in healthy proteome
Heat shock 70 kDa protein 1A	P0DMV8	HSPA1A	10.1074/mcp.M111.008128		Mass Spec	abdominal		>65	M		
Heat shock cognate 71 kDa protein	P11142	HSPA8	10.1074/mcp.M111.008128		Mass Spec	abdominal		>65	M		
Heat shock protein beta-1	P04792	HSPB1	10.3892/ijmm.2012.985, 10.1074/m	4	Mass Spec	ascending, abdominal		48.3,>65	B,M	BAV, unknown	
Heat shock protein beta-6	O14558	HSPB6	10.3892/ijmm.2012.985	1	Mass Spec	thoracic					
Heat shock protein HSP 90-alpha	P07900	HSP90AA1	10.1074/mcp.M111.008128		Mass Spec	abdominal		>65	M		
Heat shock protein HSP 90-beta	P08238	HSP90AB1	10.1074/mcp.M111.008128		Mass Spec	abdominal		>65	M		
Hematopoietic progenitor cell antigen C	P28906	CD34	10.1159/000439169		Immuno	abdominal	adventitia	70.2	B		
Heme oxygenase 1	P09601	HMOX1	10.1016/j.ijcard.2015.08.053	1	Immuno	abdominal	adventitia				not in healthy proteome
Hemoglobin subunit alpha	P69905	HBA1 , HBA2	10.1074/mcp.M112.021873, 10.116	3	Mass Spec	ascending,abdominal		38,>65	B,M	Marfan,unknown	lower than in control
Hemoglobin subunit beta	P68871	HBB	10.3892/ijmm.2012.985, 10.1074/m	5	Mass Spec	ascending, thoracic,abdominal		48.3,38,>6	B,M	Marfan,BAV,unknown	lower than in control
Hemoglobin subunit delta	P02042	HBD	10.1074/mcp.M112.021873, 10.107	2	Mass Spec	abdominal		>65	M	BAV,unknown	lower than in control
Hemopexin	P02790	HPX	10.1074/mcp.M111.008128		Mass Spec	abdominal		>65	M		
Heparin cofactor 2	P05546	SERPIND1	10.1074/mcp.M111.008128		Mass Spec	abdominal		>65	M		
Hepatocyte growth factor	P14210	HGF	10.1016/j.atherosclerosis.2011.02.025, 10.1093/cvr/cvu196	2	Immuno	ascending,abdominal	adventitia;intima;media;thrombus	54	B	Marfan,BAV,degenerative	lower than in control
Heterogeneous nuclear ribonucleoprote	Q14103	HNRNPD	10.1074/mcp.M111.008128		Mass Spec	abdominal		>65	M		
Heterogeneous nuclear ribonucleoprote	P31943	HNRNPH1	10.1074/mcp.M111.008128		Mass Spec	abdominal		>65	M		not in healthy proteome
Heterogeneous nuclear ribonucleoprote	P52272	HNRNPM	10.1074/mcp.M111.008128		Mass Spec	abdominal		>65	M		
Heterogeneous nuclear ribonucleoprote	O43390	HNRNPR	10.1074/mcp.M111.008128		Mass Spec	abdominal		>65	M		
Heterogeneous nuclear ribonucleoprote	P22626	HNRNPA2B1	10.1074/mcp.M111.008128		Mass Spec	abdominal		>65	M		
Heterogeneous nuclear ribonucleoprote	P07910	HNRNPC	10.1074/mcp.M111.008128		Mass Spec	abdominal		>65	M		
High mobility group protein HMG-I/HMG	P17096	HMGA1	10.1074/mcp.M111.008128		Mass Spec	abdominal		>65	M		not in healthy proteome
Histidine-rich glycoprotein	P04196	HRG	10.1074/mcp.M111.008128		Mass Spec	abdominal		>65	M		
Histone H1.2	P16403	HIST1H1C	10.1074/mcp.M111.008128		Mass Spec	abdominal		>65	M		
Histone H1.4	P10412	HIST1H1E	10.1074/mcp.M111.008128		Mass Spec	abdominal		>65	M		
Histone H1.5	P16401	HIST1H1B	10.1074/mcp.M111.008128		Mass Spec	abdominal		>65	M		
Histone H1x	Q92522	H1FX	10.1074/mcp.M111.008128		Mass Spec	abdominal		>65	M		not in healthy proteome
Histone H2A type 1-D	P20671	HIST1H2AD	10.1074/mcp.M111.008128		Mass Spec	abdominal		>65	M		not in healthy proteome
Histone H2B type 1-B	P33778	HIST1H2BB	10.1074/mcp.M111.008128		Mass Spec	abdominal		>65	M		
Histone H2B type 1-C/E/F/G/I	P62807	HIST1H2BC	10.1074/mcp.M111.008128		Mass Spec	abdominal		>65	M		
Histone H4	P62805	HIST1H4A	10.3892/ijmm.2012.985, 10.1074/m	2	Mass Spec	abdominal,thoracic		>65	M		
HLA class II histocompatibility antigen, D	P01903	HLA-DRA	10.1074/mcp.M111.008128		Mass Spec	abdominal		>65	M		not in healthy proteome
HLA class II histocompatibility antigen, D	P04229	HLA-DRB1	10.1074/mcp.M111.008128		Mass Spec	abdominal		>65	M		not in healthy proteome
Hsc70-interacting protein	P50502	ST13	10.1074/mcp.M111.008128		Mass Spec	abdominal		>65	M		
Hyaluronan and proteoglycan link protei	P10915	HAPLN1	10.1074/mcp.M111.008128		Mass Spec	abdominal		>65	M		same as in control
Hypoxia-inducible factor 1-alpha	Q16665	HIF1A	10.1371/journal.pone.0089830, 10.1	2	Immuno	abdominal	inflamation regions;intima;media	69	B		
IgGFc-binding protein	Q9Y6R7	FCGBP	10.1074/mcp.M111.008128		Mass Spec	abdominal		>65	M		not in healthy proteome
Immunoglobulin heavy constant alpha 1	P01876	IGHA1	10.1074/mcp.M111.008128		Mass Spec	abdominal		>65	M		
Immunoglobulin heavy constant alpha 2	P01877	IGHA2	10.1007/s00595-012-0480-6		Mass Spec	abdominal		68	B		higher than in control (atherosclerotic)
Immunoglobulin heavy constant delta	P01880	IGHD	10.1074/mcp.M111.008128		Mass Spec	abdominal		>65	M		not in healthy proteome
Immunoglobulin heavy constant gamma	P01857	IGHG1	10.1007/s00595-012-0480-6, 10.107	2	Mass Spec	abdominal		68,>65	B,M		higher than in control
Immunoglobulin heavy constant gamma	P01859	IGHG2	10.1074/mcp.M111.008128		Mass Spec	abdominal		>65	M		
Immunoglobulin heavy constant gamma	P01860	IGHG3	10.1074/mcp.M111.008128		Mass Spec	abdominal		>65	M		
Immunoglobulin heavy constant gamma	P01861	IGHG4	10.1016/j.jvs.2010.06.072, 10.1074/mcp.M111.008128	2	Immuno;Mass Spe	abdominal,thoracic	adventitia	>65	M	unknown,degenerative,atherosclerosis	not in healthy proteome
Immunoglobulin heavy constant mu	P01871	IGHM	10.1074/mcp.M111.008128		Mass Spec	abdominal		>65	M		
Immunoglobulin heavy variable 3-13	P01766	IGHV3-13	10.1074/mcp.M111.008128		Mass Spec	abdominal		>65	M		
Immunoglobulin heavy variable 3-23	P01764	IGHV3-23	10.1074/mcp.M111.008128		Mass Spec	abdominal		>65	M		not in healthy proteome
Immunoglobulin heavy variable 3-33	P01772	IGHV3-33	10.1074/mcp.M111.008128		Mass Spec	abdominal		>65	M		not in healthy proteome
Immunoglobulin heavy variable 3-7	P01780	IGHV3-7	10.1074/mcp.M111.008128		Mass Spec	abdominal		>65	M		not in healthy proteome
Immunoglobulin J chain	P01591	JCHAIN	10.1074/mcp.M111.008128		Mass Spec	abdominal		>65	M		not in healthy proteome
Immunoglobulin kappa constant	P01834	IGKC	10.1074/mcp.M111.008128		Mass Spec	abdominal		>65	M		
Immunoglobulin kappa variable 1-17	P01599	IGKV1-17	10.1074/mcp.M111.008128		Mass Spec	abdominal		>65	M		not in healthy proteome
Immunoglobulin kappa variable 1-5	P01602	IGKV1-5	10.1074/mcp.M111.008128		Mass Spec	abdominal		>65	M		not in healthy proteome

Immunoglobulin kappa variable 1D-33	P01593	IGKV1D-33	10.1074/mcp.M111.008128		Mass Spec	abdominal		>65	M		not in healthy proteome
Immunoglobulin kappa variable 2-30	P06310	IGKV2-30	10.1074/mcp.M111.008128		Mass Spec	abdominal		>65	M		not in healthy proteome
Immunoglobulin kappa variable 2D-40	P01614	IGKV2D-40	10.1074/mcp.M111.008128		Mass Spec	abdominal		>65	M		not in healthy proteome
Immunoglobulin kappa variable 3-20	P01619	IGKV3-20	10.1074/mcp.M111.008128		Mass Spec	abdominal		>65	M		not in healthy proteome
Immunoglobulin kappa variable 4-1	P06312	IGKV4-1	10.1074/mcp.M111.008128		Mass Spec	abdominal		>65	M		not in healthy proteome
Immunoglobulin lambda constant 1	P0CG04	IGLC1	10.1074/mcp.M111.008128		Mass Spec	abdominal		>65	M		
Immunoglobulin lambda variable 1-47	P01700	IGLV1-47	10.1074/mcp.M111.008128		Mass Spec	abdominal		>65	M		not in healthy proteome
Immunoglobulin lambda variable 3-21	P80748	IGLV3-21	10.1074/mcp.M111.008128		Mass Spec	abdominal		>65	M		not in healthy proteome
Inactive carboxypeptidase-like protein X	Q8N436	CPXM2	10.1074/mcp.M111.008128		Mass Spec	abdominal		>65	M		same as in control
Induced myeloid leukemia cell differenti	Q07820	MCL1	10.1074/mcp.M111.008128		Mass Spec	abdominal		>65	M		not in healthy proteome
Insulin-like growth factor I	P05019	IGF1	10.1016/j.jvs.2006.11.020	1	Immuno	abdominal		74	M	atherosclerotic	not in healthy proteome
Insulin-like growth factor-binding protei	P08833	IGFBP1	10.1159/000362997, 10.1093/cvr/cvu196	2	Immuno	ascending	media	54,69	B	unknown,Marfan,BAV,degenerative	higher than in control
Insulin-like growth factor-binding protei	P18065	IGFBP2	10.1093/cvr/cvu196	1	Immuno	ascending	adventitia	54	B	Marfan,BAV,degenerative	lower than in control
Insulin-like growth factor-binding protei	Q16270	IGFBP7	10.1074/mcp.M111.008128		Mass Spec	abdominal		>65	M		lower than in control
Insulin-like growth factor-binding protei	P35858	IGFALS	10.1074/mcp.M111.008128		Mass Spec	abdominal		>65	M		not in healthy proteome
Integrin beta-1	P05556	ITGB1	10.1074/mcp.M111.008128		Mass Spec	abdominal		>65	M		
Integrin beta-2	P05107	ITGB2	10.1074/mcp.M111.008128		Mass Spec	abdominal		>65	M		not in healthy proteome
Integrin beta-3	P05106	ITGB3	10.1016/j.atherosclerosis.2011.05.00	1	Immuno	abdominal	thrombus	70	B		
Inter-alpha-trypsin inhibitor heavy chain	P19827	ITIH1	10.1074/mcp.M111.008128		Mass Spec	abdominal		>65	M		
Inter-alpha-trypsin inhibitor heavy chain	P19823	ITIH2	10.3892/ijmm.2012.985, 10.1074/m	2	Mass Spec	abdominal,thoracic		>65	M		
Inter-alpha-trypsin inhibitor heavy chain	Q14624	ITIH4	10.1074/mcp.M111.008128		Mass Spec	abdominal		>65	M		
Inter-alpha-trypsin inhibitor heavy chain	Q86UX2	ITIH5	10.1074/mcp.M111.008128		Mass Spec	abdominal		>65	M		
Intercellular adhesion molecule 1	P05362	ICAM1	10.1371/journal.pone.0053882, 10.1	2	Immuno	abdominal		69,69	B		higher than in control
Interferon gamma	P01579	IFNG	10.1371/journal.pone.0053882, 10.1	6	Immuno	abdominal		69,74,66,7	B,M	unknown,atherosclerosis	
Interleukin enhancer-binding factor 2	Q12905	ILF2	10.1074/mcp.M111.008128		Mass Spec	abdominal		>65	M		
Interleukin-1 alpha	P01583	IL1A	10.1371/journal.pone.0053882, 10.1	2	Immuno	abdominal		69,74	M	atherosclerotic	not in healthy proteome
Interleukin-1 beta	P01584	IL1B	10.1371/journal.pone.0053882, 10.1	7	Immuno	abdominal		69,74,73, 66,71,72	B,M	unknown,atherosclerosis	higher than in control
Interleukin-10	P22301	IL10	10.1016/j.jvs.2006.11.020, 10.1016/	3	Immuno	abdominal		74,66,71	B,M	unknown,atherosclerosis	not in healthy proteome
Interleukin-12 subunit alpha	P29459	IL12A	10.1016/j.jvs.2011.06.113	1	Immuno	abdominal		66	B		not in healthy proteome
Interleukin-13	P35225	IL13	10.1371/journal.pone.0053882, 10.1	3	Immuno	abdominal		69,73,72	B		not in healthy proteome
Interleukin-15	P40933	IL15	10.1016/j.jvs.2006.11.020	1	Immuno	abdominal		74	M	atherosclerotic	not in healthy proteome
Interleukin-17A	Q16552	IL17A	10.1042/CS20070352	1	Immuno	abdominal		72	B		
Interleukin-2	P60568	IL2	10.1016/j.jvs.2006.11.020, 10.1161/	5	Immuno	abdominal		74,73,66, 71,72	B,M	unknown,atherosclerosis	
Interleukin-3	P08700	IL3	10.1016/j.jvs.2006.11.020	1	Immuno	abdominal		74	M	atherosclerotic	not in healthy proteome
Interleukin-4	P05112	IL4	10.1016/j.jvs.2011.06.113, 10.1016/	3	Immuno	abdominal		66,71,72	B		not in healthy proteome
Interleukin-5	P05113	IL5	10.1016/j.jvs.2006.11.020, 10.1016/	3	Immuno	abdominal		74,66,71	B,M	unknown,atherosclerosis	not in healthy proteome
Interleukin-6	P05231	IL6	10.1371/journal.pone.0053882, 10.1	8	Immuno	abdominal		69,69,74,7	B,M		higher than in control
Interleukin-7	P13232	IL7	10.1161/CIRCULATIONAHA.108.8065	2	Immuno	abdominal		73,72	B		not in healthy proteome
Interleukin-8	P10145	CXCL8	10.1016/j.jvs.2006.11.020, 10.1161/CIRCULATIONAHA.108.806505, 10.1016/j.jvs.2011.06.113, 10.1093/cvr/cvp048, 10.1159/000339304, 10.1016/j.jvs.2010.01.057, 10.1016/j.jvs.2014.08.088, 10.1042/CS20070352, 10.1093/cvr/cvu196, 10.1007/s10353-007-0339-z	10	Immuno	ascending,abdominal	adventitia;thrombus	74,73,66, 70,73,74, 71,54,72.6	B,M	unknown,atherosclerotic,Marfan,BAV,degenerative	higher than in control
Interstitial collagenase	P03956	MMP1	10.1159/000228900, 10.14670/HH-11-691,10.1053/hupa.2001.27107, 10.1016/j.atherosclerosis.2011.05.002, 10.1067/mva.2002.121124	5	Immuno	abdominal,thoracic,ascending	inflamation regions;intima;media;thrombus;wall lysate	71,64,70, 67.2	B,M	unknown, not Marfan	higher than in control
Kallistatin	P29622	SERPINA4	10.1074/mcp.M111.008128		Mass Spec	abdominal		>65	M		
Keratin, type I cytoskeletal 10	P13645	KRT10	10.1074/mcp.M111.008128		Mass Spec	abdominal		>65	M		
Keratin, type I cytoskeletal 14	P02533	KRT14	10.1074/mcp.M111.008128		Mass Spec	abdominal		>65	M		
Keratin, type I cytoskeletal 16	P08779	KRT16	10.1074/mcp.M111.008128		Mass Spec	abdominal		>65	M		
Keratin, type I cytoskeletal 17	Q04695	KRT17	10.1074/mcp.M111.008128		Mass Spec	abdominal		>65	M		not in healthy proteome
Keratin, type I cytoskeletal 9	P35527	KRT9	10.1074/mcp.M111.008128		Mass Spec	abdominal		>65	M		
Keratin, type II cuticular Hb4	Q9NSB2	KRT84	10.1074/mcp.M111.008128		Mass Spec	abdominal		>65	M		not in healthy proteome
Keratin, type II cytoskeletal 1	P04264	KRT1	10.1007/s00595-012-0480-6, 10.107	2	Mass Spec	abdominal		68,>65	B,M		lower than in control
Keratin, type II cytoskeletal 2 epidermal	P35908	KRT2	10.1074/mcp.M111.008128		Mass Spec	abdominal		>65	M		
Keratin, type II cytoskeletal 5	P13647	KRT5	10.1074/mcp.M111.008128		Mass Spec	abdominal		>65	M		
Keratin, type II cytoskeletal 6C	P48668	KRT6C	10.1074/mcp.M111.008128		Mass Spec	abdominal		>65	M		
Keratin, type II cytoskeletal 72	Q14CN4	KRT72	10.1074/mcp.M111.008128		Mass Spec	abdominal		>65	M		not in healthy proteome
Keratin, type II cytoskeletal 79	Q5XKE5	KRT79	10.1074/mcp.M111.008128		Mass Spec	abdominal		>65	M		not in healthy proteome
Keratinocyte proline-rich protein	Q5T749	KPRP	10.1074/mcp.M111.008128		Mass Spec	abdominal		>65	M		not in healthy proteome
Kininogen-1	P01042	KNG1	10.3892/ijmm.2012.985, 10.1074/m	2	Mass Spec	abdominal,thoracic		>65	M		not in healthy proteome
Kit ligand	P21583	KITLG	10.1016/j.jvs.2006.11.020, 10.1161/CIRCRESAHA.108.173682	2	Immuno	abdominal		74,75	B,M	unknown,atherosclerotic	higher than control
Lactadherin	Q08431	MFGE8	10.3892/ijmm.2012.985, 10.1038/la	3	Immuno;Mass Spe	thoracic, abdomina	media	>65,64	M,B	unknown, non-Marfan	same as in control
Lactotransferrin	P02788	LTF	10.1074/mcp.M111.008128		Mass Spec	abdominal		>65	M		
Lamina-associated polypeptide 2, isofor	P42166	TMPO	10.1074/mcp.M111.008128		Mass Spec	abdominal		>65	M		
Lamin-B1	P20700	LMNB1	10.1074/mcp.M111.008128		Mass Spec	abdominal		>65	M		not in healthy proteome
Lamin-B2	Q03252	LMNB2	10.1074/mcp.M111.008128		Mass Spec	abdominal		>65	M		
Laminin subunit alpha-2	P24043	LAMA2	16377578	1	Immuno	ascending		56	B	BAV	
Laminin subunit alpha-4	Q16363	LAMA4	10.1074/mcp.M111.008128		Mass Spec	abdominal		>65	M		
Laminin subunit alpha-5	O15230	LAMA5	10.1074/mcp.M111.008128		Mass Spec	abdominal		>65	M		lower than in control
Laminin subunit beta-1	P07942	LAMB1	16377578, 10.1074/mcp.M111.0081	2	Immuno;Mass Spe	abdominal,ascending		>65,56	M,B	unknown, BAV	
Laminin subunit beta-2	P55268	LAMB2	16377578, 10.1074/mcp.M111.0081	2	Immuno;Mass Spe	abdominal,ascending		>65,56	M,B	unknown, BAV	same as in control
Laminin subunit gamma-1	P11047	LAMC1	10.1155/2014/760694, 10.1074/mcp.M111.008128	2	Immuno;Mass Spe	ascending, abdominal		>65	M	Marfan&related, unknown	same as in control, Marfan higher than in control
La-related protein 1B	Q659C4	LARP1B	10.1074/mcp.M111.008128		Mass Spec	abdominal		>65	M		not in healthy proteome
Latent-transforming growth factor beta-	Q14766	LTBP1	10.1002/path.2516, 10.1074/mcp.M	2	Immuno;Mass Spe	ascending, abdomi	media	>65	M		same as in control
Latent-transforming growth factor beta-	Q14767	LTBP2	10.1074/mcp.M111.008128		Mass Spec	abdominal		>65	M		same as in control or higher than control
Latexin	Q9BS40	LXN	10.1074/mcp.M111.008128		Mass Spec	abdominal		>65	M		not in healthy proteome
Leptin	P41159	LEP	10.1016/j.jvs.2006.11.020, 10.1161/ATVBAHA.112.300543	2	Immuno	abdominal	media	74	M	unknown,atherosclerosis	
Leptin receptor	P48357	LEPR	10.1161/ATVBAHA.112.300543	1	Immuno	abdominal	media				
Leucine-rich alpha-2-glycoprotein	P02750	LRG1	10.1074/mcp.M111.008128		Mass Spec	abdominal		>65	M		
Leukocyte elastase inhibitor	P30740	SERPINB1	10.1074/mcp.M111.008128		Mass Spec	abdominal		>65	M		same as in control
LIM and cysteine-rich domains protein 1	Q9NZU5	LMCD1	10.1074/mcp.M111.008128		Mass Spec	abdominal		>65	M		
LIM and SH3 domain protein 1	Q14847	LASP1	10.1074/mcp.M111.008128		Mass Spec	abdominal		>65	M		
Lipocalin-1	P31025	LCN1	10.1074/mcp.M111.008128		Mass Spec	abdominal		>65	M		not in healthy proteome
Lipoma-preferred partner	Q93052	LPP	10.3892/ijmm.2012.985, 10.1074/m	2	Mass Spec	abdominal,thoracic		>65	M		
Lipopolysaccharide-binding protein	P18428	LBP	10.1074/mcp.M111.008128		Mass Spec	abdominal		>65	M		
L-lactate dehydrogenase A chain	P00338	LDHA	10.1074/mcp.M112.021873, 10.1074/mcp.M111.008128	2	Immuno;Mass Spe	ascending, abdominal	intima;media	>65	M	BAV,unknown	unknown aneurysm higher than in control
L-lactate dehydrogenase B chain	P07195	LDHB	10.1074/mcp.M111.008128		Mass Spec	abdominal		>65	M		
Low affinity immunoglobulin gamma Fc	P31994	FCGR2B	10.1159/000362997	1	Immuno	abdominal		69	B		higher than in control
Lumican	P51884	LUM	10.3892/ijmm.2012.985, 10.1074/m	2	Mass Spec	abdominal		>65	M		Same as control
Lymphocyte-specific protein 1	P33241	LSP1	10.1074/mcp.M111.008128		Mass Spec	abdominal		>65	M		not in healthy proteome

Lymphotoxin-alpha	P01374	LTA	10.1016/j.jvs.2006.11.020, 10.1016/j	2	Immuno	abdominal		74,66	B,M	unknown,atherosclerosis	higher than in control
Lysine-specific demethylase 3B	Q7LBC6	KDM3B	10.1074/mcp.M111.008128		Mass Spec	abdominal		>65	M		not in healthy proteome
Lysine-specific demethylase 5A	P29375	KDM5A	10.1074/mcp.M111.008128		Mass Spec	abdominal		>65	M		not in healthy proteome
Lysosomal protective protein	P10619	CTSA	10.1074/mcp.M111.008128		Mass Spec	abdominal		>65	M		not in healthy proteome
Lysosome-associated membrane glycopr	P11279	LAMP1	10.1074/mcp.M111.008128		Mass Spec	abdominal		>65	M		not in healthy proteome
Lysozyme C	P61626	LYZ	10.3892/ijmm.2012.985, 10.1074/m	2	Mass Spec	abdominal		>65	M		
Lysyl oxidase homolog 1	Q08397	LOXL1	10.1074/mcp.M111.008128		Mass Spec	abdominal		>65	M		same as in control
Macrophage colony-stimulating factor 1	P09603	CSF1	10.1016/j.jvs.2006.11.020	1	Immuno	abdominal		74	M	atherosclerotic	higher than in control
Macrophage metalloelastase	P39900	MMP12	10.1067/mva.2002.121124, 10.1074/	2	Immuno;Mass Spe	abdominal	inflamation regions;media	67.2,>65	B,M		not in healthy proteome
Macrophage migration inhibitory factor	P14174	MIF	10.3892/ijmm.2012.985	1	Mass Spec	thoracic					
Macrophage receptor MARCO	Q9UEW3	MARCO	10.1074/mcp.M111.008128		Mass Spec	abdominal		>65	M		not in healthy proteome
Macrophage-capping protein	P40121	CAPG	10.1074/mcp.M111.008128		Mass Spec	abdominal		>65	M		
Macrosialin	P34810	CD68	10.1016/j.ijcard.2015.08.053, 10.101	10	Immuno	abdominal	inflamation regions;intima;media	74,63,60,7	B,M	sporadic	higher than in control
Major vault protein	Q14764	MVP	10.1074/mcp.M111.008128		Mass Spec	abdominal		>65	M		
Malate dehydrogenase, cytoplasmic	P40925	MDH1	10.1074/mcp.M111.008128		Mass Spec	abdominal		>65	M		
Malate dehydrogenase, mitochondrial	P40926	MDH2	10.1074/mcp.M111.008128		Mass Spec	abdominal		>65	M		
Matrilin-2	O00339	MATN2	10.1074/mcp.M111.008128		Mass Spec	abdominal		>65	M		same as in control
Matrilysin	P09237	MMP7	10.1159/000228900, 10.1093/cvr/cv	2	Immuno	ascending,abdomir	inflamation regions	54,71	B	unknown,Marfan,BAV,degenerative	
Matrix Gla protein	P08493	MGP	10.3892/ijmm.2012.985, 10.1074/m	2	Mass Spec	abdominal		>65	M		same as in control
Matrix metalloproteinase-14	P50281	MMP14	10.1067/mva.2002.121124		Immuno	abdominal		67.2	B		higher than in control and less inactive than control
Matrix metalloproteinase-19	Q99542	MMP19	10.1093/cvr/cvu196	1	Immuno	ascending		54	B	Marfan,BAV,degenerative	higher than in control
Matrix metalloproteinase-9	P14780	MMP9	10.1016/j.atherosclerosis.2013.10.0	12	Immuno	ascending, abdomi	adventitia;inflamation regions;intima;media;thrombus;wall lysate	64,74,63,5	B	sporadic,Marfan,BAV,degenerative,not Marfan	same or higher than in control
Matrix-remodeling-associated protein 5	Q9NR99	MXRA5	10.1074/mcp.M111.008128		Mass Spec	abdominal		>65	M		not in healthy proteome
Membrane primary amine oxidase	Q16853	AOC3	10.3892/ijmm.2012.985, 10.1074/m	2	Mass Spec	abdominal,thoracic		>65	M		
Metal transporter CNNM4	Q6P4Q7	CNNM4	10.1074/mcp.M111.008128		Mass Spec	abdominal		>65	M		
Metalloproteinase inhibitor 1	P01033	TIMP1	10.1016/j.atherosclerosis.2010.04.0	10	Immuno;Mass Spe	ascending,abdomir	media;thrombus;wall lysate	65,71,64,6	B,M	unknown, not Marfan, Marfan,BAV,degenerative	higher than in control or not or lower
Metalloproteinase inhibitor 2	P16035	TIMP2	10.1016/j.jctvs.2006.07.036, 10.1016	6	Immuno	abdominal,ascendi	media;thrombus;wall lysate	66,65,71,6	B,M	unknown,not Marfan	higher than in control or lower
Metalloproteinase inhibitor 3	P35625	TIMP3	10.1016/j.humpath.2006.03.017, 10	3	Immuno;Mass Spe	ascending,abdominal		65,71,67.2	B,M	unknown,not Marfan	higher than in control
Metalloproteinase inhibitor 4	Q99727	TIMP4	10.1093/cvr/cvu196	1	Immuno	ascending	adventitia;media	54	B	Marfan,BAV,degenerative	lower than in control
Methyl-CpG-binding protein 2	P51608	MECP2	10.1074/mcp.M111.008128		Mass Spec	abdominal		>65	M		
Microfibril-associated glycoprotein 4	P55083	MFAP4	10.3892/ijmm.2012.985, 10.1016/j.j	4	Mass Spec	ascending, thoracic,abdominal		69,38, >65	B,M	not Marfan, Marfan,BAV,unknown	lower or higher than in control
Microfibrillar-associated protein 5	Q13361	MFAP5	10.1074/mcp.M111.008128		Mass Spec	abdominal		>65	M		same as in control
Mimecan	P20774	OGN	10.3892/ijmm.2012.985, 10.1074/m	3	Mass Spec	ascending, abdominal		>65	M	BAV,unknown	lower than in control
Mitogen-activated protein kinase 1	P28482	MAPK1	10.1016/j.jamcollsurg.2012.06.414,	4	Immuno;Mass Spe	abdominal		67,71,>65	B,M		more phosphorylated in ruptured AAA than non-ruptured and control
Mitogen-activated protein kinase 3	P27361	MAPK3	10.1016/j.ejvs.2013.02.015, 10.1111	2	Immuno	abdominal		67,71	B		more phosphorylated in ruptured AAA than non-ruptured and control
Moesin	P26038	MSN	10.1074/mcp.M111.008128		Mass Spec	abdominal		>65	M		
Monocyte differentiation antigen CD14	P08571	CD14	10.1016/j.ijcard.2015.08.053	1	Immuno	abdominal					not in healthy proteome
Mothers against decapentaplegic homol	Q15796	SMAD2	10.1016/j.ijcard.2011.08.079, 10.116	4	Immuno	ascending	intima;media	41,55	B	Marfan, BAV, degenerative, non-syndromic TAAD	higher phosphorylation than in control
Multimerin-1	Q13201	MMRN1	10.1074/mcp.M111.008128		Mass Spec	abdominal		>65	M		not in healthy proteome
Myeloblastin	P24158	PRTN3	10.1093/cvr/cvp048	1	Immuno	abdominal	adventitia;thrombus	70	M	degenerative	
Myeloperoxidase	P05164	MPO	10.1371/journal.pone.0053882, 10.1	6	Immuno;Mass Spe	abdominal		>65,69,63	B,M		higher than in control
Myocardin	Q8IZQ8	MYOCD	10.1093/cvr/cvt205	1	Immuno	ascending		63	B		same as in control
Myosin light polypeptide 6	P60660	MYL6	10.1074/mcp.M112.021873, 10.1016	3	Mass Spec	ascending, abdominal		48.3,>65	B,M	BAV,unknown	higher than in control
Myosin regulatory light chain 12B	O14950	MYL12B	10.1074/mcp.M112.021873, 10.1074	2	Mass Spec	ascending, abdominal		>65	M	BAV,unknown	BAV higher than control
Myosin regulatory light polypeptide 9	P24844	MYL9	10.3892/ijmm.2012.985, 10.1074/m	4	Mass Spec	ascending, abdominal		48.3,>65	B,M	BAV,unknown	BAV higher than in control
Myosin-10	P35580	MYH10	10.3892/ijmm.2012.985, 10.1002/pa	4	Immuno;Mass Spe	ascending,thoracic	media	38,>65	B,M	unknown,Marfan,BAV,degenerative	higher than in control
Myosin-11	P35749	MYH11	10.3892/ijmm.2012.985, 10.1111/j.1	5	Immuno;Mass Spe	ascending,thoracic	media	54,>65	B,M	Marfan,BAV,degenerative	
Myosin-9	P35579	MYH9	10.1074/mcp.M111.008128		Mass Spec	abdominal		>65	M		
N-acetylmuramoyl-L-alanine amidase	Q96PD5	PGLYRP2	10.3892/ijmm.2012.985, 10.1074/m	2	Mass Spec	abdominal		>65	M		not in healthy proteome
NACHT, LRR and PYD domains-containin	Q96P20	NLRP3	10.1016/j.atherosclerosis.2013.10.0	1	Immuno	abdominal	adventitia;intima;media	63	B	sporadic	not in healthy proteome
Neuroblast differentiation-associated pr	Q09666	AHNAK	10.1074/mcp.M111.008128		Mass Spec	abdominal		>65	M		
Neurofilament light polypeptide	P07196	NEFL	10.1074/mcp.M111.008128		Mass Spec	abdominal		>65	M		not in healthy proteome
Neutrophil collagenase	P22894	MMP8	10.1159/000228900, 10.1159/00036	8	Immuno	ascending,abdomir	inflamation regions	71,69,73,7	B,M		higher than in control
Neutrophil defensin 1	P59665	DEFA1 , DEFA1B	10.1074/mcp.M111.008128		Mass Spec	abdominal		>65	M		higher than in control
Neutrophil elastase	P08246	ELANE	10.1016/j.atherosclerosis.2011.05.0	2	Immuno	abdominal	thrombus	70	B		
Neutrophil gelatinase-associated lipocali	P80188	LCN2	10.1093/cvr/cvp048	1	Immuno	abdominal	adventitia;thrombus	70	M	degenerative	not in healthy proteome
Nidogen-1	P14543	NID1	10.1074/mcp.M111.008128		Mass Spec	abdominal		>65	M		same as in control
Nidogen-2	Q14112	NID2	10.1074/mcp.M111.008128		Mass Spec	abdominal		>65	M		same as in control
Nitric oxide synthase, endothelial	P29474	NOS3	10.1155/2014/760694	1	Immuno			30,46	B	Marfan & Marfan related	lower than in control
Nitric oxide synthase, inducible	P35228	NOS2	10.1371/journal.pone.0053882, 10.1	4	Immuno	abdominal	inflamation regions;intima;media	69,69,30,4	B	Marfan & Marfan related, unknown	higher than in control
Nuclear pore complex protein Nup133	Q8WUM0	NUP133	10.1074/mcp.M111.008128		Mass Spec	abdominal		>65	M		not in healthy proteome
Nuclease-sensitive element-binding prot	P67809	YBX1	10.1074/mcp.M111.008128		Mass Spec	abdominal		>65	M		not in healthy proteome
Nucleolin	P19338	NCL	10.1074/mcp.M111.008128		Mass Spec	abdominal		>65	M		
Nucleoside diphosphate kinase B	P22392	NME2	10.1074/mcp.M111.008128		Mass Spec	abdominal		>65	M		
Olfactomedin-like protein 1	Q6UWY5	OLFML1	10.1074/mcp.M111.008128		Mass Spec	abdominal		>65	M		not in healthy proteome
Oncostatin-M	P13725	OSM	10.1016/j.jvs.2006.11.020	1	Immuno	abdominal		74	M	atherosclerotic	higher than in control
Oral-facial-digital syndrome 1 protein	O75665	OFD1	10.1074/mcp.M111.008128		Mass Spec	abdominal		>65	M		not in healthy proteome
Osteopontin	P10451	SPP1	10.1177/1708538112472282, 10.101	5	Immuno	ascending,abdomir	media	63,66,63,6	M,B	unknown, not Marfan, not BAV	higher than in control
Palladin	Q8WX93	PALLD	10.1074/mcp.M111.008128		Mass Spec	abdominal		>65	M		
Pantothenate kinase 1	Q8TE04	PANK1	10.1074/mcp.M111.008128		Mass Spec	abdominal		>65	M		not in healthy proteome
PDZ and LIM domain protein 1	O00151	PDLIM1	10.1074/mcp.M111.008128		Mass Spec	abdominal		>65	M		
PDZ and LIM domain protein 3	Q53GG5	PDLIM3	10.1074/mcp.M112.021873, 10.1074	2	Mass Spec	ascending, abdominal		>65	M	BAV,unknown	
PDZ and LIM domain protein 4	P50479	PDLIM4	10.1074/mcp.M111.008128		Mass Spec	abdominal		>65	M		
PDZ and LIM domain protein 7	Q9NR12	PDLIM7	10.1074/mcp.M111.008128		Mass Spec	abdominal		>65	M		
Pecanex-like protein 1	Q96RV3	PCNX1	10.1074/mcp.M111.008128		Mass Spec	abdominal		>65	M		not in healthy proteome
Pentraxin-related protein PTX3	P26022	PTX3	10.1093/cvr/cvu196	1	Immuno	ascending	media	54	B	Marfan,BAV,degenerative	higher than in control
Peptidyl-prolyl cis-trans isomerase A	P62937	PPIA	10.1016/j.ejvs.2013.02.015, 10.1074	2	Immuno;Mass Spe	abdominal		67,>65	B,M		

Peptidyl-prolyl cis-trans isomerase B	P23284	PPIB	10.1074/mcp.M111.008128		Mass Spec	abdominal		>65	M		
Perforin-1	P14222	PRF1	10.1161/CIRCULATIONAHA.108.8069	2	Immuno	abdominal		72,73	B		not in healthy proteome
Periostin	Q15063	POSTN	10.3892/ijmm.2012.985, 10.1074/m	2	Immuno;Mass Spe	abdominal,thoracic		>65	M		Same as in control
Peripherin	P41219	PRPH	10.1074/mcp.M111.008128		Mass Spec	abdominal		>65	M		not in healthy proteome
Peroxidasin homolog	Q92626	PXDN	10.1074/mcp.M111.008128		Mass Spec	abdominal		>65	M		not in healthy proteome
Peroxiredoxin-1	Q06830	PRDX1	10.1074/mcp.M111.008128		Mass Spec	abdominal		>65	M		
Peroxiredoxin-2	P32119	PRDX2	10.1016/j.jvs.2008.08.097, 10.1016/	3	Immuno;Mass Spe	ascending, abdominal		73.5,48.3,	B,M	BAV,unknown	
Peroxiredoxin-4	Q13162	PRDX4	10.1074/mcp.M111.008128		Mass Spec	abdominal		>65	M		not in healthy proteome
Peroxiredoxin-6	P30041	PRDX6	10.1074/mcp.M111.008128		Mass Spec	abdominal		>65	M		
Peroxisome proliferator-activated recep	P37231	PPARG	10.1159/000439169		Immuno	abdominal	adventitia	70.2	B		not in healthy proteome
Persephin	O60542	PSPN	10.1093/cvr/cvu196	1	Immuno	ascending	media	54	B	Marfan,BAV,degener ative	higher than in control
Phosphatidylethanolamine-binding prot	P30086	PEBP1	10.3892/ijmm.2012.985	1	Mass Spec	thoracic					
Phosphatidylinositol-glycan biosynthesis	Q07326	PIGF	10.1093/cvr/cvu196	1	Immuno	ascending		54	B	Marfan,BAV,degener ative	
Phosphoglucomutase-like protein 5	Q15124	PGM5	10.3892/ijmm.2012.985	1	Mass Spec	thoracic					
Phosphoglycerate kinase 1	P00558	PGK1	10.1016/j.ejcts.2009.07.025, 10.107	2	Mass Spec	ascending,abdominal		56,>65	M		lower than in control
Phosphoglycerate mutase 1	P18669	PGAM1	10.1016/j.jvs.2011.10.033, 10.1074/	2	Mass Spec	abdominal		69,>65	B,M	not Marfan	same as in control
Phospholipase A2, membrane associate	P14555	PLA2G2A	10.1074/mcp.M111.008128		Mass Spec	abdominal		>65	M		same as in control
Phospholipase D3	Q8IV08	PLD3	10.1074/mcp.M111.008128		Mass Spec	abdominal		>65	M		not in healthy proteome
Piezo-type mechanosensitive ion channe	Q92508	PIEZO1	10.1074/mcp.M111.008128		Mass Spec	abdominal		>65	M		not in healthy proteome
Pigment epithelium-derived factor	P36955	SERPINF1	10.1074/mcp.M111.008128		Mass Spec	abdominal		>65	M		higher than in control
Plasma kallikrein	P03952	KLKB1	10.1074/mcp.M111.008128		Mass Spec	abdominal		>65	M		not in healthy proteome
Plasma protease C1 inhibitor	P05155	SERPING1	10.1074/mcp.M111.008128		Mass Spec	abdominal		>65	M		
Plasminogen	P00747	PLG	10.1093/cvr/cvu196,10.1016/S0002-	3	Immuno;Mass Spe	ascending,abdomir	adventitia;media; thrombus	54,>65	B,M	Marfan,BAV,degener ative	higher than in control
Plasminogen activator inhibitor 1	P05121	SERPINE1	10.1016/j.atherosclerosis.2011.05.0	3	Immuno	ascending,abdomi	thrombus;wall lysate	70,55,73	B	unknown,Marfan, BAV, degenerative	lower than in control
Plastin-2	P13796	LCP1	10.1074/mcp.M111.008128		Mass Spec	abdominal		>65	M		
Plastin-3	P13797	PLS3	10.1074/mcp.M111.008128		Mass Spec	abdominal		>65	M		
Platelet endothelial cell adhesion molec	P16284	PECAM1	10.1159/000228900, 10.1371/journa	5	Immuno	abdominal	adventitia;media	71,69,70,7	B		higher than in control
Platelet factor 4	P02776	PF4	10.1093/cvr/cvp048, 10.1093/cvr/cv	3	Immuno;Mass Spe	ascending,abdomir	adventitia;media; thrombus	70,54,>65	B,M	Marfan,BAV,degener ative	lower than in control
Platelet-activating factor acetylhydrolas	Q13093	PLA2G7	10.1074/mcp.M111.008128		Mass Spec	abdominal		>65	M		not in healthy proteome
Platelet-derived growth factor receptor	P09619	PDGFRB	10.1007/s00109-008-0413-4	1	Immuno	abdominal					not in healthy proteome
Platelet-derived growth factor subunit A	P04085	PDGFA	10.1093/cvr/cvu196	1	Immuno	ascending	media	54	B	Marfan,BAV,degener ative	lower than in control
Platelet-derived growth factor subunit B	P01127	PDGFB	10.1016/j.jvs.2006.11.020	1	Immuno	abdominal		74	M	atherosclerotic	not in healthy proteome
Plectin	Q15149	PLEC	10.1074/mcp.M111.008128		Mass Spec	abdominal		>65	M		
Podocan	Q7Z5L7	PODN	10.1074/mcp.M111.008128		Mass Spec	abdominal		>65	M		same as in control
Podoplanin	Q86YL7	PDPN	10.1371/journal.pone.0089830	1	Immuno	abdominal	adventitia;intima	69	B		
Poly(rC)-binding protein 2	Q15366	PCBP2	10.1074/mcp.M111.008128		Mass Spec	abdominal		>65	M		
Polymerase I and transcript release facto	Q6NZI2	PTRF	10.3892/ijmm.2012.985, 10.1074/m	2	Mass Spec	abdominal,thoracic		>65	M		
Prelamin-A/C	P02545	LMNA	10.1016/j.ejcts.2009.07.025, 10.107	2	Mass Spec	abdominal		56,>65	M		lower than in control
Pre-mRNA-processing factor 17	O60508	CDC40	10.1007/s00595-012-0480-6		Mass Spec	abdominal		68	B		higher than in control (atherosclerotic)
Probable cysteine--tRNA ligase, mitocho	Q9HA77	CARS2	10.1074/mcp.M111.008128		Mass Spec	abdominal		>65	M		
Probable G-protein coupled receptor 15	Q8NGU9	GPR150	10.1074/mcp.M111.008128		Mass Spec	abdominal		>65	M		not in healthy proteome
Probable JmjC domain-containing histon	Q15652	JMJD1C	10.1074/mcp.M111.008128		Mass Spec	abdominal		>65	M		not in healthy proteome
Probable phospholipid-transporting ATP	O94823	ATP10B	10.1074/mcp.M111.008128		Mass Spec	abdominal		>65	M		not in healthy proteome
Pro-cathepsin H	P09668	CTSH	10.1016/j.jvs.2007.08.015		Immuno	abdominal		73	B		not in healthy proteome
Procollagen C-endopeptidase enhancer	Q15113	PCOLCE	10.1074/mcp.M111.008128		Mass Spec	abdominal		>65	M		same as in control
Profilin-1	P07737	PFN1	10.1074/mcp.M111.008128		Mass Spec	abdominal		>65	M		
Profilin-2	P35080	PFN2	10.1016/j.clinbiochem.2009.10.015		Mass Spec	ascending		48.3	B	BAV, unknown	
Prokineticin-1	P58294	PROK1	10.1093/cvr/cvu196	1	Immuno	ascending	media	54	B	Marfan,BAV,degener ative	higher than in control
Prolargin	P51888	PRELP	10.1074/mcp.M111.008128		Mass Spec	abdominal		>65	M		same as in control
Proliferation marker protein Ki-67	P46013	MKI67	10.1371/journal.pone.0089830, 10.1	3	Immuno;Mass Spe	abdominal		>65,69	M,B		not in healthy proteome
Proliferation-associated protein 2G4	Q9UQ80	PA2G4	10.1074/mcp.M111.008128		Mass Spec	abdominal		>65	M		
Prolow-density lipoprotein receptor-rela	Q07954	LRP1	10.1016/j.ejvs.2013.08.006, 10.1016	3	Immuno;Mass Spe	abdominal	adventitia;media	74,58,>65	B,M	not connective diseases	lower than in control
Properdin	P27918	CFP	10.1074/mcp.M111.008128		Mass Spec	abdominal		>65	M		same as in control
Prostaglandin E synthase	O14684	PTGES	10.1194/jlr.M042481	1	Immuno	abdominal					
Prostaglandin E2 receptor EP4 subtype	P35408	PTGER4	10.1194/jlr.M042481	1	Immuno	abdominal					
Prostaglandin G/H synthase 2	P35354	PTGS2	10.1194/jlr.M042481	1	Immuno	abdominal	adventitia;media				
Proteasome activator complex subunit 1	Q06323	PSME1	10.1074/mcp.M111.008128		Mass Spec	abdominal		>65	M		
Proteasome subunit alpha type-1	P25786	PSMA1	10.1074/mcp.M111.008128		Mass Spec	abdominal		>65	M		
Proteasome subunit alpha type-6	P60900	PSMA6	10.1074/mcp.M111.008128		Mass Spec	abdominal		>65	M		
Proteasome subunit alpha type-7-like	Q8TAA3	PSMA8	10.1074/mcp.M111.008128		Mass Spec	abdominal		>65	M		
Proteasome subunit beta type-6	P28072	PSMB6	10.1074/mcp.M111.008128		Mass Spec	abdominal		>65	M		
Protein AHNAK2	Q8IVF2	AHNAK2	10.1074/mcp.M111.008128		Mass Spec	abdominal		>65	M		not in healthy proteome
Protein AMBP	P02760	AMBP	10.1074/mcp.M111.008128		Mass Spec	abdominal		>65	M		
Protein disulfide-isomerase	P07237	P4HB	10.1016/j.clinbiochem.2009.10.015,	2	Mass Spec	ascending, abdominal		48.3,>65	B,M	BAV,unknown	
Protein disulfide-isomerase A3	P30101	PDIA3	10.1074/mcp.M111.008128		Mass Spec	abdominal		>65	M		
Protein disulfide-isomerase A4	P13667	PDIA4	10.1074/mcp.M111.008128		Mass Spec	abdominal		>65	M		
Protein disulfide-isomerase A6	Q15084	PDIA6	10.1074/mcp.M111.008128		Mass Spec	abdominal		>65	M		
Protein DJ-1	Q99497	PARK7	10.1074/mcp.M112.021873, 10.107	2	Mass Spec	ascending, abdominal		>65	M	BAV,unknown	higher than in control
Protein kinase C delta-binding protein	Q969G5	PRKCDBP	10.1074/mcp.M111.008128		Mass Spec	abdominal		>65	M		
Protein kinase C-binding protein 1	Q9ULU4	ZMYND8	10.1074/mcp.M111.008128		Mass Spec	abdominal		>65	M		not in healthy proteome
Protein NPAT	Q14207	NPAT	10.1074/mcp.M111.008128		Mass Spec	abdominal		>65	M		not in healthy proteome
Protein S100-A12	P80511	S100A12	10.1161/CIRCRESAHA.109.209486	1	Immuno	ascending	media	34	M	familial TAAD	not in healthy proteome, not in control tissue
Protein S100-A4	P26447	S100A4	10.1371/journal.pone.0070057	1	Immuno	thoracic	adventitia;intima; media	43	B		higher than in control
Protein S100-A6	P06703	S100A6	10.3892/ijmm.2012.985	1	Mass Spec	thoracic					
Protein S100-A8	P05109	S100A8	10.1074/mcp.M111.008128		Mass Spec	abdominal		>65	M		higher than in control
Protein S100-A9	P06702	S100A9	10.1159/000339304, 10.1111/j.1600	4	Immuno;Mass Spe	abdominal	adventitia;media	>65,73,69	B,M		
Protein transport protein Sec23A	Q15436	SEC23A	10.1074/mcp.M111.008128		Mass Spec	abdominal		>65	M		not in healthy proteome
Protein-glutamine gamma-glutamyltrans	P21980	TGM2	10.3892/ijmm.2012.985,10.1074/mc	5	Immuno;Mass Spe	ascending, abdomi	intima;media	68,66.9, >	B,M		higher than in control or lower
Protein-lysine 6-oxidase	P28300	LOX	10.1074/mcp.M111.008128		Mass Spec	abdominal		>65	M		not in healthy proteome
Prothrombin	P00734	F2	10.3892/ijmm.2012.985, 10.1074/m	2	Mass Spec	abdominal,thoracic		>65	M		
Protocadherin Fat 3	Q8TDW7	FAT3	10.1074/mcp.M111.008128		Mass Spec	abdominal		>65	M		not in healthy proteome
Purine nucleoside phosphorylase	P00491	PNP	10.1074/mcp.M111.008128		Mass Spec	abdominal		>65	M		
Pyruvate kinase PKM	P14618	PKM	10.1074/mcp.M111.008128		Mass Spec	abdominal		>65	M		
Rab GDP dissociation inhibitor beta	P50395	GDI2	10.1074/mcp.M111.008128		Mass Spec	abdominal		>65	M		
Ras GTPase-activating-like protein IQGA	P46940	IQGAP1	10.1074/mcp.M111.008128		Mass Spec	abdominal		>65	M		
Ras-related C3 botulinum toxin substrate	P63000	RAC1	10.1074/mcp.M111.008128		Mass Spec	abdominal		>65	M		
Ras-related protein Rab-11A	P62491	RAB11A	10.1074/mcp.M111.008128		Mass Spec	abdominal		>65	M		
Ras-related protein Rab-35	Q15286	RAB35	10.1074/mcp.M111.008128		Mass Spec	abdominal		>65	M		not in healthy proteome
Ras-related protein Rab-7a	P51149	RAB7A	10.1074/mcp.M111.008128		Mass Spec	abdominal		>65	M		
Ras-related protein Rap-1A	P62834	RAP1A	10.1074/mcp.M111.008128		Mass Spec	abdominal		>65	M		
Receptor-interacting serine/threonine-p	Q13546	RIPK1	10.1161/CIRCRESAHA.116.304899	1	Immuno	abdominal	media				
Receptor-interacting serine/threonine-p	Q9Y572	RIPK3	10.1161/CIRCRESAHA.116.304899	1	Immuno	abdominal	media				higher than in control
Receptor-type tyrosine-protein phospha	P08575	PTPRC	10.1194/jlr.M042481	1	Immuno	abdominal	media				not in healthy proteome
Renin receptor	O75787	ATP6AP2	10.1016/j.atherosclerosis.2009.01.003		Immuno	abdominal		70.5	M		same as in control
Resistin	Q9HD89	RETN	10.1177/1538574410380935	1	Immuno	abdominal	media	69	B		
Retinal dehydrogenase 1	P00352	ALDH1A1	10.1016/j.jvs.2011.10.033	1	Mass Spec	abdominal		69	B	not Marfan, not inflammatory disease	same as in control

Retinol-binding protein 4	P02753	RBP4	10.1074/mcp.M111.008128		Mass Spec	abdominal		>65	M		not in healthy proteome
Rho GDP-dissociation inhibitor 1	P52565	ARHGDIA	10.1074/mcp.M111.008128		Mass Spec	abdominal		>65	M		
Ribonuclease inhibitor	P13489	RNH1	10.1074/mcp.M111.008128		Mass Spec	abdominal		>65	M		
Ribosome-binding protein 1	Q9P2E9	RRBP1	10.1074/mcp.M111.008128		Mass Spec	abdominal		>65	M		not in healthy proteome
RNA-binding protein 6	P78332	RBM6	10.1016/j.clinbiochem.2009.10.015		Mass Spec	ascending		48.3	B	BAV, unknown	not in healthy proteome
Scavenger receptor cysteine-rich type 1	Q86VB7	CD163	10.1371/journal.pone.0053882, 10.1	4	Immuno	abdominal,ascendi	adventitia;media; thrombus	69,70,64	B	not Marfan,unknown	same as in control
Secreted frizzled-related protein 3	Q92765	FRZB	10.1074/mcp.M111.008128		Mass Spec	abdominal		>65	M		same as in control
Secreted phosphoprotein 24	Q13103	SPP2	10.1074/mcp.M111.008128		Mass Spec	abdominal		>65	M		not in healthy proteome
Selenium-binding protein 1	Q13228	SELENBP1	10.1074/mcp.M111.008128		Mass Spec	abdominal		>65	M		
Septin-7	Q16181	SEPT7	10.1074/mcp.M111.008128		Mass Spec	abdominal		>65	M		
Serine protease HTRA1	Q92743	HTRA1	10.1074/mcp.M111.008128		Mass Spec	abdominal		>65	M		same as in control
Serine/arginine repetitive matrix protein	Q9UQ35	SRRM2	10.1074/mcp.M111.008128		Mass Spec	abdominal		>65	M		not in healthy proteome
Serine/arginine-rich splicing factor 1	Q07955	SRSF1	10.1074/mcp.M111.008128		Mass Spec	abdominal		>65	M		
Serine/threonine-protein kinase ATR	Q13535	ATR	10.1074/mcp.M111.008128		Mass Spec	abdominal		>65	M		
Serine/threonine-protein kinase SIK3	Q9Y2K2	SIK3	10.1074/mcp.M111.008128		Mass Spec	abdominal		>65	M		not in healthy proteome
Serine/threonine-protein phosphatase 6	Q8NB46	ANKRD52	10.1074/mcp.M111.008128		Mass Spec	abdominal		>65	M		not in healthy proteome
Serotransferrin	P02787	TF	10.1074/mcp.M112.021873, 10.1007	3	Immuno;Mass Spe	ascending, abdominal		68,48.3,>6	B,M	BAV,unknown	higher than in control or the same
Serpin H1	P50454	SERPINH1	10.1074/mcp.M111.008128		Mass Spec	abdominal		>65	M		
Serum albumin	P02768	ALB	10.1016/j.jvs.2008.08.097, 10.1510/	5	Mass Spec	ascending, abdominal		73.5,70,68	B,M		higher than in control or not
Serum amyloid A-4 protein	P35542	SAA4	10.3892/ijmm.2012.985	1	Mass Spec	abdominal					not in healthy proteome
Serum amyloid P-component	P02743	APCS	10.3892/ijmm.2012.985, 10.1074/m	4	Mass Spec	ascending, thoracic, abdominal		38,>65	B,M	Marfan,BAV, unknown	higher or lower than in control, higher than control when it is BAV dilation
Serum paraoxonase/arylesterase 1	P27169	PON1	10.1074/mcp.M111.008128		Mass Spec	abdominal		>65	M		not in healthy proteome
SH3 domain-binding glutamic acid-rich-l	O75368	SH3BGRL	10.1074/mcp.M111.008128		Mass Spec	abdominal		>65	M		
Signal transducer and activator of transc	P40763	STAT3	10.1161/CIRCULATIONAHA.108.8065	2	Immuno	abdominal		73,72	B		
Smoothelin	P53814	SMTN	10.1161/ATVBAHA.114.304412, 10.1	2	Immuno	ascending	media	41,63	B	Marfan	higher than in control
Sorbin and SH3 domain-containing prote	Q9BX66	SORBS1	10.1074/mcp.M111.008128		Mass Spec	abdominal		>65	M		
Sorbin and SH3 domain-containing prote	O94875	SORBS2	10.1074/mcp.M111.008128		Mass Spec	abdominal		>65	M		
Spatacsin	Q96JI7	SPG11	10.1074/mcp.M111.008128		Mass Spec	abdominal		>65	M		not in healthy proteome
Spectrin alpha chain, erythrocytic 1	P02549	SPTA1	10.1074/mcp.M111.008128		Mass Spec	abdominal		>65	M		not in healthy proteome
Spectrin alpha chain, non-erythrocytic 1	Q13813	SPTAN1	10.1161/CIRCULATIONAHA.108.8435	2	Immuno;Mass Spe	ascending, abdominal		38,57,>65	B,M	Marfan, BAV	increased fragmentation than in control
Spectrin beta chain, non-erythrocytic 1	Q01082	SPTBN1	10.1074/mcp.M111.008128		Mass Spec	abdominal		>65	M		
Stabilin-1	Q9NY15	STAB1	10.1074/mcp.M111.008128		Mass Spec	abdominal		>65	M		not in healthy proteome
Staphylococcal nuclease domain-contain	Q7KZF4	SND1	10.1074/mcp.M111.008128		Mass Spec	abdominal		>65	M		
Stress-70 protein, mitochondrial	P38646	HSPA9	10.1074/mcp.M111.008128		Mass Spec	abdominal		>65	M		
Stromal cell-derived factor 1	P48061	CXCL12	10.1016/j.jvs.2006.11.020	1	Immuno	abdominal		74	M	atherosclerotic	same as in control
Stromelysin-1	P08254	MMP3	10.1159/000228900, 10.14670/HH-1	3	Immuno	ascending,abdomir	inflamation regions;intima;media	71,64,54,7	B	not Marfan,Marfan,BAV, degenerative	higher than in control
Superoxide dismutase [Cu-Zn]	P00441	SOD1	10.1074/mcp.M111.008128		Mass Spec	abdominal		>65	M		
Superoxide dismutase [Mn], mitochondr	P04179	SOD2	10.1074/mcp.M111.008128		Mass Spec	abdominal		>65	M		
Synaptic vesicle membrane protein VAT-	Q99536	VAT1	10.1074/mcp.M111.008128		Mass Spec	abdominal		>65	M		
Syndecan-1	P18827	SDC1	10.1371/journal.pone.0053882, 10.1	5	Immuno	abdominal	adventitia	69,73,74,7	B,M		not in healthy proteome
Talin-1	Q9Y490	TLN1	10.1074/mcp.M111.008128		Mass Spec	abdominal		>65	M		
Target of Nesh-SH3	Q7Z7G0	ABI3BP	10.1074/mcp.M111.008128		Mass Spec	abdominal		>65	M		lower than in control
T-cell surface glycoprotein CD3 epsilon c	P07766	CD3E	10.1093/cvr/cvp048, 10.1016/j.athe	3	Immuno	abdominal	adventitia;intima; media	63,70	B,M	sporadic, degenerative,unknown	not in healthy proteome
T-cell surface glycoprotein CD4	P01730	CD4	10.1371/journal.pone.0053882, 10.1	3	Immuno	abdominal		69,74,73	M,B		not in healthy proteome
T-cell surface glycoprotein CD8 alpha cha	P01732	CD8A	10.1161/CIRCULATIONAHA.108.8065	2	Immuno	abdominal		74,73	M,B		not in healthy proteome
T-complex protein 1 subunit gamma	P49368	CCT3	10.1074/mcp.M111.008128		Mass Spec	abdominal		>65	M		
Tenascin	P24821	TNC	16377578, 10.1111/j.1440-1827.201	3	Immuno;Mass Spe	abdominal,ascending		>65,56	M,B	unknown, BAV	higher than in control
Tenascin-N	Q9UQP3	TNN	10.1074/mcp.M111.008128		Mass Spec	abdominal		>65	M		not in healthy proteome
Tenascin-X	P22105	TNXB	10.1074/mcp.M111.008128		Mass Spec	abdominal		>65	M		same as control
Tetranectin	P05452	CLEC3B	10.1074/mcp.M111.008128		Mass Spec	abdominal		>65	M		same as in control
Thioredoxin	P10599	TXN	10.1016/j.atherosclerosis.2010.05.031		Immuno	abdominal	thrombus				
Thioredoxin domain-containing protein	Q8NBS9	TXNDC5	10.1074/mcp.M111.008128		Mass Spec	abdominal		>65	M		
Thioredoxin-dependent peroxide reduct	P30048	PRDX3	10.1074/mcp.M111.008128		Mass Spec	abdominal		>65	M		not in healthy proteome
Thrombomodulin	P07204	THBD	10.1161/ATVBAHA.115.305529		Immuno	abdominal	media				in control thrombomodulin is at tunica intima
Thrombopoietin	P40225	THPO	10.1016/j.jvs.2006.11.020	1	Immuno	abdominal		74	M	atherosclerotic	same as in control
Thrombospondin-1	P07996	THBS1	10.3892/ijmm.2012.985, 10.1093/cv	3	Immuno;Mass Spe	ascending,abdomir	adventitia;media	54,>65	B,M	Marfan,BAV,degenerative	higher than in control
Thrombospondin-2	P35442	THBS2	10.1093/cvr/cvu196, 10.1074/mcp.M111.008		Immuno;Mass Spe	ascending,abdomir	media	54,>65	B,M	Marfan,BAV,degenerative	higher than in control
Thymidine phosphorylase	P19971	TYMP	10.1093/cvr/cvu196, 10.1074/mcp.M	2	Immuno;Mass Spe	ascending,abdomir	media	54,>65	B,M	Marfan,BAV,degenerative	higher than in control
Tissue-type plasminogen activator	P00750	PLAT	10.2310/6670.2006.00008, 10.1159/	2	Immuno	abdominal		73,72	B		
Titin	Q8WZ42	TTN	10.1074/mcp.M111.008128		Mass Spec	abdominal		>65	M		
Toll-like receptor 3	O15455	TLR3	10.1016/j.atherosclerosis.2015.06.01	1	Immuno	abdominal					higher than in control
Toll-like receptor 4	O00206	TLR4	10.1016/j.atherosclerosis.2015.06.01	1	Immuno	abdominal					higher than in control
Trafficking kinesin-binding protein 2	O60296	TRAK2	10.1074/mcp.M111.008128		Mass Spec	abdominal		>65	M		not in healthy proteome
Transaldolase	P37837	TALDO1	10.1074/mcp.M111.008128		Mass Spec	abdominal		>65	M		
Transcription factor AP-1	P05412	JUN	10.1161/CIRCULATIONAHA.108.8065	3	Immuno	abdominal		73,74,72	B,M		not in healthy proteome
Transcription factor p65	Q04206	RELA	10.1161/CIRCULATIONAHA.108.8065	3	Immuno	abdominal		73,74,72	B,M		not in healthy proteome
Transcription factor SOX-9	P48436	SOX9	10.1093/cvr/cvw082		Immuno	abdominal		70	M		lower than in control
Transcription initiation factor TFIID subu	Q7Z7C8	TAF8	10.1074/mcp.M111.008128		Mass Spec	abdominal		>65	M		
Transforming growth factor beta-1	P01137	TGFB1	10.1016/j.jvs.2006.11.020, 10.1093/	3	Immuno	ascending,abdomir	adventitia;media	74,54,55	M	atherosclerosis,Marfan,BAV,degererative	higher than in control
Transforming growth factor beta-1-indu	O43294	TGFB1I1	10.1074/mcp.M111.008128		Mass Spec	abdominal		>65	M		lower than in control
Transforming growth factor beta-2	P61812	TGFB2	10.1002/path.2516		Immuno	ascending	media			Marfan,BAV,degererative	same as in control
Transforming growth factor beta-3	P10600	TGFB3	10.1002/path.2516		Immuno	ascending	adventitia			Marfan,BAV,degererative	same as in control
Transforming growth factor-beta-induce	Q15582	TGFBI	10.1510/icvts.2010.238139, 10.1074	2	Mass Spec	abdominal		70,>65	B,M		higher than in control
Transgelin	Q01995	TAGLN	10.3892/ijmm.2012.985,10.1161/AT	8	Immuno;Mass Spe	ascending, thoracic	media	41,68,48.3	B,M	Marfan,BAV,unknown	higher or lower than control or the same. BAV higher than control.
Transgelin-2	P37802	TAGLN2	10.1074/mcp.M112.021873, 10.1016	2	Mass Spec	ascending, abdominal		48.3,>65	B,M	BAV,unknown	higher than in control
Transitional endoplasmic reticulum ATPa	P55072	VCP	10.1074/mcp.M111.008128		Mass Spec	abdominal		>65	M		
Transketolase	P29401	TKT	10.1074/mcp.M111.008128		Mass Spec	abdominal		>65	M		
Transthyretin	P02766	TTR	10.1074/mcp.M112.021873, 10.1016	3	Immuno;Mass Spe	ascending, abdomi	intima	48.3,>65	B,M	BAV,unknown	BAV dilation lower than in control
Trifunctional enzyme subunit alpha, mito	P40939	HADHA	10.1074/mcp.M111.008128		Mass Spec	abdominal		>65	M		
Trifunctional enzyme subunit beta, mito	P55084	HADHB	10.1074/mcp.M111.008128		Mass Spec	abdominal		>65	M		
Triosephosphate isomerase	P60174	TPI1	10.1016/j.jvs.2011.10.033, 10.1074/	2	Immuno;Mass Spe	abdominal		69,>65	B,M	not Marfan	lower than in control
Tropomyosin alpha-1 chain	P09493	TPM1	10.1016/j.clinbiochem.2009.10.015,	2	Mass Spec	ascending, abdominal		48.3,>65	B,M	BAV,unknown	
Tropomyosin alpha-3 chain	P06753	TPM3	10.1074/mcp.M111.008128		Mass Spec	abdominal		>65	M		not in healthy proteome
Tropomyosin alpha-4 chain	P67936	TPM4	10.1074/mcp.M111.008128		Mass Spec	abdominal		>65	M		
Tropomyosin beta chain	P07951	TPM2	10.3892/ijmm.2012.985, 10.1016/j.jvs.2011.10.033, 10.1074/mcp.M112.021873, 10.1016/j.clinbiochem.2009.10.015, 10.1074/mcp.M111.008128	5	Mass Spec	ascending, thoracic,abdominal		69,48.3,>65	B,M	not Marfan,BAV,unknown	higher than in control or the same
Tryptase alpha/beta-1	Q15661	TPSAB1	10.1371/journal.pone.0053882, 10.1	6	Immuno;Mass Spe	abdominal	thrombus;wall lysate	69,70,79,7	B,M		same as or higher than in control
Tubulin alpha-1A chain	Q71U36	TUBA1A	10.1074/mcp.M111.008128		Mass Spec	abdominal		>65	M		

Tubulin beta chain	P07437	TUBB	10.1074/mcp.M112.021873, 10.1074	2	Mass Spec	ascending, abdominal		>65	M	BAV,unknown	higher than in control
Tubulin beta-2A chain	Q13885	TUBB2A	10.1074/mcp.M111.008128		Mass Spec	abdominal		>65	M		
Tubulin beta-3 chain	Q13509	TUBB3	10.1074/mcp.M111.008128		Mass Spec	abdominal		>65	M		not in healthy proteome
Tubulin beta-4B chain	P68371	TUBB4B	10.1074/mcp.M111.008128		Mass Spec	abdominal		>65	M		
Tubulointerstitial nephritis antigen-like	Q9GZM7	TINAGL1	10.1074/mcp.M112.021873, 10.1074	2	Mass Spec	ascending, abdominal		>65	M		
Tumor necrosis factor	P01375	TNF	10.1016/j.jvs.2006.11.020, 10.1161/(	10	Immuno	abdominal		69,74,73,6	B,M	unknown,atherosclerosis	higher than in control
Tumor necrosis factor ligand superfamily	P50591	TNFSF10	10.1016/j.bbrc.2007.03.209	1	Immuno	abdominal		76	B		
Tumor necrosis factor receptor superfan	O00220	TNFRSF10A	10.1016/j.bbrc.2007.03.209	1	Immuno	abdominal		76	B		
Tumor necrosis factor receptor superfan	O00300	TNFRSF11B	10.1161/CIRCULATIONAHA.104.4642	3	Immuno	abdominal	adventitia	70,76,69	B, M		lower than in control
Type-1 angiotensin II receptor	P30556	AGTR1	10.1016/j.atherosclerosis.2009.01.003		Immuno	abdominal	adventitia;inflamation regions	70.5	M		higher than in control
Type-2 angiotensin II receptor	P50052	AGTR2	10.1016/j.atherosclerosis.2009.01.003		Immuno	abdominal	adventitia	70.5	M		higher than in control
Ubiquitin carboxyl-terminal hydrolase is	P09936	UCHL1	10.1074/mcp.M111.008128		Mass Spec	abdominal		>65	M		
Ubiquitin-40S ribosomal protein S27a	P62979	RPS27A	10.1074/mcp.M111.008128		Mass Spec	abdominal		>65	M		
Urokinase-type plasminogen activator	P00749	PLAU	10.2310/6670.2006.00008	1	Immuno	abdominal		72	B		not in healthy proteome
Vascular cell adhesion protein 1	P19320	VCAM1	10.1159/000339304	1	Immuno	abdominal		73	B		not in healthy proteome
Vascular endothelial growth factor A	P15692	VEGFA	10.1016/j.jvs.2006.11.020, 10.1371/journal.pone.0089830, 10.1159/000339304, 10.1093/cvr/cvu196	4	Immuno	ascending,abdominal	adventitia;media	74,69,73,5	B	unknown,Marfan,BAV,degenerative,atherosclerosis	same or lower than in control
Vascular endothelial growth factor C	P49767	VEGFC	10.1371/journal.pone.0089830	1	Immuno	abdominal		69	B		not in healthy proteome
Vascular endothelial growth factor recep	P17948	FLT1	10.1371/journal.pone.0089830	1	Immuno	abdominal		69	B		not in healthy proteome
Vascular endothelial growth factor recep	P35968	KDR	10.1371/journal.pone.0089830	1	Immuno	abdominal		69	B		not in healthy proteome
Vascular endothelial growth factor recep	P35916	FLT4	10.1371/journal.pone.0089830	1	Immuno	abdominal		69	B		not in healthy proteome
Versican core protein	P13611	VCAN	10.3892/ijmm.2012.985, 10.1074/m	2	Mass Spec	abdominal		>65	M		lower than in control
Very long-chain specific acyl-CoA dehydr	P49748	ACADVL	10.1074/mcp.M111.008128		Mass Spec	abdominal		>65	M		not in healthy proteome
Vesicle transport protein SEC20	Q12981	BNIP1	10.1139/Y09-085	1	Immuno	abdominal		70	B		not in healthy proteome
Vimentin	P08670	VIM	10.3892/ijmm.2012.985, 10.1159/000339304,10.1093/cvr/cvt205, 10.1016/j.jvs.2011.10.033, 10.1016/j.ejcts.2009.07.025, 10.1074/mcp.M112.021873, 10.1007/s00595-012-0480-6, 10.1016/j.clinbiochem.2009.10.015, 10.1074/mcp.M111.008128	9	Immuno;Mass Spe	ascending, thoracic,abdominal	intima;media	73,63,69, 56,68,48. 3,>65	B,M	not Marfan,BAV,unknown	lower than in control or the same
Vinculin	P18206	VCL	10.1161/CIRCULATIONAHA.108.8435	2	Mass Spec	ascending, abdominal		38,>65	B,M	Marfan	higher than in control
Vitamin D-binding protein	P02774	GC	10.1510/icvts.2010.238139, 10.1161	3	Mass Spec	ascending, abdominal		70,38,>65	B,M	Marfan,unknown	lower than control
Vitamin K-dependent protein S	P07225	PROS1	10.1074/mcp.M111.008128		Mass Spec	abdominal		>65	M		not in healthy proteome
Vitronectin	P04004	VTN	10.3892/ijmm.2012.985, 10.1016/j.j	4	Immuno;Mass Spe	abdominal,thoracic	adventitia;thrombus	73.5,75, >(	B,M		higher than in control
von Willebrand factor	P04275	VWF	10.1159/000228900, 10.1016/j.atherosclerosis.2011.02.025, 10.1194/jlr.M042481, 10.1093/cvr/cvu196	4	Immuno	abdominal,ascendi	intima;media	69,39,55,7	B	unknown,Marfan,BAV,degenerative	Marfan and degenerative are higher than control
Xaa-Pro dipeptidase	P12955	PEPD	10.1186/1471-2350-12-14	1	Immuno	abdominal	adventitia;media	73	M		
X-ray repair cross-complementing protei	P12956	XRCC6	10.1074/mcp.M111.008128	1	Mass Spec	abdominal		>65	M		not in healthy proteome
Zinc-alpha-2-glycoprotein	P25311	AZGP1	10.1074/mcp.M111.008128	1	Mass Spec	abdominal		>65	M		

Appendix 3. Published article

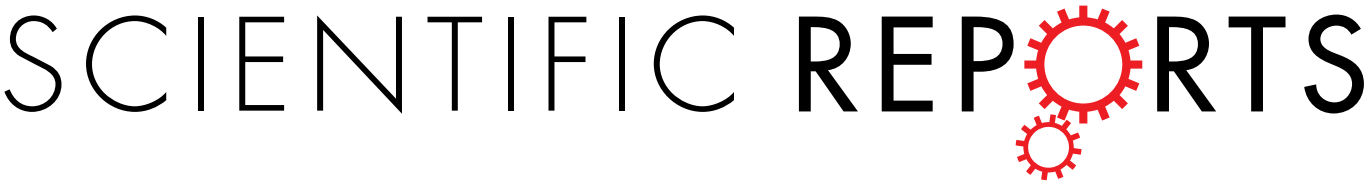

OPEN

Received: 18 August 2016
Accepted: 3 April 2017
Published online: 04 May 2017

High-Resolution Morphological Approach to Analyse Elastic Laminae Injuries of the Ascending Aorta in a Murine Model of Marfan Syndrome

Júlia López-Guimet[1], Jordi Andilla[2], Pablo Loza-Alvarez[2] & Gustavo Egea[1,3,4]

In Marfan syndrome, the tunica media is disrupted, which leads to the formation of ascending aortic aneurysms. Marfan aortic samples are histologically characterized by the fragmentation of elastic laminae. However, conventional histological techniques using transverse sections provide limited information about the precise location, progression and 3D extension of the microstructural changes that occur in each lamina. We implemented a method using multiphoton excitation fluorescence microscopy and computational image processing, which provides high-resolution en-face images of segmented individual laminae from unstained whole aortic samples. We showed that internal elastic laminae and successive 2nd laminae are injured to a different extent in murine Marfan aortae; in particular, the density and size of fenestrae changed. Moreover, microstructural injuries were concentrated in the aortic proximal and convex anatomical regions. Other parameters such as the waviness and thickness of each lamina remained unaltered. In conclusion, the method reported here is a useful, unique tool for en-face laminae microstructure assessment that can obtain quantitative three-dimensional information about vascular tissue. The application of this method to murine Marfan aortae clearly shows that the microstructural damage in elastic laminae is not equal throughout the thickness of the tunica media and in the different anatomical regions of the ascending aorta.

In mammals, the heart periodically ejects blood to the aorta, which is the main elastic artery in the body. The specific histological composition of the aorta allows an elastic response to blood ejection, which consists in the circumferential stretching of its wall and the subsequent recoil. The aortic wall is divided into three layers[1]: (i) the innermost layer named the tunica intima, composed of a monolayer of endothelial cells and subendothelial connective tissue that covers the luminal surface of the vessel; (ii) the tunica media, the thickest layer, is composed of elastic fibres arranged as fenestrated sheets (called elastic lamellae or laminae) alternating with circumferentially oriented layers of smooth muscle cells; and (iii) the tunica adventitia, the outermost layer, is composed of loose fibroelastic connective tissue enriched in collagen fibres and fibroblasts. Media elastic lamellae are concentrically arranged, with smooth muscle cells, collagen, proteoglycans and other extracellular matrix components filling the interlamellar space[2,3]. The main function of these lamellae is to provide the elasticity needed for the aorta to stretch and recoil. The lamellae are wavy when the aorta is non-pressurized, and straight when subjected to *in vivo* blood pressure[4]. The most luminal lamina, named the internal elastic lamina (IEL), serves as a frontier between intimal endothelium and the tunica media. Transversely sectioned, conventional histological preparations of the aortic wall show elastic lamellae arranged in almost equidistant parallel layers, whose number depends on the animal species, and vessel calibre[5], and is 7 to 8 on average for adult mice[6]. In addition, the surface of lamellae contains fenestrae, which are small holes of 1–10 μm in diameter[7]. Their size and density depend on the analysed

[1]Departament de Biomedicina, Facultat de Medicina i Ciencies de la Salut, Universitat de Barcelona, Barcelona, Spain. [2]ICFO-Institut de Ciències Fotòniques, The Barcelona Institute of Science and Technology, 08860, Castelldefels, Barcelona, Spain. [3]Institut de Recerca Biomèdica August Pi i Sunyer (IDIBAPS), Barcelona, Spain. [4]Institut de Nanociència i Nanotecnologia IN2UB, Universitat de Barcelona, Barcelona, Spain. Correspondence and requests for materials should be addressed to G.E. (email: gegea@ub.edu)

vessel, animal species and age[8–10]. Their role is not yet well-established, but it is thought that they facilitate the flow of nutrients and the connection between cells located in different interlamellar spaces, and contribute to the developmental modelling of the IEL[11].

It is of fundamental importance to preserve the integrity of all the aortic wall components in order to maintain effective vessel function[12]. In some pathologic conditions, the aortic structure is severely altered, which compromises its vital role in blood conduction. An example of this aberrant structure occurs in Marfan syndrome (MFS)[13]. MFS is an autosomal dominant heritable disorder that affects the cardiovascular, skeletal, ocular, pulmonary and nervous systems. MFS is caused by mutations in the fibrillin-1 gene (*Fbn1*)[14], which encodes for fibrilin-1 protein, a basic component of the medial elastic lamellae. These mutations can directly affect the assembly of the matrix of the aortic media, leading to life-threatening aortic aneurysms[15]. Conventional histological studies show that Marfan aortic samples are characterized by fragmentation and disorganization of elastic fibres, accumulation of amorphous matrix components, fibrotic collagen production, and loss of cells[12, 13]. Moreover, the elastin content in human Marfan aorta is almost 50 per cent lower[12, 16], and scanning electron microscopy demonstrates a significant loss of interlamellar fibres that link neighbouring laminae[17]. To study Marfan disease process, mice have been genetically engineered to replicate the clinical spectrum of the human disease. One of the most representative models is the $Fbn1^{C1039G/+}$ murine model, in which a cysteine is substituted with a glycine at amino acid 1039 in an EGF domain of the protein[18], mimicking the most frequent type of mutation in human MFS patients. This Marfan murine model shows the formation of ascending aortic aneurysm, with the accompanying fragmentation of elastic fibres, overactivation of TGF-β signalling, disarray of smooth muscle cells, and disorganization of the collagen network[18, 19].

The usual approach to examine the aforementioned aortic histological alterations is by conventional histological methods using fixed, dehydrated, paraffin-embedded, sectioned and stained samples. In recent decades, this approach has provided important knowledge about aneurysm initiation and progression in MFS and other aortopathies[20–22]. Nevertheless, the knowledge obtained using this methodology is inherently based on a two-dimensional perspective of the tissue, which is highly limiting to determine the location, progression and extension of the tunica media injuries when a three-dimensional (3D) microstructural analysis is required. For instance, it is not feasible to study fenestrae by classical histological methods due to their small size and distribution along the surface of lamellae. Therefore, for further insights, more sophisticated microscopy techniques have been developed and progressively applied to the cardiovascular system, including the aorta[23, 24]. In particular, multiphoton microscopy is well-suited for arterial wall imaging, since it permits visualization of almost the entire wall, without the need for exogenous fluorophores, or even sample fixation and embedding[25]. In the arterial case, multiphoton microscopy takes advantage of two nonlinear optical phenomena: two-photon excitation fluorescence (TPEF) or autofluorescence, and second harmonic generation (SHG)[26]. Based on endogenous tissue sources of nonlinear signals, the TPEF signal arises from the elastin content in elastic lamellae and the SHG signal originates from collagen fibres located at the adventitia and interlamellar spaces. Taking into account that these two matrix components make up most of the arterial tissue structure, multiphoton microscopy can disclose almost all the framework of an unstained aortic wall[25]. In addition, vascular samples can be imaged without tissue sectioning, using specific microscopy setups[27]. To date, some laboratories have used this technique to image aortic samples in a conventional transverse perspective (XZ or YZ axes)[25, 28], as in standard histological preparations. A few other groups have applied multiphoton microscopy to image the tissue in an en-face view, and subsequently generated a three-dimensional rendering of it[29, 30]. The en-face histological perspective consists of visualizing the surface of the vessel (XY axes) along the depth of its wall. An illustrative example of en-face visualization is that obtained by endoscopic imaging. This unique view is very useful for the analysis of lamellae fenestrae, since they are localized on the laminae surface. Taking into account that conventional histological preparations of arterial tissue are sectioned in the transverse plane, fenestrae have historically been visualized by scanning electron microscopy[8]. However, this technique can only display the natural surface of the tissue, and hence studies have mainly focused on the IEL[7, 8]. Furthermore, the recent application of TPEF microscopy on rat artery samples has allowed the visualization and analysis of IEL fenestrae only[10, 31], and has also been used in combination with exogenous fluorophores[32]. En-face TPEF microscopy has been used in Marfan mice to observe elastic lamellae fenestrae changes and thus report an elastolytic process, but with low-resolution imaging and very limited quantitative analysis[33, 34]. To our knowledge, no further data is available on lamellae 3D microstructure features in health or disease.

In this context, our aim was to provide further insights into the characterization of elastic lamellae microstructure, including fenestrae features, using the ascending aorta of MFS $Fbn1^{C1039G/+}$ mice as a histopathological model of tunica media alterations that typically occur in aortic aneurysms. To achieve this aim, we applied a recently implemented microscopy and computational method that we developed, which provides the en-face TPEF image of segmented individual lamellae from unstained whole aortic samples. The approach takes advantage of high resolution en-face multiphoton microscopy to characterize lamellae structural alterations in detail without sectioning the tissue. In addition, our study adds to the literature a semi-automatic image processing protocol that can isolate individual lamellae, which can be used to analyse microstructure in complex arterial wall samples. These two advantages allow the comparison of lamellae features within different anatomical regions of the vessel and within different lamellae from the same XY location. In particular, the application of our methodology to MFS murine aortae showed relevant lamellae fenestrae differences between IEL and 2nd laminae, and between the proximal-concavity and the rest of the anatomical regions in the ascending aorta.

Results

New multiphoton en-face imaging and analysis of unstained aorta. To obtain high-quality en-face images of intact mice aortae that allow a detailed assessment of lamellae microstructural alterations, we established a new method involving tissue preparation, image acquisition, processing, and analysis. To begin with, the

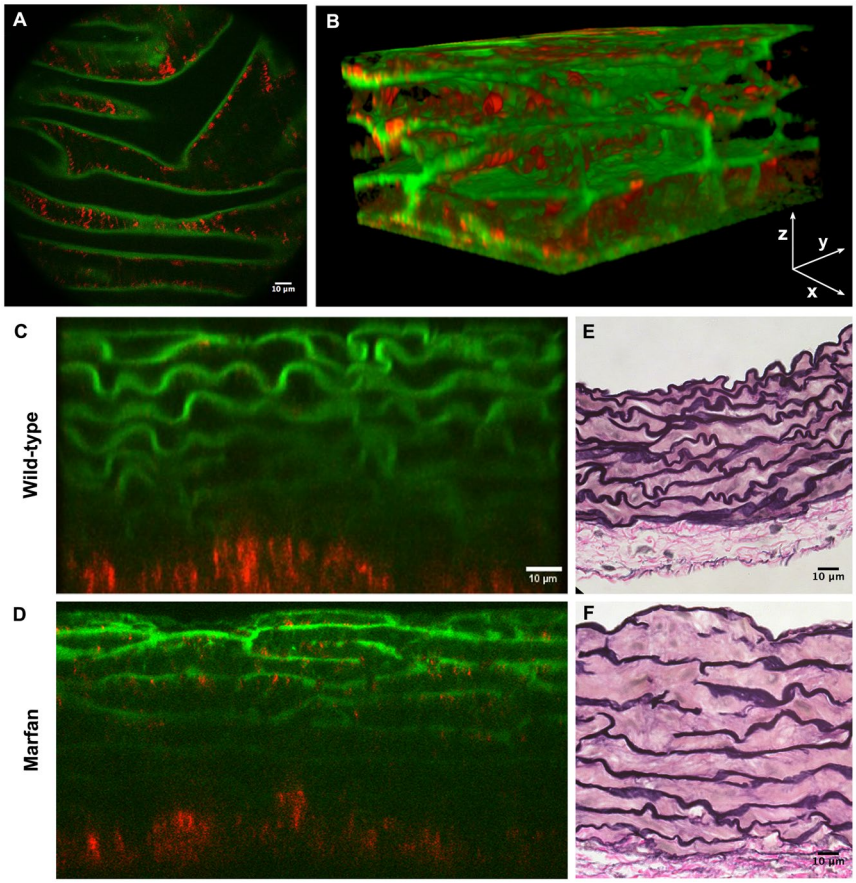

Figure 1. Aortic tissue visualizations using multiphoton microscopy. (**A**) En-face perspective of the IEL of the ascending aorta from a WT mouse using multiphoton microscopy. TPEF signal of elastin in green and SHG signal of collagen in red. (**B**) Three-dimensional rendering of a portion of the tunica media from the ascending aorta of a WT mouse. (**C** and **D**) Representative multiphoton images of the tunica media in transverse views of WT (**C**) and Marfan (**D**) mice. (**E** and **F**) Conventional histological visualization of elastic fibres using Verhoeff-van Gieson staining in WT (**E**) and Marfan (**F**) aortic tissue. Scale bar, 10 μm.

entire aorta was dissected from the animal and immediately fixed in formol. Then, the vessel was cut in half longitudinally and mounted with the tunica intima facing onto the cover slide. This sample mounting arrangement allowed en-face imaging of the vessel surface as it would be seen by *in vivo* endoscopy. In addition, mounting the sample in this way was the most suitable approach to let microscopic light get through the vessel wall from the inner intima to the outermost adventitia layer, thus avoiding the expected premature light absorption by the presence of abundant adventitial collagen. Next, the ascending portion of aortic samples was imaged using a custom-made multimodal microscope[35], which permitted simultaneous visualization of the elastic lamellae by elastin TPEF and collagen fibres by SHG. Thus, we could image the medial elastic lamellae (green) and the adventitial collagen plus the medial collagen fibres (red) (Fig. 1A–D). Acquisitions consisted of an en-face z-stack of confocal images, beginning at the tunica intima and running until the elastin signal became too low for the subsequent segmentation. Loss of signal was due to ordinary light absorption and scattering, and it was evident at ~60 μm inside the tissue (see the transverse views of 80 μm depth in Fig. 1C and D). Since acquisitions were taken en-face (XY axes) (Fig. 1A) and running into the tissue (Z axis), image stacks allowed visualization and understanding of the tissue in three dimensions (XYZ axis), and provided a vision of the entire volumetric structure of the aortic tunica media (Fig. 1B). Consequently, the transverse image of the aortic tissue can be obtained by visualizing the 3D image volume from the XZ or YZ perspectives (Fig. 1C and D), which was comparable with conventional histological preparations visualized by bright field microscopy (Fig. 1E and F).

The series of consecutive transverse images of elastin signal often showed the progression of lamella branching, small breaks, crosslinking between neighbouring lamellae and/or abrupt ending of lamellae (Supplementary Figure 1). These findings showed that aortic elastic lamellae are arranged in a 3D cage-like network[1,2], with irregularities that disrupt the apparent parallel arrangement seen in conventional histological preparations. Moreover, this view did not allow detailed lamellae microstructure visualization, and therefore segmentation of individual lamellae out of the acquired TPEF stack was then necessary. Consequently, to work with *clean* individual elastic lamella images, we developed a semi-automatic segmentation protocol in ImageJ software[36] that processed the original elastin stack (Fig. 2). Briefly, each en-face image stack (XY) was virtually resliced to

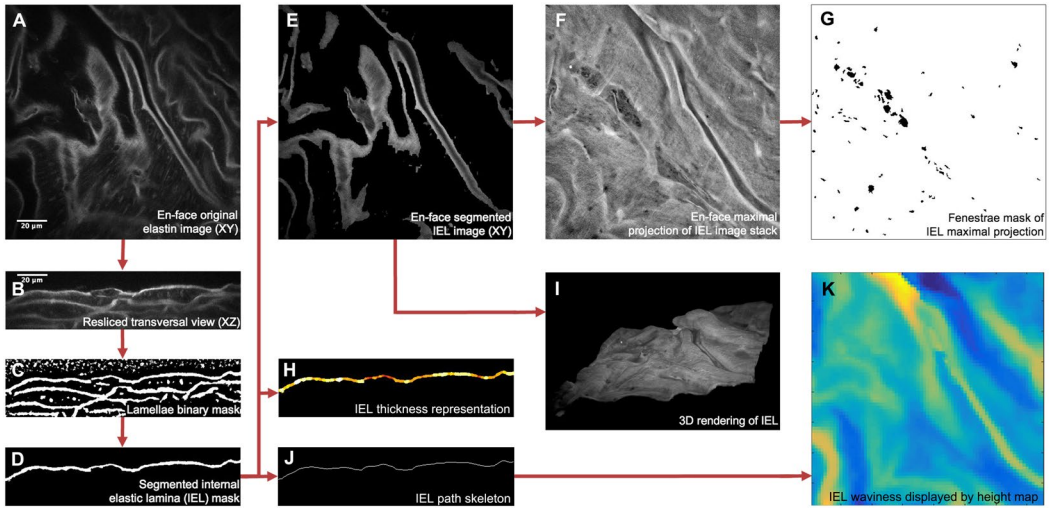

Figure 2. Image processing protocol to obtain en-face segmented elastic laminae and subsequent quantitative analysis. (**A**) Representative image of an acquired original en-face TPEF stack. Elastin TPEF and background cell autofluorescence signals are visualized in grey scale. (**B**) Representative image of the resliced original stack to transverse view. (**C**) Representative image of the binary mask stack that was subsequently obtained. Elastin signal and some background spots are automatically marked in white, the rest of the tissue is marked in black. (**D**) Representative image of segmented individual lamina mask stack. In this case, only the IEL mask was selected. (**E**) Representative image of the resulting en-face IEL stack. (**F**) En-face maximal projection comprised of all images within the IEL stack. (**G**) Binary mask of all fenestrae seen at the maximal projection (**F**). (**H**) Representative image of thickness display stack. Highest thickness is marked by white colour. (**I**) 3D rendering of the lamella obtained from the IEL stack. (**J**) Representative image of lamella skeleton image stack. (**K**) Height map showing global lamella waviness. Yellow denotes low and dark blue high heights. Scale bar, 20 µm.

build its corresponding transverse image stack (YZ) (Fig. 2A and B), and then binary auto-thresholding was used to discriminate the elastin signal from the background (Fig. 2C). The chosen elastic lamella was then manually selected, and a new mask image stack was created with only this selection (Fig. 2D). The complete lamella mask stack was resliced back to the en-face view, and finally, it was applied to the original one (Fig. 2B) to generate the image stack of the selected individual elastic lamella (Fig. 2E). The en-face lamella stack provided 3D information on an isolated lamella, which could be represented as a 3D rendering (Fig. 2I) or a maximal projection image (Fig. 2F). Either of these representations revealed topological and structural data, but we chose the latter to perform a straightforward quantitative analysis. Thus, the surface of lamellae in two dimensions was displayed in its maximal projection image, so that its microstructure could be studied. Each fenestra (i.e. dark holes) found in the maximal projection of individual lamella was selected and marked in a fenestrae map (Fig. 2G). From this map, we carried out a morphological analysis to assess the density and size of fenestrae.

Our methodology could also be used to assess lamellae thickness, without any further procedure, by applying the BoneJ plugin for ImageJ[37]. This program quantifies lamella thickness and generates a visual colour representation from blue (lowest thickness) to white (highest thickness) (Fig. 2H).

Another lamellar feature that could be evaluated from the image acquisitions was the waviness of each lamella. To this aim, we developed a new approach based on measuring the height of the lamella in each pixel position of the image stack (Fig. 2J). This procedure, however, required a single Z axis height value per X-Y position. To this aim, we created a new protocol combining ImageJ and MATLAB software, which refined each segmented lamella image stack and its subsequent skeleton. Once the lamina skeleton had been obtained (Fig. 2J), we could evaluate its waviness in terms of height variation in the Z axis. Height values were organized into histograms and waviness maps represented by colours ranging from yellow (the lowest) to dark blue (the highest) (Fig. 2K).

En-face microstructural analysis of wild-type and Marfan aortic elastic lamellae. Next, we applied the aforementioned methodology to examine in detail the elastic lamellae in the ascending aortic tissue in wild-type (WT, n = 4) and Marfan mice (MF; *Fbn1*$^{C1039G/+}$ model, n = 6). Four en-face z-stack acquisitions were randomly taken from each aorta sample, and fenestrae data were obtained from the maximal projection of each of the segmented lamellae. For each image stack, we segmented and analysed the IEL and the elastic lamina located just underneath it (2nd lamina) to obtain the mean fenestrae density and the distribution of fenestrae sizes for each lamella maximal projection. We also measured lamellae thickness and waviness for each image stack. The transverse view of the aortic wall obtained by TPEF (Fig. 1C and D) closely matched what is seen in conventional histological preparations using Verhoeff-van Gieson staining (Fig. 1E and F). Marfan tissue visualized by both techniques showed lamellae disruptions and disarrangement (Fig. 1D and F) compared to WT tissue (Fig. 1C and E).

The en-face view showed that the IEL in WT animals had a flat, continuous aspect with unevenly distributed small fenestrae, which are visualized as small black holes (Fig. 3A). The IEL in Marfan mice showed more

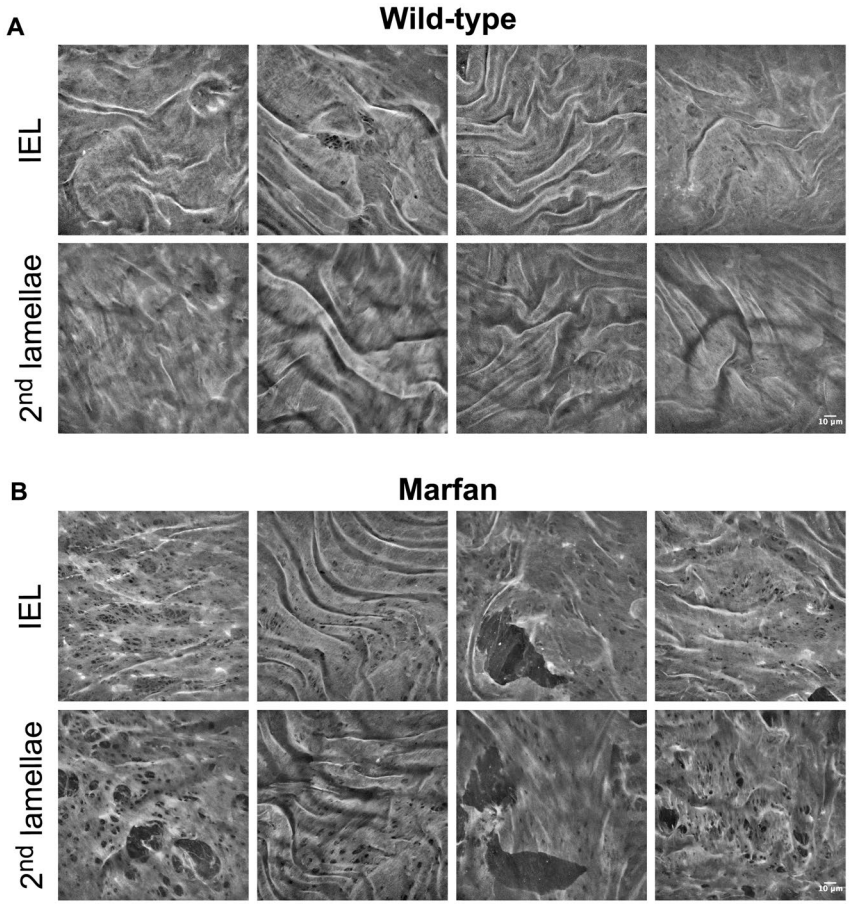

Figure 3. Representative en-face images of wild-type and Marfan elastic laminae. Maximal projections of segmented IEL and 2nd lamina of WT (**A**) and Marfan (**B**) aortae. IEL and 2nd laminae images of each column belong to the same image stack acquisition. In addition, each column corresponds to a different animal. Fenestrae are seen as black holes of variable size. Big polygonal black holes are considered ruptures, and are excluded from fenestrae quantification. Scale bar, 10 μm.

prominent fenestrae and occasional large ruptures (Fig. 3B). It could be postulated that these lamellar ruptures might be merely caused by sample handling during the surgery. To elucidate this, we measured the length of the rupture's hole at different points in the XY maximal projection. Our aim was to mimic the quantitation of the length for elastic laminae breaks when aortae are examined transversally in classic histological preparations (Fig. 1F). Thus, to resemble conventional histological sectioning, we used a standard grid that marked all the horizontal and vertical lines where length measurements should be performed for all ruptures. This way, the maximal projection rupture length was on average 20.71 μm at IEL and 30.73 μm at the 2nd lamellae. Altogether, the length of Marfan ruptures was 26.52 μm (±19.29 μm). For comparative reasons, we quantified the length of elastic laminae breaks from 24 conventional histological preparations of Marfan aortae (Fig. 1F), giving a mean length of 20.95 μm (±19.47 μm). Note that the values obtained from en-face and transversal histology are very similar and therefore, the ruptures in Marfan en-face images of IEL and 2nd lamellae (Fig. 3B, third column panels from the left) correspond to the classical elastic laminae breaks observed by conventional histological methods and not primarily caused by sample handling.

Despite having an identical genetic background, Marfan mice showed variable lamina aspect patterns. However, the differences with WT mice were clearly evident. In particular, fenestrae density was 2.5 fold higher in Marfan IEL than in WT IEL (Fig. 4A; median values: 2.14 fenestrae/mm^2 in WT vs. 5.53 fenestrae/mm^2 in MF). Marfan mice also had significantly larger fenestrae than WT mice (Fig. 4B; 2.07 μm^2 in WT vs. 2.25 μm^2 in MF). Consequently, the total area of elastic lamina occupied by fenestrae in the field of view was clearly larger in Marfan mice.

The 2nd elastic laminae were segmented and analysed in the same way as the IEL. We observed that the structural differences between WT and Marfan 2nd laminae were even more evident than in the IEL (Fig. 3). The results of quantitative analysis of the 2nd laminae were very similar to those obtained in the IEL when we compared WT and Marfan mice. Fenestrae density and size were significantly greater in the 2nd lamellae of Marfan mice than in WT mice (Fig. 4; density: 1.29 fenestrae/mm^2 WT vs. 4.34 fenestrae/mm^2 in MF; size: 2.43 μm^2 WT vs. 3.06 μm^2 in MF). No differences in fenestrae density were observed between the IEL and 2nd lamellae in WT and Marfan mice (Fig. 4A). However, there was a significant increase in the size of fenestrae between IEL and the 2nd lamellae

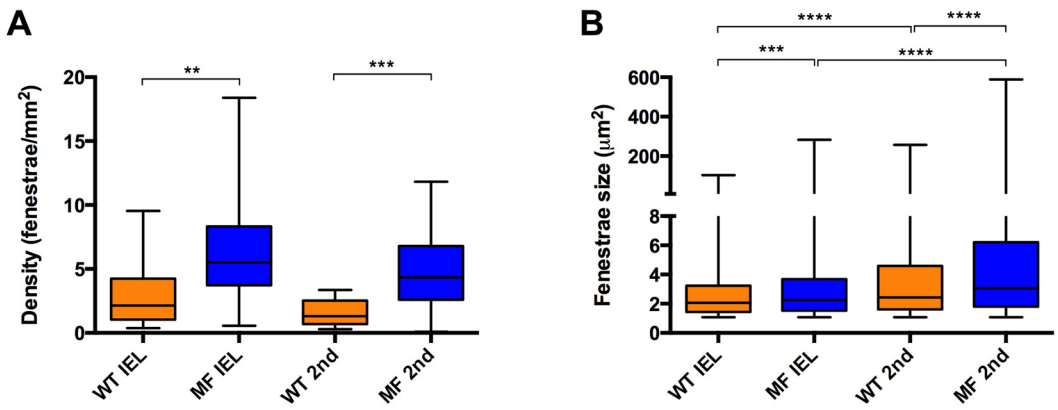

Figure 4. Quantitative analysis of density and size of fenestrae seen in IEL and 2nd elastic laminae from en-face maximal projection images. Fenestrae density (**A**) and size (**B**) seen in WT (orange) and Marfan (MF, blue) IEL and 2nd lamellae. Statistical significance between groups is indicated by asterisks, and defined in the Materials and Methods section. Interquartile boxplots with minimum and maximum whiskers. Forty maximal projections were analysed and a total of 6,400 fenestrae were quantified.

in WT and Marfan aortae (Fig. 4B), which was more pronounced in Marfan aortae (WT: 2.07 µm² in IEL vs. 2.43 µm² in 2nd lamina; MF: 2.25 µm² in IEL vs. 3.06 µm² in 2nd lamina).

Next, we performed a systematic analysis of the density and size of fenestrae in different anatomical locations of the ascending aorta. The locations were defined as proximal, central and distal in the longitudinal plane, and as concavity and convexity in the circumferential plane (Fig. 5A–C). A qualitative examination of images of the aforementioned regions revealed that laminae obtained in the convexity and proximal zones apparently had more microstructural damage (Fig. 5D and E). Indeed, statistically significant differences were observed between WT and Marfan mice in the IEL and in the 2nd elastic lamina, mainly in the proximal and convex regions. In particular, the median density of fenestrae in proximally located IEL (Fig. 6A) and 2nd laminae (Fig. 6B) were 7.5 and 6 times higher respectively in Marfan than in WT mice (IEL: 1.02 fenestrae/mm² WT vs. 7.60 fenestrae/mm² in MF; 2nd lamella: 1.14 fenestrae/mm² in WT vs. 6.74 fenestrae/mm² in MF). Moreover, Marfan fenestrae were significantly larger at proximal and distal IEL (Fig. 6C), and at proximal and central 2nd laminae (Fig. 6D).

The circumferential partition of data (Fig. 7) showed that fenestrae density in WT IEL located at the concavity (cv) was significantly higher than that at the convexity (cx) of the aorta (Fig. 7A; 1.78 fenestrae/mm² in cx vs. 5.81 fenestrae/mm² in cv). However, this was not the case for WT 2nd laminae (Fig. 7B; 1.27 fenestrae/mm² in cx, and 2.46 fenestrae/mm² in cv). In contrast, Marfan IEL fenestrae density ranges at concavity and convexity (2.8–9.1 fenestrae/mm²) were highly similar to that at WT concavity (2.7–9 fenestrae/mm²), and greater than at WT convexity (1–2.5 fenestrae/mm²) (Fig. 7A). At the 2nd laminae, Marfan fenestrae density was similar to that at the Marfan IEL (compare MFcx with MFcv in Fig. 7A and B), and higher than 2nd laminae WT density in both circumferential regions (Fig. 7B), but was only significant at the convex region. We observed a significant difference in the size of fenestrae between Marfan and WT convexities both at the IEL and the 2nd laminae (Fig. 7C and D, respectively; IEL: 1.98 µm² in WT vs. 2.25 µm² in MF; 2nd laminae: 2.52 µm² in WT vs. 3.06 µm² in MF). In summary, structural injuries in the Marfan ascending aortae were regionalized, and were preferentially accumulated in the convexity region of the circumferential plane, and mainly in the proximal region of the longitudinal plane.

Finally, we also examined potential differences between WT and Marfan mice regarding lamellae thickness and waviness. Lamellae thickness showed that in WT and Marfan, IEL and 2nd lamellae were on average 2.7–3.0 µm, without significant differences between them (Supplementary Figure 2A). In addition, the measurement of waviness showed that WT and Marfan lamellae had the same spectrum of height values (Supplementary Figure 2B).

Discussion

In this article, we report the implementation of a new multiphoton microscopy image processing method for elastic lamellae microstructure examination, based on obtaining series of en-face images from unstained aortic tissue. We used healthy and MFS murine aortae as tissue models and determined the anatomical distribution of fenestrae alterations that occur in elastic laminae. In the last decade, a lot of data have been generated about histological damage in the aortic wall in MFS, using routine histological techniques following the conventional sequence of paraformaldehyde/formol fixation, paraffin embedding, sectioning and histological (immune) staining. Technological improvements in microscopy and importantly in image processing have provided a new panorama to the histopathology field[2]. Accordingly, here we applied en-face multiphoton microscopy and a segmentation protocol to assess lamellae morphology. The advantages of our new approach are: (i) it can produce high-resolution en-face confocal stacks that enable detailed visualization of histological structures; (ii) it can obtain quantitative information belonging to the three dimensions XYZ, which increases our understanding of 3D histological arrangements; and (iii) the entire aortic vessel can be viewed, for straightforward monitoring of different anatomical regions.

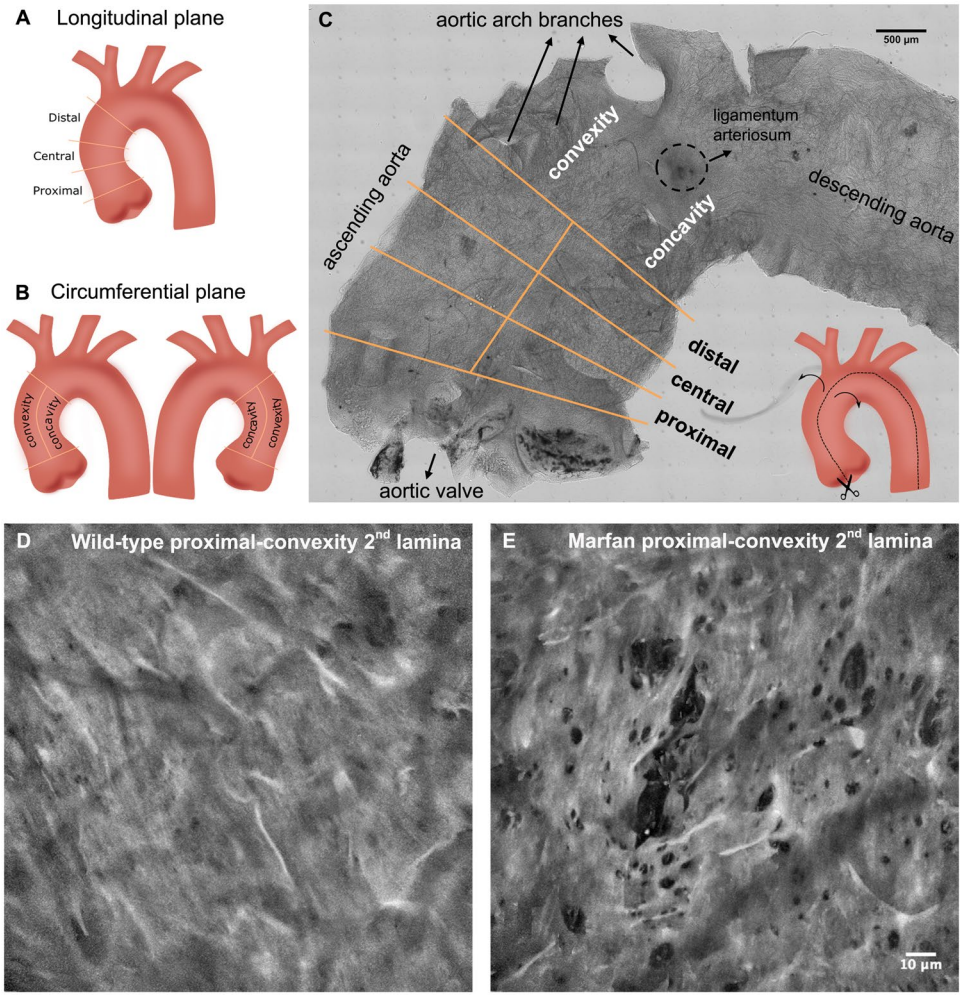

Figure 5. Anatomical regionalization of ascending aorta used in this study. (**A** and **B**) Schematic drawings of defined ascending aorta anatomical regions used in our study in longitudinal (**A**) and circumferential (**B**) planes. (**C**) Bright field image map of the longitudinally open aorta (as shown in the inset schematic drawing) and the corresponding regions. (**D** and **E**) Representative maximal projections acquired in the proximal-convex region of WT (**D**) and Marfan (**E**) aortae. Scale 500 µm in (**C**) and10 µm in (**D**,**E**).

Although TPEF confocal microscopy has been used to obtain the elastin signal of vessels in other studies[25], our report is the first to our knowledge in which a semi-automatic image processing protocol is systematically implemented to segment individual lamellae and quantitatively analyse histological microstructural changes. Furthermore, this unique analysis was performed on en-face images of ascending aorta tunica media of a murine model of MFS, in which elastic fibre ruptures are known to be associated with the formation and progression of aortic aneurysm[18]. Related previous studies in MFS reported "disruptions" in en-face images from pressurized adult MF mice descending aortae, but without any quantitative analysis[33]; and also reported a ≈40 µm "hole" diameter measurement based on non-segmented lamellae of diseased tissues only (from another MFS murine model)[34]. In addition, the measurement of elastic laminae features of transversely viewed parts of Marfan mice aortae obtained by multiphoton microscopy was reported as an alternative to conventional histological methods[38]. Here, we complement these studies and highlight the relevance of en-face multiphoton microscopy and image processing for generating quantitative 3D microstructural data on individual elastic lamellae. We report new histopathological alterations in the aortic media in the murine *Fbn1*$^{C1039G/+}$ model of MFS: lamellae in the ascending aorta show larger and more fenestrae than WT tissue. The density of fenestrae in Marfan elastic laminae is at least double that found in WT. These fenestrae alterations probably represent lamellar micro-damage, which could be directly related to the characteristic elastic lamellae fragmentation and disarrangement happening in Marfan aortae[38].

Interestingly, our results show that alterations in the density and size of fenestrae did not occur uniformly in the entire Marfan ascending aortic media, but were mostly restricted to the proximal and convex regions. This is in accordance with results reported by ref. 39 in the ascending aorta of angiotensin II-infused ApoE$^{-/-}$ mice. Using conventional histological techniques, they reported that the largest aortic wall dissections occurred in the outer convex quadrant, which corresponds to the central part of the aortic convexity. We speculate that the

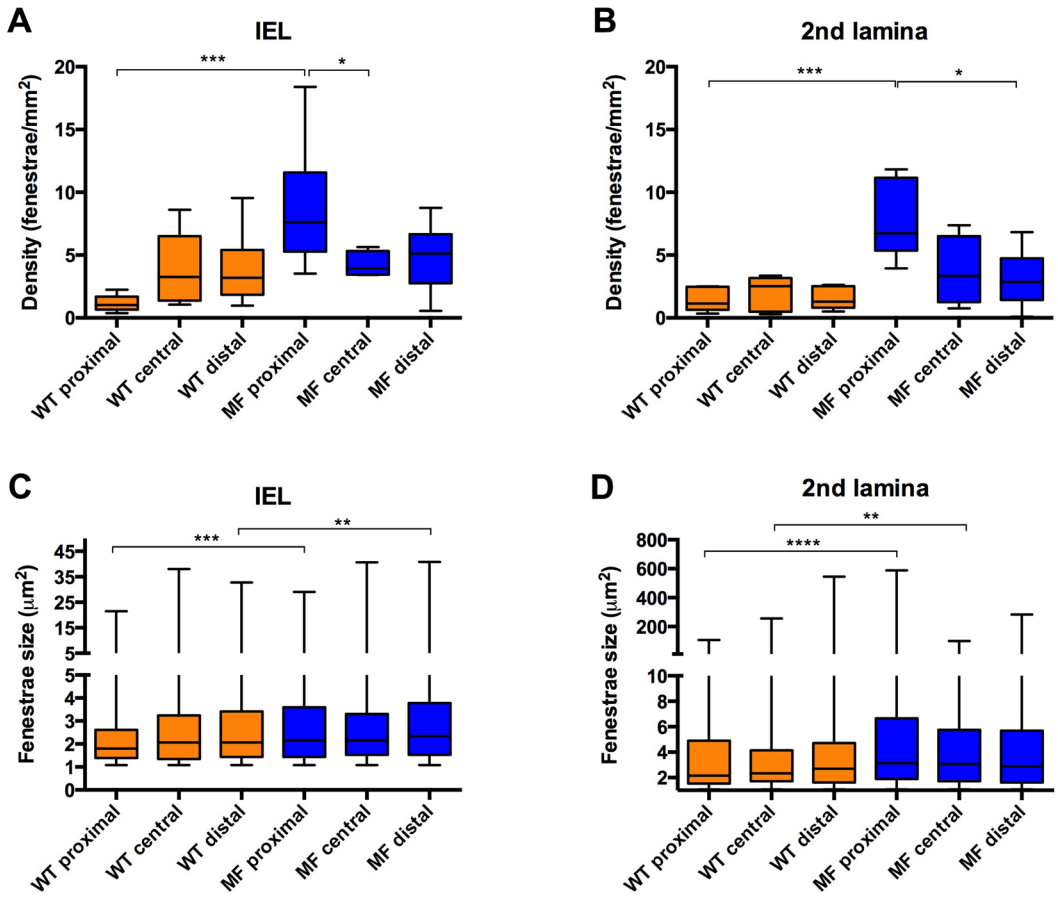

Figure 6. Quantitative analysis of fenestrae in IEL and 2nd laminae in the longitudinal plane of the ascending aorta. The density of fenestrae in the IEL (**A**) and 2nd lamina (**B**), and their respective individual fenestrae size (**C** and **D**) measured at different longitudinal plane locations (proximal, central and distal) of WT (orange) and Marfan (MF, blue) ascending aortae. Statistical significance between groups is indicated by asterisks. Interquartile boxplots with minimum and maximum whiskers. Forty maximal projections were analysed and a total of 6,400 fenestrae were quantified.

regionalized structural changes reported here could be due to a preferential impact of the blood flow on the convex and proximal ascending aortic regions. It is known that deviant blood flow can be caused by aortic valve dysfunction[40]. In particular, the convexity of ascending aorta is the preferential blood flow impact zone found in bicuspid aortic valve disease[41], which is accompanied by differential lamellae fragmentation and matrix protein expression patterns in comparison to the concavity[42]. In the case of MFS patients, aortic root dilatation usually entails aortic valve dysfunction[43], which in turn causes aortic blood flow disturbance[43,44] leading to mild or moderate aortic regurgitation[44,45]. Therefore, it is reasonable to hypothesize that MFS disturbed flow could be mainly impacting on this particular anatomical zone, just as happens in bicuspid aortic valve pathology. This premise should be confirmed by further detailed hemodynamic studies on Marfan patients and murine models, which to our knowledge are not currently available.

A recent paper[39] reported a transmural gradient of lamellar injury, in which elastic laminae break number varies significantly amongst lamellae. In particular, central lamellae including the 2nd showed more breaks than peripheral ones. The results of our comparisons of fenestrae density and size between the IEL and the 2nd lamina also suggest a histological injury gradient, where the damage is more severe in the 2nd lamina than in the IEL. Again, we can only speculate about the significance of this difference. It could be related to intrinsic robustness of the IEL, whose structure and organization might be better adapted to support the mechanical impact of blood flow than the rest of laminae. In this respect, aortic transmural mechanical behaviour has been studied in relation to transmural structural properties[46,47]. Results show that the porcine thoracic descending aorta wall is divided into transverse outer and inner tunica media halves, which differ in their mechanical and molecular composition. In addition, the alignment of bovine elastic and collagen fibres due to mechanical load varies in lamellae localized close to the endothelium and in the subsequent lamellae[48]. We are aware that this variance cannot be directly extrapolated to mice, due to differences in the animal model used and the aortic portion examined in terms of wall thickness and lamellae number. Nonetheless, it cannot be discarded that similar structural variance between lamellae occurs in mice as well. Our results suggest that this variance might take place between IEL and successive lamellae. In the case of Marfan mice aortae, we hypothesise that the weakness of the tunica media[16,49] plus the

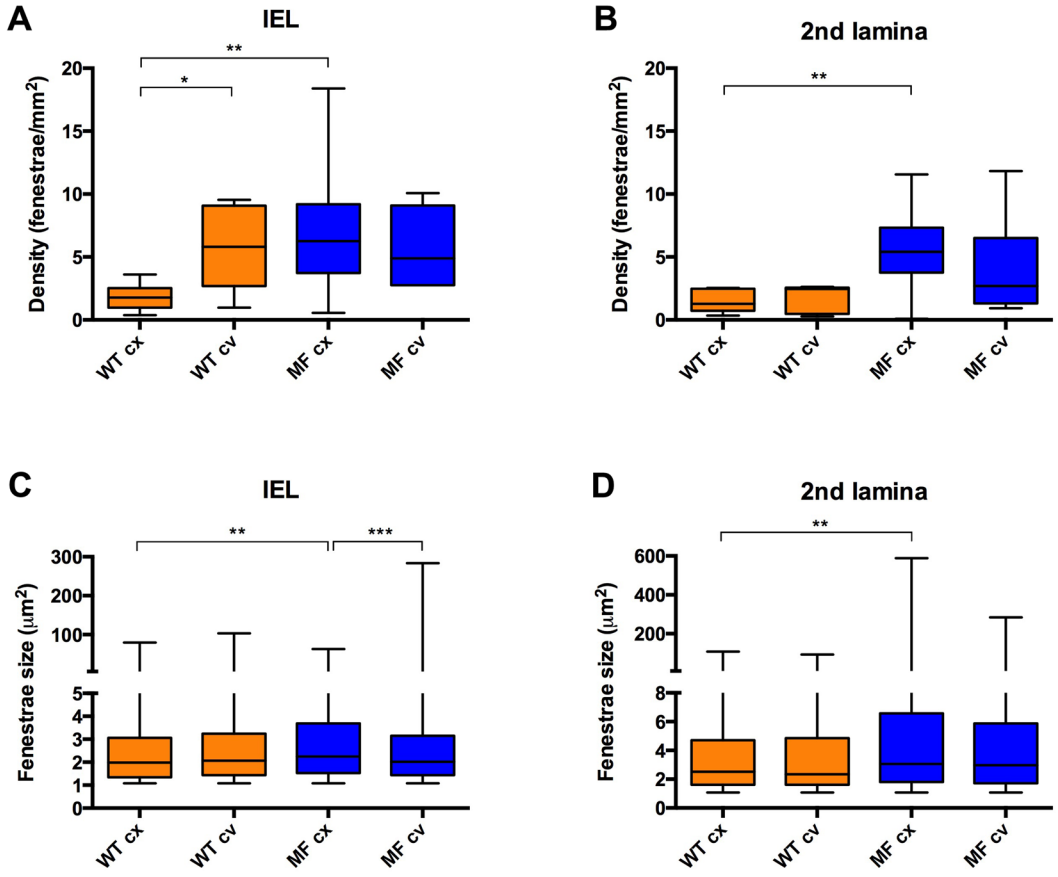

Figure 7. Quantitative analysis of fenestrae in IEL and 2nd laminae in the circumferential plane of the ascending aorta. The density of fenestrae at the IEL (**A**) and 2nd lamina (**B**), and their respective individual fenestrae size (**C** and **D**) measured at different circumferential plane locations (convexity/cx and concavity/cv) of WT (orange) and Marfan (MF, blue) ascending aortae. Statistical significance between groups is indicated by asterisks. Interquartile boxplots with minimum and maximum whiskers. Forty maximal projections were analysed and a total of 6,400 fenestrae were quantified.

intrinsically different primary structure of each lamina could explain the here reported dissimilar injury pattern occurring between the 2nd laminae and the IEL.

Regarding the other lamellar parameters assessed by our methodology, it was previously shown by SEM that medial elastic laminae of adult rat aorta were 2–3 μm thick and had an irregular profile[50]. Moreover, an average of 2.74 μm was reported in mouse[51]. Therefore, our lamella thickness values (2.7–3.0 μm) are in accordance with those measured in mouse[51] and rat aortae[50,52].

There are few data about lamellae undulation assessment either in health or disease. Wolinsky and Glagov[4] established the waviness index, which consisted in obtaining the ratio of the lamellar length to the straight line distance between two reference points. Other developed undulation assessment techniques quantified the folding[53] and fiber angular undulation[28] of lamellae. Globally, these three methods are all based on individual transversal sections, and hence they provide 2D data. Conversely, our waviness quantification approach takes into account area values as in earth topography studies, and therefore it is much more informative about the 3D structure of the tissue. With this method, we showed no differences in lamellar waviness between WT and Marfan aortic tissue.

In conclusion, here we describe the method that we have developed, apply it to wild-type and Marfan murine aortae, and quantify morphological differences in terms of lamellae fenestrae, thickness and waviness features. Our results take advantage of multiphoton microscopy to achieve en-face images of unstained aortic tissue, which in turn provide us with novel information on lamellae 3D histopathological damage. The application of this methodology to Marfan mice aneurysm-prone tissue suggested the density of fenestrae as a potential aortic microscale damage marker, whose alterations are mainly accumulated in the proximal and convex regions of the ascending aorta. Finally, our method opens the door to study in detail 3D vessel morphology and injuries in other conditions, diseases, and animal models. The future application of our imaging and processing method as a basis for the vascular endoscopy examination of MSF patients or related diseases might provide an early evaluation tool for aortic histological damage prior to the irreversible appearance of the aneurysm.

Methods

Experimental animals and sample preparation. Nine-month-old *Fbn1*$^{C1039/+}$ mice and age-matched wild-type littermates were used in this study (n = 4 for WT and n = 6 for Marfan mice). Animal care and experimental procedures were approved by the University of Barcelona's independent Committee for Animal Welfare, according to the University of Barcelona's guidelines and the European Parliament Directive. The mice were on a C57B/6 genetic background and maintained as a heterozygous breeding colony in our animal room facility. Animals were sacrificed by isoflurane inhalation and the aorta was surgically harvested from the aortic root until its suprarenal portion, and immediately rinsed in PBS and fixed in formol 10% overnight. Thereafter, aortae were cut longitudinally (see inset in Fig. 5C). The open aorta was placed on a glass slide covered with mowiol, and some small transverse cuts were performed to keep the tissue flat. Each aorta was mounted with the tunica intima facing the coverslide. For this study, only the ascending aorta was used for imaging. A detailed map image of the entire sample was obtained by mosaic stitching of 308 bright field images of 0.8 × 0.5 mm field of view (see Fig. 5C). Bright field images were acquired using a 10 × 0.5 NA objective (Nikon) and Qimaging fast camera, with 0.46 μm pixel size.

Multiphoton microscope setup and image acquisition. The microscope setup consisted of a custom-made non-linear optics setting, based on a fully motorized Ti eclipse Nikon microscope. Multiphoton excitation was obtained using a Coherent mira900 titanium sapphire laser. The laser produced pulses of ~150 fs with a repartition rate of 76 MHz, and the power used at the back aperture of the objective was 40 mW. To perform aorta imaging, the laser wavelength was set to 810 nm, producing at 405 nm a generation of second harmonic and efficient TPEF signals. The filters were the following: Semrock FF720-SDi01-25 × 36 for TPEF/SHG generation; Semrock FF01750/SP-25 for TPEF detection; Semrock FF735-Di01-25 × 36 for SHG detection; and Semrock FF01-406/15-25 for forward SHG detection. Samples were visualized using a 40 × 1.3 NA oil objective (Nikon) and the collection of the forward second harmonic signal was performed by means of a 1.4 NA oil immersion condenser. Image stacks of both signals (TPEF/elastin and SHG/collagen) were taken simultaneously by custom-made acquisition software coded in Labview. Image stacks were carried out at z-step 0.5 μm from the intima until 60 μm deep into the tissue. Acquisitions were taken at a pixel size of 0.29 μm, field of view 512 × 512 px and averaged 5 times. Four image stacks at different anatomical locations were acquired for each aorta sample and the exact location was assessed using the bright field image map of each sample.

Image processing. Quantitative data was obtained by an image processing protocol (as indicated in Fig. 2) scripted in ImageJ macro language, available on demand. The elastin signal image stack was resliced to its YZ perspective, and automatically binary thresholded using the Niblack algorithm at radius 10 to generate an elastin binary mask. The resulting mask stack was separated into groups of 15 consecutive images (34 groups), and each group was manually processed to select the chosen elastic lamella and isolate it from the other lamellae. This segmented lamella mask stack was re-resliced to recover the XY perspective, and small errors of segmentation and thresholding were corrected by applying a binary erode routine of 50 iterations at range 5. Manual rectification of segmentation inaccuracies was executed when needed. The corrected lamella mask was applied to the original elastin image stack to obtain the isolated segmented lamella, and its maximal projection was created. Illumination intensity variations were adjusted. Sauvola local threshold at radius 5 was applied to the adjusted maximal projection image to create a fenestrae binary mask. Manual check and correction were performed to obtain a verified fenestrae dataset. From the fenestrae binary mask, individual area (μm^2) and density (fenestrae number/mm^2) of fenestrae greater than 1 μm^2 were measured for each lamella using the "analyse particles" algorithm. The number of elastic lamellae ruptures and their area were excluded from the analysis. The image processing protocol yielded maximal projections of 16 wild-type IEL, 16 wild-type 2nd lamellae, 24 Marfan IEL and 24 Marfan 2nd lamellae. A total of 6,400 fenestrae at all maximal projections were quantified.

BoneJ plugin in ImageJ was used to automatically quantify lamella thickness from the segmented lamella stacks. For an accurate measurement, image stack voxel size was rescaled by 0.6 at the X and Y axis, so that voxels had isotropic dimensions (0.5 × 0.5 × 0.5 μm). Then the BoneJ specific measurement of thickness was applied onto each segmented lamella stack mask. Data was the mean thickness ±SD of the whole stack, and the programme provided a coloured representation of local thicknesses in each stack slice.

To quantify lamella waviness in ImageJ, the YZ segmented lamella mask stack was manually checked for any error in the continuity of the lamella. Next, 9 automated series of binary erode and dilate were applied to the lamella mask in order to smooth the mask surface without losing its path. The YZ mask stack was then converted into its skeleton (by the "Skeletonize" ImageJ algorithm), depicted as a black background and white single-pixeled line tracing the core path of the lamella and branches, in each one of the stack slices. The next step was to process the skeleton stack to erase all undesired branching. We developed a complex automated algorithm run on MATLAB (The MathWorks Inc., Natick, MA) that tracked each one of the white pixels in the skeleton and classified them into skeleton segments belonging to the lamellar core path or to a branch path. Once the classification had been done in each stack slice, the algorithm joined only the core path skeleton segments to finally generate the clean lamella skeleton stack. However, due to simplification of the 3D lamella shape into a split 2D skeleton, the lamellar smooth continuity was somehow spoiled. Therefore, in ImageJ, 9 series of erode and dilate were used automatically, first in the XY perspective and then in the resulting YZ view. Finally, a complete clean accurate skeleton stack was obtained from each segmented lamella stack. Out of these, we applied another developed MATLAB algorithm to generate height data. The algorithm tracked each white pixel in the YZ skeleton to get its height value in the Z axis, and relativized each value to the minimum height value of the whole skeleton. To eliminate noise or tiny details affecting the wave pattern, the XY image (made of the relativized height values) was rescaled by 0.15. Likewise, a possible general inclination of the lamella was also corrected from the relativized

rescaled height image by subtracting its own 20px Gaussian blurred image. At the end, these final height values were displayed as a height map where yellow denotes low heights and dark blue represents high ones.

Conventional histology. Formol-fixed mice aortae were dehydrated and embedded in paraffin. Five µm transverse sections were stained with Verhoeff-Van Gieson staining for visualization of elastic fibres. The length of elastic laminae breaks was measured manually from 24 images, using ImageJ. The mean break length and standard deviation were calculated.

En-face lamellar rupture length corresponded to the rupture distance crossed by a vertical or horizontal line. To standardize, a 10×10 µm grid was superimposed on all the TPEF maximal projection images that showed lamellar ruptures (8 out of the 48 total Marfan images). Each rupture yielded multiple length values. The mean length of ruptures was calculated by averaging the multiple lengths obtained from all the ruptured images. The standard deviation was also calculated in order to show data dispersion. Ruptured images were relatively infrequent, distributed among half of the Marfan aortic samples, and their anatomical location was aleatory.

Statistical method. Data were analysed using GraphPad Prism 6, and plotted as median and interquartile boxplots with minimum and maximum whiskers. As the datasets presented diverse distribution shapes, statistical analysis was carried out using the Kolmogorov-Smirnov nonparametric test. The value of $P \leq 0.05$ was considered statistically significant. The degree of significance was assigned as follows: *for $P \leq 0.05$, **for $P \leq 0.01$, ***for $P \leq 0.001$, and ****for $P \leq 0.0001$.

Data Availability. The datasets and protocols generated during the current study are available from the corresponding author upon request.

References

1. Wagenseil, J. E. & Mecham, R. P. Vascular extracellular matrix and arterial mechanics. *Physiol Rev.* **89**, 957–89, doi:10.1152/physrev.00041.2008 (2009).
2. O'Connell, M. K. *et al.* The three-dimensional micro- and nanostructure of the aortic medial lamellar unit measured using 3D confocal and electron microscopy imaging. *Matrix Biol.* **27**, 171–81, doi:10.1016/j.matbio.2007.10.008 (2008).
3. Dingemans, K. P., Teeling, P., Lagendijk, J. H. & Becker, A. E. Extracellular matrix of the human aortic media: an ultrastructural histochemical and immunohistochemical study of the adult aortic media. *Anat Rec.* **258**, 1–14, doi:10.1002/(SICI)1097-0185(20000101)258:1<1::AID-AR1>3.0.CO;2-7 (2000).
4. Wolinsky, H. & Glagov, S. Structural Basis for the Static Mechanical Properties of the Aortic Media. *Circ Res.* **14**, 400–13, doi:10.1161/01.RES.14.5.400 (1964).
5. Wolinsky, H. & Glagov, S. A Lamellar Unit of Aortic Medial Structure and Function in Mammals. *Circ Res.* **20**, 99–111, doi:10.1161/01.RES.20.1.99 (1967).
6. Mariko, B. *et al.* Fibrillin-1 genetic deficiency leads to pathological ageing of arteries in mice. *J Pathol.* **224**, 33–44, doi:10.1002/path.2840 (2011).
7. Ushiki, T. Collagen Fibers, Reticular Fibers and Elastic Fibers. A Comprehensive Understanding from a Morphological Viewpoint. *Arch Histol Cytol* **65**, 109–26, doi:10.1679/aohc.65.109 (2002).
8. Campbell, G. J. & Roach, M. R. Fenestrations in the internal elastic lamina at bifurcations of human cerebral arteries. *Stroke* **12**, 489–96, doi:10.1161/01.STR.12.4.489 (1981).
9. Roach, M. R. The pattern of elastin in the aorta and large arteries of mammals. *Ciba Found Symp* **100**, 37–55, doi:10.1002/9780470720813.ch4 (1983).
10. Sandow, S. L., Gzik, D. J. & Lee, R. M. K. W. Arterial internal elastic lamina holes: Relationship to function? *J Anat* **214**, 258–66, doi:10.1111/j.1469-7580.2008.01020.x (2009).
11. Wong, L. C. Y. & Langille, B. L. Developmental remodeling of the internal elastic lamina of rabbit arteries: effect of blood flow. *Circ Res.* **78**, 799–805, doi:10.1161/01.RES.78.5.799 (1996).
12. Tsamis, A., Krawiec, J. T. & Vorp, D. A. Elastin and collagen fibre microstructure of the human aorta in ageing and disease: a review. *J R Soc Interface* **10**, 1–22, doi:10.1098/rsif.2012.1004 (2013).
13. Dietz, H. C., Loeys, B., Carta, L. & Ramirez, F. Recent progress towards a molecular understanding of Marfan syndrome. *Am J Med Genet Part C Semin Med Genet* **139C**, 4–9, doi:10.1002/ajmg.c.30068 (2005).
14. Dietz, H. C. *et al.* Marfan Syndrome caused by a recurrent de novo missense mutation in the fibrillin gene. *Nature* **352**, 337–339, doi:10.1038/352337a0 (1991).
15. Wu, D. *et al.* Molecular mechanisms of thoracic aortic dissection. *J Surg Res* **184**, 907–24, doi:10.1016/j.jss.2013.06.007 (2013).
16. Abraham, P. A., Perejda, A. J., Carnes, W. H. & Uitto, J. Marfan syndrome. Demonstration of abnormal elastin in aorta. *J Clin Invest* **70**, 1245–52, doi:10.1172/JCI110723 (1982).
17. Nakashima, Y. Pathogenesis of aortic dissection: Elastic fiber abnormalities and aortic medial weakness. *Ann Vasc Dis* **3**, 28–36, doi:10.3400/avd.ctiia09001 (2010).
18. Judge, D. P. *et al.* Evidence for a critical contribution of haploinsufficiency in the complex pathogenesis of Marfan syndrome. *J Clin Invest* **114**, 172–81, doi:10.1172/JCI20641 (2004).
19. Habashi, J. P. *et al.* Losartan, an AT1 antagonist, prevents aortic aneurysm in a mouse model of Marfan Syndrome. *Science* **312**, 117–21, doi:10.1126/science.1124287 (2006).
20. Schlatmann, T. J. M. & Becker, A. E. Histologic changes in the normal aging aorta: implications for dissecting aortic aneurysm. *Am J Cardiol* **39**, 13–20, doi:10.1016/S0002-9149(77)80004-0 (1977).
21. Gomez, D. *et al.* Syndromic and non-syndromic aneurysms of the human ascending aorta share activation of the Smad2 pathway. *J Pathol.* **218**, 131–42, doi:10.1002/path.2516 (2009).
22. Romaniello, F. *et al.* Aortopathy in Marfan syndrome: an update. *Cardiovasc Pathol.* **23**, 261–6, doi:10.1016/j.carpath.2014.04.007 (2014).
23. Hope, M. D. & Hope, T. A. Functional and molecular imaging techniques in aortic aneurysm disease. *Curr Opin Cardiol* **28**, 609–18, doi:10.1097/HCO.0b013e3283644beb (2013).
24. Campagnola, P. J. & Dong, C.-Y. Second harmonic generation microscopy: principles and applications to disease diagnosis. *Laser Photon Rev* **5**, 13–26, doi:10.1002/lpor.200910024 (2011).
25. Boulesteix, T. *et al.* Micrometer scale *ex vivo* multiphoton imaging of unstained arterial wall structure. *Cytom Part* **69A**, 20–26, doi:10.1002/cyto.a.20196 (2005).
26. Psilodimitrakopoulos, S. *et al.* Quantitative discrimination between endogenous SHG sources in mammalian tissue, based on their polarization response. *Opt. Express.* **17**, 10168–10176, doi:10.1364/OE.17.010168 (2009).

27. Yu, W., Braz, J. C., Dutton, A. M., Prusakov, P. & Rekhter, M. *In vivo* imaging of atherosclerotic plaques in apolipoprotein E deficient mice using nonlinear microscopy. *J Biomed Opt* **12**, 54008, doi:10.1117/1.2800337 (2007).
28. Tsamis, A. *et al.* Fiber micro-architecture in the longitudinal-radial and circumferential-radial planes of ascending thoracic aortic aneurysm media. *J Biomech.* **46**, 2787–94, doi:10.1016/j.jbiomech.2013.09.003 (2013).
29. Megens, R. T. A. *et al.* Two-photon microscopy of vital murine elastic and muscular arteries. *J Vasc Res* **44**, 87–98, doi:10.1159/000098259 (2007).
30. Zadrozny, L. M. *et al.* Study of the development of the mouse thoracic aorta three-dimensional macromolecular structure using two-photon microscopy. *J Histochem Cytochem* **63**, 8–21, doi:10.1369/0022155414559590 (2015).
31. Arribas, S. M. *et al.* Heightened aberrant deposition of hard-wearing elastin in conduit arteries of prehypertensive SHR is associated with increased stiffness and inward remodeling. *Am J Physiol Heart Circ Physiol* **295**, H2299–307, doi:10.1152/ajpheart.00155.2008 (2008).
32. Kirby, B. S. *et al.* Robust internal elastic lamina fenestration in skeletal muscle arteries. *PLoS One.* **8**, 1–11, doi:10.1371/journal.pone.0054849 (2013).
33. Haskett, D. *et al.* Altered tissue behavior of a non-aneurysmal descending thoracic aorta in the mouse model of Marfan syndrome. *Cell Tissue Res* **347**, 267–77, doi:10.1007/s00441-011-1270-y (2012).
34. Ju, X. *et al.* IL-6 regulates extracellular matrix remodeling associated with aortic dilation in a fibrillin-1 hypomorphic mgR/mgR mouse model of severe marfan syndrome. *J Am Heart Assoc* **3**, e000476–e000476, doi:10.1161/JAHA.113.000476 (2014).
35. Santos, S. I. C. O. *et al.* Collateral damage assessment of Femtosecond laser axotomy in Caenorhabditis elegans D-type motoneurons. *PLoS ONE.* **8**, e58600, doi:10.1371/journal.pone.0058600 (2013).
36. Schneider, C. A., Rasband, W. S. & Eliceiri, K. W. NIH Image to ImageJ: 25 years of image analysis. *Nature methods.* **9**(7), 671–675, doi:10.1038/nmeth.2089 (2012).
37. Doube, M. *et al.* BoneJ: free and extensible bone image analysis in Image. *J. Bone* **47**, 1076–9, doi:10.1016/j.bone.2010.08.023 (2010).
38. Cui, J. Z. *et al.* Quantification of aortic and cutaneous elastin and collagen morphology in Marfan syndrome by multiphoton microscopy. *J Struct Biol* **187**, 242–253, doi:10.1016/j.jsb.2014.07.003 (2014).
39. Trachet, B. *et al.* Ascending Aortic Aneurysm in Angiotensin II-Infused Mice: Formation, Progression, and the Role of Focal Dissections. *Arterioscler Thromb Vasc Biol* **36**, 673–681, doi:10.1161/ATVBAHA.116.307211 (2016).
40. Bäck, M., Gasser, T. C., Michel, J.-B. & Caligiuri, G. Biomechanical factors in the biology of aortic wall and aortic valve diseases. *Cardiovasc. Res.* **99**, 232–241, doi:10.1093/cvr/cvt040 (2013).
41. Atkins, S. K., Cao, K., Rajamannan, N. M. & Sucosky, P. Bicuspid aortic valve hemodynamics induces abnormal medial remodeling in the convexity of porcine ascending aortas. *Biomech Model Mechanobiol* **13**, 1209–25, doi:10.1007/s10237-014-0567-7 (2014).
42. Cotrufo, M. *et al.* Different patterns of extracellular matrix protein expression in the convexity and the concavity of the dilated aorta with bicuspid aortic valve: Preliminary results. *J Thorac Cardiovasc Surg* **130**, 504–11, doi:10.1016/j.jtcvs.2005.01.016 (2005).
43. Dormand, H. & Mohiaddin, R. H. Cardiovascular magnetic resonance in Marfan syndrome. *J Cardiovasc Magn Reson* **15**, 33–41, doi:10.1186/1532-429X-15-33 (2013).
44. Bogren, H. G., Mohiaddin, R. H., Yang, G. Z., Kilner, P. J. & Firmin, D. N. Magnetic resonance velocity vector mapping of blood flow in thoracic aortic aneurysms and grafts. *J Thorac Cardiovasc Surg* **110**, 704–714, doi:10.1016/S0022-5223(95)70102-8 (1995).
45. Hope, M. D. *et al.* Bicuspid aortic valve: four-dimensional MR evaluation of ascending aortic systolic flow patterns. *Radiology* **255**, 53–61, doi:10.1148/radiol.09091437 (2010).
46. Hemmasizadeh, A., Autieri, M. & Darvish, K. Multilayer material properties of aorta determined from nanoindentation tests. *J Mech Behav Biomed Mater* **15**, 199–207, doi:10.1016/j.jmbbm.2012.06.008 (2012).
47. Hemmasizadeh, A. *et al.* Correlations between transmural mechanical and morphological properties in porcine thoracic descending aorta. *J Mech Behav Biomed Mater* **47**, 12–20, doi:10.1016/j.jmbbm.2015.03.004 (2015).
48. Timmins, L. H., Wu, Q., Yeh, A. T., Moore, J. E. & Greenwald, S. E. Structural inhomogeneity and fiber orientation in the inner arterial media. *Am J Hear Circ Physiol* **298**, 1537–45, doi:10.1152/ajpheart.00891.2009 (2010).
49. Perejda, A. J., Abraham, P. A., Carnes, W. H., Coulson, W. F. & Uitto, J. Marfan's syndrome: structural, biochemical, and mechanical studies of the aortic media. *J Lab Clin Med* **106**, 376–383 (1985).
50. Ushiki, T. & Murakumo, M. Scanning Electron Microscopic Studies of Tissue Elastin Components Exposed by a KOH-Collagenase or Simple KOH Digestion Method. *Arch. Histol. Cytol.* **54**, 427–436, doi:10.1679/aohc.54.427 (1991).
51. Clark, T. E., Lillie, M. A., Vogl, A. W., Gosline, J. M. & Shadwick, R. E. Mechanical contribution of lamellar and interlamellar elastin along the mouse aorta. *J. Biomech.* **48**, 3599–3605, doi:10.1016/j.jbiomech.2015.08.004 (2015).
52. Briones, A. M. *et al.* Role of elastin in spontaneously hypertensive rat small mesenteric artery remodelling. *J. Physiol* **552**, 185–195, doi:10.1113/jphysiol.2003.046904 (2003).
53. Blomgren, B. & Göktürk, C. A novel method for quantification of the folding of elastic laminae in elastic arteries. *Micron* **39**, 623–630, doi:10.1016/j.micron.2007.03.010 (2008).

Acknowledgements

The authors would like to thank Yolanda Mendizábal and Laura Barberà for technical support. Júlia López-Guimet is supported by a Spanish Government FPI predoctoral fellowship (BES-2013-065962). This study was supported by grants to GE (SAF2015-64136-R and 2014SGR-334). Authors from ICFO acknowledge financial support from Laserlab-Europe (EU-H2020 654148), and the Spanish MINECO (Severo Ochoa grant SEV-2015-0522). This research has been partially supported by Fundació Cellex Barcelona and has been partially conducted at ICFO's Super Resolution Light Microscopy and Nanoscopy Facility and CERCA programme/Generalitat de Catalunya.

Author Contributions

J.L.-G. and J.A. conducted the experiments; J.L.-G., J.A., P.L.-A. and G.E. analysed the results; J.A. and G.E. conceived the experiment(s), J.L.-G. and G.E. wrote the manuscript. All authors reviewed the manuscript.

Additional Information

Supplementary information accompanies this paper at doi:10.1038/s41598-017-01620-8

Competing Interests: The authors declare that they have no competing interests.

Publisher's note: Springer Nature remains neutral with regard to jurisdictional claims in published maps and institutional affiliations.